Thomas Willum Hansen
Jakob Birkedal Wagner *Editors*

Controlled Atmosphere Transmission Electron Microscopy

Principles and Practice

Springer

Controlled Atmosphere Transmission Electron Microscopy

Thomas Willum Hansen • Jakob Birkedal Wagner
Editors

Controlled Atmosphere Transmission Electron Microscopy

Principles and Practice

Springer

Editors
Thomas Willum Hansen
Center for Electron Nanoscopy
Technical University of Denmark
Kgs. Lyngby, Denmark

Jakob Birkedal Wagner
Center for Electron Nanoscopy
Technical University of Denmark
Kgs. Lyngby, Denmark

ISBN 978-3-319-22987-4 ISBN 978-3-319-22988-1 (eBook)
DOI 10.1007/978-3-319-22988-1

Library of Congress Control Number: 2015951843

Springer Cham Heidelberg New York Dordrecht London

Printed on acid-free paper

Springer International Publishing AG Switzerland is part of Springer Science+Business Media (www.springer.com)

Preface

Electron microscopy has long been the de facto standard for materials scientists to obtain structural information that now approaches the atomic scale. Scanning electron microscopy and transmission electron microscopy, along with the many peripherals now available, provide information about three-dimensional structure, particle size and morphology, layer thickness, as well as elemental, chemical, and magnetic information, to name just a few characteristics. Traditionally, electron microscopy has been performed in high vacuum or even ultrahigh vacuum, in order to prevent sample contamination, preserve the performance of the electron source, and maintain coherence of the electron wave. However, for several applications, observing samples under vacuum conditions is far from a realistic scenario when one considers the actual working environment of the material under study.

To remedy this situation, the controlled atmosphere microscope was conceived. Using various adaptations either to the sample holder or to the microscope, a certain volume of gas can be maintained around the sample without compromising the microscope itself. Such adaptations were suggested previously by Ernst Ruska, the inventor of the transmission electron microscope in the 1940s. Since then, several experimentalists have modified electron microscopes to allow for gas entry.

Over the last three decades, the technique has become much more mainstream and instruments are now commercially available. Inspired by the developments of Boyes and Gai, the concept of differentially pumped electron microscopes now allows samples to be exposed to a gaseous atmosphere of the order of 1000 Pa. The concept has now made its way to the newer microscopy platforms and high-end microscopes.

There are many scientific challenges that can be addressed by electron microscopy. Among these are the structure and stability of two-dimensional materials such as graphene, which has been suggested as a future candidate to replace silicon for semiconductor devices when properly structured, the active state of catalytically active materials, or the structure of semiconducting devices with electrical bias applied in a gaseous environment. In order to move forward in the understanding of

the working state of these materials, a multitude of complementary characterization techniques should be applied.

This text is aimed at graduate students, but the experienced microscopist should also find it to be a valuable reference book. The book describes the development and construction of the environmental transmission electron microscope, or ETEM for short, as well as the peripherals such as cameras and detectors that allow for the thorough and exhaustive characterization of a sample. It is supplemented by several example chapters highlighting the use of the technique for different scientific cases.

We are grateful to a large number of people for fruitful discussions and providing material for the book.

Kgs. Lyngby, Denmark

Thomas Willum Hansen
Jakob Birkedal Wagner

Contents

Part I
Technique

Chapter 1
A Brief History of Controlled Atmosphere Transmission Electron Microscopy

Ai Leen Koh, Sang Chul Lee, and Robert Sinclair

Abstract In this chapter, the development of controlled atmosphere conditions to study gas-solid reactions inside the transmission electron microscope (TEM) will be presented. The two successful approaches to achieve this, namely the use of electron transparent windows and the incorporation of small-bore apertures inside the TEM combined with differential pumping, will be discussed. Finally, we will also describe the state-of-the-art instrumentation available today to study the behavior of nanomaterials in reactive gas environments, which have been largely brought about by the development of aberration correctors, monochromators, specialized TEM holders, as well as faster and more sensitive spectrometers. Examples that highlight the diverse applications in this field will be provided.

1.1 Introduction

It was clear to the original pioneers in the 1930s or so that an electron microscope requires a background high vacuum. Indeed, once the transmission electron microscope (TEM) was being applied to examine the microstructure of metals and alloys, specimen contamination, generally from breakdown of residual hydrocarbons in the TEM atmosphere, became a real issue. This was further exacerbated by the introduction of small probe work in the 1970s for microanalysis of chemical composition. The historical trend therefore required increasingly good vacuum conditions especially in the specimen and electron gun chambers.

This evolution clearly contrasts with the desire to study materials in their natural environment, such as atmospheric gaseous conditions or even in liquids. Accordingly, methods needed to be devised whereby the overall microscope vacuum environment could be maintained while viewing the sample in a controlled

A.L. Koh (✉)
Stanford Nano Shared Facilities, Stanford University, 476 Lomita Mall, McCullough Building Rm 236, Stanford, CA 94305, USA
e-mail: alkoh@stanford.edu

S.C. Lee • R. Sinclair
Department of Materials Science and Engineering, Stanford University, Stanford, CA 94305, USA
e-mail: sclee99@stanford.edu; bobsinc@stanford.edu

T.W. Hansen, J.B. Wagner (eds.), *Controlled Atmosphere Transmission Electron Microscopy*, DOI 10.1007/978-3-319-22988-1_1

environment. In this chapter, we will outline the historical progression of these developments alongside the advances in TEM itself.

The main purpose of such experiments is to derive as much information as possible about material interactions with the environment, whether under ambient conditions such as in corrosion or in vivo biological processes, or extreme conditions as might be required for catalytic reactions or non-equilibrium liquid phase processes. This clearly represents a significant broadening to the scope of in situ TEM observations whereby one examines the changes to a material system under a controlled external stimulus such as heating, cooling, electrical bias, and mechanical stress. The behavior of the specimen under high-vacuum conditions already has its own merit as many manufacturing processes are carried out in vacuum, especially for the semiconductor industry. However, the added value of the controlled environment has extensive implications. Indeed, a recent analysis of in situ TEM publications (Sinclair 2013) showed a noticeable increase in recent years attributable mainly to environmental TEM (ETEM) studies, as illustrated in Fig. 1.1, a trend which continues as noted later.

Historically, the interest for environmental chambers inside the electron microscope came about as a means to allow wet specimens to be examined in vivo (Marton 1934) while at the same time, minimizing any possible damage and artifacts associated with conventional biological specimen preparation. The presence of an environmental chamber was also thought to be advantageous in reducing specimen contamination produced by the electron beam and residual hydrocarbon gases present in the microscope. In the 1970s, the reason to pursue this expanded to include the study of chemical reactions at elevated temperatures, as described later.

In 1935, Marton (1935) suggested two methods in which gas pressure and composition could be controlled inside the electron microscope. The first involved modifying the specimen holder by placing a pair of electron transparent "windows" above and below the specimen to seal it, and the gas atmosphere, from the column. The second involved modifying the objective pole pieces of the electron microscope, by placing a pair of small apertures above and below the specimen (see also later papers by Ruska 1942, and Abrams and McBain in 1944). Gas leakage into the column is then limited to that which escapes via the apertures. These two approaches have evolved separately, and successfully, alongside the TEM and are referred to as the closed cell ("window") and "apertures," respectively, in this chapter.

In the 1970s, the term "controlled atmosphere electron microscopy" (CAEM) was coined by several groups including Feates et al. (1970) and Baker (Baker and Harris 1972; Baker 1979). Despite the sub-nanometer imaging resolution of the TEM (about 0.25 nm or so in the 1970s), its value was found to be limited because materials can only be viewed in a vacuum environment, and the tactic had been to examine a specimen before and after reaction. Of significant interest is the actual appearance of the specimen during reaction. Thus, CAEM is used to describe the technique in TEM in which reactions between gases and solids are studied at very high magnifications, while they are taking place, under realistic conditions of temperature, pressure, and reaction time (Baker 1979). The key design feature of

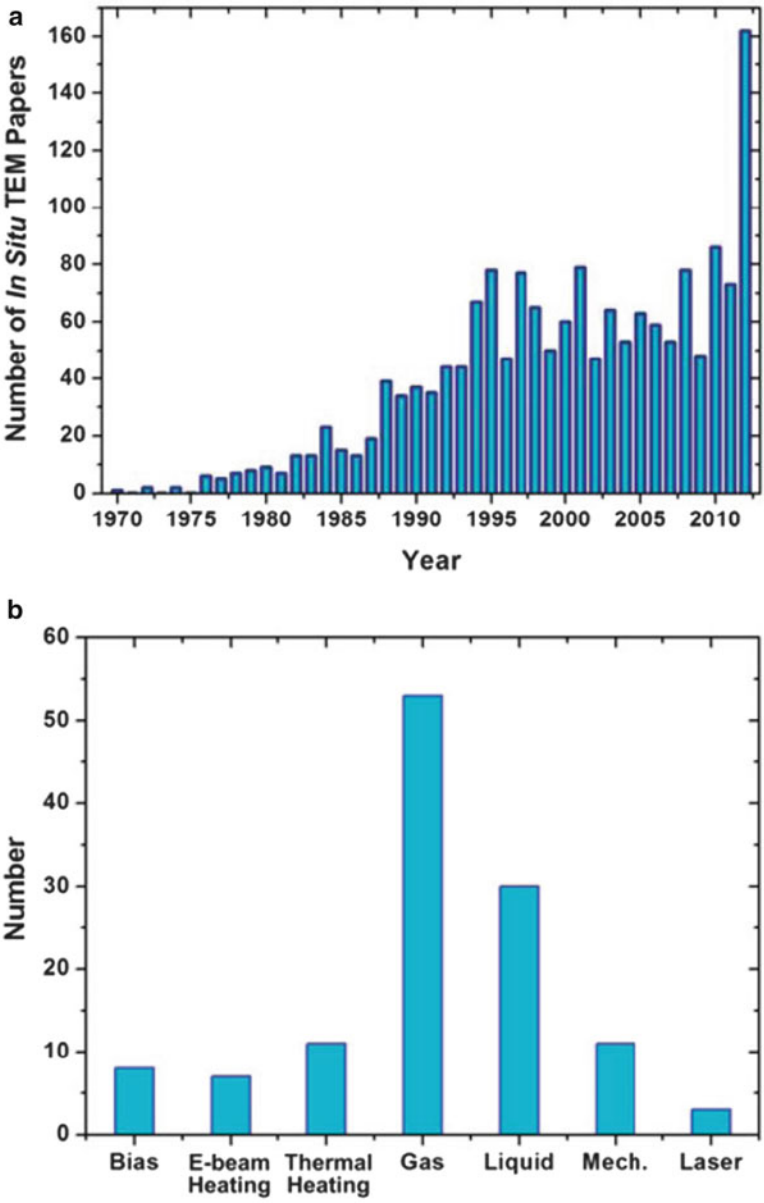

Fig. 1.1 (**a**) Number of publications identified using the keywords "in situ", "transmission electron microscopy" and "TEM", showing a steady increase over the last 20 years and a marked increase in 2012; (**b**) Breakdown by various subcategories of in situ papers presented at the 2012 Microscopy and Microanalysis Conference (USA) and the 2012 European Microscopy Conference (UK). These subcategories are in situ electrical biasing, electron beam heating, thermal heating, gaseous environment, liquid environment, mechanical loading, and laser stimulation. Reprinted with permission from Sinclair (2013)

CAEM is the ability to operate at high pressure in the specimen region (3×10^4 Pa, or 225 Torr), while maintaining very low pressure (10^{-3} Pa, or 10^{-5} Torr) in the rest of the microscope.

Since the 1970s, there have been a number of comprehensive reviews highlighting the developments in the field of CAEM, or environmental transmission electron microscopy (ETEM) as it is more commonly known today, as well as its diverse applications. Readers can refer to the articles and book chapters by Flower (1973), Allinson (1975), Butler and Hale (1981a), Sharma (2001, 2005), Sharma and Crozier (2005), Gai et al. (2007, 2008), Jinschek and Helveg (2012), publications from the Technical University of Denmark (Hansen and Wagner 2012; Wagner et al. 2012), Jinschek (2014), the Takeda group from Osaka University (Takeda et al. 2015) as well as their references therein. We have elected to present the historical developments in this field in a chronological sequence, with an emphasis toward gas-solid reactions in the TEM. For comprehensive reviews and applications for liquid-solid reactions and interactions, articles and book chapters by Parsons (1974), Parsons et al. (1974), Butler and Hale (1981b) and de Jonge and Ross (2011), and their references therein, are good starting points. A later chapter of this book also discusses liquid phase electron microscopy techniques and applications. We conclude with a number of examples spanning from the 1970s that highlight the diverse applications in this field, and where we think the future in this area lies.

1.1.1 Window Approach

The first approach to attain environmental conditions inside the transmission electron microscope is by use of a specialized specimen holder combined with a windowed cell. A pair of electron transparent "windows" is placed above and below the specimen to seal it, and the gas atmosphere, from the column. In this method, containment is total—the windows completely seal off the specimen and its surrounding gas environment so that the high vacuum of the microscope remains unchanged. The windowed design has the advantage of working with higher gas pressures (depending on the strength and thickness of the windows). Wet samples can also be imaged with this setup. The reader can refer to a later chapter in this book which describes the developments in the field of liquid cell electron microscopy.

There are several advantages using a specialized holder combined with windowed cells. First of all, the holder can be used in different TEMs without modifications to the microscope column. To date, this approach is the only one that is capable of achieving ambient pressure conditions. However, the specimen geometry and the field of view are usually significantly smaller than in a conventional TEM, and the sample can only be moved or tilted together with the windows since it is sandwiched between them. Additional scattering information from the (usually amorphous) window material is superimposed on the image and

diffraction pattern of the sample, leading to compromises in image resolution. The interaction also hinders the acquisition of energy-dispersive X-ray spectroscopy (EDS) signals. The thin films used as windows should have low gas or vapor permeability, and must be able to withstand the pressure difference between the microscope vacuum and the design pressure of the holder device when mounted. There is the possibility of windows rupturing inside the microscope during an experiment, leading to the degradation of the electron column and source vacuum.

The earliest documentation of a closed cell for electron microscopy was by Marton in 1935, who attempted to use two 0.5-μm aluminum foils as windows. In 1944, Abrams and McBain constructed a closed chamber out of two perforated platinum disks covered with plastic film windows less than 100 nm thick, and sealed to vacuum-tightness using wax. It could withstand an atmospheric pressure difference between the inside of the cell and the remainder of the electron microscope. Using this setup, the authors were able to observe the movement of liquid and bubbles inside the electron microscope. However, they found water of one micron thickness to be "practically opaque to electrons." The lack of fast, continuous recording capability also precluded the possibility of the observations of Brownian movement in colloidal particles. Moreover, the cell was completely sealed and hence capable of operating at only a single (fixed) pressure.

Variable-pressure controlled dynamic experiments were not possible until cells were designed such that a connection existed between the gas space around the specimen and the outside of the microscope. Heide (1962) constructed a specimen holder for a Siemens Elmiskop I electron microscope using two specimen grids with the flat surfaces facing each other. The separation of the two grids was controlled by pieces of thin metal foil. Both specimen grids were covered with a supporting film of low contrast, which could withstand the gas pressure over the central openings, and one of the grids served at the same time as a supporting film for the specimen. The gas inlet was sealed against the microscope column vacuum when the holder was inserted inside the microscope, and gas was injected through a tube placed in the opening of the column along the specimen holder. Air or gas pressures could be varied up to atmospheric pressure with this design.

There were a number of limitations to these earlier basic designs of the closed cells, as highlighted in the review article by Butler and Hale (1981a):

1. The single gas line does not enable experiments to be performed with gas flowing continuously over the specimen.
2. The relatively poor metal-to-metal seal between the apertures and the cartridge results in some leakage into the column.
3. The specimen cannot be heated unless it is supported independently of the windows.

Improvements in these three areas were realized in later designs. Escaig and Sella (1969) incorporated a heater and twin gas lines in their holder so that the temperature of the specimen could be varied while gas continuously circulated over it. Earlier window cells were made out of plastic which were generally not suitable

for high temperature work because of damage during heating and were thus employed mainly in the biological field to provide a hydrated environment for in vivo studies. Escaig and Sella (1966, 1968, 1969) made improvements to the windowed cells that consist of triple layers of carbon, nitrocellulose, and silica (facing the specimen), maintaining a gap of approximately 1 mm between window and specimen, which was successfully employed for in situ oxidation of copper, tungsten, and titanium (Escaig and Sella 1972).

Another limitation of the windowed cells is that they tend to bulge under pressure, resulting in a longer electron beam path length at higher pressure. In order to reduce the beam path length and stabilize the films, Fukami and Adachi (1965) developed plastic micro grids consisting of holes of 0.1–10 μm in diameter which were used as the supporting frame for a continuous carbon film. The plastic micro grids were also used as substrates in the production of micro metal grids with thicknesses >30 nm which were stronger and more resistant to heat than their plastic counterparts (Fukami et al. 1966, 1972).

In the late 1960s and 1970s, the development of high-voltage (1 MeV) electron microscopes (HVEM) led to enclosed gas reaction cells with thicker, stronger windows being developed. Dupouy (1968) designed a single gas-line room temperature device with windows constructed out of carbon/colloidion of 60 nm thickness. Twin gas-line top entry designs capable of a range of temperatures were also constructed by Fujita et al. (1976) and Doi et al. (1977). Fujita et al. (1976) built a holder for gas and liquid experiments on a 3MV-class electron microscope, which could be used in the temperature range of −100 to 1000 °C and up to a pressure close to two atmospheres. The window cell consisted of three films whose materials could be vapor-deposited aluminum, SiO_x and carbon films, depending on the purpose, and they were supported with metal (Ni) of 300 and 400 mesh in size. The specimen was set directly on the center Ni mesh, or on a vapor-deposited film coated on the Ni mesh. The specimen was directly heated by the application of a current to the Ni mesh. The increased penetration ability of the HVEM led to a significant improvement in contrast at these high operating voltages. Specimen damage was found to depend on the heat conductivity of the supporting film, and decreases when the supporting film has high heat conductivity. The use of crystalline window materials of higher strength also became a consideration for use with HVEM, and single crystal corundum which was ion-beam-thinned to ~180 nm was one possible material option (Allinson 1970). In window-limited holders, the strength and thickness of the window material determines the maximum gas pressure and, in principle, pressures as high as atmospheric pressure can be attained, although the thickness of window material needed to sustain such pressures may not be compatible with instrument performance.

Progress in the development of closed window cell systems was stalled until the 2000s, when holders based on micro-electro-mechanical systems (MEMS) technology for both gas (Creemer et al. 2008; de Jonge et al. 2010; Yokosawa et al. 2012; Yaguchi et al. 2011; Allard et al. 2012; Alsem et al. 2012) and liquid (Williamson et al. 2003; de Jonge et al. 2009; Ring and de Jonge 2010; Klein

et al. 2011) TEM applications emerged. This technique uses miniaturized, low mass heating devices and is integrated with a heater and thermal sensor which allows much more rapid thermal response than standard specimen furnace-based heating holders. The specimen drift is also stabilized at a more rapid rate, leading to better control of the reaction process and the imaging experiments. The windows are usually produced using micro-fabrication techniques and consist of a silicon frame with an electron transparent silicon nitride membrane which is tens of nanometers thick. A lot of effort was given to miniaturize the thickness of the gas volume in the windowed cell to confine the gas along the electron beam path into a layer that is as thin as possible (tens of micrometers). Consequently, these MEMS devices allow for correspondingly higher pressures without loss of resolution or damage to the electron source. Atomic resolution with holders like these have been attained, sometimes at local gas pressures of one atmosphere or more (Giorgio et al. 2006; Creemer et al. 2008; de Jonge et al. 2010; Yokosawa et al. 2012; Yaguchi et al. 2011; Allard et al. 2012; Alsem et al. 2012). Improvements are also made to the windowed cell support film. Kawasaki and coworkers (2009) demonstrated that carbon films with thickness <10 nm could withstand pressure differences greater than two atmospheres. A schematic design of the flow system for atmospheric pressure (scanning) TEM ((S)TEM) is illustrated in Fig. 1.2.

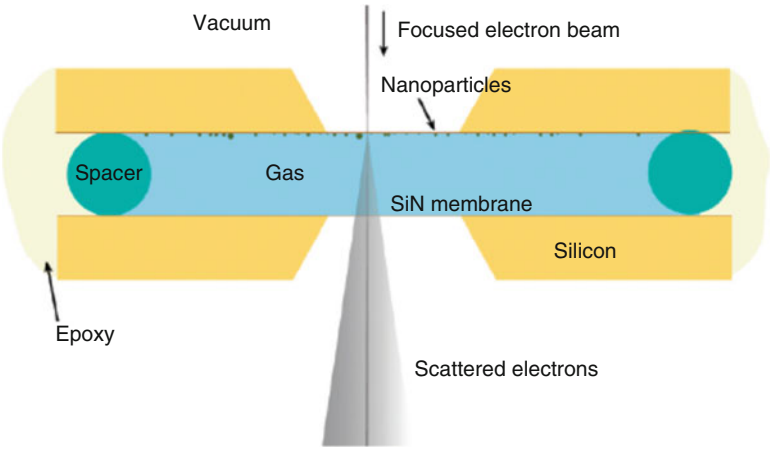

Fig. 1.2 Schematic of the flow system for atmospheric pressure (scanning) transmission electron microscopy ((S)TEM). A sample compartment filled with gas at atmospheric pressure is enclosed between two silicon microchips supporting electron-transparent SiN windows. The microchips are separated by a spacer and sealed with epoxy. Gas entry and exit are not shown in this drawing. The flow cell is placed in the vacuum of the electron microscope. Images are obtained by scanning a focused electron beam over nanoparticles attached to the *top* window and detecting elastically scattered transmitted electrons. The dimensions and angles are not to scale. Reprinted with permission from de Jonge et al. (2010)

1.1.1.1 Specimen Holders with Gas Injection Systems

An alternative specimen holder design which reduces the number of gas molecules inside the microscope column incorporates a gas injection system was developed by Kamino and coworkers in 2005 (Kamino et al. 2005). This holder is compatible for use with a 300 kV Hitachi high-resolution H-9500 TEM, which has a high-speed turbo molecular pump added to pump the specimen chamber, a 0.3 mm restricting aperture above the specimen chamber to restrict the gas leakage into the upper column, and a safety valve in the gun area to further maintain the safe high vacuum in the gun area. Specimens are supported on a fine tungsten wire which was employed as a heating element of the holder, and gas was injected onto specimens via a nozzle. The maximum pressure near specimens is ~10^{-2} Pa, while the pressure in the electron gun chamber was kept to ~3×10^{-4} Pa (2×10^{-6} Torr).[1] The holder requires no self-confined window cell and can heat the sample up to 1000 °C with the injection of gases like H_2, O_2, air, water vapor, etc. An evaporator could also be added to the design to allow for both synthesis of metal oxide support and deposition of catalyst nanoparticles in situ (Kamino et al. 2006). For pressures up to an atmosphere, a windowed environmental cell holder is necessary. Yaguchi et al. (2011) give details of a windowed environmental cell holder for Hitachi microscopes that builds on the Kamino et al. (2005) design, wherein the tungsten wire passes between two SiN windows of 15 nm thickness with a spacing of about 1 mm, and incorporates a micropressure gauge fabricated using MEMS technology, to measure the pressure inside the windowed cell accurately.

1.1.2 Aperture Approach

The second approach to controlled atmosphere transmission electron microscopy makes use of small apertures placed above and below the specimen, which restrict the flow of gas from the specimen chamber into the microscope column. The apertures must be large enough to permit the passage of incident, diffracted and scattered electron beams, and yet small enough to avoid too great a gas leak. Leakage into the column vacuum is controlled by the size of the apertures and supplemented by differential pumping. In order to maintain the pressure conditions at the specimen cell while retaining the very low pressure in the rest of the microscope, an equilibrium condition such that the effective pumping speed of the differential pumps exceeds the leak rate of the apertures should be achieved. The first pair of apertures is placed closest to the sample and most of the gas leaking through these apertures is pumped out of the system using a turbo molecular pump. The second pair of apertures is larger than the first pair (because they experience a

[1] We have, throughout this article, used pressures converted to SI units as well as those quoted in the original publications (in parentheses). The conversions are 1 Torr ≡ 1 mm Hg ≡ 1.33 mbar ≡ 133.3 Pa.

much smaller pressure drop) and is used to further restrict the leakage of gases into the microscope column.

The main advantage of the aperture type system is that the basic instrument resolution is preserved (i.e., not degraded by the presence of membranes in the windowed cell). Specimen holders that are used in a regular (high-vacuum) TEM are also compatible with this setup. However, the maximum gas pressure is limited to ~10^3 Pa (tens of Torr) at best. At higher gas pressures, the resolution deteriorates because of the rather thick gas layer (5–10 mm depending on pole-piece gap).

The first aperture environmental cell inside the TEM was reported and constructed by Ito and Hiziya in 1958 to enable direct and continuous observations of chemical reactions in a heated gas environment. The specimen chamber of a JEM electron microscope was modified and diaphragms were introduced to prevent diffusion of the gas from the chamber to the electron source. The gas pressure ranged from about 10^{-2} to 133 Pa (10^{-4} to 1 mm Hg), and the specimen could be heated up to 1000 °C using a high temperature furnace which the group had constructed two years earlier (Takahashi et al. 1956).

In the same year, Hashimoto and coworkers (1958) constructed a specimen chamber with a metallic wire with a high melting temperature (e.g., tungsten) as the heating device. Gas pressures of up to ~1.33 Pa (10^{-2} Torr) could be introduced through a valve of the holder to react with the specimen at elevated temperature. The range of pressure was expanded to about 40 kPa (300 Torr) in a later design which included differential pumping (Hashimoto et al. 1966, 1968). In both versions, the wire was placed between two Pt apertures of diameters 50–100 μm and spaced 0.3–0.5 mm apart. The specimen stage could be taken out of the electron microscope column through an airlock system without breaking the vacuum. These efforts led to the production of a commercially available (JEOLCO JEM AGI attachment) gas reaction stage, and the image resolution achievable was 5–10 nm with an air pressure of 40 kPa (300 Torr).

The Hashimoto cell was adapted by Feates et al. (1970) onto a JEOL 7A microscope with continuous recording facilities. The latter was made possible by incorporating a 20 mm diameter hole in the center of the fluorescent viewing screen to allow the electron beam to strike a secondary screen with a transmission phosphor. The underside of the phosphor was viewed by a 25 mm "Plumbicon" television camera, and the image was displayed on a television screen (300 mm diameter), which increased the effective magnification of the instrument to greater than 2.5 million times. Additional refinements included direct recording of the image on videotape, slow-motion replay facilities, and the provision of permanent records on 16 mm cine film.

In the 1960s and 1970s, a number of electron microscopes were adapted to incorporate gas reaction attachments. Gallegos (1964) converted an existing hot stage for a JEM-6A electron microscope into a gas reactor by attaching a syringe needle to the hot stage. The gas nozzle was shaped into a slit, which facilitated the impingement of gas onto the specimen. The column vacuum was maintained at about 0.1 Pa (1×10^{-3} mm Hg) in this setup. Fryer (1968a, 1968b) investigated the oxidation of graphite catalyzed by palladium by heating the specimen to 500 °C

using a heating stage in a Siemens Elmiskop I electron microscope in high vacuum (1.33×10^{-3} Pa, or 10^{-5} Torr), and then introducing dry air over the specimen by means of a special attachment, and recording the specimen behavior over photographic plates and video tape (by means of closed circuit television). In the same year, Mills and Moodie (1968) designed, constructed, and installed an electron microscope stage on a Hitachi HU-11A microscope which included gas injection capability via a curved capillary. There was no differential pumping mechanism. Rather, the column pumps, working through the same capillary, established a rate adequate for the evacuation of the line between the taps and the valves, and for the adjustment of pressure in the fixed volume.

The need for differential pumping was recognized as a means of increasing the range of allowable pressures in the apertured chamber. Besides the modified Hashimoto (1966, 1968) design, Baker and Harris (1972) incorporated a modified JEOL AGI gas reaction attachment onto a 100 kV JEOL JEM-7A "high-resolution" electron microscope wherein the specimen chamber was evacuated by a three-stage diffusion pump backed by a rotary pump. The attachment consisted of only one aperture, which compromised the maximum allowable pressure up to 30 kPa (or 225 Torr) instead of 40 kPa (300 Torr) in the Hashimoto design, but retained its full diffraction capability. In addition, a glove box was added to the entry port of the microscope to load specimens into the microscope in a high purity argon atmosphere. A high sensitivity Plumbicon camera viewed the underside of the transmission phosphor and its output was monitored and recorded continuously on videotape, with an effective exposure time of 40 ms and a total recording time of 1 h per tape. Ward and Mitchell (1972) from the Cavendish Laboratory in Cambridge also produced an environmental chamber by mounting two 20 μm apertures 0.75 mm apart in the gap of the objective pole piece. The space between the apertures was effectively separated from the rest of the microscope column, and its environment may thus be varied independently. The addition of a diffusion pump with its own backing system to the microscope's normal pumps enabled the pressure in this space to be increased to one atmosphere (10^5 Pa) without significantly altering the column pressure.

With the advent of HVEMs in the 1960s and 1970s, Swann and Tighe (Swann and Tighe 1971; Swann et al. 1972; Swann 1972) designed and constructed an environmental cell for the 1 MV AE1-EM7 electron microscope. The environmental specimen chamber was located between the objective pole pieces of the microscope. It consisted of four apertures which were machined concentrically with the upper objective pole piece thus obviating the need for special aperture alignment facilities inside the microscope. The specimen chamber itself was surrounded by a second, differentially pumped chamber which further reduced the leakage rate of the reaction gas into the microscope column. The specimen holder was of the side-entry type and could be translated ± 1.5 mm using the normal, side-entry specimen stage. The specimen rod was supported at its tip by a conical socket inserted into the normal side-entry stage. The distance between the specimen apertures was 5.5 mm which was large enough to accommodate a tilting hot stage and yet short enough to obtain satisfactory images of crystalline samples at pressures up to 10^5 Pa

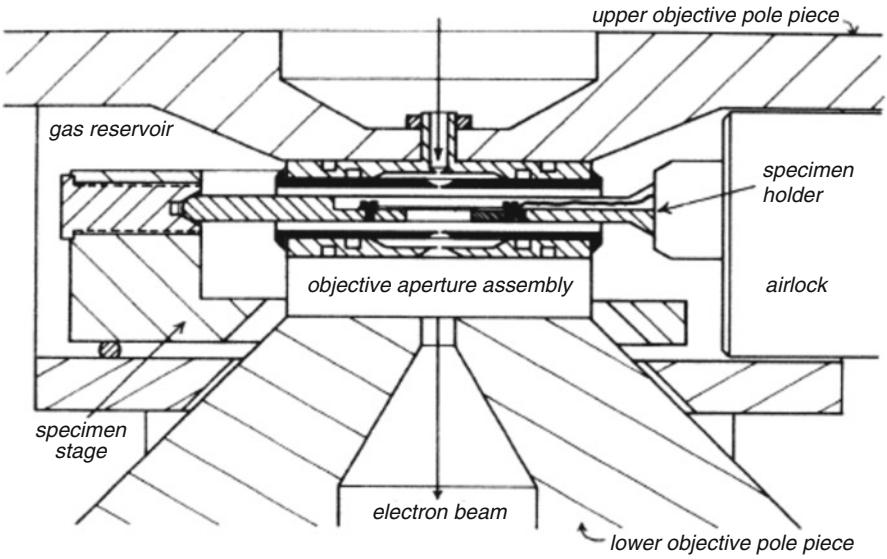

Fig. 1.3 Environmental specimen chamber situated between the objective pole pieces of the AEI EM7 one million volt electron microscope, with the side entry, single tilt hot stage shown in position. Reprinted with permission from Swann (1972)

(760 Torr) of He or 20 kPa (150 Torr) of air. The specimen and differential chamber apertures were large enough to transmit complete diffraction rings at 1 MV from crystal planes with spacings larger than 0.05 nm. A movable objective aperture system was provided below the gas reaction cell and was hermetically sealed to prevent gas leaking into the lower part of the microscope column. The superior penetrating power of the high-voltage electron microscope, compared to 100 kV instruments that were commonly available during that time, facilitated the observations of thin foils with micrometer thicknesses (Swann and Tighe 1977). The resolution achievable was about 10 nm in 20 kPa (150 Torr) of air. Increasing gas pressure led to a decrease in image intensity and contrast, with the latter better in dark-field imaging mode at all pressure levels (Fig. 1.3).

In the 1980s, improvements in the objective lens pole-piece design led to the development of atomic-resolution medium-voltage (200–400 kV) TEMs which allowed in situ heating experiments in vacuum at atomic resolution (e.g., Sinclair et al. 1988). This further led to resurgence in the interest in the environmental cell designs in the 1980s and 1990s, with several groups modifying the objective pole pieces of various TEMs. Differential pumping was incorporated in all the modifications.

Rodriguez and coworkers (1990) modified the specimen chamber region of a JEOL 200CX TEM/STEM to accommodate a specially designed environmental cell and specimen heating stage to continuously observe changes in the appearance of a specimen as it underwent reaction with a beam of atomic oxygen.

The environmental cell was differentially pumped making it possible to work at an oxygen pressure of 2 kPa (15 Torr) and at the same time maintain a vacuum of 1.3×10^{-4} Pa (10^{-6} Torr) in the rest of the microscope column. The microscope setup also included a closed circuit television link in conjunction with a videotape recorder so that dynamic events occurring during the reaction could be captured and replayed later for analyses. The output from the camera was continuously monitored and stored on a Sony ¾″ VO-7600 videocassette recorder. In situ electron diffraction of the reacting specimen was also possible.

Lee and coworkers (1991) designed an objective pole piece for a JEOL 4000 (400 kV) TEM with a gap of 14 mm. Five apertures were used, and additional holes were machined into the pole piece to accommodate the extra gas handling equipment and to provide extra pumping ports. Differential pumping between the primary and secondary apertures, and pumping of the volume surrounding the pole piece and the upper secondary aperture and the condenser stack aperture, was accomplished by four turbo molecular pumps. The point-to-point resolution of the pole piece in the modified state was 0.41 nm. The column vacuum was in the lower 10^{-5} Pa (10^{-7} Torr) range with no gas in the cell. At 400 kV, the maximum diffraction angle that could be observed corresponds to 24 mrad ($d = 0.08$ nm). The cell was pressurized to 9.3 kPa (70 Torr) with H_2 gas for several hours with no adverse effects on microscope performance. Images could be recorded on conventional microscope plates or on high-resolution video tape via a Gatan TV camera.

Doole and coworkers (1991) modified a JEOL 4000 EX TEM by introducing differential pumping apertures and achieved a resolution of 0.31 nm at 400 kV under a pressure of 560 Pa (4.2 Torr) of H_2 and at temperature of 670 °C. Apart from the gas, the microscope was effectively unaltered (Goringe et al. 1996). Specimen shifts and tilts and heating capabilities were all available, as were the standard imaging apertures. A thin-window for energy-dispersive X-ray spectroscopy (EDS) and a parallel electron energy-loss spectrometer were available for analytical work.

Boyes and Gai (Boyes et al. 1996; Boyes and Gai 1997), then at DuPont, permanently modified the objective lens area of a Philips CM30T TEM/STEM system with a pole-piece gap of 9 mm, by introducing two pairs of apertures above and below the specimen. The apertures were mounted inside the bores of the objective pole pieces rather than between them as in previous designs. With this approach, regular specimen holders compatible with conventional TEMs could be used, as well as objective apertures for diffraction contrast experiments. The controlled environment (ECELL) volume was the regular specimen chamber of the microscope, and was separated from the rest of the column by the apertures in each objective pole piece and by the addition of a gate valve, which was normally closed, in the line to the regular ion-getter pump (IGP) at the rear of the column. A schematic of the basic geometry of their ECELL aperture system is illustrated in Fig. 1.4. A turbo molecular pump as well as an additional IGP was added to the microscope. Differential pumping was introduced at the sample area of the ECELL and at the level of the second condenser (C2) lens and selected area (SA) apertures. (111) lattice fringes of gold islands of 0.24 nm could be resolved at 500 °C in 40 Pa

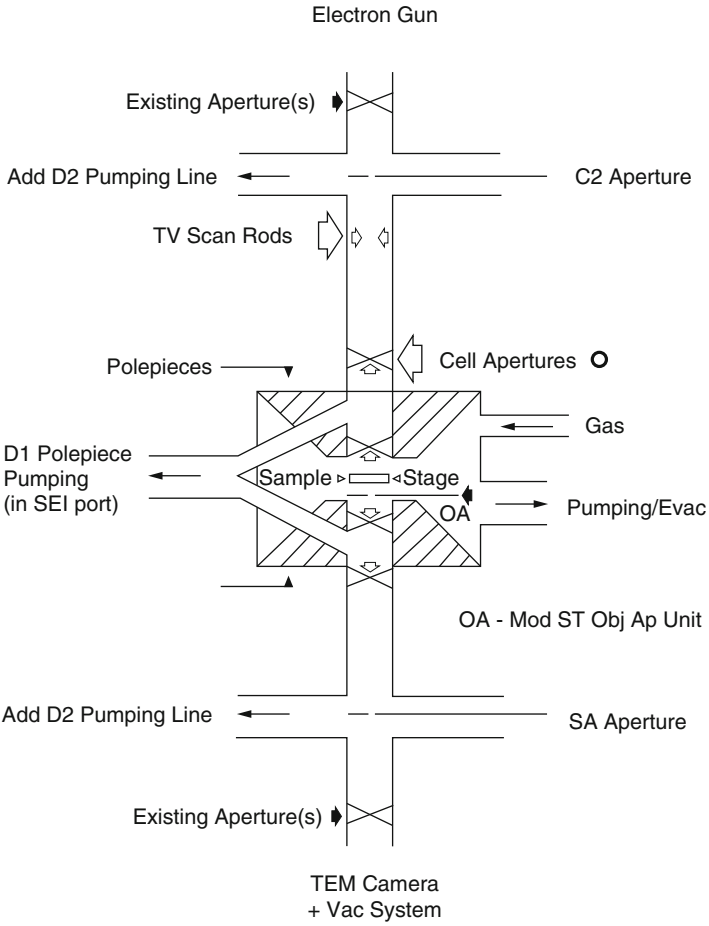

Fig. 1.4 Schematic of the basic geometry of the ECELL aperture system from Boyes and Gai (1997)

(0.3 Torr) N_2 at 200 kV accelerating voltage. The maximum allowable pressure in this design was 5 kPa (50 mbar) (Boyes and Gai 1997). At 200 kV, diffraction patterns extend out to a real space equivalent of <0.07 nm. Regular, small probe scanning TEM (bright-field and annular dark-field) imaging and chemical and crystallographic analyses capabilities were also available.

In Arizona State University, Sharma and coworkers (1994) modified a Philips 400-T TEM operated at 120 kV to include a differentially pumped environmental cell, based on the Swann (Swann and Tighe 1971; Swann et al. 1972) design. Then in 1998, a Philips EM 430 (300 kV LaB_6 source) high-resolution TEM was modified by fitting a differentially pumped environmental cell (E-cell) in the objective lens pole-piece gap (Sharma and Weiss 1998). It consisted of two sets of apertures placed

above and below the sample. Smaller apertures were used for the upper apertures to reduce the leak rate to the electron gun source. The larger lower aperture in the E-cell makes high-angle electron diffraction possible. {422} diffraction rings of Au showing reflections out to 0.083 nm were achieved. The E-cell could handle up to 2.7 kPa (20 Torr) of gas pressure. Regular single- and double-tilt heating holders could be used to heat the samples up to 1300 °C and 850 °C, respectively. This was likely the first E-cell setup to include a post projector energy filter (Gatan Inc.) to filter the inelastic scattering from the gases/thick samples as well as to obtain energy-filtered images (chemical maps). The Gatan Imaging Filter (GIF) could also be used as a parallel electron energy-loss spectrometer to obtain chemical information in the sample composition during the reactions.

In the 2000s, TEM manufacturer Philips Electron Optics (now known as FEI Company) adapted the Boyes and Gai design and further improved the image resolution by incorporating a field emission gun (FEG) and a SuperTwin objective lens which has a narrower pole-piece gap (about 5 mm). An extra pumping stage is introduced to protect the FEG better (Hansen et al. 2006). FEI Company custom built ETEMs for Haldor Topsøe (a chemical company in Denmark) (Hansen et al. 2001), Osaka University in 2005 (Yoshida and Takeda 2005; Yoshida et al. 2007), and Arizona State University (Sharma and Crozier 2005) as part of a collaborative effort.

The latest series of ETEMs from FEI Company is based on the Titan platform, which is a three-condenser lens (scanning) TEM system. Technological improvements in electron microscopy over the past 15 years can be incorporated into these state-of-the-art ETEMs. For example, the spatial resolution is better than 0.1 nm when the microscope is operated at 300 kV with an aberration corrector (Haider et al. 1998a, b) in the image-forming (objective) lens. Spherical aberration correction of the objective lens minimizes image delocalization and leads to directly interpretable TEM images. This is especially crucial for in situ ETEM experiments where reactions and processes are dynamic, leaving little time for the recording of through-focal series images. The addition of a monochromator (Tiemeijer 1999) reduces the energy spread of the incident electron beam to better than 0.2 eV. An energy filter for imaging and electron energy-loss spectroscopy, an energy-dispersive X-ray spectrometer, scanning capabilities for STEM and bright-field and dark-field detectors can be incorporated in the setup. The instrument is also equipped with a residual gas analyzer to monitor the composition of the gases, and a plasma cleaner in the specimen chamber (Fig. 1.5).

On other fronts, Gai and Boyes (now at the University of York) are developing an ETEM equipped with aberration correctors in both the image- and probe-forming lenses as part of a collaboration with JEOL, which is another major electron microscope company (Gai and Boyes 2009; Boyes et al. 2013; Boyes and Gai 2014a, b). The instrument has both a gas tolerant turbo molecular pumping vacuum system and a wider gap objective lens pole piece in order to accommodate a 1000 °C hot stage, and aims to retain the original full function (S)TEM imaging and chemical analysis capabilities while operating at temperatures of >500 °C in a controlled gas environment. The increase in pole-piece gap is found to have little

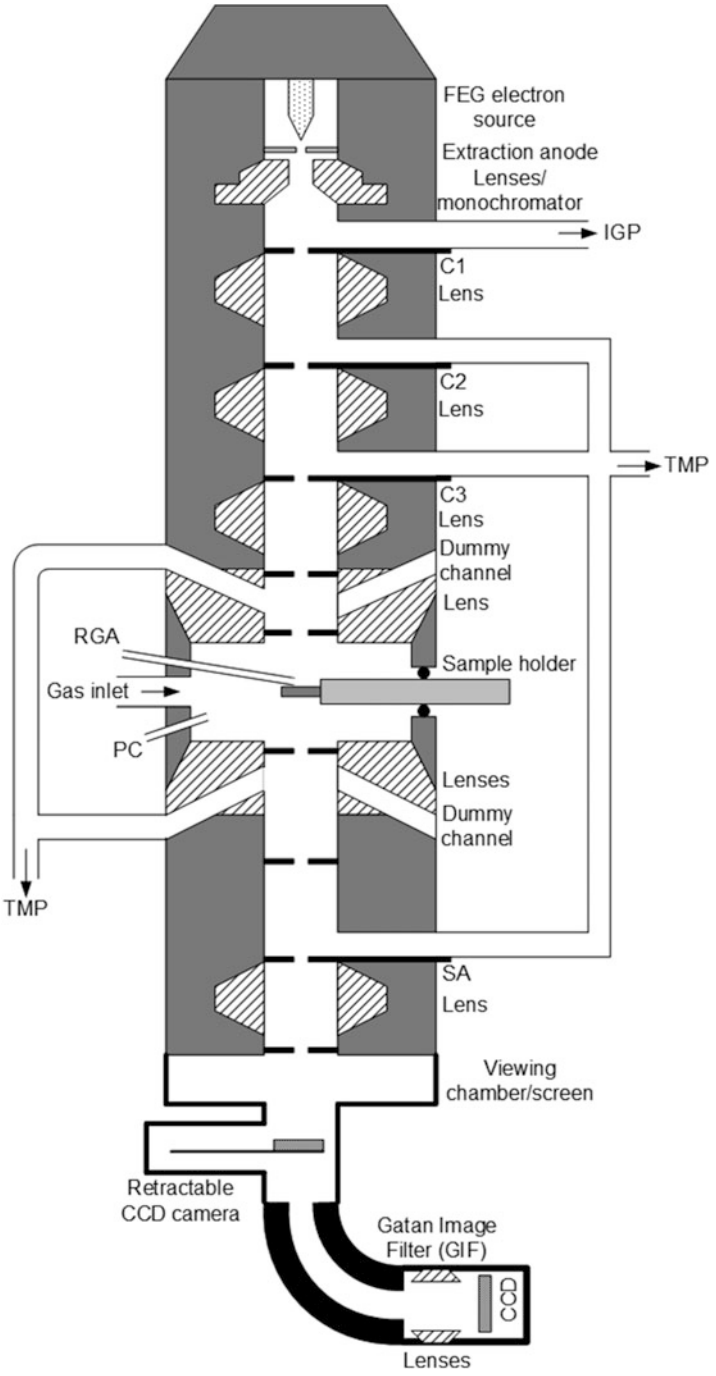

Fig. 1.5 Schematic diagram of differentially pumped TEM column (FEG, field emission gun, ion-getter pump (IGP), turbo molecular pump (TMP), residual gas analyzer (RGA), plasma cleaner (PC), first condenser aperture (C1), selected area aperture (SA) in an FEI Titan environmental transmission electron microscope (ETEM). Reprinted with permission from Hansen et al. (2010)

effect on spatial resolution owing to the aberration correctors. Currently, the system operates in both (E)STEM and (E)TEM modes with up to 5 kPa (50 mbar) in gas pressure.

There is also a possibility of the resurgence of HVEM for environmental studies, as exemplified by researchers at Nagoya University (Tanaka et al. 2013, 2014) who have been developing the reaction science high-voltage electron microscope (RSHVEM), which is a 1 MV high-voltage (S)TEM that can be used to observe nanomaterials under gas, liquids, and illuminating light conditions. Samples of micrometer thicknesses can be observed. The microscope vacuum is supported by a three-stage differential pumping system comprising five turbo molecular pumps. It is also equipped with electron tomography, energy-filtered TEM and electron energy-loss spectroscopy capabilities.

1.1.3 Development of UHV TEM for Epitaxial Growth Studies

The desire to image atomically clean surfaces and to perform epitaxial growth studies has led to the development of ultrahigh-vacuum (UHV) specimen environments in TEMs. Because of the highly reactive nature of the starting materials, a UHV specimen environment is required so that a clean initial surface can be prepared, usually by annealing at high temperatures. To perform controlled environment studies, McDonald and coworkers (1989) modified a JEOL 200CX high-resolution TEM with point resolution of 0.25 nm, to obtain an UHV environment of ~1.3×10^{-7} Pa (10^{-9} Torr) (cf. vacuum of 1.3×10^{-5} Pa, or 10^{-7} Torr in regular TEMs) in the specimen region. This was achieved by isolating the specimen chamber from the manufacturer's vacuum system, incorporating differential pumping, and using larger pumps, pumping manifolds, improved vacuum seals, and replacing or removing non-vacuum-compatible materials from the specimen chamber. The modified design permitted a variety of different experiments at pressures from <13 Pa (0.1 Torr) to ~1.3×10^{-7} Pa (10^{-9} Torr). The system was fitted with a calibrated leak valve for the introduction of gases, and in situ heating and evaporation capabilities were also added to the specimen viewing position, where high resolution could be maintained at temperatures exceeding 600 °C. In situ cleaning and thin film deposition capabilities were also added.

Hammar and coworkers from the IBM Research Lab (1996) modified a Hitachi 9000 UHV-TEM operated at 200 kV, with a base pressure in the column of 3×10^{-8} Pa (2×10^{-10} Torr) with the beam on or off. The modifications consist of a gas inlet system for the introduction of oxygen or germane in the column, and a double-tilt heating stage which allows the application of precise dark-field conditions and in which the samples can be heated with direct current up to 1400 °C during observation. This setup has been used extensively to study the growth of nanowires in situ (see Applications section).

1.2 Applications

Controlled atmosphere transmission electron microscopy has been applied in a variety of materials research problems. In this section, we highlight its major uses in the areas of oxidation and reduction processes, growth of one-dimensional materials as well as catalysis. The reader can also refer to the chapters on growth experiments and catalysis studies in this book for more examples within these topics.

1.2.1 Oxidation and Reduction Processes

Early applications of CAEM focused on oxidation and reduction processes, often at high temperature, using both aperture- and window-type cells. Using their aperture environmental cell, Ito and Hizaya (1958) observed the oxidation of Al into γ-Alumina at 400 °C in 13.3 Pa (0.1 Torr) of air and the reduction of Cu_2O to Cu at 300 °C in 13.3 Pa (0.1 Torr) of H_2 by monitoring the changes in the diffraction patterns of the specimens. Hashimoto and coworkers (1958) observed the growth of needle-like tungsten oxide crystals on the surface of a tungsten filament at 850 °C in 400 Pa (3 Torr) of air. Diffraction analyses showed that the needles were composed of γ-tungsten oxide, which transformed to the α-phase (WO_3) upon further heating to 1400–1600 °C. WO_3 was found to evaporate above 2000 °C. Hashimoto and coworkers (1968, 1966, 1970) performed similar work on ammonium molybdate $(NH_4)_6MO_7O_{24}.4H_2O$ at 700 °C in air pressure of 1.3–20 kPa (10–150 Torr), and cuprous iodide (CuI) at 700 °C in hydrogen gas of pressure 6.7–20 kPa (50–150 Torr). Using the gas nozzle apparatus on a JEM microscope, Gallegos (1964) performed oxidation studies on Fe, Cu, and Ni which had been vacuum evaporated onto carbon support grids at high temperatures, as well as the reduction of these oxides.

The environmental cell for the 1 MeV AE1-EM7 high-voltage electron microscope designed by Swann and Tighe (1972) was utilized in a variety of redox experiments, including Ti oxidation at 450–850 °C (Flower and Swann 1974), hematite (Fe_2O_3) reduction to magnetite (Fe_3O_4) (Swann 1972; Swann and Tighe 1977), and oxidation of Ni-30Cr and TDNiCr (Flower and Wilcox 1977). It was also used to observe the microstructural changes in Ta during in situ heating in nitrogen (Swann et al. 1973). The high penetrating power of the 1 MeV HVEM permits continuous observation of foils which were mechanically much stronger than those suitable for medium voltage work. It was thus possible to follow the oxidation of a single grain from 100 % metal to 100 % oxide without any problems of foil buckling or fracture. In these experiments, the early stages of nucleation and growth could be followed and the morphology and crystallography of the reactant products could be established, and models to explain the growth kinetics during oxidation (or reduction) could be deduced, albeit at limited resolution (on the order of 10 nm).

Using the JEOL TEM modified with a UHV system (Mcdonald et al. 1989), Ross and Gibson (1992) observed in real time the nature and motion of the silicon (111) surface steps during in situ oxidation inside the microscope, at temperatures from room temperature to 900 °C, by both O_2 and H_2O at pressures from 1.3×10^{-6} to 0.13 Pa (10^{-8} to 10^{-3} Torr), as well as in one atmosphere O_2. By using an imaging technique based on the behavior of forbidden reflections in Si, they showed that surface steps of two monolayers in height do not move noticeably during oxidation of several atomic layers of the silicon specimen. In contrast, bilayer step movement was observed in the "etching" of silicon by oxygen at higher temperatures.

With the increasing interest in nanomaterials in recent years, Crozier and coworkers (1998) subjected Pd catalyst particles to oxidation and reduction cycles and studied the changes in particle structure and morphology with in situ electron diffraction and imaging, and found that many of the oxide particles form voids when reduced to Pd metal. The decrease in volume that occurs during reduction is often accompanied by a combination of particle shrinkage and void formation. Koh et al. (2013) reported the first direct study on the oxidation of carbon nanotubes (CNTs) at the resolution of an aberration-corrected environmental transmission electron microscope (ETEM), as the same nanotubes were located and their changes identified as they underwent oxidation at increasing temperatures in situ in the ETEM. Their findings show that only the outside graphene layer is being removed and, on occasion, the interior inner wall is oxidized, presumably due to oxygen infiltrating into the hollow nanotube through an open end or breaks in the tube, contrary to earlier reports based on ex situ observations that CNT oxidation initiates at the cap of the tube and proceeds along its length.

1.2.2 Catalysis

Another major area which has benefited greatly from the development of environmental TEM is catalysis. The active surface sites of heterogeneous catalysts facilitate conversion of reactants into products and their properties depend on a number of factors including the type and number of surrounding atoms at the surface, the supporting material, and the presence of reactants and products (Molenbroek et al. 2009). A thorough understanding of the nanoparticle structure and its correlation to activity is therefore important to establish rational catalyst design strategies, and electron microscopy is invaluable in this regard owing to its sub-nanometer resolving ability. Although nanoparticles may be synthesized with predefined shapes and surface sites, the morphology of the as-synthesized particles may be influenced by reaction conditions. There is therefore tremendous interest in obtaining atomic level structural and chemical information on the catalysts in situ, in their working conditions. A much more detailed review is given in a later chapter, and we confine our comments to those which illustrate the growth of the field historically.

1.2.2.1 Catalyst Deactivation Studies

The pioneering experiments of catalytic decomposition of hydrocarbons on metallic surfaces were conducted by Baker and coworkers in the 1970s. Using CAEM (Baker and Harris 1972), Baker and coworkers were able to directly observe the formation of carbon filaments on metal surfaces (Fe, Co, Cr) when reacted in hydrocarbon environments (Baker et al. 1972a, b). The authors noted that the presence of a small particle located at the growing end of each filament appeared to catalyze the growth of the carbonaceous structure. From the experimental data, a mechanism to describe the filament growth process was developed, and activation energies for filament growth were determined (Baker et al. 1973, 1979). The growth of filamentous carbon is a major concern in many industrial processes involving blast furnaces, steam cracking, fuel pins, and boiler tubes of nuclear reactors and various heterogeneous catalyst systems, where the catalyst deactivates due to the spatial limitations imposed on the filamentous carbon growth (coke formation and fouling) by the reactor (Baker 1989, 1990). The motivation for studies relating to the formation of carbon filaments has been the drive to inhibit the growth of this form of carbon deposit.

Besides fouling, catalyst deactivation can also occur from sintering. Gai and Boyes (1997) studied the dynamic effect of Cu-Pd intermetallic alloy particle catalysts supported on carbon at 250 °C in an H_2/He and CO/He environments, and found that the particles were more faceted in CO than in H_2 and sinter faster in H_2. Liu et al. (2004) used in situ ETEM to study the sintering mechanisms on Al_2O_3-supported Pd catalysts in an oxidizing environment. For fresh catalysts, particle sintering occurred via a traditional ripening and coalescence mechanism and was significant at temperatures from 700 °C. In the case of used catalysts, gasification of carbonaceous material around these particles in an oxidizing environment resulted in movement and coalescence at temperatures as low as 350 °C. Simonsen and coworkers (2010) performed time-resolved imaging of Pt nanoparticles dispersed on amorphous Al_2O_3 support during exposure to 1 kPa (10 mbar) of synthetic air at 650 °C inside an ETEM, and showed that Pt nanoparticle sintering was mediated by an Ostwald ripening process.

1.2.2.2 Investigations on Catalysts and Their Supports

The properties of heterogeneous catalysts are often determined by the interactions between the catalyst nanoparticles and their supports (typically metal oxides). Molecules can restructure the surfaces of heterogeneous catalysts under reaction conditions. The nature of the support has important influence on the properties of supported metal catalysts and this has been an interest in the ETEM community over the years. Here, we present a summary of work performed on Au and Cu catalysts, and ceria supports.

(a) *Au catalysts*

While bulk Au is chemically inert, supported Au nanoparticles (Au NPs) (on selected oxides such as CeO_2 and TiO_2) catalyze a wide variety of reactions such as CO oxidation (Haruta 1997), water-gas shift reactions (WGSR) (Fu et al. 2003), and selective and total oxidation of hydrocarbons (Hayashi et al. 1998). The catalytic performances of Au markedly depend on particle size, dispersion, supports, and preparation methods. For example, catalytic activity measurements of Au particles of 1–7 nm deposited on rutile TiO_2 show that smaller particles have higher activity (Williams et al. 2010). Au nanoparticles supported on TiO_2 have been shown to have higher catalytic rates than those supported on Al_2O_3 in CO oxidation and WSGR (Arrii et al. 2004; Sandoval et al. 2007)

Using an aberration (image)-corrected ETEM, Yoshida, Takeda, and coworkers (Yoshida et al. 2012; Takeda and Yoshida 2013) showed that adsorbed carbon monoxide molecules caused the facets of a Au nanoparticle supported on CeO_2 to reconstruct during CO oxidation at room temperature (Fig. 1.6). By operating at a lower accelerating voltage (80 kV), which improved the image contrast of light-element atoms, they also observed bright and dark contrast features extruded from the reconstructed facets of gold nanoparticles. Using image simulations in combination with ab initio electronic calculations, they showed that the electron micrograph allowed deduction of an energetically favorable model for CO adsorption (Fig. 1.7). Uchiyama and coworkers (2011) examined a large number of Au/CeO_2 catalysts using ETEM and found that the morphology of Au nanoparticles changes from faceted during CO oxidation in CO/air to becoming more round with decreasing CO partial pressure relative to air. They also examined Au nanoparticles supported on a non-oxide (TiC) crystal and observed no morphological changes in the Au nanoparticles supported on TiC when switching the gases. Using aberration-corrected ETEM, Kuwauchi et al. (2013) show that catalytically active Au NPs move reversibly and stepwise by approximately 0.09 nm on a CeO_2 support surface at room temperature and in a reaction environment. The lateral displacements and rotations occur back and forth between equivalent sites, indicating that Au nanoparticles are loosely bound to oxygen-terminated CeO_2 and may migrate on the surface with low activation energy.

Kuwauchi and coworkers (2012) studied the intrinsic structure of Au/TiO_2 catalysts at room temperature under various gas reaction conditions with the ETEM (high vacuum, O_2 at 100 Pa, N_2 at 100 Pa and 1 % vol CO in air at 100 Pa), and observed that the Au NPs changed their morphology systematically depending on the environment. Based on the ETEM observations, structural evolution diagrams depicting the morphology of the catalysts as a function of electron current density and dose in various gas environments were derived.

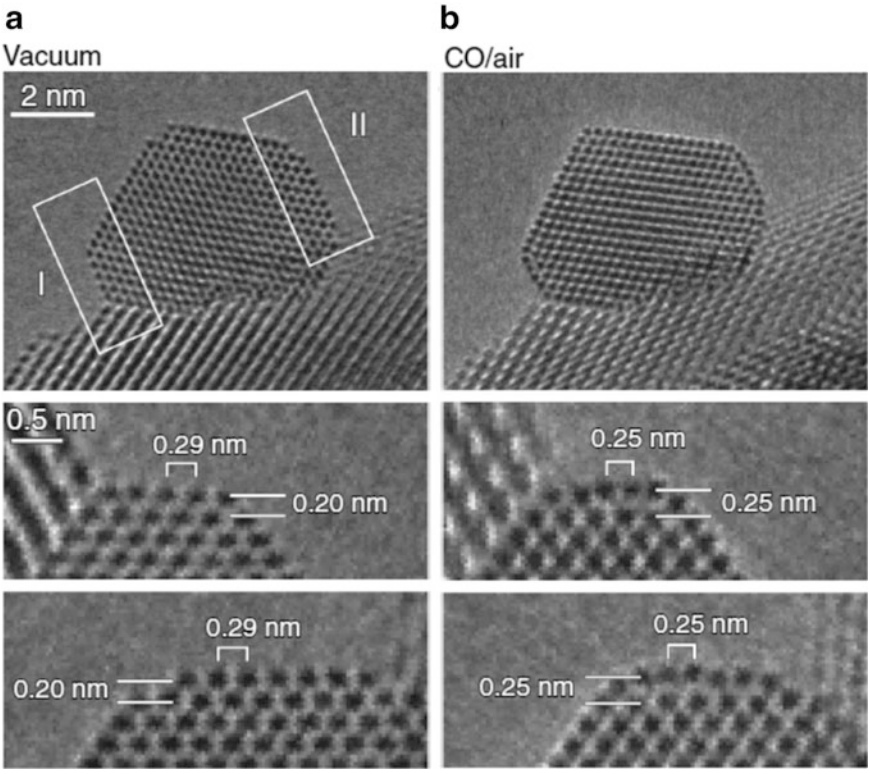

Fig. 1.6 Au{100}-hex reconstructed surface under catalytic conditions. GNP supported on CeO_2 in (**a**) a vacuum and (**b**) a reaction environment (1 vol.% CO in air gas mixture at 45 Pa at room temperature). Two {100} facets are present in the rectangular regions indicated by I and II in (**a**). The enlarged images of these regions in vacuum and in the CO in air gas mixture are shown at the bottom of (**a**, **b**), respectively. In vacuum, the distance between the topmost and the second topmost {100} surface layers of 0.20 nm was the same as the interplanar distance of the {200} planes in crystalline bulk gold. The average distance of the adjoining Au atomic columns on the topmost surface layer of 0.29 nm was the same as the corresponding distance in a {100} plane in crystalline bulk gold. In the reaction environment, both the average distance of the adjoining Au atomic columns and the interplanar distance changed to 0.25 nm. These changes in positions of the Au atomic columns correspond well to those of the Au{100}-hex reconstructed surface structure. To reduce random noise, the images in (**a**, **b**) were obtained by averaging four successively acquired images. Figure reprinted with permission from Yoshida et al. (2013)

(b) *Cu catalysts*

Another catalyst material that is of interest is Cu. Cu nanoparticles on supports are used as catalysts for methanol synthesis and hydrocarbon conversion processes for fuel cells. Cu alone may work as a methanol synthesis catalyst, but the activity increases significantly for Cu supported by ZnO. Hansen et al. (2002) examined Cu nanoparticles dispersed on ZnO and silica supports and found that for the Cu/ZnO catalysts, the shape of the particles changes with varying gas composition. The addition of water to hydrogen gas

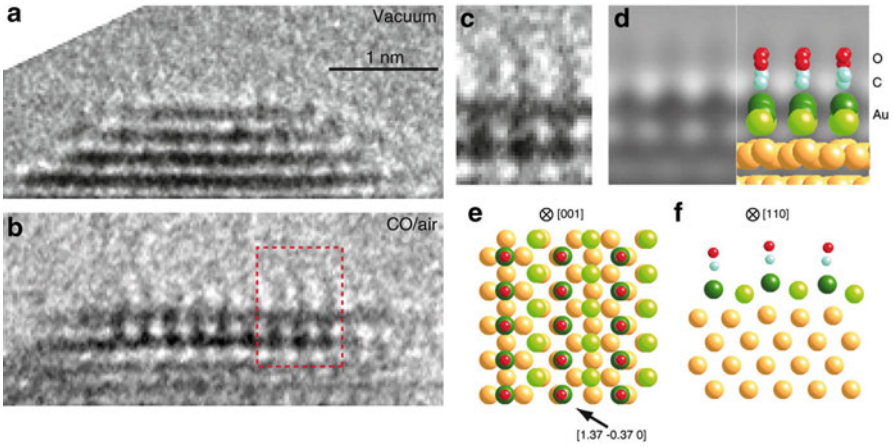

Fig. 1.7 Adsorbed CO molecules on a Au{100}-hex reconstructed surface under catalytic conditions. Aberration-corrected ETEM images in (**a**) vacuum and (**b**) a reaction environment (1 vol.% CO in air at 100 Pa at room temperature) taken using 80 keV electrons using an under-defocus condition. (**c**) The observed image in the rectangular region in (**b**) at higher magnification. (**d**) A simulated image based on an energetically favorable model. The model is superimposed on the simulated image. The model in (**e**) plan view along the [001] direction of crystalline gold and (**f**) cross-sectional view along the [110] direction of crystalline gold to show the undulating topmost Au layer. C atoms, blue colored balls; O atoms, red colored balls; CO adsorbed Au atoms within the surface hexagonal lattice, darker green colored balls; the other Au atoms within the surface hexagonal lattice, brighter green colored balls; the Au atoms within and below the second topmost surface layer, gold colored balls. By fitting the simulated images with the observed images, the viewing direction in (**a–c**) was determined to be the [1.37, –0.37, 0] direction of the crystalline Au NP. As shown in models (**d**, **e**), the [1.37, –0.37, 0] direction is nearly parallel to one side of the surface hexagonal lattice. To reduce random noise, the images in (**a–c**) were obtained by averaging four successively acquired images. Figure reprinted with permission from Yoshida et al. (2013)

transforms the Cu crystals into a more spherical morphology, whereas the removal of H_2O from H_2 causes the Cu crystals to revert to their original form. For Cu nanocrystals supported on silica, the support was found to have negligible influence on the structure. Vesborg and coworkers (2009) performed time-resolved measurements of the methanol synthesis reaction over a Cu/ZnO-based catalyst using a laminar flow tube reactor and compared the activity measurements with ETEM observations of Cu/ZnO particles during exposure to comparable reaction conditions. Using ETEM, it was revealed that qualitatively, the Cu particles appear to be more flat under more reducing conditions and more spherical when exposed to a more oxidizing environment. The gas-dependent morphology of the Cu nanoparticles is consistent with the dynamic microkinetic model proposed by other research groups. Wagner and coworkers (2003) utilized electron energy-loss spectroscopy (EELS) to investigate metal-support interaction in a Cu/ZnO catalyst by examining the energy-loss near edge structure (ELNES) at the Cu L_3 ionization edge as the catalysts are heated in a CO/H_2 environment in the ETEM. The intensity of the ELNES reflects modifications in the electronic structure of Cu. They found that in the Cu/SiO_2 system, the ELNES intensities were

constant, reflecting that no structural changes of the Cu nanocrystals are observed. Changes in the ELNES were observed when the particles were dispersed on a ZnO support, and were interpreted as a tensile strain in the Cu nanoclusters induced by the ZnO support, as well as a Cu-Zn alloy formation induced to a degree depending on the severity of the reduction treatment of the catalyst.

(c) *Ceria particles and ceria-based supports*

Cerium-based oxides continue to attract considerable attention because of their current and potential use in metal-supported oxide catalyst applications, e.g., in automobile three-way catalytic converters, solid oxide fuel cell anodes, and water-gas shift reactions. The valence state of cerium changes from Ce^{3+} to Ce^{4+} during the associated phase transformations $(2CeO_2 \leftrightarrow CeO_3 + 0.5O_2)$, and the ability of this material to reversibly accept or contribute oxygen to its surroundings is the basis for its use in catalytic applications where redox processes are important. Parkinson (1989) envisaged feasibility of directly studying atomic rearrangements in catalysts and catalyst supports under reaction conditions by electron microscopy, when he presented HRTEM images of the ceria lattice, taken under flowing nitrogen at 2.7 kPa (20 Torr) which revealed lattice fringes from the {111} planes (separation = 0.312 nm). Such studies show promise of providing a detailed understanding of the mechanisms involved in certain types of heterogeneous catalyst.

Sharma and coworkers (2004) characterized the reduction behavior of high-surface-area (HSA) and low-surface-area (LSA) CeO_2 catalysts in hydrogen gas at elevated temperatures using EELS by analyzing the Ce $M_{4,5}$ white line intensity ratio. The relative intensities of the M_5 and M_4 peaks in the Ce EEL spectra depend on the oxidation state of Ce. The authors found a direct correlation between the extent of reduction and surface area, with significant Ce reduction occurring by 600 °C in the HSA sample whereas with the LSA sample, significant reduction took place around 700–800 °C.

Wang and coworkers (2008, 2009) followed the dynamic redox process taking place in individual ceria and ceria–zirconia nanoparticles. The samples were progressively heated and cooled while maintaining the same H_2-rich atmosphere. Re-oxidation may occur rapidly at temperatures below 600 °C due to residual background oxygen/water vapor in the sample area or in the ETEM column, and the structure and chemistry were monitored using high-resolution TEM imaging, electron diffraction, and electron energy-loss spectroscopy (EELS) (Fig. 1.8). The studies show that for ceria nanoparticles with an average size of 20 nm, oxygen vacancies present in the reduced ceria undergo rapid ordering leading to the immediate formation of Ce_2O_3. The reduced ceria has a C-type lattice in which the lattice parameter is doubled compared to that of the parent fluorite structure. In the ceria–zirconia nanoparticles, the more active structure has predominantly disordered cations and shows no evidence for oxygen vacancy ordering during reduction.

Cargnello et al. (2013) studied CeO_2 which has been found to be an "active support" in terms of increasing the rates of redox reactions. By tailoring the

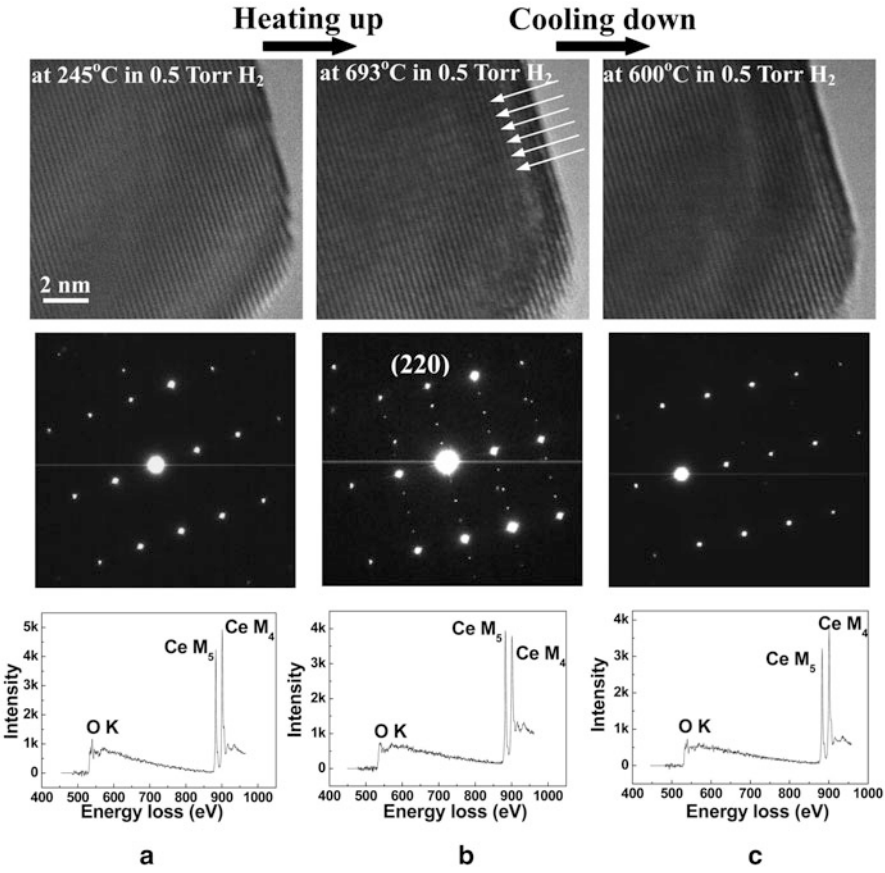

Fig. 1.8 Dynamic changes of atomic-level structure characterized by high-resolution imaging (upper row) and electron diffraction (middle row) and chemistry analyzed by the electron energy-loss spectrum (lower row) at (**a**) 245, (**b**) 693, and (**c**) 600 °C in 67 Pa (0.5 Torr) of H_2 along the [21-1] zone axis from the same individual ceria nanoparticle during the redox process. (**b**) After reduction, arrows in the high-resolution image and extra spots along the (220) plane in the electron diffraction pattern show the superstructure formed during reduction. The reversal of Ce M_5/M_4 intensity indicates the reduction and re-oxidation from Ce^{4+} to Ce^{3+} and from Ce^{3+} to Ce^{4+} during heating and cooling, respectively. Figure reprinted with permission from Wang et al. (2009)

"length" of a ceria-metal interface, through the use of monodisperse Ni, Pd, and Pt nanocrystals, CO oxidation in ceria-based catalysts was found to be greatly enhanced at the ceria-metal interface sites, and the metals deposited on ceria had higher catalytic rates than their alumina-supported counterparts, as evidenced by the much lower temperatures needed to completely oxidize CO.

(d) *Catalyst promoters*
Besides catalysts themselves, there are also catalyst promoters which cause more than proportional increases in activity or selectivity when added to a catalyst, and are therefore essential to achieve the required activity or selectivity in catalysts. Hansen et al. (2001) performed in situ TEM imaging of Ba-promoted Ru catalysts in their working conditions in an ETEM, and suggested that the increased activity to be related to a two-dimensional barium-oxygen overlayer on the Ru crystals.

(e) *Electron energy-loss spectroscopy (EELS) for quantification of gases and catalytic products*
With the developments of electron energy-loss spectrometers and their attachments onto modern ETEMs, redox reactions in catalysts and other materials system can be studied by monitoring changes in the EELS spectra of the specimens. EELS thus offers another avenue of TEM characterization in addition to imaging and diffraction capabilities. For example, López-Cartes and coworkers (2003) performed ETEM studies on $Rh/Ce_{0.8}Pr_{0.2}O_{2-x}$ catalysts under H_2 conditions at temperatures ranging from 298 to 1223 K, and observed the occurrence of consecutive reduction of Pr^{4+} and Ce^{4+} ions, and the formation of an oxygen-deficient $Ln_{16}O_{30}$ (Ln: Ce, Pr) ordered phase, by analyzing the fine structure in EELS spectra of their $M_{4,5}$ edges. The group at Arizona State University (Sharma et al. 2004 and Crozier et al. 2008) studied the dynamic changes taking place during redox reactions in ceria and ceria–zirconia nanoparticles in a hydrogen atmosphere by monitoring the white lines in the Ce EELS spectra, and determining the Ce oxidation state by its M_5/M_4 intensity ratio.

Crozier and Chenna (2011) show that, while modern ETEMs are fitted with residual gas analyzers to monitor the composition of the gases, one can also perform quantitative analysis of gases in an ETEM with in situ EELS with an accuracy of 15 % or better (provided that some precautions are taken during the acquisition to account for the extended gas path lengths associated with the reaction cell). They have since employed this technique to detect and quantify catalytic products directly inside the ETEM (Chenna and Crozier 2012). Ru nanoparticles supported on SiO_2 spheres were used as the model catalyst for CO oxidation and CO methanation. CO oxidation reaction was performed by flowing $He:CO:CO_2$ in 50:8:4 ratio in the ETEM. CO has a carbon π^* peak of 286.4 eV, and as the temperature of the specimen was increased inside the ETEM, the C π^* peak from CO_2 (at 289.7 eV) was found to increase in intensity, indicating that the greater percentage of CO had been converted to CO_2. There was good agreement between the EELS measurements and the results obtained using an ex situ catalytic reactor. In CO methanation, a CO_2 and H_2 gas mixture of 4:1 pressure ratio was admitted to the environmental cell and EEL spectra were collected at different temperature. A shoulder peak at about 286.4 eV started to appear at 400 °C, corresponding to CO formation, and became more dominant at increasing temperatures.

A key challenge to successfully applying EELS in catalysis is the peak overlap between reactant and product gases. This can be overcome by the use

of electron microscopes equipped with monochromators, which significantly improves the energy resolution from 1 to 0.2 eV or better. Baldi and coworkers (2014) utilized monochromated EELS in an ETEM to observe hydrogen absorption and desorption in individual Pd nanocrystals by directly probing the bulk plasmon resonance mode of the Pd nanoparticle. On hydrogen absorption, individual Pd nanocrystals exhibit large red shifts (exceeding 2 eV) in their bulk plasmon resonance, and these shifts are reversible on desorption. The individual particle spectra are then correlated with particle size and crystallinity using the high spatial resolution of aberration-corrected TEM imaging, and hydrogen loading and unloading isotherms of individual Pd nanocrystals were then deduced.

(f) *Photocatalysis*
Photocatalysts are also an important class of catalyst materials with applications relating to sustainable energy development. Several groups have recently explored different ways for light irradiation of samples inside the (E)TEM. One approach is the use of specialized lens-based or fiber-based TEM specimen holders that permit specimens to be illuminated with light and electrons at the same time (Shindo et al. 2009; Cavalca et al. 2012). Combining the use of these holders with an ETEM, Cavalca and coworkers (2012, 2013) investigated the photoreduction of cuprous oxide (Cu_2O). Water vapor was leaked into the ETEM specimen chamber and the specimen was exposed to light with 405 nm wavelength for various time periods while the electron beam was blanked. Then, the column was evacuated to $\sim 1.3 \times 10^{-4}$ Pa (10^{-6} mbar) pressure for 5 h to reduce the water vapor in the column before the electron beam was illuminated on the sample to record changes post-reaction. TEM images show that Cu_2O nanocubes were degraded after photoreduction. Diffraction patterns show the transformation of the cubes from Cu_2O to Cu, and the change in oxidation state of Cu is also elucidated in the Cu $L_{2,3}$ edge using EELS. The group at Arizona State University (Miller and Crozier 2013) designed an illuminating system for the ETEM whereby light is introduced through a port on the microscope, and they observed surface amorphization in TiO_2 nanocrystals when the latter were irradiated with light while exposed to water vapor inside the ETEM (Zhang et al. 2013).

1.2.3 Nucleation and Growth of One-Dimensional Nanomaterials

Another application of ETEM is the in situ nucleation and growth of one-dimensional nanomaterials such as carbon nanotubes and nanowires, as described in a later chapter.

Since their discovery in 1991 carbon nanotubes (CNTs) (Iijima 1991) have found an increasing number of applications, most notably as field emission electron sources in displays or in X-ray tubes for medical applications (e.g., Rinzler

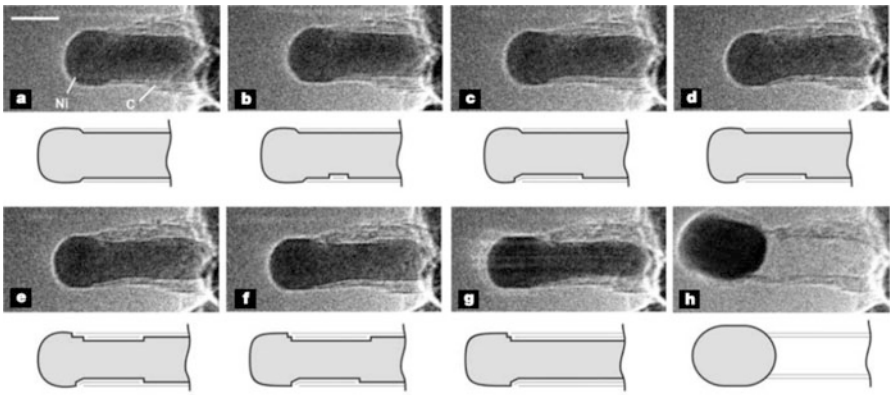

Fig. 1.9 Image sequence of a growing carbon nanofibre. Images (**a**–**h**) illustrate the elongation/contraction process. Drawings are included to guide the eye in locating the positions of mono-atomic Ni step edges at the C–Ni interface. The images are acquired in situ with CH_4:H_2 ratio of 1:1 at a total pressure of 210 Pa (2.1 mbar) with the sample heated to 536 °C. All images are obtained with a rate of 2 frames per sec. Scale bar, 5 nm. Figure reprinted with permission from Helveg et al. (2004)

et al. 1995; de Heer et al. 1995; Wang et al. 1998; Choi et al. 1999; Sugie et al. 2001). Observations of carbon nanotube growth can be made in situ using ETEM and was reported by two groups in 2004. Helveg et al. (2004) formed carbon nanofibers from methane decomposition over Ni nanocrystal catalysts supported on $MgAl_2O_4$ (CH_4:H_2 ratio = 1:1), at temperatures 500–540 °C and total pressure of 200 Pa (1.5 Torr), and observed, in real time, the growth of the nanofibers at the high resolution of the TEM (Fig. 1.9). Carbon nanofibers were found to develop through a reaction-induced reshaping of the Ni nanocrystals, with the nucleation and growth of graphene layers assisted by a dynamic formation and restricting of mono-atomic step edges at the Ni surface. Sharma and Iqbal (2004) used a Ni/SiO_2 catalyst and acetylene as the precursor gas. The catalysts–supports were dry loaded on 400 mesh Ni grids, and heated at 400 °C for 30–60 min in vacuum or in 133–266 Pa (1–2 Torr) of H_2 using a furnace-based heating holder. When 13.3–200 Pa (100–1500 mTorr) of acetylene (C_2H_2) was introduced into the ETEM at a temperature ~450 °C, catalytic decomposition of C_2H_2 on the Ni/SiO_2 catalysts led to the growth of carbon nanotubes. Multiwall nanotubes formed at temperatures as low as 450 °C while only single-wall carbon nanotubes (SWNTs) formed at higher temperatures ~700 °C and above. The growth rate, structure, and morphology of the CNTs are found to be dependent upon reaction temperature and pressure. When the growth temperature was maintained at 480 °C, multiwalled CNTs are observed to grow in a zigzag manner, forming waves, spirals or loops, at an average rate of 35–40 nm/s under C_2H_2 pressures of 2.67–13.3 Pa (20–100 mTorr), whereas SWNTs with diameters ~3.5 nm form at growth rates of 6–9 nm/s observed at C_2H_2 pressures <1.33 Pa (10 mTorr) (Sharma et al. 2005). When the C_2H_2 pressure was maintained at 0.13 Pa (1 mTorr) and the growth temperature varied from 450 to

650 °C, both the inner and outer nanotube diameters were found to decrease with increasing temperature (Sharma et al. 2007).

The catalyst plays an important role in the growth of CNTs via the CVD process. For example, the size of the catalysts dictates the SWNTs diameters grown (Zhang et al. 2002). For surface-bound CVD, the interactions between the catalyst and support play a critical role in controlling catalyst size distribution (Lolli et al. 2006). A fundamental question of interest is the physical and chemical state of the catalyst during the CNT growth process. Yoshida and coworkers (2008) vacuum-evaporated 1 nm-thick Fe on SiO_2 and heated the substrate in an ETEM to 600 °C in high vacuum, and subsequently, in a mixture of C_2H_2:H_2 = 1:1 at 10 Pa (0.08 Torr). They concluded, from real-time observations of the nucleation and growth processes of CNTs, that the nanoparticle catalysts are fluctuating crystalline cementite (Fe_3C) particles. Hofmann et al. (2009) studied catalyst–support and catalyst–carbon interactions during the CVD growth of SWNTs using a combination of ETEM and in situ, time-resolved X-ray photoelectron spectroscopy, and found the active state of Fe and Ni catalysts to be the crystalline metallic nanoparticles. Pd (silicides) and Au are catalytically less efficient for C_2H_2 dissociation compared to Fe and Ni.

The growth of ultra-long, vertically oriented SWNT carpets or forests using CVD (Chattopadhyay et al. 2001; Hinds et al. 2004) is also of interest because of their suitability in a number of potential applications. To promote and sustain the growth of SWNT carpets, an approach known as "super growth" was developed by the Iijima group, whereby the introduction of H_2O led to an increased activity and lifetime of the catalysts (Hata et al. 2004). Amama and coworkers (2009) showed *a posteriori* that the addition of H_2O promotes super growth of SWNTs by inhibiting Ostwald ripening in the Fe catalyst nanoparticles on Al_2O_3 support. Kim et al. (2010) demonstrated using both ex situ quantitative measurements of CNT growth rate and in situ ETEM observations that termination of SWNT carpet growth can be linked to the evolution of the catalyst morphology and Fe subsurface migration. Yoshida and coworkers (2009) also demonstrated that the deposition of a proper quantity of Mo on substrates with Fe catalysts leads to the formation of Fe-Mo carbide nanoparticle catalysts of $(Fe,Mo)_{23}C_6$ structures as well as Fe_3C. Mo suppresses the nucleation of iron silicates which inhibits catalytic activity in the growth of CNTs, thereby increasing the CNT yield.

The electronic properties of carbon nanotubes are influenced by their chirality (e.g., Odom et al. 1998; Wilder et al. 1998). Existing synthesis methods cannot controllably produce nanotubes with a specific type of conductivity. Harutyunyan and coworkers (2009) show that by varying the noble gas (He or Ar) during thermal annealing of the catalyst in combination with oxidative and reductive species, the yield of nanotubes with metallic conductivity can be significantly increased. TEM characterization reveals a strong difference in the morphological behavior of Fe nanoparticles depending on the gas environment at 500 °C, with all particles in He exhibiting stronger faceting whereas those in Ar were more round shaped.

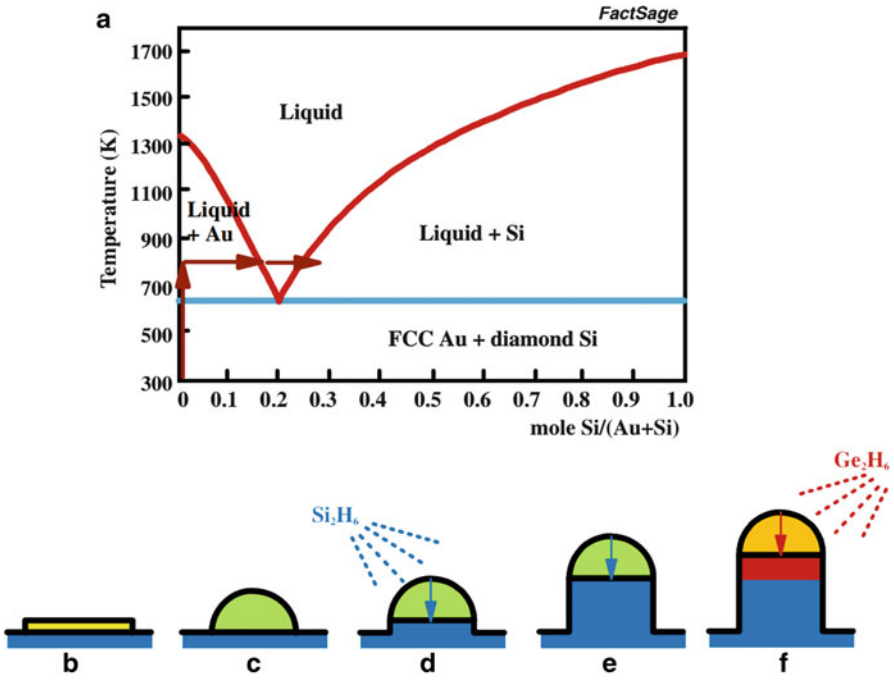

Fig. 1.10 (**a**) Phase diagram for the Au–Si binary system. The typical reaction path for Si nanowire growth is indicated by arrows. (**b**–**f**) Schematic diagrams of the process of Si and Ge nanowire growth from Au: (**b**) Au is deposited on HF-dipped Si. (**c**) Heating above 370 °C forms AuSi eutectic droplets containing ~20 % Si. (**d**) Exposure to a source gas such as disilane which adsorbs preferentially at the droplet surface and supersaturates the droplet with Si. (**d**, **e**) Si precipitates beneath the droplet. (**f**) Heterostructures such as Si/Ge nanowires are grown by changing the source gas. Figure reprinted with permission from Ross (2010)

In situ TEM has also been used to probe the vapor-liquid-solid (VLS) mechanism for the growth of semiconductor nanowires. One of the simplest forms of nanowire growth is by chemical vapor deposition (CVD), whereby a catalytic droplet (commonly a liquid Au-semiconductor eutectic) is formed on a surface and then exposed to a gas supply of the growth material, as illustrated in Fig. 1.10. Ross and coworkers (2010) from IBM studied semiconductor (Si and Ge) nanowires during the growth process in situ using a UHV-TEM which has been modified to enable chemical vapor deposition (CVD) and evaporation processes in situ (Hammar et al. 1996; Ross 2000). In the Si nanowire growth experiments, a Si (111) wafer cleaned with an HF dip and heated above 1200 °C to desorb any surface oxide was evaporated with Au (the catalytic material), and then mounted in the microscope with the Au-covered side vertical. Wire growth was then initiated by heating the specimen (using direct current) and exposing it to disilane gas. When nanowires grow epitaxially, perpendicular to the surface, they are also

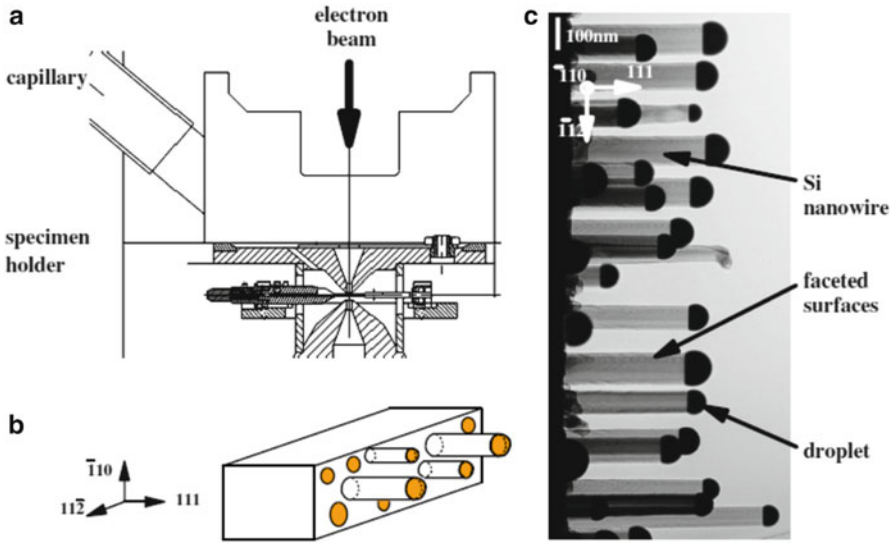

Fig. 1.11 (**a**) The pole-piece region of the UHV TEM showing the specimen holder and the capillary tube through which gas is introduced. (**b**) The specimen, cut from a Si(111) wafer, showing AuSi droplets and the nanowire growth direction. The nanowires are shown as cylinders although their surfaces are actually faceted. (**c**) Typical TEM image of nanowires during growth, in this case at 550 °C and 1.3×10^{-4} Pa (1×10^{-6} Torr) Si_2H_6. Figure reprinted with permission from Ross (2010)

perpendicular to the electron beam, With this geometry, the nanowire/catalyst interface is parallel to the electron beam so that phenomena at the growth interface can be resolved easily (see Fig. 1.11, and Ross 2010).

In situ growth studies of nanowires have led to new insights into the VLS growth mechanism. Ross and coworkers (2005) found that Si nanowires growing from a Si-Au eutectic show periodic sawtooth facets, which are at an angle to the growth direction. The wire surface is not smooth. Rather, growth occurs at a (111) facet at the end of the wire, and the size and shape of this facet oscillates periodically during growth. At higher temperatures and lower pressures, the presence of small amounts of oxygen was found to change the morphology of Si nanowires grown using the VLS process with Au (Kodambaka et al. 2006). Wires of almost constant diameter and several micrometers in length can be formed in the presence of oxygen, in contrast with wires grown in disilane alone, which show significant changes in diameter over sub-micrometer length. Contrary to the conventional VLS growth model assumptions, Au diffusion during nanowire growth determines the length, shape, and sidewall properties of the nanowires (Hannon et al. 2006). Au can diffuse from one catalyst droplet to another during growth, i.e., Au migrates over the surface as well as up and down the nanowire sidewalls, and Ostwald ripening during growth can lead to the termination of growth due to the disappearance of the Au catalyst. Using the same experimental setup, Kim et al. (2008) obtained quantitative

measurements on the nucleation and growth kinetics of Si from a Au-Si eutectic liquid, and by using a simple kinetic model, provided insights into the nanowire growth process.

In some cases, it is also possible to grow nanowires in a high-vacuum TEM without supplying the growth material as a gas precursor. Instead, evaporation from the sample provides the flux required for the growth mechanism to be activated. For example, Stach and coworkers (2003) observed in real-time TEM observations of the growth of GaN nanowires via a self-catalytic VLS mechanism. These nanowires nucleate and grow from Ga droplets formed during thermal decomposition of GaN at elevated temperatures in a vacuum of ~1.3×10^{-5} Pa (1×10^{-7} Torr).

Metals other than Au are also of great interest for VLS growth studies because they allow flexibility in designing electronic properties such as doping type and doping level in as-grown nanowires (Ross 2010). They also provide the opportunity to grow nanowires with different surface structures. Wen et al. (2009) added Al to Au catalysts to raise the eutectic temperature with Si or Ge, and formed compositionally abrupt interfaces in Si-Ge and Si-SiGe heterostructure nanowires using the vapor-solid-solid (VSS) method. Chou et al. (2012) grew Si/Ge nanowires and heterojunctions with compositionally abrupt interfaces using a catalyst based on alloying Ag with Au. Hofmann and coworkers (2008) demonstrated that an environmental TEM with higher base pressure compared to the UHV-TEM can also be used to grow Si nanowires from Pd and Au catalysts.

1.2.4 Windowed Cell Holder Applications

A key limitation in differentially pumped ETEM systems is that the maximum gas pressure allowed is usually not more than 2 kPa (20 mbar), which is about three orders of magnitude lower than the ambient pressure condition at which many applications are concerned. This "pressure gap" can be bridged by the use of closed window gas cell TEM holders, as described in Sect. 1.1. In this section, some of the applications arising from the use of such closed cell systems in the area of solid-gas reaction studies are described. The reader can also refer to a later chapter about how the windowed cell setup can be used to study specimens in their native liquid medium.

Using the MEMS-based nanoreactor developed by Creemer et al. (2008), Yokosawa and coworkers (2012) investigated the (de)hydrogenation behavior of Pd islands at H_2 pressure up to 4.5×10^5 Pa (4.5 bar) and temperature up to 400 °C, and observed, in electron diffraction mode, Pd crystal lattice expansion and shrinkage owing to hydrogenation and dehydrogenation, respectively. Vendelbo et al. (2014) also used a similar MEMS reactor which has been fitted with quantitative mass spectrometry, to analyze gases exiting the nanoreactor, and reaction calorimetry, to study the oscillatory behavior exhibited in catalytic reactions occurring under fixed conditions (in this case, at 10^5 Pa, or 1 bar, of $CO:O_2$:He of 3 %:42 %:55 % ratio and temperatures 659–729 K). Pt nanoparticles, which

catalyze the oxidation of CO, gradually transformed from a more spherical shape toward a more facetted shape as the CO conversion increased rapidly, and transformed back to the more spherical shape on decrease in CO conversion, and retained that shape until CO conversion increased steeply again. Their studies showed a direct coupling between the oscillatory CO conversion behavior and the Pt nanoparticle shape changes.

With an MEMS-based environmental holder developed by Protochips Inc., Ghassemi and coworkers (2014) studied the mechanism of transformation of two-dimensional Ti_3C_2, also known as "MXene", into a TiO_2/carbon hybrid material during oxidation at different temperatures and under different heating rates. The specimens which consisted of delaminated $Ti_3C_2T_x$ (where T stands for the "terminating group" and x is the number of surface groups per Ti_3C_2 unit cell) flakes were dropcast on holder-compatible chips with electron transparent windows, sealed in ambient air, and flash-oxidized (by increasing the temperature stepwise to 950 °C) or slowly heated to 450 °C at a rate of 0.1 °C/s and maintained at 450 °C for 2 h. With flash oxidation, TiO_2 particles were first formed in a planar thin film morphology and subsequently shrank laterally and grew vertically into 3D particles with the anatase phase, whereas slow heating led to the formation of planar nanocrystals of mainly rutile phase.

1.3 Current Status and Outlook

This chapter review illustrates that numerous researchers have contributed virtually since the original construction of the TEM to improving and applying the ability to observe material reactions in an encompassing environment, at the resolutions uniquely available with the transmission electron microscope, and with its improving analytical capability. Moreover, with the increasing development of specimen holders for both windowed and aperture systems, the breadth of experimentation (as illustrated by the compilation in the present text) is only broadening, and at an impressively rapid rate. An update of the analysis summarized in Fig. 1.1 to include the date of the 2014 International Microscopy Congress is shown in Fig. 1.12. It appears that there has been another significant jump in the numbers of in situ TEM publications, and that the trend noticed in Sinclair (2013) has been firmly established. The environmental (gas and liquid) contributions to this trend remain at over 50 %, as alluded in Fig. 1.12b. It is our conclusion that environmental studies in the TEM will continue to grow, both in numbers and in innovation, and that they will provide ever more insight into material reactions of scientific and technological interest.

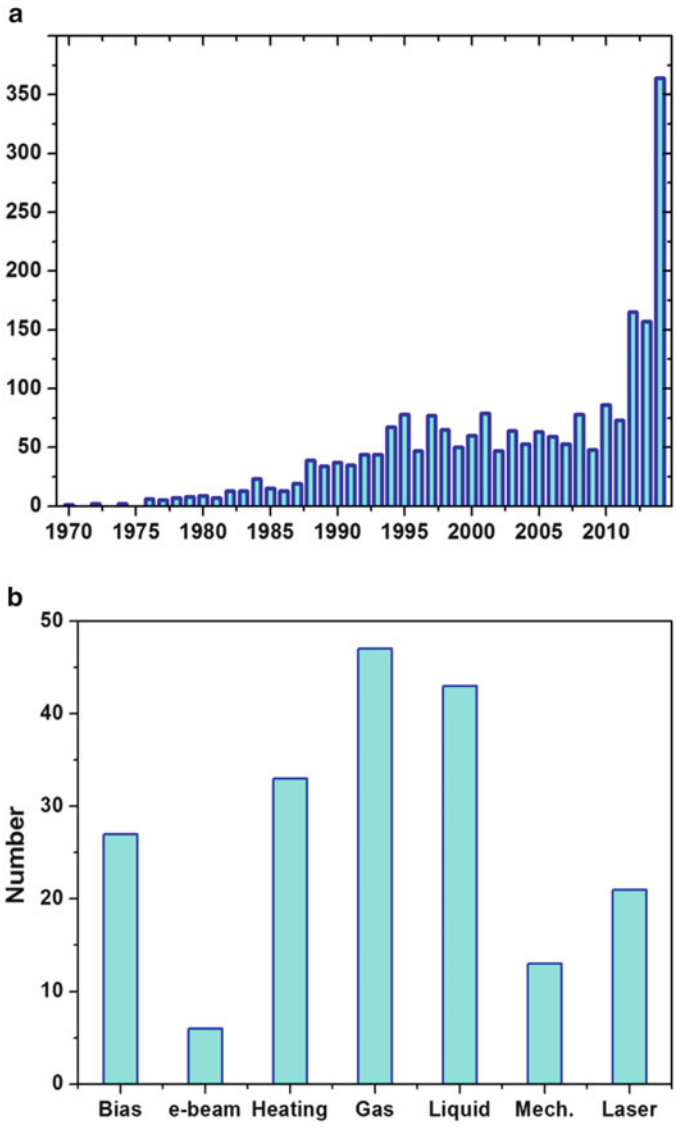

Fig. 1.12 (**a**) Number of publications until 2014 identified using the keywords "in situ", "transmission electron microscopy" and "TEM"; (**b**) Breakdown by various subcategories of in situ papers presented at the 2014 Microscopy and Microanalysis Conference (USA) and the 2014 International Microscopy Congress (Czech Republic). These subcategories are in situ electrical biasing, electron beam heating, thermal heating, gaseous environment, liquid environment, mechanical loading, and laser stimulation

Acknowledgements A.L.K. is grateful for the support from the Stanford Nano Shared Facilities. S.C.L. and R.S. acknowledge funding support from the Center of Nanostructuring for Efficient Energy Conversion (CNEEC) at Stanford University, an Energy Frontier Research Center funded by the U.S. Department of Energy, Office of Science, Office of Basic Energy Sciences under award no. DE-SC0001060. R.S. also acknowledges funding from the National Cancer Institute grant CCNE-T U54CA151459-02.

References

I.M. Abrams, J.W. McBain, A closed cell for electron microscopy. J. Appl. Phys. **15**, 607–609 (1944)

L.F. Allard, S.H. Overbury, W.C. Bigelow, M.B. Katz, D.P. Nackashi, J. Damiano, Novel MEMS-based gas-cell/heating specimen holder provides advanced imaging capabilities for in situ reaction studies. Microsc. Microanal. **18**, 656–666 (2012)

D.L. Allinson, Environmental cell for use in a high voltage electron microscope, in *Proc. 7th Int. Congr. Electron Microscopy*, Grenoble, 1970, pp. 169–170.

D.L. Allinson, Environmental devices in electron microscopy, in *Principles and Techniques of Electron Microscopy Biological Applications*, ed. by M.A. Hayat, vol. 5 (Van Nostrand Reinhold, New York, 1975)

D.H. Alsem, R.R. Unocic, G.M. Veith, K.L. More, N.J. Salmon, In-situ Liquid and Gas Transmission Electron Microscopy of Nano-Scale Materials. Microsc. Microanal. **18**(Suppl 2), 1158–1159 (2012)

P.B. Amama, C.L. Pint, L. McJilton, S.M. Kim, E.A. Stach, P.T. Murray, R.H. Hauge, B. Maruyama, Role of water in super growth of single-walled carbon nanotube carpets. Nano Lett. **9**, 44–49 (2009)

S. Arrii, F. Morfin, A.J. Renouprez, J.L. Rousset, Oxidation of CO on gold supported catalysts prepared by laser vaporization: Direct evidence of support contribution. J. Am. Chem. Soc. **126**, 1199–1205 (2004)

R.T.K. Baker, P.S. Harris, Controlled atmosphere electron microscopy. J. Physics E: Sci. Instruments **5**, 793–797 (1972)

R.T.K. Baker, M.A. Barber, P.S. Harris, F.S. Feates, R.J. Waite, Nucleation and growth of carbon deposits from the nickel catalyzed decomposition of acetylene. J. Catalysis **26**, 51–62 (1972a)

R.T.K. Baker, F.S. Feates, P.S. Harris, Continuous electron microscopic observation of carbonaceous deposits formed on graphite and silica surfaces. Carbon **10**, 93–96 (1972b)

R.T.K. Baker, P.S. Harris, R.B. Thomas, R.J. Waite, Formation of filamentous carbon from iron, cobalt and chromium catalyzed decomposition of acetylene. J. Catalysis **30**, 86–95 (1973)

R.T.K. Baker, In situ electron microscopy studies of catalyst particle behavior. Catal. Rev. Sci. Eng. **19**(2), 161–209 (1979)

R.T.K. Baker, Catalytic growth of carbon filaments. Carbon **27**, 315–323 (1989)

R.T.K. Baker, Electron microscopy studies of the catalytic growth of carbon filaments, in *Carbon Fibers Filaments and Composites*, ed. by J.L. Figueiredo et al. (Kluwer Academic, Dordrecht, 1990), pp. 405–439

A. Baldi, T. Narayan, A.L. Koh, J.A. Dionne, In situ detection of hydrogen-induced phase transitions in individual palladium nanocrystals. Nature Mater. **13**(12), 1143–1148 (2014)

E.D. Boyes, P.L. Gai, L.G. Hanna, Controlled environment (ECELL) TEM for dynamic in-situ reaction studies with HREM lattice imaging. Mat. Res. Soc. Symp. Proc. **404**, 53–60 (1996)

E.D. Boyes, P.L. Gai, Environmental high resolution electron microscopy and applications to chemical science. Ultramicroscopy **67**, 219–232 (1997)

E.D. Boyes, M.R. Ward, L. Lari, P.L. Gai, ESTEM imaging of single atoms under controlled temperature and gas environment conditions in catalyst reaction studies. Ann. Phys. (Berlin) **525**(6), 423–429 (2013)

E.D. Boyes, P.L. Gai, Aberration corrected environmental STEM (AC ESTEM) for dynamic in-situ gas reaction studies of nanoparticle catalysts. Journal of Physics: Conference Series **522**, 012004 (2014a)

E.D. Boyes, P.L. Gai, Visualising reacting single atoms under controlled conditions: Advances in atomic resolution in situ environmental (scanning) transmission electron microscopy (E(S) TEM). C. R. Physique **15**, 200–213 (2014b)

E.P. Butler, K.F. Hale, In situ studies of gas-solid reactions, in *Dynamic Experiments in the Electron Microscope*, ed. by A.M. Glauert. Practical Methods in Electron Microscopy, vol. 9 (North-Holland, Amsterdam, 1981a)

E.P. Butler, K.F. Hale, Wet cell microscopy, in *Dynamic Experiments in the Electron Microscope*, ed. by A.M. Glauert. Practical Methods in Electron Microscopy, vol. 9 (North-Holland, Amsterdam, 1981b)

M. Cargnello, V.V.T. Doan-Nguyen, T.R. Gordon, R.E. Diaz, E.A. Stach, R.J. Gorte, P. Fornasiero, C.B. Murray, Control of metal nanocrystal size reveals metal-support interface role for ceria catalysts. Science **341**, 771–773 (2013)

F. Cavalca, A.B. Laursen, B.E. Kardynal, R.E. Dunin-Borkowski, S. Dahl, J.B. Wagner, T.W. Hansen, In situ transmission electron microscopy of light-induced photocatalytic reactions. Nanotechnology **23**, 075705 (2012) (6 pp.)

F. Cavalca, A.B. Laursen, J.B. Wagner, C.D. Damsgaard, I. Chorkendorff, T.W. Hansen, Light-induced reduction of cuprous oxide in an environmental transmission electron microscope. ChemCatChem **5**, 2667–2672 (2013)

D. Chattopadhyay, I. Galeska, F. Papadimitrakopoulos, Metal-assisted organization of shortened carbon nanotubes in monolayer and multilayer forest assemblies. J. Am. Chem. Soc. **123**, 9451–9452 (2001)

S. Chenna, P.A. Crozier, Operando transmission electron microscopy: A technique for detection of catalysis using electron energy-loss spectroscopy in the transmission electron microscope. ACS Catal. **2**, 2395–2402 (2012)

W.B. Choi, D.S. Chung, J.H. Kang, H.Y. Kim, Y.W. Jin, I.T. Han, Y.H. Lee, J.E. Jung, N.S. Lee, G.S. Park, J.M. Kim, Fully sealed, high-brightness carbon-nanotube field-emission display. Appl. Phys. Lett. **75**, 3129–3131 (1999)

Y.-C. Chou, C.-Y. Wen, M.C. Reuter, D. Su, E.A. Stach, F.M. Ross, Controlling the growth of Si/Ge nanowires and heterojunctions using silver-gold alloy catalysts. ACS Nano **6**, 6407–6415 (2012)

J.F. Creemer, S. Helveg, G.H. Hoveling, S. Ullmann, A.M. Molenbroek, P.M. Sarro, H.W. Zandbergen, Atomic-scale electron microscopy at ambient pressure. Ultramicroscopy **108**, 993–998 (2008)

P.A. Crozier, R. Sharma, A.K. Datye, Oxidation and reduction of small palladium particles on silica. Microsc. Microanal. **4**, 278–285 (1998)

P.A. Crozier, R. Wang, R. Sharma, In situ environmental TEM studies of dynamic changes in cerium-based oxides nanoparticles during redox processes. Ultramicroscopy **108**, 1432–1440 (2008)

P.A. Crozier, S. Chenna, In situ analysis of gas composition by electron energy-loss spectroscopy for environmental transmission electron microscopy. Ultramicroscopy **111**, 177–185 (2011)

W.A. de Heer, A. Châtelain, D. Ugarte, A carbon nanotube field-emission electron source. Science **270**, 1179–1180 (1995)

N. de Jonge, D.B. Peckys, G.J. Kremers, D.W. Piston, Electron microscopy of whole cells in liquid with nanometer resolution. Proc. Natl. Acad. Sci. U. S. A. **106**, 2159–2164 (2009)

N. de Jonge, W.C. Bigelow, G.M. Veith, Atmospheric pressure scanning transmission electron microscopy. Nano Lett. **10**, 1028–1031 (2010)

N. de Jonge, F.M. Ross, Electron microscopy of specimens in liquid. Nature Nano **6**, 695–704 (2011)

M. Doi, M. Yoshida, M. Nonoyama, S. Arai, T. Imura, A modified window-type environmental cell for use with HVEM, in *Proc. 5th Int. Conf. High Voltage Electron Microscopy,* Kyoto, 1977, p. 155.

R.C. Doole, G.M. Parkinson, J.M. Stead, High resolution gas reaction cell for the JEM 4000. Institute of Physics Conference Series **119**, 157–160 (1991)
G. Dupouy, Electron microscopy at very high voltages, in *Advances in optical and electron microscopy*, ed. by R. Barer, V.E. Cosslett, vol. 2 (Academic Press, London, 1968), p. 167
J. Escaig, C. Sella, Cellule porte-objet permettent l'observation des specimens chauffes sous atmosphere controlee, in *Proc. 6th Int. Cong. Electron Microsc*., 1966, vol. 1, p. 177
J. Escaig, C. Sella, Application d'une nouvelle cellule a atmosphere controlee a l'etude de quelques problems d'oxydation et de depot par decomposition termique en phase vapeur, in *Proc. 4th Europ. Conf. Electron Microsc.,* 1968, vol. 1, 241.
J. Escaig, C. Sella, Nouvelle microchambre pour observation en microscopie-electronique, a haute temperature et sous atmosphere controlee. C. r. hebd. Séanc. Acad. Sci., Paris **268**, 532 (1969)
J. Escaig, C. Sella, Observation in situ au microscope electronique de l'oxydation desc couches minces metalliques. C. r. hebd. Séanc. Acad. Sci., Paris **274**, 27 (1972)
F.S. Feates, H. Morley, P.S. Robinson, Controlled atmosphere electron microscopy, in *Proc. 7th Int. Congr. Electron Microscopy*, Grenoble, 1970, pp. 295–296
H.M. Flower, High voltage electron microscopy of environmental reactions. J. Micros. **97**, 171–190 (1973)
H.M. Flower, P.R. Swann, An *in situ* study of Titanium oxidation by high voltage electron microscopy. Acta Metall. **22**, 1339–1347 (1974)
H.M. Flower, B.A. Wilcox, *In situ* oxidation of Ni-30 Wt% Cr and TDNiCr in the high voltage electron microscope. Corros. Sci. **17**, 253–264 (1977)
J.R. Fryer, Oxidation of graphite catalyzed by palladium. Nature **220**, 1121–1122 (1968a)
J.R. Fryer, The direct observation of gas solid reactions inside the electron microscope. Siemens Review **35**, 13 (1968b)
Q. Fu, H. Saltsburg, M. Flytzani-Stephanopoulos, Active nonmetallic Au and Pt species on ceria-based water-gas shift catalysts. Science **301**, 935–938 (2003)
H. Fujita, M. Komatsu, I. Ishikawa, A universal environmental cell for a 3MV-class electron microscope and its applications to metallurgical sciences. Jap. J. Appl. Phys. **15**(11), 2221–2228 (1976)
A. Fukami, K. Adachi, A new method of preparation of a self-perforated micro plastic grid and its application (I). J. Electron Microscopy **14**(2), 112–118 (1965)
A. Fukami, K. Adachi, M. Katoh, On a study of new micro plastic grid and its applications, in *Proc. 6th Int. Congr. Electron Microscopy*, Kyoto, 1966, pp. 262–264
A. Fukami, K. Adachi, M. Katoh, Micro grid techniques (continued) and their contribution to specimen preparation techniques for high resolution work. J. Electron Microscopy **21**(2), 99–108 (1972)
P.L. Gai, E.D. Boyes, Environmental high resolution electron microscopy in materials science, in *In-situ microscopy in materials research*, ed. by P.L. Gai (Kluwer Academic, Boston, 1997)
P.L. Gai, E.L. Boyes, S. Helveg, P.L. Hansen, S. Giorgio, C.R. Henry, Atomic-resolution environmental transmission electron microscopy for probing gas-solid reactions in heterogeneous catalysis. MRS Bulletin **32**, 1044–1050 (2007)
P.L. Gai, R. Sharma, F.M. Ross, Environmental (S)TEM studies of gas-liquid-solid interactions under reaction conditions. MRS Bulletin **33**, 107–114 (2008)
P.L. Gai, E.D. Boyes, Advances in atomic resolution in situ environmental transmission electron microscopy and 1Å aberration corrected in situ electron microscopy. Microsc. Res. Tech. **72**, 153–164 (2009)
E.J. Gallegos, Gas reactor for hot stage transmission electron microscopy. Rev. Sci. Instrum. **35** (9), 1123–1124 (1964)
H. Ghassemi, W. Harlow, O. Mashtalir, M. Beidaghi, M.R. Lukatskaya, Y. Gogotsi, M.L. Taheri, In situ environmental transmission electron microscopy study of oxidation of two-dimensional Ti_3C_2 and formation of carbon-supported TiO_2. J. Mater. Chem. A **2**, 14339–14343 (2014)
S. Giorgio, S. Sao Joao, S. Nitsche, D. Chaudanson, G. Sitja, C.R. Henry, Environmental electron microscopy (ETEM) for catalysts with a closed E-cell with carbon windows. Ultramicroscopy **106**, 503–507 (2006)

M. Goringe, A. Rawcliffe, A. Burden, J. Hutchison, R. Doole, Observations of solid-gas reactions by means of high-resolution transmission electron microscopy. Faraday Discuss. **105**, 85–102 (1996)

M. Haider, S. Uhlemann, E. Schwan, H. Rose, B. Kabius, K. Urban, Electron microscopy image enhanced. Nature **392**, 768–769 (1998a)

M. Haider, H. Rose, S. Uhlemann, E. Schwan, B. Kabius, K. Urban, A spherical aberration-corrected 200 kV transmission electron microscope. Ultramicroscopy **75**, 53–60 (1998b)

M. Hammar, F. LeGoues, J. Tersoff, M.C. Reuter, R.M. Tromp, In situ ultrahigh vacuum transmission electron microscopy studies of hetero-epitaxial growth. I. Si(009)/Ge. Surf. Sci. **349**, 129–144 (1996)

P.L. Hansen, J.B. Wagner, S. Helveg, J.R. Rostrup-Nielsen, B.S. Clausen, H. Topsøe, Atom-resolved imaging of dynamic shape changes in supported copper nanocrystals. Science **295**, 2053–2055 (2002)

P.L. Hansen, S. Helveg, A.K. Datye, Atomic-scale imaging of supported metal nanocluster catalysts in the working state. Adv. Catal. **50**, 77–95 (2006)

T.W. Hansen, J.B. Wagner, P.L. Hansen, S. Dahl, H. Topsøe, C.J.H. Jacobson, Atomic-resolution in situ transmission electron microscopy of a promoter of a heterogeneous catalyst. Science **294**, 1508–1510 (2001)

T.W. Hansen, J.B. Wagner, R.E. Dunin-Borkowski, Aberration-corrected and monochromated environmental transmission electron microscopy: challenges and prospects for materials science. Mater. Sci. Technol. **26**(11), 1338–1344 (2010)

T.W. Hansen, J.B. Wagner, Environmental transmission electron microscopy in an aberration-corrected environment. Micros. Microanal. **18**, 684–690 (2012)

J.B. Hannon, S. Kodambaka, F.M. Ross, R.M. Tromp, The influence of the surface migration of gold on the growth of silicon nanowires. Nature **440**, 69–71 (2006)

M. Haruta, Size- and support-dependency in the catalysis of gold. Catal. Today **36**, 153–166 (1997)

A.R. Harutyunyan, G. Chen, T.M. Paronyan, E.M. Pigos, O.A. Kuznetsov, K. Hewaparakrama, S.M. Kim, D. Zakharov, E.A. Stach, G.U. Sumanasekera, Preferential growth of single-walled carbon nanotubes with metallic conductivity. Science **326**, 116–120 (2009)

H. Hashimoto, K. Tanaka, E. Yoda, A specimen treating device at high temperature for the electron microscope. J. Electron Microscopy **6**, 8–11 (1958)

H. Hashimoto, T. Naiki, T. Eto, K. Fujiwara, M. Watanabe, Y. Nagahama, Specimen chamber for observing the reaction process with gas at high temperature, in *Sixth Int. Congress for Electron Microscopy*, 1966, pp. 181–182.

H. Hashimoto, T. Naiki, T. Eto, K. Fujiwara, High temperature gas reaction specimen chamber for an electron microscope. Jpn. J. Appl. Phys. **7**(8), 946–952 (1968)

S. Hashimoto, S. Urai, H. Yotsumoto, J. Sawamori, Morphology and structure of Mo oxides formed by thermal decomposition of the ammonium salt, in *Proc. 7th Int. Congr. Electron Microscopy*, Berlin, 1970, p. 87.

K. Hata, D.N. Fubata, K. Mizuno, T. Namai, M. Yumara, S. Iijima, Water-assisted highly efficient synthesis of impurity-free single-walled carbon nanotubes. Science **306**, 1362–1364 (2004)

T. Hayashi, K. Tanaka, M. Haruta, Selective vapor-phase epoxidation of propylene over Au/TiO_2 catalysts in the presence of oxygen and hydrogen. J. Catal. **178**, 566–575 (1998)

H.G. Heide, Electron microscopic observation of specimens under controlled gas pressure. J. Cell. Bio. **13**, 147–152 (1962)

S. Helveg, C. Lopez-Cartes, J. Sehested, P.L. Hansen, B.S. Clausen, J.R. Rostrup-Nielsen, F. Abild-Pedersen, J.K. Nørskov, Atomic-scale imaging of carbon nanofibre growth. Nature **427**, 426–429 (2004)

B.J. Hinds, N. Chopra, T. Rantell, R. Andrews, V. Gavalas, L.G. Bachas, Aligned multiwalled carbon nanotube membranes. Science **303**, 62–65 (2004)

S. Hofmann, S. Sharma, C.T. Wirth, F. Cervantes-Sodi, C. Ducati, T. Kasama, R.E. Dunin-Borkowski, J. Drucker, P. Bennett, J. Robertson, Ledge-flow-controlled catalyst interface dynamics during Si nanowire growth. Nature Mater. **7**, 372–375 (2008)

S. Hofmann, R. Blume, C.Y. Wirth, M. Cantoro, R. Sharma, C. Ducati, M. Hävecker, S. Zafeiratos, P. Schnoerch, A. Oestereich, D. Teschner, M. Albrecht, A. Knop-Gericke, R. Schlögl, J. Robertson, State of transition metal catalysts during carbon nanotube growth. J. Phys. Chem. C **113**, 1648–1656 (2009)

S. Iijima, Helical microtubules of graphitic carbon. Nature **354**, 56–58 (1991)

T. Ito, K. Hiziya, A specimen reaction device for the electron microscope and its applications. J. Electron Microscopy **6**, 4–8 (1958)

J.R. Jinschek, S. Helveg, Image resolution and sensitivity in an environmental transmission electron microscope. Micron **43**, 1156–1168 (2012)

J.R. Jinschek, Advances in the environmental transmission electron microscope (ETEM) for nanoscale in situ studies of gas–solid interactions. Chem. Commun. **50**, 2696–2706 (2014)

T. Kamino, T. Yaguchi, M. Konno, A. Watabe, T. Marukawa, T. Mina, K. Kuroda, H. Saka, S. Arai, H. Makino, Y. Suzuki, K. Kishita, Development of a gas injection/specimen heating holder for use with transmission electron microscope. J. Electron. Microsc. **54**, 497–503 (2005)

T. Kamino, T. Yaguchi, M. Konno, A. Watabe, Y. Nagakubo, Development of a specimen heating holder with an evaporator and gas injector and its application for catalyst. J. Electron Microsc. **55**, 245–252 (2006)

T. Kawasaki, K. Ueda, M. Ichihashi, T. Tanji, Improvement of windowed type environmental-cell transmission electron microscope for in situ observation of gas-solid interactions. Re. Sci. Instrum. **80**, 113701 (2009)

B.J. Kim, J. Tersoff, S. Kodambaka, M.C. Reuter, E.A. Stach, F.M. Ross, Kinetics of individual nucleation events observed in nanoscale vapor–liquid–solid growth. Science **322**, 1070–1073 (2008)

S.M. Kim, C.L. Pint, P.B. Amama, D.N. Zakharov, R.H. Hauge, B. Maruyama, E.A. Stach, Evolution in catalyst morphology leads to carbon nanotube growth termination. J. Phys. Chem. Lett. **1**, 918–922 (2010)

K.L. Klein, I.M. Anderson, N. de Jonge, Transmission electron microscopy with a liquid flow cell. J. Microscopy **242**, 117–123 (2011)

S. Kodambaka, J.B. Hannon, R.M. Tromp, F.M. Ross, Control of Si nanowire growth by oxygen. Nano Lett. **6**, 1292–1296 (2006)

A.L. Koh, E. Gidcumb, O. Zhou, R. Sinclair, Observations of carbon nanotube oxidation in an aberration-corrected environmental transmission electron microscope. ACS Nano **7**, 2566–2572 (2013)

Y. Kuwauchi, H. Yoshida, T. Akita, M. Haruta, S. Takeda, Intrinsic catalytic structure of gold nanoparticles supported on TiO_2. Angew. Chem. Int. Ed. **51**, 7729–7733 (2012)

Y. Kuwauchi, S. Takeda, H. Yoshida, K. Sun, M. Haruta, H. Kohno, Stepwise displacement of catalytically active gold nanoparticles on cerium oxide. Nano Lett. **13**, 3073–3077 (2013)

T.C. Lee, D.K. Dewald, J.A. Eades, I.M. Robertson, H.K. Birnbaum, An environmental cell transmission electron microscope. Rev. Sci. Instrum. **62**, 1438–1444 (1991)

R.-J. Liu, P.A. Crozier, C.M. Smaith, D.A. Hucul, J. Blackson, G. Salaita, In situ electron microscopy studies of the sintering of palladium nanoparticles on alumina during catalyst regeneration processes. Microsc. Microanal. **10**, 77–85 (2004)

G. Lolli, L.A. Zhang, L. Balzano, N. Sakulchaicharoen, Y.Q. Tan, D.E. Resasco, Tailoring (n, m) structure of single-walled carbon nanotubes by modifying reaction conditions and the nature of the support of CoMo catalysts. J. Phys. Chem. B **110**, 2108–2115 (2006)

C. López-Cartes, S. Bernal, J.J. Calvino, M.A. Cauqui, G. Blanco, J.A. Pérez-Omil, J.M. Pintado, S. Helveg, P.L. Hansen, In situ transmission electron microscopy investigation of Ce(IV) and Pr(IV) reducibility in a Rh (1%)/$Ce_{0.8}Pr_{0.2}O_{2-x}$ catalyst. Chem. Commun. **5**, 644–645 (2003)

L. Marton, Electron microscopy of biological objects. Nature **133**, 911 (1934)

L. Marton, La microscopie electronique des objets biologiques. Bull. Acad. r. Belg. Cl. Sci. **21**, 553 (1935)

M.L. McDonald, J.M. Gibson, F.C. Unterwald, Design of an ultrahigh-vacuum specimen environment for high-resolution transmission electron microscopy. Rev. Sci. Instrum. **60**(4), 700–707 (1989)

B.K. Miller, P.A. Crozier, System for in situ UV-visible illumination of environmental transmission electron microscopy samples. Microsc. Microanal. **19**, 461–469 (2013)
J.C. Mills, A.F. Moodie, Multipurpose high resolution stage for the electron microscope. Rev. Sci. Instrum. **39**, 962–969 (1968)
A.M. Molenbroek, S. Helveg, H. Topsøe, B.S. Clausen, Nano-particles in heterogeneous catalysis. Top Catal **52**, 1303–1311 (2009)
T.W. Odom, J.-L. Huang, P. Kim, C.M. Lieber, Atomic structure and electronic properties of single-walled carbon nanotubes. Nature **391**, 62–64 (1998)
G.M. Parkinson, High resolution, in-situ controlled atmosphere transmission electron microscopy (CATEM) oh heterogeneous catalysts. Catal. Lett. **2**, 303–308 (1989)
D.F. Parsons, Structure of wet specimens in electron microscopy. Science **186**, 407–414 (1974)
D.F. Parsons, V.R. Matricardi, R.C. Moretz, J.N. Turner, *Electron microscopy and diffraction of wet unstained and unfixed biological objects, in: Advances in Biological and Medical Physics (Volume 15)*. Edited by J. H. Lawrence, J (W Gofman and T. L. Hayes. Academic Press, New York, 1974)
E.A. Ring, N. de Jonge, Microfluidic System for Transmission Electron Microscopy. Microsc. Microanal. **16**, 622–629 (2010)
A.G. Rinzler, J.H. Hafner, P. Nikolaev, L. Lou, S.G. Kim, D. Tomimek, P. Nordlander, D.T. Colbert, R.E. Smalley, Unraveling nanotubes: Field emission from an atomic wire. Science **269**, 1550–1553 (1995)
N.M. Rodriguez, S.G. Oh, W.B. Downs, P. Pattabiraman, R.T.K. Baker, An atomic oxygen environmental cell for a transmission electron microscope. Rev. Sci. Instrum. **61**(7), 1863–1868 (1990)
F.M. Ross, J.M. Gibson, Dynamic observations of interface propagation during silicon oxidation. Phys. Rev. Lett. **68**(11), 1782–1786 (1992)
F.M. Ross, Growth processes and phase transformations studied by in situ transmission electron microscopy. IBM J. Res. Develop. **44**, 489–501 (2000)
F.M. Ross, J. Tersoff, M.C. Reuter, Sawtooth faceting in silicon nanowires. Phys. Rev. Lett. **95**, 146104 (2005)
F.M. Ross, Controlling nanowire structures through real time growth studies. Rep. Prog. Phys. **73**, 114501 (2010) (21 pp.)
F.M. Ross, C.-Y. Wen, S. Kodambaka, B.A. Wacser, M.C. Reuter, E.A. Stach, The growth and characterization of Si and Ge nanowires grown from reactive metal catalysts. Phil. Mag. **90**, 4679–4778 (2010)
V.E. Ruska, Beitrag zur ubermikroskopischen Abbildung bei höheren Drucken. Zolloid-Z **100**, 212–219 (1942)
A. Sandoval, A. Gomez-Cortes, R. Zanella, G. Diaz, J.M. Saniger, Gold nanoparticles: Support effects for the WGS reaction. J. Mol. Cat. A: Chemical **278**, 200–208 (2007)
R. Sharma, K. Weiss, M. McKelvy, W. Glaunsinger, Gas reaction chamber for gas–solid interaction studies by high resolution transmission electron microscopy, in *Proceedings of the 52nd Annual Meeting of the Microscopy Society of America*, 1994, pp. 494–495
R. Sharma, K. Weiss, Development of a TEM to study in situ structural and chemical changes at an atomic level during gas-solid interactions at elevated temperatures. Micros. Res. Tech. **42**, 270–280 (1998)
R. Sharma, Design and applications of environmental cell transmission electron microscope for in situ observations of gas-solid reactions. Microsc. Microanal. **7**, 494–506 (2001)
R. Sharma, Z. Iqbal, In situ observations of carbon nanotube formation using environmental transmission electron microscopy. Appl. Phys. Lett. **84**, 990–992 (2004)
R. Sharma, P. Crozier, Z.C. Kang, L. Eyring, Observation of dynamic nanostructural and nanochemical changes in ceria-based catalysts during in-situ reduction. Philosophical Magazine **84**, 2731–2747 (2004)
R. Sharma, An environmental transmission electron microscope for in situ synthesis and characterization of nanomaterials. J. Mater. Res. **20**(7), 1695–1707 (2005)

R. Sharma, P.A. Crozier, Environmental transmission electron microscopy in nanotechnology, in *Handbook of Microscopy for Nanotechnology*, ed. by N. Yao, Z.L. Wang (Kluwer Academic Publishers, New York, 2005), pp. 531–565

R. Sharma, P. Rez, M.M.J. Treacy, S.J. Stuart, In situ observation of the growth mechanisms of carbon nanotubes under diverse reaction conditions. J. Electron Microsc. **54**, 231–237 (2005)

R. Sharma, P. Rez, P. Brown, G. Du, M.M.J. Treacy, Dynamic observations of the effect of pressure and temperature conditions on the selective synthesis of carbon nanotubes. Nanotechnology **18**, 125602 (2007) (8pp)

D. Shindo, K. Takahashi, Y. Murakami, K. Yamazaki, S. Deguchi, H. Suga, Y. Kondo, Development of a multifunctional TEM specimen holder equipped with a piezodriving probe and a laser irradiation port. J Electron Microsc **58**, 245–249 (2009)

S.B. Simonsen, I. Chorkendorff, S. Dahl, M. Skoglundh, J. Sehested, S. Helveg, Direct observations of oxygen-induced platinum nanoparticle ripening studied by in situ TEM. J. Am. Chem. Soc. **132**, 7968–7975 (2010)

R. Sinclair, T. Yamashita, M.A. Parker, K.B. Kim, K. Holloway, A.F. Schwartzman, The development of in situ high resolution electron microscopy. Acta Crystallogr. Sec. A **44**, 965–975 (1988)

R. Sinclair, In situ high-resolution transmission electron microscopy of material reactions. MRS Bulletin **38**, 1065–1071 (2013)

E.A. Stach, P. Pauzauskie, T. Kuykendall, J. Goldberger, P. Yang, Watching GaN nanowires grow. Nano Lett. **3**, 867–869 (2003)

H. Sugie, M. Tanemura, V. Filip, K. Iwata, K. Takahashi, F. Okuyama, Carbon nanotubes as electron source in an X-Ray tube. Appl. Phys. Lett. **78**, 2578–2580 (2001)

P.R. Swann, N.J. Tighe, High voltage microscopy of gas oxide reactions. Jernkont. Annaler **155**, 497–501 (1971)

P.R. Swann, High voltage microscope studies of environmental reactions in electron microscopy and structure of materials, in *Proceedings of the Fifth International Materials Symposium, September 13-17, 1971*, ed. by G. Thomas, R.M. Fulrath, R.M. Fisher (University of California Press, Berkeley, 1972), pp. 878–904

P.R. Swann, N.J. Tighe, Performance of a differentially pumped environmental cell, in *The AEI EM7. Proc. Fifth European Congress on Electron, Microscopy*, 1972, pp. 360–361

P.R. Swann, G. Thomas, N.J. Tighe, In situ observations of the nitriding of tantalum. J. Microscopy **97**, 24–257 (1973)

P.R. Swann, N.J. Tighe, High voltage microscopy of the reduction of hematite to magnetite. Metallurgical Transactions B **8B**, 479–487 (1977)

N. Takahashi, T. Takeyama, K. Ito, T. Ito, K. Mihama, M. Watanabe, High temperature furnace for the electron microscope. J. Electron Microscopy **4**, 16–23 (1956)

S. Takeda, H. Yoshida, Atomic-resolution environmental TEM for quantitative in-situ microscopy in materials science. Microscopy **62**(1), 193–203 (2013)

S. Takeda, Y. Kuwauchi, H. Yoshida, Environmental transmission electron microscopy for catalyst materials using a spherical aberration corrector. Ultramicroscopy **151**, 178–190 (2015)

N. Tanaka, J. Usukura, M. Kusunoki, Y. Saito, K. Sasaki, T. Tanji, S. Muto, S. Arai, Development of an environmental high-voltage electron microscope for reaction science. Microscopy **62**(1), 205–215 (2013)

N. Tanaka, J. Usukura, M. Kusunoki, Y. Saito, K. Sasaki, T. Tanji, S. Muto, S. Arai, Development of an environmental high voltage electron microscope and its application to nano and bio-materials. Journal of Physics: Conference Series **522**, 012008 (2014)

P.C. Tiemeijer, Measurement of Coulomb interactions in an electron beam monochromator. Ultramicroscopy **78**, 53–62 (1999)

T. Uchiyama, H. Yoshida, Y. Kuwauchi, S. Ichikawa, S. Shimada, M. Haruta, S. Takeda, Systematic morphology changes of gold nanoparticles supported on CeO_2 during CO oxidation. Angew. Chem. Int. Ed. **50**, 10157–10160 (2011)

S.B. Vendelbo, C.F. Elkjær, H. Falsig, I. Puspitasari, P. Dona, L. Mele, B. Morana, B.J. Nelissen, R. van Rijn, J.F. Creemer, P.J. Kooyman, S. Helveg, Visualization of oscillatory behaviour of Pt nanoparticles catalysing CO oxidation. Nat. Mater. **13**, 884–890 (2014)

P.C.K. Vesborg, I. Chorkendorff, I. Knudsen, O. Balmes, J. Nerlov, A.M. Molenbroek, B.S. Clausen, S. Helveg, Transient behavior of Cu/ZnO-based methanol synthesis catalysts. J. Catal. **262**, 65–72 (2009)

J.B. Wagner, P.L. Hansen, A.M. Molenbroek, H. Topsøe, B.S. Clausen, S. Helveg, In situ electron energy loss spectroscopy studies of gas-dependent metal-support interactions in Cu/ZnO catalysts. J. Phys. Chem. B **107**, 7753–7758 (2003)

J.B. Wagner, F. Cavalca, C.D. Damsgaard, L.D.L. Duchstein, T.W. Hansen, Exploring the environmental transmission electron microscope. Micron **43**, 1169–1175 (2012)

Q.H. Wang, A.A. Setlur, J.M. Lauerhaas, J.Y. Dai, E.W. Seelig, R.P.H. Chang, A Nanotube-Based Field-Emission Flat Panel Display. Appl. Phys. Lett. **72**, 2912–2913 (1998)

R. Wang, P.A. Crozier, R. Sharma, J.B. Adas, Measuring the redox activity of individual catalytic particles in cerium-based oxides. Nano Lett. **8**(3), 962–967 (2008)

R. Wang, P.A. Crozier, R. Sharma, Structural transformation in ceria nanoparticles during redox processes. J. Phys. Chem. C **113**, 5700–5704 (2009)

P.R. Ward, R.F. Mitchell, A facility for electron microscopy of specimens in controlled environments. Journal of Physics E: Scientific Instruments **5**, 160–162 (1972)

C.-Y. Wen, M.C. Reuter, J. Bruley, J. Tersoff, S. Kodambaka, E.A. Stach, F.M. Ross, Formation of compositionally abrupt axial heterojunctions in Si/Ge nanowires. Science **326**, 1247–1250 (2009)

J.W.G. Wilder, C. VenemaL, A.G. Rinzler, R.E. Smalley, C. Dekker, Electronic structure of atomically resolved carbon nanotubes. Nature **391**, 59–62 (1998)

W.D. Williams, M. Shekhar, W.-S. Lee, V. Kispersky, W.N. Delgass, F.H. Ribeiro, S.M. Kim, E.A. Stach, J.T. Miller, L.F. Allard, Metallic corner atoms in gold clusters supported on rutile are the dominant active site during water-gas shift catalysis. J. Am. Chem. Soc. **132**, 14018–14020 (2010)

M.J. Williamson, R.M. Tromp, P.M. Vereecken, F.M. Ross, Dynamic microscopy of nanoscale cluster growth at solid-liquid interface. Nat. Mat. **2**, 532–536 (2003)

T. Yaguchi, M. Suzuki, A. Watabe, Y. Nagakubo, K. Ueda, T. Kamino, Development of a high temperature–atmospheric pressure environmental cell for high-resolution TEM. J. Electron Microsc. (Tokyo) **60**(3), 217–225 (2011)

T. Yokosawa, T. Alan, G. Pandraud, B. Dam, H. Zandbergen, In-situ TEM on (de)hydrogenation of Pd at 0.5–4.5 bar hydrogen pressure and 20–400°C. Ultramicroscopy **112**, 47–52 (2012)

H. Yoshida, S. Takeda, Image formation in a transmission electron microscope equipped with an environmental cell: Single-walled carbon nanotubes in source gases. Phys. Rev. B **72**, 195428 (2005)

H. Yoshida, T. Uchiyama, S. Takeda, Environmental Transmission Electron Microscopy Observations of Swinging and Rotational Growth of Carbon Nanotubes. Jap. J. Appl. Phys. **46**, L917–L919 (2007)

H. Yoshida, S. Takeda, T. Uchiyama, H. Kohno, Y. Homma, Atomic-scale in-situ observation of carbon nanotube growth from solid state iron carbide nanoparticles. Nano Lett. **8**, 2082–2086 (2008)

H. Yoshida, T. Shimizu, T. Uchiyama, H. Kohno, Y. Homma, S. Takeda, Atomic-scale analysis on the role of molybdenum in iron catalyzed carbon nanotube growth. Nano Lett. **9**, 3810–3815 (2009)

H. Yoshida, Y. Kuwauchi, J.R. Jinschek, K. Sun, S. Tanaka, M. Kohyama, S. Shimada, M. Haruta, S. Takeda, Visualizing gas molecules interacting with supported nanoparticulate catalysts at reaction conditions. Science **335**, 317–319 (2012)

L. Zhang, B.K. Miller, P.A. Crozier, Atomic level in situ observation of surface amorphization in anatase nanocrystals during light irradiation in water vapor. Nano Lett. **13**, 679–684 (2013)

Y. Zhang, Y. Li, W. Kim, D. Wang, H. Dai, Imaging as-grown single-walled carbon nanotubes originated from isolated catalytic nanoparticles. Appl. Phys. A **74**, 325–328 (2002)

Chapter 2
Development of the Atomic-Resolution Environmental Transmission Electron Microscope

Pratibha L. Gai, Edward D. Boyes, Kenta Yoshida, and Thomas W. Hansen

Abstract The development of the novel atomic-resolution environmental transmission electron microscope (atomic-resolution ETEM) for directly probing dynamic gas–solid reactions in situ at the atomic level under controlled reaction conditions consisting of gas environment and elevated temperatures is described. Applications of the ETEM include investigations of catalytic reactions such as biofuel synthesis from biomass, hydrogenation reactions of interest in synthetic fuel cell technologies, and hydrocarbon oxidation along with various other mainly supported metal catalysts. In other fields, the ETEM is used to study steels, graphene, nanowires, etc. In this chapter, the experimental setup of the microscope column and its peripherals *are* described.

2.1 Introduction

The transmission electron microscope has generated substantial results and various fields. From heterogeneous catalysis (Boyes and Gai 1997; Gai and Kourtakis 1995; Haggin 1995; Gai 1998, 1999, 2002a; Hansen et al. 2001, 2002; Jacoby 2002; Gai and Boyes 2003; Lopez-Cartes et al. 2003; Liu et al. 2004; Helveg et al. 2004; Helveg and Hansen 2006; Gai et al. 2007) to studies of carbonaceous materials and devices (Helveg et al. 2004; Hofmann et al. 2007). However, traditionally, these

P.L. Gai (✉)
The York JEOL Nanocentre, University of York, Heslington, York YO10 5DD, UK
e-mail: pratibha.gai@york.ac.uk

E.D. Boyes
Department of Physics, Chemistry, and Electronics, University of York, York YO10 5DD, UK
e-mail: ed.boyes@york.ac.uk

K. Yoshida
Institute for Advanced Research, Nagoya University, Nagoya, Japan

T.W. Hansen
Center for Electron Nanoscopy, Technical University of Denmark,
Kgs. Lyngby 2800, Denmark

T.W. Hansen, J.B. Wagner (eds.), *Controlled Atmosphere Transmission Electron Microscopy*, DOI 10.1007/978-3-319-22988-1_2

investigations have been carried out in high vacuum conditions. Typically not the working environment of the samples in question. In a quest to expose samples to more realistic surroundings, various modifications and adaptations are made to the microscope setup. These include holders for interacting with the sample in the form of adding heat, contacting, indenting, magnetizing, etc. Modifications could also be allowing for the samples to be exposed to a gaseous atmosphere. These latter modifications will be the topic of this chapter.

Mainly two routes have been pursued in order to maintain a locally high pressure around the sample inside the microscope. One approach involves encapsulating the sample between electron-transparent windows. The other approach involves confining the gas around the sample using small apertures and evacuating the gas using pumps in sequential steps. Whereas the former approach, known as the windowed method, can be realized using a specially designed sample holder, the latter approach, known as the differentially pumped column, requires modifications to the microscope column itself. In either case, the sample region is often referred to as the Environmental Cell or ECELL. The technique of exposing samples to gases is frequently referred to as ETEM.

In differentially pumped column approach (Boyes and Gai 1997), the ECELL capabilities have been combined in a single instrument allowing atomic resolution (HRTEM), STEM, and PEELS/GIF functionalities. The combination is required to aid simultaneous determination of the dynamic structure and composition of the reactor contents. The ETEM system is used as a nanolaboratory with multi-probe measurements. Design of novel reactions and nanosynthesis are possible. The windowed approach will be discussed in a different chapter. The structure and chemistry of dynamic catalysts are revealed by atomic imaging, electron diffraction, and chemical analysis while the sample is immersed in controlled gas atmospheres and at the operating temperature. For chemical microanalyses, a commercial energy filter system (or an EDX detector) can be fitted, to provide elemental analysis during in situ experiments with low gas pressures and fast and minimally invasive high-resolution chemical mapping with filtered TEM images, in addition to an EDX detector. The analysis of the oxidation state in intermediate phases of a catalytic reaction is possible. In studies including the determination of the size and subsurface location of particles, the dynamic STEM system (integrated with ETEM) provides complementary methods for chemical and crystallographic analyses.

Many technological processes occur at the gas–solid or liquid–solid interface at the atomic scale. For example, in heterogeneous catalysis, chemical reactions catalyzed by solid surfaces take place at the atomic level and play a major role in the production of industrial chemicals, energy sources, and environmental emission controls. The dynamic atomic structure of catalysts under reaction conditions plays a crucial role on their performance in these reactions. It is often not possible to infer the dynamic state of the material from postmortem examinations of the static material, and these data often cannot be obtained directly by other means. Atomic-resolution environmental transmission electron microscopy (atomic-resolution ETEM) for direct in situ observation of the dynamic nanostructural evolution at

the solid surface under controlled reaction conditions of gas/vapor/liquid and temperature environments is therefore a powerful scientific tool in the materials and chemical sciences for the nanostructure-dependent information.

Of particular interest are the properties of solid-state heterogeneous catalysts of interest for gas reactions in technological processes; to better understand the fundamental reaction mechanisms and the atomic scale structure–property relationships is important in the development of new materials and processes. Atomic-resolution ETEM under controlled operating environments is of vital importance to probe catalyst structure–property relationships under working conditions in catalysis. Probing catalysts directly under reaction environments is key to gaining insights into catalytic reaction mechanisms, active reaction sites, defect structural evolution, and the nature of bonding in redox reactions. The unique contribution of atomic-resolution ETEM under operating conditions is the ability to characterize the dynamic catalyst local structures, which may be aperiodic (such as dislocations), and determine their nature, composition, and adjacency of particles of different types.

Since chemical reactions take place at the atomic level, this chapter focuses on the novel development of *atomic-resolution* environmental transmission EM (atomic-resolution ETEM) with a new design of an integrated environmental cell (gas reaction cell) reactor. For earlier in situ studies carried out with an old and different environmental cell (ECELL) technology using (ex situ) reactor aperture assembly (jig), inserted between polepieces of the objective lens (Butler and Hale 1981; Gai et al. 1990) in the microscope column (or window cells) to carry out reactions at modest resolutions, readers are referred to other chapters in this book. Such jigs were made interchangeable, necessitating the frequent opening of the microscope to air to insert the jig and rebuilding of the microscope to effect the changeover in functionality. Window cells that have been used to contain gases, solvent vapors, and hydrated samples may present difficulties in reliably sustaining a large pressure difference across a window that is thin enough to permit electron penetration; and in heating and tilting samples.

Several approaches have been taken in order to maintain a controlled atmosphere over a sample in a transmission electron microscope while imaging. The main aim is to limit the high-pressure region to as small as possible a region around the sample in the z direction so that the electrons only have to traverse a thin slab of gas at relatively high pressure. This ensures that the sample is exposed to as high a pressure as possible while maintaining the performance of the microscope with only limited effect of the gas. For gas–solid reactions, the complications and potential for failure of windows can be avoided by substituting small apertures above and below the sample to restrict the diffusion of gas molecules, but to allow the penetration of the electron beam. Typically, pairs of apertures are added above and below the sample with differential pumping lines attached between them.

In most cases, the gas atmosphere is provided by a gas injection system in conjunction with a differential pumping system for evacuating the injected gas from the sample region. The differential pumping system is typically separate from

the conventional pumping system often consisting of ion getter pumps. Such system can sustain pressures approaching 2000 Pa.

In order to inject gases in a controlled way into the sample region of the microscope, certain modifications have to be made. A port for letting in the gas has to be made, and a differential pumping system has to be constructed. These are described below.

Atomic-resolution ETEM under controlled reaction conditions provides dynamic information on processes which take place at the atomic level, performance-critical defect structures, and subsurface diffusion of catalytic species. However, the development of ETEM for directly visualizing reactions under extreme conditions of gas pressures and temperatures at the atomic level is highly challenging.

2.2 Design and Development of the Differentially Pumped ETEM

The quest to probe gas molecule–solid catalyst reactions directly at the atomic level resulted in the pioneering development of in situ atomic-resolution ETEM at DuPont, USA, by Gai and Boyes (Boyes and Gai 1997; Gai and Kourtakis 1995). This development demonstrated for the first time that catalyst studies of gas–solid reactions at the atomic resolution was possible under controlled dynamic reaction conditions of gas pressure of a few millibars and at elevated temperatures. The development was featured by the American Chemical Society's Chemical and Engineering News (Haggin 1995). In this development, a new approach was taken to design an integrated atomic-resolution ETEM instrument that is dedicated to environmental cell (ECELL, or gas reaction cell) operations, and the ECELL is permanently mounted and integrated with HRTEM. Firstly, it was based on a modern computer-controlled Philips CM30T TEM/STEM system with proven high-resolution crystal lattice imaging performance. Secondly, the whole microscope column, and not just the region around the sample, has been redesigned for the ECELL functionality using the microscope sample chamber itself as the ECELL reactor. Thirdly, a custom set of polepieces incorporating radial holes for the first stage of differential pumping, with no deleterious effect on imaging, was designed for the instrument (Fig. 2.1).

The basic configuration of the ETEM is a short ($<$10 mm) path length of controlled environment with gas/vapor introduced, or in some cases with liquid injected onto the sample, and containing the microscope specimen in an otherwise high vacuum TEM column. The limited sample area is the only part of the system shared by both the chemical reactor stream and the microscope.

The basic geometry of the atomic-resolution ETEM system design (Boyes and Gai 1997) is a four-aperture system, in pairs above and below the sample (Fig. 2.1), but with the apertures now mounted in the bores of the objective lens polepieces

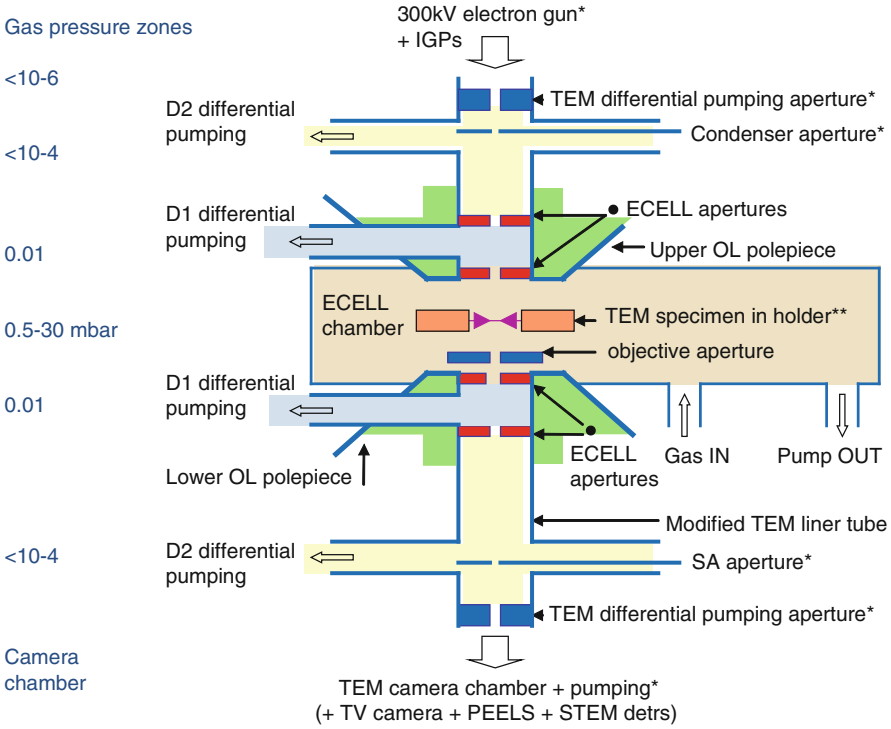

Fig. 2.1 Schematic (not to scale) of key elements of the pioneering development of the atomic-resolution ETEM design to probe gas–solid reactions at the atomic level (Boyes and Gai 1997; Gai and Kourtakis 1995). The basic geometry of the aperture system consists of radial holes through objective polepieces (OL) for gas lines at *D*. The OL polepieces are above and below the specimen holder, and the lower OL polepiece are indicated. Gas inlet, the first stage of differential pumping lines (*D1*) between the environmental cell (ECELL) apertures, condenser aperture, a second stage of pumping (*D2*) at the condenser lens, selected area (SA) diffraction aperture, parallel electron energy loss spectroscopy (PEELS), and TEM camera vacuum are indicated. The ECELL chamber is the gas reaction cell. The atomic-resolution ETEM design (Boyes and Gai 1997) is used for commercial production and now used by researchers worldwide

with regular microscope apertures in bushes in the polepieces. The controlled environment ECELL volume is the regular sample chamber of the microscope. Differential pumping systems connected between the apertures consist of molecular drag pumps (MDP) and turbomolecular pumps (TMP). This permits high gas pressures in the ECELL sample region. With regard to potential X-ray emissions, a combination of innovative internal Al-shielded Ta X-ray beam stops and extensive additional external lead shielding was used, with stringent auditing of both design and implementation. The manufacturing tolerances on the centering of selected regular microscope apertures and on machining tolerances for mounting them in a fixed alignment are fully adequate for the purpose. In this design (Boyes and Gai 1997), the regular adjustable objective aperture is retained inside the ETEM's ECELL section (Fig. 2.1) for its usual useful TEM functions.

Subsequent ETEMs have field emission guns (FEG) (Hansen et al. 2001, 2009, 2013; Yoshida et al. 2011, 2012, 2014a) and require additional stages of differential pumping added to the configuration described here. Fortunately, the vacuum conditions in the modern ETEM are significantly better than those in a regular TEM, greatly reducing the contamination issues critical for chemistry—and with which the ETEM apertures and gas flow can help even in older systems.

A conventional reactor-type gas manifold system enables the inlet of flowing gases into the ECELL of the ETEM apparatus, and a sample hot stage allows samples to be heated. A mass spectrometer is fitted to the ETEM for gas analysis. The atomic-resolution ETEM provides facilities for dynamic in situ experiments in an atomic resolution (<0.2 nm) TEM under controlled conditions of gas/vapor environment at regular operating pressures up to ~5000 Pa, and at selected and accurately known temperatures from 150 to 1100 °C, and in a few cases up to 2000 °C (Boyes and Gai 1997). Reviews of the important scientific impact of ETEM in solid-state chemistry and related fields, including catalysis research, are provided by references (Gai 1999, 2002a; Hansen et al. 2013; Hansen and Wagner 2014). For dynamic atomic resolution, a few millibars of gas pressure are used in the ECELL. Higher gas pressures are possible, but this compromises the resolution (due to multiple scattering effects of the electron beam through thicker gas layers). A video system connected to the ETEM apparatus or CCD camera facilitates digital image processing and real-time recording of dynamic events.

The atomic-resolution ETEM development of Gai and Boyes has been adopted for commercial production by EM manufacturers (Gai et al. 2007) and is being used by researchers worldwide (Hansen et al. 2001; Hofmann et al. 2007; Chenna et al. 2011; Booth et al. 2011).

In the ETEM the sample—but nothing much else—is shared between the chemical reactor on the horizontal axis and the vertical microscope column (Fig. 2.1). It is essential to ensure the effect of the electron beam is minimally invasive; or eliminated, in part by using low electron beam doses and sensitive recording methods, and by rigorous audit of results with and without the sample exposed to the electron beam continuously, under careful experimental conditions. In any scientific study, a hot stage at controlled and accurately known temperatures should be used; rather than uncontrolled beam heating of indeterminate intensity, wide variations in local effect and mostly completely alien to the real world. Of course, a rigorous approach is experimentally demanding; especially to obtain the most informative continuous dynamic data from a small selected area or feature at high resolution and magnification, as the environment, temperature, or other controlled conditions are varied systematically. After the basic data are recorded, they must always be confirmed in a rigorous comparison end-point experiment with the beam turned off during the reaction sequence, and used only for analysis at the end of the experiment. Data found to be influenced in any way by the electron beam are usually artifacts and should be discarded. This is obviously very dependent on materials and conditions, but it seems to be a much bigger problem using electron beam energies above 200 kV. Atomic-resolution ETEM can add valuable spatially resolved microstructure and defect data to wider studies, but must always be related to them.

Electronic image shift and drift compensation help to stabilize high-resolution images for data recording on film or with real-time digitally processed video. Minimally invasive electron beam techniques and calibration studies (described in the preceding paragraphs) are used throughout.

We want to point out that any modifications to an electron microscope, and especially a higher voltage TEM column, must be undertaken with a well-informed plan and rigorous procedures to ensure the outcome is as safe as the base instrument.

The emphasis in ETEM is on dynamic in situ studies of reaction and other change mechanisms under controlled, near real world, conditions of environment and temperature; with minimally invasive microscopy for analysis. Any compromises in TEM performance with the ETEM functionality added are now very limited.

2.3 Gas Injection and Cleaning

Being able to evacuate gases from the column microscope column is only half the challenge of environmental transmission electron microscopy. The other part is controlled injection of gases around the sample. In order to maintain the stability needed to acquire images with atomic resolution, the flow around the sample need to be stable. Furthermore, for many experiments a mixture of gases is desired. Whereas gas mixtures can easily be purchased, it is undesirable to compromise the vacuum by opening it in order to mount new gas supplies.

A versatile system can be constructed by using mass flow controllers and a battery of different gases permanently mounted to the ETEM system. By using digitally controlled mass flow controllers, high stability can be achieved and the flows of the individual gases can easily be controlled and changes can be made on the fly. However, as the gas flows involved in ETEM experimentation are typically low, on the order of 10 mL/min, the residence time of the gases in the system can be quite long, and the time it takes for gases to reach the sample can be longer than expected. The time it takes for a certain gas to reach the sample can be monitored using residual gas analysis by mass spectrometry around the sample.

When working at low flows and pressures, cross-contamination can be a serious issue. Hence, experiments are often grouped in reduction and oxidizing experiments and experiments involving gases that can be challenging to desorb from the interior of the microscope column and separated in time. While extensive pumping can minimize the risk of cross-contamination considerably, a more thorough cleaning is sometimes necessary. This can be done by mounting a plasma cleaner on the ECELL itself (Hansen et al. 2010). Regular use of a plasma cleaner can lower the base pressure within the microscope column and limit undesired contamination of samples. Further measures that can be taken in order to limit the risk of sample contamination include plasma cleaning of the sample prior to inspection in the microscope and keeping holders under vacuum when not used along with frequent baking of the inlet and pumping lines.

2.4 Aberration Correction

Correction of aberrations is very important in ETEM (Gai and Boyes 2009), in helping to simplify image interpretation, particularly between 0.1 and 0.25 nm, improving imaging of small particle structures against a support background, allowing the use of wider gap polepieces with space for more stage manipulations and other in situ facilities such as straining. Therefore, aberration correction (AC) for atomic-resolution E(S)TEM under controlled environments was proposed (Gai et al. 2005). Aberration correction plays a key role in in situ ETEM studies as a single image close to zero defocus with full range of spatial frequencies without the contrast transfer function oscillations is possible as shown in Fig. 2.2 for a JEOL 2200FS double AC (S)TEM (Gai and Boyes 2009). Figure 2.3 shows an example of a multiply twinned particle (MTP) of gold in an AC atomic-resolution ETEM with gas modifications with the corresponding FFT (Walsh et al. 2012). The image illustrates displaced MTP axis (indicated by the yellow circle) and asymmetric strain fields, important in the surface structure and reactivity of gold nanoparticles (Walsh et al. 2012).

Because of the small amounts of solid reactant in the microscope sample, measurement of reaction products is generally performed on larger samples in a microreactor operating under similar conditions and used for the correlation between the catalyst structure and performance. The correlation is crucial for a better understanding of gas–solid reactions to aid the development of improved materials and processes. However, some attempts at monitoring reactions have been taken. These are described in a later chapter. Under carefully controlled conditions, data from in situ ETEM can be directly related to structure–activity relationships in technological processes (Gai and Boyes 2003; Miller and Crozier 2014; Chenna and Crozier 2012; Crozier and Chenna 2011; Hansen and Wagner 2012).

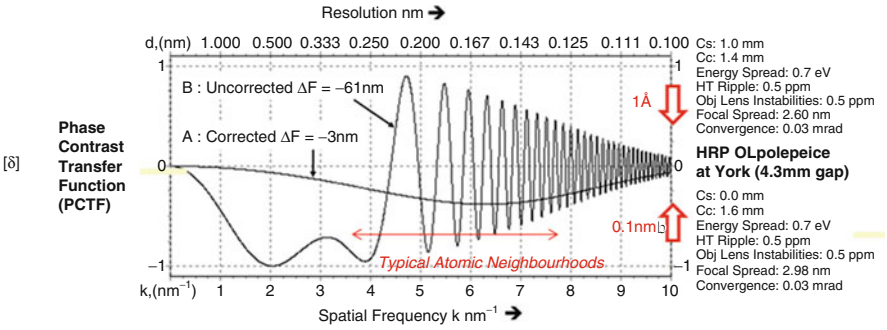

Fig. 2.2 Calculated contrast transfer functions (CTFs) for an aberration corrected (**a**) imaging conditions of the HRP version of the double aberration corrected JEOL 2200FS FEG TEM/ STEM at the University of York (UK) (Gai and Boyes 2009) (CTF for the uncorrected conditions is shown in (**b**) for comparison

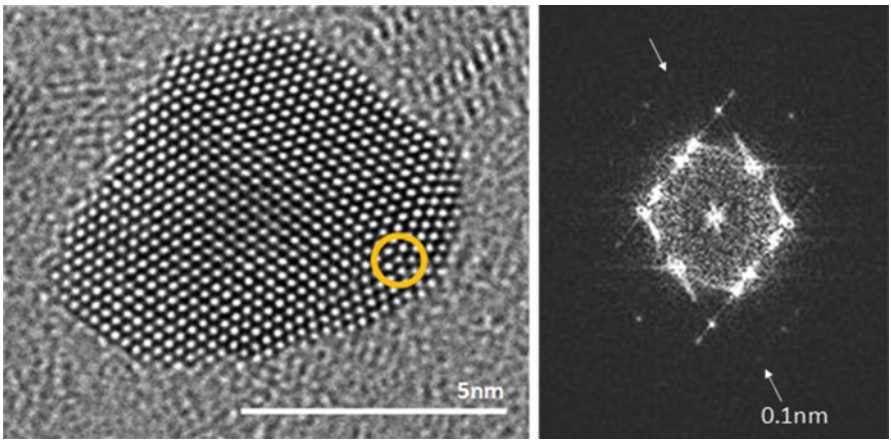

Fig. 2.3 Multiple twinned particle decahedral particle with fivefold axis shifted close to the surface (Walsh et al. 2012)

2.5 Instrument Performance

Naturally, the presence of gas around the sample will interfere with the imaging capabilities of the microscope. As the beam electrons impinge on the gas molecules above and below the sample, they can be scattered. Apertures and other parts of the microscope intercept most of these scattered electrons. Hence, the main result of this interaction is a loss of total intensity. With light molecules such as hydrogen and helium, this is usually not a big issue. But with heavier molecules such as oxygen, nitrogen, and carbon monoxide which are often used in experiments with catalysts, a substantial amount of the beam electrons can be lost when working in the higher end of the pressure range (above 500 Pa). Figure 2.4 shows the measured intensity on the fluorescent screen as a function of pressure for various gases often used in ETEM experiments. Whereas only a few percent of the total intensity is lost for hydrogen and helium at 300 kV, more than 80 % is lost for oxygen and nitrogen at 80 kV.

The presence of gas also has an effect on the resolution of the microscope. The resolution depends on several parameters: the gas pressure, the gas specie, and the beam current. Figure 2.5 shows the power spectra of an amorphous carbon films at increasing argon pressure. The loss of intensity variation is observed by the dampening of the intensity (Hansen and Wagner 2012). Figure 2.6 shows the resolution as a function of beam current in 400 Pa nitrogen. The resolution is measured by a Young's fringe experiment. As the beam current is increased, a significant loss of resolution is observed (Bright et al. 2013). The electron–gas molecule interaction is further described in a later chapter.

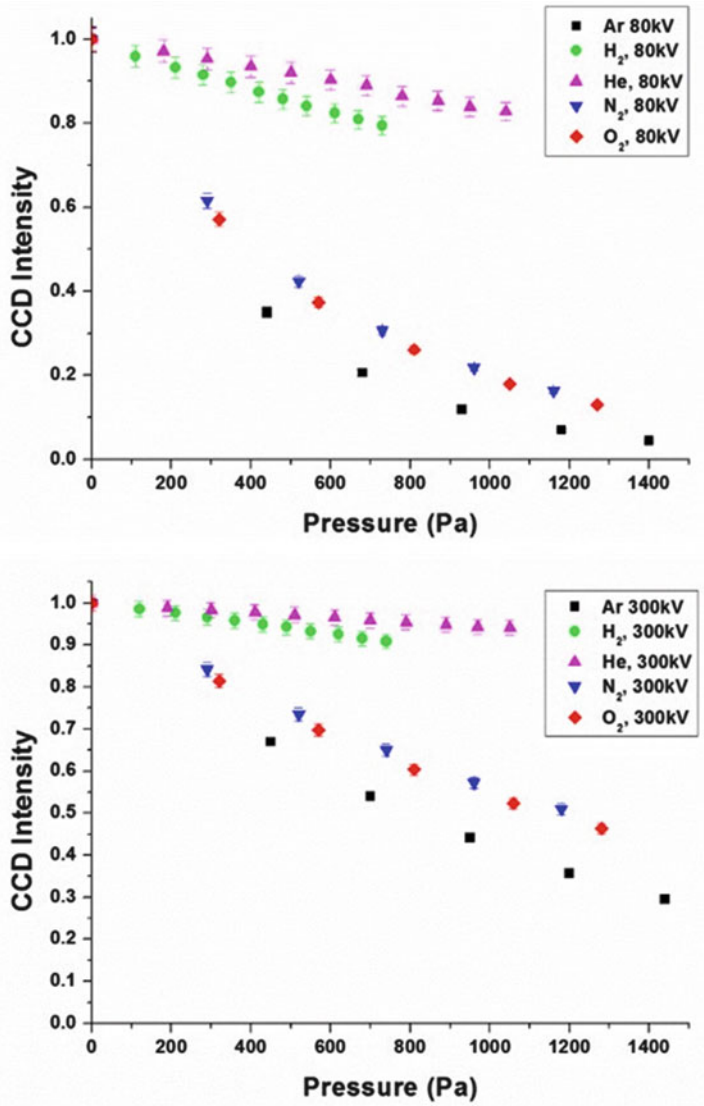

Fig. 2.4 Intensity recorded on the CCD camera as a function of gas pressure for 80 kV (*top*) and 300 kV (*bottom*) (Hansen and Wagner 2012)

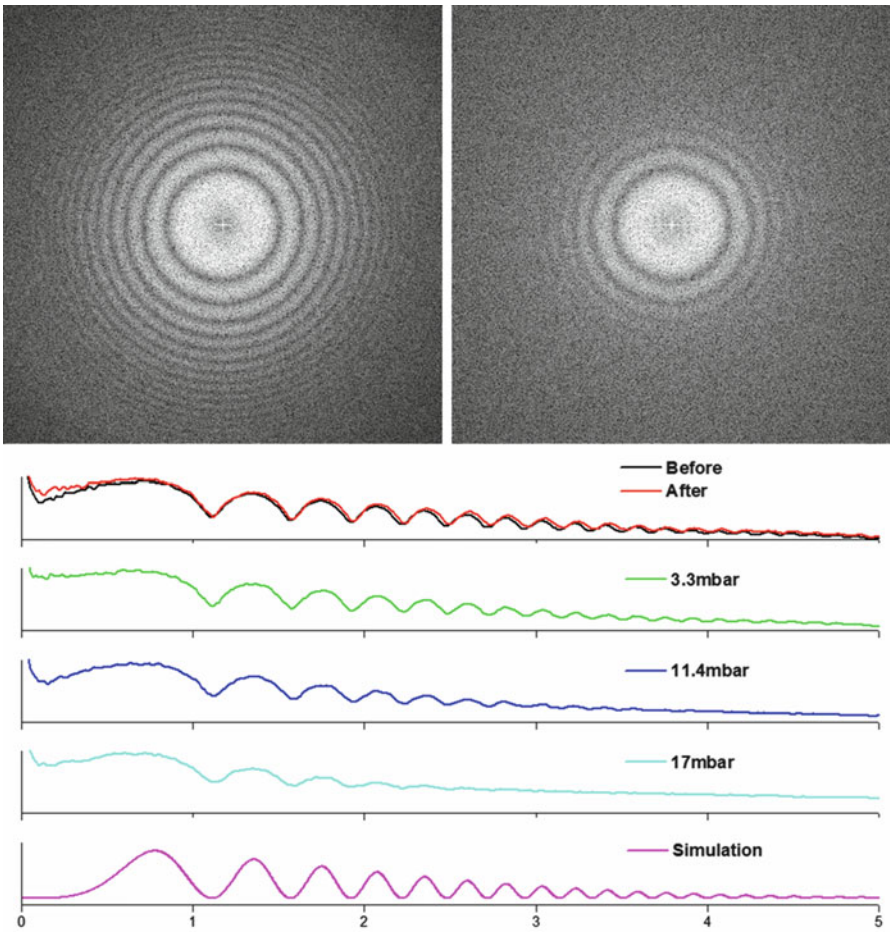

Fig. 2.5 Fourier transforms of images acquired from an amorphous carbon film in vacuum (*top left*) and at 1700 Pa argon gas (*top right*). From the FFTs, the radial intensity has been extracted (*bottom*). Values at intermediate pressures and a simulation made using CTFExplorer are also included in the plot (Hansen and Wagner 2012)

2.6 Atomic-Resolution Wet-ETEM: Reactions in the Liquid Phase

Many commercial hydrogenation and subsequent polymerization processes take place in liquid-gas environments or in liquids at operating temperatures and take place on the atomic or molecular scale. Probing reactions in solutions at the atomic level in the atomic-resolution ETEM, hereafter referred to as wet-ETEM, is therefore of great importance in the development of advanced catalytic technologies. In the past, to examine samples in hydrated environments for imaging at modest

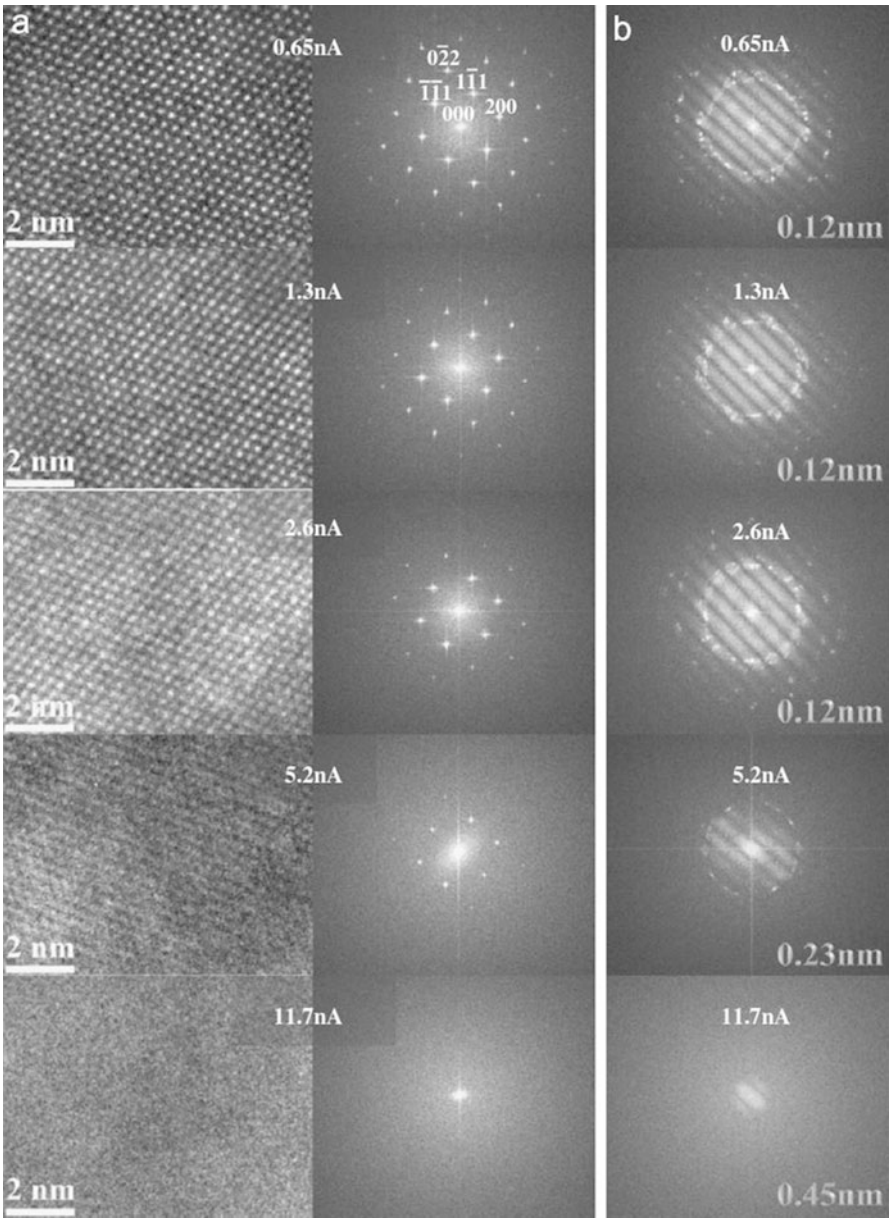

Fig. 2.6 HRTEM images taken with 4 mbar of nitrogen gas as a function of the total beam current (measured without gas). (**a**) Si <114> crystal lattice images with corresponding diffractograms, (**b**) Diffractograms of AuPd/carbon cross-grating HRTEM images used for measurement of information limit (displayed *bottom right*) (Bright et al. 2013)

resolution wet cells have been used, including windows to contain liquids, but without heating capabilities (Butler and Hale 1981). A wet holder for the atomic-resolution wet-ETEM has therefore been developed for atomic scale studies of polymerization reactions in liquids and liquid-gas environments over solid catalysts at operating temperature (Gai 2002b). Water vapor is also a major component in selective oxidation of hydrocarbons and in advanced fuel cell reactions. To visualize the influence of moisture on the performance of catalysts in real time at the atomic scale, an AC wet-ETEM system under moisturizing environments has been developed and water vapor is transported to the sample via a carrier gas (Yoshida et al. 2014a). This development involves the introduction of a thermostatic chamber and mass spectrometer enabling a stable moisturized N_2 environment in the ECELL and allows the direct detection of H_2O. The wet-ETEM system for the differential pumping ECELL with quadrupole mass spectrometer is shown in Fig. 2.7. This system plays a key role in investigating directly in situ reactions under water environments of importance in fuel cells and hydrocarbon catalysis (Yoshida et al. 2014a). An example in Fig. 2.8 shows the atomic scale modifications in copper supported ceria in carbon monoxide and water environments (Yoshida et al. 2014b).

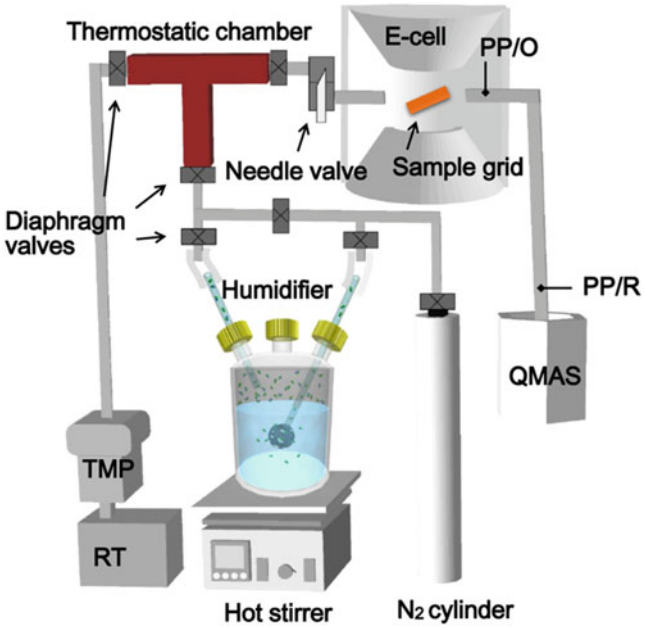

Fig. 2.7 Wet-ETEM system for the ECELL with humidifier and quadrupole mass spectrometer (QMAS) (Yoshida et al. 2014a). Wet-ETEM system for the ECELL with humidifier and quadrupole mass spectrometer (QMAS) (Yoshida et al. 2014a). *The figure reference is from the authors' (Yoshida, Boyes and Gai et al.) work in Nanotechnology 25, 425702 (2014) which is reproduced with permission by the Institute of Physics Publishers (IOPP)*

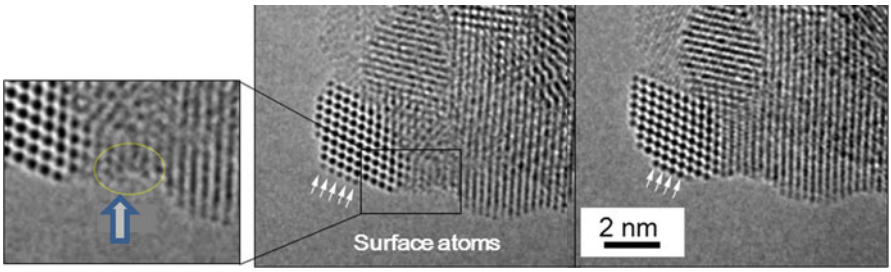

Fig. 2.8 Example of CO + water reaction on transition metals (Cu) supported on ceria. Surface atom movement on ceria (indicated by *small arrows*) is observed under hydrated conditions. The presence of Cu is shown by the *yellow circle* which also undergoes movement (Yoshida et al. 2014b)

In addition to calibration experiments, several conditions are required for successful studies using the ETEM. Electron-transparent samples and ultrahigh-purity heater materials and sample grids are required (such as stainless steel, Ti or Mo). For high-temperature studies in gas environments, samples are normally supported on finely meshed-grids of Ti or Mo with experiments carried out on crystals protruding from the edge of grid bars. Carbon support films are not suitable at high temperatures.

2.7 Sample Heating

For many experiments, samples need to be heated in situ in the microscope. This poses a challenge as the geometry is already considerably confined within the sample region of the transmission electron microscope. Typically, samples are heated using a heating holder. These come in mainly two types. The most widely used is the furnace type holder. Here, the sample is placed in a cup containing an embedded heating filament, and the temperature can be measured using a thermocouple attached to the exterior of the cup. This design can accommodate samples of various geometries such as powders, focused ion beam (FIB) prepared samples, and wires. Different materials can be used for the sample cup providing compatibility with different gas environments and obtainable temperatures. For ETEM experiments, stainless steel (Inconel) is often used as this material is compatible with most gases and will resist corrosion at the high temperatures typically associated with catalysis. Whereas the versatility provided by this system offers a lot of advantages; there are also drawbacks. Thermal expansion of the cup during heating results in significant sample drift and makes imaging during temperature ramping challenging. Furthermore, residual magnetic fields caused by the heating filament may result in a loss of resolution.

The other approach for sample heating is using an MEMS (Micro-Electro-Mechanical Systems) fabricated heater chip. Two different approaches are used for MEMS heaters. Heating is either done by using an embedded heater filament (Creemer et al. 2008) or by passing a current through a thin film acting as a tiny hot plate (Allard et al. 2009). In both approaches, holes can be fabricated in the heater structure allowing for unhampered imaging. In both MEMS type heaters, only a very small amount of material is heated and hence the issue of thermal expansion is minimized. The drawback of this approach is the limited space for sample deposition and the lack of a direct temperature measurement.

2.8 Examples of the Atomic-Resolution ETEM

2.8.1 In Situ Catalyst Activation for Biofuel Synthesis

Atomic-resolution ETEM has been used to study the formation of biofuels from vegetable plant biomass. The biofuel reaction involves the esterification of triglycerides into fatty esters and glycerol. The activation of nanoscale magnesium hydroxide methoxide slurry precursors (containing a mixture of amorphous and crystalline regions) carried out in situ in the AC atomic-resolution ETEM revealed increased crystallinity and defects during the activation process. The defects form along <111> directions in (110) projection of nano-magnesium oxide (which adopts a cubic structure, with $a = 0.4212$ nm). Figure 2.9 illustrates the in situ reaction sequence at room temperature (RT), 500 °C and 700 °C, respectively. Defect analyses showed that they were formed by simple atomic movement (called Gai glide shear mechanism) (Gai et al. 2009). The study found excellent correlation between surface glide defects and the catalytic activity, with the glide defects creating active sites for the biofuel synthesis (Gai et al. 2009; Gai and Boyes 2012). During the activation, the glide

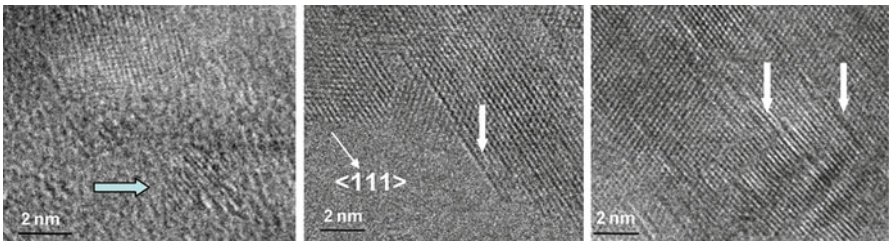

Fig. 2.9 In situ, real-time, dynamic studies of the activation of magnesium hydroxide methoxide precursors for biofuel synthesis at: (**a**) room temperature (RT); nanocrystals of only about 3–5 nms (*arrowed*) and amorphous areas are indicated. Crystallinity increases as the temperature is increased leading to nano-MgO. (**b**) Surface profile imaging of defects at 500 °C (indicated, e.g., by an *arrow*): The defects are along <111> direction and are at or near the surface. The defect analyses show that they are formed by simple atomic movement called glide shear; (**c**) profile image at 700 °C shows many defects (Gai et al. 2009)

defects are formed to accommodate the shape misfit between the reduced anion-deficient catalyst surface and the subsurface without collapsing the catalyst structure which is critical to the sustained operation of the catalyst. Other applications of atomic-resolution ETEM include carbon nanotube and filament growth and solid-state reaction mechanisms (Hofmann et al. 2007; Chenna et al. 2011).

Dynamic in situ experiments can be very efficient, and productive of data, in scanning a range of experimental conditions in a single session, and in mechanistic studies. Moreover, as is generally in the case of catalysis the active phase is metastable with respect to temperature and environment, the key data can only be obtained from dynamic in situ studies. The limits on the systems are a maximum gas pressure in the mbar range dictated by electron scattering and finally leakage into the gun. These in situ conditions are generally adequate to ensure the reacting surface is flooded with the desired species.

Acknowledgements We are most grateful to Leland Hanna and Ellis Daniels at DuPont and Ian Wright at the University of York for their technical assistance in developing the atomic-resolution ETEM and AC ETEM. We thank EPSRC (UK) for critical mass research grant EP/J0118O58/1 awarded to PLG and EDB. TWH gratefully acknowledges the A. P. Møller and Chastine Mc-Kinney Møller Foundation for its contribution towards the establishment of the Center for Electron Nanoscopy in the Technical University of Denmark.

References

L.F. Allard, W.C. Bigelow, M. Jose-Yacaman, D.P. Nackashi, J. Damiano, S.E. Mick, A new MEMS-based system for ultra-high-resolution imaging at elevated temperatures. Microsc. Res. Techniq. **72**, 208–215 (2009)

T.J. Booth, F. Pizzocchero, H. Andersen, T.W. Hansen, J.B. Wagner, J.R. Jinschek, R.E. Dunin-Borkowski, O. Hansen, P. Bøggild, Discrete dynamics of nanoparticle channelling in suspended graphene. Nano Lett. **11**, 2689–2692 (2011)

E.D. Boyes, P.L. Gai, Environmental high resolution electron microscopy and applications to chemical science. Ultramicroscopy **67**, 219–232 (1997)

A.N. Bright, K. Yoshida, N. Tanaka, Influence of total beam current on HRTEM image resolution in differentially pumped ETEM with nitrogen gas. Ultramicroscopy **124**, 46–51 (2013)

E.P. Butler, K.F. Hale, *Dynamic Experiments in the Electron Microscope* (North-Holland, Amsterdam, 1981), p. 457

S. Chenna, P.A. Crozier, Operando transmission electron microscopy: a technique for detection of catalysis using electron energy-loss spectroscopy in the transmission electron microscope. ACS Catal. **2**, 2395–2402 (2012)

S. Chenna, R. Banerjee, P.A. Crozier, Atomic-scale observation of the Ni activation process for partial oxidation of methane using in situ environmental TEM. ChemCatChem **3**, 1051–1059 (2011)

J.F. Creemer, S. Helveg, G.H. Hoveling, S. Ullmann, A.M. Molenbroek, P.M. Sarro, H.W. Zandbergen, Atomic-scale electron microscopy at ambient pressure. Ultramicroscopy **108**, 993–998 (2008)

P.A. Crozier, S. Chenna, In situ analysis of gas composition by electron energy-loss spectroscopy for environmental transmission electron microscopy. Ultramicroscopy **111**, 177–185 (2011)

P.L. Gai, Direct probing of gas molecule solid catalyst interactions on the atomic scale. Adv. Mater. **10**, 1259–1263 (1998)

P.L. Gai, Environmental high resolution electron microscopy of gas-catalyst reactions. Top. Catal. **8**, 97–113 (1999)
P.L. Gai, Developments in in situ environmental cell high-resolution electron microscopy and applications to catalysis. Top. Catal. **21**, 161–173 (2002a)
P.L. Gai, Development of wet environmental TEM (Wet-ETEM) for in situ studies of liquid-catalyst reactions on the nanoscale. Microsc. Microanal. **8**, 21–28 (2002b)
P.L. Gai, E.D. Boyes, *Electron Microscopy in Heterogeneous Catalysis*, vol. Series in Microscopy and Materials Science (CRC Press, Boca Raton, 2003)
P.L. Gai, E.D. Boyes, Advances in atomic resolution in situ environmental transmission electron microscopy and 1 angstrom aberration corrected in situ electron microscopy. Microsc. Res. Techniq. **72**, 153–164 (2009)
P.L. Gai, E.D. Boyes, Atomic-resolution environmental transmission electron microscopy, in *Handbook of Nanoscopy*, ed. by G. van Tendeloo, D. van Dyck, S.J. Pennycook (Weinheim, Wiley, 2012)
P.L. Gai, K. Kourtakis, Solid-state defect mechanism in Vanadyl pyrophosphate catalysts—implications for selective oxidation. Science **267**, 661–663 (1995)
P.L. Gai, B.C. Smith, G. Owen, Bulk diffusion of metal particles on ceramic substrates. Nature **348**, 430–432 (1990)
P.L. Gai, L. Hanna, E.D. Boyes, Atomic resolution in situ environmental-TEM (ETEM) studies of novel nanostructures for hydrogenation and hydrogen energy economy. Microsc. Microanal. **11**(Suppl 2), 1526–1527 (2005)
P.L. Gai, E.D. Boyes, S. Helveg, P.L. Hansen, S. Giorgio, C.R. Henry, Atomic-resolution environmental transmission electron microscopy for probing gas-solid reactions in heterogeneous catalysis. MRS Bull. **32**, 1044–1050 (2007)
P.L. Gai, J.M. Montero, A.F. Lee, K. Wilson, E.D. Boyes, In situ aberration corrected-transmission electron microscopy of magnesium oxide nanocatalysts for biodiesels. Catal. Lett. **132**, 182–188 (2009)
J. Haggin, In situ electron microscopy technique probes catalysis at atomic level. Chem. Eng. News **73**, 39–41 (1995)
T.W. Hansen, J.B. Wagner, Environmental transmission electron microscopy in an aberration-corrected environment. Microsc. Microanal. **18**, 684–690 (2012)
T.W. Hansen, J.B. Wagner, Catalysts under controlled atmospheres in the transmission electron microscope. ACS Catal. **4**, 1673–1685 (2014)
T.W. Hansen, J.B. Wagner, P.L. Hansen, S. Dahl, H. Topsøe, C.J.H. Jacobsen, Atomic-resolution in situ transmission electron microscopy of a promoter of a heterogeneous catalyst. Science **294**, 1508–1510 (2001)
P.L. Hansen, J.B. Wagner, S. Helveg, J.R. Rostrup-Nielsen, B.S. Clausen, H. Topsøe, Atom-resolved imaging of dynamic shape changes in supported copper nanocrystals. Science **295**, 2053–2055 (2002)
T.W. Hansen, J.B. Wagner, J.R. Jinschek, R.E. Dunin-Borkowski, The Titan environmental transmission electron microscope: specifications. Considerations and first results. Microsc. Microanal. **15**, 714–715 (2009)
T.W. Hansen, J.B. Wagner, R.E. Dunin-Borkowski, Aberration corrected and monochromated environmental transmission electron microscopy: challenges and prospects for materials science. Mater. Sci. Technol. **26**, 1338–1344 (2010)
T.W. Hansen, A.T. Delariva, S.R. Challa, A.K. Datye, Sintering of catalytic nanoparticles: particle migration or Ostwald ripening? Acc. Chem. Res. **46**, 1720–1730 (2013)
S. Helveg, P.L. Hansen, Atomic-scale studies of metallic nanocluster catalysts by in situ high-resolution transmission electron microscopy. Catal. Today **111**, 68–73 (2006)
S. Helveg, C. Lopez-Cartes, J. Sehested, P.L. Hansen, B.S. Clausen, J.R. Rostrup-Nielsen, F. Abild-Pedersen, J.K. Nørskov, Atomic-scale imaging of carbon nanofibre growth. Nature **427**, 426–429 (2004)

S. Hofmann, R. Sharma, C. Ducati, G. Du, C. Mattevi, C. Cepek, M. Cantoro, S. Pisana, A. Parvez, F. Cervantes-Sodi, A.C. Ferrari, R. Dunin-Borkowski, S. Lizzit, L. Petaccia, A. Goldoni, J. Robertson, In situ observations of catalyst dynamics during surface-bound carbon nanotube nucleation. Nano Lett. **7**, 602–608 (2007)

M. Jacoby, Microscopist chemists—transmission electron microscopy has evolved into a powerful tool for chemistry research. Chem. Eng. News **80**, 26 (2002)

R.J. Liu, P.A. Crozier, C.M. Smith, D.A. Hucul, J. Blackson, G. Salaita, In situ electron microscopy studies of the sintering of palladium nanoparticles on alumina during catalyst regeneration processes. Microsc. Microanal. **10**, 77–85 (2004)

C. Lopez-Cartes, S. Bernal, J.J. Calvino, M.A. Cauqui, G. Blanco, J.A. Perez-Omil, J.M. Pintado, S. Helveg, P.L. Hansen, In situ transmission electron microscopy investigation of Ce(IV) and Pr(IV) reducibility in a Rh (1%)/Ce0.8Pr0.2O_2-x catalyst. Chem. Commun. **5**, 644–645 (2003)

B.K. Miller, P.A. Crozier, Analysis of catalytic gas products using electron energy-loss spectroscopy and residual gas analysis for operando transmission electron microscopy. Microsc. Microanal. **20**, 815–824 (2014)

M.J. Walsh, K. Yoshida, M.L. Pay, P.L. Gai, E.D. Boyes, On the effect of atomic structure on the activity and deactivation of catalytic gold nanoparticles. ChemCatChem **4**, 1638–1644 (2012)

K. Yoshida, M. Makihara, N. Tanaka, S. Aoyagi, E. Nishibori, M. Sakata, E.D. Boyes, P.L. Gai, Specific surface area and three-dimensional nanostructure measurements of porous titania photocatalysts by electron tomography and their relation to photocatalytic activity. Microsc. Microanal. **17**, 264–273 (2011)

H. Yoshida, Y. Kuwauchi, J.R. Jinschek, K.J. Sun, S. Tanaka, M. Kohyama, S. Shimada, M. Haruta, S. Takeda, Visualizing gas molecules interacting with supported nanoparticulate catalysts at reaction conditions. Science **335**, 317–319 (2012)

K. Yoshida, A.N. Bright, M.R. Ward, L. Lari, X. Zhang, T. Hiroyama, E.D. Boyes, P.L. Gai, Dynamic wet-ETEM observation of Pt/C electrode catalysts in a moisturized cathode atmosphere. Nanotechnology **25**, 425702 (2014a)

K. Yoshida, E.D. Boyes, L. van de Water, M. Watson, P.L. Gai, *In-situ studies of ceria supported copper nanocatalysts at the atomic level using wet-environmental TEM, in 18th International Microscopy Congress* (Czech Republic, Prague, 2014b)

Chapter 3
Gas–Electron Interaction in the ETEM

Jakob B. Wagner and Marco Beleggia

Abstract Imaging in a differential pumped environmental TEM (ETEM) results in general in a degradation of the image quality. Scattering of electrons by gas molecules in the pressurized volume between the pole pieces blurs the image and decreases the signal-to-noise ratio of the acquired images. The somewhat simple picture of a plane wave interacting with the sample of interest is no longer valid. Furthermore, the exit wave from the sample is altered by scattering events taking place after the sample in the direction of propagation. In this chapter, the effect of the increased gas pressure between the pole pieces in an aberration-corrected high-resolution transmission electron microscope is discussed in order to shine some light on the additional phenomena occurring in ETEM compared to conventional HRTEM. Both direct effects on the image quality and more indirect effects rising from gas ionization are discussed.

3.1 Introduction

Ever since the proposal and first attempts of in situ electron microscopy involving non-vacuum imaging in the early days of electron microscopy (see Chap. 1) addressing the influence of the gas on the fast electron pathway has been crucial. The higher the pressure and the longer gas path the fast electrons have to pass, the larger is the probability of scattering events between electrons and gas species.

J.B. Wagner (✉)
Center for Electron Nanoscopy, Technical University of Denmark, Kgs. Lyngby, Denmark
e-mail: jakob.wagner@cen.dtu.dk

M. Beleggia
Center for Electron Nanoscopy, Technical University of Denmark, Kgs. Lyngby, Denmark

Helmholtz-Zentrum Berlin for Materials and Energy, Berlin, Germany

T.W. Hansen, J.B. Wagner (eds.), *Controlled Atmosphere Transmission Electron Microscopy*, DOI 10.1007/978-3-319-22988-1_3

The scattering on gas molecules results in a significant loss of electrons (intensity) on the viewing screen depending on the gas species, total pressure and energy of the primary electrons. Furthermore, the spatial resolution will decrease both for scanning transmission electron microscopy (STEM) and for broad beam electron microscopy. The contrast in the resulting images might be influenced as well depending on the scattering power of the gas molecules.

Not only the spatial resolution and contrast of the acquired micrographs will be affected by the electron–gas interaction, but the observations will also be influenced indirectly by ionization of gas species, which can lead to more reactive gas species and charge transfer effects. For example, the ionized gas species can be used for charge compensation since ionized gas species act as charge carriers compensating for charging of the sample during electron beam irradiation.

The effect on the special resolution might be easier to understand qualitatively in the case of scanning transmission electron microscopy. The highly focussed beam gets more diffuse on the sample as the fast electron scatters on gas species above the specimen. This beam broadening effect has been studied in great detail in the SEM community for decades (Danilatos 1988; Belkorissat et al. 2004; Mansour et al. 2009, 2013; Danilatos et al. 2011). However, the understanding of the effects on intensity, resolution, and (phase) contrast for broad beam electron microscopy is still in its infancy, and it is the focus of the present chapter.

In TEM where the spatial resolution relies on the coherency of the fast electron beam, the scattering effects taking place both above and below the sample strongly influence the resolution and signal to noise. Figure 3.1 illustrates the reduction of a cobalt oxide surface layer embedding a Co nanoparticles supported on α-Al_2O_3. The striking difference between the two images is the removal of the oxide layer. However, the signal-to-noise of the image in general is decreased when imaging in 740 Pa of CO (used as reducing agent). The insets in Fig. 3.1c, d clearly show that the high spatial frequency information is damped in the presence of CO in the microscope.

Obviously the effect of the gas species is related to the amount of gas present in the electron path (pressure of gas), but also the electron-optical conditions such as total beam current, current density, and primary beam energy have been found to influence the image quality to a greater extent when imaging in the presence of gas compared to traditional imaging in vacuum. In order to understand these direct effects on the image quality or instrument performance the geometry of the instrument and the scattering events taking place during the electron beam passage of the high-pressure volume have to be described in detail. In the present chapter effects of electron gas scattering is described and discussed to elucidate some of the aspects, which have to be considered in differential pumped environmental microscopy.

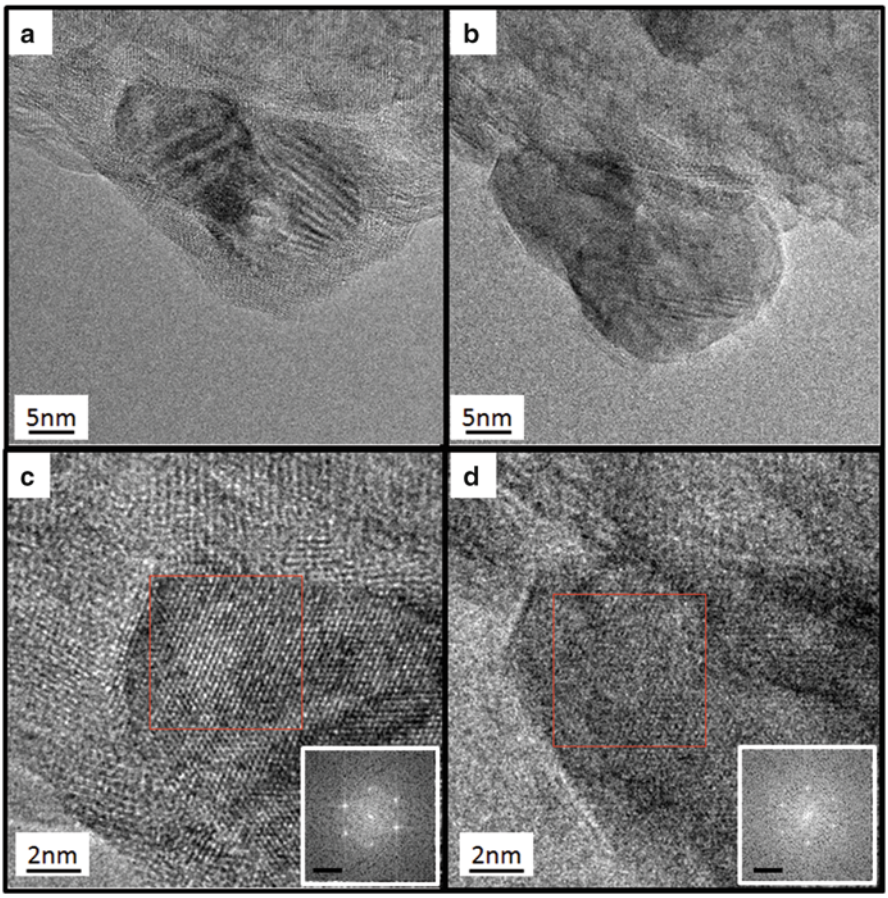

Fig. 3.1 Co/α-Al_2O_3 imaged in (**a**) high vacuum and (**b**) in the presence of 740 Pa of CO at 250 °C. (**c**, **d**) Close-up and FFT of marked areas in vacuum and presence of CO, respectively. The interaction of the fast electrons with the gas molecules decrease the resolution and signal to noise of the final image. Acquisition time and optical parameters of the electron microscope are the same for the two images

3.2 Influence on Instrument Performance

3.2.1 Geometric Considerations

The effect of the scattering of the swift electron on gaseous molecules near the sample of interest on the image quality and information transferred to the imaging system is dependent on the exact geometry of the high-pressure volume surrounding the sample.

As described in detail in dedicated chapters in the present book two main paths are pursued in order to allow controlled atmosphere around the sample:

(1) The windowed cell, which encapsulate the high-pressure gas around the sample by electron transparent windows and (2) the differential pumped version where a direct line of sight is available and the pressure is confined by pressure-limiting apertures.

Whereas the windowed cell usually limits the high-pressure volume to a thickness less than 50 μm in the direction of the propagating electron beam, the differentially pumped version have the high-pressure zone confined in the full volume between the pole pieces—the typical distance between the pressure-limiting apertures in commercially available ETEMs is in the order of 5–7 mm.

As described above, electrons should traverse the shortest possible path through gas in order to minimize the artefacts due to scattering of electrons on gas molecules. This is accomplished in the windowed cell, but on the expense of having two solid membranes interacting with the swift electrons as well disturbing the wave function. Thinner membranes are constantly developed in order to minimize this artefact maintaining the strength to withstand the pressure difference as further described in Chap. 6. The effect of the membranes on the spatial resolution has been studied in detail by Yaguchi et al. (2011), who, not surprisingly, found that 200 nm Si_3N_4 membranes cause a more significant loss in spatial resolution of the final image compared to the use of 15 nm Si_3N_4 membranes for the windowed cell. With membranes designed specifically to minimize their bulging during high pressure while maintaining a relatively large field of view, lattice fringe images can be recorded at pressures of more than 100 kPa (Creemer et al. 2008; Vendelbo et al. 2013, 2014). In this case the pathway of the fast electrons through the high-pressure zone is limited to around 50 μm.

Comparing the pathway of the high energetic electrons through the high-pressure zone in a differential pumped environmental TEM such as the aberration corrected FEI Titan 80-300 ETEM gives an indication of the pressure resulting in a similar amount of scattering event as described above. The high-pressure zone is confined by the pressure-limiting apertures placed at the pole pieces resulting in a pathway of around 7 mm (Hansen et al. 2010). The pathway is around two orders of magnitude longer in the aperture-limiting setup compared to the windowed solution. The upper limit of pressure allowing lattice fringe imaging is around two orders of magnitude lower for the aperture-limiting setup. Virtually compressing a 7 mm slab of gas at 1 kPa into the same atomic density as a solid results in a "solid" of around 10 nm in thickness—a typical value that allows for good lattice fringe imaging conditions. However, the scattering on gas molecules takes place over the full pathway between the pole pieces and not only in the intended object plane for conventional samples. The extended volume of scattering events includes the front focal and back focal plane as indicated in Fig. 3.2. This implies that the scattering geometry of the electron–gas interaction has to be revised. The rather complex trajectories which the scattered electron now follows lead to a loss of intensity in the final image as electrons being scattered above and below the sample are captured by apertures (or the column itself). In the windowed cell approach, the electron–gas scattering takes place closer to the intended objective plane and the conventional tracing of scattering event is more suitable in this case.

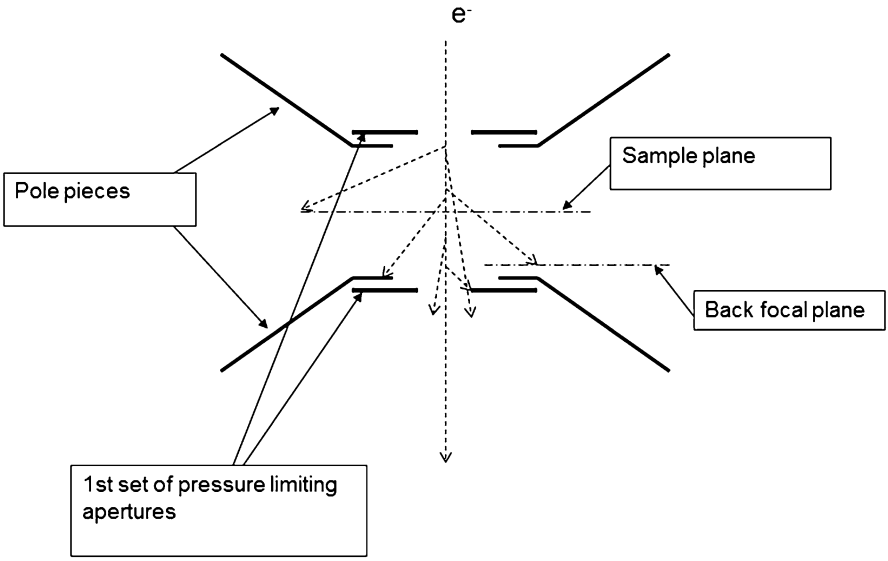

Fig. 3.2 Scattering of electrons on gas molecules in a differential pumped ETEM. (**a**) Scattering of electrons on gas molecules (indicated by *hatched lines*) takes place mainly between the first set of pressure-limiting apertures, which extend the focal length of the objective lens. The effect of the objective lens on the electron "trajectories" is not included in this drawing. The sketch is not to scale. Modified from Wagner et al. (2012)

3.2.2 Loss of Intensity

One of the immediate observed effects of letting gas into the microscope is the significant loss of intensity in the image. Measuring the intensity by summing the counts on the CCD at a given magnification and optical configuration as a function of gas pressure, gas composition, and acceleration voltage reveals that the intensity can be reduced as much as 95 % within the pressure range compatible with the differentially pumped ETEM. Figure 3.3 shows the normalized CCD count (count per pixel) in the absence of a solid sample. The intensity is normalized with respect to the measured intensity in traditional high vacuum mode ($P = 10^{-4}$ Pa). The measurements are plotted as function of pressure in different gases (H_2, He, N_2, O_2, and Ar). The gases represent a range of molecular mass typically for the gases used in the ETEM. The measurements are performed at three different acceleration voltages of the microscope as well. It is obvious that the measured intensity at the CCD in general is decreasing with increasing gas pressure. The density of gas molecules in the path of the electron beam increases with increasing pressure and thereby increases the probability of an electron–gas scattering event resulting in the electron being stopped by apertures in the microscope column.

The cross section of scattering events between fast electrons and molecules depends on the energy of the swift electrons: the higher the energy the lower the

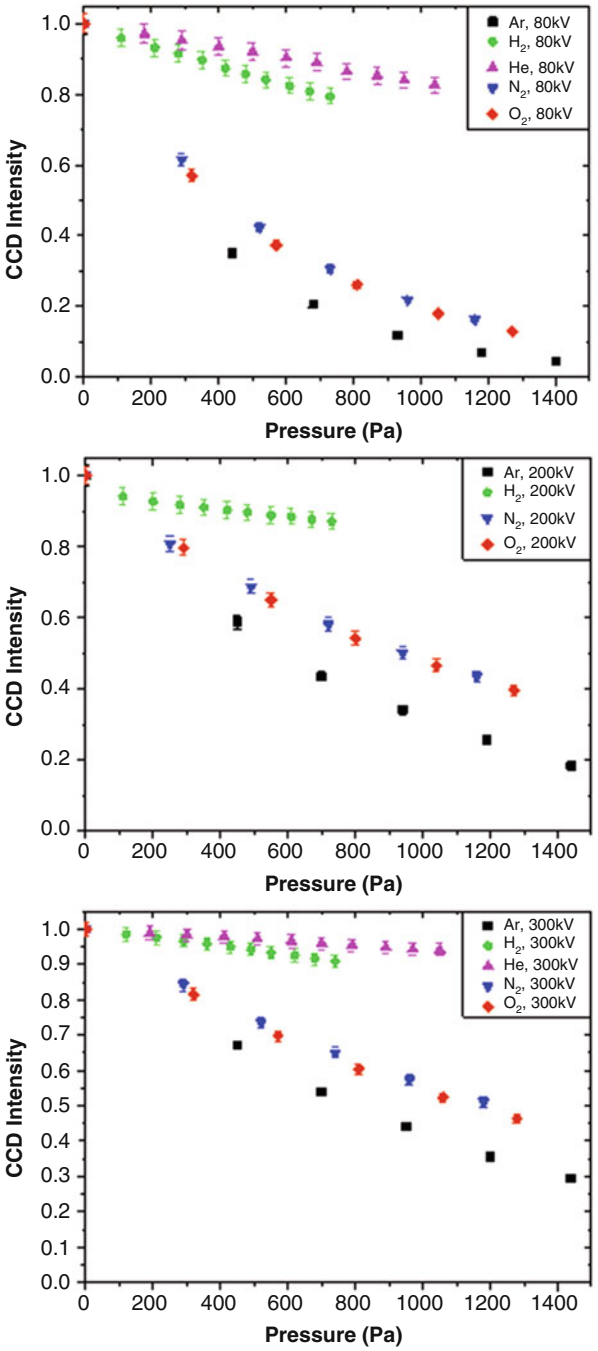

Fig. 3.3 The effect of the primary electron beam scattering on gas molecules in a differentially pumped environmental TEM. Normalized image intensity (without a specimen present) measured on a pre-GIF Ultrascan CCD camera, plotted as a function of gas pressure for various gas molecules at 80, 200, and 300 kV. The significant loss of intensity (counts) at the camera results in general in lower signal-to-noise ratio of the acquired images

cross section, as the electrons have less time to interact with the molecules along their path, decreasing the probability of interaction. Figure 3.3 shows clearly that the loss of intensity is, in general, larger for experiments performed at lower acceleration voltage of the primary electron beam in the presence of gas.

The measured intensity of the electron beam varies also with the atomic number of the gas species. Whereas the measured intensity only varies little for lighter molecules such as hydrogen and helium, the recorded intensity is less than 30 % of the vacuum value in 1400 Pa of argon using 300 kV primary electrons. With 80 kV electrons, the remaining intensity is less than 10 %. These observations indicate that the scattering cross section needs to be taken into account when estimating the loss of intensity for a TEM experiment. The scattering of electrons by gas molecules follows the atomic number.

Both the elastically and inelastically scattered electrons are contributing to the measured intensity. Electron energy-loss spectroscopy (EELS) reveals both low-loss and core-loss features corresponding to ionization of the gas molecules present between the pole pieces. As the pressure in the objective lens is increased, the ratio between the low-loss features and the zero-loss peak increases as expected. The fraction of the total intensity of the inelastically scattered electrons is indicative of the gas pressure in the pole piece gap.

The same trend in loss of intensity for the differentially pumped pathway of having gas in the microscope has been reported by Jinschek and Helveg (2012) for N_2 in a ETEM operated at 300 kV at different pressures. As a result of the decreased intensity the signal-to-noise ratio is also decreased with increasing gas pressure between the pole pieces. This will of course influence the image quality and thereby the spatial resolution obtainable from images at a given electron dose. Compensating by increasing the total dose during imaging will not always be a valid opportunity as both sample drift and beam damage might influence the observations as discussed below.

One way to minimize the loss of intensity in the acquired images is to decrease the total probability of electron–gas scattering at a given pressure by decreasing the gas path length. Decreasing the gas path length by encapsulating the high-pressure gas zone between impermeable membranes allows for higher pressures without losing too much intensity. Calculations by Yaguchi et al. show that the amount of unscattered 300 kV electrons is reduced by 70 % in 1×10^5 Pa of air having a 0.5 mm gas path length (Yaguchi et al. 2011). Comparing to the measured values in Fig. 3.3 it is found that a similar intensity loss is found for approximately 800 Pa gas (O_2–N_2) in a pole piece gap of 7 mm. The projected density of gas molecules is comparable in the two cases. Advantages and disadvantages of the membrane solution for high-pressure TEM measurements are addressed in more detail in Chap. 6.

3.2.3 Resolution in TEM

Besides the loss of intensity of the acquired images when having gas species in the microscope, the spatial resolution in general decreases with increasing gas pressure. To explore the effects of gas–electron interaction on the degradation of spatial

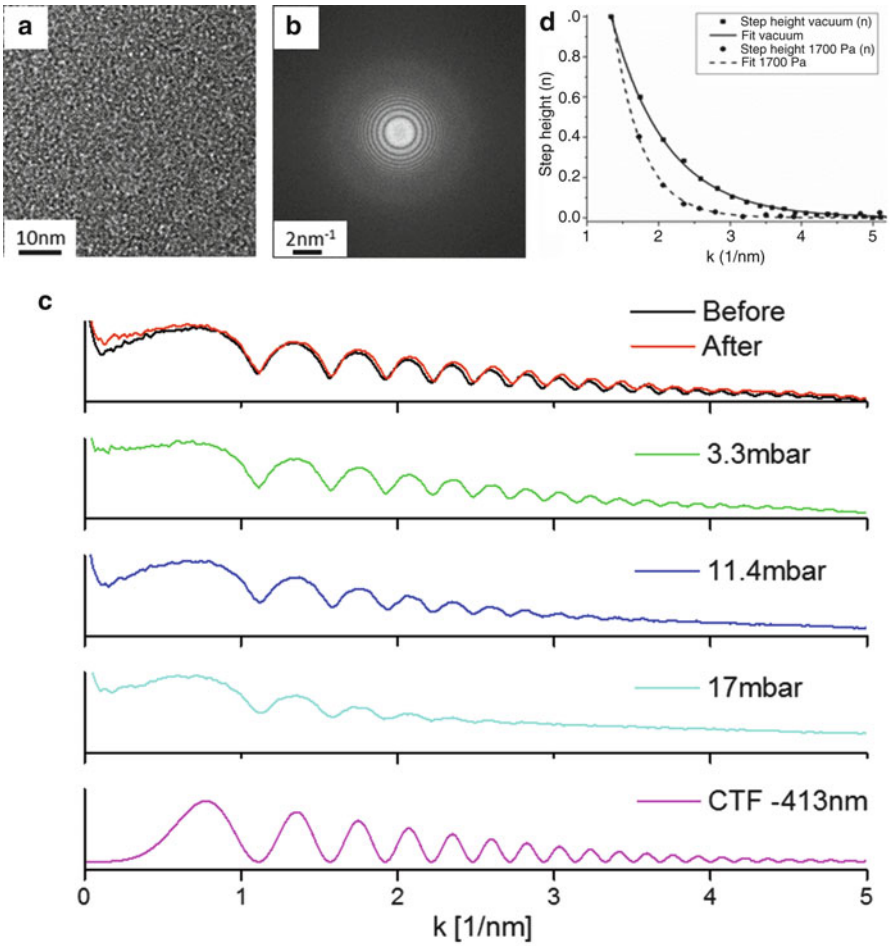

Fig. 3.4 Contrast transfer in presence of gas. (**a**) Amorphous carbon imaged out of focus. (**b**) Fourier transform of (**a**) showing the Thon rings. (**c**) From the FFT in (**b**), the radial intensity has been extracted. Values at intermediate pressures and a simulation made using CTFExplorer (Sidorov 2003) are also included in the plot. (**d**) The step height defined as peak to valley value of the radial intensity of the FFTs is plotted for vacuum and 1700 Pa Ar. Figure modified from Hansen et al. (2012)

resolution, we acquired images of a pristine amorphous carbon film at increasing gas pressure of argon as shown in Fig. 3.4. Prior to each acquisition the defocus value was adjusted to 410 nm as estimated by the aberration-corrector software from the Thon rings. The small change in calculated defocus value after each change of pressure is accredited to thermal drift as the gas temperature might be slightly different compared to the sample temperature.

The radial intensity profiles of the power spectra shows the minima and maxima well aligned as a result of adjusting the defocus value. The apparent damping of the

information from higher spatial frequencies in the image changes clearly with gas pressure. Due to the large defocus value used for the acquisition, the spatial resolution is far from optimum even in the case of imaging in vacuum. Quantifying the contrast transfer by measuring the step height of the oscillations in the FFT being the top-to-valley value shows that damping of the CTF decreases the information transferred at higher spatial frequencies. In the case of imaging in vacuum, 10 % transfer is observed up to 3.2 nm^{-1}, whereas having 1700 Pa argon between the pole pieces results in the maximum spatial frequency being transferred with at least 10 % being around 2 nm^{-1}. Similar observations (not shown here) at 80 kV show a much faster decrease of the contrast transfer. In the presence of lighter gas molecules, this dampening is significantly less pronounced.

A more severe effect of the presence of gas around the sample is damage on the sample and support film primarily in the form of etching, which can be minimized by keeping the beam current density low. For this reason, the current density was deliberately kept low for the present observations, on the order of 1 A/cm^2. The effect on the amorphous film was monitored by recording an image in vacuum after the experiment. The FFT of this image indicates that the damage sustained by the film was insignificant as observed from Fig. 3.4.

The loss of lattice fringe resolution as a function of pressure can be described in terms of a damping of the Contrast Transfer Function (CTF). The scattering events taking place in the high-pressure zone is represented by the CTFs. Energy spread by inelastic scattering induces the defocus Δf due to chromatic aberration and the elastic scattering alters the wave direction Δk leading to an increment in the angular spread. Both leads to damping of the CTF as described by Yaguchi et al. (2011; Suzuki et al. 2013). An estimation based on the calculated CTFs indicates that resolution is not influenced much by 1×10^4 Pa air in a 1.0 mm gas path length (including 15 nm Si_3N_4 membranes). However increasing the pressure just by a factor of 10 to 1×10^5 Pa essentially kills all phase contrast.

In order to get deeper into the understanding of the gas–electron scattering and its effect on the lattice fringe resolution and intensity, Suzuki et al. divided the gas–electron scattering into two regimes (Suzuki et al. 2013). The gas–electron scattering occurring above the specimen does not influence the coherence of each electron and thereby only the angular deflection and the energy loss deteriorate the construction of the image at the image plane. The gas–electron scattering occurring below the sample results in destruction of the coherence and will thereby not contribute to the information transfer from sample to image.

The loss of resolution in terms of decreasing phase contrast at higher spatial frequencies does not only depend on the gas composition and pressure in the ETEM. The total current in the electron beam is found to influence the spatial resolution keeping the current density (electrons per sample area) constant (Jinschek and Helveg 2012; Bright et al. 2013).

To illustrate the effect of the current density and the total electron beam current on the transferred information and thereby the resolution of the microscope operated with gas surrounding the specimen, amorphous carbon has been imaged in 270 Pa of O_2. The images are acquired at a relative high defocus value in order to

identify a number of Thon rings in the FFTs. In Fig. 3.5, the FFTs achieved from images in the presence of gas at different current density and total beam current are shown. The absolute values of the total beam current and the current density are measured without the presence of gas under given optical conditions, which then is used for imaging in gas as well.

Varying the current density keeping the total current and acquisition time constant results in an increased damping of information at higher spatial frequencies (and thereby the resolution) at lower current densities as shown in Fig. 3.5a. This phenomenon is related to the loss of intensity as the signal-to-noise ratio (SNR) is becoming smaller at lower dose. Repeating this experiment without the

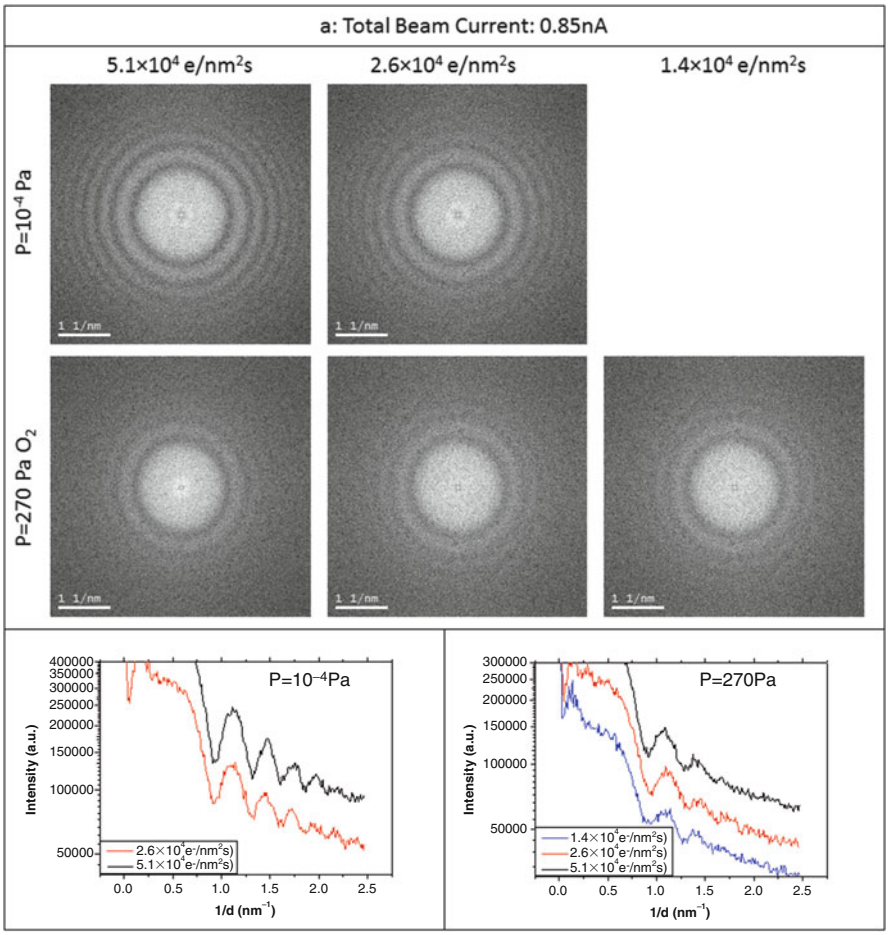

Fig. 3.5 Fast Fourier transforms of images of amorphous carbon as a function of (**a**) current density and (**b**) total beam current. The damping of the information transferred to the image is highly dependent on the total electron beam current in the presence of gas. The resolution of the images acquired in conventional vacuum mode do not show the same dependency

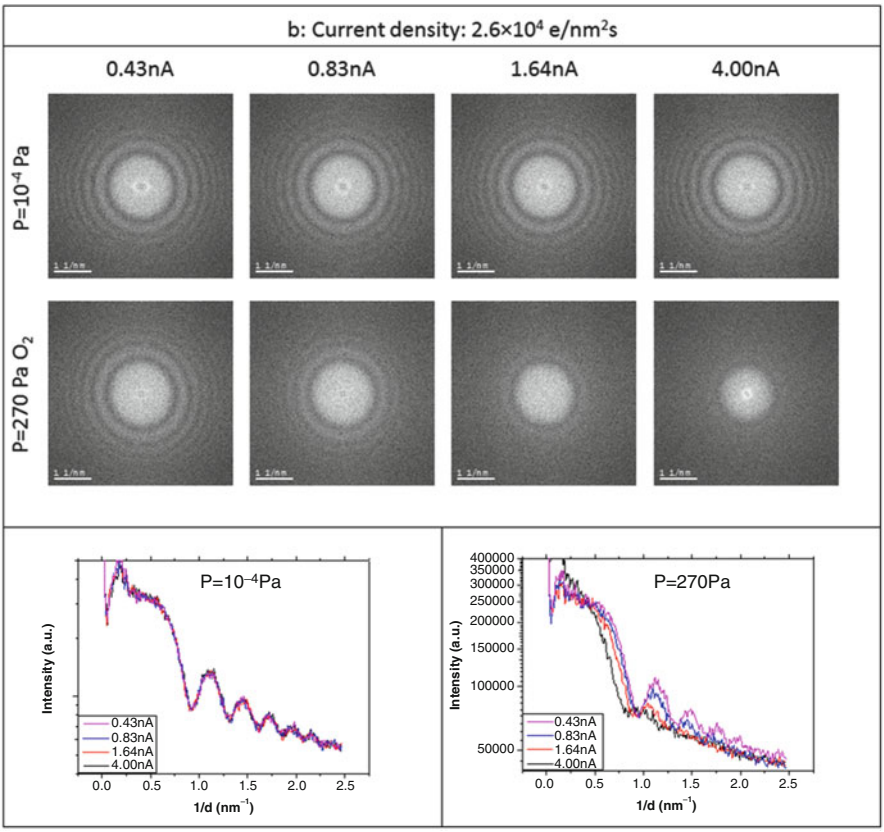

Fig. 3.5 (continued)

presence of surrounding gas molecules gives a similar effect information transfer at high spatial frequencies; however, the SNR is in general higher as the absolute number of electrons contributing to the image is significantly higher without the gas present as seen from Fig. 3.3. Although the SNR plays a role in the loss of resolution, it cannot account for the full effect. Images acquired with similar acquisition time resulting in similar total count on the CCD and similar SNR shows poorer spatial resolution in the presence of gas compared to vacuum in terms of information transfer at high spatial frequencies.

Keeping the current density constant but changing the total current of the electron beam (by changing condenser aperture) results in a significant loss of resolution at higher total beam current in the presence of gas as shown in Fig. 3.5b. The SNR is not affected significantly by the varying total beam current and is observed for a current density range spanning several orders of magnitude (Fig. 3.5; Bright et al. 2013). The resolution of the acquired images in conventional vacuum mode appears to be independent on the total beam current. The current density of the electron beam is measured on the viewing screen and is calibrated to the sample

plane. The electron trajectories of unscattered electrons give rise to a varying beam diameter throughout the pole piece gap. This implies that the current density in the back focal plane is dependent on the total current, even if the current density in the sample plane is kept constant.

3.2.4 Contrast of Bright field images

The resolution and contrast has been discussed above in terms of phase contrast for high-resolution imaging. However, lot of interesting studies have been done over the past decades by means of lower magnification ETEM (Ross et al. 2005; Zhou et al. 2006, 2012; Kodambaka et al. 2007; Li et al. 2009; Sharma 2009; Jeangros et al. 2010; Nasibulin et al. 2010; Costa et al. 2010; Cabié et al. 2010; Janbroers et al. 2011; DeLaRiva et al. 2013; Hansen et al. 2013; Vendelbo et al. 2014). The loss of intensity will of course influence the image quality, but how is electron–gas scattering and interaction affecting the contrast in low-magnification images?

In order to elucidate the relation between image intensity loss caused by electron–gas scattering and the possible related loss of contrast, an edge of a lacey-carbon amorphous film has been imaged at room temperature for varying argon pressures (Fig. 3.6). The edge of the lacey carbon film shows a contrast reflecting the thickness variation of the film corresponding to three distinct thicknesses (thinnest in the upper right corner). The lower left corner of the image corresponds to vacuum (no sample). The intensity profile of the image measured perpendicular to the edge shows four distinct intensities corresponding to the four distinct thicknesses (named 1–4). The overall intensity of the area of interest strongly depends on the total pressure of argon. The intensity decreases by more than 60 % for pressures above 1000 Pa in good agreement with the data presented in Fig. 3.3—the acceleration voltage of the present measurements is 300 kV. Normalizing the intensity of the images to the value measured in the region without any solid sample present (Region 1) shows that the contrast is much less affected. Besides a small spatial shift in the intensity measured between Region 2 and 3 caused by sample drift and possible etching, the contrast remains constant over the pressure range used. The extra scattering of electrons in the presence of gas does not affect the mass-thickness contrast; however, the signal to noise is decreased with increasing gas pressure.

The measurements presented in Fig. 3.6 were all acquired with an objective aperture corresponding to an acceptance angle of 2.7 mrad. The contrast in low-magnification images is strongly related to the size of the objective aperture as it filters the specimen-scattered electrons. Figure 3.7 shows the plot of the intensity measured around a lacey carbon edge. Without any gas present in the microscope column, the image intensity measured at the solid sample decreases with decreasing objective aperture size (Region 2 and 3). As no scattering occurs in Region 1 of the image (without gas) the intensity is constant with varying objective aperture size.

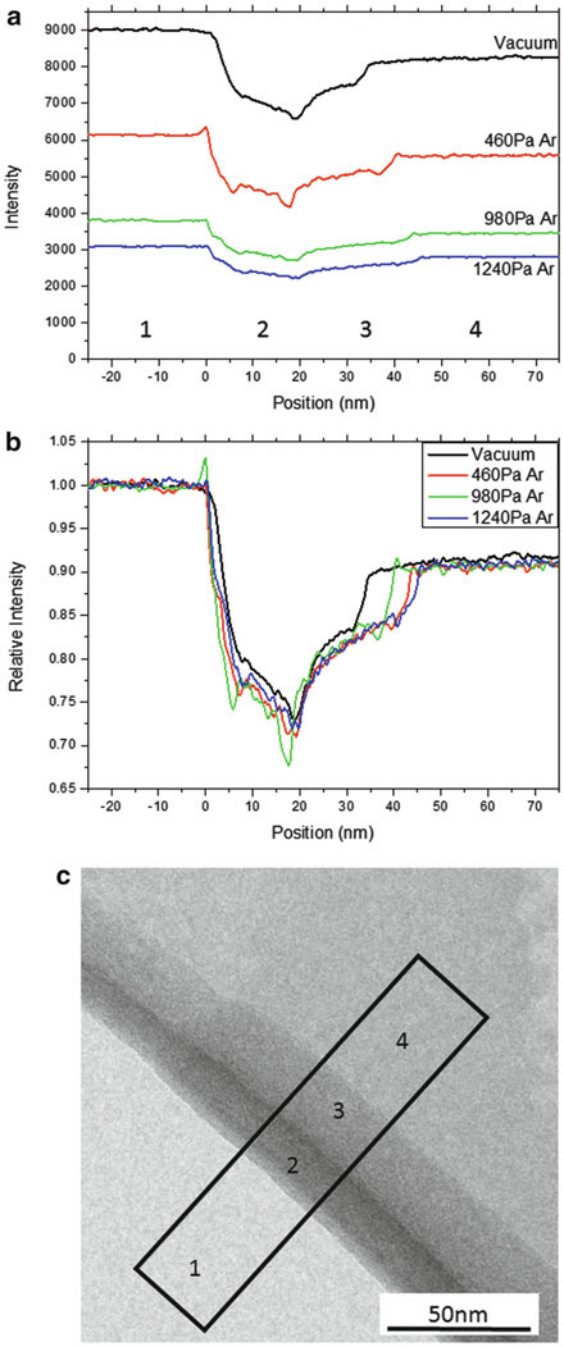

Fig. 3.6 Contrast of amorphous carbon film imaged in presence of Argon. (**a**) Absolute intensity measured on images. (**b**) Normalized intensity revealing an insignificant change in the contrast. The slight shift in intensity around 40 nm is due to sample drift and damage. The numbers 1–4 in the plots refer to the areas indicated in (**c**)

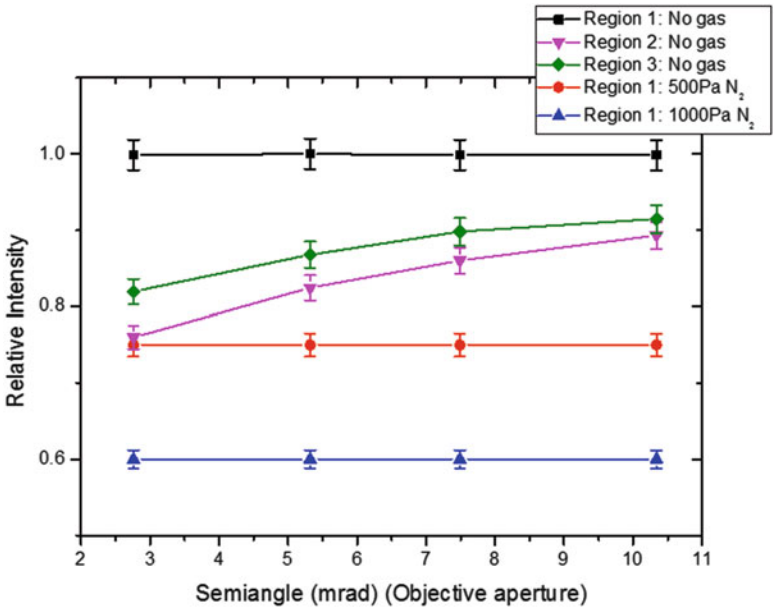

Fig. 3.7 The relative intensity of the carbon edge images in vacuum and nitrogen presented as function of the maximum allowed scattering angle for the electrons forming the image as defined by the objective aperture. The region numbers in the legend refer to the areas defined in Fig. 3.7

Changing the objective aperture in the presence of gas does not have the same effect on the contrast of the image. The intensity is constant with varying objective aperture size in depicted area without any solid sample (as seen in Fig. 3.7). As the scattering of the electrons on the gas molecules takes place over the full gas path between the pole pieces and not only in the plane of the solid sample (see Fig. 3.2), the objective aperture is no longer placed in the back focal plane of the scattering event (object plane).

Furthermore, comparing the intensity of the image in the presence of gas to the intensity measured of the solid carbon sample gives another indication of the ill-defined scattering geometry. Assuming that a gas path of 7 mm of 500 Pa and 1000 Pa N_2 has a projected atom density similar to 5 nm and 10 nm of solid, respectively, justifies the comparison of the measured intensity of the imaged solid without gas present and the measured intensity of imaged gas without solid present. The measured intensity of the gas-only scattered electrons is significantly lower than the measured intensity of the solid-only scattered electrons as illustrated in Fig. 3.7.

This indicates that the limiting aperture for electrons scattered on the gas molecules present in a distance from the sample plane is relatively small (in angular terms) compared to the “normal” objective aperture.

3.3 On the Propagation of Electrons in an ETEM

The observed independence, within experimental uncertainties, of the total current reaching the detector on the objective aperture radius (Fig. 3.7), coupled with the pressure-dependent net loss of electrons (Fig. 3.3), has two important consequences: (1) the angular distribution of the electron beam appears to be very narrow in spite of electron–gas scattering and (2) what "absorbs" electrons cannot be the objective aperture. To explain these findings, we need to move beyond the simple picture of a neutral gas modeled essentially as a low-density amorphous slab with thickness equal to the extension of the gas chamber. In fact, the characteristic elastic scattering angle θ_0 from typical low-Z atomic or molecular gasses (e.g., O_2, N_2, and Ar) is typically of the order of 15 mrad: following Egerton's (1996) introduction to elastic scattering based on the Lenz (1954) model, $\theta_0 = (\lambda Z^{1/3})/(2\pi a_0)$, or $\theta_0 = 6\,Z^{1/3}$ if measured in mrad and with 300 kV electrons, resulting in, for example, about 15 mrad for O_2. Since the fraction of electrons elastically scattered at angles beyond θ_0 is, by definition, 50 %, an Objective Aperture (OA) will necessarily start "absorbing" electrons when its radius approaches θ_0. On the contrary, the data (see Fig. 3.7) indicates unequivocally that no electrons are intercepted in the OA plane outside a very narrow window of just 2 mrad (the smallest aperture used was 10 μm in diameter, located approximately 2.5 mm below the sample plane, giving about 5 μm/2.5 mm = 2 mrad radius). Possible geometrical adjustments, such as considering scattering events happening higher up in the gas chamber, resulting in an effective z-dependent aperture angular radius, are not a sufficient reconciliation. In fact, if the objective aperture physical radius is selected to allow any $<$15 mrad scattered electrons from the sample plane, any electron that is 15 mrad scattered above or below the sample plane will not intercept the aperture.

This can be seen from the diagram in Fig. 3.8, where we calculated the effective aperture radius for axial electrons 15 mrad scattered from an arbitrary location within the 7.5 mm wide gas chamber (indicated by the blue vertical dashed lines). In the diagram, distances are measured from the objective lens mid-gap ($z = 0$ mm), the horizontal dashed line gives the 15 mrad reference, the sample plane (indicated by the purple line) is positioned to receive planar illumination from the nearest cross-over (located above the entrance aperture of the gas chamber at $z = -4.7$ mm for the chosen parameter set) and to form its Fraunhofer diffraction pattern at the OA plane (red line), located at $z = 2.5$ mm. As evident from the diagram, no gas-scattered electron will be absorbed by the OA just because it was scattered above or below the sample: gas-scattered electrons above the sample will be kept within the OA mainly by the focusing effect of the Objective Lens (OL), while those scattered below the sample will effectively see a larger and larger aperture as the location of the scattering event approaches the OA plane. Those electrons that are scattered below the OA plane (where there is still gas) will obviously see no aperture at all. The focusing effect of the pre-field is particularly important in determining the effective aperture size, as just by considering straight trajectories and the geometrical angles involved, one would expect a portion of the electrons

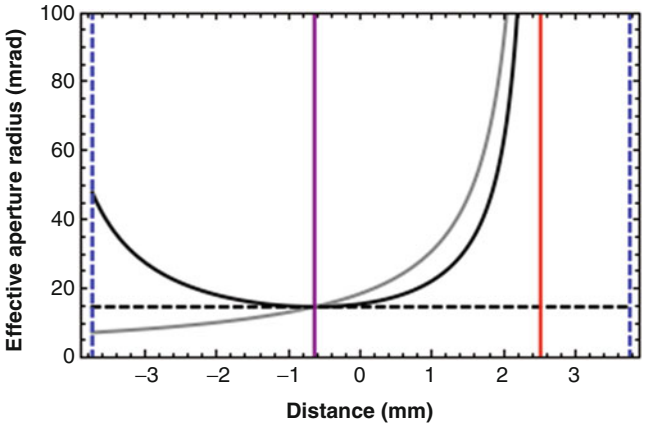

Fig. 3.8 Effective angular size (*black line*) of a nominal 15 mrad objective aperture (*black dashed line*) when referred to a scattering event occurring within the gas chamber at a coordinate z along the optic axis. The curve differs from a simple geometrical estimate based on straight trajectories (*gray line*) due to the focusing effect of the objective lens' field. Additional *colored lines* indicate the position of sample plane (*purple*), objective aperture plane (*red*), and pressure-limiting apertures (*dashed blue*)

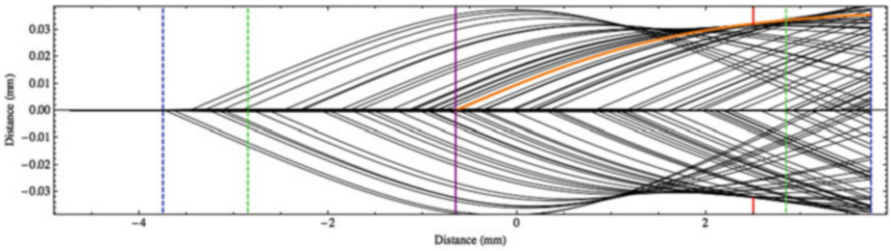

Fig. 3.9 Set of trajectories representing electrons scattered at 15 mrad from a random location along the optic axis illustrating how, regardless of where scattering occurs, no electron is intercepted by the objective aperture (*red line*). The *orange line* highlights a 15 mrad scattering event originating at the sample plane (*purple line*), reaching precisely the edge of the objective aperture. *Other colored lines* indicate the positions of the pressure-limiting apertures (*blue*), and objective lens pole pieces (*green*)

scattered above the sample to be intercepted by the aperture, as illustrated by the gray line.

To further illustrate the concept and role of an effective position-dependent aperture size, we have calculated a set of 10,000 trajectories (100 of which are plotted in Fig. 3.9) for electrons that are scattered at 15 mrad from a random location along the optic axis within the gas chamber. In Fig. 3.9, we have added a 15 mrad "Bragg beam" (thick orange line) originating from the sample and used to choose the appropriate OA radius (about 30 μm in this case). We have also added two dashed green lines indicating the positions of the pole pieces bounding the OL gap. A standard Glaser

model was used for the OL field ($B_{max} = 2.2$ T, $a =$ OL gap/2 $= 2.85$ mm) to facilitate the computation.

Visual inspection of Fig. 3.9 reveals an important piece of information: while pre-sample scattering does not remove electrons from the beam, it does influence dramatically the illumination characteristics. In absence of gas scattering, and with the chosen electron-optical setup (position of the cross-over, position of the sample, OL axial field model, etc.) the sample would be illuminated by a 1-μm patch of planar illumination, while electrons scattered at 15 mrad higher up in the gas chamber, may end up as far as 30 μm off-axis at the sample plane. This simple observations hints already at what might be responsible for the observed net decrease of electrons reaching the CCD: a field-limiting aperture positioned further down the column, for example, the selected area aperture (SAA), or one of the entrance diaphragm of the image-corrector. This is better visualized by zooming the trajectory plot out to the first image plane, in this case located about 6 cm down the column.

Figure 3.10 reveals that the reference "Bragg beam" originating at the sample plane makes its way through the OA, and is kept paraxial down to the image plane where it recombines with all other beams from the sample to form the image. The rightmost purple line indicates the position of the image plane, and it has an aperture that corresponds to the 1-μm illumination patch on the sample plane once rescaled for the OL magnification factor. Almost all trajectories, corresponding to electrons scattered at almost any position other than the sample plane, are intercepted by the purple field-limiting aperture. Some electrons are also intercepted by the lower 400-μm pressure-limiting aperture positioned 17 mm below the first one (both indicated by the blue lines in the illustration).

The considerations exposed so far provide us with a qualitative explanation as to why the OA plays no role in "absorbing" gas-scattered electrons while at the same time the net count reaching the detector may be very small. However, the data underpinning this analysis tell us that the OA plays no role even for angular apertures much smaller than the expected neutral-gas characteristic elastic

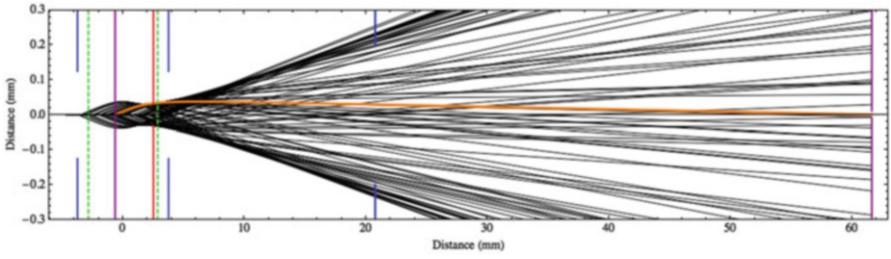

Fig 3.10 Same set of trajectories as in Fig. 3.9, plotted over a larger scale and illustrating the importance of further apertures positioned down the column. The third *blue line* at $z = 70$ mm indicates a 400 μm aperture that is part of the ETEM system, while the second *purple line*, positioned at the image plane, indicates a field-limiting aperture (selected area-type) conjugate with the 1 μm illumination patch on the sample

scattering angle, and this is clearly at odds with the diagrams presented above: if we imagine to reduce the OA radius from 30 μm down to 5 μm (the smallest OA used), while keeping the gas-scattered electrons at 15 mrad, we would definitely start "absorbing" electrons directly in the OA plane.

Since the analysis of the effective position-dependent aperture revealed that the nominal aperture angular radius (referred to scattering from the sample plane) is a lower limit, in the sense that it is effectively bigger for electrons that are gas-scattered anywhere else within the gas chamber, we can only conclude that the characteristic angle for gas scattering is much smaller than what we estimated on the basis of the Lenz model. Since the atomic weight of the gas is fixed, and so are temperature, pressure, and beam energy, the only parameter that might result in a substantial decrease of the characteristic angle is ionization of the gas. We may imagine, in fact, that as soon as the beam is turned on and electrons start crossing the gas chamber, a fraction of them will undergo inelastic scattering while ionizing the gas. In fact, ionization losses are clearly observed in the EELS signal (see Chap. 4), indicating that the primaries trigger and sustain the generation of free electrons and ions in the chamber; their recombination will then kick-in, until a dynamic steady-state equilibrium is reached in the form of a plasma. The charge-carrier density of the plasma will depend on generation and recombination rates, and it is important to estimate the beam-induced plasma characteristics, in particular its Debye length, because the typical elastic scattering angle will depend on it.

In a single-scattering approximation, by combining the stopping power S (in units of energy/length) of the gas as given by the NIST ESTAR database (Berger et al. 2005) the mean observed energy loss E_i associated with ionization of the gas molecules, and a primary beam current density J_p, we can write the volume generation rate G (in units of number density per unit time, or $1/(\mathrm{m}^3\mathrm{s})$) of electrons as

$$eG = J_\mathrm{p} S / E_\mathrm{i}$$

For example, considering $P = 1$ mbar He at room temperature, having a number density of $n_\mathrm{He} = P/k_\mathrm{B}T = 2.4 \times 10^{22}/\mathrm{m}^3$ (equivalent to a mass density of $4n_\mathrm{He}u = 1.6 \times 10^{-7}\ \mathrm{g/cm}^3$) ESTAR estimates a stopping power for 300 keV electrons of about 36 eV/m, corresponding to a mean loss of 0.27 eV (or 11 ionization events per 1000 primaries) over the 7.5 mm gas chamber. The generation rate according to (3.1) considering a primary current density of 16 $\mathrm{kA/m}^2$ and the He ionization energy $E_\mathrm{i} = 25$ eV is then $G = 1.5 \times 10^{23}\ 1/\mathrm{m}^3\mathrm{s}$, which is a very small number: for comparison, the typical electron-hole pair generation rate in a solar cell under solar illumination can be 5–7 orders of magnitude higher, and EBIC effects with solid targets might originate from even larger generation rates. Of course, such a large difference arises from the low gas density with respect to that typical of solids.

The generated electrons and ions, in the example above He^+, will start recombining, and a steady state is reached when the generation and recombination rates are equal. Considering a recombination term with the form Knp, and noting that in this simple picture that disregards the variety of ionic species and charge

states that are interacting and evolving in higher-Z molecular gasses, the electron and He^+ densities are equal, i.e., $n = p$, the plasma charge density at steady state is simply $n_p = (G/K)^{1/2}$. A representative value for the recombination constant K (Fugol et al. 1971) is about 1×10^{-15} m^3/s at room T, independent on P, giving a plasma density of just $n_p = 1.2 \times 10^{19}\,m^{-3}$, corresponding to an average gas ionization degree $n_p/n_{He} = 250$ ppm. The characteristic time for achieving the steady state can be estimated as $\tau = (GK)^{-1/2}$, or 75 μs.

Increasing the gas pressure fourfold leads to a 4× larger gas density, 4× higher generation rate, 2× larger plasma density, 2× faster steady state achievement, and 2× *smaller* degree of ionization.

Having neglected generation of higher ionic charge states, as well as core-losses and secondary ionization, the estimated plasma density is most likely a lower bound. We have also considered one particular beam current density in this example, representative of the value it has near the sample plane in our experiments. The simple equation $G = Kn^2$ we have employed to predict the steady state plasma density is the residual term of the drift-diffusion transport equation when both drift and diffusion are absent, i.e., when the charge density in the plasma is uniform, so that no electric fields and no concentration gradients are present. However, as the beam converges towards the focal point, the beam current increases by orders of magnitude, and so does the generation rate, leading to a higher plasma density in the OA plane. Even more rapid is the decay of the primary current density at the rim of the illumination patch, where the generation rate drops to zero over a sub-micron length scale. As a consequence, we cannot expect a uniform charge concentration throughout the gas chamber, which triggers diffusion followed by the formation of space-charge regions with non-negligible electric fields that, in turns, may modify the whole electron-optical configuration in the OL field region. In particular, measurable variations of the focal length are conceivable due to the plasma field acting as a weak electrostatic lens on top of the much stronger OL. Achieving a satisfactory description of the beam-induced plasma in the gas chamber requires necessarily the full, self-consistent solution of the drift-diffusion equation in a circularly symmetric three-dimensional volume with the spatially varying magnetic field of the OL included as an additional term as it affects the plasma dynamics. As this treatment is beyond the scope of this chapter, we extend the basic picture developed so far only by considering, when needed, a z-dependence of the plasma density according to

$$n_p(z) = [J_p(z)S/(eKE_i)]^{1/2}$$

while abandoning any quantitative intention.

Once equilibrium is reached, free electrons wandering in the gas chambers start playing a fundamental role: screening of the ionic Coulomb potential. As it happens in any physical system with co-existing charge carriers of opposite sign in a dynamic equilibrium, for example, in semiconductors, electrolytes, or in the ionosphere of our planet, an added external charge polarizes the environment resulting

in an electric field that decays with distance faster than in vacuum. In particular, the Coulomb potential of an isolated charge in vacuum turns into a Yukawa potential, also called "screened Coulomb potential"

$$V(r) = e/(4\pi\varepsilon_0 r)\exp(-r/\lambda_D)$$

decaying exponentially over a length scale λ_D named "Debye length," which is defined for a Maxwellian free electron gas with fixed neutralizing background ("jellium" model) as

$$\lambda_D = \left(\varepsilon_0 k_B T/n_p e^2\right)^{1/2}$$

For the 1.2×10^{19} 1/m^3 He plasma density calculated earlier when the pressure is 1 mbar, the resulting Debye length at room T is approximately 350 nm. Since the plasma density depends on the square root of pressure via the stopping power, and the Debye length depends on the inverse square root of the plasma density, ultimately we have a relatively weak dependence of λ_D on pressure, i.e., $\lambda_D \sim P^{-1/4}$. At 10 mbar pressure, for example, the Debye length is about 200 nm. As we illustrate in the following, plasma screening occurring at a Debye length scale is the key concept needed to address the puzzling experimental results, as it affects dramatically the mean elastic scattering angle we expect from a partially ionized gas.

The elastic cross sections for electron scattering by ions are very different from those for neutral atoms. As shown by Peng et al. (2004), ionic scattering factors for an atomic number Z are decomposed into two terms: the first arising from the fully screened atom potential $f_0(q)$ for a virtual neutral atom with atomic number $Z - Z_i$, (Z_i is the ionic charge) the second originating from the long-range Coulomb potential of a bare point charge with magnitude Z_i, and resulting in a pure Rutherford term:

$$f_{\text{ion}}(q) = f_0(q) + 2\gamma Z_i/\left(a_0 q^2\right)$$

where a_0 is the Bohr radius and $q = 4\pi/\lambda \sin(\theta/2)$ is the magnitude of the momentum transfer for a scattering angle θ. Note that we have adopted the notation of Egerton (1996), while scattering factors in Peng et al. (2004) are tabulated as a function of $s = \sin(\theta/4)/\lambda$ rather than as a function of q. At small angles, s and q are simply related by $q = 8\pi s$.

As visible in Fig. 3.11, where we consider Au only for illustration purposes since its scattering factors are readily available, neutral atom and ionic scattering factors differ in particular at small angles due to the long-range potential of the unscreened ionic charge capturing electrons at large impact parameters. The small-angle divergence of the Rutherford cross section for an isolated charge poses a normalization problem. Having a finite total cross section is a necessary prerequisite for proper accounting of the incoming vs. scattered electrons: if the cross section goes

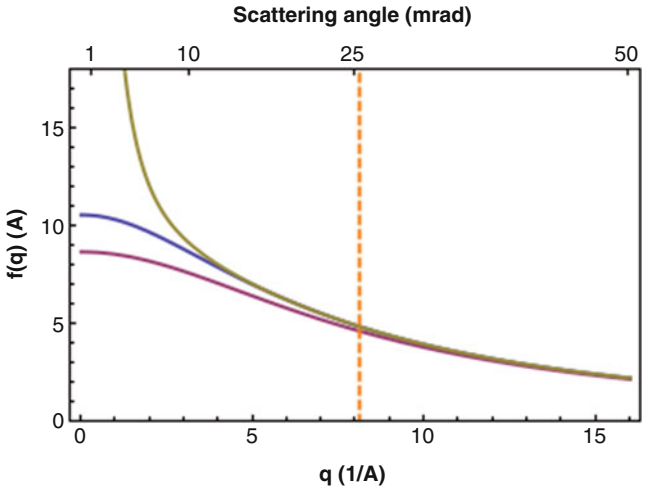

Fig. 3.11 Scattering factor for neutral Au (*blue curve*) and Au+ (*yellow curve*). The purple curve represents $f_0(q)$, originating from the screened portion of the atom potential. The dashed orange line indicates the characteristic elastic scattering angle for neutral Au, $\theta_0 = 6 \times 79^{1/3} = 25$ mrad, corresponding to $q = 8.1$ A^{-1} for 300 keV electrons

to infinity, every electron, no matter how far from the ion, is captured and undergoes elastic scattering, although essentially all of them are scattered at very small angles.

In plasmas, however, as discussed above, screening provides a cutoff that keeps the total cross section finite. To estimate the characteristic plasma-scattering angle, we proceed heuristically. For neutral atoms, the large-angle (low impact parameter) cross section is Rutherford, while for small angle it is dictated by Thomas-Fermi screening of the nucleus potential over a characteristic length $r_0 = a_0 Z^{-1/3}$ (as already used above when estimating θ_0). For ions in a plasma, large-angle scattering remains Rutherford, but small-angle scattering now becomes, and this is our ansatz, Debye-screening limited, with characteristic length set by the plasma density-dependent Debye length.

If we then revisit the derivation of the scattering factor in presence of a different type of Yukawa potential, with screening parameter now equal to the Debye length in the plasma, we obtain an approximation for the elastic cross section from ions, which remains finite at $q \to 0$ and allows to calculate the total cross section thereby giving us the opportunity to estimate the effect of ionization on the beam.

Modifying then the Rutherford term in the ionic scattering factor by replacing q^2 with $q^2 + \lambda_D^{-2}$, and estimating the screened term $f_0(q)$ as if it originated from a neutral atom with atomic number $Z - Z_i$, we arrive at

$$f_{\text{ion}}(q) = 2\gamma/a_0 \left[(Z - Z_i)/\left(q^2 + r_0^{-2}\right) + Z_i/\left(q^2 + \lambda_D^{-2}\right) \right]$$

Note that $f_{\text{ion}}(q) \to f(q)$ when either $Z_i = 0$ or $\lambda_D \to r_0$.

Since the differential cross section is the square modulus of the scattering amplitude, by integrating $|f_{\text{ion}}(q)|^2$ over the unit sphere we obtain the total elastic cross section of a Debye-limited ion, of which we keep only the (overwhelmingly) dominant term proportional to λ_D:

$$\sigma_{\text{e,ion}} = 4\pi\gamma^2 Z_i^2 \lambda_D^2 / \left(a_0^2 k_0^2\right)$$

to be compared with the neutral atom total elastic cross section calculated within the Lenz model

$$\sigma_e = 4\pi\gamma^2 Z^{4/3} / k_0^2$$

Since, the ratio $\sigma_{\text{e,ion}}/\sigma_e$ is proportional to λ_D^2/a_0^2, and the Debye length, typically sub-micron as found earlier, we conclude that the elastic cross section is plasma-enhanced by several orders of magnitude. Imagining the total cross section as a circle, its radius expands from something at the Angstrom scale, to something much larger, comparable or larger than the beam size (depending on where we are along the optic axis). While consistent with the diverging trend of the Rutherford cross section for an unscreened charge, this implies that we cannot remain in the single-scattering approximation, or consider concepts such as "fraction of scattered (or unscattered) electrons," "scattering probability" as meaningful in presence of an ionized gas, even when the degree of ionization is low. In fact, reconsidering the plasma density (250 ppm of the gas number density) obtained at 1 mbar pressure, this corresponds on average to just a few ions per cubic micron, and therefore every primary will be elastically scattered several thousand times over its 7.5 mm long path within the gas chamber. Each time, the angular distribution broadens a little according to a Lorentzian-type probability density function, exactly as from a neutral atom, except that the characteristic angle now is $\theta_p = 1/(k_0\lambda_D)$ instead of $\theta_0 = 1/(k_0 r_0)$. For 300 keV electrons and $\lambda_D = 350$ nm, $\theta_p = 1$ μrad.

We have plotted in Fig. 3.12 ten unscattered (grey curves) and 1-μrad scattered (orange curve) trajectories for electrons traversing the gas chamber (bounded by the blue dashed lines) under the influence of the OL field (OL gap bounded by the green

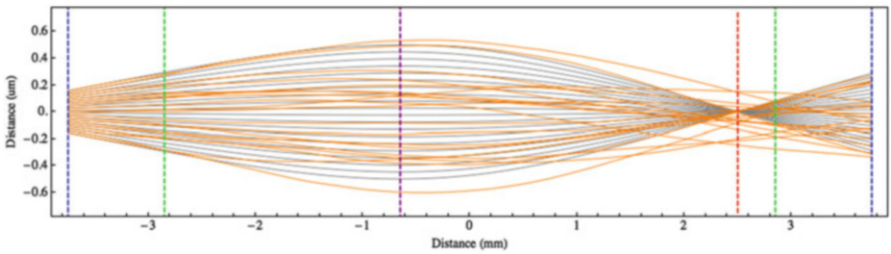

Fig. 3.12 Unscattered (*gray*) and 1-μrad gas-scattered (*orange*) trajectories within the gas chamber. The effects of gas scattering are visible both at the sample plane (*purple line*) and at the OA plane (*red line*), as the spatial and angular distributions of the illumination broaden progressively

dashed lines). As before, the electron-optical configuration was chosen to simulate a 1-μm patch of planar illumination at the sample plane (indicated by the dashed purple curve) forming its Fraunhofer pattern at the OA plane (red dashed line). Scattered and unscattered trajectories coincide at the entrance aperture of the chamber, and they progressively differentiate as scattering from the gas ions accumulates.

To better visualize how the beam evolves in presence of gas, we have sampled the spatial and angular distribution of the beam in the sample, OA and image plane, and created histograms representing the beam spatial and angular profiles in those planes. The histograms are shown in Fig. 3.13, for He pressure of 1 and 20 mbar, corresponding to mean scattering angles of 1 and 2 μrad, respectively. As sketched in Fig. 3.13, in absence of scattering the beam has a top-hat/delta (spatial/angular) profile in the sample plane, a delta/top-hat profile in the OA plane, and a top-hat/top-hat profile in the image plane. Gas scattering broadens progressively all distributions, with the most significant effect occurring in the image plane where about 11 % of the incoming electrons are transferred outside the illumination patch, thereby lowering proportionally the observed intensity per pixel around the central portion of the illuminated area.

3.3.1 *Influence on Material Observations*

As discussed above, scattering of electrons on the gas molecules present near the sample of interest in environmental TEM has a significant impact on the microscope performance. However, the interaction between the gas and fast primary electrons as well as secondary electrons might change the properties of the gaseous environment and thereby lead to artefacts in the sample observations.

However, the combination of the electron beam and gas molecules in the transmission electron microscope can been used for electron beam-induced deposition (van Dorp et al. 2011) and is thereby not always to be considered as an artefact.

In the following, a few examples of the more indirect influence on the microscopy observations originating from the interactions between the gas molecules and the free electrons are discussed.

3.3.2 *Ionization of Gas Molecules*

Damage or modifications of the observed samples due to the, at times, high current density is a well-documented phenomenon in the electron microscopy society. In general, two types of beam damage are considered in the TEM: Knock-on damage and radiolysis. The former is caused by displacement of atoms in the sample by momentum transfer from fast primary electrons to atoms in the sample. Usually,

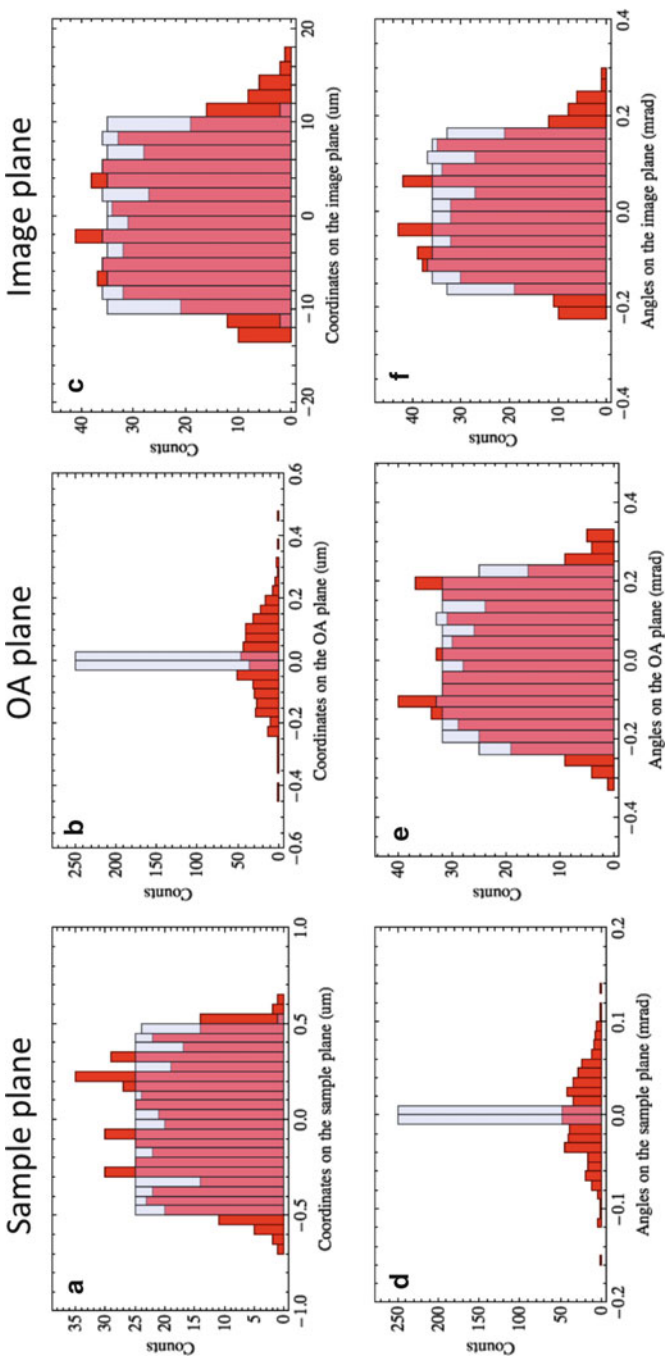

Fig. 3.13 Histograms of the spatial (**a**–**c**) and angular (**d**–**f**) profile of the illumination with (*red bins*) and without (semi-transparent *blue bins*) gas scattering at 1 mbar He pressure. The histograms represent snapshots of the collection of electron trajectories intersecting the three sample (**a**, **d**), OA (**b**, **e**) and image (**c**, **f**) planes

this can be minimized by lowering the energy of the electron beam (Egerton et al. 2010; Smith and Luzzi 2001). Radiolysis is caused by fast electrons modifying the chemical bonds in the sample, leading to changes in the electronic structure and thereby stability of the sample. This type of damage is usually larger for lower electron beam energies due to the larger interaction cross section. Examples of beam-induced chemistry can be found in the electron beam-induced reduction of molybdenum and vanadium oxides as described by Su et al. (Su et al. 2001; Wang et al. 2004). In addition to the beam damage observed in conventional TEM, ionization of gas molecules as a result of the interaction between free electrons and gas leads to increased reactivity. Therefore, it is very important to perform the ETEM experiments as a function of beam current density to explore the effects of ionized gas molecules near the sample.

As an example, the development of MgO smoke particles covered with Au nanoparticles in the presence of water vapor has been studied in situ in the electron microscope. MgO smoke particles produced by ignition of an Mg metal ribbon form close-to-perfect cubes exposing the MgO (100) surfaces. These cubes serve as a perfect substrate for studying nanoparticle-support interactions and especially the interface between. Gold is sputter-coated onto the cubes forming 2–6 nm epitaxially oriented Au nanoparticles.

Figure 3.14 summarizes our findings on the effect of electron dose and water vapor pressure in the vicinity of the sample. All experiments are performed at room temperature. The images are extracted frames from movies after approximately 30 min exposure in each case. At low pressure ($P = 10^{-5}$ Pa) and relative low electron dose rate (0.1 A/cm^2) the surface mobility is observed to be relatively small. In conventional high-vacuum TEM mode (including the use of a cold trap to minimize the water vapor pressure), the column base-pressure is ca. 10^{-5} Pa. Increasing the electron dose or the pressure by leaking in water vapor increases the mobility of MgO species on the surface resulting in the formation of kinks and steps. At increasing water vapor pressure, the species diffusing at the MgO surfaces start to accumulate at the Au/MgO interface. At relatively high electron dose rate (1.0 A/cm^2) and a pressure of 10^{-4} Pa pillars grow from the cubes apparently catalyzed by the Au nanoparticles. Au-catalyzed MgO pillar growth has been reported earlier (Ajayan and Marks 1989; Nasibulin et al. 2010), but in the present study, the effect of the environment has been addressed in greater detail. Even a low partial pressure of water vapor (10^{-5} Pa) has an apparent effect on surface species mobility in the Au/MgO system.

Pure MgO-smoke particles are known to hydroxylate under electron irradiation in the presence of water (Gajdardziska-Josifovska and Sharma 2005) modifying the perfect (100) surfaces of the MgO cubes. MgO species (Mg^+, $(MgO)^+$) are mobile on the surface of the cubes as a result of the energy transferred from both primary and secondary electrons (Kizuka 2001) creating steps and kinks on the MgO (100) surfaces.

The Au/MgO interface acts as a collection point (due to negatively charged metal particles) where the highly mobile MgO species are trapped and recrystallize in pillars. The presence of water species in the surrounding environment influences the charge transfer in the system changing the overall energy landscape. The change in behavior of the system in the presence of water vapor under electron beam

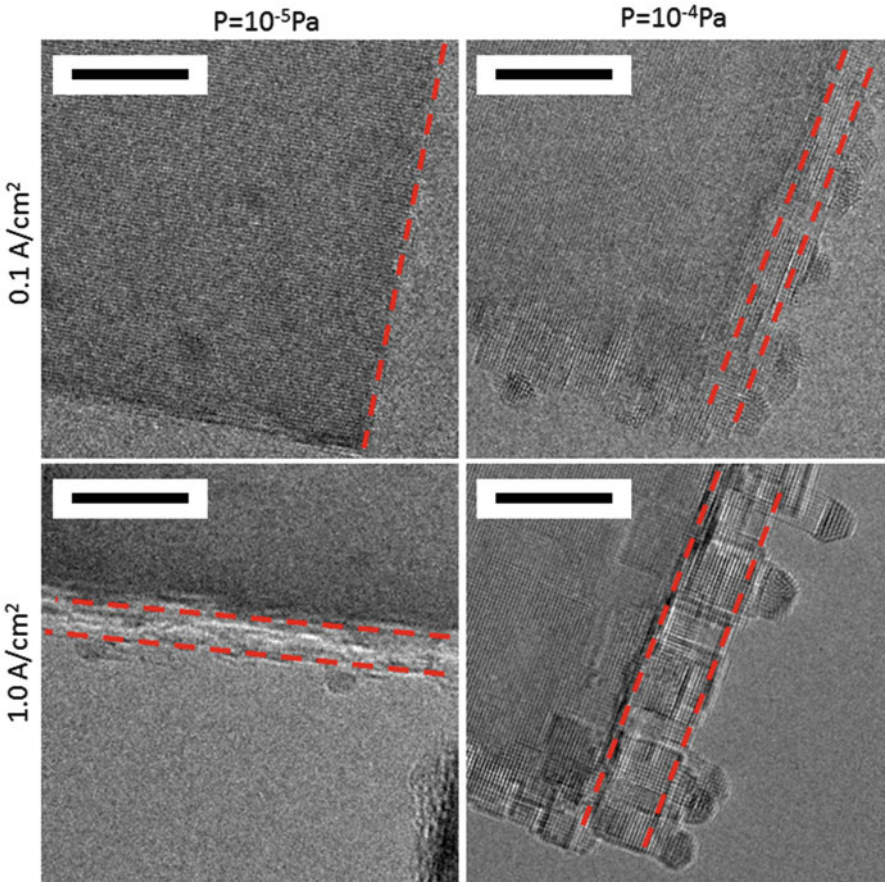

Fig. 3.14 TEM images of Au on MgO smoke cubes. The images are stills extracted from movies acquired at 300 kV in a FEI Titan ETEM. The Au/MgO sample was exposed to different electron dose rates (0.1 and 1.0 A/cm^2) at different pressures (10^{-5} and 10^{-4} Pa) for approximately 30 min in each case. The scale bars are 5 nm. Figure adapted from Duchstein et al. (2014)

irradiation illustrates the necessity for addressing the additional energy and radicals introduced when dealing with gases, even at room temperature. The thresholds of these beam- and gas-induced effects are strongly dependent on the material system and have to be studied systematically in each case.

As illustrated above the presence of gas molecules and especially water, even in low concentration, can change the observation in the electron microscope drastically. Cavalca et al. has been studying the photodegradation of cuprous oxide in the presence of water in situ in the electron microscope by means of a purpose-built TEM sample holder capable of letting light into the microscope in a controlled manner (Cavalca et al. 2012, 2013). The degradation of the cubed cuprous oxide nanoparticles observed by the authors in the presence of water and light to metallic copper is due to electron transfer to water molecules absorbed on the Cu_2O surface.

The electron transfer is facilitated by creation of electro-hole pairs by means of light. The observations had to be performed in a pseudo in situ manner as the electron beam accelerated the process by orders of magnitude. The electron beam did not degrade the Cu_2O nanocubes without the presence of water in the sample vicinity. That implied that imaging of the process had to be performed in the absence of water and a "stop-and-go" protocol was used by alternating between imaging in vacuum and treating the sample in water and the presence of light, but without irradiating the sample with electrons (see also Chap. 8).

It is obvious that extra care has to be taken when performing electron microscopy experiments in the presence of gas. The observations by environmental TEM have to be compared at different beam currents and beam current densities. Ideally, the observations have to be evaluated without the electron beam as well (Hansen et al. 2013). These blank experiments will, together with complementary experiments by other means than electron microscopy, help to justify the observations made in the presence of gas in situ in the microscope (Hansen et al. 2002). An example of the importance of studying the electron beam effect in environmental TEM experiments is reported by Simonsen et al. (2010). The authors studied the electron beam effect on the observation of Pt nanoparticle sintering mediated by Ostwald ripening. The shrinkage rate of Pt nanoparticles supported on Al_2O_3 was measured with an electron beam current density from 0.07 to 1.0 A/cm^2 in the presence of 1000 Pa air at 400 °C. The shrinkage rate showed a clear linear dependency on the beam density in the measured range as viewed in Fig. 3.15. The lack of shrinkage without the electron beam or with electron beam in pure N_2

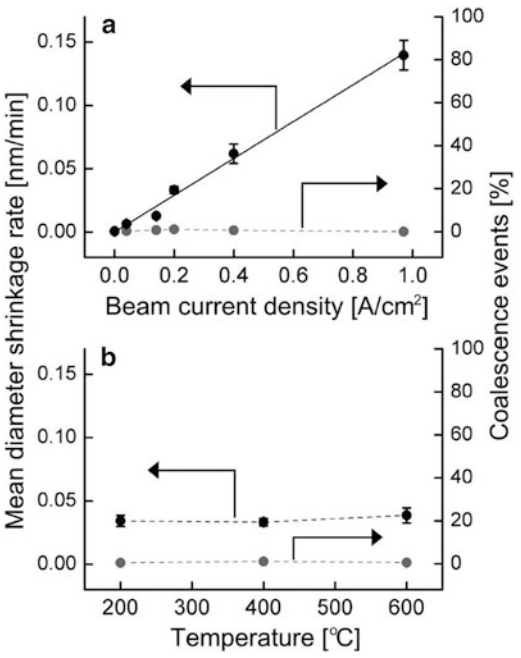

Fig. 3.15 The mean particle diameter shrinkage rate and the number of coalescence events of the Pt/Al_2O_3 catalyst during exposure to 1000 Pa air as a function of beam current density at constant temperature (400 °C). Figure adapted from Simonsen et al. (2010)

concludes that the effect is a combined electron beam and oxidizing gas effect. In order to follow the dynamical time-resolved Ostwald ripening the authors minimized the beam current to 0.07 A/cm^2 and only acquired snapshots during several hours of treatment arguing that the observed electron beam-induced nanoparticle shrinkage could be neglected at the given total electron dose in comparison to the total effect observed.

It is not only the beam current but also the total dose, which plays a role in the electron beam-induced phenomena observed during ETEM experiments. The structure evolution under electron beam irradiation of the Au/TiO_2 system for CO oxidation is studied in detail by Kuwauchi and co-workers (2012). The Au-TiO_2 is found to be strongly influenced by the surrounding gas in combination with the intense electron beam as summarized in Fig. 3.16. In the presence of oxygen or

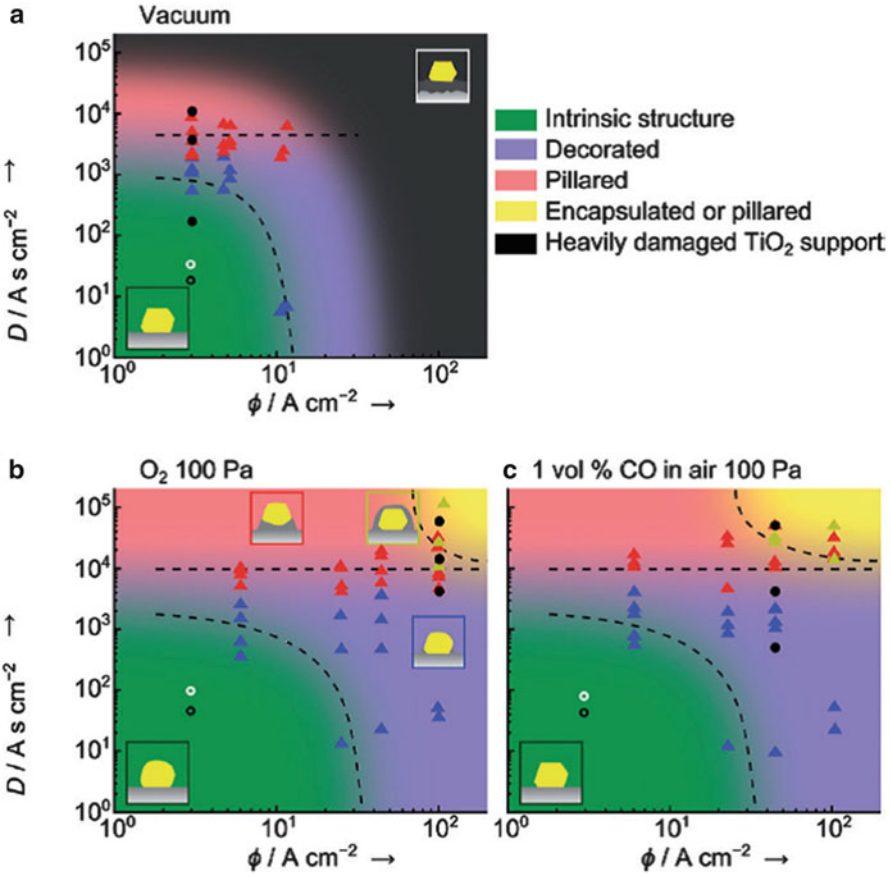

Fig. 3.16 Structural changes of Au/TiO_2 catalyst under different gases varying the electron current density, φ, and the total dose, D, observed in ETEM. (**a**) Vacuum, (**b**) 100 Pa of O_2, (**c**) 100 Pa of CO/air (1:100). All observations at room temperature. The color coding represents the categorized types of structural changes of the Au/TiO_2 system. Figure adapted from Kuwauchi et al. (2012)

carbon monoxide and an intense electron beam, TiO_2 decorates and encapsulates the Au nanoparticles at higher beam current. An interesting observation is that the decoration of Au nanoparticles by TiO_2 is found even without gas present, although at lower beam currents, but the complete encapsulation requires CO or O_2. Increasing the beam current in vacuum results in a heavily damaged TiO_2 support at beam currents above approx. 50 A/cm^2. This is not observed in the presence of CO or O_2 at similar beam currents. This indicated that the electron beam-induced damage of the TiO_2 support is compensated by the gas species in the sample vicinity. Ionized gas species might act as oxygen donor to the support. The authors showed that both the current density of the beam and the total dose of the high-energetic electrons have to be taken into consideration when designing the experiment.

3.4 Conclusion and Outlook

The interactions between the electron beam and the gas surrounding the sample results in a non-negligible effect on the microscope performance. The more pronounced effects are the loss of intensity and loss of resolution with increasing pressure, increasing atom-number of the gas, and decreasing acceleration voltage of the microscope. However, by getting a better insight in the physics behind the gas–electron scattering and the contribution to the resulting electron microscope image, quantitative ETEM might be obtainable.

The conventional approached for gaining three-dimensional information of the materials in the TEM, such as electron tomography, is usually not possible in ETEM dynamical ETEM experiments due to the relative long acquisition time. However by relating the intensities and contrast of single images to the sample geometry as demonstrated by Jia et al. (2014) in conventional aberration corrected electron microscopy will add significantly to the dynamic studies where tomography is not an option. In order to adapt the single-shot three-dimensional imaging a full understanding of the imaging process is required, including the electron–gas interactions occurring throughout the microscope column.

Furthermore, the increased reactivity of ionized gases has to be taken into account. A good practise when performing ETEM experiments is to study the influence on beam current density and total dose on the observations and ideally compare with complementary non-electron beam based techniques.

References

P.M. Ajayan, L.D. Marks, Experimental-evidence for quasimelting in small particles. Phys. Rev. Lett. **63**(3), 279–282 (1989)

R. Belkorissat, A.E.D. Kadoun, M. Dupeyrat, B. Khelifa, C. Mathieu, Direct measurement of electron beam scattering in the low vacuum SEM. Microchimica Acta **147**(3), 135–139 (2004). doi:10.1007/s00604-004-0182-x

M.J. Berger, J.S. Coursey, M.A. Zucker, J. Chang, *ESTAR, PSTAR, and ASTAR: Computer Programs for Calculating Stopping-Power and Range Tables for Electrons, Protons, and*

Helium Ions (version 1.2.3) (National Institute of Standards and Technology, Gaithersburg, 2005)

A.N. Bright, K. Yoshida, N. Tanaka, Influence of total beam current on HRTEM image resolution in differentially pumped ETEM with nitrogen gas. Ultramicroscopy **124**, 46–51 (2013). doi:10.1016/j.ultramic.2012.08.007

M. Cabié, S. Giorgio, C.R. Henry, M.R. Axet, K. Philippot, B. Chaudret, Direct observation of the reversible changes of the morphology of Pt nanoparticles under gas environment. J. Phys. Chem. C **114**(5), 2160–2163 (2010). doi:10.1021/jp906721g

F. Cavalca, A.B. Laursen, B. Kardynal, R.E. Dunin-Borkowski, S. Dahl, J.B. Wagner, T.W. Hansen, F. Cavalca, A.B. Laursen, B. Kardynal, R.E. Dunin-Borkowski, S. Dahl, J.B. Wagner, T.W. Hansen, In situ transmission electron microscopy of light-induced photocatalytic reactions. Nanotechnology **23**(7), 075705 (2012). doi:10.1088/0957-4484/23/7/075705

F. Cavalca, A.B. Laursen, J.B. Wagner, C.D. Damsgaard, I. Chorkendorff, T.W. Hansen, Light-induced reduction of cuprous oxide in an environmental transmission electron microscope. Chemcatchem **5**(9), 2667–2672 (2013)

P.M.F.J. Costa, T.W. Hansen, J.B. Wagner, R.E. Dunin-Borkowski, Imaging the oxidation of ZnS encapsulated in carbon nanotubes. Chem. Eur. J **16**(39), 11809–11812 (2010). doi:10.1002/chem.201001301

J.F. Creemer, S. Helveg, G.H. Hoveling, S. Ullmann, A.M. Molenbroek, P.M. Sarro, H.W. Zandbergen, Atomic-scale electron microscopy at ambient pressure. Ultramicroscopy **108**(9), 993–998 (2008). doi:10.1016/j.ultramic.2008.04.014

G.D. Danilatos, *Foundations of Environmental Scanning Electron Microscopy*. Advances in Electronics and Electron Physics, vol. 71 (Academic Press, Boston, 1988), pp. 109–250

G. Danilatos, J. Rattenberger, V. Dracopoulos, Beam transfer characteristics of a commercial environmental SEM and a low vacuum SEM. J. Microsc. **242**(2), 166–180 (2011). doi:10.1111/j.1365-2818.2010.03455.x

A.T. DeLaRiva, T.W. Hansen, S.R. Challa, A.K. Datye, In situ transmission electron microscopy of catalyst sintering. J. Catal. **308**, 291–305 (2013). doi:10.1016/j.jcat.2013.08.018

L.D.L. Duchstein, C.D. Damsgaard, T.W. Hansen, J.B. Wagner, Low-pressure ETEM studies of Au assisted MgO nanorod growth. J. Phys. Conf. Ser. **522**, 012010 (2014). doi:10.1088/1742-6596/522/1/012010

R.F. Egerton, *Electron Energy-Loss Spectroscopy in the Electron Microscope*, 2nd edn. (Plenum Press, New York, 1996)

R.F. Egerton, R. McLeod, F. Wang, M. Malac, Basic questions related to electron-induced sputtering in the TEM. Ultramicroscopy **110**(8), 991–997 (2010). doi:10.1016/j.ultramic.2009.11.003

I.Y. Fugol, V.N. Samovaro, M.G. Starkov, Electron-ion recombination and diffusion in a cryogenic helium plasma. Sov. Phys. JETP USSR **33**(5), 887 (1971)

M. Gajdardziska-Josifovska, R. Sharma, Interaction of oxide surfaces with water: Environmental transmission electron microscopy of MgO hydroxylation. Microsc. Microanal. **11**(6), 524–533 (2005). doi:10.1017/s1431927605050403

P.L. Hansen, J.B. Wagner, S. Helveg, J.R. Rostrup-Nielsen, B.S. Clausen, H. Topsoe, Atom-resolved imaging of dynamic shape changes in supported copper nanocrystals. Science **295** (5562), 2053–2055 (2002). doi:10.1126/science.1069325

T.W. Hansen, J.B. Wagner, R.E. Dunin-Borkowski, T.W. Hansen, J.B. Wagner, R.E. Dunin-Borkowski, Aberration corrected and monochromated environmental transmission electron microscopy: challenges and prospects for materials science. Mater. Sci. Technol. **26**(11), 1338–1344 (2010). doi:10.1179/026708310X12756557336355

T.W. Hansen, J.B. Wagner, T.W. Hansen, J.B. Wagner, Environmental transmission electron microscopy in an aberration-corrected environment. Microsc. Microanal. **18**(4), 684–690 (2012). doi:10.1017/S1431927612000293

T.W. Hansen, A.T. Delariva, S.R. Challa, A.K. Datye, Sintering of catalytic nanoparticles: particle migration or Ostwald ripening? Acc. Chem. Res **46**(8), 1720–1730 (2013)

Q. Jeangros, A. Faes, J.B. Wagner, T.W. Hansen, U. Aschauer, J. Van Herle, A. Hessler-Wyser, R.E. Dunin-Borkowski, In situ redox cycle of a nickel-YSZ fuel cell anode in an environmental transmission electron microscope. Acta Mater. **58**(14), 4578–4589 (2010). doi:10.1016/j.actamat.2010.04.019

C.L. Jia, S.B. Mi, J. Barthel, D.W. Wang, R.E. Dunin-Borkowski, K.W. Urban, A. Thust, Determination of the 3D shape of a nanoscale crystal with atomic resolution from a single image. Nat. Mater. (2014). doi:10.1038/nmat4087

J.R. Jinschek, S. Helveg, Image resolution and sensitivity in an environmental transmission electron microscope. Micron **43**(11), 1156–1168 (2012)

S. Kodambaka, J. Tersoff, M.C. Reuter, F.M. Ross, Germanium nanowire growth below the eutectic temperature. Science **316**(5825), 729–732 (2007). doi:10.1126/science.1139105

T. Kizuka, Formation and structural evolution of magnesium oxide clusters under electron irradiation. Jpn. J. Appl. Phys. Pt. 2: Lett **40**(10A) (2001)

Y. Kuwauchi, H. Yoshida, T. Akita, M. Haruta, S. Takeda, Intrinsic catalytic structure of gold nanoparticles supported on TiO_2. Angew. Chem. Int. Ed. Engl. **124**(31), 7849–7853 (2012)

F. Lenz, Zur Streuung Mittelschneller Elektronen in Kleinste Winkel. Z. Naturforsch. A **9**(3), 185–204 (1954)

P. Li, J. Liu, N. Nag, P.A. Crozier, In situ preparation of Ni–Cu/TiO_2 bimetallic catalysts. J. Catal. 262(1):73–82 (2009). doi:http://dx.doi.org/10.1016/j.jcat.2008.12.001

O. Mansour, K. Aidaoui, A.E.D. Kadoun, L. Khouchaf, C. Mathieu, Monte Carlo simulation of the electron beam scattering under gas mixtures environment in an HPSEM at low energy. Vacuum **84**(4), 458–463 (2009). doi:10.1016/j.vacuum.2009.09.004

O. Mansour, A. Kadoun, L. Khouchaf, C. Mathieu, Monte Carlo simulation of the electron beam scattering under water vapor environment at low energy. Vacuum **87**, 11–15 (2013). doi:10.1016/j.vacuum.2012.06.006

M. Sidorov (2003). http://www.maxsidorov.com/ctfexplorer/

A.G. Nasibulin, L. Sun, S. Hämäläinen, S.D. Shandakov, F. Banhart, E.I. Kauppinen, In situ TEM observation of MgO nanorod growth. Crystal Growth Des. **10**(1), 414–417 (2010). doi:10.1021/cg9010168

L.-M. Peng, S.L. Dudarev, M.J. Wheelan, *High-Energy Electron Diffraction and Microscopy* (Oxford University Press, Oxford, 2004)

F.M. Ross, J. Tersoff, M.C. Reuter, Sawtooth faceting in silicon nanowires. Phys. Rev. Lett. **95** (14), 146104 (2005). doi:10.1103/PhysRevLett.95.146104

S. Janbroers, P.A. Crozier, H.W. Zandbergen, P.J. Kooyman, A model study on the carburization process of iron-based Fischer–Tropsch catalysts using in situ TEM–EELS. Appl. Catal. B. 102 (3–4):521-527(2011). doi:http://dx.doi.org/10.1016/j.apcatb.2010.12.034

R. Sharma, Kinetic measurements from in situ TEM observations. Microsc. Res. Tech. **72**(3), 144–152 (2009). doi:10.1002/jemt.20667

S.B. Simonsen, I. Chorkendorff, S. Dahl, M. Skoglundh, J. Sehested, S. Helveg, Direct observations of oxygen-induced platinum nanoparticle ripening studied by in situ TEM. J. Am. Chem. Soc. **132**(23), 7968–7975 (2010). doi:10.1021/Ja910094r

B.W. Smith, D.E. Luzzi, Electron irradiation effects in single wall carbon nanotubes. J Appl Phys **90**(7), 3509–3515 (2001). doi:10.1063/1.1383020

D.S. Su, M. Wieske, E. Beckmann, A. Blume, G. Mestl, R. Schlögl, Electron beam induced reduction of V_2O_5 studied by analytical electron microscopy. Catal. Lett. **75**(Part 1/2), 81–86 (2001)

M. Suzuki, T. Yaguchi, X.F. Zhang, High-resolution environmental transmission electron microscopy: modeling and experimental verification. Microscopy **62**(4), 437–450 (2013). doi:10.1093/jmicro/dft001

W.F. van Dorp, I. Lazic, A. Beyer, A. Gölzhäuser, J.B. Wagner, T.W. Hansen, C.W. Hagen, W.F. van Dorp, I. Lazic, A. Beyer, A. Gölzhäuser, J.B. Wagner, T.W. Hansen, C.W. Hagen,

Ultrahigh resolution focused electron beam induced processing: the effect of substrate thickness. Nanotechnology **22**(11), 115303 (2011). doi:10.1088/0957-4484/22/11/115303

S.B. Vendelbo, P.J. Kooyman, J.F. Creemer, B. Morana, L. Mele, P. Dona, B.J. Nelissen, S. Helveg, Method for local temperature measurement in a nanoreactor for in situ high-resolution electron microscopy. Ultramicroscopy **133**, 72–79 (2013). doi:10.1016/j.ultramic.2013.04.004

S.B. Vendelbo, C.F. Elkjaer, H. Falsig, I. Puspitasari, P. Dona, L. Mele, B. Morana, B.J. Nelissen, R. van Rijn, J.F. Creemer, P.J. Kooyman, S. Helveg, Visualization of oscillatory behaviour of Pt nanoparticles catalysing CO oxidation. Nat. Mater. **13**(9), 884–890 (2014). doi:10.1038/NMAT4033

J.B. Wagner, F. Cavalca, C.D. Damsgaard, L.D.L. Duchstein, T.W. Hansen, Exploring the environmental transmission electron microscope. Micron **43**(11), 1169–1175 (2012). doi:10.1016/j.micron.2012.02.008

D. Wang, D.S. Su, R. Schlögl, Electron beam induced transformation of MoO_3 to MoO_2 and a new phase MoO. Z. Anorg. Allg. Chem **630**(7), 1007–1014 (2004). doi:10.1002/zaac.200400052

T. Yaguchi, M. Suzuki, A. Watabe, Y. Nagakubo, K. Ueda, T. Kamino, Development of a high temperature-atmospheric pressure environmental cell for high-resolution TEM. J. Electron Microsc. (Tokyo) **60**(3), 217–225 (2011). doi:10.1093/jmicro/dfr011

G.W. Zhou, L. Wang, R. Birtcher, P. Baldo, J. Pearson, J. Yang, J. Eastman, Cu_2O island shape transition during Cu-Au alloy oxidation. Phys. Rev. Lett. **96**(22), 226108 (2006). doi:10.1103/PhysRevLett.96.226108

G. Zhou, L. Luo, L. Li, J. Ciston, E.A. Stach, J.C. Yang, Step-edge-induced oxide growth during the oxidation of Cu surfaces. Phys. Rev. Lett. **109**(23), 235502 (2012). doi:10.1103/PhysRevLett.109.235502

Chapter 4
Spectroscopy of Solids, Gases, and Liquids in the ETEM

Peter A. Crozier and Benjamin K. Miller

Abstract The use of various nanospectroscopies for determining the nanoscale composition and electronic structure of materials in the environmental transmission electron microscope (ETEM) is described and illustrated. ETEM is a powerful approach for determining the atomic level changes taking place in materials as a result of interactions with ambient gas or liquid environments. A variety of different composition changes may occur with the details depending on the sample composition, gas composition, temperature, and other stimuli. Changes in the elemental and bonding information associated with gas–solid interactions can be detected and quantified using electron energy-loss spectroscopy (EELS) and energy dispersive X-ray spectroscopy (EDX). When these spectroscopies are used in combination with the sub-nanometer electron probes associated with scanning transmission electron microscopy (STEM), they provide a powerful tool for determining composition and bonding information at the atomic level. It may also be important to monitor the surrounding gas or liquid composition during in situ experiments. The use of EELS and mass spectrometry, usually a residual gas analyzer (RGA), for gas measurement during ETEM experiments is described and compared. Examples of the application of nanospectroscopies to in situ analysis of compositional changes in a number of metal and oxide systems are given. Combining gas analysis with structural determination opens the door to an *operando* approach to TEM. Several examples of *operando* TEM applied to catalytic CO oxidation reactions are given. The impact of current and future instrument development on the analytical capability of ETEM is briefly described.

P.A. Crozier (✉) • B.K. Miller
School for Engineering of Matter Transport and Energy, Arizona State University, Tempe, AZ 85287, USA
e-mail: crozier@asu.edu

T.W. Hansen, J.B. Wagner (eds.), *Controlled Atmosphere Transmission Electron Microscopy*, DOI 10.1007/978-3-319-22988-1_4

4.1 Introduction

The environmental transmission electron microscope is a powerful approach for determining the atomic level changes taking place in materials as a result of interactions with ambient gas or liquid environments. The evolution of the material may be in the form of structural rearrangement in the bulk or surface of the materials. A variety of different composition changes may occur with the details depending on the sample composition, gas composition, temperature, and other stimuli. A schematic illustration of the types of stimuli that are currently available for in situ TEM is shown in Fig. 4.1. In some cases such as electrical biasing, most of the compositional changes are associated with a redistribution of the elements in the samples, e.g., lithiation and de-lithiation in battery electrodes. In the presence of reactive gases and/or heating, mass exchange with the ambient atmosphere leads to a compositional change in the TEM sample. The changes in the composition may be very obvious as in the case of growth of nanotubes or nanowires from a gaseous precursor. In other cases, the sample may undergo phase changes such as complete oxidation of a metal or complete reduction of an oxide. Differential surface segregation may take place in, for example, alloys where the less noble component may segregate and react with surface oxygen species. More subtle chemical changes may occur such as oxygen vacancy introduction in oxides or the formation

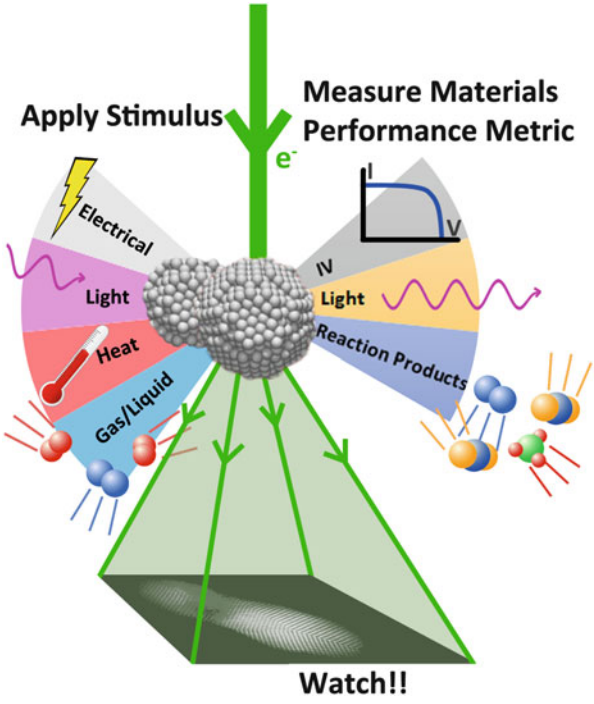

Fig. 4.1 Schematic diagram illustrating in situ and *operando* approaches to TEM. In situ TEM involved the application of some form of stimuli as shown on the *left-hand side*. *Operando* TEM involves simultaneous quantitative measurement of some materials functionality as illustrated on the *right-hand side*

of thin oxide or metallic layers on the surface of a material. To fully describe the dynamic materials evolution it is critical to determine the compositional changes occurring in the material at nanometer or sub-nanometer resolution.

Imaging and diffraction techniques provide information on structural changes taking place in the material but cannot provide specific information on changes in the elemental composition of the system. Elemental and bonding information associated with gas–solid interactions in the ETEM can be detected using electron energy-loss spectroscopy (EELS) (Egerton 2011) and energy dispersive X-ray spectroscopy (EDX) (Lyman et al. 1994). When these spectroscopies are used in combination with the sub-nanometer electron probes associated with scanning transmission electron microscopy (STEM) they provide a powerful tool for determining composition and bonding information at the atomic level (Watanabe et al. 2011; Kimoto et al. 2007; Muller et al. 2008).

Discussion of the physics underlying these two forms of spectroscopy is given in Sect. 4.2. A simplified description of the electron–sample interaction is illustrated schematically in Fig. 4.2. The EELS and EDX signal arise from the inelastic scattering processes taking place between the fast incident electron and the electrons in the sample. In general, when the fast electron inelastically interacts with the sample, it will lose energy and be scattered through a certain angle as illustrated in the real space representation of Fig. 4.2a. The same processes are illustrated on an electronic structure diagram in Fig. 4.2b. Many inelastic scattering events cause

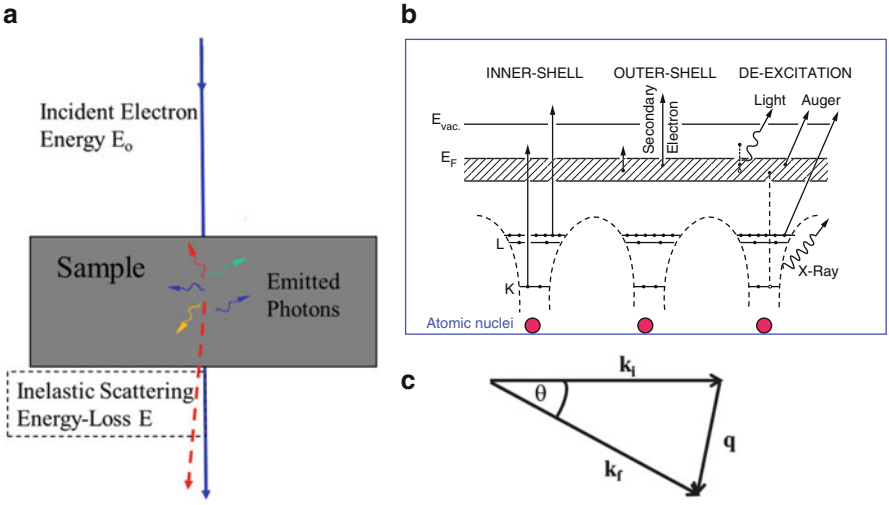

Fig. 4.2 (**a**) Schematic illustration of inelastic electron scattering through some angle θ and isotropic photon emission leading to the EELS and EDX signals, respectively. (**b**) Energy level diagram illustrating electronic excitation processes responsible for EELS and EDX signals ((**b**) is adapted from Egerton 2011). (**c**) Vector diagram showing relationship between incident and scattered wavevectors, $\mathbf{k_i}$ and $\mathbf{k_f}$, respectively for electron inelastically scattered through an angle of θ. The change in wavevector is $\mathbf{q}$

atomic electrons to make transitions to states above the Fermi level. The fast electron can scatter off a deeply bound inner-shell level or a more loosely bound valence-shell electron. The energy lost by the fast electron will be determined by the type of excitation taking place in the solid. By collecting and analyzing the energy spectrum of the transmitted electrons, detailed information about the composition and bonding in the materials can be obtained. This is the principle behind EELS. The hole that is generated in the energy band or level of the solid can then undergo relaxation in which the vacancy is filled by an electron from a higher shell. This may result in the emission of a photon whose energy is characteristic of the element being excited. By collecting and analyzing the energy spectrum of the emitted photon, detailed information about the composition in the materials can be obtained. This is the principle behind EDX.

EDX and EELS have been extensively used to characterize materials in the TEM and EELS is compatible with the reactive gas environment in the ETEM. The current generation of EDX detectors may be damaged by high gas pressures in the column so they can only be employed with some care when the gas pressure in the cell is rather low (see, for example, Nylese 2014). With the growing number of ETEM applications, there is increasing recognition of the need to spectroscopically analyze not only the solid sample but also the surrounding gas or even liquid medium. In many systems of interest, the composition can be dynamic, changing due to varying conditions inside the ETEM. Thus, it is important to measure the composition within the environmental cell.

The area where this dynamic behavior has received the most study thus far is catalysis (Helveg et al. 2015; Jinschek 2014; Hansen and Wagner 2014; Yoshida et al. 2012, 2013; Jeangros et al. 2013; He et al. 2012; Chee and Sharma 2012; Ross 2010; Cabie et al. 2010; Gai and Boyes 2009; Giorgio et al. 2008; Gai et al. 2008; Crozier and Hansen 2015; Miller and Crozier 2014; Zhang et al. 2013; Sharma et al. 2012; Chenna and Crozier 2012a, b; Chenna et al. 2011a; Wang et al. 2008, 2009; Crozier et al. 2008). If a gaseous catalytic reaction is being studied in the ETEM, this process will, by definition, alter the gas composition inside the cell. Measurements of the changing gas composition within the cell can be correlated with catalyst structure as the reaction proceeds. Mass spectrometry has been used for at least a decade in ETEM systems to measure gas compositions (Gai et al. 2005; Hansen et al. 2006). A residual gas analyzer (RGA) cannot operate at the higher pressures typically used in environmental TEM experiments (Miller and Crozier 2014). Consequently the RGA is differentially pumped, sitting behind a leak valve placed either on the first stage of cell differential pumping (as seen in Fig. 4.3), or at the end of a long capillary "sniffer" tube (the implementation currently used for the FEI Titan microscopes). These gas analyzers are also usually placed some distance away from the TEM column because of space limitations and possible interference with electron optical performance.

EELS can also be employed to determine the composition of the gas in the reaction cell (Crozier and Chenna 2011). EELS was found to be a relatively simple method for detecting changes in gas composition directly in the cell. Energy-loss

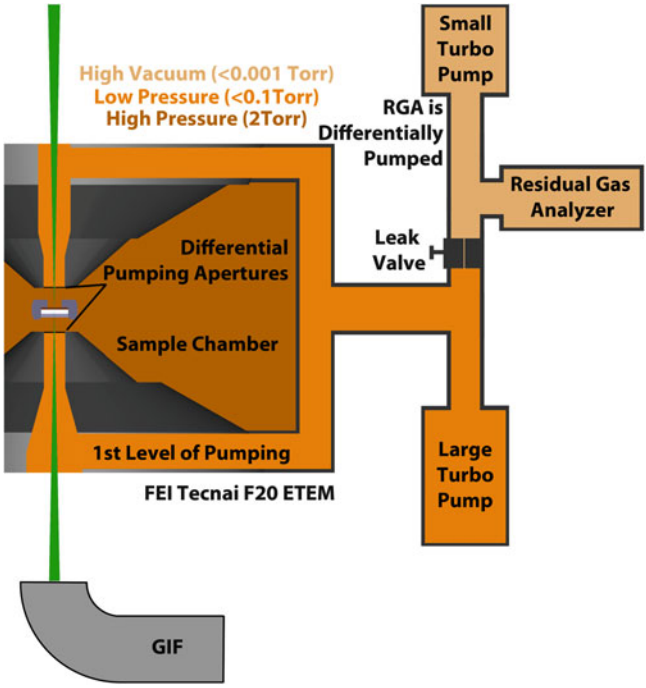

Fig. 4.3 A schematic diagram showing one way in which an RGA can be interfaced to the reaction cell of the ETEM (connected to the first stage of differential pumping). A leak valve and a small turbo pump are used to maintain the low pressure required by the RGA. Reproduced with permission from (Miller and Crozier 2014) © 2014 Microscopy Society of America

spectra of gases are also readily quantifiable. Quantification can be performed using the core-loss approach described in Sect. 4.2.2 or by finding the linear combination of individual gas spectra that best fits the observed spectrum from a gas mixture. Some individual gas spectra in the low-loss region are shown in Fig. 4.4.

In this chapter we discuss fundamental aspects of EELS, EDX, and RGA and illustrate their application in the TEM and ETEM. To begin, Sect. 4.2.1 gives a description of the inelastic electron scattering processes that underpin EDX and EELS.

4.2 Primary Spectroscopies for the ETEM

In this section, EELS and EDX are first discussed because they are the most common techniques employed in the ETEM. The use of residual gas analysis to determine gas composition and pressure changes in the ETEM is also discussed.

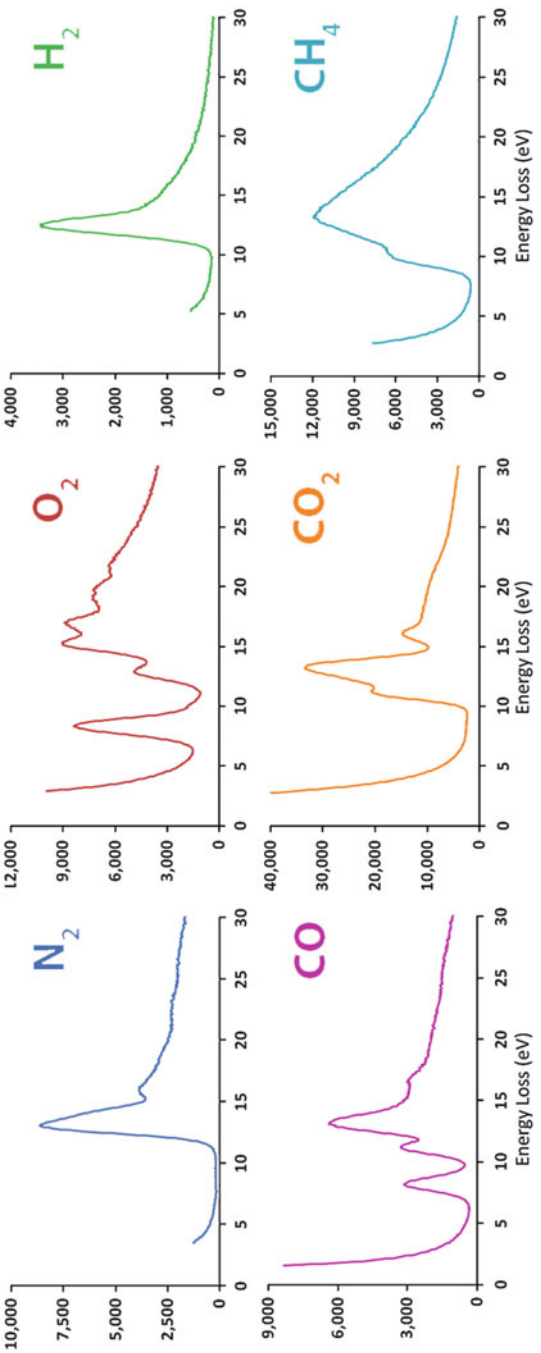

Fig. 4.4 Different gas molecules result in distinctive low-loss spectra in EELS. These can be measured easily in the ETEM, and used to quantify mixtures of gases. Modified with permission from (Crozier and Chenna 2011). © 2011 Elsevier

4.2.1 Inelastic Electron Scattering

When fast electrons strike the atoms in a solid or a gas they may undergo a variety of different scattering events which are often classified as *elastic* or *inelastic* processes. A detailed discussion of electron scattering processes can be found in the many textbooks on electron imaging and spectroscopy such as Egerton (2011), Williams and Carter (2009), and Pennycook and Nellist (2011). A schematic diagram of electron–solid interactions and the subsequent relaxation processes are illustrated in Fig. 4.2a, b. Scattering involving direct interaction of the fast electron with the nucleus or crystal lattice has traditionally been called elastic scattering with small energy transfers on the order of a few eV or less because of the large difference in mass between the electron and the nucleus. This type of scattering gives rise to *vibrational losses* which can now be observed in monochromated EELS. Scattering involving interaction of the fast electrons with the electrons in the solid can involve much larger energy transfers of hundreds or thousands of eV. This type of *electronic excitation* has traditionally been called inelastic scattering and it is the fundamental interaction behind EDX as well as plasmon and inner-shell EELS.

Inelastic scattering involves electronic excitation of different groups of electrons in the material and the energy transfers are characteristic of the electronic binding energies of the material as shown in Fig. 4.2b. A fast electron, with incident energy E_o, may scatter off a particular atomic shell causing an atomic electron to undergo a transition from the initial state Ψ_i of energy E_i to an empty state Ψ_f above the Fermi level of energy E_f. In general, the incident electron with wave vector $\mathbf{k_i}$ will be scattered through an angle θ, undergo a momentum change of h$\mathbf{q}$, and have a final state with wave vector $\mathbf{k_f}$ (see Fig. 4.2c). The energy, E, transferred from the fast electron is equal to the energy difference between the two atomic states involved, i.e., $E = E_f - E_i$. The spectrum of such energy transfers contains information about both the elements present and the type of bonding in the sample and is the basis for the technique of EELS. For inner-shell spectroscopy, the resulting ionization edges are named in terms of the initial state of the electron making the transition. For example, excitation of an electron in an initial state with principal quantum number $n = 1$ (i.e., 1*s* orbital), gives rise to the K edge, $n = 2$ to the L edge, $n = 3$ to the M edge, etc. ... The core-hole left behind can undergo relaxation either by Auger electron emission or photon emission processes with the latter forming the basis for EDX.

The probability of inelastic scattering occurring from different groups of electrons in the material is often expressed in terms of a *scattering cross section*, σ, with larger cross sections corresponding to larger inelastic scattering probabilities. This problem was first considered quantum mechanically by Hans Bethe in 1930 using an approximation called the plane wave Born approximation (Bethe 1930). For more information on this Bethe theory, the interested reader is referred to the review article by Inokuti (1971). The incident and scattered fast electron wave functions are described as plane waves. The wave functions of the atomic electrons

are solutions to the Schrodinger equation for the electrostatic potential of the atom. The cross section varies with scattering angle and can be written in a form that is differential with respect to solid angle Ω as (e.g., Egerton 2011),

$$\frac{d\sigma}{d\Omega} = \left(\frac{m_o}{2\pi\hbar^2}\right)\frac{k_f}{k_i}\left|\int V(\mathrm{r})\Psi_\mathrm{i}\Psi_f^*\exp(iq.\mathrm{r})dV\right|^2 \tag{4.1}$$

where V is the interaction potential between the fast electron and the atom, $\mathrm{m_o}$ is the rest mass of the electron, and $\hbar = h/2\pi$ with h Planck's constant. The squared term is often called the *inelastic scattering form factor*. This equation can be further simplified and the integral over wave functions is often incorporated into a quantity known as the *generalized oscillator strength*, *df/dE*. In this case, the inelastic scattering cross section differential with respect to solid angle and energy-loss can be written as (Egerton 2011; Inokuti 1971),

$$\frac{d^2\sigma}{d\Omega dE} = \frac{4\gamma^2 R}{Eq^2}\frac{k_f}{k_\mathrm{o}}\frac{df(q,E)}{dE} \approx \frac{4\gamma^2 R}{Eq^2}\frac{df(q,E)}{dE} \tag{4.2}$$

with R the Rydberg constant and $\gamma = (1-(v^2/c^2))^{-0.5}$. This form of the differential cross section can be integrated over energy transfer and scattering angle to determine the exact form of the cross section that would apply to spectral acquisition conditions in the electron microscope. These so-called Bethe cross sections play a central role in quantification schemes for performing elemental analysis in EELS and EDX. For inner-shell excitation, the initial state Ψ_i is spatially localized near the atom core. Thus, the exponential in (4.1) can be expanded and, for moderate scattering angles, only the first term of the form **q.r** need be retained. This form of the form factor appears in expressions for calculating the transition probability for photon absorption. This approximation applies when **q** is small and it will always be small when the scattering angle is small and when the energy-loss, E, is relatively small compared to the incident electron energy E_o. This approximation is called the *dipole approximation* and it highlights the connection between inelastic electron scattering and optical absorption measurements. Moreover, the dipole inelastic scattering form factor is only non-zero if the initial and final state angular momentum quantum number l changes by one, i.e., $\Delta\mathrm{l} = +/-1$.

For most applications in EELS, the scattering angles are typically rather small and it is useful to express the differential cross section explicitly in terms of scattering angle as

$$\frac{d^2\sigma}{d\Omega dE} = \frac{8\mathrm{a_o^2R^2}}{Em_\mathrm{o}\nu^2}\frac{1}{\theta^2+\theta_E^2}\frac{df}{dE} \tag{4.3}$$

where v is the electron velocity, θ is the scattering angle, and a_o is the Bohr radius. The quantity θ_E is known as the characteristic scattering angle and it is defined as

$$\theta_E = \frac{E}{\gamma m_o v^2} \approx \frac{E}{2E_o} \tag{4.4}$$

with the approximate version on the right-hand side corresponding to the nonrelativistic limit.

Equation (4.3) gives some information on the behavior of the inelastic electron scattering taking place in the electron microscope. The cross section depends on the square of the velocity of the electron which means that both EELS and EDX signals become stronger at lower accelerating voltage. At small scattering angles, the generalized oscillator varies only slowly, so the angular distribution of the scattering is dominated by the Lorentzian term in (4.3). The scattering is strongly forward peaked and the intensity falls by 50 % when $\theta = \theta_E$. The generalized oscillator term contains the dependence on both the atomic number and the electronic shell involved in the scattering. For inner-shell scattering it can be calculated using atomic models such as the simple hydrogenic model or more sophisticated Hartree–Slater models.

The formulation of inelastic scattering in terms of the generalized oscillator strength is useful for elemental analysis, which primarily employs the electronic excitation of inner-shell levels. The inelastic interaction between the fast electron and the sample can also be described in terms of a complex dielectric response function of the solid $\varepsilon(\mathbf{q},E)$ (Raether 1967; Batson and Silcox 1983; Howie and Walsh 1991; García de Abajo and Aizpurua 1997). This formulation is more suitable for phenomena that involve optical properties and collective behaviors such as plasmon or phonon excitations. Such effects can be investigated with EELS but play no role in contemporary EDX analysis because of the limited energy resolution of modern EDX detectors. The energy differential cross section can be written in a form very similar to (4.3) as (Egerton 2011),

$$\frac{d^2\sigma}{d\Omega dE} = \frac{1}{\pi^2 a_o m_o \nu^2 n_a}\left\{\frac{1}{\theta^2 + \theta_E^2}\right\}\mathrm{Im}\left[-\frac{1}{\varepsilon(E,q)}\right] \tag{4.5}$$

where the term Im means the imaginary part of the function $-1/\varepsilon$. Comparison of (4.5) and (4.3) shows that the dielectric function plays a similar role to the generalized oscillator strength and controls the response of the electrons in the material to the interaction with the fast electrons (Inokuti 1971).

4.2.2 Electron Energy-Loss Spectroscopy

The inelastically scattered electrons that are transmitted through the sample can be collected and separated into their different energy components to form the electron energy-loss spectrum. The dispersion of the electrons with respect to energy is usually accomplished using a magnetic prism spectrometer as illustrated in Fig. 4.5.

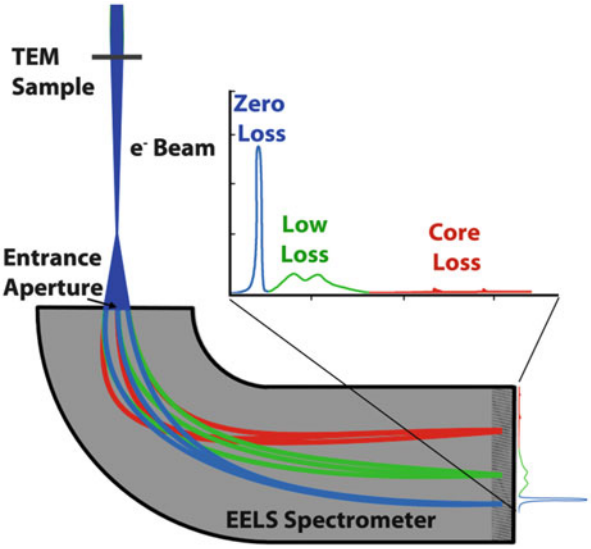

Fig. 4.5 Schematic illustration of magnetic prism spectrometer coupled to TEM using a projector lens crossover. A series of additional post spectrometer lenses transfer the spectrum to the detector system

The spectrum is formed at the output of the spectrometer in the so-called dispersion plane. The opening in the spectrometer is defined by a spectrometer entrance aperture. This aperture may define the so-called *collection semi-angle*, β, which is the range of scattering angles that contribute to the spectrum. The collection semi-angle may affect the energy resolution and the signal-to-noise in the spectrum and usually lies in the range 5–100 mrad. The energy-loss range measured in a spectrum usually lies somewhere between 0 and 3000 eV. Beyond this range the signal is very weak. An electron detector is placed in the dispersion plane to measure the intensity of the spectrum. Indirect electron detection is typically employed in EELS because of the very large dynamic range across the energy-loss spectrum. Most detectors consist of a scintillator (typically yttrium aluminum garnet) to convert the electron signal into an optical signal. The light is then transferred to a two-dimensional charge-coupled device (CCD) using a fiber optic. The pixel intensity is summed in the nondispersive direction and then plotted as a function of energy-loss. The energy resolution obtainable with EELS is determined by the electron source, and whether the gun is equipped with a monochromator. For non-monochromated systems, the energy resolution is typically 0.8–1 eV for a Schottky thermally assisted field emission source and around 0.3–0.4 eV for a cold field emission source (Krivanek and Paterson 1990; Paterson and Krivanek 1990). With a monochromator, the typical energy resolution is 100 meV (Mitterbauer et al. 2003; Brink et al. 2003) but 10 meV is now possible on the most recent generation instruments (Krivanek et al. 2014).

A typical spectrum from a thin TEM sample is shown in Fig. 4.6 and consists of three main regions. A large peak centered on energy loss of zero, the *zero-loss peak*, is the most prominent feature in the spectrum and arises from electrons that have

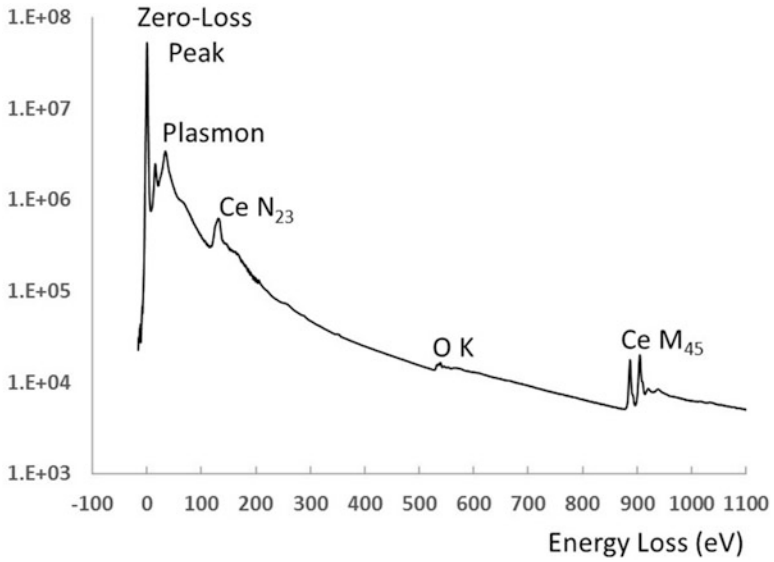

Fig. 4.6 Energy-loss spectrum from sample of Ca doped CeO_2 showing zero-loss peak, low-loss region with plasmon and core-loss region with ionization edges (Spectrum courtesy of William Bowman)

not suffered significant energy loss compared to the system energy resolution. The second region of the spectrum is called the *low-loss* or *valence-loss region* and may arise due to vibrational excitation or excitation of the outer shell or valence shell electrons. This part of the spectrum (usually up to about 40 eV) consists of a series of peaks and contains information on the optical properties of materials including phonon and plasmon modes as well as interband transitions. Above 40 eV, the spectral intensity generally drops rapidly but the decline is punctuated with somewhat abrupt ionization edges due to electronic excitation of the *inner-shell*, or *core-levels*, of the material. This is the third region of the spectrum and it provides information on the elemental composition and the electronic structure of the material.

4.2.2.1 Elemental Analysis with EELS

Analysis of the location and intensity of the inner-shell ionization edges is the primary method of performing elemental analysis of solids with EELS. Each occupied energy level in the material gives rise to an inner-shell edge at an energy corresponding to the binding energy of the level. Thus it is relatively easy to identify the elements present in the sample simply by consulting a table of inner-shell energy levels. For example, Fig. 4.7 shows the core-loss region of a spectrum from NiO with an O K-edge at 532 eV (due to excitation of the oxygen 1*s* electrons)

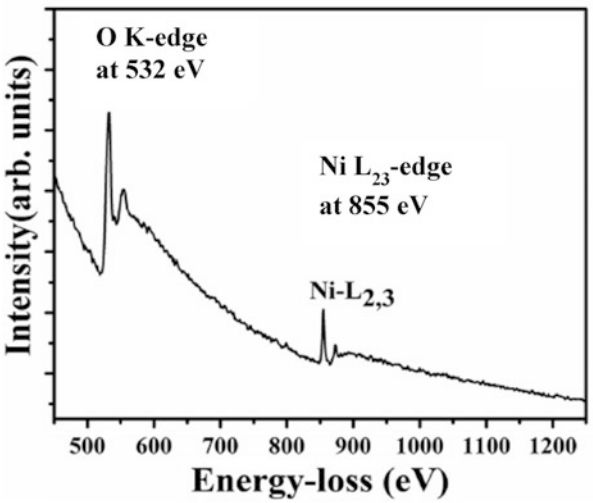

Fig. 4.7 Energy-loss spectrum from a sample of NiO showing the oxygen K-edge and Ni L_{23} edge

and a Ni L_{23} edge at 855 eV (due to excitation of the Ni 2*p* electrons). Performing quantitative elemental analysis is accomplished by determining a concentration ratio between two elements of interest, A and B. The process to determine the ratio of the number of atoms per unit area of the two elements, denoted by N_A and N_B, can be broken down into several steps:

1. Acquire a spectrum from a region of suitable sample thickness.
2. Remove the background under the ionization edges of interest.
3. Integrate the ionization edge intensities over a suitable energy range.
4. Convert the integrated intensities into concentration ratios using suitable ionization cross section ratios.

For simple cases, the background before the ionization edge is often modeled with an inverse power law function which is then extrapolated beyond the ionization edge. The background-subtracted signals are then integrated over an energy range of Δ and the resulting intensities, I_A and I_B, can be converted to a concentration ratio of C_{AB} through the equation,

$$C_{AB} = \frac{N_A}{N_B} = \frac{I_A \sigma_B}{I_B \sigma_A} \tag{4.6}$$

where σ_A and σ_B are inelastic scattering cross sections obtained by integrating (4.3) over the collection semi-angle β and the energy integration window Δ. This is the basic equation for determining elemental compositions with inner-shell EELS. It applies not only to solids, but also to gases, and can thus be employed to perform in situ gas analysis in the ETEM.

The accuracy of this procedure varies and depends on factors such as sample thickness, background removal, and ionization cross sections. Equation (4.6) is

derived assuming there is not a strong plural scattering component to the spectrum. The probability of inelastic scattering can be expressed in terms of an *inelastic mean free path* λ, which is the average distance an electron will travel in the material before undergoing inelastic scattering. The mean free path is materials dependent and can be determined from the inelastic scattering cross sections. As a rough rule of thumb, it is generally safe to assume that plural scattering can be ignored if the ratio of sample thickness, t, to the mean free path is less than 0.5, i.e., $t/\lambda < 0.5$. For electrons of energy E_0 in the range 100–300 keV, the mean free path typically lies in the range 50–100 nm so this means that the sample should be less than 50 nm.

For incoherent inelastic scattering, Poisson's equation can be employed to derive a simple expression relating the inelastic intensity in the measured energy-loss spectrum to the t/λ value (Johnson et al. 1974). Under the Poisson assumption, this can be expressed as

$$\mathrm{t}/\lambda = \ln\left(\mathrm{I_{tot}}/\mathrm{I_o}\right) \tag{4.7}$$

where I_o is the intensity in the zero-loss peak and I_{tot} is the total intensity in the spectrum (the sum of the zero-loss peak and all the inelastic part of the signal). This equation can be evaluated rapidly at the microscope and can be employed to determine the importance of plural scattering in energy-loss spectra from solids or gases. In cases where large t/λ values are unavoidable, the effects of plural scattering may be removed by using deconvolution techniques, yielding the so-called single scattering distribution as first described by Johnson and Spence (1974). Such procedures are available in most EELS processing packages but require measurement of both the core-loss and low-loss spectral regions. Of course, as with all deconvolution routines, the correction must be used with some caution because of the introduction of artifacts and noise amplification (Egerton and Crozier 1988).

The background under the ionization edge is often modeled using an inverse power law of the form AE^{-r} or logarithmic polynomial functions. The accuracy and suitability of this approach depends on the details of the spectral form and simple curve fitting methods will fail in cases where there is severe edge overlap. In such cases, more sophisticated approaches using filtering, differentiation techniques, or reference spectra must be employed (see, e.g., see references Bowman et al. 2015; Narayan et al. 2014). The choice of ionization cross sections requires some consideration depending on the edges of interest and the signal integration range. Theoretical inner-shell cross sections have been calculated using both hydrogenic and more sophisticated Hartree–Slater models (Egerton 2011; Leapman et al. 1980). The cross sections and cross section ratios have been compared with experimental measurements (Hofer 1989, 1991; Hofer and Golob 1988; Hofer and Wilhelm 1993; Crozier 1990). The theoretical atomic K-shell cross sections for light elements are good to within about 5 % if signal integration ranges of 50–100 eV are employed to average out bonding effects. For heavier elements or smaller integration ranges, it may be preferable to determine the relevant cross

section ratios from solid or gas standards of well-defined composition. The Bethe cross sections calculated based on atomic models may give large errors when signal integration windows are small compared to the energy range over which significant near-edge fine structure intensity modulations occur. For this reason, an energy integration range of 50 eV or higher is desirable while simultaneously avoiding large background extrapolation errors.

4.2.2.2 Near-Edge Fine Structure and Bonding

The oscillations within 30 eV of the ionization edge onset are associated with local bonding and coordination. This *near-edge fine structure* is related to the unoccupied density of states above the Fermi level and it provides a powerful method for exploring local variations in bonding at surfaces, interfaces, and grain boundaries. It can be exploited to great benefit in ETEM work to detect chemical changes taking place in the materials as a consequence of gas–solid interactions. Examples of the near-edge fine structure from two forms of TiO_2, anatase and rutile, are shown in Fig. 4.8. The data were recorded using the monochromated Nion ultraSTEM at Arizona State University and the sharpest spectral features have a full width half maximum of around 0.4 eV in part as a result of broadening due to the relatively short lifetime of the core hole (Krause and Oliver 1979; Lazar et al. 2003; Brydson et al. 1989). The difference in the relative intensities of the peak heights makes it very easy to differentiate between anatase and rutile structures. In favorable cases, it is possible to fully interpret the nature of the bonding in the material by calculating the fine structure using, for example, the multiple scattering or multiplet theories developed for X-ray absorption spectroscopy (Rehr et al. 2010; Stavitski and de Groot 2010). These approaches must be used with some caution as many-body effects such as excitons may not be accurately reproduced in the calculations.

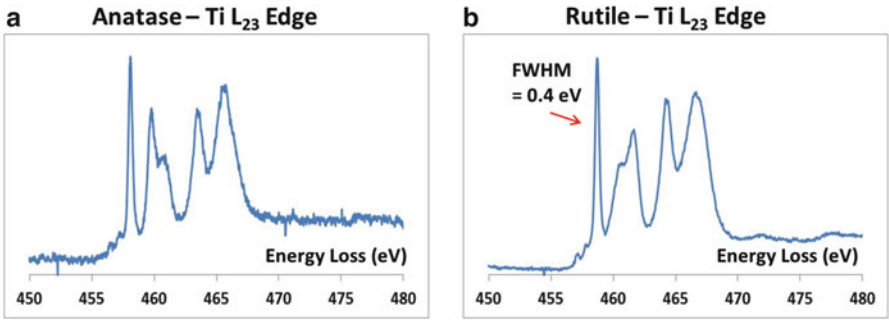

Fig. 4.8 The Ti L_{23} edge for (**a**) anatase and (**b**) rutile recorded from the Nion monochromated microscope. The edges are characterized by five peaks but the relative intensity is different in the two structures (spectra courtesy of Liuxian Zhang and Toshi Aoki)

The near-edge fine structure for transition metals is often associated with prominent peaks (so-called white lines) at the edge thresholds. This is particularly pronounced for the L_{23} edges for 3*d* transition metals and the M_{45} edges for rare earth elements. By measuring the change in relative intensity of these peaks it is often possible to identify the oxidation state of the element (Manoubi et al. 1990; Pearson et al. 1993). This is a relatively simple indicator of the oxidation state of cations in oxides and is an important tool for monitoring redox reactions in the ETEM.

4.2.2.3 EELS of Gases in the ETEM

The basic physics of the interactions of a fast electron with atoms in a solid and with atoms in a gas are similar, but there are several practical differences relative to the conditions in the ETEM. First, at the (low to atmospheric) pressures used in ETEM, individual gas molecules have negligible electronic interaction with each other, and can be assumed to be independent entities. This means that the signal obtained from a single gas molecule in a gas mixture will be the same as that obtained from the single gas molecule alone. This contrasts sharply with the behavior of atoms or molecules in solids or liquids, whose electronic interactions cause changes in the fine-structure of the core-loss EELS edges, as well as the long-range interactions which are probed in the plasmon peaks of the valence-loss region of the spectrum.

Second, for a differentially pumped environmental TEM, electrons undergoing identical inelastic scattering processes at the top and bottom of the gas cell several mm apart may follow very different trajectories through the objective lens and the lower section of the TEM column. This will give rise to a difference between the fraction of inelastically scattered electrons entering the spectrometer (Crozier and Chenna 2011). For example, if the C and O core-loss edges from CO gas are observed, a larger fraction of the C than of the O signal is collected resulting in a systematic error in the relative collection efficiencies of the two edges. This causes errors in elemental quantification if the standardless methods described in Sect. 4.2.2.1 for inner-shell spectra are applied without taking this effect into account. In principle, it is possible to estimate a correction factor based either on a detailed calculation of electron trajectories for electrons scattered at different points in the gas cell or through the use of gas standards containing edges at different energy. However, the effect is likely to be largest for larger angle scattering events and the magnitude of this effect should be smaller when smaller collection angles are employed. Acquisition of core-loss spectra of gases should therefore be performed with small collection angles. This may not be an issue for holder-based ETEM cells, in which the gas is confined to a thin layer near the eucentric height of the microscope.

Electron energy-loss spectra of gases may be acquired and quantified from both the core-loss and valence-loss regions (Miller and Crozier 2014; Crozier and Chenna 2011). In the valence-loss region, each gas molecule has a distinctive signature from 5 to 25 eV loss. A series of low-loss spectra from a variety of

different gases is shown in Fig. 4.4. These spectra show significant differences both in the number and location of the peaks present and quantification is straightforward for these gases. These signals overlap, but since the component gases present in the gas mixture are usually known, it is simple to determine the molar concentrations. The valence-loss spectrum from the gas mixture can be expressed as a linear combination of the individual component gas valence-loss spectra. For suitably normalized spectra, the weighting coefficients in the linear combination can be directly related to the molar concentrations of the components.

To determine the relationship between the valence-loss spectra and the gas composition, the gas volume is assumed to be homogeneous with an effective thickness in the electron beam direction of t. Each gas can be characterized with a mean free path λ which will vary with pressure P. If the values of t, λ, and P are known for the reference spectra of individual gases, then the composition (aA + bB) of a mixture of two gases A and B (with a and b the molar concentrations) can be obtained from the linear combination coefficients α and β of the normalized reference spectra by the following equation (Crozier and Chenna 2011):

$$\frac{a}{b} = \frac{\alpha\left(\frac{\lambda}{t}\right)_{\mathrm{A}} P_{\mathrm{A}}}{\beta\left(\frac{\lambda}{t}\right)_{\mathrm{B}} P_{\mathrm{B}}} \tag{4.8}$$

This equation is valid provided the scattering parameters are small and plural scattering is similar in all the spectra employed for the analysis. This approach is easily extended to mixtures of several gases.

A MATLAB code was written to automate the process of determining α and β by a weighted least squares method and also accounts for differences in the tails of the zero-loss peak (Miller and Crozier 2014). To do this, the code first normalizes the reference spectra so their integrated intensities are all unity over the energy range of 4–44 eV. Next, the linear combination of selected gases that best fits the spectrum from the gas mixture in the TEM is computed by a weighted least squares method, where the weights are set equal to the square of the intensity to emphasize peaks in the spectra. It is often seen that the residuals from this fit show a clear functional dependence, as seen in Fig. 4.9b. This is due to the zero-loss tails of the reference and mixture spectra being slightly different. No background removal is performed on either the reference or mixture spectra to attempt to completely remove the zero loss tails; instead the backgrounds of the reference and mixture spectra were matched by fitting the residuals of the linear combination fit using an inverse power law, and subtracting the power law fit from the measured spectrum. This procedure, shown in Fig. 4.9, is equivalent to performing background subtraction on both the mixture and reference spectra, to remove the zero loss tail. However, it is more robust in this case, where only a small window prior to the peak onset is available, making traditional background fitting and subtraction difficult. After the residual fit has been subtracted from the measured spectrum, a linear combination fit to the spectrum is found again, yielding a new fit. This process of matching the background is repeated as necessary until no clear power law dependence of the

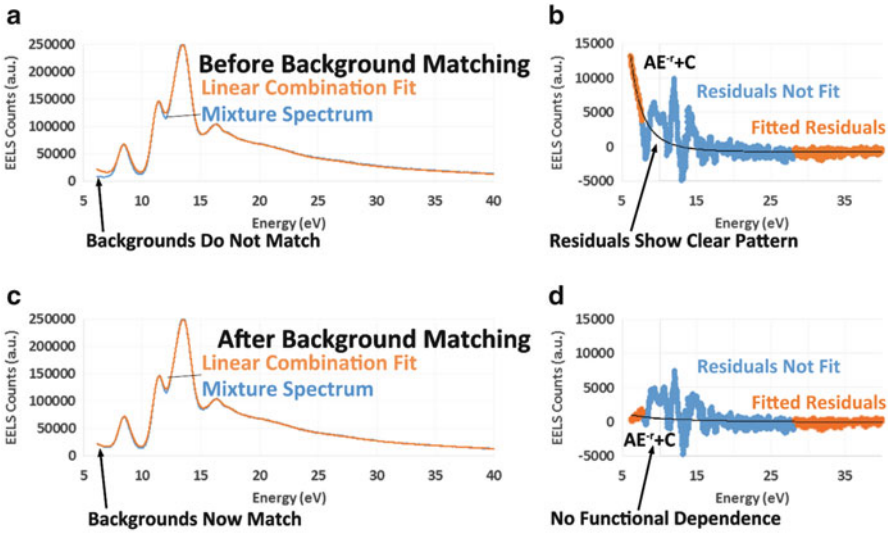

Fig. 4.9 The background matching method used for the low-loss EELS analysis automation. (**a**) After fitting a linear combination of experimentally obtained spectra of individual gases (*orange*) to a spectrum from a gas mixture (*blue*), the background of the composite spectrum and mixture spectrum do not match. (**b**) The residuals from the fit show a clear pattern. This pattern can be fit quite well with a power law function (*black*). (**c**) Subtracting this fitted function yields a mixture spectrum with a background that more closely matches that of the individual reference spectra so that no clear functional dependence is seen in the residuals (**d**). Reproduced with permission from (Miller and Crozier 2014) © 2014 Microscopy Society of America

residuals is found (Fig. 4.9d). No procedure for deconvolution of plural scattering need be applied, if plural scattering is small for the combination of gas pressure and cell-thickness used. Once the linear combination coefficients have been determined, information about the reference spectra is used to compute the gas partial pressures according to (4.8).

As detailed in Sect. 4.2.2.1, the elemental composition of solids can be determined by analysis of core-loss spectra, in which ionization cross sections or standard reference spectra are used to convert the ratio of integrated peak areas into a ratio of elemental composition. EELS core-loss spectra from gases can be quantified similarly (Crozier and Chenna 2011). As previously stated, if small collection semiangles are employed (a few mrad), gas compositions can be determined using standard atomic cross sections to within 5–10 %. If reference spectra of single gases are acquired, and these are used to determine empirical cross section ratios, the results may be more accurate. For some unique cases, like carbon K-edges of CO and CO_2, prominent peaks at the edge threshold are several eV apart, so a linear combination method similar to the valence loss method may be employed, yielding greater accuracy (Miller and Crozier 2014).

The low-loss and core-loss EELS techniques used to quantify gas mixtures each have advantages and disadvantages, depending on the gases being analyzed. In the

application of this technique to the study of CO oxidation (Miller and Crozier 2014; Chenna and Crozier 2012a) which is covered in detail in Sect. 4.4.3, the core-loss spectra are easily quantified, since the peaks from CO and CO_2 are close together, but not overlapped; thus, this technique is primarily used for the CO oxidation application. The low-loss technique is quite versatile, since any mixture of gases can be analyzed over the same small energy range. Additionally, for quantification of mixtures containing hydrogen gas, the low-loss region must be used since that is the region of the spectrum containing the H_2 edge.

To check the accuracy of the linear-combination-based quantification techniques, low-loss and core-loss spectra from a nominally 50–50 mixture of CO and CO_2 were acquired and processed (Miller and Crozier 2014). To measure the low-loss spectra, the spectrometer was set to a dispersion of 0.05 eV per channel, using an entrance aperture of 2 mm, and an exposure time of 4 s. With such a long exposure time, the zero loss peak must be shifted off the detector to prevent saturation. The mixture spectrum was quantified to be 49.2 % CO_2, and 50.8 % CO, with a standard deviation of 0.7 %. The core-loss spectra were acquired in TEM diffraction mode. The dispersion, entrance aperture, and acquisition time were identical to the low-loss case. The convergence and collection semi-angles were 2.4 and 2 mrad, respectively. The spectra were fit over the entire acquisition range of about 50 eV, and the result obtained was a composition of 51.0 % CO_2 49.0 % CO, with a standard deviation of 0.4 %. This is quite close to the nominal composition, and in good agreement with the low-loss EELS result.

4.2.3 Energy Dispersive X-ray Spectroscopy

The other main spectroscopic technique for performing elemental analysis is energy dispersive X-ray spectroscopy. The X-ray emission is associated with relaxation of the core-hole generated from the inner-shell inelastic scattering process. During relaxation, an electron from a higher orbital falls into the empty core hole of lower energy. The difference in initial and final state electron energy is accommodated either via photon emission or Auger electron emission. Any state of energy greater than the core-hole may provide the electron to fill the vacancy. The emitted X-rays are named in terms of the initial and final state of the electron making the transition. For example, a core hole in a state with principal quantum number, $n = 1$ (i.e., $1s$ orbital), gives rise to the K lines, $n = 2$ gives L lines, etc. ... Greek letters are typically used to differentiate the initial state of the electron making the transition. A transition from the $n = 2$ to $n = 1$ state gives rise to a Kα X-ray and a transition from $n = 3$ to $n = 1$ gives rise to a Kβ X-ray.

Solid state detectors are usually employed in the TEM to detect and measure the energy of the emitted X-ray, giving rise to the technique of EDX. These detectors are often composed of Si or Ge single crystals, and are typically 50 mm^2 in size. The characteristic X-rays are emitted isotropically (into a solid angle of 4π steradians (sr)) so it is important to get the detector crystal as close to the sample as possible to

increase the collection efficiency. The square shape of the detector and the geometric constraints around the objective lens pole pieces make it difficult to collect a large fraction of the emitted solid angle. A typical detector will only subtend around 0.2 sr, so the collection efficiency is $0.2/4\pi = 1.6$ % which is very small. There are newer, more efficient, systems in which up to four detectors are positioned around the sample but these have not been installed on environmental TEMs to date (von Harrach et al. 2009). When the X-ray enters the detector crystal it will be absorbed and the resulting cascade process generates a large number of electron-hole pairs. The average number of electron-hole pairs depends on the energy of the incoming X-ray. A voltage bias is placed across the crystal to separate the electron-hole pairs. The number of electron-hole pairs is determined using a suitable pulse counting system in order to determine the energy of the X-ray.

Each element in the sample will emit a series of X-ray lines which can be measured and quantified to determine sample composition. Figure 4.10 is a typical X-ray spectrum from a Ni-doped ceria sample and shows characteristic X-ray peaks sitting on top of a continuum background which arises from bremsstrahlung. The quantification procedure follows similar steps to those employed for EELS and has been described in detail in many places (Watanabe et al. 2006, 2011; Williams and Carter 2009; Chapman et al. 1984; Reimer 1989). First the continuum background is removed using standard curve fitting and interpolation techniques. The intensity of the characteristic X-ray line depends on the elemental concentration and parameters related to the underlying atomic physics. The probability of the vacancy being generated in a particular orbital can be obtained from the Bethe theory described in Sect. 4.2.1. For X-ray generation, we are only interested in the cross section for creating a vacancy in the atomic shell, σ_V, so the appropriate cross section is obtained by integration of (4.3) over all energy loss and scattering angles, i.e.,

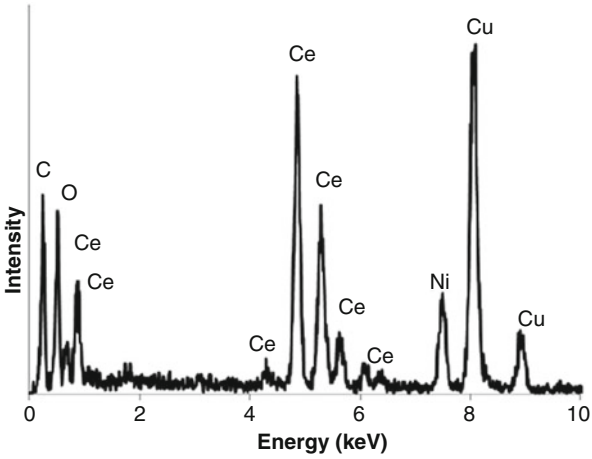

Fig. 4.10 EDX spectrum from Ni doped CeO_2 sample showing O, Ce and Ni lines. The C and Cu come from a carbon support film on copper grids (Spectra courtesy of Rio Cavendish)

$$\sigma_V = \int_{E_k}^{E_o} \int_0^{4\pi} \frac{d^2\sigma}{d\Omega dE} dE d\Omega. \tag{4.9}$$

With suitable approximations, Bethe was able to perform the integral and demonstrated that the form for generating the core-hole vacancy for inelastic scattering from a subshell of binding energy E_k could be written as

$$\sigma_V = \frac{6.51 \times 10^{-20} b_s n_s}{E_o E_k} \log\left[\frac{c_s E_o}{E_k}\right] \tag{4.10}$$

with cross sections in cm^2 and energies in keV. n_s is the number of electrons in the subshell being excited and the parameters b_s and c_s are typically between 0.5 and 1 and have been discussed by many authors. The cross sections have been tabulated (see various references above) and are incorporated into many of the commercially available EDX quantification routines.

There are other factors that must be taken into account to predict the intensity of the characteristic X-ray peak in a spectrum. The probability of relaxation occurring through photon emission is known as the fluorescence yield ω. This is generally small for light elements and higher for heavier elements. For a particular X-ray line, it is also necessary to know the probability s, that the core hole will be filled by the relevant transition from higher shell. Finally, even if the X-ray enters the detector, the efficiency of detection, ε, is usually less than 100 % and varies with X-ray energy. Taking all these factors into account, it can be shown that the concentration ratio between two elements A and B (giving characteristic peaks at energies E_A and E_B) can then be written as

$$C_{AB} = \frac{N_A}{N_B} = \frac{I_A \sigma_B \omega_B s_B \varepsilon(E_B)}{I_B \sigma_A \omega_A s_A \varepsilon(E_A)} = k_{AB} \frac{I_A}{I_B} \tag{4.11}$$

The term on the right-hand side of (4.11) combines all the atomic physics terms together with the detector efficiency terms into a constant k_{AB}. This is the so-called Cliff–Lorimer equation that is commonly employed to perform quantitative EDX in the TEM (Cliff et al. 1975). The constant k_{AB} can be determined for the elements of interest and will in general be instrument dependent because of the detector efficiency terms.

Equation (4.11) is attractive because of its simplicity, but it is important to remember that, like its EELS analog, (4.3), it is built on assumptions that are valid only for thin films. In thicker samples, X-ray absorption and fluorescence effects in the sample can introduce large errors into the quantification if not taken into account. For details on these effects, the reader is referred to some of the general EDX references (Watanabe et al. 2011; Williams and Carter 2009; Reimer 1989).

The combination of both EDX and EELS provides a powerful tool for probing the compositional and bonding changes taking place during gas–solid interactions

in the ETEM. When combined with STEM, both EDX and EELS allow information to be probed with sub-nanometer and atomic resolution.

4.2.4 Residual Gas Analysis

The gas composition within the reaction call can also be probed with a residual gas analyzer (RGA). An RGA is a type of mass spectrometer used to detect small quantities of gases in vacuum systems. Often a quadrupole mass spectrometer is employed which uses an electron beam to ionize gas molecules and accelerates the resulting charged species through a set of quadrupoles. The ions are separated according to their mass-to-charge ratio and the ion currents are measured using a Faraday cup and/or secondary electron multiplier (O'Hanlon 2003).

The placement of an RGA in the vacuum system of the ETEM is of primary importance. Ideally, the RGA would sample gas directly from the environmental cell of the ETEM. The pressure in the RGA must be maintained below ~10^{-3} Pa, which is orders of magnitude lower than the pressures typically used in ETEM experiments. To achieve this, the RGA must be located behind a leak valve or capillary, with a backing pump to maintain the low pressure. This may be accomplished using several configurations. The differentially pumped FEI Titan ETEM has an RGA which samples the gas near the TEM sample using a long capillary "sniffer" tube, which begins close to the sample in the environmental cell, and ends near the RGA's leak valve. At Arizona State University, experiments on an FEI Tecnai ETEM were performed with the RGA behind a leak valve located just before the turbo pump used for the 1st stage of differential pumping, as seen in Fig. 4.3 (Miller and Crozier 2014). MEMS-based gas cell holders can also be interfaced to RGAs so the gas entering or exiting the reactor can be measured, again with a leak valve and pump to reduce the pressure entering the RGA (Vendelbo et al. 2014).

Raw analog data from an RGA is given in Fig. 4.11, where peaks for CO, CO_2, and several other gases present in the TEM vacuum can be seen. The background gas pressure in the ETEM cell is easily detectable in the RGA and this background varies from day to day, depending on the most recently performed experiments. The raw analog signal from the background and from a nominally 50–50 mixture of CO and CO_2 is shown in Fig. 4.11. In practice, selected peaks are automatically measured by the RGA software at set intervals, and these peak intensities are monitored as a function of time (Miller and Crozier 2014; Vendelbo et al. 2013).

The RGA is not intended for rigorous quantification, but rather for simple gas identification (O'Hanlon 2003). Quantification of the gas composition present in the RGA is possible, but must be done carefully, with knowledge of the complications inherent to the system. First, the RGA signal for any single gas is not linearly dependent on the partial pressure of that gas. In addition, several gases may contribute to the same peak, as is the case with N_2 and CO, which both have a

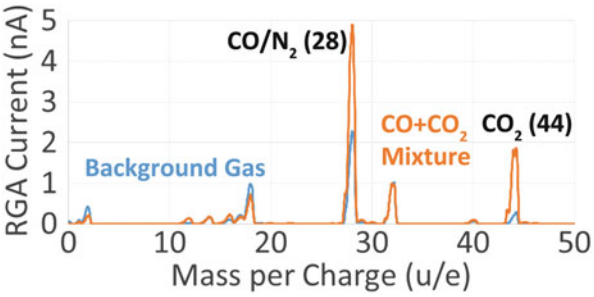

Fig. 4.11 Raw analog data from the RGA for a 50–50 mixture of CO/CO_2 (*orange*), as well as a background spectrum acquired just prior to beginning the gas flow (*blue*). Peaks for CO/N_2, CO_2, as well as 13 others are monitored by the RGA software over time to yield the usual RGA data. Reproduced with permission from (Miller and Crozier 2014) © 2014 Microscopy Society of America

mass of 28 amu. Sources other than the ETEM cell may also contribute background signals to the RGA spectrum as seen in Fig. 4.11, and this background varies from day to day. Finally, even if the RGA signal can be correctly interpreted and quantified, the placement of the RGA far from the TEM sample, along with the RGA's differential pumping system, may result in the gas composition in the RGA being different from that in the reaction cell due to mass transport issues in the vacuum system and the many background signals that are often present.

A first approximation for quantification of RGA data would be to subtract a background based on the signal obtained before beginning gas flow, and then simply take the ratio of the currents from two mass peaks, divided by known standard ionization cross sections for the main gases contributing to those peaks. A more thorough treatment would require reference spectra to be obtained for all the gases present in the ETEM, so that the experimental spectrum could be fit by a linear combination of the single-gas references (O'Hanlon 2003).

Even with the limitations of the RGA previously described, mass spectrometry is a useful semi-quantitative technique for monitoring the gas composition within the ETEM. The main benefit of the technique is its independence from the operation of the microscope. The RGA can collect data during imaging, EELS acquisition, or even with the electron beam blanked. Thus, data can be acquired continuously over the course of an entire experiment. Furthermore, the data can be easily visualized live while the user is operating the microscope, allowing any changes in gas composition to be identified and acted upon immediately.

4.2.5 Comparison Between RGA and EELS of Gases Techniques

All the techniques used to measure the gas composition inside the TEM should ideally yield identical results if correctly implemented and quantified. To determine

whether this was the case, RGA data were also obtained during the EELS comparison experiment previously described, in which a 50–50 mixture of CO and CO_2 was flowed through the ETEM cell, and the composition measured over 70 min (Miller and Crozier 2014). For the first 20 min, the low-loss EELS method was used, and for the final 20 min core-loss spectra were taken. During the entire experiment, data from the RGA were collected simultaneously.

The ratio of CO_2 to the total $CO + CO_2$ as a function of time for the comparison experiment was obtained by first subtracting a background (the RGA signal before gas is admitted to the reaction cell) and then simply taking the ratio of the currents from CO and CO_2, divided by known standard ionization cross sections (O'Hanlon 2003). This yielded a value that ranged from 48.5 % CO_2 to 50.3 % CO_2 over the course of 70 min, which essentially agrees with the 49.2 % CO_2 and 51.0 % CO_2 determined from the low-loss and core-loss spectra, respectively.

The EELS and RGA techniques have advantages and disadvantages. The EELS techniques are quantitative, and probe the gas in the environmental cell directly. In either EELS technique, a disadvantage for *operando* studies is that the beam cannot be used for high resolution imaging while it is employed to detect the gases via EELS. This is in contrast to the mass spectrometry technique using the RGA, which, as mentioned previously, can gather data continuously during the course of the experiment. The RGA is, however, a less reliable technique for accurate quantification of gas compositions, and probes the gas in the vacuum system far from the ETEM reaction cell. The RGA and EELS techniques are thus complimentary, and ideally suited to simultaneous use.

4.3 Determining Dynamic Chemical Changes in Solids with EELS

In this section, some of the ways in which spectroscopy can be employed to follow the chemical changes taking place in solids in reactive gas environments are presented. Because this process is central to the study of catalysis, many of the examples come from heterogeneous catalysts. Catalytic nanomaterials undergo an evolutionary life cycle starting from the preparation process moving through activation, operation, deactivation, and possible regeneration. The phase transformations taking place in the catalyst during these processes are often driven by interactions with the surrounding gas or liquid and exposure to heat, light, or electric fields. The structural changes are generally assumed to be strongly correlated with catalytic activity and generating baseline data on the structure of the catalyst under different reaction conditions is a critical part of developing a fundamental understanding of the catalytic functionality in nanoparticle systems. ETEM is an ideal tool for exploring these changes down to the atomic level using a broad range of imaging, diffraction, and spectroscopy techniques. Spectroscopy allows us to determine compositional changes due to mass exchange between the

sample and the surrounding gas. With STEM EELS it is also possible to monitor elemental redistributions that are often driven by interaction with the gas phase. Several examples are given, mainly of oxides, metals, and hydrides that demonstrate how spectroscopy can provide fundamental information about changes in the materials that cannot be obtained from imaging.

4.3.1 Oxides

Reducible oxides may undergo changes in reactant atmospheres associated with Mars van Krevelen type mechanisms in which oxygen for a reaction with an adsorbate comes directly from the oxide lattice. Consequently, there has been interest in exploring the changes that take place in oxides under redox conditions. While catalysis takes place on the surface, the introduction or elimination of oxygen vacancies on the surface may be influenced by processes taking place in the bulk. Ceria-based oxides play an important role in three-way automotive catalysts and have potential applications in intermediate-temperature solid oxide fuel cells and electrolyzers (Trovarelli 2002; Mogensen et al. 2004, 2011; Gaudillere et al. 2010; Bernal et al. 2008; Yeste et al. 2009). (It is also of interest for soot abatement in the exhaust from diesel engines. The nanoscale kinetics of soot oxidation with ceria was determined by direct observation of soot gasification at the soot-ceria interface (Simonsen et al. 2008).) Ceria is an interesting oxide in which the Ce cation can exist in the +3 or +4 oxidation state. It also has a high oxygen ionic conductivity and reasonable electronic conductivity under reducing conditions (Mogensen et al. 2004; Omar et al. 2009; Tuller 2000). In a reducing atmosphere, oxygen vacancies produced at the surface may diffuse to subsurface sites, resulting in an overall reduction of the entire ceria nanoparticles. The particle reduction and re-oxidization is extremely important in automotive three-way catalysts where the ceria component of the catalyst serves as an oxygen storage buffer. The ease with which this process takes place can be controlled by doping the ceria with other elements and Zr is commonly employed to provide enhanced oxygen storage capacity at lower temperatures (e.g., Yeste et al. 2009; Fornasiero et al. 1996, 1999; Izu et al. 1998; Otsuka-Yao-Matsuo et al. 1998; Montini et al. 2005).

In situ electron energy-loss spectroscopy in the ETEM has been employed to determine the local oxidation state of cerium and thus the degree to which oxygen vacancies are present in cerium-based oxides (Sharma and Crozier 1999; Sharma et al. 2004; Lopez-Cartes et al. 2003). This approach has also been employed to investigate surface restructuring and reversible oxygen vacancy ordering under reducing conditions (Wang et al. 2009; Crozier et al. 2008). Figure 4.12 shows images, electron diffraction patterns, and EELS data from a redox cycle for a CeO_2 crystal where the temperature is cycled in about 1.3 mbar of H_2. The energy-loss spectrum from the Ce shows sharp peaks at the onsets of the Ce M_5 and Ce M_4 edges, the so-called M_{45} white lines. At 693 °C the relative intensity of the Ce M_{45} white lines show an abrupt change, indicating that the cation has transformed from

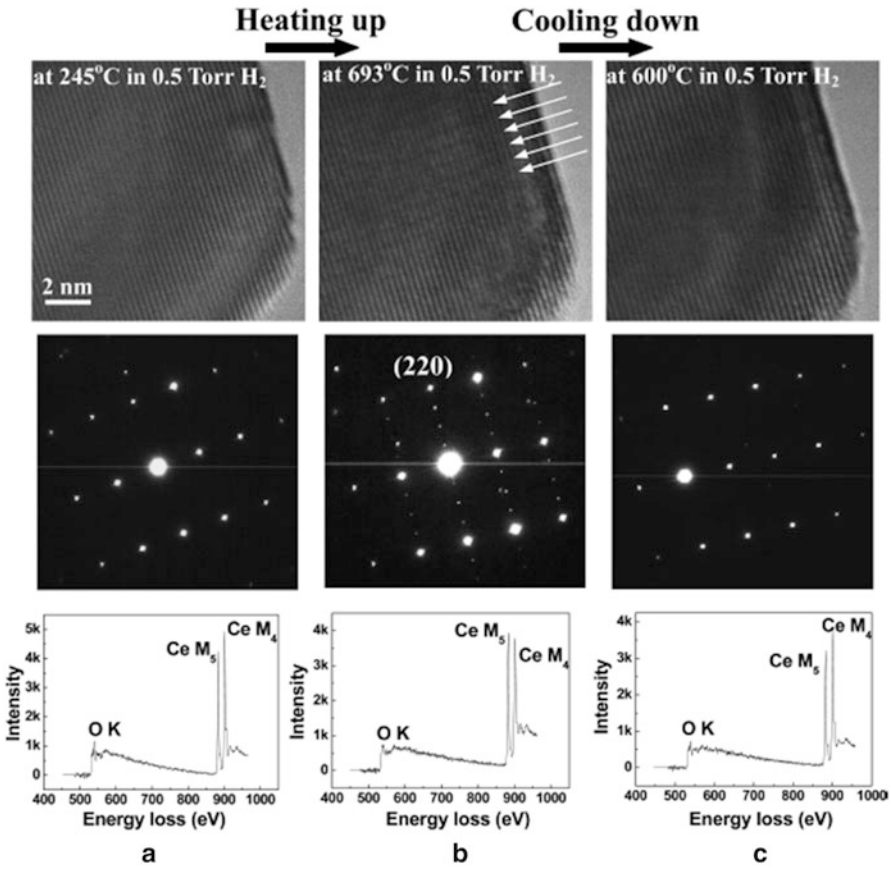

Fig. 4.12 Dynamic changes in atomic-level structure characterized by high-resolution imaging (*upper*), and electron diffraction (*middle*), and oxidation state change determined from electron energy-loss spectroscopy (*lower*) at (**a**) 245 °C, (**b**) 693 °C, and (**c**) 600 °C in 0.65 mbar of H_2 along the $[21\bar{1}]$ zone axis from the same individual CeO_2 nanoparticle during a redox cycle. After reduction (**panel b**), the *arrows* in the high-resolution image show the new periodicity, and the extra spots along the (220) plane in the electron diffraction pattern also show the superstructure formed during reduction (from Wang et al. 2009) © 2009 American Chemical Society

a +4 to *a* +3 oxidation state. Associated with the change in the Ce white lines, superlattice fringes appear in the atomic resolution image and superlattice spots in the electron diffraction pattern. The combination of the oxidation state data from the spectroscopy together with the structural information from imaging and diffraction allows us to conclude that a large number of oxygen vacancies have been introduced to the structure and undergone ordering. Interestingly, the reaction is completely reversible and the structure vanishes on cooling to 600 °C as the ceria re-oxidizes. The phase transformation is associated with a doubling of the lattice parameter and the formation of a body-centered cubic structure (Wang et al. 2009).

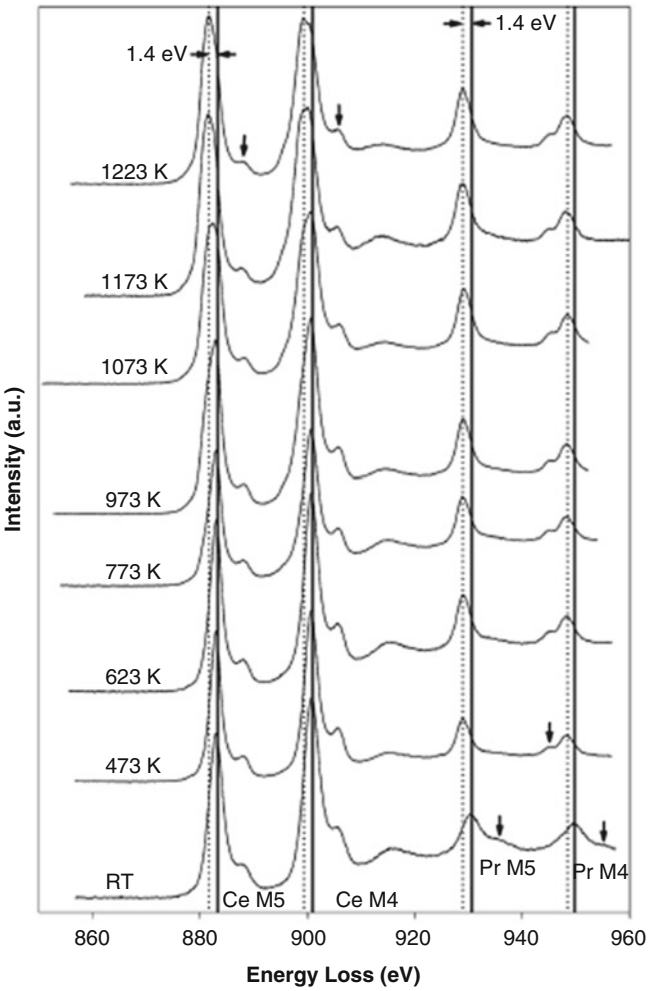

Fig. 4.13 Rh(1 %)/$Ce_{0.8}Pr_{0.2}O_{2-x}$ catalyst. Spectra recorded with 4 mbar H_2 in the ETEM cell at the indicated temperatures. The peak positions for some of the characteristic features of Ln^{4+} and Ln^{3+} species are marked by the *solid* and *dashed vertical lines*, respectively (from Lopez-Cartes et al. 2003) © 2009 Royal Society of Chemistry

A similar approach can be employed in more complex oxides such as Pr doped CeO_2 (Lopez-Cartes et al. 2003). The change in the Ce M_{45} and Pr M_{45} edge onsets and white line ratios are shown in Fig. 4.13 for $Rh_{1wt.\%}$ $Ce_{0.8}PrO_{2-x}$ catalyst when heated in an H_2 atm. In this case, Pr white-line peaks do not show a significant change in relative intensity but undergo a shift of about 1.5 eV when the Pr^{+4} reduces to Pr^{+3} at 473 K. The Ce remained in the +4 oxidation state until the temperature reached 1073 K. This approach has been used to explore the reversible redox activity of individual $Ce_xZr_{1-x}O_2$ nanoparticles of nominally identical size

and composition (Wang et al. 2008). The oxidation state of Ce was found to vary from particle to particle at least in part because of cation ordering which inhibits reversible redox behavior.

Many of the catalysts composed of metal particles on reducible oxides rely on interactions that take place under oxidizing and reducing conditions between the metal and the support. The interaction between the metal and support can also give rise to long range changes in the structure of the catalyst and ETEM has the potential to explore these phenomena. The most famous example of this long-range phenomenon is the so-called strong-metal-support interaction which often takes place in reducible oxides under reducing conditions (Tauster 1987; Tauster et al. 1978, 1981). In this case, under reducing conditions, oxide diffuses over the surface of the metal particles and effectively de-activates the catalyst (partial coverage has also been observed, Li et al. 2006a). Another related example of a potential long-range change is related to spillover phenomenon, in which molecules dissociate on metal particles and the dissociated fragments spill onto the oxide support and undergo further reaction. In situ EELS was used to characterize a hydrogen-spillover in nickel-loaded Pr-doped ceria (Sharma et al. 2012). Energy-loss spectra were recorded from the underlying oxide support adjacent to a Ni nanoparticle and tens of nanometers away. A preferential reduction of the ceria in the vicinity of a Ni particle at temperatures of 420 °C was observed and is shown in Fig. 4.14. This is much lower than the Ce reduction temperature of pure Pr-doped ceria which was about 700 °C. The experimentally measured spatial extent of the reduction zone was found to be approximately 20 nm. It is worth pointing out that the oxide support had an amorphous structure in this case and no changes between the reduced and unreduced ceria could be observed in the images. This demonstrates that spectroscopic analysis is often essential to understand the complete interplay between the solid and gas phases.

4.3.2 Metals

In situ EELS has been successfully employed to explore the changes taking place on metallic and bimetallic nanoparticles especially for catalyst applications. Developing and understanding new and existing methodologies for catalyst preparation is important for developing improved catalysts (Ertl et al. 1999; De Jong 1998; Moser 1996). For supported metal catalysts, traditional preparation methods such as metal salt impregnation remain widely used especially for industrial applications because of their relatively low cost and simplicity (Pinna 1998). Ex situ transmission electron microscopy (TEM) has been employed to investigate the various stages of impregnation processes on real high surface area supports (De Jong 1998; Sietsma et al. 2008a, b). ETEM has also been employed to follow the evolution of metal-supported catalysts during calcination and reduction. For example, the metal reduction is often the final step in preparing a supported metal catalyst and removal of surface oxide layers may also be a necessary step in catalyst activation.

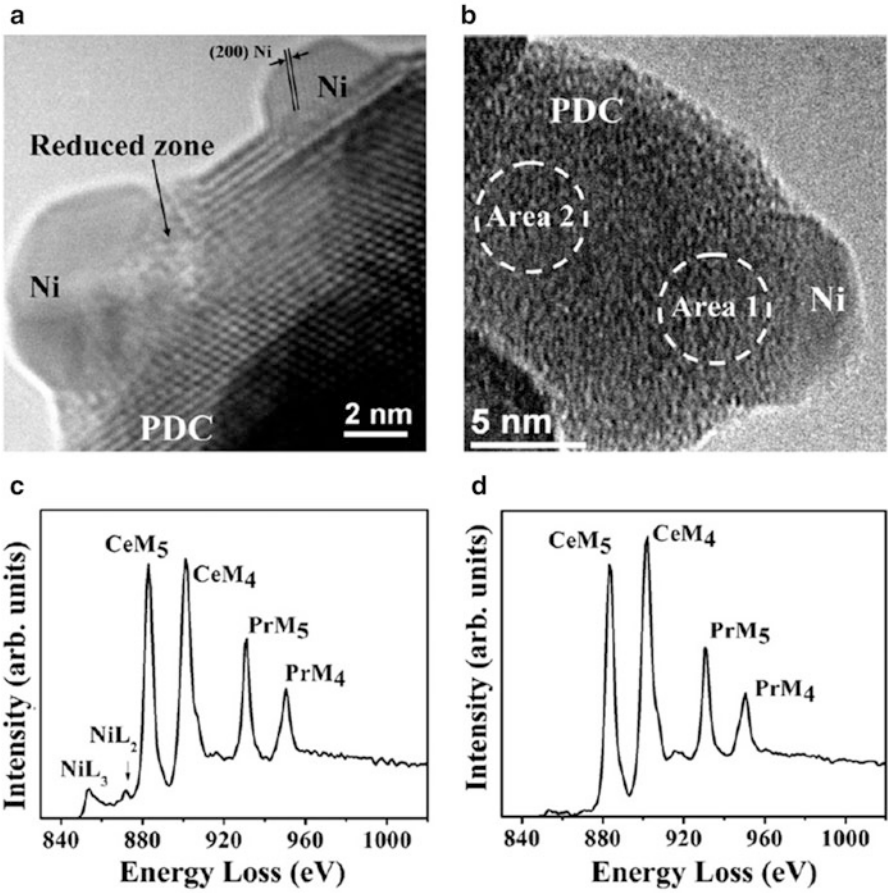

Fig. 4.14 (**a**) High resolution image of Ni–PDC interface in H_2 environment: (**a**) at 650 °C and (**b**) at 420 °C in 1.3 mbar of H_2 following an ex situ pre-reduction treatment; (**c**, **d**) energy loss spectra from the region next to the Ni–PDC interface (*Area 1*) and away from the interface (*Area 2*), respectively, of (**b**) (from Sharma et al. 2012) © 2012 Elsevier

Consequently a growing number of ETEM studies have been undertaken to investigate morphological and compositional evolution during the final reduction step. One advantage of the ETEM approach is that it allows the spatial distributions of the salt, the oxide, and the final metal from the same region of the catalytic material to be correlated (Li et al. 2005, 2006b, 2009); Banerjee et al. 2012).

Spectroscopic analysis becomes critical when more than one metal is involved in the catalyst formulation. Bimetallic systems can have many different configurations including homogeneous alloying, core-shell structures and complete separation of the two metals. Li et al. have investigated the morphological and nanoscale compositional changes during the preparation of 3 wt% Ni−1 wt% Cu/TiO_2(Li et al. 2009). Particles nucleated from the nitrate precursors grew via

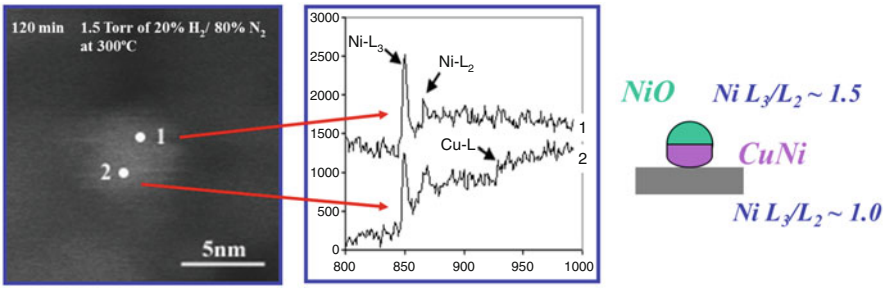

Fig. 4.15 (**a**) In situ *Z*-contrast image of a CuNi/NiO particle and (**b**) the in situ EELS precision nanoprobe chemical analysis inside the particle. The experiments were performed at 300 °C under 2 mbar of 20 % H_2/80 % N_2. (**c**) Schematic diagram of the particles structure and estimate Ni *white line* ratio showing that the CuNi lower region is metallic while the upper Ni region is NiO. Li et al. 2009, © 2009 Elsevier

both Ostwald ripening and particle migration and coalescence. Pure CuO particles reduced to metal at 300 °C, pure NiO reduced at 400 °C, and particles containing both Cu and Ni reduced to the metallic state in 2 mbar of 20% H_2−80% N_2 at 300 °C. High spatial resolution EELS is a powerful approach for following the nanoscale compositional evolution at different points within a single metal particle as shown in Fig. 4.15. This shows an annular dark-field STEM image recorded at 300 °C in H_2 from a 6 nm particle at an intermediate stage of reduction. High spatial resolution energy-loss spectra were recorded from different points on the particle using the sub-nanometer electron probe. Both spectra show the presence of Ni, but the lower half of the particle (labeled point 2 in Fig. 4.15) also shows that there is roughly 30 at.% Cu present. The L_{23} white lines on the Ni edge show that at point 1, the Ni is still oxidized and is predominantly NiO. In the lower part of the particle which contains Cu, the Ni white lines indicate that the Ni is mostly metallic. This demonstrates the promotional effect of Cu in reducing Ni in bimetallic particles. It is interesting because it clearly demonstrates that there can be substantial variations in the oxidation state of Ni under identical reactor conditions. The oxidation state depends not only on the reactive gas and temperature but also on the local materials environment adjacent to the Ni.

Other in situ spectroscopic studies with EELS have shown similar compositional heterogeneity in bimetallic systems. Li also explored the phase transformations taking place during the preparation of bimetallic catalysts including a model Fischer–Tropsch catalyst 20 wt% Co−2 wt% Ru/γ-Al_2O_3 (Li et al. 2006b). During reduction, small particles nucleated from the metal precursor and grew mainly by coalescence. By comparing the Ru-promoted Co system with monometallic cobalt, they were able to show with in situ STEM EELS that, in gentle reducing conditions (1.3 mbar of 10% H_2–90% N_2) at 400 °C, small metallic Ru and CoRu metal particles co-existed with larger CoO_x particles demonstrating that Ru enhanced the reduction of Co. Dehghan et al. have also investigated the reducibility of cobalt oxide on 12 wt% Co/α−Al_2O_3 with and without a 0.5 wt% Re promoter (Dehghan

et al. 2011). They were able to show with imaging and EELS that in 2.5 mbar of H_2, the initial Co_3O_4 started to transform to CoO at 180 °C and that Co metal started to appear at 260 °C, with complete reduction at 360 °C. In this case, the Re appeared to be uniformly distributed over the support and there was no difference in the reducibility between the promoted and non-promoted catalysts. A similar result was also found for a CoO_x/SiO_2 composite system and also showed nucleation and growth of metal particles during reduction (Xin et al. 2012).

The combination of in situ imaging, electron diffraction, and spectroscopy is able to provide direct nanoscale information about the structure, composition, and transport processes at different stages of catalyst preparation. A major advantage of the ETEM approach is that it explicitly reveals the atomic level evolution of the structural and compositional heterogeneity present in the system. Even on a highly controlled model catalyst, considerable heterogeneity may exist at the nanometer scale during the intermediate stages of, for example, calcination and reduction processes. This heterogeneity may also be present in the catalyst under operating conditions when both oxidizing and reducing species are present.

EELS is also useful for monitoring the evolution of bimetallic catalysts under reactor conditions to help establish structure–reactivity relations by correlating structural changes with changes in activity and selectivity. This can be performed by comparing a carefully designed set of in situ experiments with ex situ catalytic testing (Chenna and Crozier 2012b; Chenna et al. 2011a). (An alternative approach is to perform *operando* measurements as described in Sect. 4.4.3 of this chapter). Phase changes in the Ni system have also been correlated directly with changes in catalytic properties for hydrocarbon reforming (Chenna and Crozier 2012b; Chenna et al. 2011a). These authors used ETEM to determine the phase changes taking place on the 2.5 and 7.5 wt% Ni/SiO_2 catalysts during reactor ramp-up and were able to correlate these changes with the evolution of the catalyst activity and selectivity. During the temperature ramp-up in 1.3 mbar of $2CH_4 + O_2$, at 350 °C, the initial metallic Ni particles convert to NiO void particles, which catalyze complete oxidation of CH_4 resulting in the production of CO_2 and H_2O. As the temperature continues to rise, all the oxygen in the reactor gets converted and the atmosphere becomes reducing, resulting in the NiO being reduced to Ni metal at about 700 °C. At this point reforming begins and the products change from CO_2 and H_2O to CO and H_2. Data showing the initial transformation to NiO voids during the initial temperature ramp-up is given in Fig. 4.16.

The changes taking place in a single metal system can be followed using mostly imaging and diffraction techniques. However, when bimetallic catalysts are used for reforming, high spatial resolution spectroscopy must be employed to characterize the compositional changes taking place in the catalyst. This approach has been successfully applied to the behavior of the bimetallic $NiRu/SiO_2$ for the partial oxidation of methane. Using a combination of imaging and in situ STEM-EELS, it was shown that initially homogeneous NiRu particles undergo two distinct changes during ramp-up in mixtures of CH_4 and O_2 (Chenna et al. 2011b). Figure 4.17 shows an image of a 50–50 M ratio NiRu particle supported on SiO_2 recorded at 400 °C in H_2. The composition of the particle is confirmed by EELS which shows

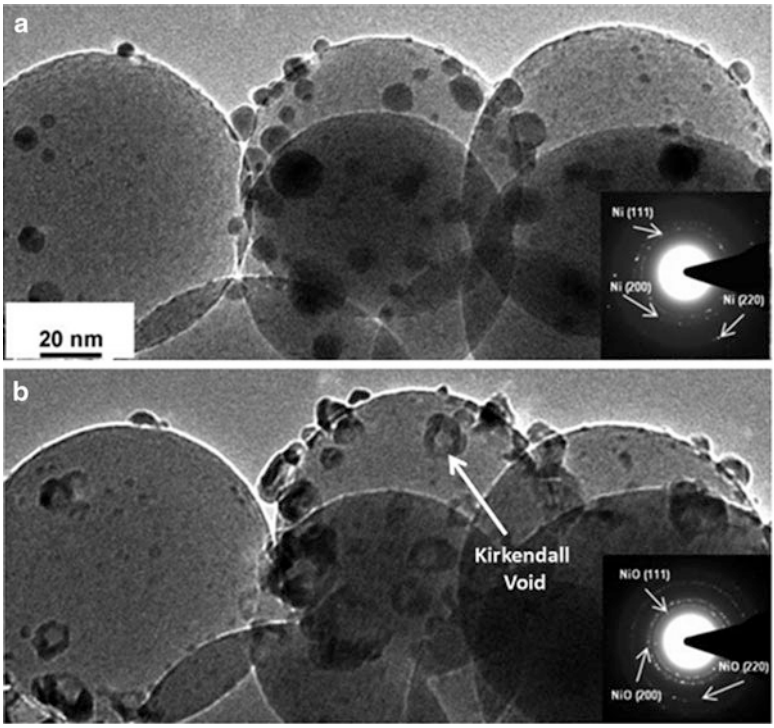

Fig. 4.16 In situ environmental transmission electron microscopy images and electron diffraction patterns of Ni/SiO_2: (**a**) in the presence of 1.5 mbar of H_2 at 400 °C and (**b**) from the same region in the presence of 1.5 mbar of a mixture of CH_4 and O_2 in a 2:1 ratio at 400 °C. *Inset*: Schematic of the structure–reactivity relation (from Chenna et al. 2011b) © 2011 Wiley-VCH Verlag GmbH&Co, KGaA, Weinheim)

the presence of the Ru M_{45} edge at about 300 eV and the Ni L_{23} edge at 855 eV. When exposed to a 1.3 mbar mixture of CH_4 and O_2 in a 2:1 ratio, a core-shell structure forms at around 350 °C. In situ EELS shows that the shell is predominantly NiO and the core is Ru metal as seen in Fig. 4.17.

A more detailed picture of the compositional evolution of the particle can be obtained by performing EELS line-scans on the initial and final structures. Figure 4.18 shows an ADF image recorded from a 10 nm particle at 400 °C in H_2. A line scan was performed by scanning the beam across the particles and recording a spectrum about every 0.5 nm. The spectra in the series were processed using the techniques described in Sect. 4.2.2, and the Ni and Ru integrated signals are plotted as a function of position in Fig. 4.18b. The figure shows that the two signals (when scaled to each other) almost completely superimpose indicating the presence of a fairly uniform mixing between the Ni and Ru. The same particle is then exposed to the CH_4 and O_2 mixture at 400 °C and this time the EELS line-scan shows that the Ni profile is displaced with respect to the Ru signal indicating that Ni has diffused to

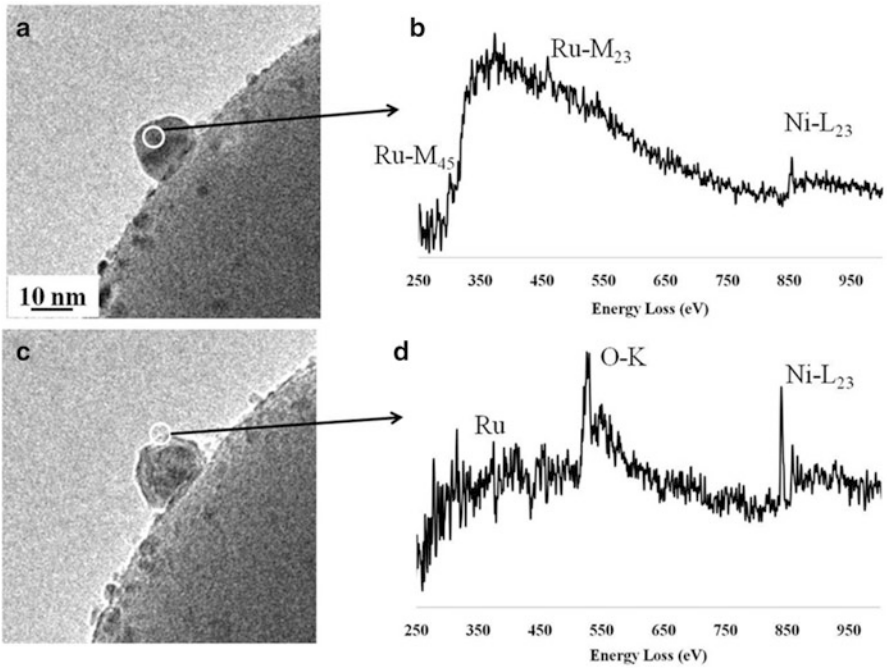

Fig. 4.17 In situ ETEM images of Ni–Ru/SiO_2: (**a**) In presence of 1.3 mbar of H_2 at 400 °C and (**b**) energy-loss spectrum from the same particle. (**c**) Image from the same region in presence of 1.3 mbar of mixture of CH_4 and O_2 in 2:1 ratio at 400 °C and (**d**) corresponding EELS spectrum

the surface and oxidized, giving rise to a NiO/Ru core-shell structure. Comparison with ex situ catalytic reactor data shows that at this temperature, the catalyst is performing complete oxidation of CH_4 and no syngas is produced.

Once again, reactor data show that, as the temperature is increased, the consumption of O_2 results in a reducing atmosphere being created because of the high concentration of CH_4. These conditions can also be recreated in the ETEM, and EELS linescans used to track the compositional evolution taking place in the bimetallic particles. Figure 4.19 shows a particle at 400 °C in the CH_4 and O_2 reforming atmosphere with the EELS line-scan showing the same core-shell structure. As the O_2 pressure is lowered in the ETEM, the particle undergoes a phase change and the NiO reduces to Ni metal. The EELS linescan shows that the particle no longer has a surface layer that is enriched in Ni and indicates that the two metals have remixed. However, the Ni and Ru profiles do not superimpose on each other, showing that the resulting particle is not compositionally uniform but consists of domains which are either rich in Ru or Ni. It is reasonable that the two metals do not form a solid solution because Ni is fcc and Ru hcp and the bulk phase diagram predicts separation between the metals.

The compositional evolution of the catalyst can be summarized schematically and superimposed on the catalytic data recorded from an ex situ reactor.

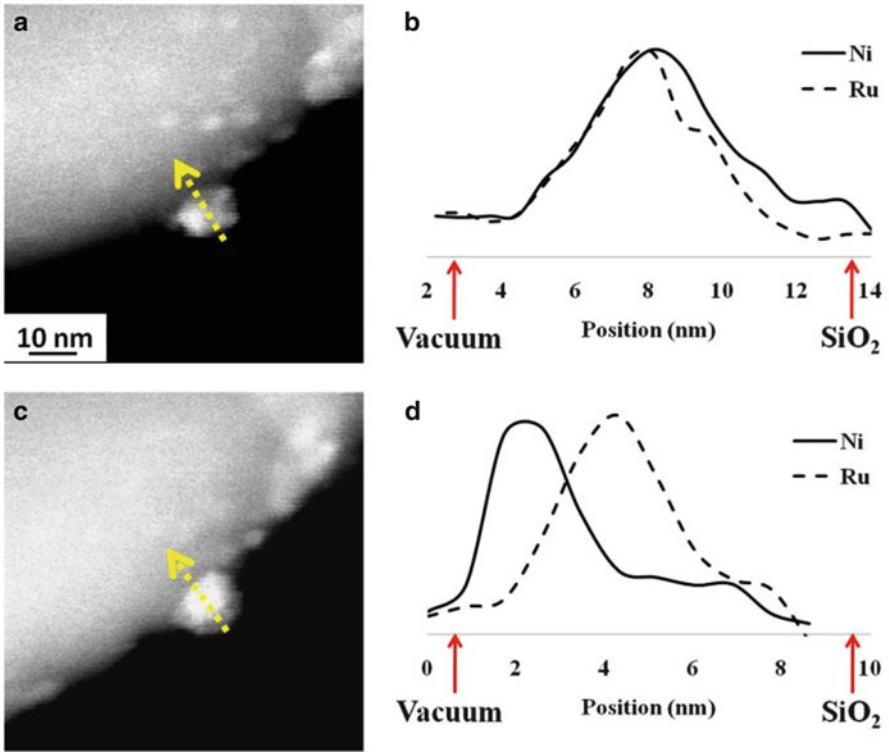

Fig. 4.18 In situ environmental STEM images and EELS line scans from Ni–Ru/SiO_2 (**a**) In presence of 0.4 mbar of H_2 at 400 °C and (**b**) from the same nanoparticle in presence of 0.4 mbar of mixture of CH_4 and O_2 in 2:1 ratio at 400 °C. (**b**, **d**) Corresponding EELS linescans showing spatial variation in Ni and Ru signals

This structure–reactivity correlation is shown in Fig. 4.20. The particles start out being approximately homogeneous and then transform to core-shell structures enriched in NiO and function as complete oxidation catalysts for methane. At around 500 °C, all the O_2 in the reactor is consumed and the atmosphere becomes reducing. At this point the particles reduce back down to the metallic state and reforming begins (i.e., H_2 and CO are produced). The active reforming catalyst is a compositionally heterogeneous NiRu particle.

4.3.3 Hydride Detection

Recently it has been shown that in situ low-loss EELS can be employed to detect the formation of hydrides (Baldi et al. 2014). Experiments have been performed on palladium nanocubes cooled to −27 °C and exposed to different pressures of H_2. A typical set of energy-loss spectra are shown in Fig. 4.21. Upon exposure to a high

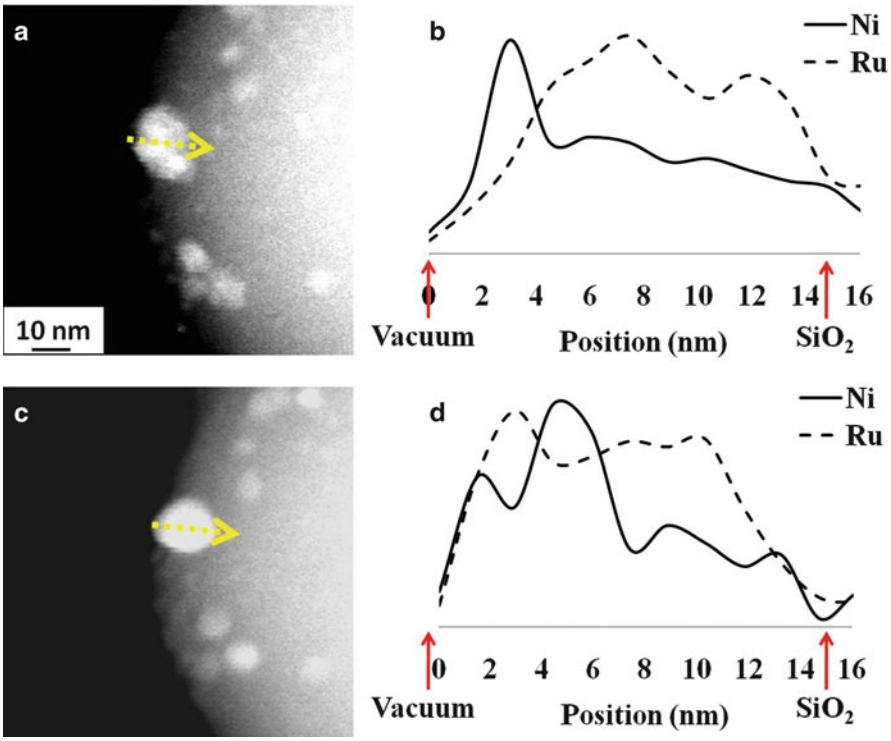

Fig. 4.19 In situ environmental STEM images and EELS line scans from Ni–Ru/SiO_2 (**a**) in the presence of 0.4 mbar of CH_4 and O_2 in 2:1 ratio at 400 °C (**b**) corresponding composition profile obtained from EELS (**c**) from the same nanoparticle in the presence of 0.4 mbar of mixture of CH_4 at 600 °C (**d**) corresponding composition profile obtained from EELS

pressure of H_2, a peak appears at around 5.6 eV in the low-loss spectrum corresponding to β hydride formation. Lowering the H_2 pressure causes the peak to vanish as the sample transforms to the α phase (which is mostly metallic Pd). There is very little change in the appearance of the cubes when this phase transformation is cycled. By employing the spectroscopic approach, the nanostructural factors which control the kinetics of the phase transformation may be investigated.

4.4 Applications Characterizing Local Gas and Liquid Environments

Using spectroscopic techniques to quantify the gas composition around the ETEM sample is a recent development, and much remains to be explored, but a few applications have been published. The study of catalysts which drive reactions

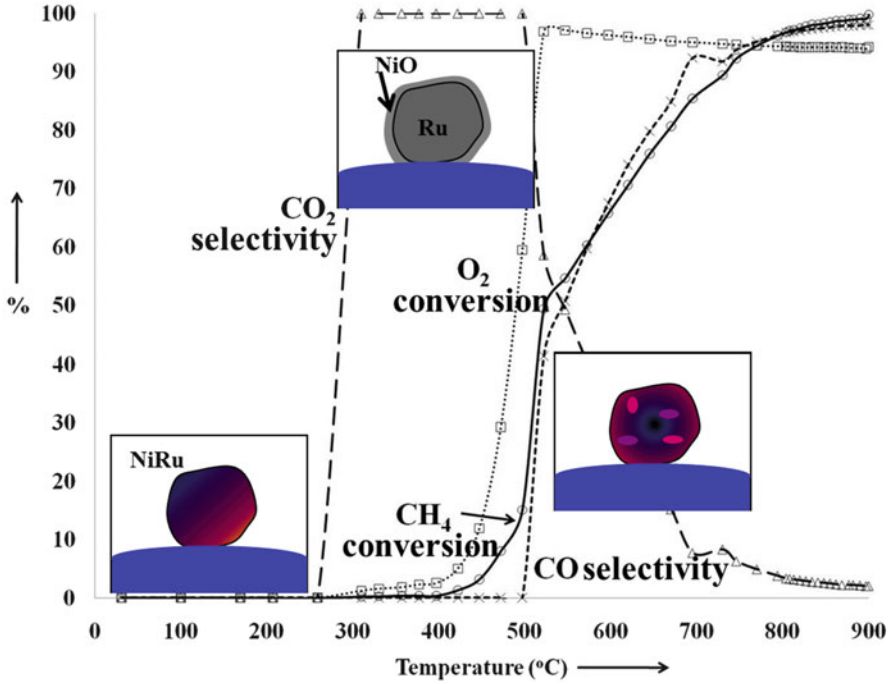

Fig. 4.20 Structure–reactivity relations for activation of $NiRu/SiO_2$ catalyst for partial oxidation of methane. Schematic diagrams of the bimetallic particle evolution determined from ETEM are positioned at the corresponding locations on the catalytic data

that change the composition of their surrounding environment is a major driving force for these techniques, though a few other possible uses for spectroscopy of gases and liquids are being explored.

4.4.1 Local Temperature Measurement

Spectroscopy techniques have been applied to gases mainly to determine the gas composition around catalytic materials, but other applications, including the measurement of temperature and of cell thickness in MEMS-based holder experiments have also been demonstrated. The local temperature of a gas cell heating holder was measured by Vendelbo et al. using EELS (Vendelbo et al. 2013). The average temperature of the cell, which is heated by a platinum element patterned on the top SiN membrane, was determined by measuring the resistance of the platinum element, and comparing this to the resistance of the same element heated in an oven of known temperature. The thickness of the gas inside the cell at these

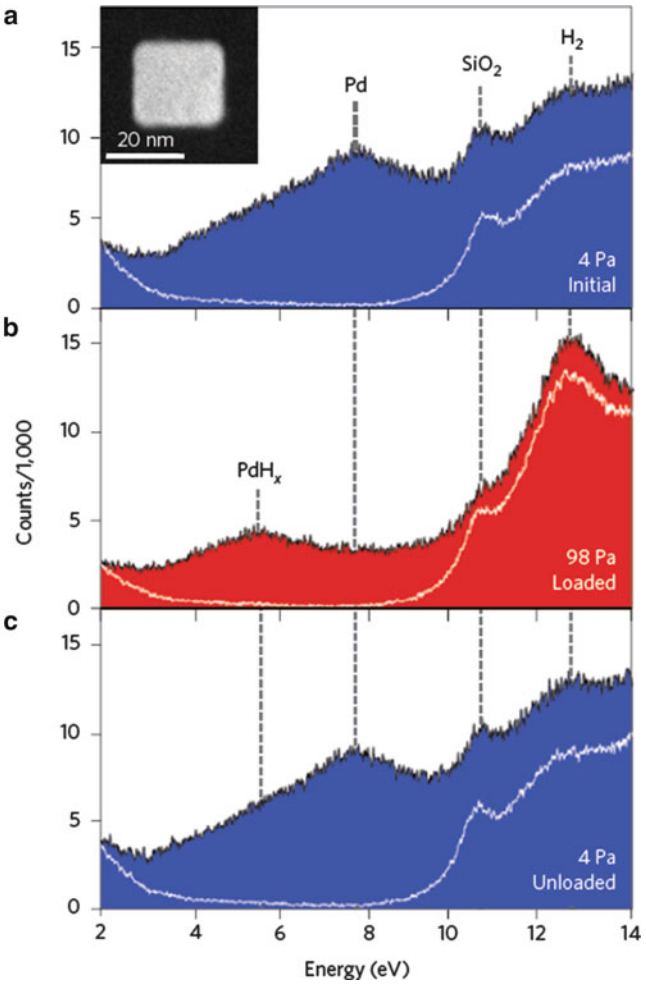

Fig. 4.21 Low loss energy-loss spectrum from cubic Pd nanoparticle (*inset*) showing (**a**) unloaded (4 Pa of H_2), (**b**) loaded with H_2 (98 Pa of H_2) and (**c**) unloaded (4 Pa of H_2). Spectrum (**b**) confirms the presence of hydrogen-rich β palladium hydride. White spectra were taken from the supporting SiO_2, near the Pd particle (from Baldi et al. 2014) © 2014 Nature Publishing Group

locations was determined by measuring the difference in focus between minimum contrast at the top and bottom membranes. A temperature of 77 °C was taken to be the reference temperature, and EELS spectra of the gas-filled cell were acquired at windows near the center and edge of the heated area. The intensity of the H_2 plasmon peak relative to the zero-loss peak will change depending on the total number of H_2 molecules which the beam interacts with, as seen in Fig. 4.22. For a constant gas pressure, this number depends only on the thickness of the gas and the

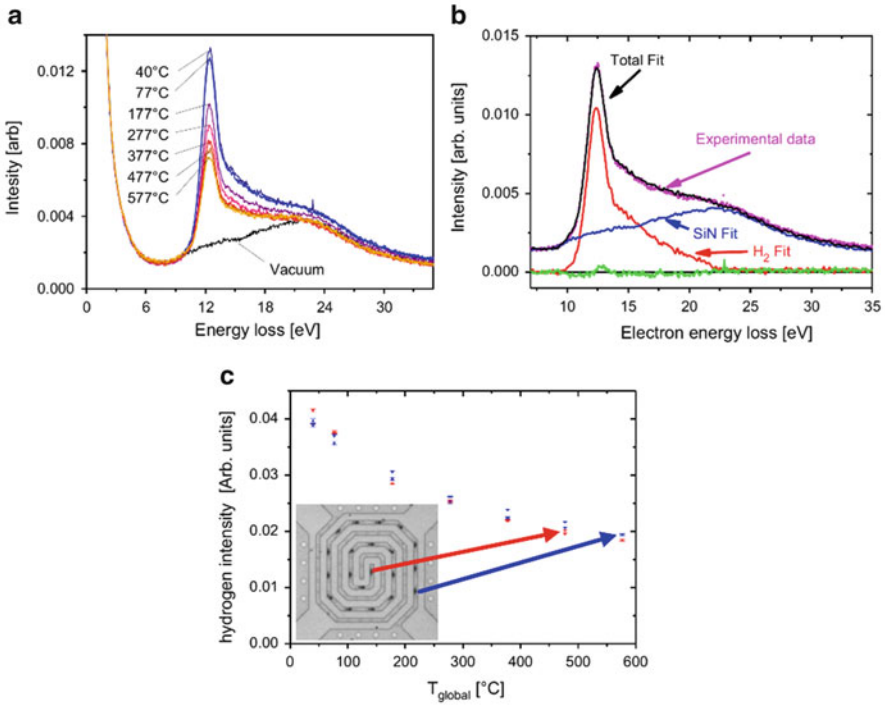

Fig. 4.22 (**a**) EELS spectra from a SiN windowed cell with 1.2 bar H_2 gas at (global) temperatures from 40 to 577 °C. (**b**) EELS spectrum from the cell at 40 °C, showing that the spectrum can be fit by a linear combination of the spectrum from SiN and the spectrum from H_2 gas. (**c**) The intensity of the H_2 gas spectrum is plotted against the global temperature of the cell, showing that the rate of change for the window at the center is different from that at the edge of the cell, due to the temperature gradient across the cell. This temperature change can be quantified using (4.12) as shown in (Vendelbo et al. 2013). Modified with permission from (Vendelbo et al. 2013) © 2013 Elsevier

temperature. The temperature of the locations previously considered can thus be expressed in terms of the reference temperature T_σ, pressure p, gas thickness t, H_2 low-loss intensity I_{H_2} and the zero loss peak intensity I_0 according to (4.12) which is derived in Vendelbo et al. (2013).

$$T_{\text{local}} = \frac{p\ t}{p_\sigma t_\sigma} \frac{\ln(1 + I_{H_{2\sigma}}/I_{0\sigma})}{\ln(1 + I_{H_2}/I_0)} T_\sigma \tag{4.12}$$

The temperature difference between the center and the edge of the cell when heated to a global temperature of 577 °C with 1.2 bar of stagnant H_2 was found to be 100 °C using this method.

4.4.2 EELS and Characterization of Liquid Environments

Electron energy-loss spectra from liquids were obtained for both low-loss and core-loss regimes (Holtz et al. 2013). Multiple scattering from the liquid limits the usefulness of this technique for thick liquid layers. It was found that core-loss edges could only be observed in layers thinner than 2–3 times the inelastic mean free path λ. This is seen in Fig. 4.23 where the O K edge is only visible in the thinnest water layer ($t/\lambda = 2.7$) observed. Valence-loss features in the EELS spectra are more visible, but were only resolved in liquid layers thinner than 6.5λ, which corresponds to about 700 nm of water. Despite these limitations, core-loss and valence-loss data of solids and liquids were still obtained in thin layers of aqueous solutions, demonstrating the possibility of using EELS for reactions in liquid cells, provided that the liquid layers are kept very thin. Additionally it was shown that the thickness of the liquid layer, which is determined mainly by the bulging of the electron transparent windows, can be measured with high spatial resolution using EELS.

4.4.3 Operando *TEM*

ETEM analysis of the catalyst structure and composition in the presence of reactive gases is important but it does not confirm that catalysis is actually taking place in the microscope. Indeed the need for techniques which simultaneously measure

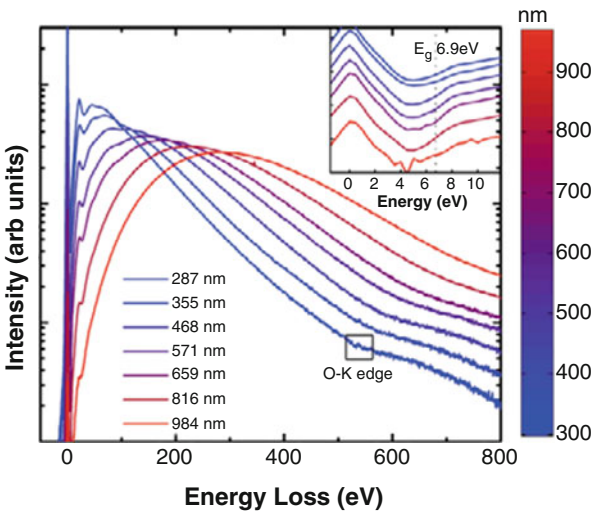

Fig. 4.23 EELS spectra of a SiN membrane cell filled with liquid water at room temperature at different locations around the electron-transparent window. The bulging of the window can be quantified by analysis of the intensity of the zero loss peak. The O K-edge from the water can be seen only in the thinnest liquid layer. Reproduced with permission from (Holtz et al. 2013) © 2013 Microscopy Society of America

catalyst structure and activity has been recognized for some time and was developed for Raman spectroscopy where the term *operando* was introduced (Bañares and Wachs 2002). The ability to determine structure and activity in the same experiment is a powerful approach to catalysis research, and both RGA and EELS can be employed to monitor gas composition in the e-cell. It has been demonstrated that EELS can be employed to quantitatively measure the composition of catalytic product gases, thus opening the door to *operando* TEM for catalysis research using EELS (Chenna and Crozier 2012a; Crozier and Chenna 2011). This makes it possible to follow the course of reactions, monitoring the changes in catalyst conversion and structure simultaneously. The correlation between the relative catalyst activity and the catalyst structure will now be much tighter.

In a traditional TEM sample, the minute amount of catalyst inside the microscope will yield a correspondingly small number of product gas molecules. In a windowed cell setup, it may be possible to detect this small number of product gas molecules in the outlet flow from the holder, since the total flow is quite small (Vendelbo et al. 2014). In a differentially pumped ETEM however, the reactant-gas flow is much larger, so the partial pressures of product gases will be smaller. If the product gas partial pressures are near the detection limit or the same gas species is present in the background of the system, it will be difficult to accurately measure the catalyst's changing activity. A simple solution to this problem is to increase the amount of catalyst present in the TEM, so that an easily quantifiable amount of product gas is produced. This requires the development of unique TEM sample preparation techniques. Standard ETEM samples for studying catalytic nanoparticles usually consist of a metal grid onto which catalyst nanoparticles are dispersed. To increase the total surface area of the TEM sample, a 3 mm diameter porous Pyrex pellet was created which had a surface area nearly 50 times larger than a standard grid, allowing products generated by the now abundant catalyst to be monitored in the microscope. The pellet was fabricated by firing crushed Pyrex wool packed inside a quartz tube, cutting sections, and then grinding it to a thickness between 0.5 and 0.8 mm. The pellet was then filled with the silica-supported catalyst using a wet-impregnation technique. Because the Pyrex pellet fibers are insulating and charge under the electron beam, a metal grid also loaded with the supported catalyst was still loaded into the holder along with the pellet (Miller et al. 2015).

CO oxidation was chosen as an ideal reaction to study using this new operando TEM technique since the chemistry is relatively simple, and the reaction well-studied. The particular catalyst studied was 5–15 nm ruthenium nanoparticles supported on amorphous silica spheres which are approximately 200 nm in diameter. Ex situ reactor studies (Chenna and Crozier 2012a) showed that the oxidation reaction to form CO_2 occurs above a temperature of about 150 °C. For the operando experiments, CO and O_2 were mixed in stoichiometric quantities, flowed through a carbon filter to eliminate carbonyls, and into the microscope to achieve a pressure of around 2.6 mbar in the ETEM cell. The ETEM used was a differentially pumped FEI Tecnai F20 operating at 200 kV. The temperature was measured and controlled

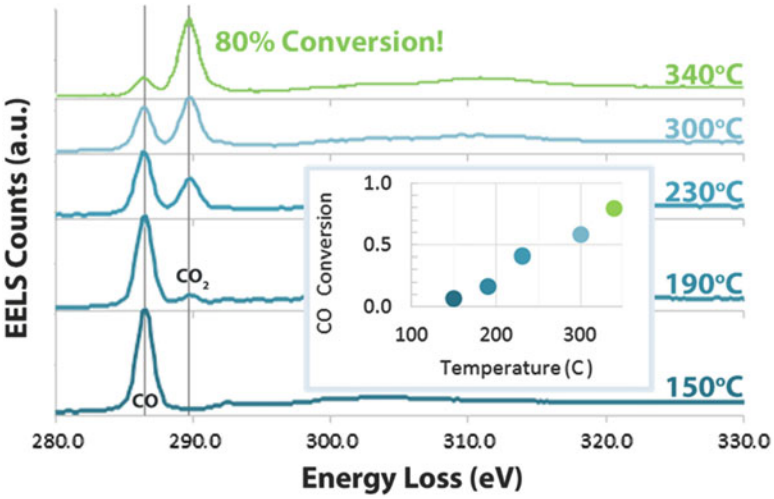

Fig. 4.24 Core-loss spectra showing the carbon K-edge recorded as a function of temperature from a CO oxidation experiment with a Pyrex-fiber pellet. The inlet gas was a stoichiometric ratio of CO and O_2 at 2.6 mbar. The spectra were quantified by fitting a linear combination of reference spectra and the calculated conversions are shown in the *inset*. Reproduced with permission from (Miller and Crozier 2014) © 2014 Microscopy Society of America

using a Gatan Ta hot stage, and was held at various temperatures from 150 °C up to 340 °C. To measure the catalytic conversion in the cell during an operando CO oxidation experiment, core-loss spectra were acquired (Miller and Crozier 2014). Some data showing high conversions achieved using the sample preparation just described is shown in Fig. 4.24.

RGA was also used by Miller and Crozier (2014) to monitor the gas composition during an in situ CO oxidation experiment. As the catalyst was heated from 130 to 230 °C, a large increase in the amount of CO_2 produced by the catalyst was observed. The data in Fig. 4.25a show this qualitative increase clearly, though the RGA data have not been quantified. Instead, EELS spectra were also acquired at specific times throughout the experiment, and these were quantified as shown in Fig. 4.25b. Experiments like this, coupled with atomic resolution images acquired in an aberration-corrected ETEM should shed light on the surface structures which are most active for CO oxidation.

Vendelbo et al. have recently reported on the use of an RGA to monitor rapid oscillations in gas composition inside a MEMS-based gas flow cell (Vendelbo et al. 2014). Under the right conditions, a well-known oscillation in the conversion of CO to CO_2 occurs over Pt (Imbihl and Ertl 1995). Ion currents in the quadrupole RGA were monitored at 4, 28, 32, and 44 amu, corresponding to He, CO, O_2, and CO_2, respectively. These were sampled with a 0.1 s dwell time and 1.8 s total spectrum acquisition time. This did not define the temporal resolution of the technique however, which was determined by space-time broadening of the gas in the tubing connecting the nanoreactor to the RGA. This broadening was found to

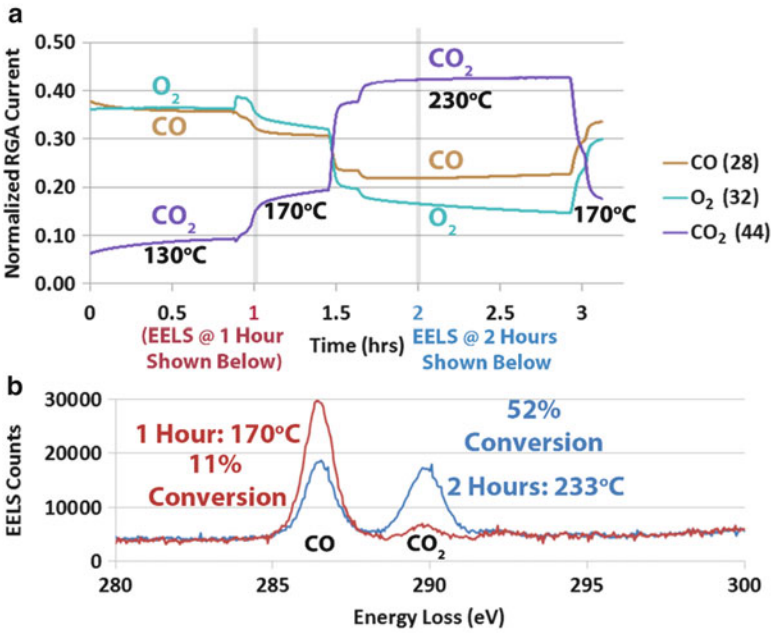

Fig. 4.25 (**a**) RGA data over several hours from masses 28, 32, and 44 amu, showing the clear increase in CO_2, and corresponding decrease in CO and O_2, within the ETEM cell as the temperature is increased from 130 to 230 °C. (**b**) EELS spectra were also acquired at several points during the experiment, including the two shown and quantified here

be on the order of 20 s, with a delay of 5 s between gas leaving the nanoreactor and being detected by the RGA, as seen in Fig. 4.26c. Fast oscillations in the reaction rate (which were still detected by monitoring the heater-power used to maintain a constant nanoreactor temperature) could therefore not be observed using the RGA (Fig. 4.26a), but oscillations with a period of about 30 s were clearly resolved (Fig. 4.26b). These authors were able to correlate the variations in the gas composition in the cell with atomic level images that showed oscillations in the faceting of the Pt nanoparticles. This is the first *operando* ETEM experiment that correlates changes in catalyst structure with activity.

4.5 Future Prospects

EELS, RGA, and EDX are the primary spectroscopic tools currently being utilized in ETEM, but future developments in instrumentation will guarantee that these spectroscopies will continue to improve and that new spectroscopies will become available. In terms of the current spectroscopies, several improvements are currently available now or in the near future. EDX is certainly compatible with

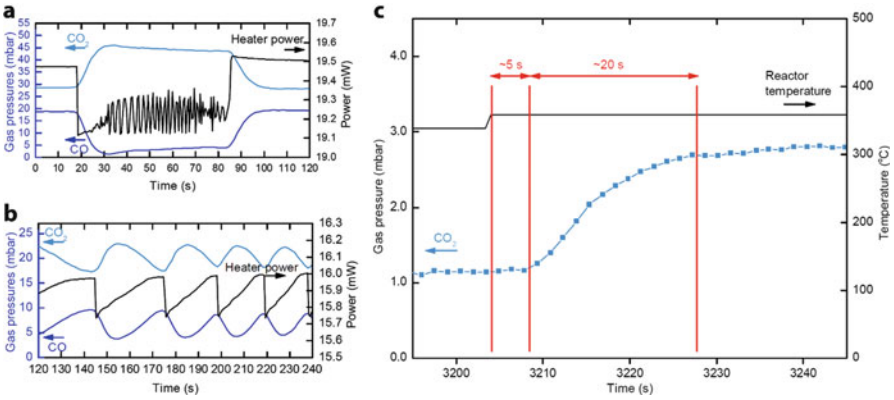

Fig. 4.26 Partial pressure and heater power data during oscillatory CO oxidation over Pt nanoparticles. (**a**) 1.0 bar 4.2% CO:21.0% O_2:74.8% He at 455 °C. At $t = 19$ s, the temperature was increased by 0.5 °C to induce the oscillatory cycle. (**b**) 1.0 bar 3% CO:42% O_2:55% He at 286 °C. At $t = 12$ s, the temperature was increased by 0.5 °C. (**c**) Response of the RGA to an instantaneous change in the gas composition which was induced by a sudden increase in the temperature of a Pt-loaded nanoreactor during CO oxidation. The change in the CO_2 pressure is delayed by 5 s between the reactor and the RGA where the composition was measured, and broadened by ~20 s. Reproduced with permission from (Vendelbo et al. 2014) © 2014 Macmillan Publishers Limited

windowed cells but the sensitivity of the technique is often compromised by the cell design. For improved detection limits, the cell must be designed in such a way that the spurious background associated with the materials in the body of the cell is minimized. This will require careful consideration of the shape and amount of bulk material supporting the electron transparent windows. EDX detectors should be made more robust so that they can be used at the moderate gas pressures (~1 mbar) associated with differentially pumped ETEM systems. Better mass spectrometers would improve quantification of gas composition within the cell. Having a response that is closer to linear with partial pressure would make interpretation of the RGA signal more straightforward.

The continued development of monochromators for the electron microscope could have a major impact on the EELS capability for the ETEM. The recently developed Nion UltraSTEM system has achieved an energy resolution on the order of 10 meV and this has allowed vibrational spectroscopy to now be accomplished (Krivanek et al. 2014). The high energy resolution is not helpful for core-loss EELS because of lifetime broadening effects but it can reveal completely new features in the low-loss spectrum that were previously impossible to observe by TEM EELS. The low energy associated with vibrational excitations may lead to the signal being delocalized by up to 50 nm or more. This may be negative in the sense that spatial resolution is compromised but it is still possible to correlate the de-localized vibrational spectrum with atomic resolution features determined with more highly localized imaging and spectroscopy signals.

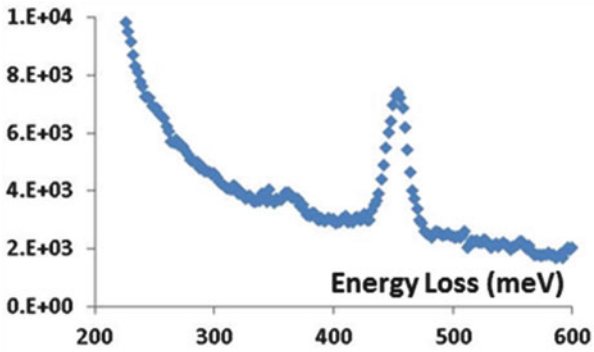

Fig. 4.27 Aloof mode spectrum showing OH vibrational peak at 454 meV from H_3BO_3

However, the question of localization and vibrational spectroscopy is far from resolved and high momentum transfer scattering may lead to atomic resolution (Rez 2014; Egerton 2014; Dwyer 2014). The delocalized nature of the low-loss spectrum also makes it possible to use the aloof beam spectral acquisition mode (García de Abajo and Aizpurua 1997; Echenique et al. 1987; Howie and Milne 1985). In this mode, the STEM probe is parked outside the sample, and sample damage that may result from radiolysis or knock-on is reduced or eliminated. A vibrational EELS spectrum recorded in aloof beam mode from boric acid is shown in Fig. 4.27 and clearly shows the OH stretch mode at 453 meV. It may be possible to employ this localized vibrational spectroscopy to probe surface adsorbates on nanoparticles and correlate this with localized surface defects. Thus improving the energy resolution of EELS will dramatically improve the spectroscopic probing capability of EELS for ETEM applications.

There is considerable interest in expanding the number of spectroscopic probes that can be employed to characterize the gas–solid interactions in the ETEM. Sharma et al. have recently added an optical system to their ETEM which can perform Raman spectroscopy and cathodoluminescence (Picher et al. 2015). This allows vibrational spectroscopy to be measured directly on the sample from an area determined by the laser beam diameter (currently 11 μm). It has been successfully employed to characterize carbon nanotube growth. It also provides a powerful method to measure local temperature because the Raman lines are temperature dependent. Temperature measurements with an accuracy of better than ± 10 °C are possible with this system.

It is likely that the number of spectroscopic configurations will continue to grow over time. The recent report by the US Department of Energy on the Future of Electron Scattering and Diffraction highlights the need to dramatically expand the number of probes available for in situ electron microscopy (DOE et al. 2014). This development of spectroscopic methods for ETEM will continue to expand and improve, providing researchers with powerful tools to study dynamic changes in materials.

Acknowledgments Sections of this work have been supported from National Science Foundation under award numbers CTS-0306688 (ceria redox studies), CBET 0553445 (NiCu bimetallic catalysts), and CBET 1134464 (EELS of gases, RGA analysis, operando EELS) and US Department of Energy, Office of Science, Basic Energy Science under award numbers DE-FG02-07ER46442 (hydrogen spillover) and DE-SC0004954 (monchromated and vibrational EELS). We gratefully acknowledge the use of facilities within the LeRoy Eyring Center for Solid State Science at Arizona State University.

References

A. Baldi, T.C. Narayan, A.L. Koh, J.A. Dionne, Nat. Mater. **13**, 1143–1148 (2014)
M.A. Bañares, I.E. Wachs, J.Raman Spectrosc. **33**, 359 (2002)
R. Banerjee, P.A. Crozier, J. Phys. Chem. C **116**, 11486–11495 (2012)
P.E. Batson, J. Silcox, Phys. Rev. B. **27**, 5224–5239 (1983)
S. Bernal, G. Blanco, J.J. Calvino, J.C. Hernandez, J.A. Perez-Omil, J.M. Pintado, M.R. Yeste, J. Alloy Compd. **451**, 521–525 (2008)
H.A. Bethe, Ann. Phys. **397**, 325–400 (1930)
W.J. Bowman, J. Zhu, R. Sharma, P.A. Crozier, Solid State Ion. **272**, 9–17 (2015)
H.A. Brink, M.M.G. Barfels, R.P. Burgner, B.N. Edwards, Ultramicroscopy **96**, 367–384 (2003)
R. Brydson, H. Sauer, W. Engel, J.M. Thomas, E. Zeitler, N. Kosugi, H. Kuroda, J. Phys. Condens. Matter **1**, 797–812 (1989)
M. Cabie, S. Giorgio, C.R. Henry, M.R. Axet, K. Philippot, B. Chaudret, J. Phys. Chem. C **114**, 2160–2163 (2010)
J.N. Chapman, W.A.P. Nicholson, P.A. Crozier, J. Microsc. **136**, 136–179 (1984)
S.W. Chee, R. Sharma, Micron **43**, 1181–1187 (2012)
S. Chenna, P.A. Crozier, ACS Catalysis **2**, 2395–2402 (2012a)
S. Chenna, P.A. Crozier, Micron **43**, 1188–1194 (2012b)
S. Chenna, R. Banerjee, P.A. Crozier, ChemCatChem **3**, 1051–1059 (2011a)
S. Chenna, Ph.D., Arizona State University (2011)
G. Cliff, G.W. Lorimer, J. Microsc. Oxf. **103**, 203–207 (1975)
P.A. Crozier, Philos. Mag. B **61**, 311–336 (1990)
P.A. Crozier, S. Chenna, Ultramicroscopy **111**, 177–185 (2011)
P.A. Crozier, T.W. Hansen, MRS Bull. **40**, 38–45 (2015)
P.A. Crozier, R. Wang, R. Sharma, Ultramicroscopy **108**, 1432–1440 (2008)
K.P. De Jong, CatTech **3**, 87 (1998)
R. Dehghan, T.W. Hansen, J.B. Wagner, A. Holmen, E. Rytter, O. Borg, J.C. Walmsley, Catal. Lett. **141**, 754–761 (2011)
DOE, *Future of Electron Scattering & Diffraction* (US Department of Energy, Office of Science, 2014)
C. Dwyer, Phys. Rev. B. **89**, 5 (2014)
P.M. Echenique, A. Howie, D.J. Wheatley, Philos. Mag. B. **56**, 335–349 (1987)
R.F. Egerton, *Electron Energy-Loss Spectroscopy in the Electron Microscope*, 3rd edn. (Plenum Press, New York, NY, 2011)
R.F. Egerton, Microsc. Microanal. **20**, 658–663 (2014)
R.F. Egerton, P.A. Crozier, Scan. Microsc. Int. Suppl. **2**, 245–254 (1988)
H. Ertl, J. Knozinger, G. Weitland (eds.) *Preparation of Solid Catalysts* (Wiley-VCH, New York, 1999)
P. Fornasiero, G. Balducci, R. Di Monte, J. Kaspar, V. Sergo, G. Gubitosa, A. Ferrero, M. Graziani, J. Catal. **164**, 173–183 (1996)
P. Fornasiero, J. Kaspar, V. Sergo, M. Graziani, J. Catal. **182**, 56–69 (1999)

P.L. Gai, E.D. Boyes, Microsc. Res. Tech. **72**, 153–164 (2009)
P.L. Gai, K. Kourtakis, E.D. Boyes, Catal. Lett. **102**, 1–7 (2005)
P.L. Gai, R. Sharma, F.M. Ross, Mater. Res. Soc. Bull. **33**, 107 (2008)
F.J. García de Abajo, J. Aizpurua, Phys. Rev. B. **56**, 15873–15884 (1997)
C. Gaudillere, P. Vernoux, C. Mirodatos, G. Caboche, D. Farrusseng, Catal. Today **157**, 263–269 (2010)
S. Giorgio, M. Cabie, C.R. Henry, Gold Bull. **41**, 167–173 (2008)
T.W. Hansen, J.B. Wagner, ACS Catalysis **4**, 1673–1685 (2014)
P. L. Hansen, S. Helveg, A. K. Datye, in *Advances in Catalysis* (Elsevier, Amsterdam, 2006), vol. 50, pp. 77–95.
M.S. He, B.L. Liu, A.I. Chernov, E.D. Obraztsova, I. Kauppi, H. Jiang, I. Anoshkin, F. Cavalca, T.W. Hansen, J.B. Wagner, A.G. Nasibulin, E.I. Kauppinen, J. Linnekoski, M. Niemela, J. Lehtonen, Chem. Mater. **24**, 1796–1801 (2012)
S. Helveg, C.F. Kisielowski, J.R. Jinschek, P. Specht, G. Yuan, H. Frei, Micron **68**, 176–185 (2015)
F. Hofer, Microsc. Microanal. Microstruct. **2**, 215–230 (1991)
F. Hofer, P. Golob, Micron Microsc. Acta **19**, 73–86 (1988)
F. Hofer, J. Microsc. Oxf. **156**, 279–283 (1989)
F. Hofer, P. Wilhelm, Ultramicroscopy **49**, 189–197 (1993)
M.E. Holtz, Y. Yu, J. Gao, H.D. Abruña, D.A. Muller, Microsc. Microanal. **19**, 1027–1035 (2013)
A. Howie, R.H. Milne, Ultramicroscopy **18**, 427–434 (1985)
A. Howie, C. Walsh, Microscopy. Microanal.Microstruct. **2**, 171–181 (1991)
R. Imbihl, G. Ertl, Chem. Rev. **95**, 697–733 (1995)
M. Inokuti, Rev. Mod. Phys. **43**, 297–347 (1971)
N. Izu, T. Omata, S. Otsuka-Yao-Matsuo, J. Alloy Compd. **270**, 107–114 (1998)
Q. Jeangros, T.W. Hansen, J.B. Wagner, C.D. Damsgaard, R.E. Dunin-Borkowski, C. Hebert, J. Van Herle, A. Hessler-Wyser, J. Mater. Sci. **48**, 2893–2907 (2013)
J.R. Jinschek, Chem. Commun. **50**, 2696–2706 (2014)
D. Johnson, J. Spence, J. Phys. D. **7**, 771–780 (1974)
K. Kimoto, T. Asaka, T. Nagai, M. Saito, Y. Matsui, K. Ishizuka, Nature **450**, 702–704 (2007)
M.O. Krause, J.H. Oliver, J. Phys. Chem. Ref. Data **8**, 329–338 (1979)
O.L. Krivanek, J.H. Paterson, Ultramicroscopy **32**, 313–318 (1990)
O.L. Krivanek, T.C. Lovejoy, N. Dellby, T. Aoki, R.W. Carpenter, P. Rez, E. Soignard, J. Zhu, P.E. Batson, M.J. Lagos, E. R. F. and P. A. Crozier. Nature **514**, 209–212 (2014)
S. Lazar, G.A. Botton, M.-Y. Wu, F.D. Tichelaar, H.W. Zandbergen, Ultramicroscopy **96**, 535–546 (2003)
R.D. Leapman, P. Rez, D.F. Meyers, J. Chem. Phys. **72**, 11–29 (1980)
P. Li, J. Liu, N. Nag, P.A. Crozier, J. Chem. Phys. B **109**, 13883–13890 (2005)
P. Li, J. Liu, N. Nag, P.A. Crozier, Surf. Sci. **600**, 693–702 (2006a)
P. Li, J. Liu, N. Nag, P.A. Crozier, Appl. Catal. A **307**, 212–221 (2006b)
P. Li, J. Liu, N. Nag, P.A. Crozier, J. Catal. **262**, 73–82 (2009)
C. Lopez-Cartes, S. Bernal, J.J. Calvino, M.A. Cauqui, G. Blanco, J.A. Perez-Omil, J.M. Pintado, S. Helveg, P.L. Hansen, Chem. Commun. **7**, 644–645 (2003). doi:10.1039/b211786j
C.E. Lyman, J.I. Goldstein, D.B. Williams, D.W. Ackland, S. von Harrach, N. A.W. and P. J. Statham. J. Microsc. **176**, 85–98 (1994)
T. Manoubi, C. Colliex, P. Rez, J. Electron. Spectrosc. Relat. Phenom. **50**, 1–18 (1990)
B.K. Miller, P.A. Crozier, Microsc. Microanal. **20**, 815–824 (2014)
B.K. Miller, T. Barker, P.A. Crozier, *Ultramicroscopy*, **156**, 18–22 (2015)
C. Mitterbauer, G. Kothleitner, W. Grogger, H. Zandbergen, B. Freitag, P. Tiemeijer, F. Hofer, Ultramicroscopy **96**, 469–480 (2003)
M. Mogensen, D. Lybye, N. Bonanos, P.V. Hendriksen, F.W. Poulsen, Solid State Ion. **174**, 279–286 (2004)

D. Mogensen, J.D. Grunwaldt, P.V. Hendriksen, K. Dam-Johansen, J.U. Nielsen, J. Power Sources **196**, 25–38 (2011)
T. Montini, N. Hickey, P. Fornasiero, M. Graziani, M.A. Banares, M.V. Martinez-Huerta, I. Alessandri, L.E. Depero, Chem. Mater. **17**, 1157–1166 (2005)
W.R. Moser (ed.), *Advanced Catalysts and Nanostructured Materials -Modern Synthetic Methods* (Academic, New York, 1996)
D.A. Muller, L.F. Kourkoutis, M. Murfitt, J.H. Song, H.Y. Hwang, J. Silcox, N. Dellby, O.L. Krivanek, Science **319**, 1073–1076 (2008)
R.D. Narayan, J.K. Weiss, P. Rez, Microsc. Microanal. **20**, 798–806 (2014)
J. O'Hanlon, *A user's guide to vacuum technology, Wiley-Interscience, Hoboken NJ, 3rd*, edth edn., 2003
S. Omar, E.D. Wachsman, J.L. Jones, J.C. Nino, J. Am. Ceram. Soc. **92**, 2674–2681 (2009)
S. Otsuka-Yao-Matsuo, T. Omata, N. Izu, H. Kishimoto, J. Solid State Chem. **138**, 47–54 (1998)
J.H. Paterson, O.L. Krivanek, Ultramicroscopy **32**, 319–325 (1990)
D.H. Pearson, C.C. Ahn, B. Fultz, Phys. Rev. B **47**, 8471 (1993)
S.J. Pennycook, P.D. Nellist (eds.), *Scanning Transmission Electron Microscopy* (Springer, New York, 2011)
M. Picher, S. Mazzucco, S. Blankenship, R. Sharma, Ultramicroscopy **150**, 10–15 (2015)
F. Pinna, Catal. Today **41**, 129–137 (1998)
H. Raether, Surface Sci. **8**, 233–246 (1967)
J.J. Rehr, J.J. Kas, F.D. Vila, M.P. Prange, K. Jorissen, Phys. Chem. Chem. Phys. **12**, 5503–5513 (2010)
L. Reimer, *Transmission electron microscopy* (Springer, Berlin, 1989)
P. Rez, Microsc. Microanal. **20**, 671–677 (2014)
F.M. Ross, Rep. Prog. Phys. **73**, 21 (2010)
R. Sharma, P.A. Crozier, Inst. Phys. Conf. Ser. **61**, 569–572 (1999)
R. Sharma, P.A. Crozier, Z.C. Kang, L. Eyring, Philos. Mag. **84**, 2731–2747 (2004)
V. Sharma, P.A. Crozier, R. Sharma, J.B. Adams, Catal. Today **180**, 2–8 (2012)
J.R.A. Sietsma, H. Friedrich, A. Broersma, M. Versluijs-Helder, A.J. van Dillen, P.E. de Jongh, K.P. de Jong, J. Catal. **260**, 227–235 (2008a)
J.R.A. Sietsma, J.D. Meeldijk, M. Versluijs-Helder, A. Broersma, A.J. van Dillen, P.E. de Jongh, K.P. de Jong, Chem. Mater. **20**, 2921–2931 (2008b)
S.B. Simonsen, S. Dahl, E. Johnson, S. Helveg, J. Catal. **255**, 1–5 (2008)
E. Stavitski, F.M.F. de Groot, Micron **41**, 678–694 (2010)
T.L. Nylese, Microsc. Microanal. **20**, 1330–1331 (2014)
S.J. Tauster, Acc. Chem. Res. **20**, 389–394 (1987)
S.J. Tauster, S.C. Fung, R.L. Garten, J. Am. Chem. Soc. **100**, 170–175 (1978)
S.J. Tauster, S.C. Fung, R.T.K. Baker, J.A. Horsley, Science **211**, 1121–1125 (1981)
A. Trovarelli, *Catalysis by ceria and related materials* (Imperial College Press, London, 2002)
H.L. Tuller, Solid State Ion. **131**, 143–157 (2000)
S.B. Vendelbo, P.J. Kooyman, J.F. Creemer, B. Morana, L. Mele, P. Dona, B.J. Nelissen, S. Helveg, Ultramicroscopy **133**, 72–79 (2013)
S.B. Vendelbo, C.F. Elkjær, H. Falsig, I. Puspitasari, P. Dona, L. Mele, B. Morana, B.J. Nelissen, R. van Rijn, J.F. Creemer, P.J. Kooyman, S. Helveg, Nat. Mater. **13**, 884–890 (2014)
H.S. von Harrach, P. Dona, B. Freitag, H. Soltau, A. Niculae, M. Rohde, Microsc. Microanal. **15**, 208–209 (2009)
R. Wang, P.A. Crozier, R. Sharma, J.B. Adams, Nanoletters **8**, 962–967 (2008)
R. Wang, P.A. Crozier, R. Sharma, J. Phys. Chem. C **113**, 5700–5704 (2009)
M. Watanabe, D.W. Ackland, A. Burrows, C.J. Kiely, D.B. Williams, O.L. Krivanek, N. Dellby, M.F. Murfitt, Z. Szilagyi, Microsc. Microanal. **12**, 515–526 (2006)
M. Watanabe, in *Scanning Transmission Electron Microscopy*, eds. S. J. Pennycook and P. D. Nellist, Springer, New York, 2011, pp. 291–351.

D.B. Williams, C.B. Carter, *Transmission electron microscopy - A textbook for materials science*, 2nd edn. (Plenum Press, New York, 2009)
H.L.L. Xin, E.A. Pach, R.E. Diaz, E.A. Stach, M. Salmeron, H.M. Zheng, ACS Nano **6**, 4241–4247 (2012)
M.P. Yeste, J.C. Hernandez, S. Bernal, G. Blanco, J.J. Calvino, J.A. Perez-Omil, J.M. Pintado, Catal. Today **141**, 409–414 (2009)
H. Yoshida, Y. Kuwauchi, J.R. Jinschek, K.J. Sun, S. Tanaka, M. Kohyama, S. Shimada, M. Haruta, S. Takeda, Science **335**, 317–319 (2012)
K. Yoshida, X.D. Zhang, A.N. Bright, K. Saitoh, N. Tanaka, Nanotechnology **24**, 7 (2013)
L.X. Zhang, B.K. Miller, P.A. Crozier, Nano Lett. **13**, 679–684 (2013)

Chapter 5
Image Detectors for Environmental Transmission Electron Microscopy (ETEM)

Ming Pan and Cory Czarnik

Abstract Camera (Imaging) systems are rapidly becoming the limiting factor for information (quality and quantity of data) captured during in situ TEM experiments. The latest TEM electron optic designs, coupled with sample holder in situ capabilities, are pushing the performance-limiting factors further "downstream" to the point, where imaging detectors (and data management systems) are now the bottleneck for advancing the understanding of critical in situ experiments.

The performance of TEM imaging cameras has traditionally been limited by both the scintillator that converts high-energy electrons to photons and the optical path for the photons to reach the imaging sensor. By eliminating the scintillator and the optical path, direct detection cameras have significantly improved the performance in output speed, image resolution, and sensitivity. The adoption of direct detection cameras for the in situ community will be major driver in the coming years to extend spatial and temporal resolution across a very wide variety of experiments.

In this chapter, we will discuss details of camera parameters that are important to in situ TEM, limitations of traditional imaging cameras, and state-of-the-art direct detection cameras with specific examples.

5.1 Introduction

In situ TEM studies the time-dependent behaviors of specimen properties inside an electron microscope under the influence of some external stimulus, possibly including heating, cooling, mechanical strains, external fields, gases, and/or liquids. Environmental TEM (ETEM) is a subset of in situ microscopy that requires more complicated gas or liquid handling capabilities (Boyes and Gai 1997; Gai 1998; Hansen et al. 2001, 2002; Oleshko 2002; Crozier et al. 2008). Image detectors or cameras are a critical part of an integrated in situ microscopy system. Detectors have become even more relevant given the significant progress that has been made in the ETEM design or specialized TEM specimen chamber/holders for ETEM

M. Pan (✉) • C. Czarnik
Gatan, Inc., 5794 W. Las Positas Blvd., Pleasanton, CA 94588, USA
e-mail: mpan@gatan.com

T.W. Hansen, J.B. Wagner (eds.), *Controlled Atmosphere Transmission Electron Microscopy*, DOI 10.1007/978-3-319-22988-1_5

applications in the last decade that have made image detectors the main performance limiting factor. The expectation for imaging detectors is to allow users to extract critical information from experimental image data that is generated by an ETEM or in situ TEM with increasingly higher demands on both resolution and sensitivity.

For more than three decades, imaging cameras for in situ TEM have slowly but steadily evolved from the early analog video cameras to current high speed digital cameras with better resolution and sensitivity (Alani and Pan 2001; Pan 2010). The evolution has gone through several phases of changes: analog video (TV rate of 25–30 fps) to digital cameras (1 k × 1 k); small to large format (~4 k × 4 k); slow (fractional fps) to fast (>1500 fps); general purpose imaging to optimized performance for in situ TEM (speed, sensitivity, and resolution); recording movie files using Video Cassette Recorder (VCR) to directly saving image sequentially to solid-state memory at high speed in raw data format along with the meta data (e.g., TEM and in situ parameters).

Digital cameras have historically used one of two types of imaging sensors—CCD (Charge-Coupled Device) and CMOS (Complementary Metal Oxide Semiconductor). CCD-based cameras were first adapted for electron microscopy application in mid-80s (Mochel and Mochel 1986; Spence and Zuo 1988) and have since been the more popular sensor technology for imaging until the most recent generation of CMOS sensors that are specifically designed for TEM applications. In the last decade, significant digital technology advancement has been made in data handling and processing such as FPGA (Field Programmable Gate Array) performance, vastly increased memory densities and speed (e.g., SSD—solid-state drives) using flash memory, CMOS wafer processing, and high speed data architecture systems (e.g., fiber optic design). Leveraging these various technologies has led to the development of a new generation of CMOS-based digital cameras that can process images and store data orders of magnitude faster than just a few years ago. Performance demanding applications such as in situ TEM will benefit greatly from this renaissance in new camera technology.

Imaging cameras suitable for in situ TEM applications need to have high speed (high temporal resolution). However, speed improvement must be made in the context of capturing adequate amount of signal (primary electrons) per image frame. As cameras run faster, the total number of electrons captured per image becomes less, thus making it more difficult to produce images with adequate signal-to-noise ratio (SNR).

Any discussion of a high performance imaging system for in situ microscopy should also include the imaging camera and software. The digital imaging system must be optimized for high-resolution quality data (spatial and temporal) while software must address fidelity and efficiency of handling large volume of data produced by a high speed camera system. Readers will quickly realize the challenges of working with large volumes of image data of in situ microscopy. This book chapter attempts to give readers an overview on digital cameras, specific requirements for an in situ camera system, the role of software and the authors' view on future integrated in situ systems.

5.2 In Situ Camera System

To help readers better understand in situ camera systems, and how to obtain/interpret quality in situ data, we first describe the basics of a digital camera system.

5.2.1 Type of Image Sensors

Two main types of image sensors (CCD and CMOS) are being used in today's digital cameras. CMOS technology (Wanlass and Sah 1963) was invented earlier than the CCD (Boyle and Smith 1970). However, it is CCD technology that found early success in scientific imaging applications due to better overall performance and manufacturability. Common to both CCD and CMOS sensors is the photodiode, a P-N junction diode in each sensor pixel that converts photons of the incoming light incident on the junction into proportional amount of charge (sensor electrons).

The difference is that the charge produced in a CCD pixel is transferred to a special buffer before being converted to voltage, amplified, digitized, and readout. In CMOS sensors, charge in a pixel is processed in the same pixel and converted to an output voltage. Figure 5.1 contrasts the architecture of CCD and CMOS sensors. CMOS sensors offer more integration on the chip, can consume much less power to operate, and have greater potential to scale to the highest frame rates. Since the turn of the twenty-first century, the advancements in the manufacturing of semiconductor chip devices increasingly make CMOS the emerging, and promising sensor for the next generation high performance image cameras.

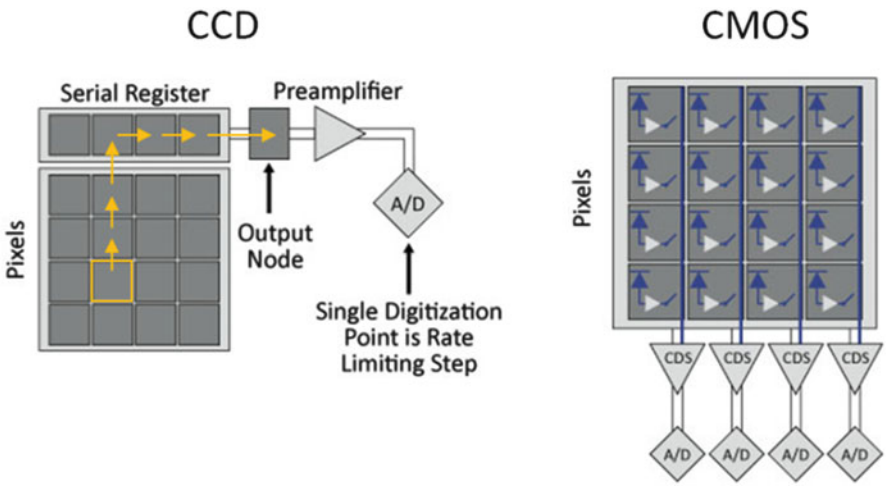

Fig. 5.1 CCDs move charge from pixel to pixel and convert it to voltage at an output node. CMOS imagers convert charge to voltage inside each pixel (Courtesy of QImaging®)

Due to their early success, CCD cameras have long been the choice of image detectors for electron microscopy including in situ. There are three main types of CCD sensors considered for TEM imaging—full frame, interline, and frame transfer (Janesick and SPIE, for Optical Engineering IS 2001). Full frame CCD sensors require that no incoming light is present during sensor readout. This means that the electron beam must be switched off during image readout. This is realized by using the electron beam shutter or blanker of an electron microscope. Interline and frame transfer CCDs do not require any beam blanking during image readout as charge can be accumulated and readout simultaneously. In these cases, the charge accumulated in each pixel is transferred to a storage area that is not photo sensitive; this allows each pixel's charge to be read out while the next frame is accumulated. As a result, these types of CCD cameras eliminate the speed of the shutter for blanking and unblanking as a limiting factor for useful frame rates versus full frame CCDs (effectively 100 % duty cycle for accumulating charge in interline CCDs vs. full frame CCDs). The trade-off with CCDs is that typically larger pixel size in full frame CCD sensors leads to higher image quality as more signal (primary electrons) can be captured per pixel, and there can be 100 % photo-sensitive area (100 % fill factor as opposed to 100 % duty cycle.) Since the importance of high frame rate and high temporal resolution is paramount for in situ microscopy and ETEM, interline CCD cameras were the preferred choice for many years as digital cameras gained popularity over film.

The name of CMOS refers to the manufacturing technique of the sensor rather than how the image is formed. For example, a CMOS sensor may use a traditional scintillator and fiber- or lens-coupling to transfer the light to the sensor. Other CMOS sensors can be designed to directly detect incoming electrons without converting the electrons to light, but need to be optimized for radiation hardness. CMOS image sensors do not generally require beam blanking during image readout. Images are captured by the on-chip shutter (rolling shutter), similar to how most cell phone and digital cameras operate today. More details on how rolling shutter works can be found in the next section.

5.2.2 Shutters/Beam Blankers

Shuttering is an integral part of an imaging sensor, and there are multiple ways to accomplish this, either in the TEM column and/or on the sensor itself. Shuttering requirement for a given sensor depends on how the sensor is read out.

Shuttering is a general term that refers to the ability to isolate the sensor from receiving new signals (electrons) from the TEM while the sensor is being readout. This functionality can be required for various purpose such as avoid blurring of the image during image transfer (e.g., full frame CCD readout of each frame), camera calibrations (dark images), avoid possible sensor damage due to overexposure or extended exposure to the electron beam, or other automated sensor operations.

5.2.2.1 TEM Shutter

The TEM column is capable of deflecting the beam at multiple points. Particularly for beam-sensitive samples, it is important to discern between "pre-specimen" and "post-specimen" shutters.

While using the TEM column to control exposures of the sensor to the electron beam, if the user is relying on the TEM to control exposure times, the speed (deflection both in and out) needs to be considered. These values can vary considerably between TEM models and can be quite important if the desired frame exposure time approaches the blanking/un-blanking time of any given TEM model. For example, if a 30 ms exposure time is desired, and the shutter blanking/un-blanking time is ~50 ms, there will be significant blurring of the image due to the relatively long time spent during blanking relative to the exposure time of the sensor.

Post-specimen Shutters

This is a standard setup on a TEM and works well for beam-stable samples. However, one should pay attention to the shutter speed as mentioned above. If the shutter speed is too low, the only option is to use an imaging camera that does not require beam blanking, for example, interline CCDs or CMOS-based cameras.

Pre-specimen Shutters

This option is typically used with beam-sensitive materials (e.g., porous or organic materials or other soft polymers), where sample structures disintegrate rapidly under electron beam irradiation. In these cases, the main priority is to minimize specimen exposure to electron beam by setting up TEM shutter and imaging sensor in advance. The electron beam is blanked at the default setting and un-blanked only for the duration of image acquisition to achieve the minimum beam damage.

5.2.2.2 Rolling Shutter

This refers to the method of readout of CMOS sensors where during continuous exposure, each row of the sensor is read out in sequence. Once the readout reaches the bottom of the sensor, it will immediately jump back to the top of the sensor and start reading out the new frame. Rolling shutter provides the fastest method of sensor readout as the camera can be continuously in readout mode with effectively 100 % duty cycle. Figure 5.2 illustrates the operation of the rolling shutter.

Rolling shutter mode maximizes the camera frame rate and charge collection efficiency, thus maximizing the camera's temporal response and image quality.

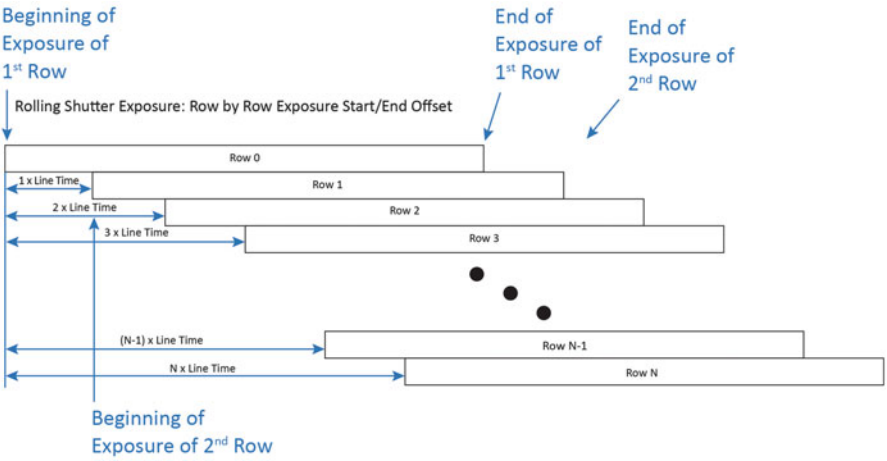

Fig. 5.2 Diagram demonstrating the time delay between each row of pixels in a rolling shutter readout mode with a CMOS camera (Courtesy of QImaging®)

Frame rate is determined by the readout time for each row (or the speed of analog-to-digital converter) and the number of rows on the sensor.

It should be pointed out that while rolling shutter mode maximizes the camera frame rate it also affects the image readout. In a single image frame, the sequential readout means that each row is read out at a slightly different moment in time. This may cause concerns with respect to potential image distortion when using the rolling shutter mode to capture in situ TEM images, where motion vs. change is of primary interest. The percentage of image distortion due to rolling shutter can be estimated as below:

$$\delta(\%) \sim \tau \cdot \mathrm{v} \tag{5.1}$$

Where δ is the relative image distortion in %, τ the row readout time, and v the sample moving velocity with unit of pixels/s.

For modern CMOS sensors operating at a frame rate of 25 fps or above, typical row readout time (τ) is ~10 μs while the frame time is about 40 ms. Note that the relative distortion (δ) is independent of the sample feature size and the CMOS sensor size. To give a practical example, for a CMOS camera operating at 25 fps @ 4 k × 4 k resolution, for 1 % of image distortion caused by the rolling shutter, the object would have to move ~1000 pixels/s. Assuming the calibrated pixel size is 0.05 nm, the motion velocity would be 50 nm/s.

Thus, image distortion caused by the use of rolling shutter is indeed extremely small due to the very fast readout of each row (~10 μs). Therefore, this distortion can be safely ignored for most of in situ experiments. Under extreme situations where samples move faster than 1000 pixels/s to limit the distortion within 1 % higher frame rate cameras are required. However, these are rare use cases.

In most cases, the advantages of using a rolling shutter outweigh any limitations assuming that the rolling shutter is fast relative to motion of interest. Rolling shutters that operate at ~1 fps will have much higher distortions than cameras with many pixels that run at video frame rates or beyond. The advent of the rolling shutter and improving the frame rates of cameras will offer significantly improved temporal resolution vs. cameras from just a few years ago.

5.2.2.3 Global Shutter

Global shutters work as the traditional shutter or beam blanker in the sense that it can switch on and off the signal reaching the image sensor to ensure an image is captured by the sensor pixels at the same moment in time, but with much lower temporal resolution. This is in contrast to the rolling shutter that reads out each row of a sensor at different moment in time—sequentially. A global shutter CMOS sensor can direct each pixel to simultaneously convert charge to voltage, effectively "freezing" an image for a fixed duration in time. This is typically done through the addition of additional transistors at the expense of frame rate, sensitivity (less photo-sensitive area on the chip), and production complexity and cost. The trade-off between global and rolling shutters generally favors rolling shutters in all but the most extreme cases, and the promise of faster rolling shutter frame rates suggests that it will be able to provide a better long-term experience and trade-off than global shuttering for most use cases.

5.2.3 Duty Cycle

Duty cycle (D) is defined (5.2) as the fraction of time that image detector collects signal in an operation cycle relative to the total time (exposure time and idle time when the sensor is busy reading out signal). For in situ microscopy, the goal for duty cycle is ~100 %. This means the image detector is able to collect data across the entire temporal space of the experiment, as opposed to having to pause while it reads out a given image. This guarantees that no given event will be lost in time due to the camera being in a "busy" state.

$$D = \frac{T_{\text{exp}}}{T_{\text{total}}} \times 100\% = \frac{T_{\text{exp}}}{\left(T_{\text{exp}} + T_{\text{idle}}\right)} \times 100\% \tag{5.2}$$

Some CCD sensors (interline or frame transfer devices) allow signal recording and data reading out at the same time. Hence, there is no idle time for the camera. The duty cycle for these cameras is approximately 100 %. Cameras with duty cycle of 100 % do not require any external beam shutter to blank the electron beam while image data is read out. Examples include interline CCDs or rolling shutter for most CMOS cameras.

5.2.4 *Detective Quantum Efficiency*

Detective quantum efficiency (DQE) is an objective measure of sensitivity and resolution of an imaging device (Mooney et al. 2004; Mooney 2007; Li et al. 2013a). It is defined as the ratio of signal-to-noise (SNR) squared of the output over that of the input of an imaging device (5.3).

$$\mathrm{DQE}(s) = \frac{\mathrm{SNR}^2_{\mathrm{out}}(s)}{\mathrm{SNR}^2_{\mathrm{in}}(s)} \tag{5.3}$$

If noise in an image is dominated by the noise in the electron beam (most practical cases in electron microscopy), one can rewrite DQE as follows:

$$\mathrm{DQE}(s) = \frac{\mathrm{SNR}^2_{\mathrm{out}}(s)}{N} \tag{5.4}$$

or

$$\mathrm{SNR}_{\mathrm{out}}(s) = \sqrt{\mathrm{DQE}(s) \times N} \tag{5.5}$$

where N is the average dose in number of electrons and s spatial frequency in nm^{-1}.

DQE measures the ability of an imaging device to generate image contrast above noise. For a given noise level, if a camera can produce enough signal (image contrast) to allow a specimen feature to be detected above the noise, this camera is said to be "sensitive." With this qualitative interpretation, it is intuitive to understand that it becomes more difficult for a camera to generate signals for higher resolution details above noise levels. This means that DQE value will decrease with spatial resolution.

A high performance image camera should have high DQE values, i.e., a high efficiency in making use of limited number of electrons to produce image details. For a given electron dose rate, i.e., the number of electrons arriving at each pixel in an image sensor per unit time, as the speed of the camera increases the number of electrons captured per image pixel in an image will decrease. So it is highly desirable to design a camera that has the ability to produce higher quality images with fewer numbers of electrons, i.e., high DQE values. This is the same requirement as that for cryo electron microscopy (cryoEM), where electron dose rate is typically limited below ~10 e^-/pixel/s (Li et al. 2013b).

Figure 5.3 shows DQE measurement at 300 kV (1) fiber-optical coupled CCD camera (Gatan Ultrascan US4000 camera with an ultra-sensitive scintillator; (2) direct detection camera (Gatan K2) operated in intensity integration or in situ (IS) mode, and (3) in electron counting and super-resolution mode. It is clear that intensity integration improves DQE by a factor of >3× (@ ½ Nyquist) over the fiber-optical coupled cameras while electron counting and super-resolution result in

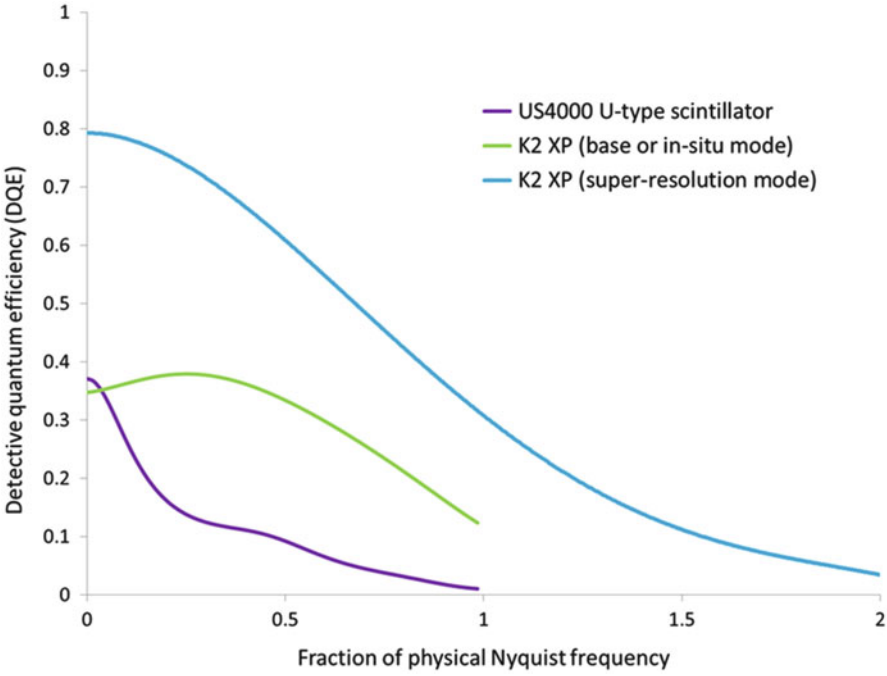

Fig. 5.3 DQE measurement at 300 kV for K2 direct detection camera with the new XP sensor and scintillator-based CCD camera. *Purple*: fiber-optical coupled CCD camera (US4000 with a U-type of scintillator); *Green*: K2 IS (intensity integration) mode; *Blue*: counting and super-resolution mode. Electron counting and super-resolution yield the highest DQE at all spatial frequencies

the largest DQE improvement. This means that direct electron counting cameras have the ability of capturing high-quality images at low electron doses (i.e., highest sensitivity).

It should be pointed out that in order to achieve reliable counting results electron scattering events during detection need to be well separated in both temporal and spatial domains to avoid counting errors (e.g., missing counts). This requires that the camera readout speed be fast enough to separate the incoming electrons under a given electron dose rate so that the probability of two electrons landing on the same pixel during exposure is negligible. With the K2 direct detection camera, experimental data demonstrates that reliable counting results can be achieved with an image readout speed of 400 fps @ 4 k × 4 k resolution for electron dose rate below 10 e^-/pixel/s (Li et al. 2013b). Furthermore, super-resolution requires that electron entry point on the image detector be predicted with accuracy better than ½ pixel (Booth 2012). The benefit of operating cameras in super-resolution mode is the fourfold increase in field of view (FOV) as the microscope magnification is decreased by 2×.

The improvement of DQE requires reducing or eliminating noise levels from all sources. The noise associated with electron beam follows Poisson statistics. As

electron dose decreases, beam noise deceases at a rate proportional to the square root of the electron dose. At some point, readout noise from image camera can become the dominant noise, thus limiting DQE. Electron counting has drastically reduced the electron scattering noise (variations in energy deposited in the CMOS detecting sensor) and removed the camera readout noise, resulting in significant improvement in DQE at all frequencies as shown in Fig. 5.3.

K2 direct detection camera offers two main distinct operation modes. In K2 IS mode, users can run high frame rate (e.g., >1500 fps) while operating the camera in intensity integration mode. In electron counting mode, users can capture and save images continuously to memory at a rate of ~40 fps @ 4 k × 4 k resolution. For certain types of in situ experiments that do not require the highest frame rate, one should consider operating the direct detection camera in counting mode to take full advantage of the superior DQE performance at low electron dose rate. Samples sensitive to electron beam irradiation should benefit greatly from this mode of operation.

5.2.5 Software

So far, we have limited our discussion mostly on image camera hardware such as beam shutter, speed, sensitivity, and DQE. Software (both in terms of control and also user interface) is another critical component for defining a high performance, in situ camera system. While it handles the normal tasks of image normalization per frame, at ever-increasing frame rates, the same software is expected to manage the large volume of image data acquired from the camera system and store the data to disk in real time without compromising quality. Additional tasks that need to be handled in real time include specimen event triggering for image recording, effective mining of the recorded image data, data extraction based on region of interest (ROI) in both spatial and temporal domains, and post-collection processing of the data stream via binning, averaging of frames, drift correction, sub-area discrimination in terms of time or space, as well as third party support for additional evaluation of a stream of images.

We discuss these aspects in more details below.

5.2.5.1 Synchronize Images with In Situ Meta Data

Meta data refers to any non-camera-specific parameters that are associated with an image, for example, the operating parameters of an in situ device such as temperature, stress, gas pressure, and biasing voltage. The meta data can also include the TEM parameters such as magnification, voltage, sample position, and stage tilt angles. As external stimulus from an in situ device is applied to a sample and corresponding in situ image series are recorded by the camera system, it is essential

to maintain a high degree of correlation of each acquired image with the meta data at the moment when the image was being recorded.

Software for a high performance in situ camera system should have the ability to communicate with the in situ device and the host TEM, capture, and store images synchronously with the meta data stream.

5.2.5.2 Strategy for Data Acquisition and Storage

As temporal resolution improves, the number of images captured by an in situ camera system will increase accordingly. In addition, as cameras increase the number of pixels and the bit depth of each pixel, the image data size will also increase over time. For in situ TEM analysis, it is highly desirable to have each image frame stored in real time directly to computer memory without loss of image quality. Even though the cost of memory decreases every year, it is still inconceivable to store all the image data an in situ camera produces and back up 100 % of the accumulated data.

Figure 5.4 shows the evolution of camera data rate since early 1990s. With the rapid advancement of digital technologies, the data rate has increased several orders of magnitudes over the last 25 years. This has significantly raised the bar for software that must handle the data volume it captures from an in situ camera system.

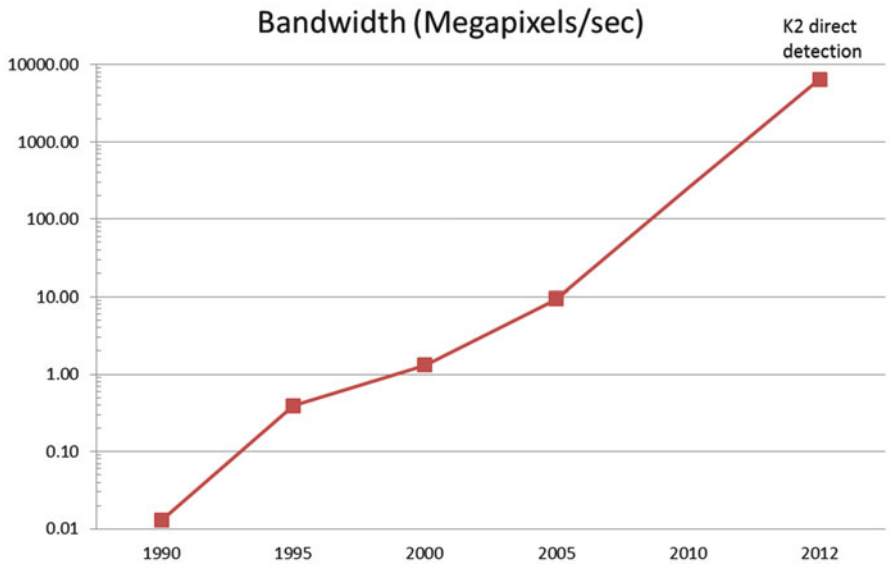

Fig. 5.4 Evolution of camera data rate since the first generation of commercial digital cameras in 1990. Current state-of-the-art K2 direct detection camera tops the chart at 6.4 Gigapixels/s

The current generation cameras are capable of directly outputting and storing images at ~400 Megapixels/s. The state-of-the-art system (K2 direct detection camera) can further push this data bandwidth to 6.4 Gigapixels/s! With these data rates, it is possible to generate petabyte (1 petabyte = 1024 terabyte) data volume annually. Such volume of data exceeds the capacity of current available data storage system for most EM user facilities. Therefore, it is not practical to attempt to back up all the images produced by a state-of-the-art in situ camera system.

A practical solution to handle this large amount of image data is to capture and store only the relevant images and discard the rest. Using event triggering (data recording is controlled by specific in situ event) can significantly reduce the waste of data storage space. By monitoring change in observed images as in situ reaction unfolds, it is possible to use the change (event) as a trigger to start the recording of an in situ reaction in its entirety, i.e., without ever missing the most important onset of any in situ reaction. Additionally, only keeping the regions of interest (ROI) in both time and space for a given data set will reduce the overall data size. This is a big challenge for current image acquisition software.

5.2.5.3 Data Mining and Analysis

Obviously manipulating the large amount of data volume of an in situ experiment is a challenging and labor-intensive task. Software that handles in situ data must allow users to easily browse the recorded data volume on a frame by frame basis, extract data subsets of interest in both spatial and temporal domains, perform image analysis and processing (e.g., image drift alignment, frame averaging, and noise reduction), and output the final data volume in standard multimedia format (avi, mpeg, wms, etc.). While the ability to quickly extract useful 3D image data also makes use of data storage space more efficiently as mentioned early, the additional ability to develop application-specific filters for particular data sets will accelerate the analysis of these large data sets through additional automation and scripting.

5.3 Scintillator-Based Cameras

5.3.1 Camera Construction

Since their debut in late 1980s (Mooney et al. 1990; Kujawa and Krahl 1992; Krivanek and Mooney 1993; Fan and Ellisman 1993), scintillator-based cameras remain the mainstream image cameras for electron microscopy applications. CCD sensors were exclusively used in this type of camera design until early 2000s when significant advancement was made in CMOS technology. Figure 5.5 is a schematic representation of the scintillator-based camera design. Electrons in the TEM column (primary electrons) impinge on the scintillator that comprises phosphor and

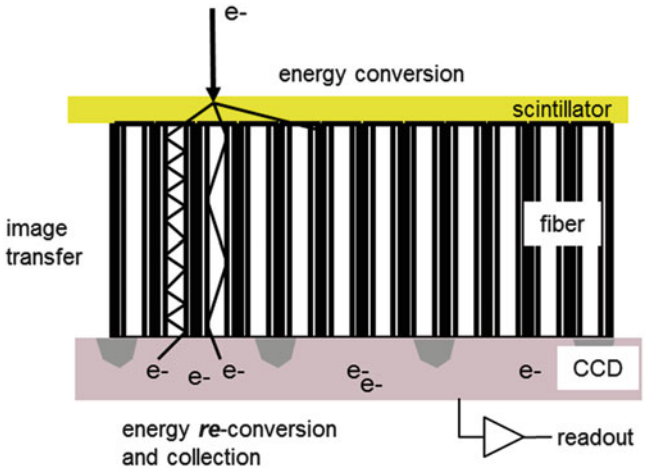

Fig. 5.5 Schematic diagram showing the detection process of primary electrons by a scintillator-fiber coupled camera. The scintillator (*yellow*) converts electrons into visible light that is guided by an optical fiber bundle to the imaging CCD sensor. The light excites electrons in the sensor before detection

other minor elements. Visible light is emitted from the scintillator from the electron—phosphor interaction. Optical coupling in the form of either optical fibers or lens then guides the light onto the image sensor, where the signal is converted to sensor electrons and then read out as an image.

Historically, there are two main reasons for adopting the scintillator design for TEM imaging, (1) sensor radiation hardness and (2) slow readout speed. First, most semiconductor devices are susceptible to radiation damage by high-energy charged particles. While direct detection sensors have been tested for many years, the limited lifetime was the major limiting factor to incorporating them into mainstream adoption. As a result, scintillators have been widely adopted to convert electrons to photons before detection. Secondly, the conversion rate of a high-energy electron (e.g., 100 keV) to sensor electrons was so high that the CCD pixel storage (storing sensor electrons) would be saturated with a few hundred primary electrons (Krivanek and Mooney 1993). This means that the image would have very poor SNR. With a slow readout speed of a few seconds to read out a 1 k × 1 k CCD sensor, it was not practical to build a direct detection camera because it would take too long to collect enough primary electrons to have an image with good SNR. Scintillators offer the ability to optimize the sensitivity (i.e., the amount of light generated per incoming electron), that makes the CCD sensor readout time better aligned with the exposure time.

Scintillator-based cameras can offer high dynamic range that is essential for imaging applications such as electron diffraction, electron energy-loss spectroscopy (EELS), and high contrast objects. In addition, it is possible to run the cameras in multi-mode operations: these can include fast readout modes via binning of pixels,

readout of a smaller area for faster response, or "high-quality" mode for final image capture after all setup is complete.

Using optical fibers to couple the light output from the scintillator to the imaging sensor results in better light collection than using optical lens configuration. The low light collection efficiency and effect of image vignette have seriously limited the use of lens-coupled cameras for performance demanding EM applications such as in situ that require the highest signal (SNR) transfer in each image without artifacts from edge effects of light transmission or other limitations due to lens effects (Liu et al. 2000).

The performance of imaging cameras is determined by the inherent design of scintillator, optical coupling, control electronics, sensor characteristics, and the deposited electron energy during the electron–phosphor interaction. For in situ applications, it is important to optimize the speed (i.e., frame rate) of the imaging cameras with sensitivity and resolution to ensure individual image frames contain useful information with enough SNR.

5.3.2 Examples of In Situ TEM

When considering the "speed" of cameras for in situ applications, most users want at least a movie-like response, which translates to ~30 fps. This is a critical benchmark for camera performance as users have to tune focus, stigmation, etc. in the TEM column and having immediate feedback greatly assists in this process.

For in situ TEM while it is useful to observe dynamic events with a fast camera, it is more important to have the ability to acquire/save images continuously during an experiment. The ability to synchronize the start of an experiment and the simultaneous recording of each individual "image" (frame output) to storage is a significant bottleneck given the data transmitted. Current generation sensors can output data rates up to 80 Gb/s. "Off the shelf" technology exists to store this data stream in real time, but the issues surrounding backup, long-term storage, and transferring data to remote sites are still unresolved within the EM community. Unlike synchrotron applications, there is not a single user base agreed on a single standard and requirements for use.

Figure 5.6 is an ETEM example of the growth of Si nanowires (SiNW) from Au/Pd catalyst particles under disilane (Si_2H_6) gas environment (Hofmann et al. 2008). Digital streaming video (DSV) was recorded with a 7 Megapixel fiber-optical coupled camera (ORIUS model 831) operated at ~14 fps (~70 ms temporal resolution). The DSV file was created from DigitalMicrograph software (Gatan 2005) and had 8-bit depth (256 Gy levels) after compression from 14 bit. Figure 5.6 shows the extracted image frames from the DSV file.

It is worth mentioning that the creation of the in situ video in Fig. 5.6 was very labor intensive. To demonstrate the difficulty of capturing this growth video, it is necessary to take a look at the workflow of typical ETEM experiments. After setting the TEM in the desired operating condition (e.g., magnification, illumination,

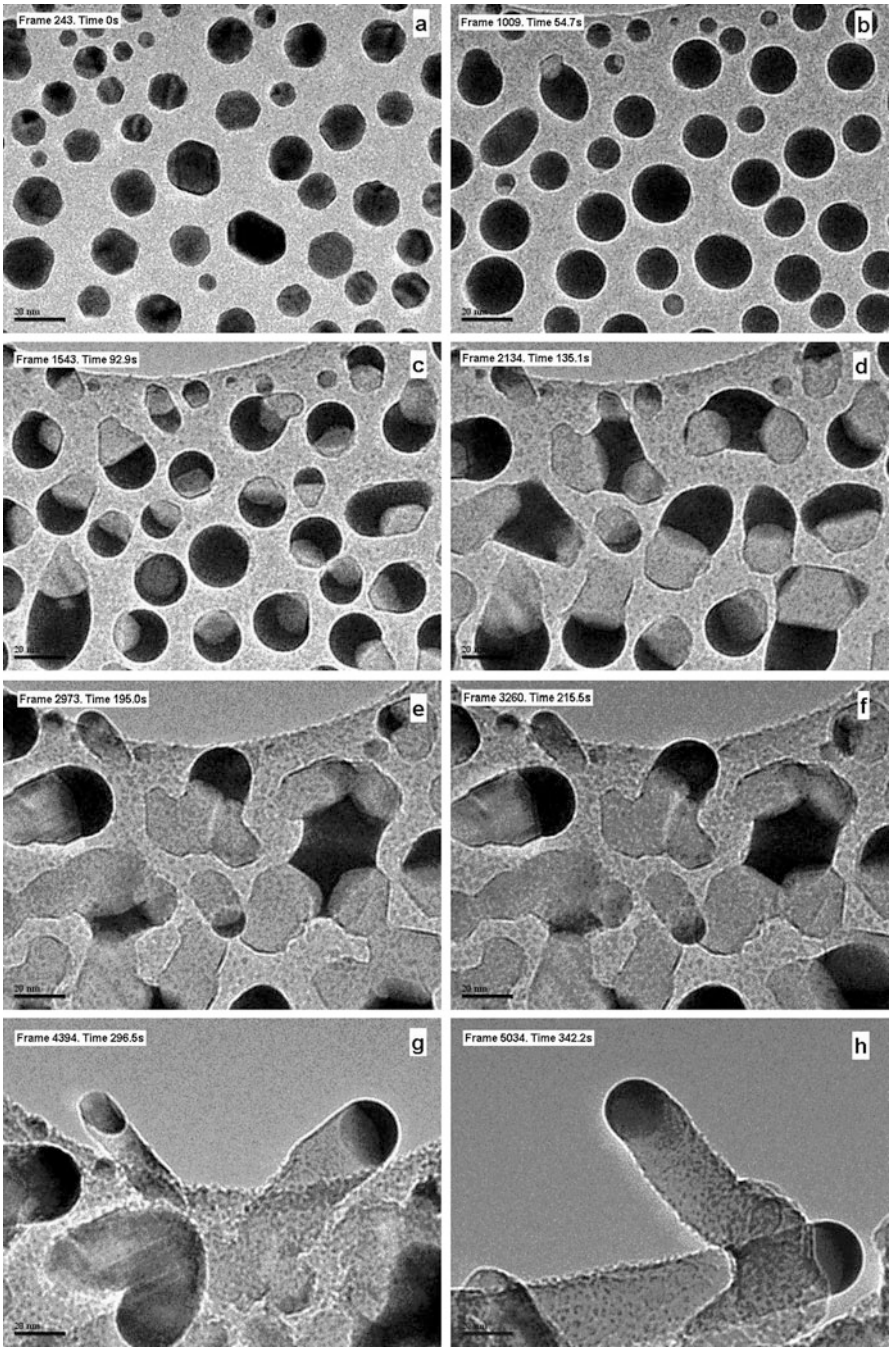

Fig. 5.6 Growth of Si nanowires from Au/Pd catalyst particles under disilane (Si_2H_6) gas environment at 200 kV. The dynamic process was recorded by ORIUS model 831 fiber-optical coupled camera. Individual image frames were extracted from the recorded DSV (14 fps). The time resolution in the DSV was ~70 ms. (**a**) Original state of the evaporated Au particles before the introduction of disilane gas; (**b**) the liquid Au-Si alloy; (**c**, **d**) Si nucleation (light contrast) and the beginning of the SiNW growth; (**e–h**) the growth of SiNW (the dark tip is Au–Si alloy). The growth conditions are: ~1.3×10^{-4} mbar Si_2H_6 at 590 °C (Images courtesy of R. Sharma at NIST, MD, USA)

apertures, focus, stigmation) and adjusting the gas mixture and pressures, one searched for suitable sample area for imaging. Once an area is found and image focus optimized, one has to patiently wait for the onset of the growth. It is a daunting task to attempt capture the entire growth process as it is nearly impossible to predict the growth onset which can occur suddenly. When growth onset occurs, one has to immediately start the video capture and check image focus and manage potential image drift, while at the same time take note of values of the external stimuli (meta data). This is clearly a frustrating experience since one must be multitasking to simultaneously manage these multiple inputs.

It is obvious that software can play a key role in managing this data acquisition process and improving the user experience by simultaneously storing images along with the meta data in real time. As mentioned in Sect. 5.2.5.2, event triggering can drastically improve the user's experience. One example would be synchronizing the change in particle size and/or shape to trigger the start or stop of recording of the "video capture" (keeping in mind that there is no video . . . . Each image is stored individually based on frame exposure, which can be sub-ms timing). Leveraging a real-time ring buffer of memory, it is possible to have "look-back" data capture, where data is continuously stored to disk (and thrown away after the buffer expires), and when the user begins a capture the stored data can be appended to the beginning of the final stored data set. In this way, the in situ user is guaranteed to "never miss the start of a reaction" again.

5.4 Direct Detection Cameras

5.4.1 Design and Construction

In 1982, Robert et al. made the first attempt of direct detecting high-energy electrons (20–100 keV) with a CCD sensor (Roberts et al. 1982). Despite the excellent linearity of the input and output signal and the high intrinsic gain, the camera suffered from radiation damage by the energetic electrons that effectively halted the development of direct detection cameras.

Since the beginning of the twenty-first century, significant progress was made in the design and production of CMOS sensors that is largely driven by the rapid increase in demand in consumer electronics market. At the same time, the development of CMOS active pixel sensor (APS) (Turchetta et al. 2001; Evans et al. 2005; Faruqi et al. 2005) for scientific imaging purpose has led to performance improvement in radiation hardness, noise, and linearity. This has re-energized the pursuit of direct electron detection and great effort was made toward using the CMOS APS in the design of next generation imaging cameras.

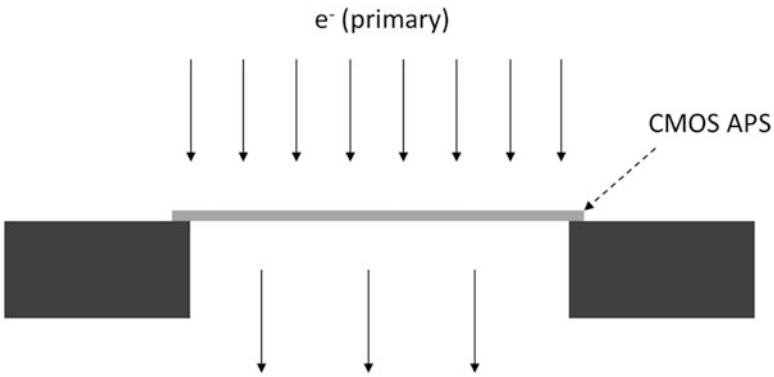

Fig. 5.7 Schematic drawing of a direct electron detection camera with a transmission CMOS APS sensor. The transmission CMOS sensor eliminates the electron backscattering common to scintillator-fiber coupled cameras. Direct detection and electron counting result in significant improvement in cameras' DQE

Figure 5.7 represents a schematic diagram showing a simplified design of direct detection camera, where electrons are detected by a back-thinned CMOS APS sensor. The design of direct detection cameras completely removes the scintillator and fiber or lens coupling. As a result, the interaction of high-energy electrons with the CMOS sensor is drastically minimized by the thin and transmission sensor. This has led to much improved DQE (Fig. 5.3) and image resolution.

For scintillator-fiber coupled cameras, electrons can be scattered in the optical fibers back to the scintillator generating additional light. This electron backscattering noise is one of the major sources for the poor DQE measured. With the introduction of a thinned direct detection sensor, this source of noise is eliminated for each image, thereby improving SNR and ultimately, improves the DQE performance.

The radiation hardness for current generation CMOS has been greatly improved by pixel design elements that make direct detection imaging practical, i.e., imaging without the need of frequent replacement of the CMOS sensor due to radiation damage. It should be pointed out that it is the design and fabrication of CMOS sensors that ultimately determine the performance of the CMOS cameras (speed, DQE, resolution, radiation hardness, etc.).

5.4.2 Recent Examples

Since CMOS sensor converts charge to voltage in each pixel while CCDs typically have a small number of A/D converters handling a large fraction of a given sensor,

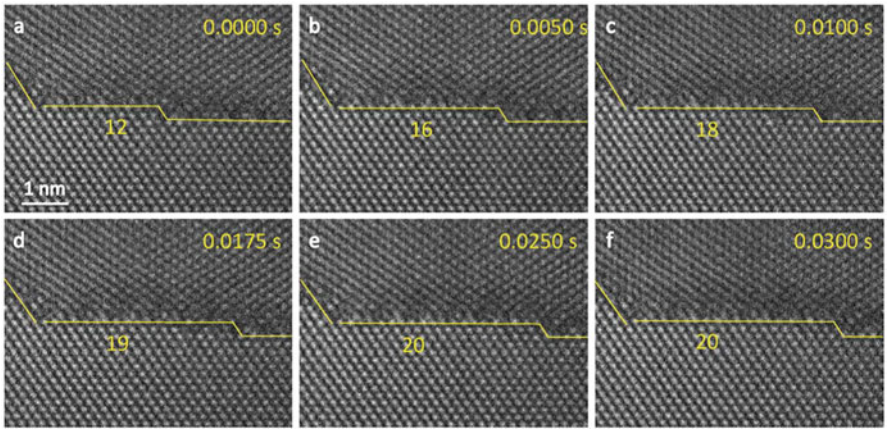

Fig. 5.8 Sequence of images showing propagation of a step (2 atomic planes high) recorded at 300 kV with K2 IS camera at 217 °C. Step position marked as the number of plane spacing from 12 to 20 (Images courtesy of T. Radetic at National Center for Electron Microscopy, LBNL, Berkeley, CA, USA and Faculty of Technology & Metallurgy at University of Belgrade, Serbia)

CMOS-based cameras can have an intrinsic speed advantage over interline or frame transfer CCD cameras when operating with a rolling shutter. CMOS sensors can operate at a typical speed of 100s–1000s fps. The best temporal resolution of state-of-the-art direct detection camera, 4 k × 4 k sensor (subsequently binned ×2) is 2.5 ms with each frame being stored to disk in real time. The temporal resolution can be further improved to sub-ms by scaling the readout to a smaller sensor area. The increased temporal resolution has led to new discoveries of materials behaviors at time scales an order of magnitude faster than possible just a few years ago.

One example of new materials behavior is shown in Fig. 5.8 that demonstrates the dynamic behavior of an atomic step (two layers high) in the 90° [110] tilt grain boundary of Au at a temperature of ~217 °C (Radetic et al. 2014). With 2.5 ms temporal resolution, the number of plane spacing in the step was observed to change between 12 and 20 as indicated in Fig. 5.8.

It is noted that the entire image sequence (5.8a–f) corresponds to a single frame at 30 fps. On a longer time scale, this step was observed to move back and forth randomly. Such detailed observation of atomic step moving at the grain boundary has never been made before. With additional investigation, these kinds of observations may improve our understanding of materials behavior at atomic level.

Figure 5.9 is a recent ETEM (liquid cell) example of Pt nanotube growth initiated by the electron beam irradiation (Liao et al. 2014). The individual images in Fig. 5.9 demonstrate the growth process of a single Pt nanotube. The top row shows experimental images after summing 5 image frames (2.5 ms each frame) to boost the SNR. The bottom row shows simulated images using a growth model that takes into account of Pt nanocrystal shape, crystal tilt, and defocus. For the first time, the atomic pathway of nanocrystal facet development was established after analyzing thousands of image frames of individual Pt clusters.

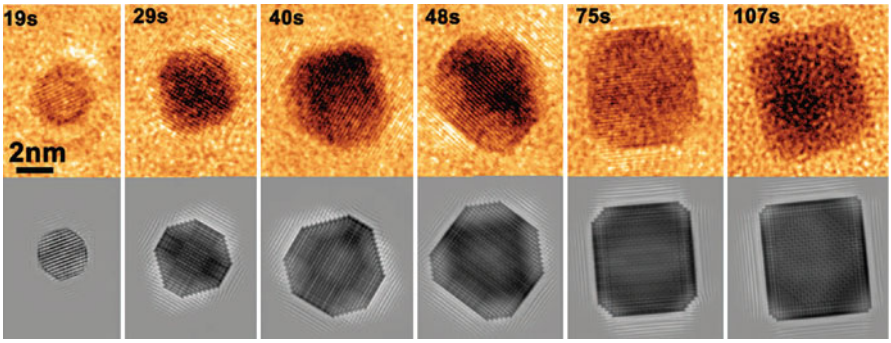

Fig. 5.9 High-resolution TEM images captured at 200 kV by K2 IS direct detection camera operated at 400 fps (time resolution = 2.5 ms). (*Top row*) Extracted images (average 5 image frames) show the growth of a Pt nanocube; (*bottom row*) simulated TEM images of the Pt nanoparticle. The simulation takes into account of Pt nanoparticle shape, particle tilt, and image defocus (Liao et al. 2014)

The main discovery by Liao et al. (2014) is that all low index facets initially have similar growth rates until the {100} facets stop growth, followed by {110} and {111} to grow into a nanotube. This finding is in contradiction to the Wulff construction theory (Hansen et al. 2002; Ringe et al. 2011) that has been extensively used to predict the equilibrium shape of crystals for almost 150 years.

In this example, there are more than 8 TB data collected (more than 30 min of recording). At 400 fps, the total number of image frames exceeds 700,000, each a 4 megapixel image! Analyzing such large number of images is both time consuming and labor intensive without new software capabilities to make it practical.

Using a region-of-interest (ROI) tool to track and extract the feature of interest (e.g., the growth of an individual particle) from the original data set has greatly reduced the storage space and made possible the detailed analysis of particle growth. Individual particle images shown in Fig. 5.9 are from the reduced data set when particle tracking is enabled during the analysis.

Another useful software feature is the quick navigation of the large in situ image data set that allows specific time points to be defined to extract the useful image data for further analysis (a sort of ROI in time for the experiment). This has further reduced the data volume, saving storage space.

Managing the large volume of image data from fast in situ cameras presents challenges to the EM community due to lack of familiarity with technologies and standards for storing, moving, and analyzing large data sets. Collaboration by the user group and camera manufacturers is required to develop the effective software tools to manipulate the large image data set and extract critical information. Current consensus is that data extraction in both spatial and temporal domains is highly effective in data volume reduction. Future development should incorporate the meta data stream into the image data set with synchronization accuracy matching the temporal resolution of the high speed cameras.

5.5 Summary and Future Outlook

The recent development of high speed and high performance cameras has created both challenges and opportunities for the in situ EM community. The generation of large volume of image data by the fast cameras will create the need to develop experience in high speed data networking/transfer and storage. Since it is not practically viable to back up all the image data acquired, users must develop a different philosophy toward saving, storing, and evaluating data sets; development effort must focus on effective management of storage space by saving only relevant images and prioritizing which data sets are analyzed. Event triggering and the use of temporary image storage facilities can be a step toward this goal, but will also require an increased focus on discipline of evaluating data sets and reducing them at an early stage in experiments. Data extraction in both spatial and temporal dimension can further make the use of memory storage more efficient but when planning new TEM installations users would be well advised to include budget for storage and transfer of data sets (both short term and long term). The ultimate goal is to obtain critical information about the in situ sample by image analysis and processing. Therefore, software must be capable of handling large data set (GBs or TBs) with high efficiency for both viewing and data mining.

To improve the fidelity of in situ image data, it is critical to maintain a high degree of synchronization between the image and the meta data from the in situ device. This requires full integration of the in situ device in the host image acquisition environment. Given that the large storage requirements are driven by the camera, it is expected that the camera software will be used to store and manage other experimental meta data associated with a given experiment.

Direct detection cameras have redefined the performance standard for in situ microscopy. The previous history of cameras with insufficient quality and resolution, combined with sub-video frame rates has become a memory of the past. The new high speed cameras have demonstrated the sub-ms temporal resolution satisfying sensitivity and full sensor resolution requirements. In the near future, there is still an opportunity for speed improvement—perhaps by as much as 5× compared with cameras today. Information captured per image will continue to increase by improving the cameras' DQE or creating more independent pixels. Optimizing the performance of direct detection cameras at lower kV (e.g., 60 or 80 kV) also represents an opportunity for future development.

It is worth pointing out that the ultimate improvement in image quality for in situ applications requires significant investment and collaboration from both manufacturers of image detectors and electron microscopes. Brighter and more coherent electron source combined with higher speed cameras with better DQE will undoubtedly push in situ microscopy to an uncharted territory. The future of in situ microscopy is full of opportunities to expand our understanding of fundamental materials systems with significantly better spatial and temporal resolution than just a few years ago.

References

R. Alani, M. Pan, In situ transmission electron microscopy studies and real-time digital imaging. J. Microsc. **203**(Pt 1), 128–133 (2001)

C. Booth, K2: A super-resolution electron counting direct detection camera for cryo-EM. Microsc. Microanal. **18**(S2), 78–79 (2012). doi:10.1017/S1431927612002243

E.D. Boyes, P.L. Gai, Environmental high resolution electron microscopy and applications to chemical science. Ultramicroscopy **67**(1-4), 219–232 (1997). doi:10.1016/S0304-3991(96)00099-X

W.S. Boyle, G.E. Smith, Charge coupled semiconductor devices. Bell Sys. Tech. J. **49**(4), 587–593 (1970). doi:10.1002/j.1538-7305.1970.tb01790.x

P.A. Crozier, R. Wang, R. Sharma, In situ environmental TEM studies of dynamic changes in cerium-based oxides nanoparticles during redox processes. Ultramicroscopy **108**(11), 1432–1440 (2008). doi:10.1016/j.ultramic.2008.05.015

D.A. Evans, P.P. Allport, G. Casse, A.R. Faruqi, B. Gallop, R. Henderson, M. Prydderch, R. Turchetta, M. Tyndel, J. Velthuis, G. Villani, N. Waltham, CMOS active pixel sensors for ionising radiation. Nucl. Instrum. Methods Phys. Res. A **546**(1-2), 281–285 (2005). doi:10.1016/j.nima.2005.03.108

G.Y. Fan, M.H. Ellisman, High-sensitivity lens-coupled slow-scan CCD camera for transmission electron microscopy. Ultramicroscopy **52**(1), 21–29 (1993). doi:10.1016/0304-3991(93)90019-T

A.R. Faruqi, R. Henderson, M. Pryddetch, P. Allport, A. Evans, Direct single electron detection with a CMOS detector for electron microscopy. Nucl. Instrum. Methods Phys. Res. A **546**(1-2), 170–175 (2005). doi:10.1016/j.nima.2005.03.023

P.L. Gai, Direct probing of gas molecule-solid catalyst interactions on the atomic scale. Adv. Mater. **10**(15), 1259–1263 (1998). doi:10.1002/(SICI)1521-4095(199810)10:15<1259::AID-ADMA1259>3.3.CO;2-X

Gatan (2005) Digital Micrograph. http://www.gatan.com/products/tem-analysis/gatan-microscopy-suite-software.

T.W. Hansen, J.B. Wagner, P.L. Hansen, S. Dahl, H. Topsoe, C.J.H. Jacobsen, Atomic-resolution in situ transmission electron microscopy of a promoter of a heterogeneous catalyst. Science **294**(5546), 1508–1510 (2001). doi:10.1126/science.1064399

P.L. Hansen, J.B. Wagner, S. Helveg, J.R. Rostrup-Nielsen, B.S. Clausen, H. Topsoe, Atom-resolved imaging of dynamic shape changes in supported copper nanocrystals. Science **295**(5562), 2053–2055 (2002). doi:10.1126/science.1069325

S. Hofmann, R. Sharma, C.T. Wirth, F. Cervantes-Sodi, C. Ducati, T. Kasama, R.E. Dunin-Borkowski, J. Drucker, P. Bennett, J. Robertson, Ledge-flow-controlled catalyst interface dynamics during Si nanowire growth. Nat. Mater. **7**(5), 372–375 (2008). doi:10.1038/nmat2140

J.R. Janesick, SPIE, for Optical Engineering IS, *Scientific charge-coupled devices* (SPIE Press, Bellingham, 2001)

O.L. Krivanek, P.E. Mooney, Applications of slow-scan CCD cameras in transmission electron microscopy. Ultramicroscopy **49**(1-4), 95–108 (1993). doi:10.1016/0304-3991(93)90216-K

S. Kujawa, D. Krahl, Performance of a low-noise CCD camera adapted to a transmission electron microscope. Ultramicroscopy **45**(1-4), 395–403 (1992)

X. Li, P. Mooney, S. Zheng, C.R. Booth, M.B. Braunfeld, S. Gubbens, D.A. Agard, Y. Cheng, Electron counting and beam-induced motion correction enable near-atomic-resolution single-particle cryo-EM. Nat. Methods **10**(6), 584–90 (2013a). doi:10.1038/nmeth.2472

X. Li, S.Q. Zheng, K. Egami, D.A. Agard, Y. Cheng, Influence of electron dose rate on electron counting images recorded with the K2 camera. J. Struct. Biol. **184**(2), 251–260 (2013b). doi:10.1016/j.jsb.2013.08.005

H.-G. Liao, D. Zherebetskyy, H. Xin, C. Czarnik, P. Ercius, H. Elmlund, M. Pan, L.-W. Wang, H. Zheng, Facet development during platinum nanocube growth. Science **345**(6199), 916–919 (2014). doi:10.1126/science.1253149

H. Liu, H. Jiang, L.L. Fajardo, A. Karellas, W.R. Chen, Lens distortion in optically coupled digital x-ray imaging. Med. Phys. **27**(5), 906–912 (2000). doi:10.1118/1.598956

M.E. Mochel, J.M. Mochel, A CCD imaging and analysis system for the VG HB5 STEM, in *Proc. 44th Annual Meeting EMSA, Albuquerque, NM* (San Francisco Press, San Francisco, 1986), pp. 616–617

P. Mooney, Optimization of image collection for cellular electron microscopy. Methods Cell Biol. **79**, 661–719 (2007)

P.E. Mooney, G.Y. Fan, C.E. Meyer, K.V. Truong, D.B. Bui, O.L. Krivanek, Slow-scan CCD camera for transmission electron microscopy, in *Proc. XIIth Int'l Congr. Elec. Microsc., Seattle, WA* (San Francisco Press, San Francisco, 1990)

P.E. Mooney, M. Pan, G. Van Hoften, F. De Haas, Quantitative evaluation of fiber-optically coupled CCD cameras for use in cryo-microscopy. Microsc. Microanal. **10**(2), 168–169 (2004). doi:10.1017/s143192760488084x

V.P. Oleshko, In situ real-time environmental TEM of gas phase Ziegler-Natta catalytic polymerization of propylene. J. Electron. Microsc. **51**(90001), S27–S39 (2002). doi:10.1093/jmicro/51.Supplement.S27

M. Pan, Developing image detectors for *in-situ* TEM applications. J. Chin. Electron Microsc. Soc. **29**, 295–310 (2010)

T. Radetic, A. Gautam, C. Ophus, C. Czarnik, U. Dahmen, High resolution observations of interface dynamics using a direct electron detection camera. Microsc. Microanal. **20**(S3), 1594–1595 (2014). doi:10.1017/S1431927614009702

E. Ringe, R.P. Van Duyne, L.D. Marks, Wulff construction for alloy nanoparticles. Nano Lett. **11**(8), 3399–3403 (2011). doi:10.1021/nl2018146

P.T.E. Roberts, J.N. Chapman, A.M. MacLeod, A CCD-based image recording system for the CTEM. Ultramicroscopy **8**(4), 385–396 (1982)

J.C.H. Spence, J.M. Zuo, Large dynamic range, parallel detection system for electron diffraction and imaging. Rev. Sci. Instrum. **59**(9), 2102–2105 (1988). doi:10.1063/1.1140039

R. Turchetta, J.D. Berst, B. Casadei, G. Claus, C. Colledani, W. Dulinski, Y. Hu, D. Husson, J.P. Le Normand, J.L. Riester, G. Deptuch, U. Goerlach, S. Higueret, M. Winter, Monolithic active pixel sensor for charged particle tracking and imaging using standard VLSI CMOS technology. Nucl. Instrum. Methods Phys. Res. A **458**(3), 677–689 (2001). doi:10.1016/s0168-9002(00)00893-7

F.M. Wanlass, C. Sah, Nanowatt logic using field-effect metal-oxide semiconductor triodes, in *Solid-State Circuits Conference*, Digest of Technical Papers, vol. VI (IEEE International, Philadelphia, 1963), pp. 32–33. doi:10.1109/ISSCC.1963.1157450

Chapter 6
Closed Cell Systems for In Situ TEM with Gas Environments Ranging from 0.1 to 5 Bar

A.K. Erdamar, S. Malladi, F.D. Tichelaar, and H.W. Zandbergen

Abstract The ability to carry out reactions with gas mixtures in a TEM is becoming an increasingly important field of study, known as environmental transmission electron microscopy (ETEM). Different approaches exist to expose the material to a gas while imaging in a TEM: an open system employing differential pumping and a closed system using microelectromechanical systems (MEMS). The latter approach using electron transparent windows in a device holding the specimen and the gas came up during the last decade, enabling a gas pressure of several bars. Here, we present this closed cell approach based on a functional MEMS device known as "nanoreactor" to investigate gas–material interactions inside a TEM. We discuss the design and the development of different kinds of nanoreactors, along with the necessary accessories to carry out drift-stabilized, atomic-resolution environmental TEM studies. Finally, examples showing the applications of the nanoreactor to investigate several gas–liquid–material interactions are presented.

6.1 Introduction

TEM experiments are almost always performed with a 10^{-7} mbar environment around the specimen. This has to be done because the electrons have such a strong interaction with matter (and thus also gas molecules) that even a low gas pressure in the electron microscope results in a strong blurring of the TEM image. Over the last two decades, the development of environmental TEMs (ETEM) has made it possible to increase the pressure around the specimen while maintaining an acceptable vacuum in other parts of the TEM. This was realized by adding extra pumps and pumping apertures. A disadvantage is that the maximum pressure around the specimen for high-resolution imaging is about 10 mbar. This limitation is caused by

A.K. Erdamar (✉) • S. Malladi • F.D. Tichelaar • H.W. Zandbergen
Kavli Institute of Nanoscience, Delft University of Technology, Lorentzweg 1, 2628 CJ Delft, The Netherlands
e-mail: a.k.erdamar@tudelft.nl

T.W. Hansen, J.B. Wagner (eds.), *Controlled Atmosphere Transmission Electron Microscopy*, DOI 10.1007/978-3-319-22988-1_6

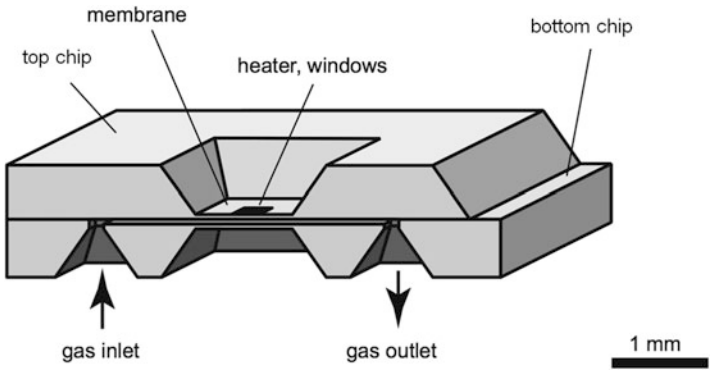

Fig. 6.1 Schematic presentation of a nanoreactor composed of two chips

the geometries in an ETEM. More than a decade ago, we realized that in order to do experiments at realistic pressures, it was necessary to develop a system with a shorter gas column. The gas column in an ETEM is about 10 mm and had to be shortened by several orders of magnitude to allow pressures of 1 bar and more. Practically, this shortening can be achieved best by developing a small microreactor or nanoreactor (NR) based on semiconductor production techniques. Figure 6.1 shows the design of the first type of NR (Creemer et al. 2008). Several prototype NRs have been designed and manufactured, which allowed getting atomic resolution images at 1 bar gas pressure and 700 °C.

6.2 The Nanoreactor Developments in Delft

The research in Delft employing MEMS to create a 1 bar environment around the sample started in 2001 with the use of a sandwich nanoreactor in which two MEMS-processed chips were aligned with respect to each other and fixed with a two-component glue. This type of ensemble was successfully used for various in situ experiments at 1 bar (Creemer et al. 2008). However, when we tried to use these glued NRs more routinely, it turned out that carbon contamination (C-contamination), ease of use (including making it airtight), and the yield were major bottlenecks.

Various routes have been explored to solve the C- contamination issue: (1) finding an organic-based glue that does not outgas, (2) using an inorganic glue (water glass) (Yokosawa et al. 2012), (3) using a Viton O-ring to make an airtight connection between the bottom and top chip, (4) making the NR as one complete chip (Creemer et al. 2011). Note that apart from the NR, contamination can also originate from hydrocarbon impurities in the rest of the gas system (in the holder and in the gas supply system). Several organic-based glues have been tried, but we could not find glue that did not result in C-contamination. Alternatively, water glass

(a solution of sodium metasilicate, Na_2SiO_3) has been used as glue. Being inorganic, it was possible to achieve C-contamination-free experiments several times, but achieving airtightness with this glue has been quite challenging. To solve the problem of possible leakage through water glass seal, the holder has been modified such that leakage through the interface between the two chips is not a problem for the vacuum of the TEM. A drawback of gluing the two chip halves is that once glued, it is nearly impossible to separate them. For this reason, we developed a third method for the sandwiched chip NR, where the sealing is achieved through O-rings without glue. In this design, the two chips are clamped together (see Sect. 6.4), but can be separated after the in situ TEM experiments to allow additional experiments on the same sample, for instance using a highly surface sensitive technique which requires the absence of the top chip. We have also developed an NR that consists of one component only (Creemer et al. 2011). One-chip and sandwiched chip NRs are similar in size and can therefore be loaded in the same holder.

Concerning the required vacuum tightness, the NRs and holders and their interfacings have to be vacuum sealed. Due to the very limited space in TEM holders, this is not a trivial task. For standard high vacuum connections, one normally uses O-rings of a shore diameter of 2–3 mm. But because of the space limitations in particular along the electron beam direction such O-ring sizes cannot be used. All the NR-holder components (lid, NR top, O-ring, NR bottom, O-ring, holder) have to fit within 2–3 mm. As a result, the O-rings must have a shore of about 0.40 mm. The typical tolerance for an O-ring of 0.40 mm is 0.08 mm, which is more than the tolerance of about 0.02 mm in compression of the O-ring needed for vacuum tightness. Thus, a careful selection and optimization of all components of the assembly is needed.

6.3 Different Types of Nanoreactors

Two major types of NRs (see Fig. 6.2) are used in Delft: the sandwiched chip NR and the one-chip NR consisting of a bottom chip with heater and top chip. Both types can be used in a static gas system, i.e., the gas must be loaded outside the TEM, and in a flowing gas system, i.e., the gas is led from a gas handling system outside the TEM through tubes in the TEM holder and through the NR and back. The sandwiched chip NR has two types of heaters: a spiral-shaped heater with electron transparent windows in between the Pt heater spiral, or a flat center heater with a larger area for specimen mounting. A brief comparison between both the NR designs is given in Table 6.1. Information on the fabrication of both kinds of NRs is given further in the chapter (Table 6.1).

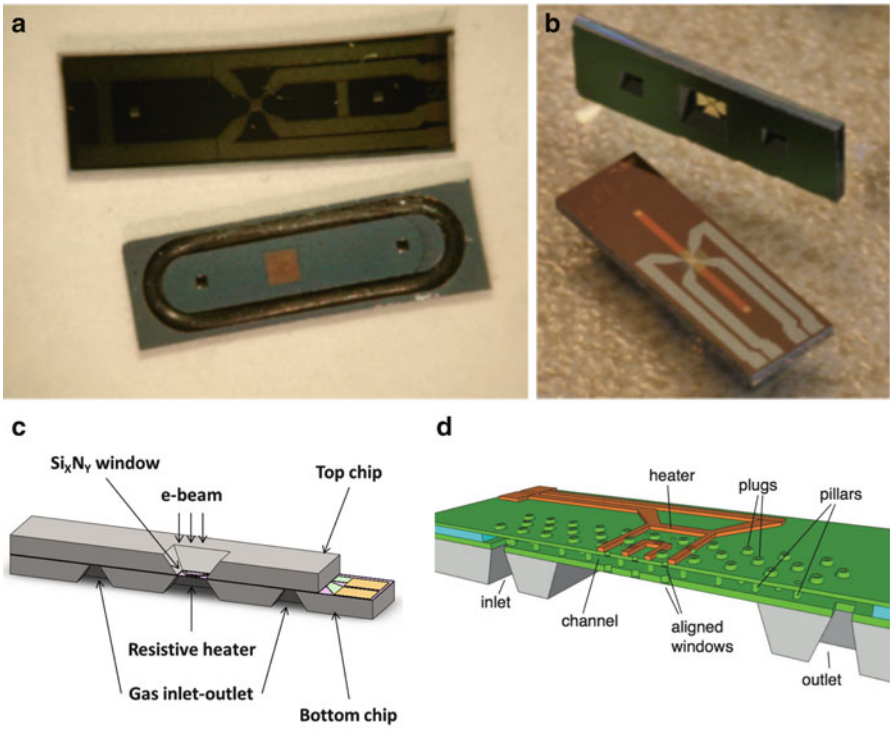

Fig. 6.2 Optical images of the two chip halves of the sandwich NR (**a**) and one-chip NR seen from top and bottom (**b**). (**c**) 3-D sketch of the sandwich NR, consisting of a bottom chip with the heater and the contact pads for connection of the heater to the heater control. (**d**) 3-D sketch of the all-in-one NR. For clarity, the thin-films' thicknesses have been drawn thicker than they are in reality. The channel is 4.6 mm long and 0.3 mm wide

6.4 The NR Holders Used in Delft

The NR has to be supported by a holder, whereby the combination of NR and holder should allow: (1) full vacuum tightness, (2) a resolution better than 1 Å, (3) reliable electrical contacts for the MEMS heater in the NR, and (4) a gas inlet and outlet in the case of the flowing gas holder.

Note that the gas tubes and the wiring for the electrical contacts have to fit into the TEM holder. This limits possible upgrades like adding valves in the tubes or preheating of the gas in the tube. Differences in the size of the holders influence the design of the NR. As an example, FEI and JEOL holders are shown in Fig. 6.3. Obviously, the JEOL holder with its much larger diameter provides more space for add-ons in the holder. Nevertheless, up till now we have always been able to realize all features in the FEI holders (with an inner bore of the narrow part of the holder tube being less than 5.5 mm) in which the most complicated one was a double tilt vacuum transfer heating-holder.

Table 6.1 Advantages (in *upright*) and disadvantages (in *italics*) of sandwiched chips and one-chip NRs

Sandwiched chips NR	One chip NR
Samples of any size can be loaded	*Only particles can be loaded with a dispersion led through the gas channel*
Sample can be positioned at a desired location (only in middle of heater)	*The whole inside space of the NR will contain particles*
Sample is only present on the heater membrane	Sample is present on both membranes
Channel height can increase from 5 to 35 μm upon gas pressure.	Channel height (e.g., 2 μm) independent on pressure
Top chip can be removed for further analysis (tomography, surface analysis, etc.)	*Top membrane cannot be removed*
O-rings thickness between NR chips is critical	NR itself is leak-tight
Assembly process may cause contamination	It is easier to prevent contamination
The fragile parts of the two chips are well protected	*Top of the chip is very fragile*
Alignment of two chips could fracture a membrane	Alignment is not an issue in this case
A modification (e.g., add biasing line) is fairly easy	*Modification is complicated*
More than one sample can be loaded and studied at the same time	*The loading of the suspension could clog the channel*
An NR can be used several times, e.g., in case of metal lamella	*Reusing this system also requires thorough cleaning which is not feasible in all cases.*
External dirt particles can be present during the assembly	Dust particles is limited to the suspension only

Fig. 6.3 A comparison of the shapes of a JEOL and an FEI flowing gas holder

Figure 6.4 shows our latest flowing gas holder for an FEI TEM, which has been used for the 1 bar corrosion experiment discussed in Sect. 6.10.3. The gas system (all components that are in contact with the gas that is lead through the NR) can be taken out of the holder for dedicated cleaning. We used two types of materials for this: Pt and Ti. In the example shown in Fig. 6.4, the material is Ti. The construction

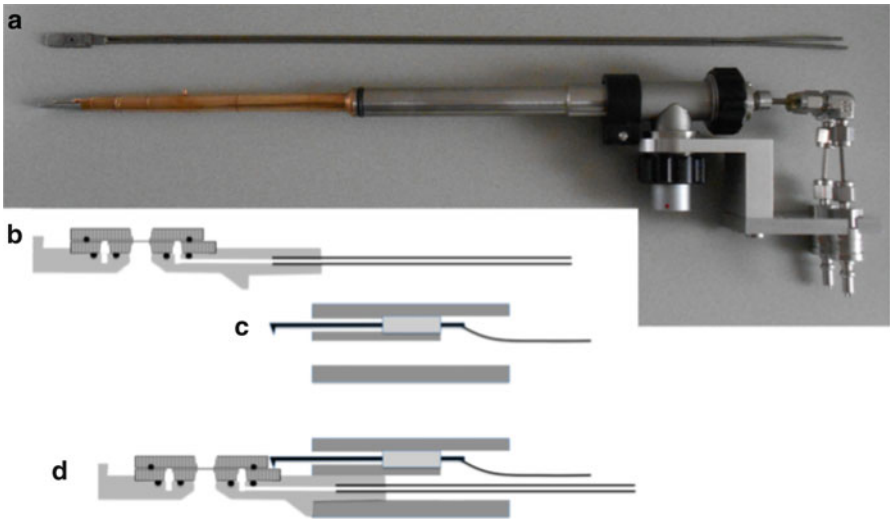

Fig. 6.4 The flowing gas holder (**a**) shows a holder that has been realized and has been used for corrosion experiments. Above the holder the tip/tubing combination is shown that can be removed as one piece. (**b**–**d**) Cross-sectional sketches of the holder tip disassembled and assembled onto the holder. The inlet and outlet tubes run all the way to the other side of the holder (extending outside of the TEM), where they are attached to a gas supply system. The tip and gas tubes of the holder shown in (**a**) are completely composed of Ti (except for the *O-rings* in the tip). This tip-tubes system can be taken out from the holder and be cleaned, for instance by a bake-out in vacuum at 300 °C

on the right side of the holder shown in Fig. 6.4 is to prevent strain on the Ti tube coming out of the holder, which could induce a leak due to the creep of the tubes.

Figure 6.5 shows our static gas holder. The holder has a separable tip, which contains an airtight chamber that can store gas with a volume of 1–10 mm^3. Gas is loaded in or pumped out through a valve in the tip (see *arrow* in Fig. 6.5b). The NR is similar to that of the flowing gas holder, but could also be made more dedicated, for instance with a build-in pressure meter. In the experiments we did up till now, we used our standard NRs, which allow both static and gas-flow experiments.

Figure 6.6 shows a previously used holder, in which the NR is allowed to be leaky between the two chip halves. The advantage is that this connection between the two chips is not critical in the airtightness, for instance allowing glues that are not sealing very well but do not contain hydrocarbons. The disadvantage is that the lid (with a hole of 1.0 mm over the membrane area) to make the chamber in which the NR is located has been thick because the large O-ring has to be pressed down everywhere sufficiently by two screws of the far ends of the lid.

Some advantages and disadvantages of the static gas holder and the flowing gas holder are indicated in Table 6.2.

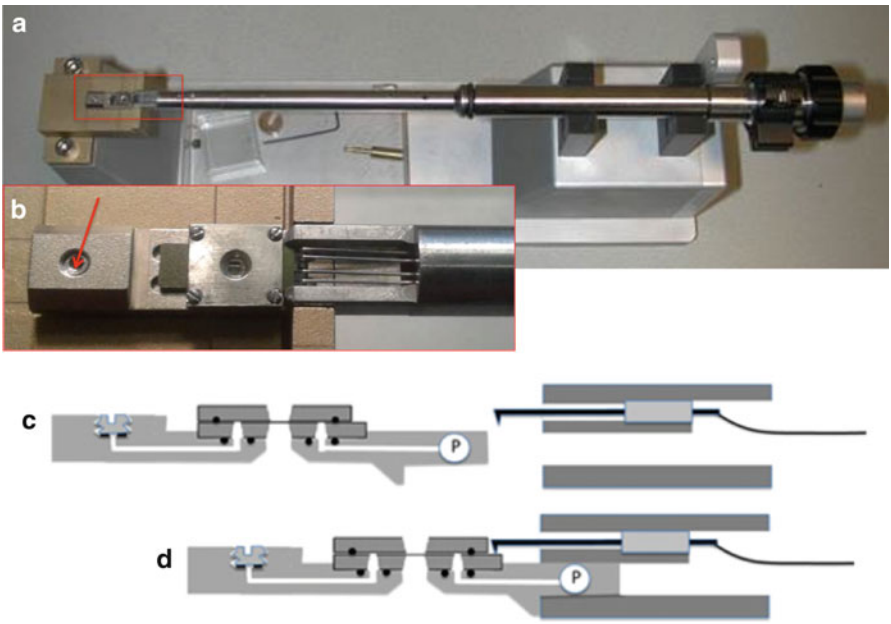

Fig. 6.5 (**a**) Image of the static gas holder and (**b**) an enlarged view of the tip part with the square lid on top. The *red arrow* indicates the valve to open or close the tip, (**c**, **d**) show cross-sectional sketches of the holder tip disassembled and assembled onto the holder, respectively. *P* indicates a pressure meter . The lid to clamp the two chips together is not given in (**c**) and (**d**) but can be seen in (**b**)

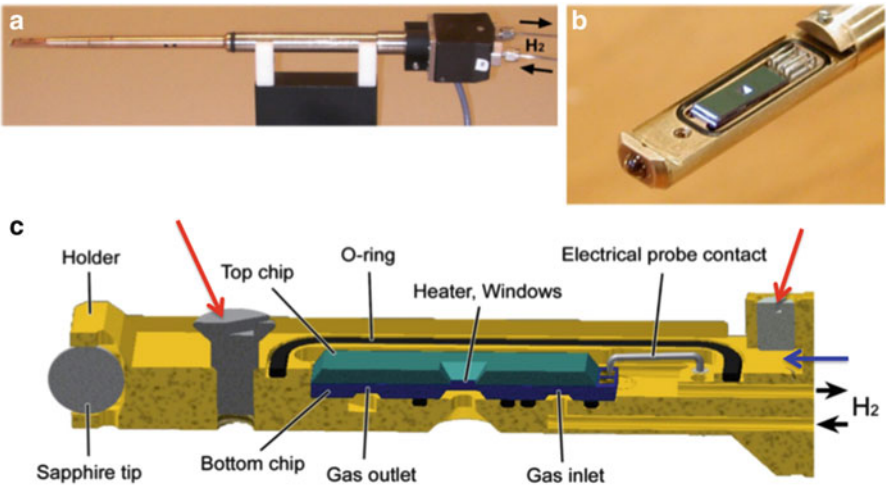

Fig. 6.6 Sample holder used for the 4.5 bar hydrogen gas experiments. (**a**) Sample holder. (**b**) NR inserted in the sample holder. The lid of the holder is removed for a better view. Mounting of the lid is done by sliding it into an opening indicated by the *blue arrow* and next tightening the screws indicated by the *red arrows*. (**c**) Schematic diagram of the NR inserted in the sample holder

Table 6.2 Comparison of using NR with static gas or flowing gas, advantages (in *upright*) and disadvantages (in *italics*)

Flowing gas system	Static gas system
Gas handling system near TEM is complicated	Simple setup at the TEM
Gas pressure regulation possible	*Pressure cannot be regulated, is dependent on T, and may drop due to leakage*
Alternating different gases possible	Because price of tip is small compared to whole holder, running several experiments in parallel (e.g., ageing) is well doable
Allowed leakage can be much higher than in static gas situation	*Even a very small leak results in significant pressure drop*
	Tiny gas volume allows for special/expensive gases
High hazard gases not possible	Also high hazard gases can be loaded outside the TEM area.
	Transfer to another analysis tool is easy
	Because price of tip is small compared to whole holder, running several experiments in parallel (e.g., ageing) is well doable

6.5 The Alignment Tool

The windows of the top and bottom chip have to be aligned to allow investigation of a sample on top of one of the windows by TEM. This is feasible with the alignment tools shown in Fig. 6.7. Two NR halves are placed on top of each other in the central part of the alignment tool. Next, the lid is placed on top of it. From this point on, two methods can be used. Method 1 involves (1) Slight tightening of the lid, (2) Alignment of the top chip to the bottom chip with micromanipulators, and (3) Further tightening of the lid. Method 2 consists of (1) Slight tightening of the lid-NRs ensemble with the block shown in Fig. 6.7b, (2) alignment of the chips, (3) tightening of the block, and (4) tightening of the lid with the four screws. The advantage of the latter method is that the force to the lid-NRs ensemble is mainly vertically applied which is important to prevent a breakage of one of the chips due to torsion. For the alignment, one needs a good optical microscope that allows clear imaging of the electron transparent windows (see also Fig. 6.18e). In general, one can see that the two membranes of the NR halves are close to each other using Newton rings.

6.6 The Gas Supply Systems in Delft

An important component of the NR in situ TEM experiments is the gas supply system. In the case of the static gas holder (see Fig. 6.8), loading the NR with the gas of interest is relatively straightforward. The tip of the holder is placed in an

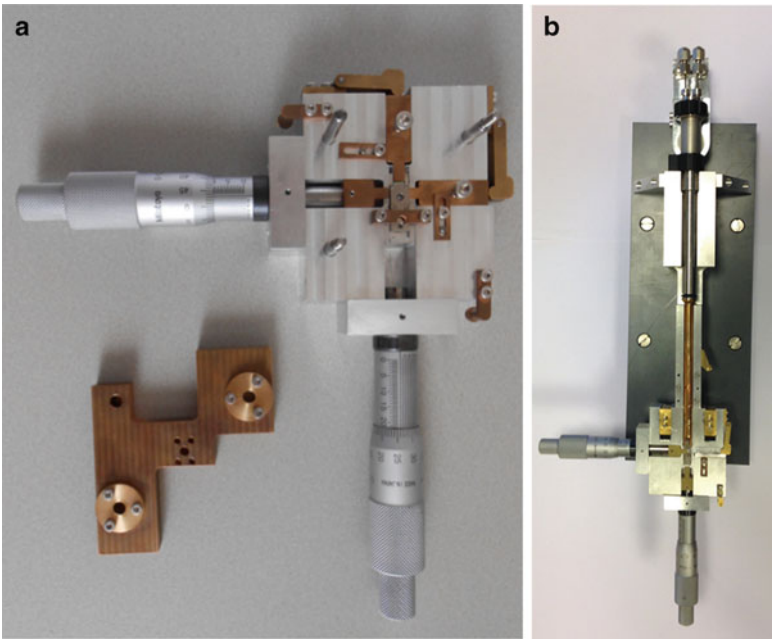

Fig. 6.7 (**a**) The alignment tool for a static gas holder. (**b**) The alignment tool for a gas-flow holder. The latter alignment tool is much larger because the holder has to be supported in one direction

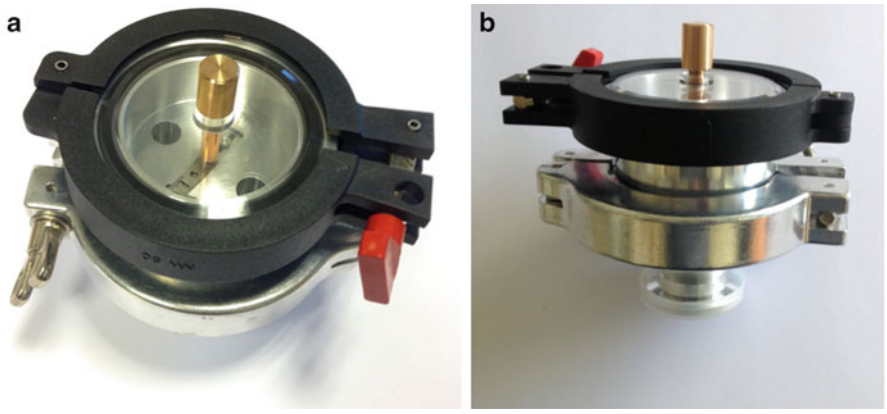

Fig. 6.8 The gas loading system seen from the *top* (**a**) and the *side* (**b**). The tip can be seen through the glass slide. The screw in the tip, acting as an airlock can be tightened (*closed*) or loosened (*open*), with the screw driver. The system has a standard NW16 connection at the bottom

enclosure. The valve in the tip is then opened and the chamber along with the NR is evacuated. Subsequently, the reactive gas of interest is introduced into the chamber at the pressure required for the in situ TEM study (typically 1 bar). The tip is left in

this configuration with the valve open for duration of 30 min to load the NR with reactive gas and the valve is then closed. This relatively long time is preferred because the gas has to travel to the gas chamber part through a thin gap in the NR. The NR is now set up for in situ TEM investigation. The handling becomes slightly more sophisticated when the flow-gas holder is used. The primary requirements for a successful in situ gas-flow experiment are a continuous gas supply at a constant pressure and a constant pressure on the outlet side of the NR. An inlet gas should be very clean to avoid any contamination during the investigation. More importantly, the gas supply system should account for all the safety standards by using a protective mechanism. This system shuts down the gas supply instantaneously in case of damage to the NR by reducing the gas leakage into the column to a minimum. Note that the NRs operate at nominal pressures of a few millibars to as high as 4.5 bar. Also, it is sometimes necessary to have a mixture of a gas and liquid (aerosols). Considering all these factors, different gas-flow systems for gases as well as aerosols have been developed.

Figure 6.9a shows the flow diagram for a gas supply system that allows multiple gas sources (currently three, but it can be modified to more gas sources). The front panel of this gas supply system is shown in Fig. 6.9b, which has been divided into a part for gas pressures lower than 2 bar and another part for gas pressures higher than 2 bar. This gas supply system has been assembled from a cuboidal framework of aluminum pillars to which the gas bottles are securely fastened with a front panel of aluminum sheet fitted with standard Swagelok valves and pressure gauges. All the tubes and components that come into contact with flowing gas are made of low-carbon stainless steel tubes. This assures corrosion resistivity against most of the commonly used gas mixtures like, e.g., H_2, O_2, CO, and CO_2. As indicated in the flow diagram (Fig. 6.9a), the gas bottles are connected to a flow tube through a series of check valves, three-way valves, and toggle valves. The three-way valves divide the gas-flow system to a low-pressure part and high-pressure part. Both parts are essentially identical; the main difference is the presence of different filters in each section. Depending on the experimental requirements, the system can be operated either at high pressures or at low pressures by the flick of a switch. The system allows the choice of either a single gas or a mixture of two or three gases. In order to avoid the contamination of the gas bottles by other gases, check valves allowing unidirectional flow only have been fitted before the gas enters the mixing tube. A relief valve and a manometer monitoring the pressure of the gas after the mixing tube have been added as a safety mechanism in case of an excess pressure. Any residual moisture due to condensation in the tubes is detrimental to the TEM investigation. Therefore, the gas mixture flows through a charcoal filter and a needle valve before entering the TEM holder. The pressure behind this filter is monitored by a digital manometer, and its value is considered to be the pressure on the inlet of the NR.

A membrane pump is used to flow the gas and to maintain pressure differences between the inlet and the outlet of the holder. The outlet of the holder is connected to the membrane pump through a toggle valve, whereas the remainder of the gas

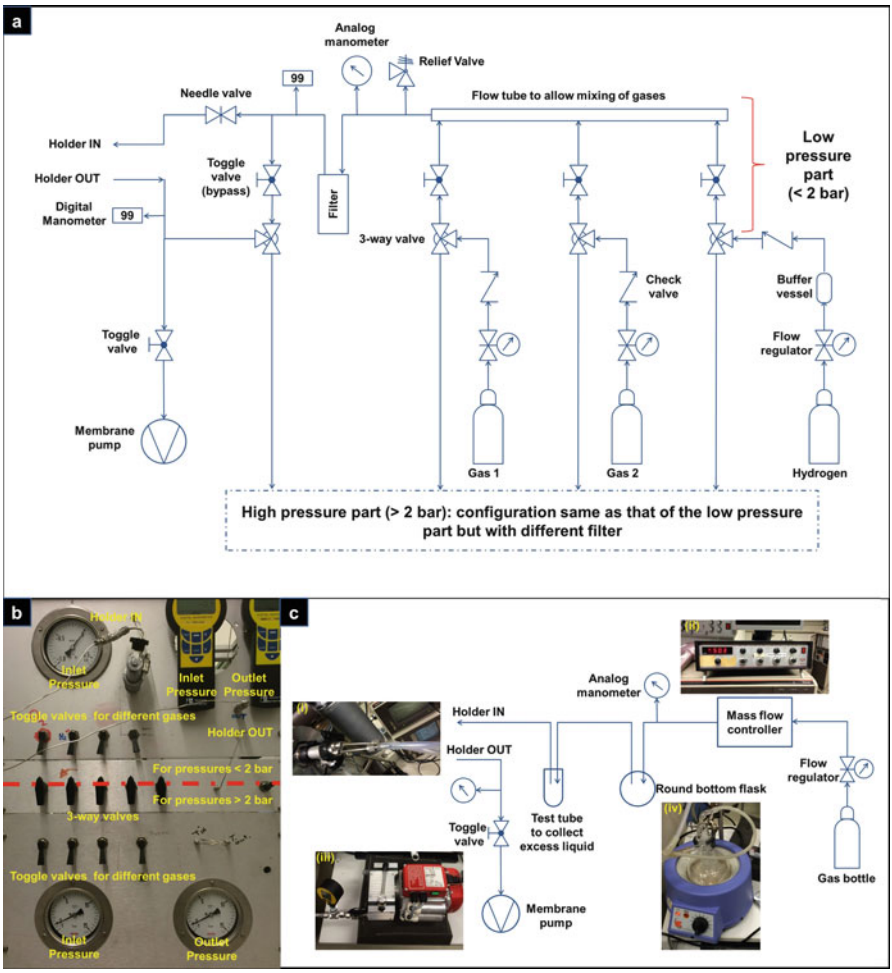

Fig. 6.9 Schematic representation of the gas supply system for the gas-flow holder (**a**) flow diagram for gas supply system allowing multiple gas sources, (**b**) front panel of gas supply system, (**c**) simplified version of gas flow system for reaction mixtures

supply system is connected to this pump through a three-way valve and a toggle valve (a bypass valve). The bypass valve connects the inlet part of the gas supply system (which is maintained at higher pressure) to the outlet part of the gas supply system. The outlet part is at a low pressure, typically around 15 mbar, determined by the membrane pump. When the bypass valve is open, the gas does not enter the TEM holder, which adds to additional safety of the microscope by preventing any excess gas leakage into the column.

In short, if the system is operational under pressures of 2 bar as shown in the figure, the experimental sequence is as follows: (1) Connect the TEM holder to the gas supply system and switch on the membrane pump with the bypass valve open; (2) Once the pressure on the digital manometers on the inlet and outlet has reached

almost the same value (this indicates the gas supply system is nearly evacuated), close the bypass valve to pump through the holder; (3) By carefully regulating the toggle valves and the needle valve before the inlet, it is possible to maintain a constant pressure difference between the inlet and the outlet of the holder.

Sometimes for certain in situ experiments, it is necessary to use aerosols, like in the case of aluminum alloys, where the corrosion in oxygen bubbled through aqueous HCl is studied. In certain cases, gases like H_2S are required. When such corrosive gases or aerosols are used, it is necessary to avoid contamination of the gas-flow system or to prevent the corrosion of stainless steel components. As an alternative, the gas supply system shown in Fig. 6.9c can be used. For aerosols, the carrier gas flowing from a bottle is regulated through a flow meter, which bubbles through a glass flask containing the solution of interest (typically aqueous). This creates an aerosol enriched with extremely fine droplets of the solution. Prior to the inlet tube of the holder, there is a test tube with two disconnected tubes, which acts as a sink for any excess liquid. The outlet of the holder is connected to the membrane pump through a toggle valve, and the pressure on the outlet is monitored. Likewise, the pressure on the inlet is monitored and regulated through the needle valves of the mass-flow controller.

6.7 Manufacturers of Nanoreactor Systems

There are three major companies that produce holders and chips for different types of in situ TEM experiments at pressures that cannot be realized in an ETEM: DENSsolutions (Guo et al. 2006), Hummingbird (Jenichen and Engler 2009), and Protochips (López Nieto et al. 2003).

The Hummingbird gas holder provides single and multichannel gas delivery systems, which are used to study solid–gas interactions at or just above atmospheric pressure. When the holder is fitted with a heating chip, it also supports real-time observation of catalysis reactions in the TEM. The sample can be heated up to ~800 °C. The temperature is controlled with closed-loop temperature control software that works with the calibrated sensor on the chip. Protochips has gas and liquid flow holders, giving the opportunity to study the real-time material behavior inside the TEM at pressure and temperature up to 1 bar and 1000 °C, respectively. Note that the presence of a gas allows heat exchange with its environment. When the temperature calibration was done in vacuum, this leads to wrong temperature indications (see further information below). Most of our own NR developments described in this chapter are or will be commercialized by DENSsolutions (He and Hull 2012). Several examples of applications of the gas holders are: (1) The solid–gas interactions related to oxidation reaction of cobalt-based nanocatalysts uncovering in situ evolution of the Kirkendall effect (Xin et al. 2013); (2) The oxidation of two-dimensional Ti_3C_2, also known as "Mxhene," whereby the production of carbon-supported TiO_2 was shown as a function of the heating rate, the temperature range, and the exposure time (Ghassemi et al. 2014);

(3) The formation of mesoporous Pd powder with a pore diameters of 7 or 13 nm in vacuum and H_2 gas; (4) The (de)hydrogenation of Pd at pressures up to 4.5 bar (Yokosawa et al. 2012).

The three companies also have or will soon have liquid (flow) holders, which enable research to be carried out in a static or dynamic liquid environment, also see review by the de Jonge and Ross (2011)

Examples of this kind of in situ TEM are (1) in situ quantification of the electrochemical nucleation and growth of copper clusters on gold from a 0.1 M $CuSO_4.5H_2O$ 1 vol.% H_2SO_4 solution (Radisic et al. 2006); (2) direct observation of calcium carbonate crystal nucleation which enables future research on the role of living organisms on this type of nucleation (Nielsen et al. 2014); (3) the use of ETEM in closed liquid cells or in liquid flow devices. The authors claimed that atomic resolutions can be achieved in liquid enclosures with 50 nm thick SiN membranes (de Jonge et al. 2014); (4) the electrochemical charging of a battery in a TEM liquid flow cell by imaging of electrochemically active ions in the electrode and electrolyte in electrical energy storage systems at nanoscale (Holtz et al. 2014); and (5) the structural evolution and electrochemical response of Pt–Fe nanocatalysts, which showed that the particles growth rate depends on both site and the potential (Zhu et al. 2014).

6.8 Design Requirements for the Nanoreactors

Several general requirements can be listed for the NRs:

1. The windows of the NRs must be sufficiently electron transparent, on the one hand, and able to withstand the applied pressure on the other hand.
2. The NR should allow heating of the gas and the specimen with a high accuracy in temperature.
3. The NR should allow straightforward loading of the specimens.
4. The NR should allow a controllable gas or liquid flow.
5. The NR and the holder should not be in conflict with normal TEM operation.

Furthermore, a few more specific requirements can be given:

6. The NR should be relatively easy to operate.
7. The carbon contamination should be negligible.
8. The electron transparent membranes of the NR should be uniform in thickness and amorphous.
9. The length of the gas or liquid column along the e-beam direction should be small (matching the required resolution).
10. It is preferable to have the resolution the same as that of the standard holder.
11. The drift should be small enough to record high-resolution images.

6.8.1 Requirement 1: Electron Transparent Windows that Withstand 10 bar

An MEMS NR consists of two parallel membranes of about 500 nm thick with a gas in between them. These two membranes contain several ultra-thin regions (e.g., 15 nm thick) that act as electron transparent windows. Most of the time we and other NR developers have used SiN as membrane material, but other materials such as SiC and SiO_2 are also possible. In this subsection, we write SiN membrane, but it should be read as a class of materials that are relatively inert, can withstand high temperatures, and are preferably amorphous.

When the goal is to obtain a gas pressure of 10 bar, the requirement for a reliable NR is that the big relatively thick membrane and the very thin electron transparent windows must survive exposure to this gas pressure. Modeling can be done on the mechanical response of different window geometries under uniform pressure to determine the limits of various designs. Furthermore, Alan et al. (2012) did an experimental study to characterize the reliability of certain window thicknesses. The simulations and the experiments show that high-pressure operation can easily be obtained by simple design rules for the SiN membranes and windows.

Nonlinear finite element ABAQUS software was used to map the deflections and stress distributions for the membranes under the influence of 10 bar uniform pressure to estimate the failure probability of the devices. Two components have to be modeled: (1) The larger membrane that contains, e.g., the microheater and (2) the electron transparent windows. The stress distribution in the large membrane is shown in Fig. 6.10. It can be seen that the largest stress is present near the location, where the membrane is attached to the Si chip. Note that these stresses can be reduced by changing the size and shape of the windows which is discussed in Fig. 6.12. In addition to larger membrane calculations, several different window geometries (elongated and circular) were tested as illustrated in Fig. 6.11 and Table 6.3. The maximum stress values decrease with decreasing lateral dimensions. Circular structures have lower maximum stresses, due to their symmetry.

Next, the simulations were repeated by taking the corner stress singularities into account. Figure 6.12 shows the models for two calculations: a 90° corner and a tapered shape. The calculations show that the tapered corner has reduced stresses (from 2.85 to 1.95 GPa), and hence increases reliability significantly.

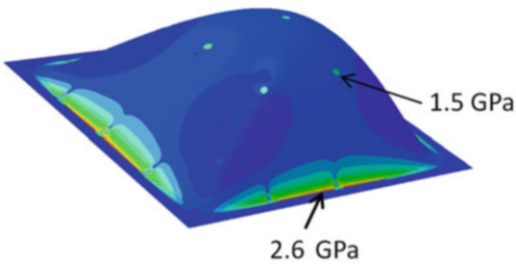

Fig. 6.10 Stress distribution in the large membrane and the electron transparent circular SiN windows (small *green areas*, one indicated by an *arrow*)

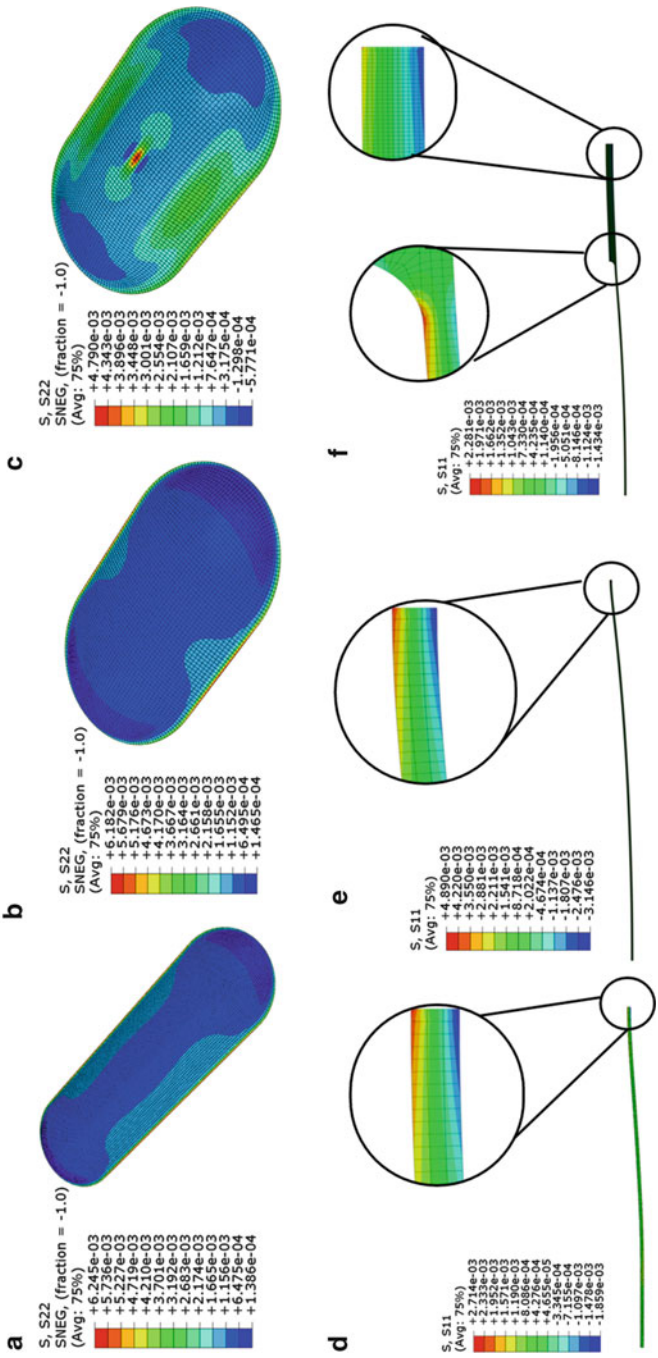

Fig. 6.11 Deflected shapes of the windows and the resulting stress distributions under 1 bar uniform pressure. *Top figure*: elongated membranes with lateral dimensions (**a**) 6×20, (**b**) 6×10, and (**c**) 3×5 μm. *Bottom figure*: axis symmetric models of circular windows in cross-section having (**d**) 3 μm and (**e**, **f**) 6 μm radii. The *small circles* in (**d–f**) indicate the transition from the thin electron transparent window to the thick SiN support. In (**f**), this is two-step transition, firstly from the thin window to a thicker window as indicated in Fig. 6.12, and secondly from this window to the thick SiN support

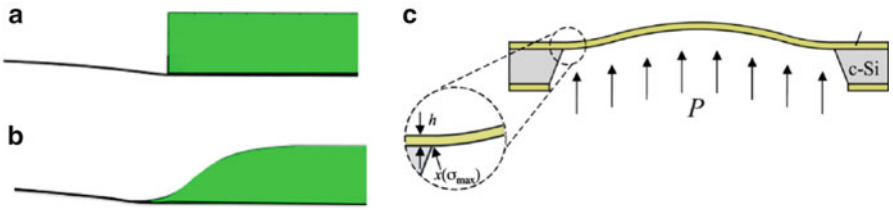

Fig. 6.12 Shapes of the models used for the calculations with (**a**) singular corners, (**b**) tapered corners, and (**c**) schematic of nanoscale bulge tests

Table 6.3 Summary of the simulated results compared to experimental failure probability

Applied load	1 MPa uniform pressure					
Membrane type	15 nm thick elongated			15 nm thick circular		
Lateral membrane dimensions (μm)	3 × 5	6 × 10	6 × 20	3	6	6
Variation in membrane thickness (nm)	–	–	–	–	–	15–60
Maximum out of plane deflection (nm)	105	215	256	66	170	115
Maximum tensile stress (10^{-3} GPa)	4.79	6.18	6.25	2.71	4.89	2.28
Failure probability	8 %	52 %	56 %	1 %	10 %	<1 %

The simulation results indicate that circular membranes have a much higher chance of survival under 10 bar pressure
Reliability and stiffness may be further enhanced by varying the thickness at the edges of the membrane

According to the simulations, the NR design with the elongated windows has an approximate 50 % chance of survival under 10 bar pressure. The results also suggest that the survival probability would increase to 99 % if the lateral window dimensions are reduced and if circular windows are taken with a varying cross-section as indicated in Table 6.3. Note that the probability of survival should be very high because failure of the membrane could result in a damaged electron source, of which a replacement costs 10,000 to 20,000 euro.

6.8.1.1 Experimental Mechanical Characterization Through Bulge Tests

It is quite common that the strength of materials shows significant deviations with changing size scales (Tsuchiya et al. 1998) and process parameters (Alan et al. 2006). Very little is known on the reliability of the use of bulk properties for simulations of the strength of ultra-thin structures. Therefore, we characterized the elastic properties and fracture strength statistics of Si-rich, low-stress SiN membranes with various thicknesses experimentally through nanoscale bulge tests (Paul and Gaspar 2008) (Fig. 6.12). To determine the mechanical properties and fracture strength statistics of SiN, 10, 16, and 1040 nm thick square and rectangular membranes with varying lateral dimensions (0.5 × 0.5 mm^2, 0.2 × 2 mm^2, 0.9 × 9 mm^2) were prepared with standard

fabrication techniques. Low-stress SiN films were deposited on an oxidized Si wafer. The wafer backsides were etched by a 33 % KOH solution, and the wafers were then immersed in a 7:1 buffered hydrofluoric acid (HF) solution releasing the membranes.

The wafers with released membranes were glued on supports that contained designated pressure feedthrough. The wafers were placed in the bulge test setup. This well-established method (Alan et al. 2012) consisted of measuring the out of plane deflection of the membranes under the influence of a uniform pressure. In the present setup, the out-of-plane deflections were monitored optically by an auto focus sensor, while pressure was applied from the KOH cavities on the wafer backside. After the dimensions of each sample were measured with an optical scan, the pressure was incremented in steps of 5 kPa. The deflected membrane profile was determined after each pressure step, and the maximum out of plane deflection at the center of the membrane was recorded. Repeating this procedure until fracture, the pressure–deflection curve and the maximum fracture load were determined for each of the tested structures. Further details of the experimental procedure can be found elsewhere (Paul and Gaspar 2008). The samples underwent deflections that were up to three orders of magnitude larger than the average film thickness and hence, the pressure–deflection curves were strongly dominated by the membrane effects. Here, the experimental data was analyzed using a model that considers the dominant membrane stresses, the rotation of the elastic supports, and the bending stresses that develop at the supporting edges. The Poisson's ratio and Young's modulus were then calculated by comparing the response of square and rectangular shaped structures based on standard membrane theory. The results are summarized in Table 6.4. The calculated elastic moduli, E, are smaller than the previously reported values (Paul and Gaspar 2008; Alan and Sarro 2008). Yet, they remain constant for different thicknesses. However, as the size scale changes from 1 μm down to 10 nm, the intrinsic stress in the films changes from tensile to compressive.

Finally, for each tested sample, the stress distribution corresponding to the fracture load was calculated. The maximum tensile stress value within each membrane was inferred as the fracture strength of the sample. Fracture strength probabilities from successive bulge tests are plotted in Fig. 6.13. As expected, there is a very strong dependence between sample size and strength. Strength increases fourfold from 2.9 to 13.5 GPa with decreasing sample thicknesses (a significant difference was not observed between the strength of 10 and 16 nm thick samples;

Table 6.4 Estimated material properties for SiN

Thickness h (nm)	Elastic modulus E (GPa)	Poisson's ratio S	Intrinsic stress σ_0 (MPa)
10	142.9	0.3	−136
16	165.6	0.3	8.3
1040	162	0.3	94

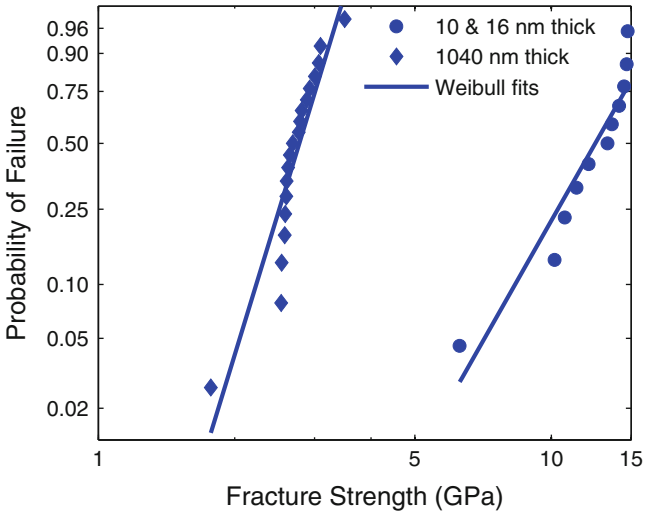

Fig. 6.13 Weibull strength distribution for rectangular membranes with different thicknesses. Strength increases from 2.9 to 13.5 GPa as membrane thickness is reduced (Alan et al. 2009)

hence, the data for both thicknesses were pooled). This size effect is generally attributed to the lower number of critical defects at smaller volumes.

6.8.2 Requirement 2: Allow Heating of Gas and Specimen with a High Accuracy in T

The MEMS heater has as big advantage that the power needed for the heating of the sample is small. In the design of the heater, this is achieved by realizing local heating inside or on top of the central part of a thin membrane. Because the heat conductance through the membrane to the supporting Si on the sides of the membrane is poor, one can easily obtain a temperature of 1000 °C in the center of the membrane, whereas the temperature of the Si hardly increases. We typically measure temperatures less than 40 °C for the Si chip for a heater temperature of 1000 °C. Note that the heat transfer to the Si chip depends on the distance from the heater to the Si and the thickness of the SiN. To reduce the heat transfer, one can increase the membrane size or reduce the thickness of the membrane, which indeed is an efficient way of heat transfer reduction, but increasing the size of the membrane width leads to more bulging of the membrane upon heating and a very substantial decrease in the membrane thickness can lead to more easy drum-like vibration of the membrane, which leads to loss of resolution when the sample is tilted.

Figure 6.14 shows a schematic presentation of the components in the heater chip and the holder that are relevant for the discussion on the drift properties of the total

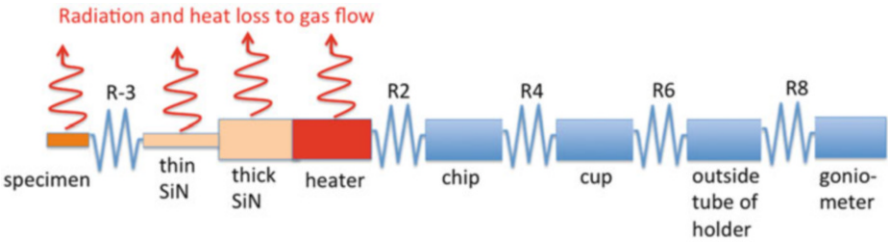

Fig. 6.14 Schematic representation of the various thermal resistors (R1–R8, where R3, R2, R4, R6, and R8 represent the connections between the various parts) that determine the heat transfer of the heater to the goniometer of the TEM. Note that the outer tube is connected to several parts of the goniometer with components that have their own thermal resistance and contacts with the final heat sink. Also the specimen itself, its contact with the support of the heater and the support-heater contact introduce thermal gradients and thus the real situation is more complicated than indicated here

system. Figure 6.14 depicts the various components as a series of thermal resistors. One can relatively easily determine the temperature of the heater by the resistance of the heater. This obviously requires a calibration, which for instance can be done on a local scale (e.g., 10 μm) using the Raman spectrum of Si (Hart et al. 1970) or carbon nanotubes (Huang et al. 1998). Once the heat distribution in the heater is characterized by local Raman spectroscopy, a pyrometer can be used to determine the temperature over a bigger area like 200 μm. The actual temperature of the specimen can be different from that of the heater because there are several thermal resistors between the sample and the heater (see Fig. 6.14). When the heater is in vacuum, a significant difference between heater and specimen only occurs if the temperature is well above 600 °C. This is because radiation becomes important above this temperature. In this case, the sample temperature will be lower than the heater temperature to an extent that is determined by the radiation losses of the various components from heater to specimen and the heat resistances of these components. For instance, we noticed a difference in the evaporation speed of the Au particles on graphene suspended over an 8 μm hole in the SiN: the evaporation was significantly slower in the central part of the graphene sheet. At low temperatures, the radiation is relatively small and one can assume that the temperature of the sample is about equal to that of the heater even if the thermal resistance between the thin window and the sample is high because there is no energy loss.

When a gas is used (either in an ETEM or an NR), the situation is very different because the gas acts as a heat exchanger between the heater/sample and the surrounding area. Since the power to obtain the set temperature is steered by measuring the resistance of the heater, the effect of heat dissipation by the surrounding gas is fully taken into account. In Tables 6.5 and 6.6, two measurements are given, one for nitrogen and one for helium. The heat exchange of helium is much larger than that of nitrogen; the latter is comparable to that of oxygen and argon. The heat exchange of hydrogen is comparable to that of helium. For example, compared to heating in vacuum, the power required to heat the Pt wire

Table 6.5 Changes in power to microheater with applied pressure (as read from the gauge from the nitrogen bottle) in a nitrogen atmosphere

P (bar)	T (°C)	R (Ω)	P (mW)	I (mA)
~10^{-3}	37	169	0.102	0.77
~10^{-3}	400	270	8.8	5.5
~0.1	400	270	20.1	8.60
~0.5	400	270	20.1	8.63
~1.0	400	270	20.2	8.65
~3.0	400	270	20.2	8.66

Table 6.6 Changes in power to microheater with applied pressure in a helium atmosphere as measured as the system was connected to a vacuum pump

P (mbar)	T (°C)	R (Ω)	P (mW)	I (mA)
Helium				
10^{-5}	30	281	0.181	0.80
10^{-5}	400	387	8.60	4.72
10^{-4}	400	387	8.60	4.71
1.4×10^{-2}	400	387	8.69	4.75
10^{-1}	400	387	9.51	5.0
5×10^{-1}	400	387	11.2	5.4
1.0	400	387	13.4	5.9
1.5	400	387	15.5	6.3
2.0	400	387	16.8	6.6
5.0	400	387	22.6	7.4
10	400	387	27.1	8.1
20	400	387	32.4	8.9
40	400	387	35.3	9.6
50	400	387	36.6	9.8
100	400	387	38.5	10
250	400	387	39.9	10.1

to 400 °C is about two times higher for 100 mbar nitrogen and four times higher for 100 mbar helium. A calibration based on a vacuum condition would lead to using an inaccurate required power to reach a certain temperature, i.e., the obtained temperature would be more than 100 °C lower in both cases. This signifies the importance of a real temperature determination, for instance based on a resistance. In fact, a four-point resistance measurement can be realized by adding another resistor than the heater, but this would require two extra electrical contacts. It would also require some extra microfabrication steps in the cleanroom because the heater and the T measurement wires will be on top of each other and need to be separated by an isolating layer such as SiN.

Thus in order to have a reliable temperature in a gas environment, the temperature has to be controlled by a device component that allows for a temperature

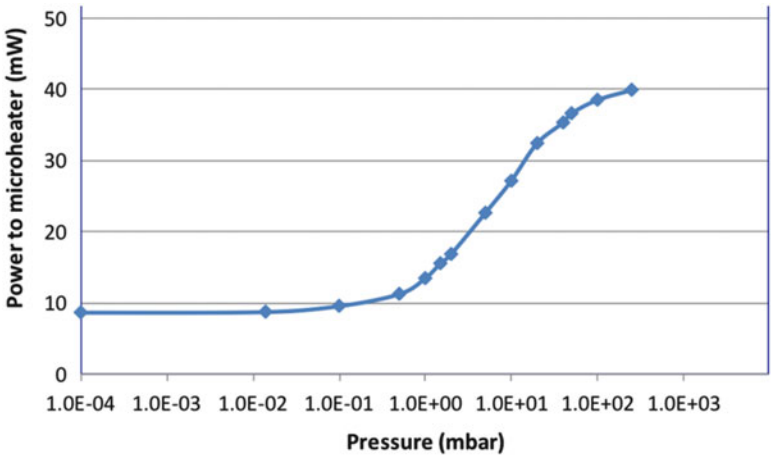

Fig. 6.15 Power needed for the microheater to maintain a temperature of 400 °C at different helium pressures

determination. This could be done for instance by constantly measuring the resistance of the heater (we are using this method) or by a Raman optical system. Note that the latter requires a dedicated TEM within-column space for the Raman optical microscope. We have used Raman for an ex situ calibration of the temperature distribution, for which we have built a dedicated measurement setup (Fig. 6.15).

Figure 6.16 shows simulations of the heat distributions in a vacuum environment of two types of heaters, a full spiral (left) and a flat center heater (right). In both cases, the thickness of the SiN is 400 nm. A disadvantage of the full spiral heater is that the central area with a diameter of about 100 μm with an equal temperature is not completely flat due to the presence of the Pt lines of about 150 nm thick. Due to this it is, for instance, difficult to place exfoliated graphene over the holes. The center part of the flat center heater is completely flat. Note that the central flat heater has a slightly lower temperature, which is due to radiation loss. An almost constant temperature for the flat center is seen for temperatures below 600 °C, where radiation losses are very small.

6.8.3 Requirement 3: Easy Loading of the Specimen

The samples to be studied with in situ TEM analysis are pieces of metals, ceramics, thin-films on substrates, or even soft biological materials. Over the years, several successful specimen preparation techniques for various kinds of materials have been developed for conventional TEM analysis. For conventional TEM studies, the most common specimen preparation techniques include electropolishing, ion-milling, grinding the specimen to extremely fine particles (<100 nm), and

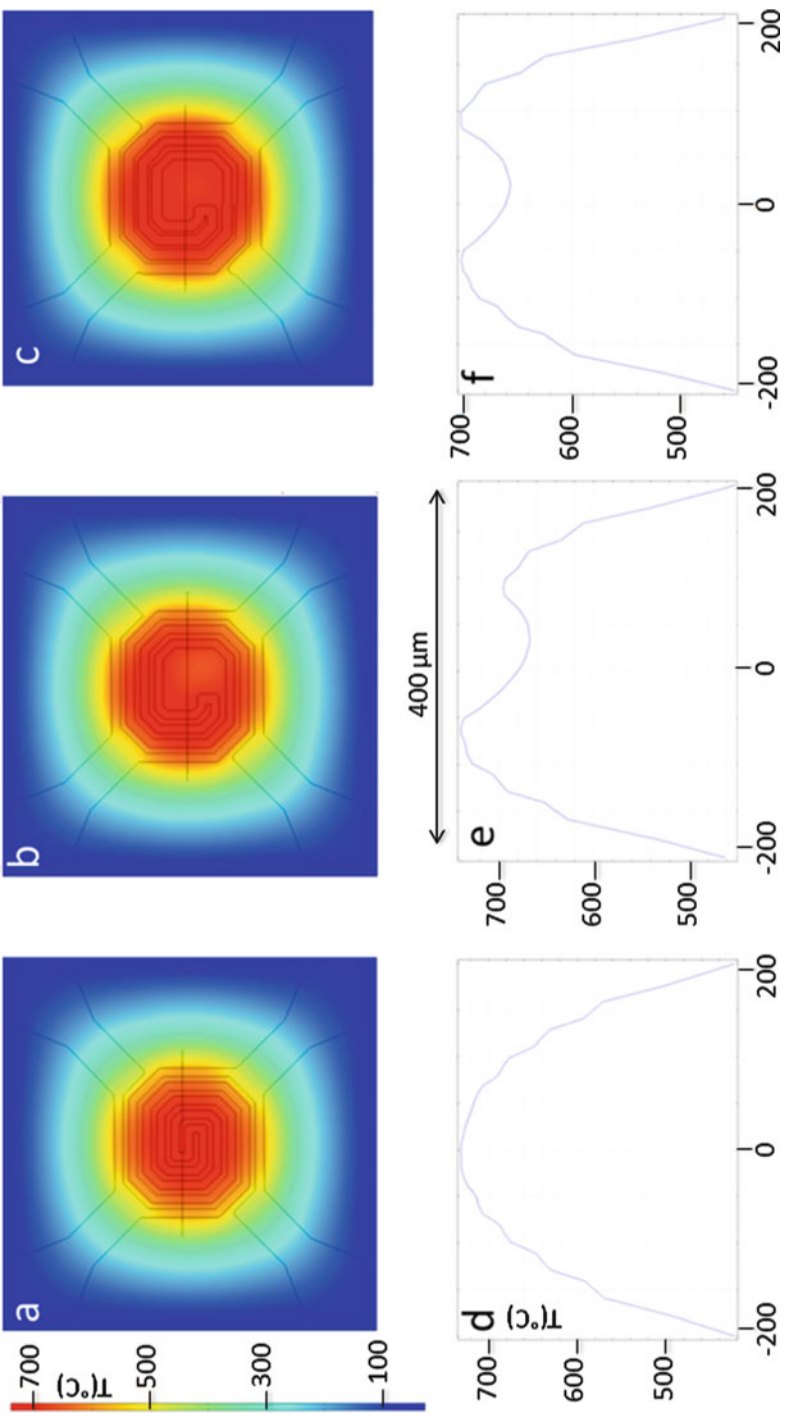

Fig. 6.16 Simulated temperature distribution across the membrane incorporating a Pt heating coil of different shapes. In (**a**), the spiral is continuous up to the center. In (**b**), a flat center area in the middle is present. On one side of the central flat area, four point lines are present and on the other side three point lines. Due to this, the temperature profile is asymmetric. In (**c**), the same asymmetry is number of lines of the heater is presented as in (**b**), but the width of the lines is adjusted such that a symmetric temperature distribution is obtained. The temperature profiles of the center 400 µm of (**a–c**) are given in (**d–f**). With two types of heating coils, one with a continuous heating coil (**a**) and one with a flat center in the middle (**b**). (**c**, **d**) Represent line-scans of the temperature distribution in the NR along the horizontal axis through the center of the heating spiral. Similar results as to (**a**) are reported by Vendelbo et al. (2014), who included the presence of a CO gas

dispersing on standard TEM grids and specialized techniques like ultramicrotomy and focused ion beam (FIB). Almost all of these techniques can be adapted for in situ TEM studies using the NR provided the specimen is transferred successfully to one of the two chips (the chip at the bottom). Useful tips for loading the sample are given by DENSsolutions (http://denssolutions.com/tips-tricks/sample-preparation/). We have carried out an experiment on the dehydrogenation of Pd deposited on the top as well as the bottom membrane as a function of temperature and hydrogen pressure and observed that the temperature difference between top and bottom chip was less than 10 K. Nevertheless, it is best to put the sample on the chip half that contains the heater. Conventional TEM specimens are 3 mm circular discs that fit in standard specimen holders. However, owing to the limited size of the microheater and the electron transparent windows the sample size in an NR is more limited. Since one wants to keep the distance between the two membranes small, the sample should also be thin over the whole lateral shape (e.g., less than 2 μm). In addition, really thin sample areas are required over some of the electron transparent windows (typically ~5 to 20 μm in diameter). Of course, the thin part of the specimen should precisely be placed on such a window.

Ceramic TEM specimens are prepared by just crushing a bulk material and putting them in suspension. Nanoparticle suspensions or suspensions of biological specimens are best transferred by sonicating the suspension for sufficient amount of time and drop casting a sample. Because the densities of these suspensions are usually high enough to cover most of the TEM windows, there is enough material to carry out in situ TEM studies.

Bulk metallic specimens and thin-films over substrates for which cross-section specimens are required, specimen preparation using FIB works best. An added advantage of using an FIB is that very specific areas of interest can be selected. Examples are cross-section samples across an interface, specimens from a special phase, and specimens corresponding to a specific crystallographic orientation (Fig. 6.17). Such specimens are typically of the size ~15 μm × 5 μm with thicknesses ≤100 nm.

Specimens can be transferred to the TEM windows of an NR very precisely by using an in situ micromanipulator available on most modern FIBs or by using the conventional ex situ micromanipulator employing a glass capillary with a sharp tip. An example of FIB cross-sectional preparation across a grain boundary in an aluminum alloy and its ex situ transfer using a glass micro capillary is shown in Fig. 6.17c–e. If there are specific areas of interest in conventional 3 mm disc specimens, these areas can be cut precisely using the FIB and transferred to the bottom chip. Upon successful transfer, the specimen is ready for either in situ heat-treatment studies using a heating-holder compatible with this bottom chip or, for in situ environmental TEM studies when the bottom chip is coupled to a top chip to make an NR as shown in Fig. 6.18.

The bottom and the top chips are first positioned facing each other in a custom-made alignment tool as shown in Fig. 6.7. The procedure of alignment starts with coarsely positioning the top chip (facing downwards) such that the large SiN windows in both the top and bottom chip coincide with each other. The alignment

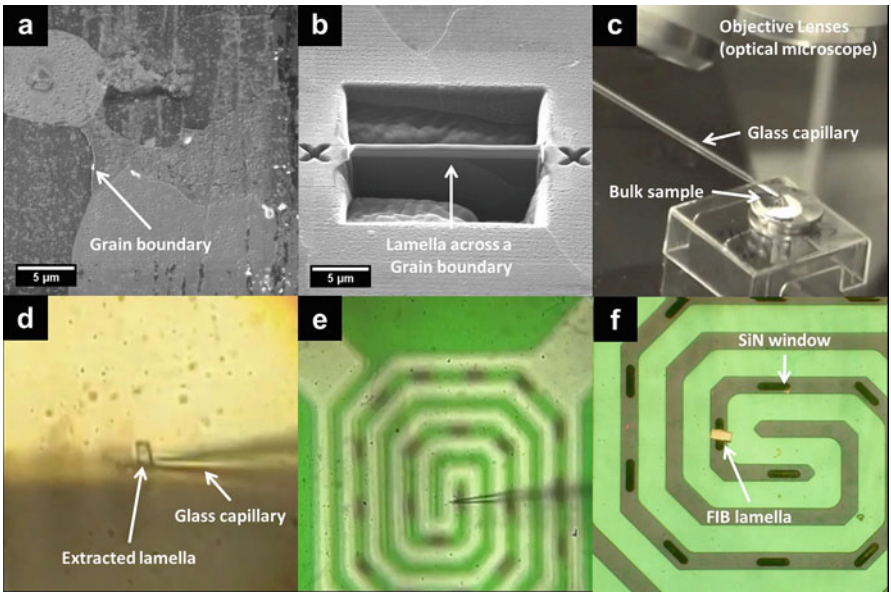

Fig. 6.17 (**a**) FIB-SEM image showing grain boundaries in an aluminum specimen. (**b**) FIB cross-sectional lamella prepared across grain boundary shown in (**a**); the lamella at this stage is cut and finally thinned to thickness <100 nm and released to stand freely in the cavity. (**c**) Photograph showing glass capillary controlled by a hydraulic micromanipulator. (**d**) Optical micrograph focused on extracted FIB lamella from a cavity as shown in (**b**). (**e**) Optical micrograph focused on glass capillary positioned precisely over a TEM window; the hydraulic micromanipulator allows positioning the lamella with an accuracy of ~2 µm. (**f**) FIB lamella deposited over a thin SiN window, ready for imaging either for in situ heating experiments, or for assembling an NR

tool consists of micrometer screws connected to metal plates which displace the top chip with ~1 µm step size. The alignment tool has the capability to precisely displace the top chip only in the *XY*-plane. In order to avoid any displacements in the *Z*-direction, the top chip is restricted to just horizontal movement by fixing the lid. Once the window(s) of the top and the bottom chip coincide, the top chip is moved down in the *Z*-direction by gently screwing down the lid. While fastening the top chip, one has to be very careful not to damage the top chip by any excessive torque. An indication of the right channel height for in situ TEM experiments is that both the top and the bottom chip are visible in the same focal plane in the optical microscope.

The alignment tool described here requires the NR to be glued either by an epoxy-based glue, super glue, or water glass. This principle of aligning the top and the bottom chips together has been extended further to avoid gluing altogether by including an O-ring in between the chips by creating a groove in the top chip. For this, the alignment tool has been adapted to allow either a retractable tip or a TEM holder with gas-flow channel. In these cases, the top chip is held in position after alignment by the lid. The O-ring in between the chips helps to maintain the NR leak-tight to allow live imaging inside the TEM.

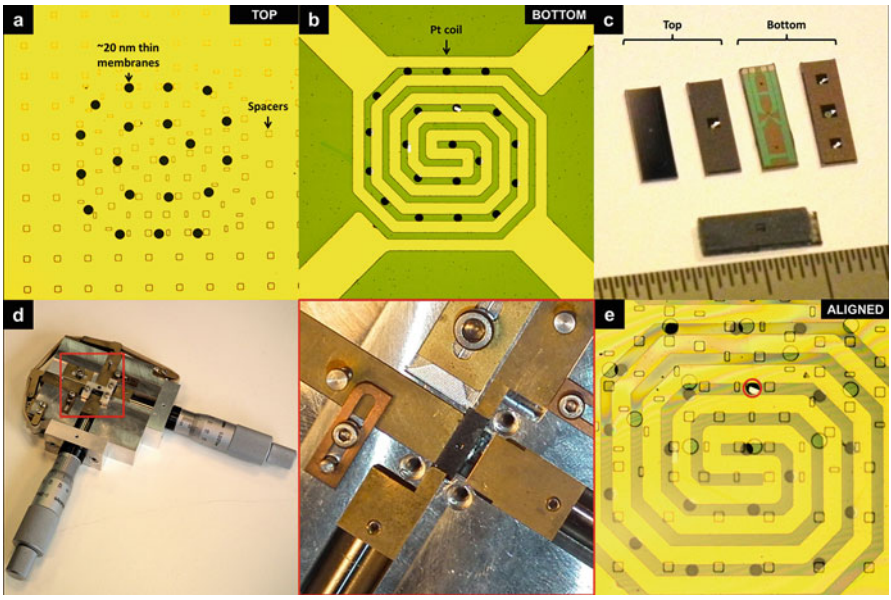

Fig. 6.18 Optical micrographs showing the large SiN windows of (**a**) the *top* chip and (**b**) *bottom* chip. These windows are at the *center* of the chips shown in (**c**). The *bottom* chip is placed facing upwards in the alignment tool shown in figure (**d**) while the *top* chip is placed facing downwards. Zoomed image of the area bounded by *red box* at the *center* of the alignment tool shows the metal plates connected to micrometer screws which displace the *top* chip with displacements as small as ~1 μm. The lid is placed over the chip assembly and tightened enough to allow displacement only in the *XY*-plane. After the window(s) in the *top* and the *bottom* chip are aligned as shown in (**e**), the NR is ready for gluing to be used either in a static gas system or a flow-gas system

6.8.4 Requirement 4: Allow a Controllable Gas

Ultimately, one would like to control the gas pressure and the composition to the extent that both can be changed instantaneously. This is, however, not possible due to the geometry of the NR and the geometry of the holder. The NR has very narrow channels creating barriers for the fast gas flow, needed for a rapid gas exchange. Thus the small size of the NR, giving on the one hand the advantage of fast temperature changes without experiment-limiting specimen drift, has on the other hand the disadvantage of slow gas exchange. Also, the NR is only hot in the center of the two membranes, and the rest of the NR is at about room temperature. Thus, some of the reaction products could be deposited on the cold part of the NR. Furthermore, the diameter of the TEM holder does not allow for electrically controlled valves close to the NR. Therefore, the gas tubes of the holder have to be pumped to exchange the gas.

If one needs only a fixed gas pressure, one could use a static gas holder for which the exchangeable tip can be extended with a pressure meter for instance. This requires extra electrical wires at the outside of the holder, making the holder

more complicated. If one needs a gas flow or a change of the gas composition, a flowing gas holder is required. As mentioned in Table 6.2, the static gas and flowing gas holders have their own advantages and disadvantages.

6.8.5 *Requirement 5: Compatibility with Normal TEM Operation*

One of the big advantages of an NR over an ETEM is that the experiments can be done in any TEM, provided that the holder is completely compatible with the normal operation of a standard TEM sample holder. This is fairly easy to realize. Note that with this approach also low-end TEMs can be used, which are actually sufficient for quite some experiments. With the possibility to use also low-end TEMs, in situ TEM is also attainable for relatively less equipped research groups. Note in this respect that for an LaB_6 type of electron source the restrictions on airtightness of the NR and the holder are less stringent. This is because in the case of a collapse of the NR, damage to the gun is less severe and replacing the gun is much less costly and time consuming than for an FEG. We have never had a problem with a collapse of the NRs, even in high-risk experiments in which we explored the maximum pressure or temperature allowed, for which we typically used our LaB_6-operated TEM.

The gas holder can be made completely compatible with a standard goniometer, such that the in situ experiments are not hampering the normal use of the microscope in any way.

6.8.6 *Requirement 6: The NR Should Be Easy to Use and Made as Disposable*

The challenges involved in in situ TEM experiments at relatively high gas pressures require sophisticated MEMS fabrication to obtain reliable miniaturization. The sample clamping and preparation need to occur at a very high control, which typically requires about 40–100 cleanroom process steps. Evidently, these challenges become more difficult when one wants to combine several external stimuli such as an electrical measurement in a gas environment. If more stimuli are added, a further miniaturization has to be realized, given the limited available space in the electron microscopes.

6.8.6.1 The Cleanroom Process for the Sandwiched NR

The design of the sandwiched NR consists of two different chips which are an MEMS-based heater chip (bottom) and O-ring chip with grooves (top). The

MEMS-based heaters that are presently used in the NRs are the same as those for in situ heating TEM studies. These heaters have been shown to be very efficient in TEM studies, such as morphological transformation of gold nanoparticles (Young et al. 2010), sculpting of graphene (Song et al. 2011), thermal stability, and degradation of nanoparticles (Yalcin et al. 2014). The heaters have platinum (Pt) as the heat-conducting material, which is embedded in a ~400 nm thick SiN membrane with 6 μm wide viewing windows of ~20 nm thick SiN. Since the embedding requires two SiN deposition steps, Pt has to be stable in the gases used in the second SiN deposition. In the case of an NR, embedding of the Pt by SiN is essential to prevent that Pt is reacting with the experimental gas. Our MEMS heater contains four electrical connections that allow for temperature determination and heating. The other chip (also called top chip) has a groove depth of ~300 μm for the O-ring. The top chip consists of a ~500 nm thick SiN membrane with 12 μm wide viewing windows of ~20 nm thick SiN. MEMS-based heaters and top chips can withstand at least 1 bar pressure.

In Fig. 6.19, the fabrication steps are shown for bottom and top chips. The steps include low-pressure chemical vapor deposition (LPCVD) of SiN, plasma-enhanced chemical vapor deposition (PECVD) of SiO_2, lithographic definition, dry and wet etching, dicing, and cleaning. Both Si wafers have an initial thickness of 500 μm. The initial step to fabricate a heater is LPCVD of 200 nm thick SiN that acts as an isolation layer between Pt and Si. The platinum layer is embedded in ~400 nm thick SiN layer in total. Subsequently, by optical lithography the viewing windows with a diameter of 6 μm are patterned onto SiN layer by anisotropic plasma etching based on AR and CHF_3. The last LPCVD step is performed to obtain 20 nm thick SiN electron transparent viewing windows. The silicon substrate is etched by KOH to get SiN membrane devices. The final steps are dicing the wafer and cleaning which leads to carbon-free, non-contaminated high quality chips.

Similar to heater chips, the production of the top chips is started from a 500 μm bare silicon wafer. PECVD of SiO_2 is used as a mask layer, and the ~300 μm depth grooves are patterned and transferred to silicon layer by SF_6-based dry etching. The mask layer SiO_2 is removed by selectively wet chemical etching with buffered HF. LPCVD SiN is performed to get membrane ~500 nm. The viewing windows with a diameter of 12 μm are patterned and transferred to SiN layer. The size of these windows is bigger than the size of the windows in the heater to increase the alignment tolerance. The thin SiN deposition is performed, and silicon is etched by KOH from the back side to create a free standing SiN membrane. The size of the top chips is slightly smaller than the heaters to have space for electrical contact pads, see Fig. 6.2.

6.8.6.2 The Cleanroom Process of the One-Chip NR

The cleanroom process of fabricating the one chip NR is sketched in Fig. 6.20 (Creemer et al. 2011). The process roughly consists of the following steps: (1) Growth of wet thermal SiO_2 on a 100 mm Si wafer (0.2 μm); (2) Deposition of low-stress SiN*x* (0.7 μm); (3) Photolithography and wet etching holes for

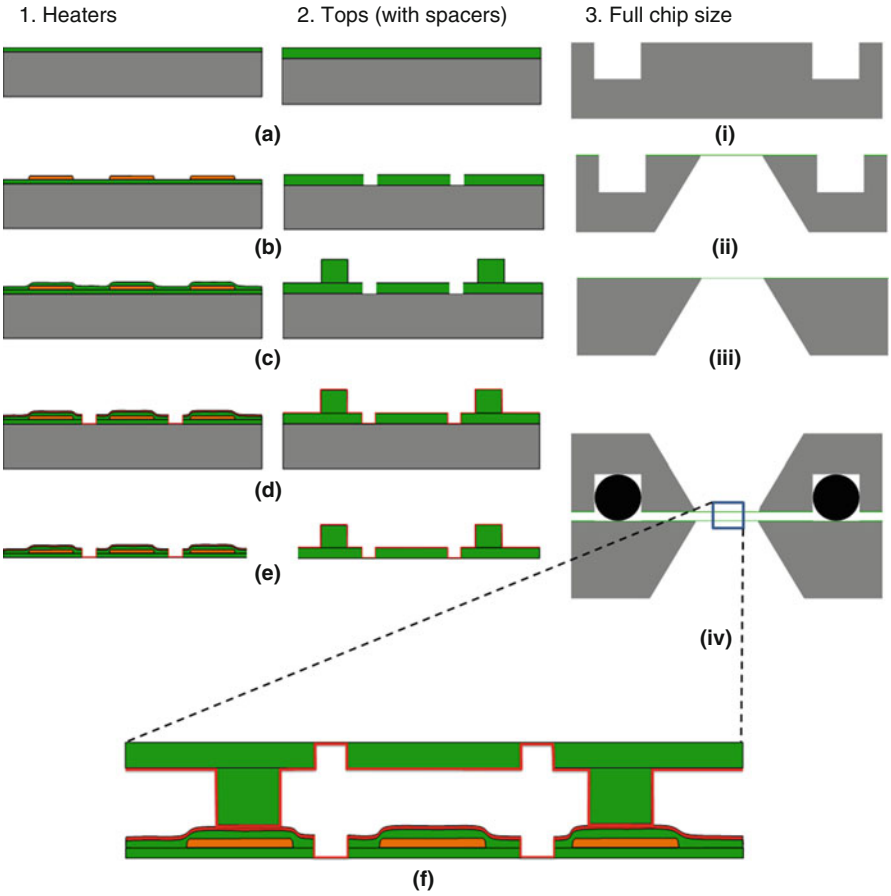

Fig. 6.19 Schematic cross-section of fabrication steps for heaters (**1**) and *top* chips (**2**) are demonstrated. (**3**) Shows the full size chip for heaters and tops for better understanding of sizes. (**1a**) and (**2a**) are deposition steps of SiN. (**1b**) is obtaining the Pt/Ta after deposition and etching, while (2b) is opening the electron transparent windows with optical lithography and dry etch of SiN. (**1c, 2c**) are LPCVD of SiN as a cladding layer for heater and spacer for *O-ring* tops, (**1d**, **2d**) after lithography of viewing windows and deposition of ~20 nm thick LPCVD SiN. (**1e**, **2e**) Are the final step of fabrication which are after back side lithography and wet etching of silicon by KOH. (**3i**) is after opening the *O-ring* grooves and (**3ii**) is after KOH etching of Si. (**3iii**) Shows the heater chip after KOH, and (**3iv**) is the full size of chips when they are mounted together including the *O-ring* rubber with the enlarged view in (**f**)

electron transparent windows; (4) LPCVD of Tetraethyl orthosilicate (TEOS) as a sacrificial layer (1.0 μm); (5) Patterning of TEOS for pillars by using buffered HF (BHF); (6) Deposition of top SiN*x* (0.5 μm) and plasma etching to create access holes to remove the TEOS in BHF; (7) Inside coating with TEOS and 15 nm SiN; (8) Plugging the access holes with SiN; (9) Creation of the Pt heater; (10) Local KOH etching of the mono Si to expose the electron transparent windows.

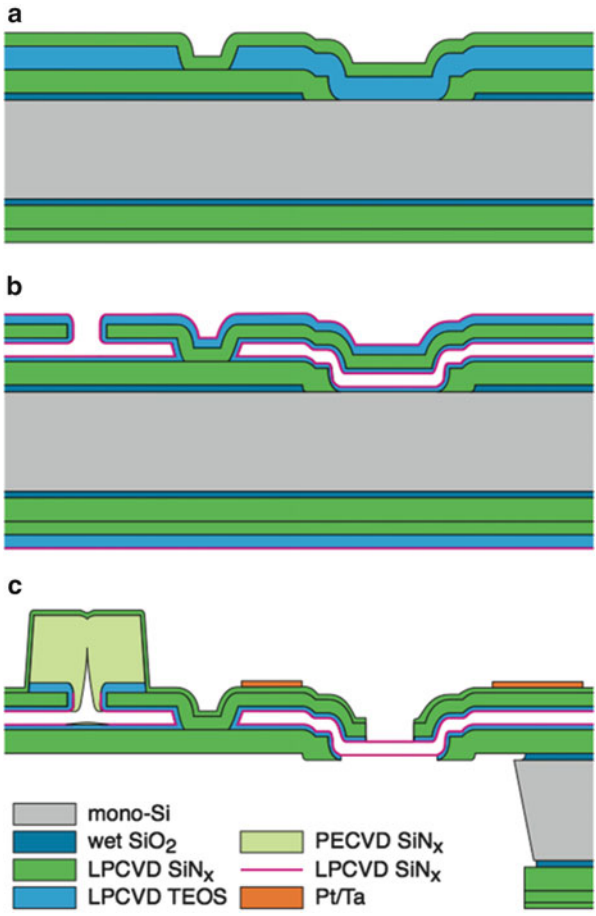

Fig. 6.20 Schematic cross-section of the NR, in different stages of the fabrication (Creemer et al. 2011). (**a**) Initial depositions of wet thermal SiO_2 and low-stress SiN*x*, followed by photolithography and wet etching holes for electron transparent windows, and deposition of LPCVD TEOS sacrificial layer. (**b**) Sacrificial etching and internal coating of the channel with the window material. (**c**) Final thin-film structure: plugged channel, released windows. *Fabrication steps*: Growth of wet thermal SiO_2 on a 100 mm Si wafer (0.2 μm). Deposition of low-stress SiN*x* (0.7 μm). Photolithography and wet etching holes for lower electron transparent windows. Deposition of LPCVD TEOS as sacrificial layer (1.0 mm). Patterning TEOS for pillars using buffered HF (BHF). Deposition of top SiN*x* (0.5 μm) and plasma etching to create access holes to remove the TEOS in BHF. Inside coating with TEOS and 15 nm SiN*x*. Plugging the access holes with SiN*x*. Creation of Pt heater. Local KOH etching of the mono Si to expose the electron transparent windows

The important concept is the introduction of a sacrificial TEOS layer that can be removed later in the process, followed by (a) the internal deposition of again an LPCVD TEOS layer as an etch stop for later steps, and (b) the LPCVD SiN*x* electron transparent 15 nm layer (exposed later by a KOH etch of the

monocrystalline Si substrate). The access holes to remove the sacrificial layer are "plugged" by a PECVD SiN local layer sealed with another PVCVD SiN layer. The resistive heater is made by evaporation of Pt (0.2 μm) on top of an adhesion layer of Ta (15 nm) with the aid of a lift-off process. The final steps are the release of the electron transparent windows using buffered HF etching. The inlets and outlets of the channel are created by plasma etching using a shadow mask.

6.8.7 Requirement 7: The Carbon Contamination Should Be Negligibly Small

Since the characterization of a material under a gas atmosphere requires that the surface is very clean, the formation of C-contamination has to be prevented during the in situ TEM experiments. If available, a reliable method to remove any carbon is required. Keeping the sample free from C-contamination usually requires the absence of hydrocarbons, whereby the presence of water accelerates the formation of C-contamination. Note that the electron beam is an extremely efficient hydrocarbon "detector" because the electron beam can crack the hydrocarbon very efficiently to C. The presence of water plays an important role because it strongly effects the surface diffusion of hydrocarbons and probably plays a role in the cracking process as well. For instance, heating a sample in vacuum at 300 °C for a few minutes allows for subsequent C-deposition-free experiments at room temperature (see Fig. 6.21). Alternatively, cooling of the NR to, e.g., −60 °C while heating of the membrane to, e.g., 400 °C will allow trapping of water and hydrocarbon molecules outside the reaction area, thereby strongly reducing the formation of C-contamination as we have verified experimentally.

In Fig. 6.21, the deposition of C can be observed well, if one defocuses. In this case, a thick contamination was deposited by a beam roughly of the size of the contamination. Note that if a larger beam size is used, most of the contamination is deposited as a ring at the edges of the beam. If the C-deposition is much smaller than that shown in Fig. 6.21a, it can be difficult to verify the absence of any C-deposition. When a hole is available, C-deposition can be observed by growth of the edge as explained in Fig. 6.21b. When a hole like the one in Fig. 6.21b is not available and the C-deposition is small, we use a small spot size of, e.g., 5 nm and keep the beam for about 10 min at the same position (so no drift should be present) with the sample at about zero focus (to be sure that the actual beam on the sample is indeed small). Note that the beam should not be so intense that a hole is drilled in the electron transparent window as in Fig. 6.21b. Next at high under focus or over focus we check whether there is a local intensity change. If there is a hole as in Fig. 6.21b, we put the beam on the edge of the hole (as the yellow dot in the inset of Fig. 6.21b and keep it there, e.g., 10 min. In the case of C contamination, the edge will "grow" along the edge of the beam. If the growth is relatively fast, one can see it if the recording is done in movie mode.

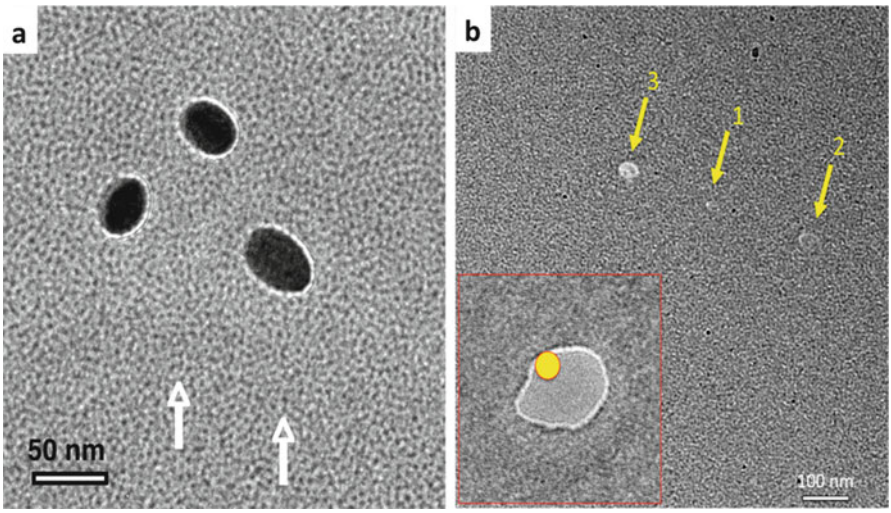

Fig. 6.21 (**a**) Three C-contamination dots deliberately created on a C film using a dirty C film on a MEMS heater, by focusing the electron beam on these three areas for 2 min. Next, the sample was heated at 200 °C for 2 min. Subsequent focusing of the electron beam at the areas indicated by the *white arrows* for several minutes did not lead to any visual contamination. Note that a strong defocus was used to image the C-contamination dots. (**b**) shows that a very intense fully focused electron beam can remove SiN finally resulting in a hole in the SiN membrane. The beam was positioned at the locations indicated by the *arrows* 1, 2, and 3 for 1, 2, and 5 min. At *arrow* 3 a hole is present. This hole can be used for a precise determination of the absence of C-contamination, by putting a beam with a relatively low intensity such that no SiN is removed at the edge of the hole as the *yellow spot* in the *inset* in (**b**). In case of any C-contamination, one can see the growth of material at the edge real time

6.8.8 *Requirement 8: The Electron Transparent Membranes Should Be Uniform in Thickness and Amorphous*

Preferably, one would like to have no effect of the presence of the two membranes, but this is not possible of course. Typically, one wants to image the sample relatively close to zero focus. In this condition, one of the two membranes will also be close to zero focus, but the other one will not be and the modification of the electron wave by this membrane can be significant. This can be seen in Fig. 6.22, where two samples are shown at zero focus and 10 μm focus. Clearly, the effect of the membrane is much less at zero focus. Furthermore, it is clear from Fig. 6.22 that thickness variations (in the form of local bumps) can have a strong effect on the image. Therefore, the interpretation of a sample between one or two windows with thickness variations will be less easy. Therefore, we have put quite some effort in making uniform windows, which are as thin as possible. During the deposition of the thick SiN for the electron transparent windows, we add an Si test wafer, which can be tested for roughness using STM. Typically, we get a roughness of 0.4 nm RMS. Note that even when one has perfectly uniformly thick electron transparent

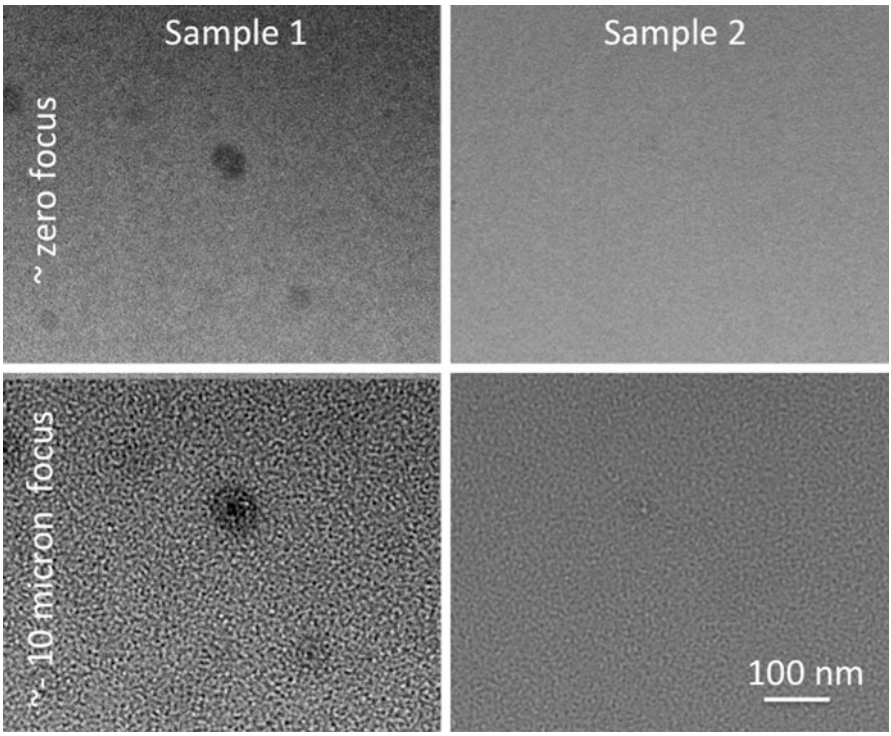

Fig. 6.22 Example of two electron transparent ~20 nm thick SiN windows at zero focus and a focus of about −10 μm. In the *left* example, SiN-like particles are present of different sizes. In the *right*, hardly any particle can be observed. Note that such particles are much better visible if the imaging is done at high under or over focus

windows, the relative positions of areas of interest can affect the measurement. For example, when both membranes are covered with particles of the sample to be studied, particles on one membrane will strongly hamper the study of particles on the other membrane if their projections partly coincide in one or more of the required viewing directions.

6.8.9 Requirement 9: The Length of the Gas (or Liquid) Column Should Be Small (Matching the Required Resolution)

We have done experiments with thin SiN electron transparent windows to determine the minimum required thickness to maintain a 1 bar pressure difference over the window without breakdown. We have noticed a significant failure rate (>10 % of 10 chips with each 16 electron transparent windows) when the windows were 10 nm or

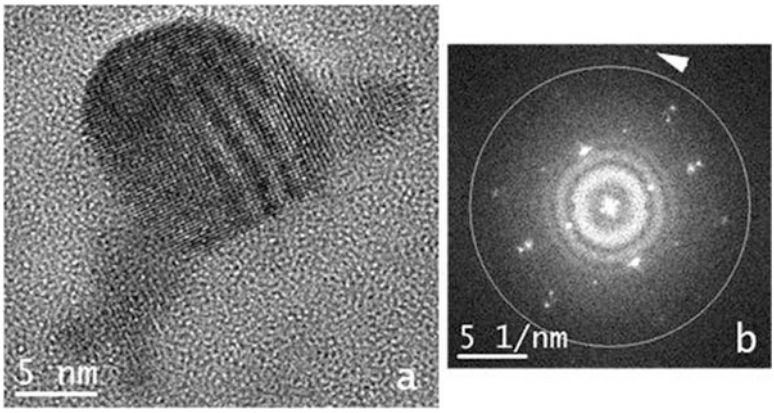

Fig. 6.23 (**a**) PdO_x nanoparticles in O_2 with pressure of 0.65 bar at 500 °C. (**b**) FFT of image (**a**), the white circle is 1 Å. The *triangle* indicates a diffraction spot with a d-spacing of 0.88 Å. Note that the rings in the FFT are from the window not carrying the particle

thinner. Note that such a test will depend strongly on the quality of the deposited SiN. A thickness of 20 nm might be required for other SiN depositions to obtain no failure.

Assuming the thickness of the SiN windows is 15 nm, the total thickness of SiN is thus 30 nm. Taking as rule of thumb that the density of a gas at 1 bar is 1000 times smaller than the solid (of the same composition), a gas column of 20 μm of O_2 gas at 1 bar will be equal to 20 nm of solid O_2. The latter has a lower scattering potential than the two 10 nm thick SiN windows. Under these conditions, a good resolution can still be achieved as it can be seen in Fig. 6.23. This back-on-the-envelope estimation also shows that a large reduction of the gas column is not very useful, if the thickness of the SiN windows is not significantly reduced.

One could use thinner SiN membranes if the failure rate is reduced or by using a lower pressure in the NR. Note however, that normally the holder is first in air and thus the pressure on the outside of the NR is 1 bar and once inside the holder this pressure drops quickly to 0 bar. Starting for instance with a pressure of 0.1 bar inside the NR, one has a pressure difference of 0.9 bar. Only if the pressure inside the NR is kept the same as outside the NR by a shunt between the inside of the NR and the vacuum of the microscope, one can use electron transparent windows that do not withstand a 1 bar pressure difference.

6.8.10 Requirement 10: The Resolution Should Preferably Be the Same as that of a Standard Holder

If an HRTEM that allows 1 Å resolution is used for the NR experiments and this resolution is lost because of the NR-holder-HREM ensemble, the reason for the resolution loss can be: the thickness of the SiN membranes, the thickness of the gas

column, specimen drift, mechanical instability of the holder/NR ensemble, charging and other electrical instabilities, and/or the holder–goniometer interface. The specimen drift is discussed in more detail below. Our experimental results in getting 1 Å resolution show that all causes for resolution loss can be overcome.

In many cases, one is interested in experiments for which a relatively large field of view is needed. For instance, if the front of the oxidation of Pd to PdO moves fast and over a big area, one gets much more information from an overview movie with a relatively low resolution than a low field of view HREM movie.

Given the contradictory requirements of a high field of view and sometimes very detailed imaging, the best option is a combination of two detectors, whereby the first detector has a hole behind which at some depth a second camera is placed. If both cameras have $4k \times 4k$ pixels and the first one has an effective pixel size of 0.1 nm/pixel and the second one a pixel size of 0.02 nm, the problem is how to display this in an efficient manner given the nature of the human eye. The display should be such that: both images are displayed on the same monitor or an array of monitors; whereby the image of the second detector is shown in the center, and the first detector is displayed around this central area with the same magnification as the second detector and thus with 5×5 pixels in the display for each pixel of this camera. In this display mode, one can use the human eye, which is fine-tuned for focusing on the center with high resolution and still be able to detect movements and rapid changes in the periphery.

6.8.11 Requirement 11: The drift Should Be Small Enough to Record High-Resolution Images

We typically set our goal for the drift to be less than 3 nm/min. This allows 1 Å resolution imaging with an exposure time of 0.5 s, which we consider as a standard recording time. Such drifts are well obtainable as shown in the example in Fig. 6.23. In the case of imaging of changes, one prefers to obtain as many images as possible, and in such case exposure times of 0.5 s are rather long. Therefore, the possibility to record high-resolution images is not limited by the holder or NR.

6.9 Electron Beam Effects

Well-known artifacts of the electron beam during TEM experiments were evaluated for example by Egerton et al. (2004), also see Banhart (1999). Major artifacts are electrostatic charging due to bad electrical connection between the specimen and the holder, structural damage, and sputtering of the sample as the result of knock-on damage (elastic scattering of electrons) and radiolysis (inelastic scattering of electrons), specimen heating caused by inelastic scattering of the incoming

electrons by the specimen, and deposition of material on the specimen and support, i.e., carbon deposition due to hydrocarbons on and around the specimen. These artifacts depend to a large degree on the electron beam energy and intensity. For example, sputtering of the specimen can be neglected at 100 kV or lower, but will occur at 200 kV for light elements like carbon or silicon.

Aside the normal electron beam artifacts, important artifacts encountered in an NR are contamination and damage of the electron transparent windows or the specimen by the electron beam. Contamination of the specimen and the SiN windows caused by cracking of hydrocarbons inside or outside the NR by the electron beam is an important issue as described above: the presence of water molecules in the system has a major impact on the contamination of the sample caused by the cracking of hydrocarbons by the electron beam on the sample surface, see the experiments described in Fig. 6.21. Sputtering of the electron transparent SiN windows must be avoided obviously, since a hole drilled by an intense electron beam will create a leaky NR. In Fig. 6.21, an example of a hole drilled with an electron beam is visible. Typical electron doses used for hole drilling were reported as ~10^8 e/nm^{2}s (5 nm beam diameter, 200 kV) in a 40 nm thick SiN/SiO_2 window (Wu et al. 2005), and ~1×10^8 Am^{-2} in 10 nm thick SiO_2 windows (using a few nm beam diameter at 300 kV) (Storm et al. 2003).

Dose rates should be kept at a low value to avoid a visible influence of the electron beam on the sample under investigation itself. Vendelbo et al. (2014) found that at dose rates of 10,000 e/nm^{2}s (300 kV) and above, the investigated Pt nanoparticles in a O_2/CO gas-loaded NR are displaced in the projected image plane. In (de)hydrogenation experiments up to 4.5 bar H_2 in an NR (Yokosawa et al. 2012), an electron dose up to 1000 e/nm^{2}s (300 kV) did not influence the phase transition temperature.

6.10 Examples of Experiments

In this section, a few case studies will be presented to show the application of different NRs in in situ TEM experiments for understanding processes involving gas–matter interactions.

6.10.1 In Situ TEM on (de)Hydrogenation of Pd at 0.5–4.5 Bar H Pressure and 20–400 °C Using a Composite Flowing Gas NR

The composite NR was used (Yokosawa et al. 2012) to study the (de)hydrogenation of Pd crystals at hydrogen pressures up to 4.5 bar. An LaB_6 electron source in a Philips CM30T TEM was used for imaging. A dedicated gas handling system with

tubing to the NR TEM holder was used to regulate the hydrogen pressures ranging from 0 to 10 bar. Image plates were used for recording images and diffraction patterns. Also movies of the dynamic diffraction patterns were recorded during phase transitions using a Gatan Fiber-Optic Coupled Camera (25 fps).

A Pd thin-film was sputtered on the SiN of the bottom chip with the heater spiral, including the electron transparent windows. Heating to ~400 °C transformed the randomly oriented Pd crystals into closed Pd islands, which were 50–1000 nm wide and 15 nm thick. The distance between the 300 μm wide SiN windows was limited to 3 μm (no bulging) at vacuum (short cut to vacuum of TEM) and to 19 μm at 3.2 bar hydrogen gas, as measured by focusing at the bottom and top electron transparent window edges. This was less than when 1000 μm (in which case the bulging was about 36 μm) wide windows were used. However, with the smaller membrane diameter the temperature gradient is larger because the neighboring Si support acts as a heat sink. This temperature gradient and the indirect heating of the Pd crystals through the gas give some uncertainty about the temperature at the crystal. However, the observed α to β phase transition temperatures (see Fig. 6.24) correspond to the bulk measurements reported (Qian and Northwood 1988).

The phase transitions due to changes in temperature or pressure were visualized by using the differences in lattice parameters of the phases. Movies of selected area diffraction patterns were recorded. In Fig. 6.25, a series of patterns is shown after a sudden temperature drop from 140 °C to room temperature in a 0.8 bar H_2 atm. The lattice expansion caused by the hydrogen absorption results in a 3 % shrinkage of the (022) reflections in the patterns during the few seconds for the transformation to occur. Both the Pd and the PdH reflection are observed for single Pd crystal transforms during 1 or 2 s. This shows that the transformation occurs gradually and that the crystal orientation of the PdH is the same as the original Pd crystal. This was also observed from careful dark-field imaging during the transition by aligning the objective aperture at the position of the PdH reflection, thereby just omitting the closely positioned Pd reflection: it showed a gradual intensity increase from a crystal upon hydrogen absorption during 4 s.

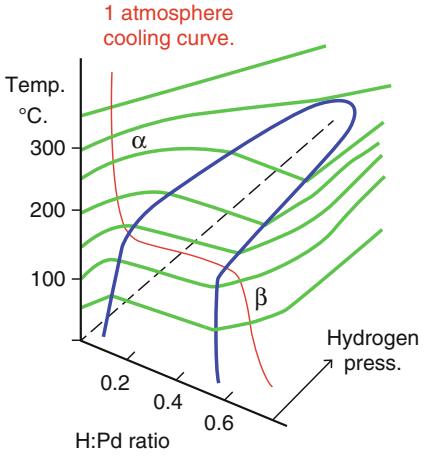

Fig. 6.24 Schematic Pd-H phase diagram. The H poor α-phase is fcc structured with lattice parameter 3.89 Å as pure Pd. The NaCl structured β-phase has lattice parameter 4.03 Å

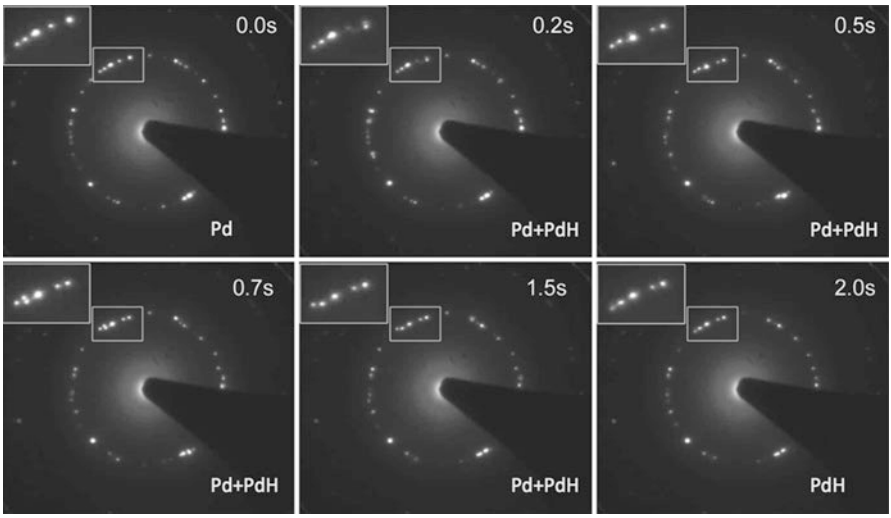

Fig. 6.25 Selected area diffraction patterns of a number of Pd particles with different orientations, after decreasing *T* from 140 °C to RT. The lattice expansion caused by the hydrogen absorption causes a 3 % shrinkage of the (022) reflections. At 0.7 s after the decrease in *T*, a "split" reflection is seen: this indicates a transition was going on from Pd to PdH during the recording of this pattern. The transformations of different crystals do not occur all at the same time

By changing the temperature in the NR gradually, a transition temperature can be found from the dynamic diffraction pattern. This is a more direct method than changing the pressure because a change in temperature is much faster. The transformation was shown to be reversible, but a hysteresis was observed between the α to β and β to α phase transition temperatures of 15 °C at 0.5 bar H_2 and 7 °C at 4.5 bar H_2. The pressure dependence of the transition temperature and the hysteresis is shown in Fig. 6.26. It is similar to the hysteresis found in bulk materials, showing the reliability of the in situ method. The in situ method presented by Yokosawa et al. (Yokosawa et al. 2012), however, showed differences in the transition behavior of individual Pd(H) particles: some particles were shown to transform consistently faster than others. Thus, the use of NRs for in situ TEM provides a tool to investigate (de)hydrogenation properties on a local scale.

6.10.2 Oscillatory CO Oxidation Catalyzed by Pt Nanoparticles Using Time-Resolved High-Resolution Transmission Electron Microscopy

For the development of catalytic materials employing nanoparticles (NPs), understanding the different reactivity of the nanoparticle surfaces and facets is a topic of constant research. For example, Pt NPs are used in the automotive

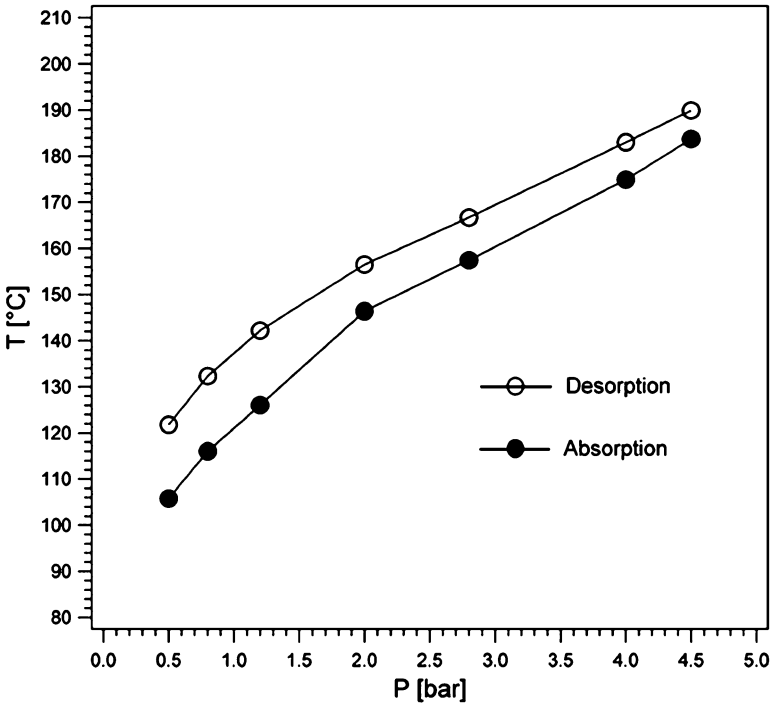

Fig. 6.26 Hydrogen absorption and desorption temperatures as a function of H_2 pressure. A hysteresis is visible between transformations upon a decrease of T (absorption) and an increase of T (desorption)

industries for the catalytic conversion of CO to CO_2 to control unwanted CO emission. The behavior of Pt catalyst NPs in a dynamic environment is also dynamic as the result of the changing free energy of the NPs surfaces with gas composition (Newton et al. 2007). Vendelbo et al. (2014) studied this behavior by in situ TEM using the all-in-one NR described above in Sect. 6.8.6.

The catalyst Pt NPs with 3–30 nm diameters were prepared by impregnation of an NR with an aqueous solution of tetraammineplatinum(II)nitrate followed by calcination in air at 573 K. A gas mixture of CO, O_2, and He (4.2 %:21.0 %:74.8 %) flowed through the NR containing the NPs into a mass spectrometer to analyze the reaction products, see Fig. 6.27. The reaction taking place at the NPs in the reaction zone is described as:

- $CO(g)+*\rightarrow CO*$
- $O_2(g)+*\rightarrow O_2*$
- $O_2*+*\rightarrow 2O*$
- $CO*+O*\rightarrow CO_2(g)+2*$

where * denotes a free surface site on a catalytic NP, and $X*$ denotes an adsorbed species. The temperature in the reaction zone was increased to a nominal value of

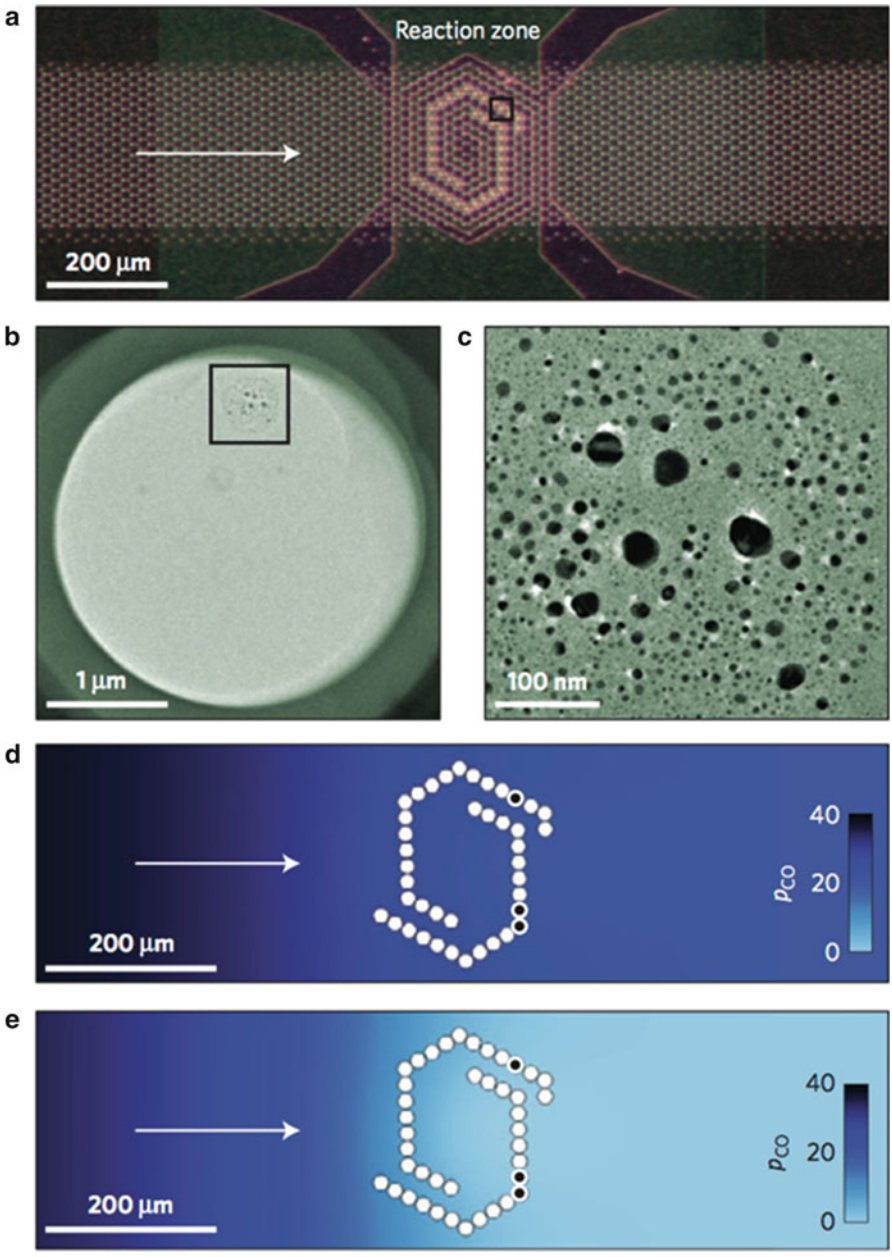

Fig. 6.27 (**a**) Light optical micrograph of the nanoreactor with the gas channel and the reaction zone including the heater spiral and electron transparent windows. (**b**) An electron micrograph of the framed window in a showing that Pt nanoparticles (*dark contrast*) are dispersed heterogeneously on the electron transparent windows (uniform, bright contrast). (**c**) An electron micrograph showing a close-up of the as-prepared Pt nanoparticles framed in (**b**). (**d**, **e**) Steady-state simulation of the CO concentration profile ([p_{CO}]: mbar) in the nanoreactor for the low conversion branch of the bistable regime at 710 K (**d**) and the high conversion branch of the bistable regime at 710 K (**e**). The *arrow* in (**a**, **d**, **e**) indicates the gas-flow direction. White discs superimposed on (**d**, **e**) indicates the positions of the electron transparent windows

710 K (total power input ~19 mW), and CO_2 was recorded in the spectrometer. The concentrations of CO_2 and CO started to fluctuate periodically spontaneously, or by a minor temperature change of 0.5–1.0 K, and were observed at temperatures in the range 659–729 K. During the oscillating reaction, the average NR temperature was kept constant by compensating the exothermic reaction heat with a reduction in the heater power. (Hence the heater power changes reflect the changes in the reactions taking place, with a faster response time as the pressure changes dampened by the tube system.)

At the same time as the spectrometer recorded the reaction product concentrations, images were recorded of NPs at a specific position in the reaction zone. At the inlet of the reaction zone, the NPs were observed to be static and more or less rounded in shape. In contrast, near the reaction zone outlet, the Pt nanoparticles switched between a more spherical and a more facetted morphology. In Fig. 6.28, the oscillations in gas pressures are demonstrated together with the morphology changes of a Pt NP near the outlet. It turns out that the morphology changes from spherical to more facetted and back is synchronous with the pressure oscillations. A high conversion is associated with a transformation towards low index Pt NP facets like {111}, while a lower conversion is associated with a conversion to high index facets.

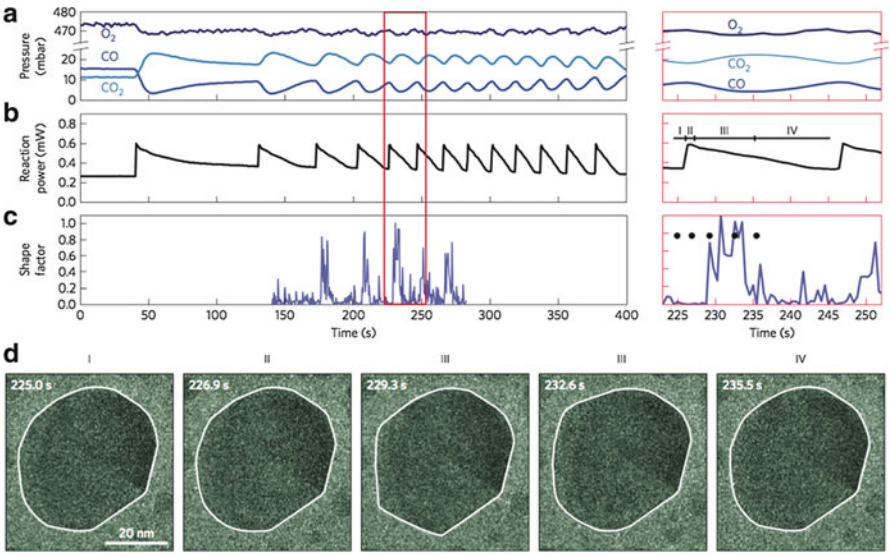

Fig. 6.28 Oscillatory CO oxidation reaction data correlated with the projected morphology changes of a Pt nanoparticle. The gas entering the reaction zone is 1.0 bar of $CO:O_2$:He at 3 %:42 %:55 % and NR temperature is 659 K. (**a–c**) Mass spectrometry of the CO, O_2, and CO_2 pressures (**a**), reaction power (**b**), and shape factor (**c**) for the Pt nanoparticle in d as a function of time. The shape factor corresponds to the relative difference in area from the best elliptical fit in *image I* in (**d**). The morphology factor is zero for the more spherical shape and deviates for more facetted particles. Part of the reaction oscillation data is highlighted by the *red rectangle*

Thus, the individual NPs near the exit from the reaction zone can undergo oscillatory and reversible shape changes with a temporal frequency matching the oscillations in reaction power, indicating that the oscillatory CO conversion and the dynamic shape change of the Pt NPs are coupled. This behavior was rationalized with a micro kinetic model using DFT calculations of the Pt surface CO and O adsorption and transition state energies, taking into account the CO pressure variation across the reaction zone. It showed that at higher CO pressures more open surfaces (high index planes like {112}) show a high CO coverage, and is stabilized, resulting in more rounded (high index surfaces) NP morphologies, as observed near the inlet, where the CO concentration is high. At lower CO pressures, the low index facets are stabilized with respect to the more open surfaces. Taking into account the flow in the NR and the morphology change rate proportional to the deviation from the equilibrium shape, an oscillatory pressure behavior coupled to periodic morphology variations could be described.

6.10.3 Corrosion and Heat-Treatment in Al Alloys

One of the applications of the NR is to understand a common metallurgical problem of localized corrosion. For example, aluminum alloys are generally considered corrosion resistive, but localized corrosion can arise from micro-galvanic couples due to extremely fine, nanometer, size precipitates, and solute depleted regions. The distribution of precipitates and solute depleted regions varies depending on the heat-treatment given to the alloys. Investigating the corrosion at the nanoscale is extremely challenging using conventional electrochemical methods. In such cases, in situ TEM studies using NR plays an important role in not just giving an understanding of the corrosion mechanisms at a submicron scale, but also on the influence of heat-treatments on the microstructural change and corrosion behavior of these alloys.

For carrying out corrosion studies inside the TEM, it is important to identify the four components of a corrosion cell: anode, cathode, conducting path and electrolyte. Due to the large density of precipitates and solute depleted zones inside the alloy, there are numerous anodes, cathodes connected by a conducting path (the Al matrix). In the presence of a suitable electrolyte, this system acts as a spontaneous corrosion cell. In order to identify an electrolyte suitable for in situ TEM studies, ex situ and quasi in situ experiments have been carried out. An aerosol of oxygen bubbled through aqueous HCl (pH = 3) has been identified to cause localized corrosion attack in reasonably short time for TEM investigation.

The specimens for in situ TEM studies (Malladi et al. 2013) are prepared using a focused ion beam (FIB). Using a dual-beam SEM/FIB, cross-sectional specimens of dimensions 15 μm × 5 μm × 100 nm are prepared across grain boundaries and other areas prone to localized corrosive attack. The specimens are then transferred to the bottom chip of the NR, which also consists of an embedded Pt heater. Upon

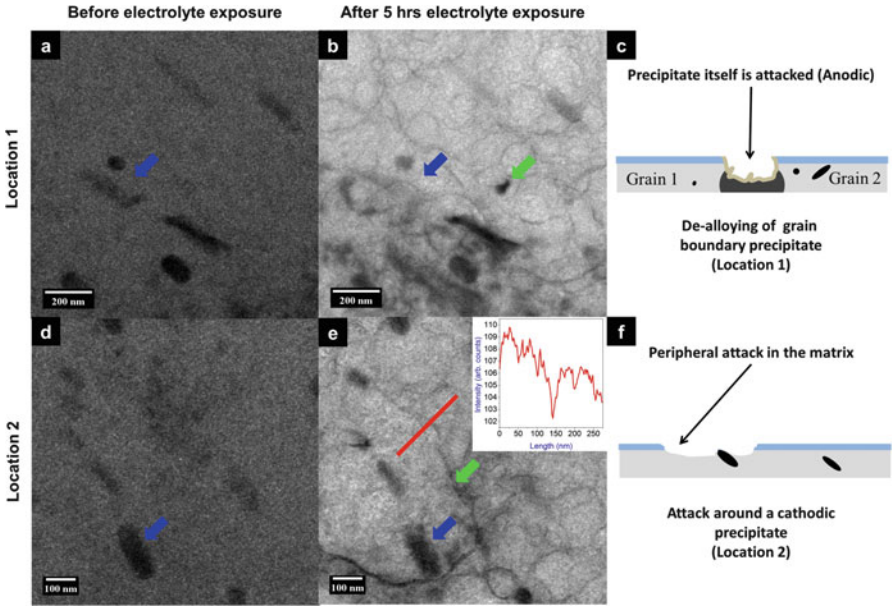

Fig. 6.29 (**a–c**) De-alloying of an anodic grain-boundary precipitate and (**d–f**), peripheral attack around cathodic matrix precipitates

combining with the top chip, the NR is assembled. The NR is placed in the flow-gas holder and introduced into the TEM for in situ TEM investigations.

Figure 6.29 shows snapshots from a movie recorded while exposing an FIB specimen of aluminum alloy AA2024-T3 to oxygen bubbled through aqueous HCl. The gas mixture was maintained at a pressure of 1 bar, and the specimen was maintained at room temperature. The bright-field TEM images from two areas of the FIB specimen show two kinds of localized corrosion attack. The location 1 (Fig. 6.29a–c) corresponds to the corrosion attack of an anodic grain-boundary precipitate. After exposing to the electrolyte for 5 h, the intensity of the grain-boundary precipitate indicated by the blue arrow diminishes significantly. EDX compositional analysis on several specimens of this alloy showed that the grain-boundary precipitates have been enriched in Mg, indicating the anodic nature of the attack. Likewise in location 2, an attack on the matrix surrounding platelet-like matrix precipitates was identified as an attack around cathodic precipitates. The precipitates have been identified as precipitates containing Cu, Mn, Fe, and Si. These two types of attacks are the origins of localized corrosion in Al alloys.

Most of the Al alloys have the unique property of improving their strength by the mechanism known as precipitation hardening. This involves a special heat-treatment given to the alloys where alloying elements are added to aluminum, heated to an elevated temperature (usually above 500 °C) to form a single-phase solid solution, and then quenched rapidly to room temperature.

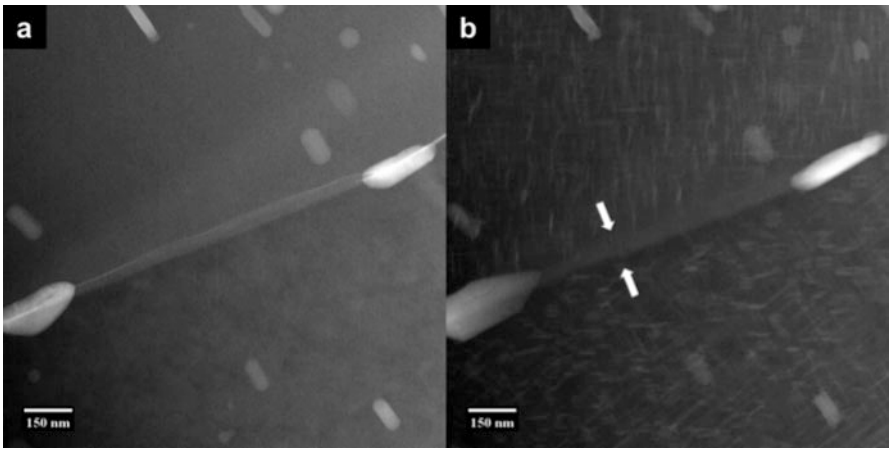

Fig. 6.30 STEM-annular dark-field images obtained from an FIB specimen of AA2024 (**a**) before and (**b**) after heat-treatment at 250 °C for 3 min. Prior to heat-treatment, there exist numerous matrix precipitates enriched in Mn, Cu, Fe, and Si, whereas heat-treatment results in precipitation of fine nanometer-sized S-type precipitates enriched in Cu and Mg. Also notice the precipitate-free zone indicated by the *arrows* next to the grain boundary

On quenching, a super-saturated solid solution is obtained, from which a distribution of numerous fine nano-sized precipitates in the matrix can be obtained by heating at slightly elevated temperatures (typically ranging from 100 to 250 °C). Fig. 6.30 shows the precipitation of numerous S-type nano-precipitates in the matrix of an FIB specimen of AA2024, heat-treated at 250 °C for 3 min. While the formation of the S-type precipitates contributes to a significant increase in the strength of the alloy, the Mg-rich S-type precipitates and the formation of precipitate-free zones next to the grain boundary have a severely detrimental effect on the corrosion behavior of this alloy.

The corrosion behavior of the heat-treated specimen can be investigated by assembling an NR and carrying out in situ corrosion experiments as described previously. The heat-treated specimen was also exposed to a gas mixture of oxygen bubbled through aqueous HCl at room temperature, at a pressure of 1 bar. The snapshots from a movie recorded during the in situ corrosion experiment are shown in Fig. 6.31. In contrast to the specimen prior to heat-treatment, Fig. 6.29, exposure to the reactive gas mixture of oxygen bubbled through aqueous HCl causes an immediate attack as shown in Fig. 6.29a. The bubble-like features observed all over the specimen indicate this, and more prominently next to the grain-boundary precipitates. As the exposure time increases, the corrosion attack progresses as observed by the growth of circular features all over the matrix after exposure of 15 min (Fig. 6.31b) and approximately 30 min (Fig. 6.31c). STEM-ADF tilt series confirms that the circular feature observed all over the specimen are pits initiating from the surface of the sample. The high density of the S-type precipitates enriched in Mg and Cu acts as numerous galvanic couples leading to such an attack. More

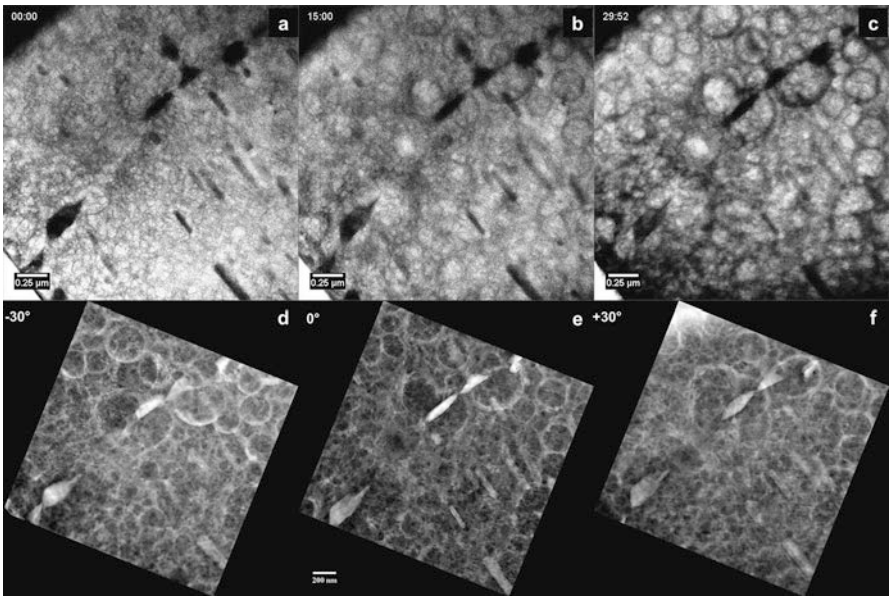

Fig. 6.31 (**a**) Surface attack and selective attack next to grain-boundary precipitates in a heat-treated FIB specimen of AA2024. The surface attack progresses rapidly after (**b**) 15 min, as indicated by the increase in the size of the circular features. The attack progresses more and the whole specimen surface is attacked after (**c**) at approximately 30 min. Projections at (**d**) −30°, (**e**) 0°, and (**f**) +30° from STEM-ADF tilt series obtained from the region shows that the *circular* features are in fact pits formed due to the corrosive attack

studies on understanding the propagation of corrosive attack by correlating with compositional analysis and other combinations of heat-treatment and corrosion are in progress.

Acknowledgements For the cleanroom work in fabricating the nanoreactors and various experiments, we acknowledge G. Pandraud, T. Alan, and L. Vicarelli. For the mechanical machining, we acknowledge T.R. de Kruijff, A. Grafhorst, L. van Luijk, and M. Camp.

The authors gratefully acknowledge the ERC project "In situ NanoElectrical Measurements in a Transmission Electron Microscope" (TSIC 69) for support.

References

T. Alan, P.M. Sarro, A comparative study of the strength of Si, SiN and SiC used at nanoscales. Mater. Res. Soc. Symp. P **1052**, 241–245 (2008)

T. Alan, M.A. Hines, A.T. Zehnder, Effect of surface morphology on the fracture strength of silicon nanobeams. Appl. Phys. Lett. **89**(9) (2006)

T. Alan, J. Gaspar, O. Paul, H.W. Zandbergen, F. Creemer, PM Sarro, Characterization of ultrathin membranes to enable TEM observation of gas reactions at high pressures, in *ASME 2009*

International Mechanical Engineering Congress and Exposition (American Society of Mechanical Engineers, 2009), pp 327–331

T. Alan, T. Yokosawa, J. Gaspar, G. Pandraud, O. Paul, F. Creemer, P.M. Sarro, H.W. Zandbergen, Micro-fabricated channel with ultra-thin yet ultra-strong windows enables electron microscopy under 4-bar pressure. Appl. Phys. Lett. **100**(8) (2012)

F. Banhart, Irradiation effects in carbon nanostructures. Rep. Prog. Phys. **62**(8), 1181–1221 (1999)

J.F. Creemer, S. Helveg, G.H. Hoveling, S. Ullmann, A.M. Molenbroek, P.M. Sarro, H.W. Zandbergen, Atomic-scale electron microscopy at ambient pressure. Ultramicroscopy **108**(9), 993–998 (2008). doi:10.1016/j.ultramic.2008.04.014

J. Creemer, F. Santagata, B. Morana, L. Mele, T. Alan, E. Iervolino, G. Pandraud, P. Sarro, An all-in-one nanoreactor for high-resolution microscopy on nanomaterials at high pressures, in *Micro Electro Mechanical Systems (MEMS), 2011 I.E. 24th International Conference on, 2011* (IEEE, 2011), pp. 1103–1106

N. de Jonge, F.M. Ross, Electron microscopy of specimens in liquid. Nat. Nanotechnol. **6**(11), 695–704 (2011)

N. de Jonge, M. Pfaffa, D.B. Peckysa, Practical aspects of transmission electron microscopy in liquid. Adv. Imag. Electron Phys **186**, 1–37 (2014)

R.F. Egerton, P. Li, M. Malac, Radiation damage in the TEM and SEM. Micron **35**(6), 399–409 (2004). doi:10.1016/j.micron.2004.02.003

H. Ghassemi, W. Harlow, O. Mashtalir, M. Beidaghi, M.R. Lukatskaya, Y. Gogotsi, M.L. Taheri, In situ environmental transmission electron microscopy study of oxidation of two-dimensional Ti_3C_2 and formation of carbon-supported TiO_2. J. Mater. Chem. A **2**(35), 14339–14343 (2014)

Y.N. Guo, J. Zou, M. Paladugu, H. Wang, Q. Gao, H.H. Tan, C. Jagadish, Structural characteristics of GaSb/GaAs nanowire heterostructures grown by metal-organic chemical vapor deposition. Appl. Phys. Lett. **89**(23), 231917 (2006). doi:10.1063/1.2402234

T.R. Hart, R.L. Aggarwal, B. Lax, Temperature dependence of Raman scattering in silicon. Phys. Rev. B Solid St **1**(2), 638 (1970)

L. He, R. Hull, Quantification of electron-phonon scattering for determination of temperature variations at high spatial resolution in the transmission electron microscope. Nanotechnology **23**(20), 205705 (2012). doi:10.1088/0957-4484/23/20/205705

M.E. Holtz, Y.C. Yu, D. Gunceler, J. Gao, R. Sundararaman, K.A. Schwarz, T.A. Arias, H.D. Abruna, D.A. Muller, Nanoscale imaging of lithium Ion distribution during in situ operation of battery electrode and electrolyte. Nano Lett. **14**(3), 1453–1459 (2014)

F.M. Huang, K.T. Yue, P.H. Tan, S.L. Zhang, Z.J. Shi, X.H. Zhou, Z.N. Gu, Temperature dependence of the Raman spectra of carbon nanotubes. J. Appl. Phys. **84**(7), 4022–4024 (1998)

A. Jenichen, C. Engler, Metal-organic chemical vapour deposition of (BInGa)P: density-functional calculations to the mechanisms. J. Cryst. Growth **312**(1), 10–15 (2009). doi:10.1016/j.jcrysgro.2009.10.001

J.M. López Nieto, P. Botella, B. Solsona, J.M. Oliver, The selective oxidation of propane on Mo-V-Te-Nb-O catalysts. Catal. Today **81**(2), 87–94 (2003). doi:10.1016/s0920-5861(03)00119-6

S. Malladi, C.G. Shen, Q. Xu, T. de Kruijff, E. Yucelen, F. Tichelaar, H. Zandbergen, Localised corrosion in aluminium alloy 2024-T3 using in situ TEM. Chem. Commun. **49**(92), 10859–10861 (2013)

M.A. Newton, C. Belver-Coldeira, A. Martinez-Arias, M. Fernandez-Garcia, Dynamic in situ observation of rapid size and shape change of supported Pd nanoparticles during CO/NO cycling. Nat. Mater. **6**(7), 528–532 (2007)

M.H. Nielsen, S. Aloni, J.J. De Yoreo, In situ TEM imaging of $CaCO_3$ nucleation reveals coexistence of direct and indirect pathways. Science **345**(6201), 1158–1162 (2014)

O. Paul, J. Gaspar, *Thin-Film Characterization Using the Bulge Test. Reliability of MEMS* (Wiley-VCH, Weinheim, 2008), pp. 67–121. doi:10.1002/9783527622139.ch3

S. Qian, D.O. Northwood, Hysteresis in metal hydrogen systems—a critical-review of the experimental-observations and theoretical-models. Int. J. Hydrogen Energy **13**(1), 25–35 (1988)

A. Radisic, P.M. Vereecken, J.B. Hannon, P.C. Searson, F.M. Ross, Quantifying electrochemical nucleation and growth of nanoscale clusters using real-time kinetic data. Nano Lett. **6**(2), 238–242 (2006)

B. Song, G.F. Schneider, Q. Xu, G. Pandraud, C. Dekker, H. Zandbergen, Atomic-scale electron-beam sculpting of near-defect-free graphene nanostructures. Nano Lett. **11**(6), 2247–2250 (2011)

A.J. Storm, J.H. Chen, X.S. Ling, H.W. Zandbergen, C. Dekker, Fabrication of solid-state nanopores with single-nanometre precision. Nat. Mater. **2**(8), 537–540 (2003)

T. Tsuchiya, O. Tabata, J. Sakata, Y. Taga, Specimen size effect of tensile strength of surface-micromachined polycrystalline silicon thin films. J. Microelectromech. S **7**(1), 106–113 (1998)

S.B. Vendelbo, C.F. Elkjaer, H. Falsig, I. Puspitasari, P. Dona, L. Mele, B. Morana, B.J. Nelissen, R. van Rijn, J.F. Creemer, P.J. Kooyman, S. Helveg, Visualization of oscillatory behaviour of Pt nanoparticles catalysing CO oxidation. Nat. Mater. **13**(9), 884–890 (2014). doi:10.1038/NMAT4033

M.Y. Wu, D. Krapf, M. Zandbergen, H. Zandbergen, P.E. Batson, Formation of nanopores in a SiN/SiO_2 membrane with an electron beam. Appl. Phys. Lett. **87**(11) (2005)

H.L.L. Xin, K.Y. Niu, D.H. Alsem, H.M. Zheng, In situ TEM study of catalytic nanoparticle reactions in atmospheric pressure gas environment. Microsc. Microanal. **19**(6), 1558–1568 (2013)

A.O. Yalcin, B. de Nijs, Z.C. Fan, F.D. Tichelaar, D. Vanmaekelbergh, A. van Blaaderen, T.J.H. Vlugt, M.A. van Huis, H.W. Zandbergen, Core-shell reconfiguration through thermal annealing in $FexO/CoFe_2O_4$ ordered 2D nanocrystal arrays. Nanotechnology **25**(5) (2014)

T. Yokosawa, T. Alan, G. Pandraud, B. Dam, H. Zandbergen, In-situ TEM on (de)hydrogenation of Pd at 0.5-4.5 bar hydrogen pressure and 20-400 degrees C. Ultramicroscopy **112**(1), 47–52 (2012)

N.P. Young, M.A. van Huis, H.W. Zandbergen, H. Xu, A.I. Kirkland, Transformations of gold nanoparticles investigated using variable temperature high-resolution transmission electron microscopy. Ultramicroscopy **110**(5), 506–516 (2010)

G.Z. Zhu, S. Prabhudev, J. Yang, C.M. Gabardo, G.A. Botton, L. Soleymani, In situ liquid cell TEM study of morphological evolution and degradation of Pt-Fe nanocatalysts during potential cycling. J. Phys. Chem. C **118**(38), 22111–22119 (2014)

Part II
Applications

Chapter 7
Growth of One-Dimensional Nanomaterials in the ETEM

Jonathan Winterstein and Renu Sharma

Abstract One-dimensional nanomaterials (nanowires and nanotubes) have a number of unique and interesting properties that have made them the subject of significant research for a wide range of applications. Electron microscopy is generally necessary for their morphological, structural, and chemical characterization due to their small dimensions. For applications such as nanomanufacturing, the synthesis process must be scalable. In the case of nanoelectronics, the tolerances are demanding, necessitating stringent control of process parameters. Catalytic chemical vapor deposition (CVD) is currently the most suitable route that allows both scalable production and selective, aligned growth directly on a substrate. Characterization of growth parameters and atomistic growth mechanisms is necessary if such nanomaterials are to be engineered for specific applications. Environmental transmission or scanning transmission electron microscopy (ETEM or ESTEM) provides the needed platform for in situ monitoring of the influence of processing parameters on nanomaterial structure and morphology. In this chapter, we present the practical aspects of experiment design, data analysis, successful examples, and the limitations of the ETEM platform for following one-dimensional nanomaterial growth processes.

7.1 Motivation and Background

1D Nanomaterials, such as nanowires and nanotubes, are a class of materials with large aspect ratios (ratio of length to diameter) and absolute diameter dimensions below approximately 100 nm. The unique and interesting phenomena observed in these materials arise due to quantum confinement effects, high surface-area-to-volume ratios, and the absence of defects result in exceptional properties.

There are a wide range of applications that take advantage of these unique properties of 1D materials. For example, nanowires (NWs) have been proposed for use in electronic devices (Yang 2005), photonic devices (Reimer et al. 2012),

J. Winterstein (✉) • R. Sharma
Nanofabrication Research Group, Center for Nanoscale Science and Technology, NIST, Gaithersburg, MD, USA
e-mail: Jonathan.Winterstein@nist.gov; renu.sharma@nist.gov

T.W. Hansen, J.B. Wagner (eds.), *Controlled Atmosphere Transmission Electron Microscopy*, DOI 10.1007/978-3-319-22988-1_7

photovoltaics, thermoelectrics (Hochbaum and Yang 2009), chemical sensors (Cui et al. 2001), catalysts, and catalyst supports (Wang et al. 2011) and recently, in the case of Si NWs, as battery electrodes for Li-ion batteries, with intriguing results (Chan et al. 2008). In many instances, to maximize the effectiveness of NWs in a specific application, it is necessary to control the growth rate and direction, and the presence and arrangement defects. The single-crystal nature of many NWs is a particularly valuable feature, which is most easily confirmed with diffraction and imaging in an electron microscope.

Nanotubes constitute a second subset of 1D materials. They differ from nanowires as they are hollow instead of solid, with an individual single-walled carbon nanotube (SWCNT)—a single sheet of carbon atoms, a graphene sheet, rolled into a tube—being the canonical example. Moreover, the structural variation in nanotubes is not limited to different aspect ratios or diameters but includes the fact that their wall thickness, i.e., the number of concentrically rolled sheets can vary from a single sheet to multiple sheets. Carbon nanotubes (CNTs) were first identified by Iijima (1991) using high-resolution transmission electron microscopy (TEM) and electron diffraction. Applications for CNTs include field-emission electron sources for displays or high-brightness electron guns, high-strength composites, transparent electrodes, high-efficiency filters, and electronics, among many others. A tremendous amount of research has therefore been performed to understand and exploit the unique electrical, thermal, and mechanical properties of CNTs (Baughman et al. 2002; Robertson 2004; Meyyappan 2005; Dresselhaus et al. 2001).

The properties of nanowires and nanotubes are strongly dependent on their crystallography and morphology. The primary goal is thus the controlled synthesis of 1D structures with the required structure and dimensions to deliver the desired properties. The transmission electron microscope is now capable of obtaining direct, atomic resolution images of crystals and their defects. Chemical composition can also be mapped with a spatial resolution below the interatomic spacing in many materials. However, the ex situ information thus obtained is often not sufficient to optimize the synthesis conditions to yield the required structure and morphology. In situ measurements that reveal the effect of synthesis parameters on nucleation and growth mechanisms, structure and morphology, are therefore the subject of intense development efforts (Ross 2010; Sharma 2005).

Environmental TEM (ETEM) is an excellent tool for growth studies because it combines synthesis with characterization capabilities. With one experiment, the crystallography, morphology, defect structure, and chemical composition can be monitored during growth with moderate temporal resolution, which now reaches into the millisecond regime. Critical measurements such as growth rates are possible with atomic-scale accuracy. Importantly, ETEM offers the possibility of measuring the growth rate of individual nanomaterials and determining the structure and chemistry of the active nanoparticle catalysts. Although the wealth of information available from ETEM experiments has improved our understanding of nanomaterial growth and enabled new science and engineering, ETEM also has a

number of limitations that must be considered during experimental design and interpretation of results (Sharma 2005, 2012; Egerton et al. 2004).

In this chapter, we will review 1D nanomaterial growth with a focus on the fundamental phenomena that can be studied in the ETEM, followed by a practical description of experimental design, the important instrumental features, sample preparation, and data analysis. We will also review examples from the literature of successful ETEM growth experiments and the scientific knowledge gained. Finally, we discuss limitations, such as beam damage and uncertainties in temperature measurement, as these must be understood for correct interpretation of ETEM results.

7.2 CVD Synthesis Process

Chemical vapor deposition (CVD) is the most widely used method for the synthesis of 1D nanomaterials because it permits growth at relatively low temperatures with a high yield and the possibility of control over growth by selection of suitable catalysts, supports, temperature, and precursor pressure. In the CVD process, metal nanoparticles act as catalysts to (a) dissociate the precursor molecules and (b) provide nucleation sites for growth. This CVD process is sometimes also referred to as catalytic CVD (CCVD). There are clear similarities between CVD of nanowires and CNTs: in both cases, a catalyst particle dissociates and absorbs atoms from a gas-phase precursor and a second-phase, 1D nanomaterial is formed as the product (Moisala et al. 2003).

Depending upon the synthesis conditions, NWs are known to grow by two mechanisms: vapor–liquid–solid (VLS) or vapor–solid–solid (VSS) (Dasgupta et al. 2014). For VLS growth, the temperature is between the elemental melting point of the catalyst (1064 °C for Au) and the eutectic temperature (363 °C for Au–Si) such that the catalyst particle is initially solid (Fig. 7.1, stage 1). In the case of the Au–Si system, introducing Si-containing gas molecules (or reaction with a clean Si substrate) increases the concentration of dissolved Si in the Au particle. As the Si concentration in the Au particle increases and shifts isothermally to the Si-rich side of the phase diagram, it crosses the Au-rich liquidus line and the catalyst melts completely (Fig. 7.1, stage 2); eventually, the composition will reach the Si-rich liquidus line and solid Si precipitates (Fig. 7.1, stage 3). Continued dissociation and absorption of the Si into the liquid Au–Si alloy catalyst feeds continued NW growth (Fig. 7.1, stage 4). Fundamental aspects of NW and whisker growth via the VLS mechanism are reviewed in (Ross 2010; Bootsma and Gassen 1971; Givargizov 1975).

On the other hand, NW nucleation and growth via the VSS mechanism occurs from supersaturated solid particles below the eutectic temperature, where both the matrix and growing phase remain solid. The mechanism of NW growth is therefore simple precipitation, but with the important feature that the metal nanoparticles provide a template for growth and may control the diameter of the NW. Reference

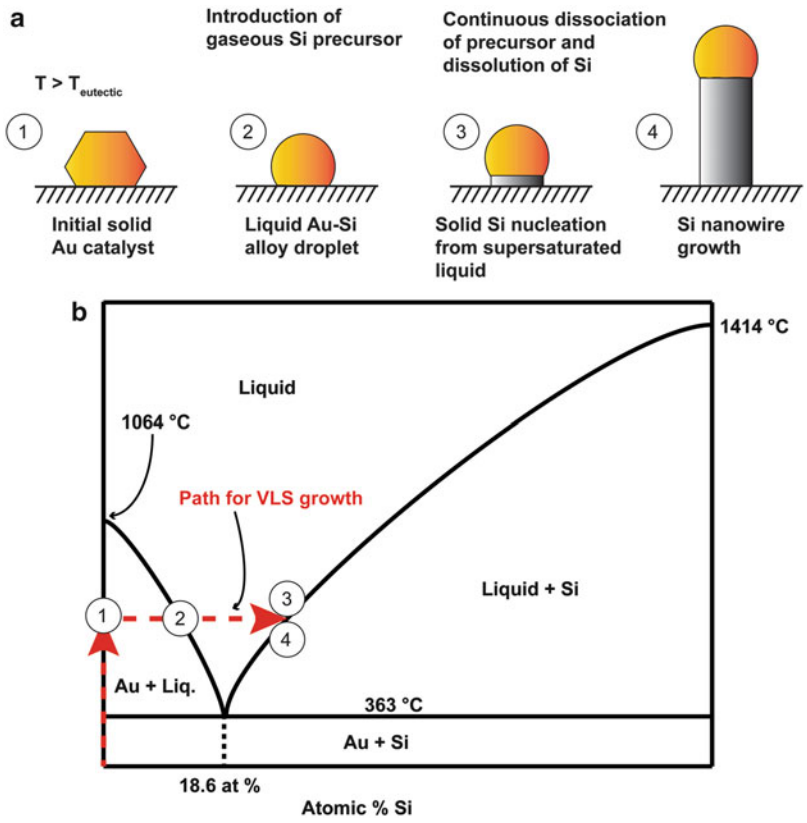

Fig. 7.1 (**a**) A schematic drawing showing the steps in growth of a Si nanowire via the VLS method and (**b**) the Au–Si phase diagram. The locations on the phase diagram corresponding to steps 1–4 in the schematic are labelled. The initially solid catalyst dissolves Si until melting completely (point 2). Once the Si concentration reaches the saturation level (point 3), the NW nucleates and grows. The phase diagram was redrawn based on information from Okamoto and Massalski (1983)

to a phase diagram is useful to understand the thermodynamics of VLS or VSS growth.

Compound semiconductor NWs are more complicated and require additional considerations as they are generally synthesized by metal organic CVD (MOCVD) process and require two or more precursor gases. Therefore, a ternary phase diagram is necessary to describe the possible phase transformations. For example, GaN NWs form by nitridation of liquid Au–Ga by ammonia (NH_3). Therefore, the composition of Au–Ga droplet has to be in the liquid region as identified in the Au–Ga phase diagram (Fig. 7.2a) and confirmed by experimental data shown in Fig. 7.2b, c (Diaz et al. 2012).

The most commonly reported gases used for NW growth are digermane and disilane for Ge and Si NWs, respectively. In situ measurements of GaN NW

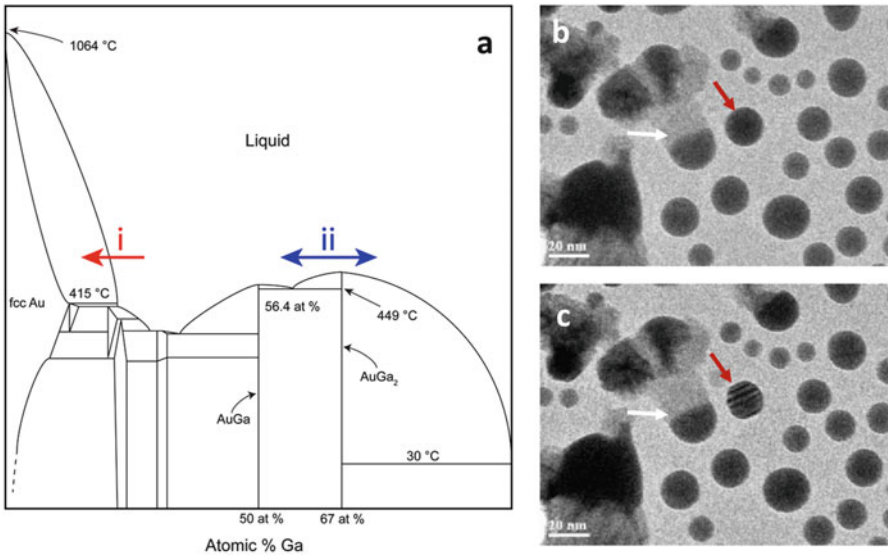

Fig. 7.2 (**a**) Au–Ga phase diagram. (**b**, **c**) time-resolved video frames recorded during GaN NW growth from Au–Ga liquid particles at 800 °C in 200 PaNH_3. *Red arrows* indicate step (i) where a liquid Au–Ga particle becomes Au rich, and thereby solid, after losing some Ga to the environment due to evaporation. *White arrows* indicate the NW growth if the particle composition is Ga rich, step (ii) in the phase diagram; the particle remains liquid

growth, using trimethylgallium (TMG) and ammonia (NH_3) have also been reported (Diaz et al. 2012). Although Au is the most commonly studied catalyst, other catalyst materials for semiconductor NW growth are also possible including Ag (Wittemann et al. 2010), Al (Wacaser et al. 2009), Ni (Purushothaman and Jeganathan 2013), Pd (Hofmann et al. 2008), Cu (Wen et al. 2009b), and alloys of these metals (Chou et al. 2012; Wen et al. 2009a; Gamalski et al. 2013; Robertson 2012).

The precise mechanisms of CVD CNT growth are still an active subject of research. Briefly, the process involves dissociation of the carbon-containing gas and the carbon adsorption on the catalyst surface, diffusion of the C atoms on the surface or in the bulk, formation of a CNT nucleus on the particle and CNT liftoff and growth. Questions remain about the chemical phase of the catalyst particle during growth, the role of bulk versus surface diffusion of C, the influence of particle size on CNT growth, and the initial nucleation and formation of a graphene layer on the catalyst particle prior to growth of the nanotube. It is likely that the details will vary significantly with growth conditions and metal catalyst used. In situ ETEM has shed light on a number of these questions as described in Sect. 7.8.2.

7.3 Advantages of In Situ Experiments

Ex situ, post-growth evaluation of nanomaterials in the TEM is a critically useful technique for understanding lattice defects, chemistry, etc. at high spatial resolution. However, it suffers from a number of limitations alleviated by direct in situ observations in the TEM. In particular, during cooling from the reaction temperature the catalyst particles may change phase, nanowires and nanotubes may change their morphology, etc. In the case of Si NW growth, Ross et al. showed sawtooth faceting on NW walls related to the presence of oxygen, and it appears that this faceting is often not observed ex situ due to changes during cooling after reaction (Ross et al. 2005). Another key advantage of in situ growth is the ability to directly measure growth rates of multiple individual nanomaterials in the same experiment. This capability has been exploited to identify time-dependent fluctuations in CNT growth (Sharma 2009) and to examine size effects in nucleation and growth of NWs (Kim et al. 2008; Kodambaka et al. 2006b).

7.4 Instrumentation Required

ETEM provides the most suitable platform for in situ growth studies as the chamber surrounding the sample can be used as a "cold wall" CVD reactor, allowing the complete set of nanoscale characterization techniques to be maintained. CVD growth studies require: (1) the ability to heat the sample (typically to temperatures in the range of ≈300 °C to ≈800 °C); and (2) the ability to introduce gas into the sample area. In an ideal situation, heating and gas introduction would occur rapidly and introduce negligible sample vibration and drift. Despite many years of effort and significant progress towards this goal, drift, and vibrations, nonetheless remain problems. The microscope design is described in more detail in Chap. 2 of this book and previously in several reviews (Sharma 2001; Boyes and Gai 1997; Hansen et al. 2010; Wagner et al. 2012) and heating holders are described in Chaps. 2 and 6, and will not be discussed here.

For gas introduction into the vacuum of the microscope column, differentially pumped systems with a gas inlet are now a commonly used design. In addition, UHV TEMs, with or without additional differential pumping, with gas-introduction hardware have been developed by a few researchers (Hammar et al. 1996; McDonald et al. 1989). The modified UHV systems start with a TEM capable of reaching base pressures below 1×10^{-7} Pa and are modified to introduce small amounts of gas (1×10^{-5} Pa) (Hammar et al. 1996; McDonald et al. 1989). One advantage of UHV systems is that by maintaining very low partial pressures of oxygen or water, reactions on clean surfaces, can be observed. For example, the effect of a low partial pressure of oxygen (~1×10^{-5} Pa) on Si NW growth was revealed using a UHV TEM (Ross 2010; Kodambaka et al. 2006a).

7.5 Experimental Design

When designing an in situ growth experiment, it is essential to consider what measures are necessary to ensure safe handling and use of the gases involved. Gas-handling systems and microscope use must be designed around safe operation in the same manner as a CVD reactor. Possible damage to the internal parts of the microscope must also be considered in the selection of reaction gases. For example, corrosive gases such H_2S and SO_2 Cl_2 should be avoided. Also, gas leak rates should be kept to a minimum level for disilane which can form silicon oxide coatings on internal microscope surfaces including apertures and vacuum pump components if the leak rate or pressure is too high.

A number of conditions for the gas-handling system must be met for successful nanomaterial growth. Both NW and CNT growth require a clean environment with very low partial pressures of water and other contaminants which can interfere with the primary catalytic reaction. Tubing on the gas-handling system should be bakeable so that water can be driven from the internal surfaces. The cleanliness of the setup is further discussed in Chap. 2.

The reaction condition (nature of gas and/or temperature) must also be compatible with the heating holders used. For example, Ta-based furnace holders should not be used with oxygen environments (Diaz et al. 2012). In addition, the grid and support materials must be carefully chosen. When using a furnace holder, metal evaporated from the grid can interact with catalyst particles (Zhang and Su 2009).

The next step in experimental design for nanomaterial growth should be checking the relevant equilibrium phase diagrams to identify possible phase transformations and the conditions necessary for growth. For example, the Au–Si phase diagram (Fig. 7.1) was used as a guide to identify VLS growth conditions for Si nanowire growth. A similar strategy was also used to determine VLS and VSS growth conditions for Ge NW and Si NW growth using Au and Pd as catalysts, respectively (Hofmann et al. 2008).

It is important to note that phase diagrams only provide information on thermodynamic equilibrium: kinetic effects must also be considered. Generally, this requires reviewing the in situ and ex situ literature for the reactions of interest. Important data to obtain include rates of gas decomposition as a function of temperature and pressure, diffusion constants, etc. It is also worth noting that nanoscale size effects can modify the stability of phases compared to what is expected from the bulk equilibrium phase diagram (Gamalski et al. 2010). The examples provided in Sect. 7.8 can be used as a guide to design ETEM experiments for similar systems.

7.6 Specimen Preparation Considerations

Specimen preparation for nanowire growth requires the creation of catalyst nanoparticles, such as Au, on a substrate. Evaporation or sputtering of metal films onto a substrate can produce the required particles for growth, where the density

and diameter of metal nanoparticles formed can be controlled by film thickness (see, e.g., Daudin et al. 2012)

In some ultra-high vacuum (UHV) TEMs, thin-film deposition is possible via evaporation within the UHV system (i.e., thin films can be deposited and samples inserted into the microscope without breaking vacuum) (Hammar et al. 1996; Ross 2010). For example, Au films of 1–2 nm thickness evaporated onto cleaned Si(111) substrates dewet in UHV to form small metal nanoparticles. The substrates were oriented so that the NWs grow perpendicular to the electron beam, a convenient geometry to image catalyst-NW interfaces and measure growth rates (Ross 2010).

Specimen preparation for CNT growth experiments must also be carefully designed to avoid certain pitfalls. Small particles (1–10 nm) are typically necessary for CNT growth and therefore the particle–substrate system must be chosen so that sintering via coalescence or Ostwald ripening of the particles does not occur at the reaction temperatures used. In the past, researchers have had success with NiO/SiO_x powder (Sharma and Iqbal 2004; Hofmann et al. 2007), $Fe–Al_2O_3$ (Amama et al. 2010), $NiO/MgAl_2O_4$ (Helveg et al. 2004), and Co–Mo/MgO (Sharma and Iqbal 2004; Picher et al. 2014). Sputtered or evaporated films may not always dewet the substrate properly to form small nanoparticles unless the combination of film and substrate is correctly chosen. In addition to the potential for particle size increase at high temperature, it has been shown that diffusion of catalyst material into the substrate can deactivate CNT growth (Kim et al. 2010b). Further discussion of catalyst–substrate interactions relevant to CNT growth in the ETEM is given by Kim et al. (2010a). One method for precise control of catalyst particle size, shape, and location is the deposition of particles in situ using electron-beam-induced deposition (EBID) (Sharma et al. 2009; Chee and Sharma 2012).

Typically, for transition metals, the nanoparticles are highly reactive and oxidize. Therefore, the particles and films are present as an oxide phase at room temperature and must be reduced to the metallic phase prior to CNT growth. Helveg et al. reduced NiO catalyst nanoparticles in ~100 Pa H_2 prior to CNT growth (Helveg et al. 2004). However, this step is not necessary as some of the C precursor gases such as acetylene or CO also act as reducing agents and have been reported to reduce iron, cobalt, and nickel oxides to the metal during the same reaction step as the growth. In fact, maintaining the nanoparticles in the oxide phase until the C precursor gas is introduced may be beneficial due to reduced sintering rates for the oxide compared to the metal nanoparticles during heating.

7.7 Data Analysis

Many software packages are available for analysis of videos or image stacks. In addition to commercial software, free and open-source software suitable for scientific analysis of time series is available, the best known of which is ImageJ (Schneider et al. 2012) (or its offshoot FIJI, Schindelin et al. 2012). Standard features of ImageJ include algorithms for thresholding, quantitative particle size

analysis, FFTs, Fourier filtering, etc. Multiple plugins are also available for spatial alignment of image stacks for this platform.

The ability to extract the growth rates of individual nanowires or nanotubes from in situ data is a key advantage of ETEM experiments. With such data in hand, it is possible to deduce the growth kinetics and identify the rate-limiting steps for the growth process and activation energies for various reactions. The general method is described by Sharma (2009) and consists of measuring growth rates at different temperatures and obtaining an Arrhenius plot to determine the activation energy. Details can be found in the relevant articles, (especially, Kim et al. 2008; Hofmann et al. 2008) and examples of kinetic information extracted from in situ measurements can be found in Sect. 7.8.

Measuring growth rates for individual CNTs is complicated due to their tubular structure and varying inner and outer diameters, thus requiring very careful analysis. For example, for a given outer tube diameter, it is not always possible to determine the number of walls, and therefore it is difficult or impossible to relate linear growth rates to the number of carbon atoms which have been incorporated into the tube and therefore it is not always possible to measure the activation energies for growth (Sharma 2009). This restriction does not apply to SWNTs or for imaging conditions which permit determination of the number of walls.

7.8 Examples of Information Gained from In Situ 1D Nanomaterial Growth Experiments

7.8.1 Nanowire Growth

The VLS mechanism had been proposed in the 1960s for growth of whiskers (Wagner and Ellis 1964), but had not been experimentally confirmed until recently. Early in situ TEM observations of Ge nanowire growth from Au catalysts were the first direct evidence of the VLS growth mechanism for nanowires (Wu and Yang 2001). In this set of experiments, the vapor source was solid material deposited on a TEM grid. Subsequent ETEM experiments using a gas-phase precursor confirmed the VLS mechanism for NW growth (Hannon et al. 2006). In situ microscopy is critical to verify if the catalyst particle is liquid during growth.

Application of semiconductor nanowires requires detailed knowledge of the parameters controlling the growth rate to permit dimensional control during fabrication and in situ ETEM offers the ability to make highly accurate measurements of the growth rates of individual NWs. The unique capabilities of UHV-ETEM have been exploited to measure the growth rates of individual NWs as their diameters tapered during growth. Theoretical predictions have suggested that the growth rate should decrease with nanowire diameter, but these direct measurements of Si NW growth rates for a range of sizes indicate that growth conditions, i.e., pressure and temperature, and not the size, affects the growth rate (Kodambaka et al. 2006b).

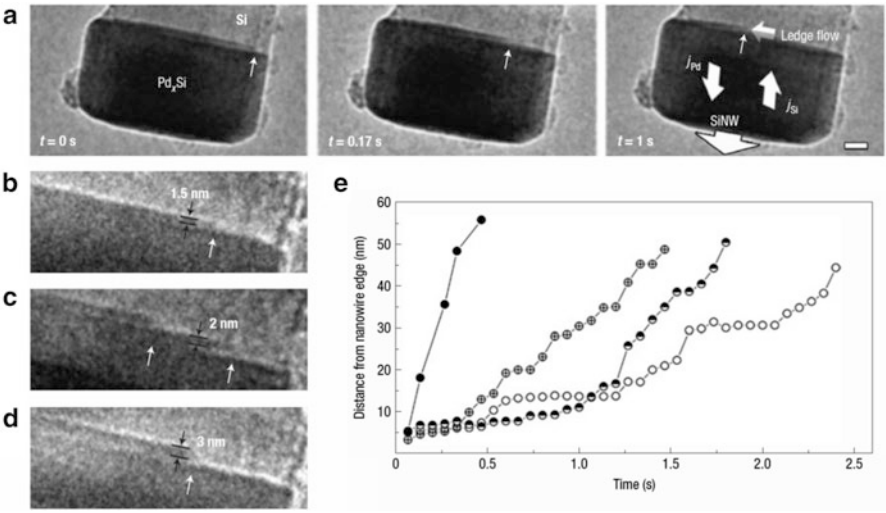

Fig. 7.3 (**a**) Sequence of images showing the growth of a Si NW from a Pd_xSi catalyst with time (t) (scale bar 10 nm), (**b–d**) various ledge configurations at the Pd_xSi/Si NW interface during growth, (**e**) measured step edge position with time for independent ledges

Another important contribution of in situ ETEM was the demonstration that the catalyst can be solid during NW growth (Kodambaka et al. 2007). Subsequent experiments have shown VSS growth in other systems such as Si NW growth from Pd and Cu catalysts (Hofmann et al. 2008; Wen et al. 2009b). These studies also revealed the existence of a ledge-flow controlled growth mechanism in which atomic-scale ledges at the interface between the solid catalyst and the nanowire move laterally resulting in the nanowire growth (see Fig. 7.3).

The nucleation rate dependence on the catalyst particle size was first reported by Hofmann et al. (2008). Direct in situ observation, using ETEM, revealed that smaller particles supersaturated, and thereby nucleated NWs, before larger particles as shown in Fig. 7.4. Incubation time for Si NW nucleation was measured to be $\propto A_o^{1/2}$, where A_o is the initial cross-sectional area of the Au particle.

They also showed that Si NWs grow via the VSS mechanism when using Pd as a catalyst. Their analysis of growth rates of Si NW growth from Pd_2Si catalysts allowed the rate-limiting step to be inferred (Hofmann et al. 2008). The activation energy and NW growth rates were inconsistent with a rate-limiting step set by an interfacial reaction. Instead, the data indicated that Pd diffusion away from the Si NW/silicide interface controlled the growth.

Useful kinetic and thermodynamic information extracted from in situ observations of individual NW nucleation and growth events also includes the quantification of the nucleation events for Si NWs (Kim et al. 2008). By quantifying the growth rate of Si crystals within multiple Au–Si liquid droplets at 585 °C, the authors were able to extract the activation energies for disilane dissociation and Si atoms joining the Si crystal from the liquid. A detailed study of the data obtained

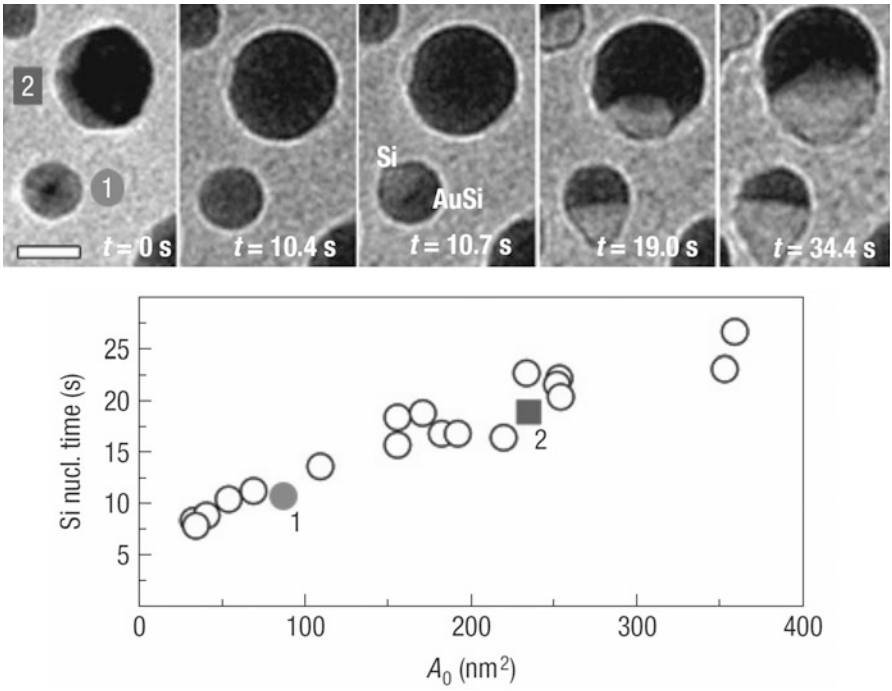

Fig. 7.4 ETEM images of the nucleation of Si NWs from Au catalysts (Hofmann et al. 2008). Analysis of multiple nucleation events indicates a size effect for nucleation. Nucleation occurs first in small Au catalyst particles

enabled many more conclusions to be drawn about the physical nature of the nucleation process (Kim et al. 2008).

An additional interesting phenomenon identified by in situ observations is the hysteresis in the state of the Au catalyst during Ge nanowire growth as a function of temperature, Ge_2H_6 pressure, and size. The catalyst particles at the tip of the growing NWs remain liquid below the eutectic temperature before solidifying abruptly. The solidification occurred as the temperature was lowered below the eutectic (undercooling) and the catalyst composition became Ge rich (Kodambaka et al. 2007). Upon reheating, catalyst particles melted at temperatures (superheating) above the eutectic point. The extent of undercooling or superheating was also observed to be dependent on the Ge_2H_6 pressure, i.e., the dissociative adsorption rate in Au particles. As a result, NWs were observed to grow both by VLS and VSS under the same growth conditions (Kodambaka et al. 2007).

ETEM growth experiments have also revealed fundamental features of growth that influence NW morphology and the introduction of defects such as kinks. ETEM was used to identify temperature regimes that produced straight or "wormy" NW growth (Fig. 7.5) (Madras et al. 2009). In particular, Si NWs that started out straight at 425 °C became kinked when the temperature was reduced to 380 °C. Real-time imaging of Si NW kinking was obtained, showing a transition in growth directions

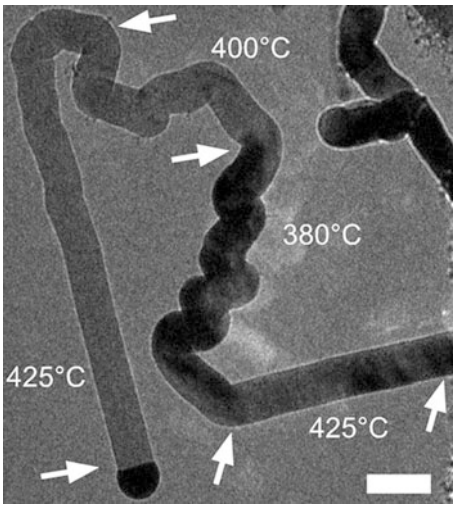

Fig. 7.5 Image of a Si NW after growth showing the changes in morphology as the growth temperature is varied. Higher growth temperatures produce straighter, unkinked NWs. Scale bar is 250 nm. Reprinted with permission from (Madras et al. 2009), Copyright 2009 American Chemical Society

between equivalent <111> directions or from <111> to <112> directions. Figure 7.5 shows an image after in situ growth where a single NW has grown straight in some regions and kinked at other points depending on the temperature, which was varied during the growth experiment. The disilane pressure also influenced the growth morphology (Madras et al. 2009).

Other research using ETEM has related kinking behavior to changes in the dimensions of the NW (Hillerich et al. 2013). If the NW diameter shrinks, an inclined facet can form and the NW can continue growing outward from the new facet (Hillerich et al. 2013). Such effects are especially prominent for hybrid structures, where a new material is grown on top of another material and the change in interfacial energies can induce NW diameter changes. Another source of NW diameter change is out-diffusion of Au from the catalyst causing shrinkage of the catalyst particle. Au diffusion is sensitive to the reaction conditions used such as oxygen partial pressure (Hannon et al. 2006; Kodambaka et al. 2006a). Au out-diffusion during growth of Si NWs introduces several other phenomena revealed by in situ ETEM experiments. For example, as Au diffuses along the NW surface the Si surface energy is modified, causing the introduction of "saw-tooth" faceting (Ross et al. 2005). Ostwald ripening of catalyst particles occurs as Au diffuses from the smaller to the larger particles, leading to changes in catalyst size during growth (Kodambaka et al. 2006a). ETEM also revealed that the presence of a small amount of oxygen in the reaction chamber prevented Au diffusion on the NW side walls (Kodambaka et al. 2006a).

While the majority of investigations of NW growth have focused on semiconductors grown from a catalyst material, metal oxide nanowires can be grown directly by a reaction of the metal with oxygen gas. Recently, Rackauskas et al. observed the growth mechanisms of CuO NWs, in situ, by exposure of Cu metal to oxygen in the ETEM (Rackauskas et al. 2014).

7.8.2 CNT Growth

In situ observations of carbon nanotube (CNT) growth in the TEM possibly extends back to the earliest days of gas–cell microscopy in the TEM when Baker and Harris obtained images of carbon filaments in a modified TEM (Baker and Harris 1972; Baker 1989). The low-resolution in situ images obtained did not clearly show the filaments to be CNTs. High-resolution images and diffraction patterns, collected post-growth, show amorphous carbon filaments as well as thick graphitic layers in some filaments indicating that their structure may be similar to multi-wall CNTs. These filaments were of interest as they were identified as a potential source of catalyst poisoning and deactivation for hydrocarbon cracking reactions. Baker et al. also presented a growth model based on carbon supersaturated particles that was widely accepted until recently (Baker et al. 1972).

ETEM observations from multiple groups have shown that the catalyst particle remains solid during CNT growth (Hofmann et al. 2009), clarifying the controversy regarding the possibility of growth from a liquid particle (Harutyunyan et al. 2005; Cantoro et al. 2006) due to proposed significant melting point depression for nanoparticles at growth temperatures. Ex situ TEM data could not, of course, confirm the state of the particle during growth. During in situ ETEM observation of carbon nanofiber (CNF) growth from Ni particles the catalyst remained solid while undergoing huge deformations which could be explained by rapid solid-state diffusion at the growth temperatures (Hofmann et al. 2007).

During the last couple of decades, unprecedented results have been obtained by direct imaging of CNT nucleation and growth process at reaction temperature using ETEM (Helveg et al. 2004; Zhu et al. 2005; Hofmann et al. 2007). Helveg et al. were also first to show that surface diffusion of carbon and not bulk diffusion is a prominent feature for CNT growth (Helveg et al. 2004). Later, Sharma and Iqbal employed ETEM to identify reaction temperatures that produced different types of CNTs using catalysts of NiO/SiO_x and Co–Mo/MgO and acetylene as the precursor (Sharma and Iqbal 2004).

Even without atomic-resolution imaging of CNT growth, ETEM experiments enable precise measurement of the growth rates of individual tubes, adding to the understanding of catalyst poisoning and growth mechanisms. Early work showed different growth regimes for a single CNT over time and eventually the slowing and end of growth even though the temperature and gas pressure were not changed (Lin et al. 2006).

Only within the last decade, with the development of higher-resolution ETEMs, has it been possible to reveal the atomic-level growth mechanisms of CNTs on catalyst particles (Helveg et al. 2004; Zhu et al. 2005; Hofmann et al. 2007). Pioneering work by several groups has provided clear evidence of a number of features of CNT growth. For example, Yoshida et al., showed that Fe catalyst particles during CNT growth are transformed to the cementite phase Fe_3C, as

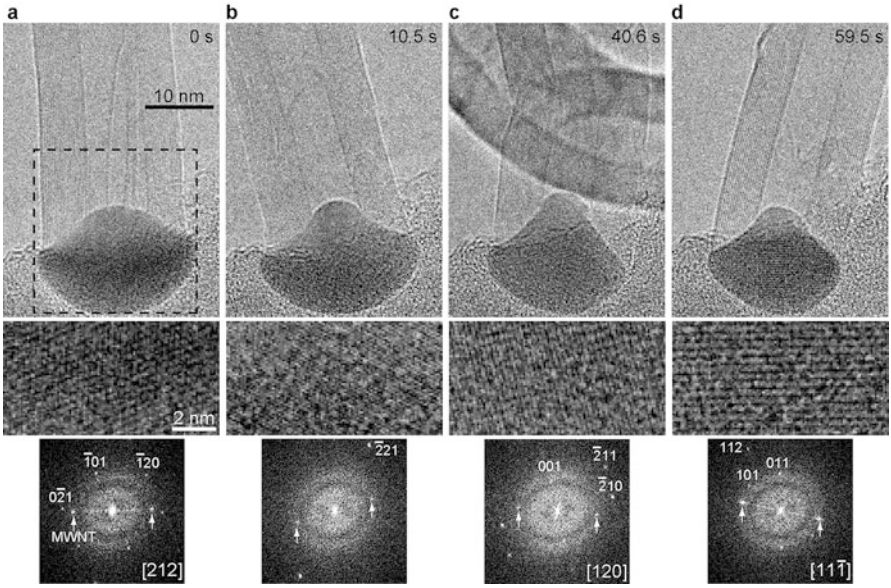

Fig. 7.6 (**a**-**d**) Low magnification in situ ETEM images during CNT growth from a Fe catalyst (*top row*). Analysis of FFTs (*bottom row*) from the lattice fringes (*middle row*) indicates the active phase during growth is cementite

illustrated in Fig. 7.6 (Yoshida et al. 2008) or a more complex Mo-containing carbide in the presence of Mo (Yoshida et al. 2012). Together with other observations, this information strongly suggested that bulk diffusion occurs during CNT growth from Fe catalysts because the entire catalyst particle adopted the observed carbide structure (Yoshida et al. 2008). Recently, the crystal structures of active and inactive particles have been identified by examining a number of HRTEM images of Fe catalysts, recorded under reaction conditions, during CNT growth and after growth termination. Experimental data show that the structure of active particles is cementite (Fe_3C) and that of inactive particles is Hägg phase (Fe_5C_2) (Mazzucco et al. 2014). In situ evidence in fact indicated that termination of CNT growth was correlated with the formation of the Hägg phase. Density functional theory (DFT) calculations further confirmed that the inactivity of the Fe_5C_2 structure is due to the lower mobility of the C atoms and the higher C–C bond formation energies on the stable (010) surface (Mazzucco et al. 2014).

The unexpected restructuring and shape changes of a solid catalyst particle, a liquid-like behavior, during CNT growth were first observed by ETEM. It was known from ex situ TEM imaging that metal particles could be incorporated into the hollow center of the nanotube (Ajayan et al. 1994), but the mechanism of incorporation was unclear. Direct in situ evidence of a Ni catalyst particle changing shape during tip growth of a nanofiber was obtained by Helveg et al. (2004) who showed elongation and contraction of the Ni catalyst. Restructuring during the

initial stages of growth was also observed for a Ni catalyst during root growth (Hofmann et al. 2007).

The driving force for the catalyst particle reshaping during growth and becoming incorporated within the CNT is still open to debate. Interpretations based on capillary forces, strong metal-carbon bonding, etc. have been proposed (Sun et al. 2006; Schebarchov and Hendy 2008). Molecular dynamics (MD) simulations and continuum modeling have been shown to reproduce observations from ETEM experiments in work reported by Moseler et al. (2010). This study indicated that enhanced diffusion of Ni interface atoms and capillary forces could explain experimental observations. It was not necessary to assume that the Ni metal particle liquefied, instead the particle remained crystalline during MD simulations as the restructuring happened. This restructuring after nucleation identifies one of the limitations of controlling CNT growth by control of the initial catalyst particle features as new crystal facets can form and the particle size can change. Shape changes of the catalyst particle during growth were observed to be associated with the formation of the so-called bamboo structures during growth in an ETEM experiment (Lin et al. 2007).

The nucleation of an SWCNT on a catalyst particle has been the subject of much research because of the importance of this step in determining the SWCNT chirality. Ex situ TEM images, diffraction patterns, and lattice-energy-based theoretical simulations suggest that the atomic arrangement of the catalyst particle surface determines the structure of the SWCNT cap (and thereby the chirality) at the nucleation stage (Reich et al. 2006; Zhu et al. 2008; Koziol et al. 2010; Picher et al. 2014). However, the nucleation period is very short and difficult to capture during ETEM observations at the typical ~30 Hz frame rates of most charge-couple device (CCD) cameras. In addition, high resolution is necessary to observe the single atomic layer of C forming the nucleus, requiring high stability from the heating holder during the beginning of the reaction. Recently, Picher et al. have reported the formation of a graphene layer that developed into an SWCNT on a Co–carbide catalyst on an MgO support (Picher et al. 2014). Time-resolved images of the nucleation step were obtained by reducing the rate of SWCNT growth. In this work, an initial graphene layer was reported to form on a (020) facet of the Co_2C particle and remained tethered to one facet as the other edge of the graphene moved stepwise across a C-terminated (210) facet until reaching and attaching to another (020) surface, at which point the CNT grew out from the particle (Fig. 7.7). DFT calculations confirmed that different works of adhesion of graphene layer for the different crystallographic surfaces determined the tethering and lift-off facets for SWCNT on the catalyst nanoparticle (Picher et al. 2014).

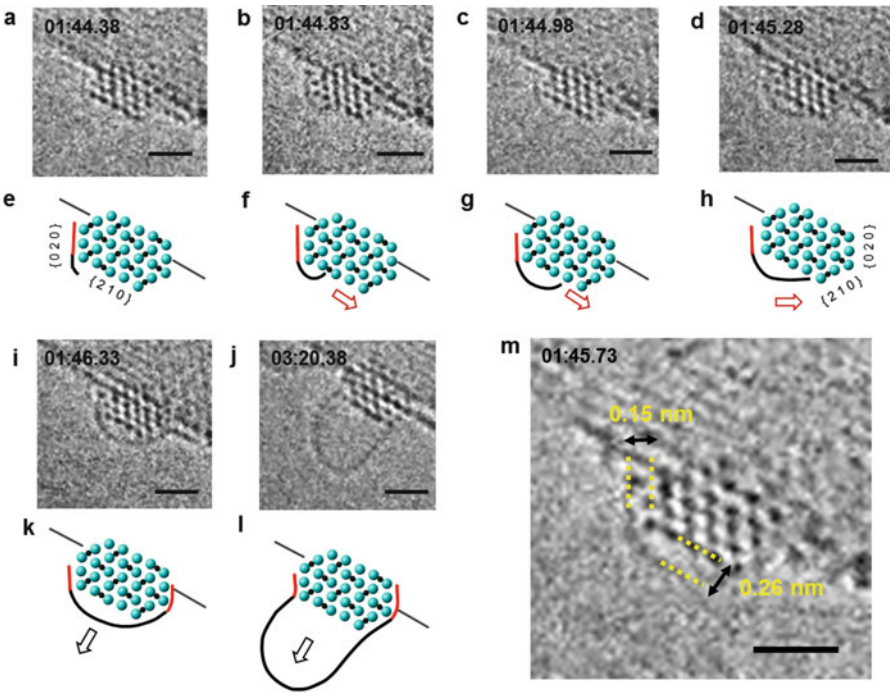

Fig. 7.7 (**a**–**d**, **i**, **j**) A series of images extracted from a video showing SWCNT growth from Co_2C nanoparticle. (**e**–**h**, **k**, **l**) Corresponding atomic models. The *red lines* indicate the stronger adhesion between graphene and metal on the two $Co_2C(020)$ surfaces and the *black line* shows slightly lifted graphene from {210} surface that results in the formation of cap, with the *arrows* indicating the SWCNT growth direction. (**m**) Snapshot showing the average distances between the growing structure and the {020} and {210} catalyst surfaces before the nanotube lift-off. Scale bars are 1 nm

7.9 Limitations

7.9.1 Electron Beam Damage

Various types of damage or other unwanted effects of electron beam irradiation can occur during in situ TEM imaging. Electron beam damage can be categorized into three main classes: (1) beam heating, (2) atom displacement and removal, and (3) contamination. Atom displacement can occur through one of several mechanisms depending on the material. It is important to keep in mind when considering radiation damage that, although the beam energy may be hundreds of thousands of electron volts, damage requires a mechanism for energy transfer from the beam electrons to the sample and higher beam energies can lead to less damage if the likelihood of the damage mechanism decreases. Ionization damage is reduced at higher voltages because the cross section for ionization decreases.

Energy absorbed in the specimen via inelastic scattering from the incident beam can heat the sample. The amount of energy deposited depends on the cross section for excitations, nature, and thickness of sample material. The important conditions to avoid are a high current in a small diameter beam with a low thermal conductivity support. A discussion of beam heating and an equation to calculate the temperature increase can be found in Egerton et al. (2004).

Perhaps the most serious result of beam irradiation for nanomaterial growth is contamination. Particularly for CNT growth, the presence of water and unwanted hydrocarbons on the sample or in the sample area can easily ruin an in situ experiment. Some recommendations for limiting contamination include: plasma clean the sample and support film when possible (Isabell et al. 1999) (carbon films can withstand short durations in a plasma cleaner of ~5 to 20 s); (McGilvery et al. 2012) avoid the use of acetone as cleaning agent or to disperse the catalyst particles on TEM grids—instead use ethanol or isopropanol of high purity from a glass container or use dry loading; heat the sample and film in a clean or inert atmosphere (heating in argon was used to clean graphene films attached to lacey carbon on copper grids for nano-area diffraction) (Tendeloo et al. 2012).

In addition to build-up of material on the sample, contaminant molecules can cause sample etching. The presence of water in particular can catalyze the etching of carbonaceous materials under the electron beam according to the following reactions which can convert C into CO and CO_2: (Hren et al. 1979).

$$H_2O \rightarrow H_2O^+ + e^-$$
$$H_2O^+ + C \rightarrow H + H^+ + CO$$

Ross has reported that the beam has little effect on growth kinetics as the NWs in unirradiated regions can be seen to be approximately the same length as NWs exposed to the beam. However, the beam can decompose the precursor gases causing deposition on the NW sidewalls (Ross 2010).

Carbon materials can be damaged by atom displacement by knock-on damage. The low atomic number of carbon means that the threshold for displacement is usually below the accelerating voltage used. To avoid atom displacement, a beam energy below ~80 kV should be used (Smith and Luzzi 2001). The results of atom displacements in CNTs include the reduction of the diameter as atoms are removed and the formation of a variety of defects. At elevated temperatures, carbon atoms are mobile in CNTs and radiation damage can cause unexpected changes in the CNTs including joining of separate CNTs (Banhart 2006).

Beam heating is expected to be negligible for CNTs as the small cross section for scattering and low thickness mean little energy is transferred to cause heating and CNTs have a high thermal conductivity that quickly removes deposited heat (Banhart 2006; Smith and Luzzi 2001). However, small nanoparticle catalysts on a thermally insulating substrate may experience some beam heating.

Under growth conditions, the anti-contamination device (cold finger) is not used, leading to the presence of a small amount of water that is particularly problematic for imaging of CNTs due to the catalytic etching effect described previously (Mølhave et al. 2007). If imaging of CNTs after growth is necessary, in the

experience of the authors, beam effects can be reduced if the sample temperature is kept at or above ~200 °C which reduces the absorption of water by the sample and allows the point defects generated by the beam to anneal.

Imaging of CNTs grown in the ETEM away from the electron beam shows that for a range of imaging and growth conditions the beam has no measurable effect as CNTs are similar in irradiated and non-irradiated regions after growth at high temperatures. However, the effect of electron radiation should always be monitored for every reaction condition.

7.9.2 Temperature Measurement

Although it had been previously recognized as a potential problem and studied to a limited extent (Baker and Harris 1972), the precise decrease in specimen temperature with gas introduction has not been measured until recently. Direct sample temperature measurements for flowing H_2 and N_2 have been made using diffraction to measure metal lattice expansion (Winterstein et al. 2014) and Raman scattering to measure changes in vibrational states (Picher et al. 2015). Temperature changes of several hundred degrees Celsius have been measured for pressures of ~100 Pa H_2. At much lower pressures (<10 Pa), the change in specimen temperature may be negligible, but it cannot be ignored for high ETEM pressures. Because the nature of nanomaterial growth is very sensitive to specimen temperature, it is important to consider the quenching effect of gases and several test runs may be necessary to identify proper conditions. This should be considered when trying to match in situ reaction conditions to ex situ results.

7.10 Future Research Directions

The features of 1D nanomaterial growth discovered by ETEM experiments confirms the value of ETEM for understanding the basic science of nanotube and nanowire growth. While ETEM experiments have answered many questions, new questions have arisen and remain to be resolved.

Looking to the future, we anticipate higher time resolution to study nucleation events and other rapid phenomena. Imaging with higher time resolution will require new cameras with frame rates greater than the typical ~30 Hz capabilities of CCDs and more stable holders to limit drift during fast heating. New, faster cameras and micro-electro-mechanical system (MEMS) holders with lower drift rates are now available and are being used (see Chap. 5). Detectors with higher quantum efficiencies, necessary for high-speed imaging, can also reduce dose requirements. New correlative techniques for more thorough analysis, e.g., combining light spectroscopy and TEM imaging, should enable a greater understanding of growth processes in the ETEM. Better control of sample temperature with the newer generation of MEMS-based holders should also permit greater accuracy in the extraction of kinetic and thermodynamic information.

References

P.M. Ajayan, C. Colliex, J.M. Lambert, P. Bernier, L. Barbedette, M. Tence, O. Stephan, Growth of manganese filled carbon nanofibers in the vapor phase. Phys. Rev. Lett. **72**(11), 1722–1725 (1994)

P.B. Amama, C.L. Pint, S.M. Kim, L. McJilton, K.G. Eyink, E.A. Stach, R.H. Hauge, B. Maruyama, Influence of alumina type on the evolution and activity of alumina-supported Fe catalysts in single-walled carbon nanotube carpet growth. ACS Nano **4**(2), 895–904 (2010). doi:10.1021/nn901700u

R.T.K. Baker, Catalytic growth of carbon filaments. Carbon **27**(3), 315–323 (1989). doi:http://dx.doi.org/10.1016/0008-6223(89)90062-6

R.T.K. Baker, P.S. Harris, Controlled atmosphere electron microscopy. J. Phys. E Sci. Instrum **5**(8), 793 (1972)

R.T.K. Baker, M.A. Barber, P.S. Harris, F.S. Feates, R.J. Waite, Nucleation and growth of carbon deposits from the nickel catalyzed decomposition of acetylene. J. Catal. **26**(1), 51–62 (1972). doi:10.1016/0021-9517(72)90032-2

F. Banhart, Irradiation of carbon nanotubes with a focused electron beam in the electron microscope. J. Mater. Sci. **41**(14), 4505–4511 (2006). doi:10.1007/s10853-006-0081-0

R.H. Baughman, A.A. Zakhidov, W.A. de Heer, Carbon nanotubes—the route toward applications. Science **297**(5582), 787–792 (2002). doi:10.1126/science.1060928

G.A. Bootsma, H.J. Gassen, A quantitative study on the growth of silicon whiskers from silane and germanium whiskers from germane. J. Cryst. Growth **10**(3), 223–234 (1971). doi:http://dx.doi.org/10.1016/0022-0248(71)90188-6

E.D. Boyes, P.L. Gai, Environmental high resolution electron microscopy and applications to chemical science. Ultramicroscopy **67**(1-4), 219–232 (1997). doi:10.1016/S0304-3991(96)00099-X

M. Cantoro, S. Hofmann, S. Pisana, V. Scardaci, A. Parvez, C. Ducati, A.C. Ferrari, A.M. Blackburn, K.-Y. Wang, J. Robertson, Catalytic chemical vapor deposition of single-wall carbon nanotubes at Low temperatures. Nano Lett. **6**(6), 1107–1112 (2006). doi:10.1021/nl060068y

C.K. Chan, H. Peng, G. Liu, K. McIlwrath, X.F. Zhang, R.A. Huggins, Y. Cui, High-performance lithium battery anodes using silicon nanowires. Nat. Nanotechnol. **3**(1), 31–35 (2008). doi:http://www.nature.com/nnano/journal/v3/n1/suppinfo/nnano.2007.411_S1.html

S.W. Chee, R. Sharma, Controlling the size and the activity of Fe particles for synthesis of carbon nanotubes. Micron **43**(11), 1181–1187 (2012). doi:http://dx.doi.org/10.1016/j.micron.2012.01.008

Y.-C. Chou, C.-Y. Wen, M.C. Reuter, D. Su, E.A. Stach, F.M. Ross, Controlling the growth of Si/Ge nanowires and heterojunctions using silver–gold alloy catalysts. ACS Nano **6**(7), 6407–6415 (2012). doi:10.1021/nn301978x

Y. Cui, Q. Wei, H. Park, C.M. Lieber, Nanowire nanosensors for highly sensitive and selective detection of biological and chemical species. Science **293**(5533), 1289–1292 (2001). doi:10.1126/science.1062711

N.P. Dasgupta, J. Sun, C. Liu, S. Brittman, S.C. Andrews, J. Lim, H. Gao, R. Yan, P. Yang, 25th Anniversary article: semiconductor nanowires—synthesis, characterization, and applications. Adv. Mater. **26**(14), 2137–2184 (2014). doi:10.1002/adma.201305929

R. Daudin, C. Revenant, G. Davi, G. Renaud, Growth and dewetting of gold on Si(111) investigated in situ by grazing incidence small angle x-ray scattering. Physica E Low Dimens. Syst. Nanostruct. **44**(9), 1905–1909 (2012). doi:http://dx.doi.org/10.1016/j.physe.2012.05.021

R.E. Diaz, R. Sharma, K. Jarvis, Q. Zhang, S. Mahajan, Direct observation of nucleation and early stages of growth of GaN nanowires. J. Cryst. Growth **341**(1), 1–6 (2012). doi:http://dx.doi.org/10.1016/j.jcrysgro.2011.09.028

M.S. Dresselhaus, G. Dresselhaus, P. Avouris, *Carbon Nanotubes: Synthesis, Structure, Properties, and Applications* (Springer, Berlin, 2001)

R.F. Egerton, P. Li, M. Malac, Radiation damage in the TEM and SEM. Micron **35**(6), 399–409 (2004). doi:10.1016/j.micron.2004.02.003

A.D. Gamalski, J. Tersoff, R. Sharma, C. Ducati, S. Hofmann, Formation of metastable liquid catalyst during subeutectic growth of germanium nanowires. Nano Lett. **10**, 2972–2976 (2010)

A.D. Gamalski, D.E. Perea, J. Yoo, N. Li, M.J. Olszta, R. Colby, D.K. Schreiber, C. Ducati, S.T. Picraux, S. Hofmann, Catalyst composition and impurity-dependent kinetics of nanowire heteroepitaxy. ACS Nano **7**(9), 7689–7697 (2013). doi:10.1021/nn402208p

E.I. Givargizov, Fundamental aspects of VLS growth. J. Cryst. Growth **31**, 20–30 (1975). doi:http://dx.doi.org/10.1016/0022-0248(75)90105-0

M. Hammar, F.K. LeGoues, J. Tersoff, M.C. Reuter, R.M. Tromp, *In situ* ultrahigh vacuum transmission electron microscopy studies of hetero-epitaxial growth I. Si(001)Ge. Surf. Sci. **349**(2), 129–144 (1996). doi:http://dx.doi.org/10.1016/0039-6028(95)01068-8

J.B. Hannon, S. Kodambaka, F.M. Ross, R.M. Tromp, The influence of the surface migration of gold on the growth of silicon nanowires. Nature **440**(7080), 69–71 (2006). doi:10.1038/nature04574

T. Hansen, J. Wagner, R. Dunin-Borkowski, Aberration corrected and monochromated environmental transmission electron microscopy: challenges and prospects for materials science. Mater. Sci. Technol. **26**(11), 1338–1344 (2010). doi:10.1179/026708310X12756557336355

A.R. Harutyunyan, T. Tokune, E. Mora, Liquid as a required catalyst phase for carbon single-walled nanotube growth. Appl. Phys. Lett. **87**(5), 87–89 (2005). doi:http://dx.doi.org/10.1063/1.2005395

S. Helveg, C. Lopez-Cartes, J. Sehested, P.L. Hansen, B.S. Clausen, J.R. Rostrup-Nielsen, F. Abild-Pedersen, J.K. Norskov, Atomic-scale imaging of carbon nanofibre growth. Nature **427**(6973), 426–429 (2004). doi:http://www.nature.com/nature/journal/v427/n6973/suppinfo/nature02278_S1.html

K. Hillerich, K.A. Dick, C.-Y. Wen, M.C. Reuter, S. Kodambaka, F.M. Ross, Strategies to control morphology in hybrid group III–V/group IV heterostructure nanowires. Nano Lett. **13**(3), 903–908 (2013). doi:10.1021/nl303660h

A.I. Hochbaum, P. Yang, Semiconductor nanowires for energy conversion. Chem. Rev. **110**(1), 527–546 (2009). doi:10.1021/cr900075v

S. Hofmann, R. Sharma, C. Ducati, G. Du, C. Mattevi, C. Cepek, M. Cantoro, S. Pisana, A. Parvez, F. Cervantes-Sodi, A.C. Ferrari, R. Dunin-Borkowski, S. Lizzit, L. Petaccia, A. Goldoni, J. Robertson, *In situ* observations of catalyst dynamics during surface-bound carbon nanotube nucleation. Nano Lett. **7**(3), 602–608 (2007). doi:10.1021/nl0624824

S. Hofmann, R. Sharma, C.T. Wirth, F. Cervantes-Sodi, C. Ducati, T. Kasama, R.E. Dunin-Borkowski, J. Drucker, P. Bennett, J. Robertson, Ledge-flow-controlled catalyst interface dynamics during Si nanowire growth. Nat. Mater. **7**(5), 372–375 (2008). doi:http://www.nature.com/nmat/journal/v7/n5/suppinfo/nmat2140_S1.html

S. Hofmann, R. Blume, C.T. Wirth, M. Cantoro, R. Sharma, C. Ducati, M. Hävecker, S. Zafeiratos, P. Schnoerch, A. Oestereich, D. Teschner, M. Albrecht, A. Knop-Gericke, R. Schlögl, J. Robertson, State of transition metal catalysts during carbon nanotube growth. J. Phys. Chem. C **113**(5), 1648–1656 (2009). doi:10.1021/jp808560p

J.J. Hren, J. Goldstein, D.C. Joy, *Introduction to Analytical Electron Microscopy* (Plenum Press, New York, 1979)

S. Iijima, Helical microtubules of graphitic carbon. Nature **354**(6348), 56–58 (1991)

T.C. Isabell, P.E. Fischione, C. O'Keefe, M.U. Guruz, V.P. Dravid, Plasma cleaning and its applications for electron microscopy. Microsc. Microanal. **5**(02), 126–135 (1999). doi:10.1017/S1431927699000094

B.J. Kim, J. Tersoff, S. Kodambaka, M.C. Reuter, E.A. Stach, F.M. Ross, Kinetics of individual nucleation events observed in nanoscale vapor-liquid-solid growth. Science **322**(5904), 1070–1073 (2008). doi:10.1126/science.1163494

S.M. Kim, C.L. Pint, P.B. Amama, R.H. Hauge, B. Maruyama, E.A. Stach, Catalyst and catalyst support morphology evolution in single-walled carbon nanotube supergrowth: growth

deceleration and termination. J. Mater. Res. **25**(10), 1875–1885 (2010a). doi:10.1557/JMR.2010.0264

S.M. Kim, C.L. Pint, P.B. Amama, D.N. Zakharov, R.H. Hauge, B. Maruyama, E.A. Stach, Evolution in catalyst morphology leads to carbon nanotube growth termination. J. Phys. Chem. Lett. **1**(6), 918–922 (2010b). doi:10.1021/jz9004762

S. Kodambaka, J.B. Hannon, R.M. Tromp, F.M. Ross, Control of Si nanowire growth by oxygen. Nano Lett. **6**(6), 1292–1296 (2006a). doi:10.1021/nl060059p

S. Kodambaka, J. Tersoff, M.C. Reuter, F.M. Ross, Diameter-independent kinetics in the vapor-liquid-solid growth of Si nanowires. Phys. Rev. Lett. **96**(9), 096105 (2006b)

S. Kodambaka, J. Tersoff, M.C. Reuter, F.M. Ross, Germanium nanowire growth below the eutectic temperature. Science **316**(5825), 729–732 (2007). doi:10.1126/science.1139105

K.K.K. Koziol, C. Ducati, A.H. Windle, Carbon nanotubes with catalyst controlled chiral angle. Chem. Mater. **22**(17), 4904–4911 (2010). doi:10.1021/cm100916m

M. Lin, J.P. Ying Tan, C. Boothroyd, K.P. Loh, E.S. Tok, Y.-L. Foo, Direct observation of single-walled carbon nanotube growth at the atomistic scale. Nano Lett. **6**(3), 449–452 (2006). doi:10.1021/nl052356k

M. Lin, J.P.Y. Tan, C. Boothroyd, K.P. Loh, E.S. Tok, Y.-L. Foo, Dynamical observation of bamboo-like carbon nanotube growth. Nano Lett. **7**(8), 2234–2238 (2007). doi:10.1021/nl070681x

P. Madras, E. Dailey, J. Drucker, Kinetically induced kinking of vapor−liquid−solid grown epitaxial Si nanowires. Nano Lett. **9**(11), 3826–3830 (2009). doi:10.1021/nl902013g

S. Mazzucco, Y. Wang, M. Tanase, M. Picher, K. Li, Z. Wu, S. Irle, R. Sharma, Direct evidence of active and inactive phases of Fe catalyst nanoparticles for carbon nanotube formation. J. Catal. **319**, 54–60 (2014). doi:http://dx.doi.org/10.1016/j.jcat.2014.07.023

M.L. McDonald, J.M. Gibson, F.C. Unterwald, Design of an ultrahigh-vacuum specimen environment for high-resolution transmission electron microscopy. Rev. Sci. Instrum. **60**(4), 700–707 (1989). doi:http://dx.doi.org/10.1063/1.1141004

C.M. McGilvery, A.E. Goode, M.S.P. Shaffer, D.W. McComb, Contamination of holey/lacey carbon films in STEM. Micron **43**(2–3), 450–455 (2012). doi:http://dx.doi.org/10.1016/j.micron.2011.10.026

M. Meyyappan, *Carbon Nanotubes: Science and Applications* (CRC Press, Boca Raton, 2005)

A. Moisala, A.G. Nasibulin, E.I. Kauppinen, The role of metal nanoparticles in the catalytic production of single-walled carbon nanotubes—a review. J. Phys. Condens. Matter **15**(42), S3011 (2003)

K. Mølhave, S.B. Gudnason, A.T. Pedersen, C.H. Clausen, A. Horsewell, P. Bøggild, Electron irradiation-induced destruction of carbon nanotubes in electron microscopes. Ultramicroscopy **108**(1), 52–57 (2007). doi:http://dx.doi.org/10.1016/j.ultramic.2007.03.001

M. Moseler, F. Cervantes-Sodi, S. Hofmann, G. Csányi, A.C. Ferrari, Dynamic catalyst restructuring during carbon nanotube growth. ACS Nano **4**(12), 7587–7595 (2010). doi:10.1021/nn102118y

H. Okamoto, T.B. Massalski, The Au−Si (Gold-Silicon) system. Bull. Alloy Phase Diagrams **4**(2), 190–198 (1983). doi:10.1007/BF02884878

M. Picher, P.A. Lin, J.L. Gomez-Ballesteros, P.B. Balbuena, R. Sharma, Nucleation of graphene and its conversion to single-walled carbon nanotubes. Nano Lett. (2014). doi:10.1021/nl501977b

M. Picher, S. Mazzucco, S. Blankenship, R. Sharma, M. Picher, S. Mazzucco, S. Mazzucco, Vibrational and optical spectroscopies integrated with environmental transmission electron microscopy. Ultramicroscopy **150**, 10–15 (2015). doi:10.1016/j.ultramic.2014.11.023

V. Purushothaman, K. Jeganathan, Investigations on the role of Ni-catalyst for the VLS growth of quasi-aligned GaN nanowires by chemical vapor deposition. J. Nanopart. Res **15**(7), 1–12 (2013). doi:10.1007/s11051-013-1789-9

S. Rackauskas, H. Jiang, J.B. Wagner, S.D. Shandakov, T.W. Hansen, E.I. Kauppinen, A.G. Nasibulin, *In situ* study of noncatalytic metal oxide nanowire growth. Nano Lett. **14** (10), 5810–5813 (2014). doi:10.1021/nl502687s

S. Reich, L. Li, J. Robertson, Control the chirality of carbon nanotubes by epitaxial growth. Chem. Phys. Lett **421**(4–6), 469–472 (2006). doi:http://dx.doi.org/10.1016/j.cplett.2006.01.110

M.E. Reimer, G. Bulgarini, N. Akopian, M. Hocevar, M.B. Bavinck, M.A. Verheijen, E.P.A.M. Bakkers, L.P. Kouwenhoven, V. Zwiller, Bright single-photon sources in bottom-up tailored nanowires. Nat. Commun. **3**, 737 (2012)

J. Robertson, Realistic applications of CNTs. Mater. Today **7**(10), 46–52 (2004). doi:http://dx.doi.org/10.1016/S1369-7021(04)00448-1

J. Robertson, Heterogeneous catalysis model of growth mechanisms of carbon nanotubes, graphene and silicon nanowires. J. Mater. Chem. **22**(37), 19858–19862 (2012). doi:10.1039/C2JM33732K

F.M. Ross, Controlling nanowire structures through real time growth studies. Rep. Prog. Phys. **73** (11), 114501 (2010)

F.M. Ross, J. Tersoff, M.C. Reuter, Sawtooth faceting in silicon nanowires. Phys. Rev. Lett. **95** (14), 146104 (2005)

D. Schebarchov, S.C. Hendy, Capillary absorption of metal nanodroplets by single-wall carbon nanotubes. Nano Lett. **8**(8), 2253–2257 (2008). doi:10.1021/nl080875s

J. Schindelin, I. Arganda-Carreras, E. Frise, V. Kaynig, M. Longair, T. Pietzsch, S. Preibisch, C. Rueden, S. Saalfeld, B. Schmid, J.-Y. Tinevez, D.J. White, V. Hartenstein, K. Eliceiri, P. Tomancak, A. Cardona, Fiji: an open-source platform for biological-image analysis. Nat. Methods **9**(7), 676–682 (2012). doi:http://www.nature.com/nmeth/journal/v9/n7/abs/nmeth.2019.html#supplementary-information

C.A. Schneider, W.S. Rasband, K.W. Eliceiri, NIH Image to ImageJ: 25 years of image analysis. Nat. Methods **9**(7), 671–675 (2012)

R. Sharma, Design and applications of environmental cell transmission electron microscope for *in situ* observations of gas–solid reactions. Microsc. Microanal. **7**(06), 494–506 (2001)

R. Sharma, An environmental transmission electron microscope for *in situ* synthesis and characterization of nanomaterials. J. Mater. Res. **20**(07), 1695–1707 (2005). doi:10.1557/JMR.2005.0241

R. Sharma, Kinetic measurements from *in situ* TEM observations. Microsc. Res. Tech. **72**(3), 144–152 (2009). doi:10.1002/jemt.20667

R. Sharma, Experimental set up for *in situ* transmission electron microscopy observations of chemical processes. Micron **43**(11), 1147–1155 (2012). doi:http://dx.doi.org/10.1016/j.micron.2012.01.007

R. Sharma, Z. Iqbal, *In situ* observations of carbon nanotube formation using environmental transmission electron microscopy. Appl. Phys. Lett. **84**(6), 990–992 (2004). doi:http://dx.doi.org/10.1063/1.1646465

B.W. Smith, D.E. Luzzi, Electron irradiation effects in single wall carbon nanotubes. J. Appl. Phys. **90**(7), 3509–3515 (2001). http://dx.doi.org/10.1063/1.1383020

B.W. Smith, D.E. Luzzi, Electron irradiation effects in single wall carbon nanotubes. J. Appl. Phys. **90**(7), 3509–3515 (2001). doi:10.1063/1.1383020

L. Sun, F. Banhart, A.V. Krasheninnikov, J.A. Rodríguez-Manzo, M. Terrones, P.M. Ajayan, Carbon nanotubes as high-pressure cylinders and nanoextruders. Science **312**(5777), 1199–1202 (2006). doi:10.1126/science.1124594

G.V. Tendeloo, D. Van Dyck, S.J. Pennycook, *Handbook of Nanoscopy* (Wiley-VCH, Weinheim, 2012)

B.A. Wacaser, M.C. Reuter, M.M. Khayyat, C.-Y. Wen, R. Haight, S. Guha, F.M. Ross, Growth system, structure, and doping of aluminum-seeded epitaxial silicon nanowires. Nano Lett. **9**(9), 3296–3301 (2009). doi:10.1021/nl9015792

R.S. Wagner, W.C. Ellis, Vapor-liquid-solid mechanism of single crystal growth. Appl. Phys. Lett. **4**(5), 89–90 (1964). doi:http://dx.doi.org/10.1063/1.1753975

J.B. Wagner, F. Cavalca, C.D. Damsgaard, L.D.L. Duchstein, T.W. Hansen, Exploring the environmental transmission electron microscope. Micron **43**(11), 1169–1175 (2012). doi: http://dx.doi.org/10.1016/j.micron.2012.02.008

D. Wang, A. Pierre, M.G. Kibria, K. Cui, X. Han, K.H. Bevan, H. Guo, S. Paradis, A.-R. Hakima, Z. Mi, Wafer-level photocatalytic water splitting on GaN nanowire arrays grown by molecular beam epitaxy. Nano Lett. **11**(6), 2353–2357 (2011). doi:10.1021/nl2006802

C.-Y. Wen, M.C. Reuter, J. Bruley, J. Tersoff, S. Kodambaka, E.A. Stach, F.M. Ross, Formation of compositionally abrupt axial heterojunctions in silicon-germanium nanowires. Science **326** (5957), 1247–1250 (2009a). doi:10.1126/science.1178606

C.Y. Wen, M.C. Reuter, J. Tersoff, E.A. Stach, F.M. Ross, Structure, growth kinetics, and ledge flow during vapor−solid−solid growth of copper-catalyzed silicon nanowires. Nano Lett. **10** (2), 514–519 (2009b). doi:10.1021/nl903362y

J. Winterstein, P. Ann Lin, R. Sharma, Measurement of local specimen temperature under flowing Gas ambient in the environmental scanning transmission electron microscope (ESTEM) using diffraction. Microsc. Microanal. **20**(S3), 1596–1597 (2014). doi:10.1017/S1431927614009714

J.V. Wittemann, W. Münchgesang, S. Senz, V. Schmidt, Silver catalyzed ultrathin silicon nanowires grown by low-temperature chemical-vapor-deposition. J. Appl. Phys. **107**(9), 096105 (2010). doi:http://dx.doi.org/10.1063/1.3393601

Y. Wu, P. Yang, Direct observation of vapor−liquid−solid nanowire growth. J. Am. Chem. Soc. **123**(13), 3165–3166 (2001). doi:10.1021/ja0059084

P. Yang, The chemistry and physics of semiconductor nanowires. MRS Bull **30**, 85–91 (2005)

H. Yoshida, S. Takeda, T. Uchiyama, H. Kohno, Y. Homma, Atomic-scale in-situ observation of carbon nanotube growth from solid state iron carbide nanoparticles. Nano Lett. **8**(7), 2082–2086 (2008). doi:10.1021/nl080452q

H. Yoshida, H. Kohno, S. Takeda, *In situ* structural analysis of crystalline Fe–Mo–C nanoparticle catalysts during the growth of carbon nanotubes. Micron **43**(11), 1176–1180 (2012). doi:http://dx.doi.org/10.1016/j.micron.2012.04.008

Z. Zhang, D. Su, Behaviour of TEM metal grids during in-situ heating experiments. Ultramicroscopy **109**(6), 766–774 (2009). doi:http://dx.doi.org/10.1016/j.ultramic.2009.01.015

H. Zhu, K. Suenaga, A. Hashimoto, K. Urita, K. Hata, S. Iijima, Atomic-resolution imaging of the nucleation points of single-walled carbon nanotubes. Small **1**(12), 1180–1183 (2005). doi:10.1002/smll.200500200

H. Zhu, K. Suenaga, J. Wei, K. Wang, D. Wu, A strategy to control the chirality of single-walled carbon nanotubes. J. Cryst. Growth **310**(24), 5473–5476 (2008). doi:http://dx.doi.org/10.1016/j.jcrysgro.2008.09.174

Chapter 8
The Structure of Catalysts Studied Using Environmental Transmission Electron Microscopy

Thomas W. Hansen and Jakob B. Wagner

8.1 Introduction

In the chemical industry, approximately 85–90 % of all chemicals are made via catalytic processes (Chorkendorff and Niemantsverdriet 2003). Catalysts are used in processes ranging from synthesis of fine chemicals over fuel refinement to abatement of pollution. Heterogeneous catalysts often comprise metal nanoparticles supported on a substrate providing a high dispersion and stabilization of the particles. The nanoparticle surfaces hold the active sites responsible for the conversion of reactants to products. The atomic arrangement at the specific surfaces has large influence on the reaction rate, making it of high importance to be able to study this arrangement on a local scale. Something, which has become a reality with the advent of aberration corrected transmission electron microscopy (TEM) (Hansen and Wagner 2012; Yoshida et al. 2012). Whereas this information could be obtained from more conventional high vacuum microscopy (Honkala et al. 2005; Carlsson et al. 2006; Janssens et al. 2006), the atomic arrangement, and distribution of specific surfaces are most likely different when the catalyst is in a reactive environment.

During reaction, catalysts are often exposed to harsh environments with high temperatures and corrosive gases inside the reactor resulting in a change of the structure of both active nanoparticles and substrate. Effectively this means that the surface of the nanoparticles can oxidize, be poisoned by adsorbing species, or the particles could sinter resulting in larger particles. All these phenomena result in the loss of active surface area. In order to unravel the dynamic entities as a function of the reaction coordinate, structural and spectroscopic studies under a reactive environment are needed (Grunwaldt et al. 2000).

T.W. Hansen (✉) • J.B. Wagner
Center for Electron Nanoscopy, Technical University of Denmark,
Kgs. Lyngby 2800, Denmark
e-mail: twh@cen.dtu.dk

T.W. Hansen, J.B. Wagner (eds.), *Controlled Atmosphere Transmission Electron Microscopy*, DOI 10.1007/978-3-319-22988-1_8

In situ electron microscopy in general and environmental transmission electron microscopy (ETEM) in particular can provide detailed information on a local scale such as particle size distributions, shape of catalytically active nanoparticles, atomic structure and composition of surfaces, etc.—all giving insight in the gas–solid interactions taking place during catalytic activity (Hansen and Wagner 2014). Such knowledge combined with a quantum chemical treatment of the problem using density functional theory and microkinetical models enables prediction of the conversion of reactants to products and hence derivation of an overall reaction rate (Honkala et al. 2005; Brodersen et al. 2011). However, addressing site-specific turnover numbers (Boudart 1995) remains a daunting challenge.

Although atomic resolution of the catalyst in action is of great importance, the overall performance of a catalytic system is dependent on features at different length scales (Grunwaldt et al. 2013). Electron microscopy has the necessary resolution and flexibility to characterize samples at magnifications spanning five orders of magnitude and has had a large impact in heterogeneous catalysis science (Datye 2003; Hansen et al. 2006; Zhang et al. 2013a; Gai et al. 2007).

Even though electron microscopy in general and ETEM in particular are powerful techniques for the catalyst society, they rely considerably on complementary techniques in order to ensure that local effects probed by TEM are representative for the sample as a whole. As an example, the combination of ETEM and in situ EXAFS has been used for studying the morphology of Cu nanoparticles (Grunwaldt et al. 2000; Hansen et al. 2002a). However, the studies are performed in separate experimental setups. Bringing more characterization techniques together in one instrument might, despite the increased complexity, be a beneficial addendum to the ETEM community. As an example, several groups bring light into the microscope via special TEM sample holders facilitating light input by fiber optics or add the light source directly to the microscope column (Cavalca et al. 2012; Miller and Crozier 2013). Light can be guided out of the microscope in the same way. Cathodoluminescence is already possible with dedicated equipment in the microscope, but to the authors knowledge it has not been reported used in combination with a gaseous environment. Having the light-in and the light-out capabilities, it is straightforward to imagine the combination of electron spectroscopy and optical spectroscopy such as Raman spectroscopy and Plasmon resonance spectroscopy in environmental TEM by optimizing the collection solid angle of the optical response signal.

Recently, more sensitive cameras have been developed for TEM allowing for shorter acquisition times and thereby better temporal resolution of the dynamic processes. These include CMOS-based technology and direct electron detection. Both types have improved sensitivity and read out speed compared to traditional CCD-based cameras. See earlier chapters for more information on electron detection. On the sample holder side, MEMS technology is now extensively used. MEMS technology allows for closed cell sample holders compatible with pressures exceeding atmospheric pressure. Using an MEMS-based close cell holder, Vendelbo et al. were able to correlate shape changes of a platinum nanoparticle with changes in the gas composition at 100,000 Pa total pressure (Vendelbo et al. 2014).

Furthermore, miniaturized heaters can be fabricated, where the heated area is only a few hundred micron resulting in a considerable reduction in drift compared to traditional furnace type holders. More information on MEMS technology and its application to sample holders can be found in a later chapter. Aberration correction has also made its way to ETEM experimentation thus bringing the resolution of the microscopes down to below 1 μm.

Recent development in 4D ultrafast electron microscopy (4D UEM) gives the possibility for imaging processes in the femtosecond regime (Flannigan and Zewail 2012). The basic idea behind these highly specialized TEMs is the synchronization of an electron pulse used for imaging and a stimulus of the sample (e.g., heating). This way, high temporal resolution of irreversible reactions can be obtained. In order to have enough electrons in the electron pulse, to image the sample the density of electrons is so high that Coulomb repulsion is limiting the coherence of the electron beam. That results in a somewhat lower spatial resolution than can be obtained in more traditional TEMs. However, 4D UEM shows great potential for imaging at the time scale of chemical reactions.

8.2 Applications Within Catalysis

For supported catalysts, a parameter of interest is typically the particle size distribution. Unlike many other techniques such as X-ray diffraction (XRD), X-ray photoelectron spectroscopy (XPS), and X-ray absorption spectroscopy (XAS) TEM can provide not only the mean particle size but also the size distribution. Admittedly, such a distribution will be obtained from only a limited subset of the particles where XRD, for instance, can provide an estimate of the average size from a macroscopic amount of the sample. However, TEM can provide information far beyond the particle size distribution. ETEM provides an invaluable tool for supporting the current trend in catalysis of engineering particles with a specific functionality.

As catalytic materials are exposed to various gas species at elevated temperatures, accommodate the change in surface energy caused by adsorbed species by redistributing the area of difference facets. Furthermore, after prolonged exposure to a reactive environment, catalyst nanoparticles tend to deactivate by sintering or poisoning of specific surfaces and their surfaces could restructure. The restructured and often dynamic surface forms the basis for the "active" sites during a catalytic reaction. Although morphology changes of the catalysts are observed under gaseous atmosphere in the ETEM linking it directly to the activity of the catalyst is difficult as quantitative measurements of conversion and selectivity is far from an easy task in the ETEM setup. In the pursuit of measuring reaction products, the group at Arizona State University has made significant progress by measuring the electron energy-loss signal of the gas phase. In this way, they have successfully measured the conversion of carbon monoxide to carbon dioxide (Chenna and Crozier 2012). These efforts are further described in an earlier chapter.

Whereas products of catalytic reactions are challenging to measure in the ETEM, the conditions to which the samples are exposed mimic those found in the catalytic converter, albeit typically at much lower pressure. Still, most of the pressure gap between UHV experimentation and industrial catalysis has been bridged. Experimental observations from a single technique should never stand alone. Interpretations should be done on conjunction with other techniques capable of extending the bridge to fully cover the gap.

Contrary to many other experimental techniques, electron microscopy provides detailed information about specific sites on a local scale. This means that for example the refaceting of an individual nanoparticle as its surroundings vary or the trajectory of individual mobile nanoparticles can be followed. This is not possible with any other technique. The following sections are meant to illustrate the capabilities of the electron microscope within catalysis taking advantage of the recent developments mentioned above.

8.3 On the Active State of Supported Metal Catalysts

8.3.1 Cu/ZnO: Methanol Synthesis

As the environment around metal nanoparticles changes, the fraction of different gases adsorbed on the surfaces changes. This can result in a change of the specific surface energy allowing for a restructuring of the particle. Using the first ETEM equipped with a field emission electron source, Hansen et al. demonstrated this effect on a Cu/ZnO methanol synthesis catalyst (Hansen et al. 2002a).

As summarized in Fig. 8.1, the catalyst was exposed to various environments found in the methanol synthesis reactor: H_2, H_2/H_2O and H_2, CO, all at 220 °C. In pure hydrogen, the copper particles appeared faceted exposing the low-index facets (100), (110), and (111). As the surroundings became more oxidizing by adding H_2O, the particles adopted a more spherical shape due to relative change in the facet-specific surface energies by adsorption of OH species. Under these conditions, the particles remained metallic as determined by HRTEM analysis. When switching the environment to a more reducing environment by adding CO to the hydrogen, the particles again exposed facets but the distribution of the different facets changed and the particle wetted the ZnO surface. Two explanations, which might both contribute to the observed effect, were suggested. First, the surface energy of the copper particles changes as CO adsorbs on the particle surface. Secondly, the surface of the zinc oxide support is slightly reduced offering a different interface energy to the copper particle. In contradiction to the morphology changes observed as an effect of the H_2O treatment, the wetting of the Cu particles was observed to be irreversible when CO was removed after the CO/H_2 treatment indicating that the major effect is caused by surface reduction of the ZnO. The chemical state of the Cu nanoparticles under the different environments was further

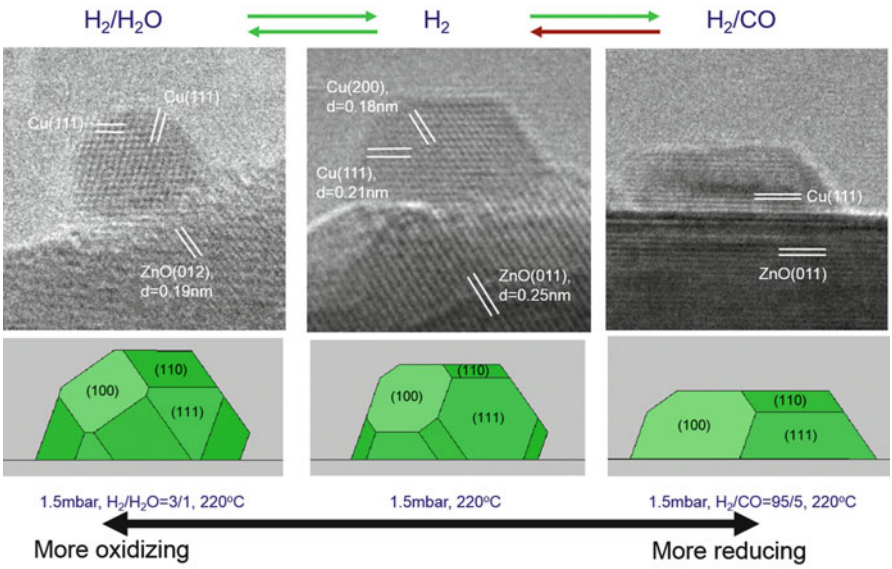

Fig. 8.1 TEM images showing the reversible shape change of a Cu nanoparticle. The same Cu nanoparticle is imaged at 220 °C under (**a**) H_2 at 150 Pa, (**b**) H_2:H_2O (3:1) at a total pressure of 150 Pa, and (**c**) H_2 at 150 Pa. Reproduced from (Hansen et al. 2002a). Copyright 2002 American Association for the Advancement of Science

studied by electron energy-loss spectroscopy (EELS). In all cases described above, Cu was found to be in the metallic state (Wagner et al. 2003). The findings from the ETEM studies were consistent with the results from Grunwaldt et al. who studied a similar catalyst system. Using EXAFS, it was determined that the Cu–Cu coordination number change reversibly during changes in the reaction conditions indicating a morphology change of the Cu nanoparticles (Grunwaldt et al. 2000). The study also confirmed that alloys of Zn and Cu do not form under methanol synthesis conditions. The metallic state of copper under reaction conditions was also confirmed in an infrared spectroscopy (FTIR) study by Topsøe and Topsøe (Topsoe and Topsoe 1999). The morphology change of the Cu particles has been used as input for microkinematical models in order to relate the distribution of facets to the activity (Askgaard et al. 1995; Wagner et al. 2002; Topsøe and Topsøe 1999).

In a more recent study by Cabié et al.(2010), a similar phenomenon was observed for platinum nanoparticles. The platinum nanoparticles were mainly truncated by (001) facets in O_2 and mainly by (111) facets in H_2. Refaceting was again observed when the same set of nanoparticles was re-exposed to oxygen. The same group studied the refaceting further including other catalyst systems including Au and Ag nanoparticles as well (Giorgio et al. 2008; Molina et al. 2011).

8.3.2 Au/Oxides: CO Oxidation

Typically, the outermost layers of a nanoparticle will restructure depending on the composition of the surrounding gas atmosphere. Observing the atomic configuration under a reactive environment is necessary in order to unravel the nature of the active site for a given reaction.

Despite gold being chemically inert in the bulk (Hammer and Nørskov 1995), gold nanoparticles below about 10 nm are highly active for the oxidation of carbon monoxide to carbon dioxide even at temperatures below room temperature (Haruta et al. 1989, 1993). Gold nanoparticles have been studied extensively using electron microscopy, focusing specifically on nanoparticle sizes, surface structure, support interface, and growth (Akita et al. 2013). For gold, nanoparticle growth is particularly important as all activity is lost when the nanoparticles exceed a certain size (Akita et al. 2001).

Using an aberration corrected ETEM, Yoshida et al. investigated gold nanoparticles supported on cerium dioxide (Yoshida et al. 2012). The catalyst was first observed in vacuum, where the surface did not restructure as viewed in the <110> zone axis—see Fig. 8.2. As the sample was exposed to a mixture of 1 % CO in air, the outermost gold layer expanded from 0.20 nm (as also observed in

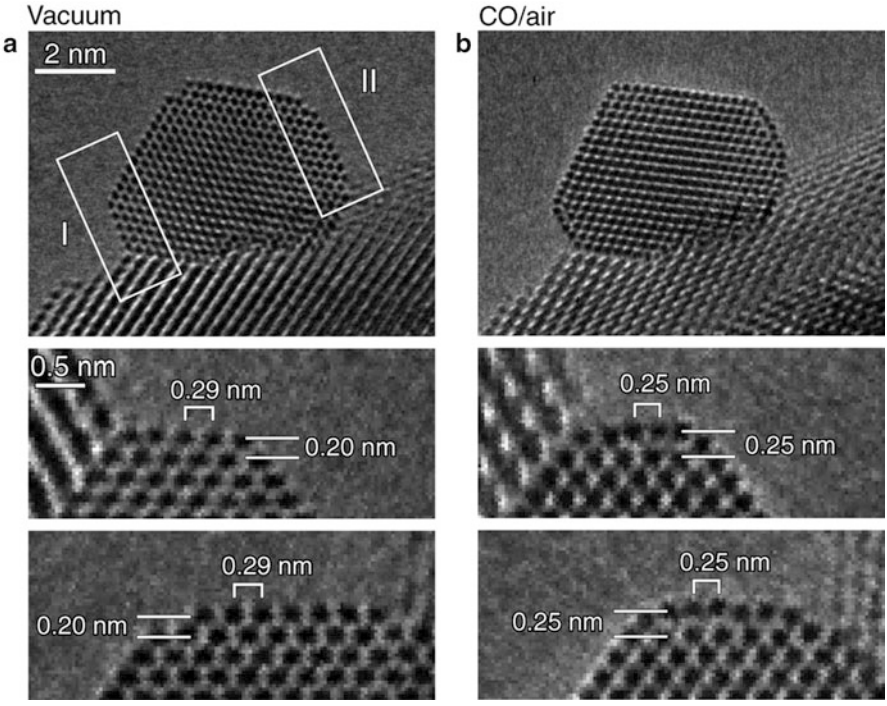

Fig. 8.2 Au {100} reconstructed surface under catalytic conditions. The CeO_2-supported gold nanoparticle in (**a**) vacuum and (**b**) a reaction environment (1 vol.% CO in air gas mixture at 45 Pa at room temperature). Reproduced from (Yoshida et al. 2012). Copyright 2012 American Association for the Advancement of Science

bulk Au) to 0.25 nm. The combination of the ETEM observations with ab initio calculations using the VASP package (Kresse and Hafner 1993) show that the restructured gold nanoparticle surface accommodates a higher surface coverage of CO molecules compared to the bulk terminated structure due to an unusual bonding arrangement with the second gold layer. Similarly, Uchiyama et al. studied the shape of gold nanoparticles supported on cerium oxide in different atmospheres. Their main observations were that when exposed to CO/air mixtures, the gold nanoparticles were truncated by low energy {111} and {100} facets (Uchiyama et al. 2011).

8.3.3 Ru/BN: Ammonia Synthesis

Supported ruthenium nanoparticles have been found to be a highly active catalyst for ammonia synthesis (Jacobsen 2001). Studies of Ru nanoparticles supported on carbon, boron nitride, magnesium aluminum spinel, and alumina have shown these catalysts to be significantly more active than traditional iron-based catalysts (Hansen et al. 2001, 2002b; Kowalczyk et al. 1996). The addition of barium as promoter increased the integral reaction by more than a factor of 10. Hence, obtaining insight into the role of the promoter phase could provide valuable insight into workings of this catalyst system.

When imaged in high vacuum at room temperature, the surface of the ruthenium nanoparticles was covered by a layered structure identified as hexagonal boron nitride, a strong indication of strong metal support interactions (SMSI) (Tauster et al. 1978; Tauster 1987). This layer entirely disguised the surface structure of the metal nanoparticles, see Fig. 8.3a, b. When exposed to a reactive environment consisting of a 3:1 mixture of H_2 and N_2 in the ETEM at a total pressure of about 500 Pa at ca. 550 °C, the surface layer was removed exposing the surface of the metal particles, see Fig. 8.3c, d. A similar surface coverage was observed by Kowalczyk and coworkers for ruthenium supported on carbon (Kowalczyk et al. 1999). After treatment in H_2/N_2, the surfaces of the metal particles revealed a periodic structure, see Fig. 8.3d, which by EELS was shown to contain barium. As the promoter phase was observed on the surface of the active metal particles, the promotional effect was believed to be of electronic nature. This was, however, contested by other studies (Szmigiel et al. 2002; Raróg et al. 2000).

The striking difference in surface structure from vacuum to a reactive environment shows the significance of imaging catalytic metal nanoparticles under conditions resembling the operating environment if the true nature of the active site is to be unraveled. Furthermore, it stresses the importance of imaging catalysts under reactive environments if any information about active sites is to be obtained.

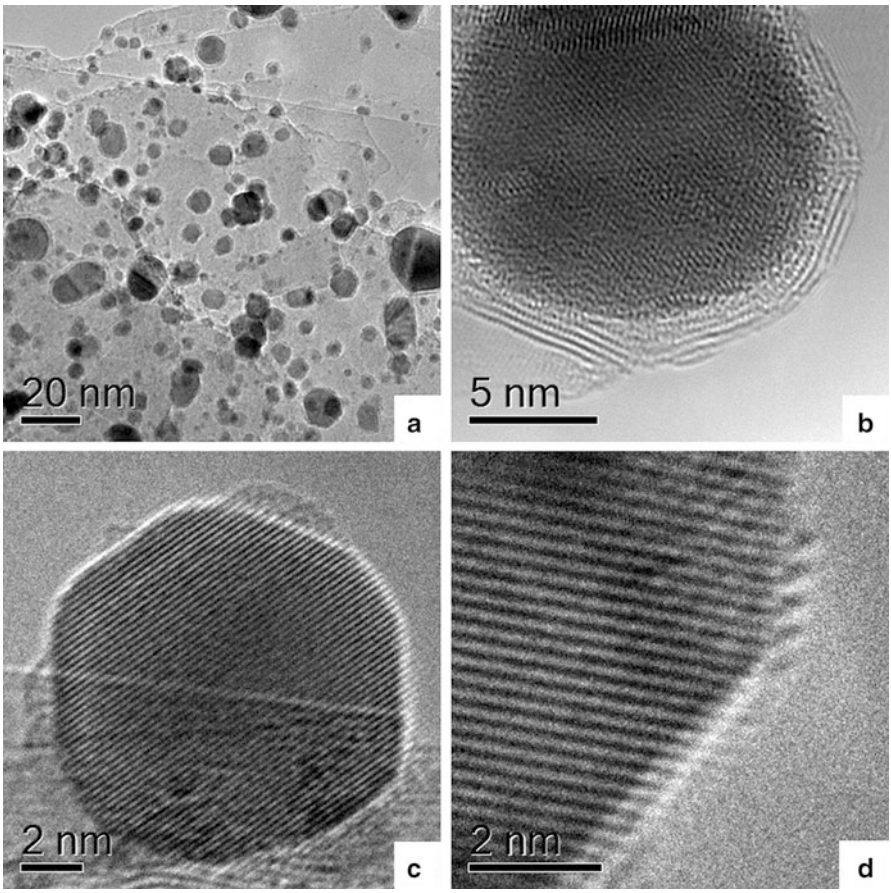

Fig. 8.3 Ruthenium nanoparticles supported on boron nitride. In vacuum (**a**, **b**), all particles are encapsulated in boron nitride layers. Ruthenium nanoparticles supported on boron nitride in 3:1 H_2/N_2 at 450 °C (**c**, **d**) the surfaces are exposed to the gas phase. Reproduced from (Hansen et al. 2001). Copyright 2001 American Association for the Advancement of Science

8.3.4 Photocatalysis

Photocatalysis, where light irradiation provides most of the energy for a reaction, has great potential for solar fuels (Kudo and Miseki 2009). In order to understand structure-reactivity relations at the atomic level, it is necessary to introduce light as a stimulus in the ETEM in addition to a gaseous phase, typically water vapor.

Allowing sample irradiation with light has been accomplished in two distinct ways. Either light has been coupled to the sample via a port on the objective lens of the microscope (Miller and Crozier 2011) or through the barrel of the sample holder (Cavalca et al. 2012; Shindo et al. 2009). Each approach comes with its own

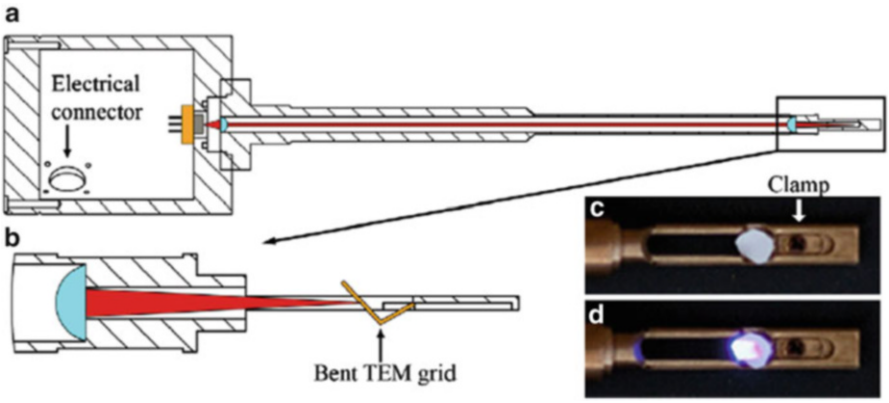

Fig. 8.4 Schematic cross-sectional view of the lens-based specimen holder. (**a**) The feedthrough on the left hosts a laser diode, which is connected through a mini-DIN connector installed in the lateral port. Two lenses (shown in *blue*), selected for the chosen laser wavelength, collimate and focus the light onto the sample. (**b**) A close-up cross-sectional side view of the tip. The sample (shown in *yellow*) is bent in order to allow it to be exposed to both light and electron beams. (**c**, **d**). Photographs of the tip with the illumination off and on, respectively (Cavalca et al. 2012)

advantages and complexities. Whereas the former approach allows for using different holder with additional functionality, e.g., heating, the latter construction offers the possibility of compatibility with different microscopes. Figure 8.4 shows the design of a holder with an integrated lens focusing the light onto the sample. A laser diode is fitted into the housing of the holder. In a similar design, optical fibers are inserted into the barrel of the holder guiding the light all the way to the sample. When inserting the fibers through the objective lens of the microscope, special considerations have to be made regarding the termination of the optical fiber inside the microscope in order to achieve an even illumination of the sample.

Using in situ illumination, Cavalca et al. studied the evolution of cuprous oxide in an aqueous atmosphere. Cu_2O nanocubes in the range 100–200 nm were dispersed onto a lacey carbon film on a gold TEM grid. The sample was characterized using TEM, electron diffraction, and EELS prior to exposure to water vapor and light. Figure 8.5 shows the evolution via the three techniques. All data clearly indicates a reduction from oxide to metal during light illumination.

Miller and Crozier adapted and ETEM to include an optical fiber into the sample region via the microscope column (Miller and Crozier 2011). Using this setup, Zhang et al. studied the amorphization of anatase titanium dioxide, a stable catalyst for water splitting. In their investigation, an amorphous layer formed on top of initially crystalline facets (Zhang et al. 2013b). Figure 8.6 shows a titania particle exposed to light and water vapor for 12 h showing a disordered layer on the (101) and (002) facets. The process was found to be self-limiting as the thickness of the layer did not increase after prolonged exposure to light and water vapor. This is in agreement with the stability of the catalyst.

ETEM compatible light illumination has been developed, and interested readers should see the references (Cavalca et al. 2012, 2013; Miller and Crozier 2011, 2012, 2013).

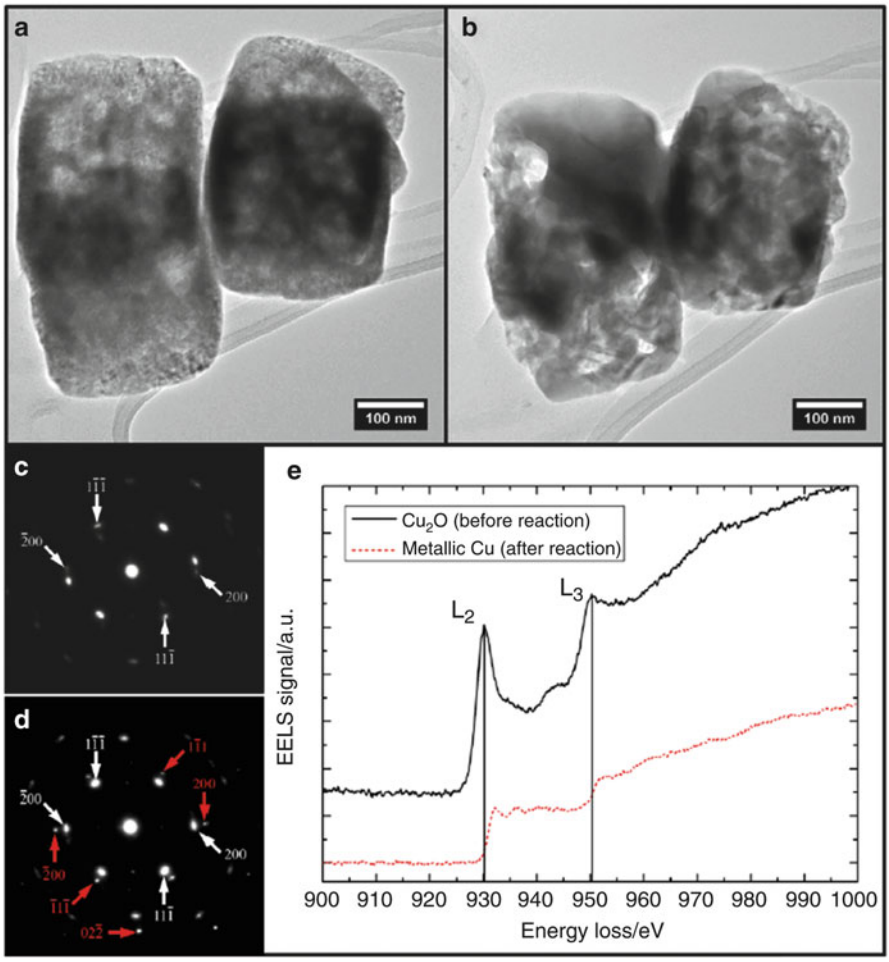

Fig. 8.5 (**a**, **b**) Bright-field TEM images of Cu_2O nanocubes before and after reaction, respectively, showing changes in particle shape and morphology (Cavalca et al. 2012). No significant damage to the supporting carbon film was observed. The growth of large single crystals of Cu is observed. (**c**, **d**) Selected area diffraction patterns in the [011] zone axis, indexed for Cu_2O (**c**) and for both Cu_2O and Cu (**d**). The area sampled by the selected area aperture is 400 nm in diameter and encompasses at least two of the particles shown in (**a**, **b**). After the reaction, (**d**) contains spots representative of metallic copper, labeled in *red*. Spots from Cu_2O are still present as some portions of the particles are not completely reduced. (**e**) Electron energy-loss spectra of the same nanocubes. The *upper curve* is offset vertically for ease of comparison. The positions of the peaks of the L_2 and L_3 EELS edges are indicated by the *vertical black lines*

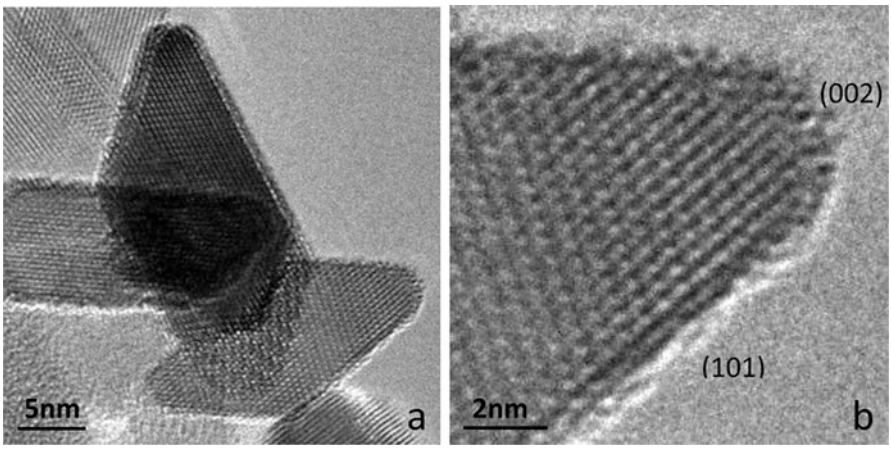

Fig. 8.6 (**a**) Fresh anatase particles after 40 h in H_2O gas at 150 °C, light exposure 12 h; (**b**) magnified images of the (101) and (002) surfaces after illumination. The image was taken in 20 s including adjusting the focus (Zhang et al. 2013b)

8.4 Catalyst Deactivation

8.4.1 Dynamic Studies: Growth and Oxidation of Carbon Structures

Catalyzed growth of extended carbon nanofiber structures in the form of either filaments or tubes have been a major point of interest for decades. Before the constructive use of carbon nanotubes in materials science, the formation of carbon nanofiber structures has been acknowledged as a severe problem in heterogeneous catalysis. For instance, in nickel-based steam-reforming catalysts, the growth of carbon nanofibers resulting from low H_2O/C ratio or high temperature can have catastrophic effects (Rostrup-Nielsen and Christiansen 2011). When fibers grow inside catalyst pellets, they can break up the pellet structuring leaving granulates blocking the reactor resulting in a high pressure drop (Rostrup-Nielsen 1975).

Helveg et al. studied the formation of fibrous carbon structures in a nickel-based steam-reforming catalyst using environmental TEM (Helveg et al. 2004). In a 1:1 mixture of hydrogen and methane, growth of both carbon filaments or whiskers and carbon nanotubes (CNTs) was observed. Figure 8.7 illustrates the dynamical behavior of the Ni catalysts during CNT growth. Based on the experimental observation of the growth process and modelling by density functional theory (DFT), the authors concluded that individual graphene layers of the carbon filaments were formed at step edges as the carbon atoms bind more strongly here. Details on the experiment are described by Helveg et al. (2004) and corresponding supplementary movies showing the growth.

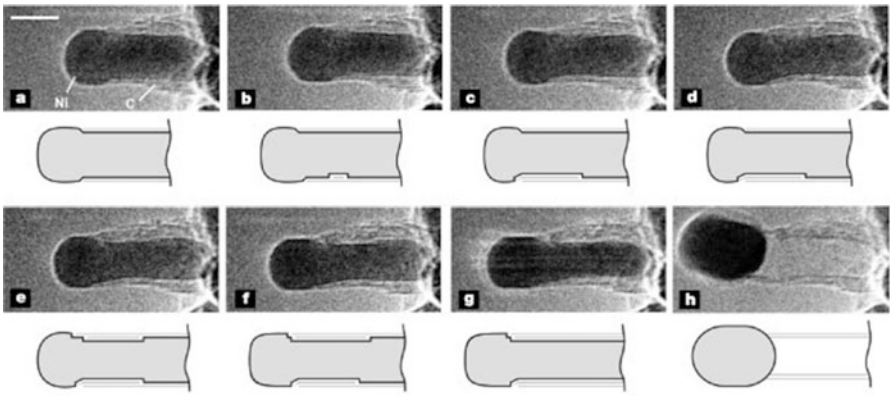

Fig. 8.7 Image sequence of a growing carbon nanofiber illustrating an elongation/contraction process. Mono-atomic Ni steps are found to be the point of formation for the carbon layers (guide-to-the-eye drawings are included in the figure). The images are acquired in situ with CH_4:H_2=1:1 at 210 Pa with the sample heated to 536 °C. Reproduced from (Helveg et al. 2004). Copyright 2004 Nature Publishing Group (Helveg et al. 2004)

With stricter demands on emission control being enforced worldwide, oxidation of particulate matter from particularly diesel engines is a topic of increasing interest (van Setten et al. 2001). Simonsen et al. studied the oxidation of soot over a ceria catalyst (Simonsen et al. 2008) for vehicle emission control with emphasis on the soot-ceria interface under oxidizing conditions. As model soot, 30 nm carbon black particles were used. The study concluded that the oxidation occurs solely at the soot-ceria interface. A motion of the particles towards the interface, which established a continuous interface and an efficient reaction point, accompanied the oxidation of soot.

8.4.2 Sintering of Supported Metal Catalysts

Sintering or growth of nanoparticles is a deactivation route that plagues supported metal catalysis (Sehested 2006). The phenomenon has been studied at great length using TEM under a controlled atmosphere from the time the technique became available (Baker et al. 1974). More recent studies include both model systems (Simonsen et al. 2010, 2011; Benavidez et al. 2012) as well as technical catalysts (Hansen 2006; Hansen et al. 2013; Liu et al. 2004).

Two mechanisms of mass transfer are suggested to be responsible for sintering of metal nanoparticles. One mechanism suggests that atomic species or small entities can migrate from smaller to larger particles due to a difference in chemical potential; this is known as Ostwald ripening (OR). The other mechanism is particle migration and coalescence (PMC), where particles migrate on the substrate and coalesce into single particles as they encounter each other. Both mechanisms play a

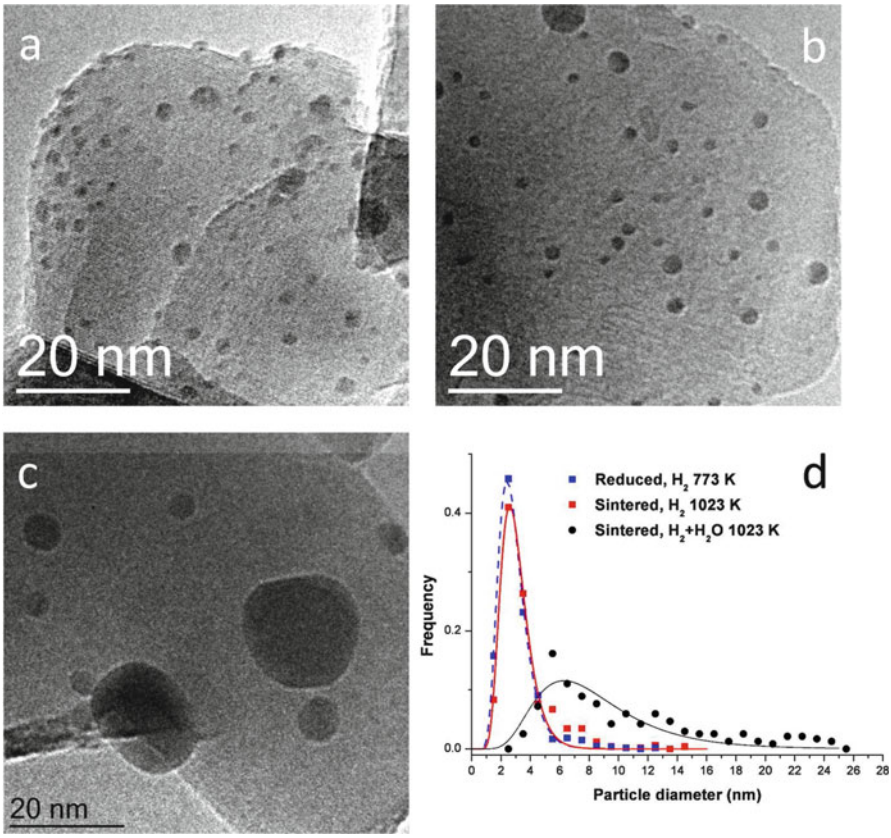

Fig. 8.8 TEM images of a $Ni/MgAl_2O_4$ sample. (**a**) After reduction in 300 Pa H_2 at 500 °C; (**b**) after sintering for 5 h in 200 Pa H_2 at 750 °C; (**c**) after sintering for 5 h in 200 Pa H_2 and 200 Pa H_2O at 750 °C; (**d**) particle size distributions for the three cases. Reproduced from (Hansen et al. 2013). Copyright 2013 American Chemical Society

role in industrial catalysis, the dominant mechanism being determined by the reaction conditions. Traditionally, the shape of the particle size distribution after a given time on stream has been used to determine the mechanism of sintering. A tail on the small diameter side of the mean size indicated an OR mechanism, whereas a tail on the large diameter side of the mean indicates growth by PMC (Wynblatt and Gjostein 1975; Granqvist and Buhrman 1975).

Figure 8.8 shows images and size distributions of spinel-supported nickel nanoparticles determined from TEM images. First, the sample was reduced in 300 Pa H_2 at 500 °C (Fig. 8.8a), and then exposed to the sintering environment, 200 Pa H_2 at 750 °C (Fig. 8.8b) and 200 Pa H_2 and 200 Pa H_2O at 750 °C (Fig. 8.8c) for 5 h. The particle size distributions after reduction and after sintering determined from a set of TEM images are shown in Fig. 8.8d. Both distributions after sintering show a tail on the large diameter side of the mean indicating that the growth

occurred via PMC and a strong effect of atmosphere composition is observed. In order to further document the sintering mechanism, the particles were imaged during exposure to the sintering environments (Hansen et al. 2013). Based on these observations along with observation of the initial exposure to a reactive environment (DeLaRiva et al. 2013; Challa et al. 2011), Hansen et al. suggested that the sintering of supported metal nanoparticles could be divided into three phases (Hansen et al. 2013). In phase 1, a rapid decrease of activity is observed, and sintering is dominated by OR. During this stage, the catalyst reaches its operating temperature and the metal particles attain their equilibrium shape. In phase 2, sintering slows down but particles still grow in size, mainly via particle migration. Phase 3 represents the stable operation of the catalyst; the active particles have reached a size, where migration is very slow.

The same authors have also investigated the phenomenon of anomalous particle growth (Benavidez et al. 2012). Here, some particles grow to sizes significantly larger than the ensemble mean size. The phenomenon was already described in the mid 1970s by Wynblatt and Gjostein (1975). Platinum particles were physically deposited on a silicon oxide film and investigated in the ETEM. The sample was exposed to a flow of oxygen at 560 Pa, and the temperature was increased to 550 °C. Sets of images were acquired in intervals over 10 h while keeping the electron beam off between image acquisition in order to minimize the electron exposure of the sample, see Fig. 8.9. After prolonged exposure to the sintering conditions, particles with a diameter considerably larger than the mean started to evolve. The emergence of these particles does not result in a significant shift in the particle size distribution (Fig. 8.10).

Traditionally, the migration of nanoparticles has been a strong function of the particle size (r^{-4} dependence). Whereas such a behavior may be true on a perfectly flat substrate, other observations have been made recently. Hansen et al. studied the mobility of nickel particles on a magnesium aluminum spinel substrate. Here, particles were observed to migrate be creeping along steps on the support. However, contrary to conventional knowledge, the smallest particles were rarely the most mobile. Larger particles were observed to be more mobile and coalesce with

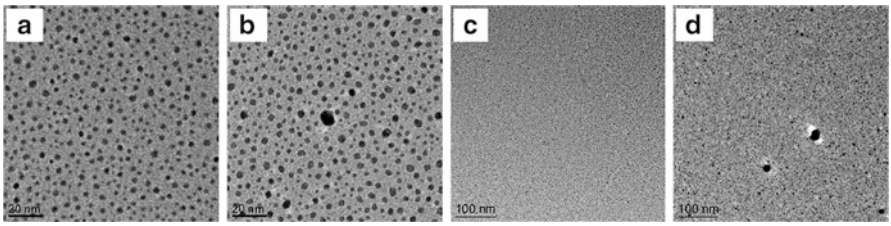

Fig. 8.9 Platinum NPs supported on SiO_2/Si_3N_4 acquired in 560 Pa O_2 at 550 °C. Panels (**a**, **b**) are acquired after 30 min and panels (**c**, **d**) after 10 h. Panels (**a**, **b**) show high magnification images recorded after 30 min and 10 h, respectively, and used for determination of PSDs. Panels (**c**, **d**) show medium magnification images recorded after the same times. At medium magnification, panels (**c**, **d**), a larger field of view is captured and the appearance of anomalously large particles is evident (Benavidez et al. 2012)

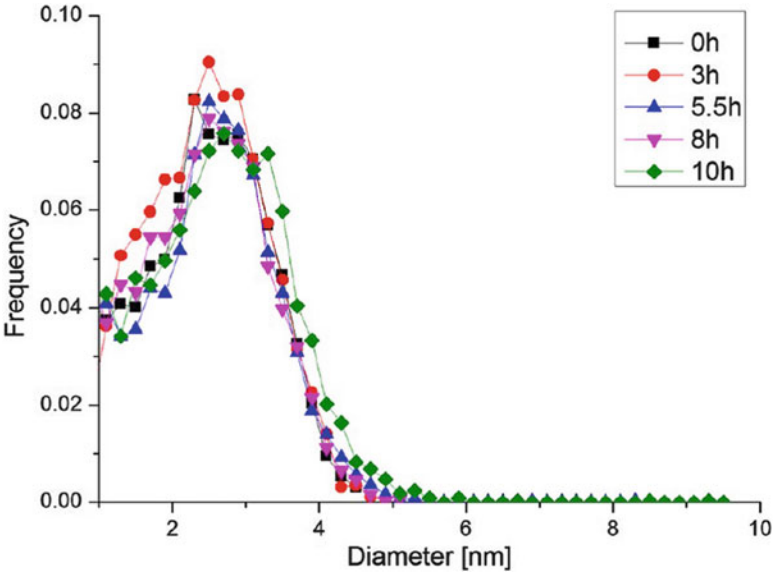

Fig. 8.10 PSDs determined after 0, 3, 5.5, 8, and 10 h, respectively, from images acquired at high magnification. The distributions appear very similar up to 8 h after which a slight shift to larger particles is observed. The bin size is 0.2 nm (Benavidez et al. 2012)

smaller particles on their route. The smallest particles appear to be stable whereas the larger particles migrate, see Fig. 8.11. These observations indicate that the structure of the support may play a significant role in stabilizing catalytic nanoparticles.

Even though sintering in practice is challenging to control, knowledge of the governing processes is crucial if more sintering stable catalysts are to be developed. Modifications of the support material creating more anchoring sites is one possibility that may limit particle migration or even reduce migration speeds of single atoms or small clusters reducing Ostwald ripening. Such materials engineering could greatly benefit society.

8.4.3 Fuel Cells

Fuel cells are one of the most promising technologies for decentralized energy production. They exist in various forms operating at various temperatures. The class of fuel cells known as solid oxide fuel cells (SOFC) are candidates for power production up to a few megawatts. The name stems from the use of a solid oxide as the electrolyte transporting the negatively charged oxygen ions from the cathode to the anode. The anode of an SOFC typically consists of nickel oxide and yttria-stabilized zirconia (YSZ). It is synthesized by sintering NiO particles with YSZ

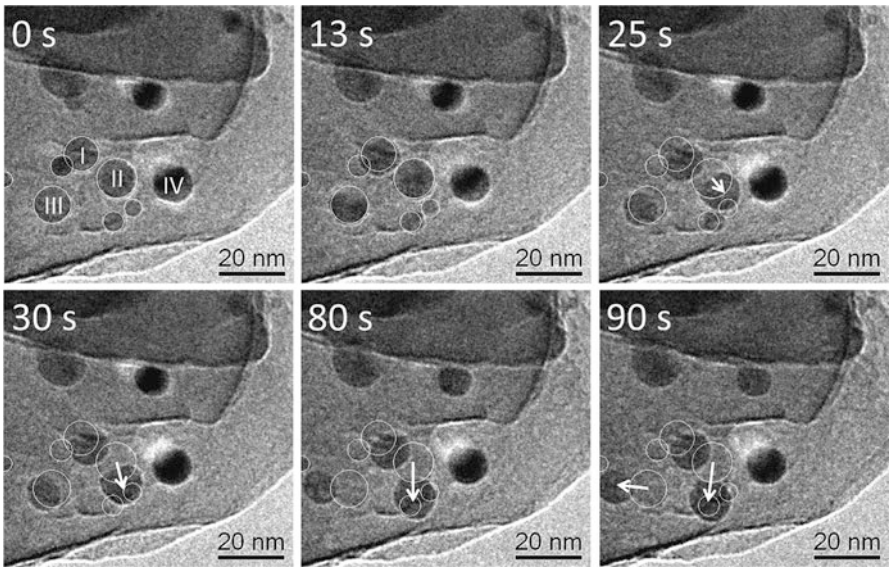

Fig. 8.11 TEM images of $Ni/MgAl_2O_4$ catalyst. This is an image sequence acquired in 200 Pa H_2O and 200 Pa H_2 at 750 °C. Individual frames have been aligned to make it easier to see the motion of individual nanoparticles and to allow us to track these particles. The frames are acquired at 0, 13, 25, 30, 80, and 90 s. The *white circles* indicate the initial positions of the particles and four particles that survived at the end of the treatment are indicated with numbers I–IV. *Arrows* show the particle mobility seen in the next frame. The image sequence shows that the larger particles are more mobile than the smaller particles, and the particles appear to nucleate preferentially at steps on the support (Hansen et al. 2013)

followed by a reduction process. During the reduction, pores are formed in the anode-enhancing gas permeability. During standard operating conditions, the nickel is kept in the reduced state. However, various types of failures including seal leakage and uncontrolled shut downs may result in reoxidation.

Jeangros et al. studied the reduction and reoxidation of a slice of an SOFC using environmental transmission electron microscopy (Jeangros et al. 2010). The slice was prepared using focused ion beam (FIB) and was attached to a TEM grid for mounting in a heating holder. First, the samples were exposed to 140 Pa of flowing hydrogen, and the temperature was ramped up to 200 °C. After allowing 30 min for stabilization, after which the temperature was further increased to first 300 °C in two steps and then to 500 °C in 10 °C steps. From 300 °C and onwards, bright-field images, diffraction patterns, and EELS were acquired in order to monitor the oxidation state of nickel, see Fig. 8.12. The reduction was observed to initiate as nanovoids at the NiO/YSZ interfaces starting at 340 °C. At 420 °C, the free surfaces of the NiO grains start to reduce and the porosity fills the entire NiO grains. After reaching 500 °C, the temperature was maintained for 2 h and then ramped down to room temperature, still in flowing H_2. After reaching room temperature, the H_2 was evacuated from the ETEM and oxygen was introduced at a pressure of 320 Pa and a

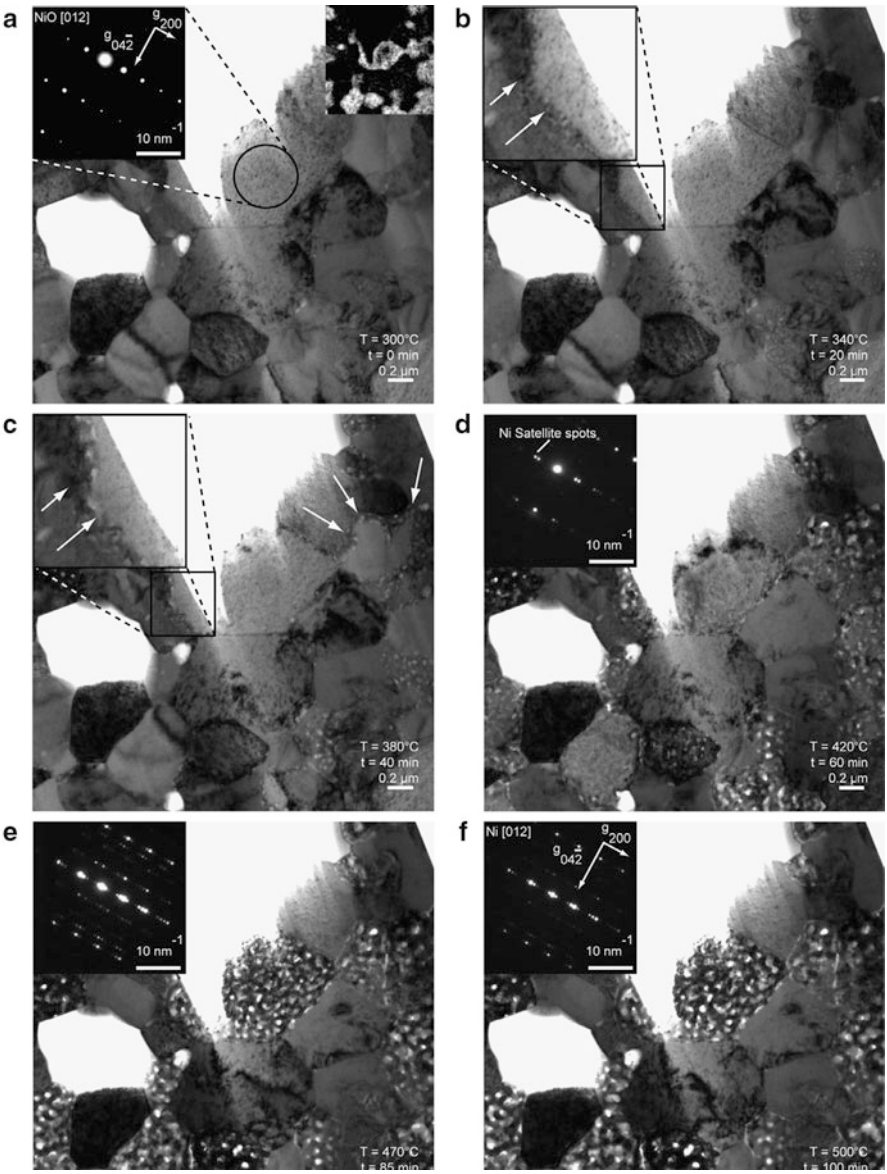

Fig. 8.12 Bright-field TEM images acquired during in situ reduction of a NiO/YSZ anode precursor in 140 Pa of H_2. Higher magnification images, diffraction patterns, and a nickel map obtained using energy-filtered TEM are shown as *insets*. The *arrows* in (**b**, **c**) show the nanovoids (Jeangros et al. 2010)

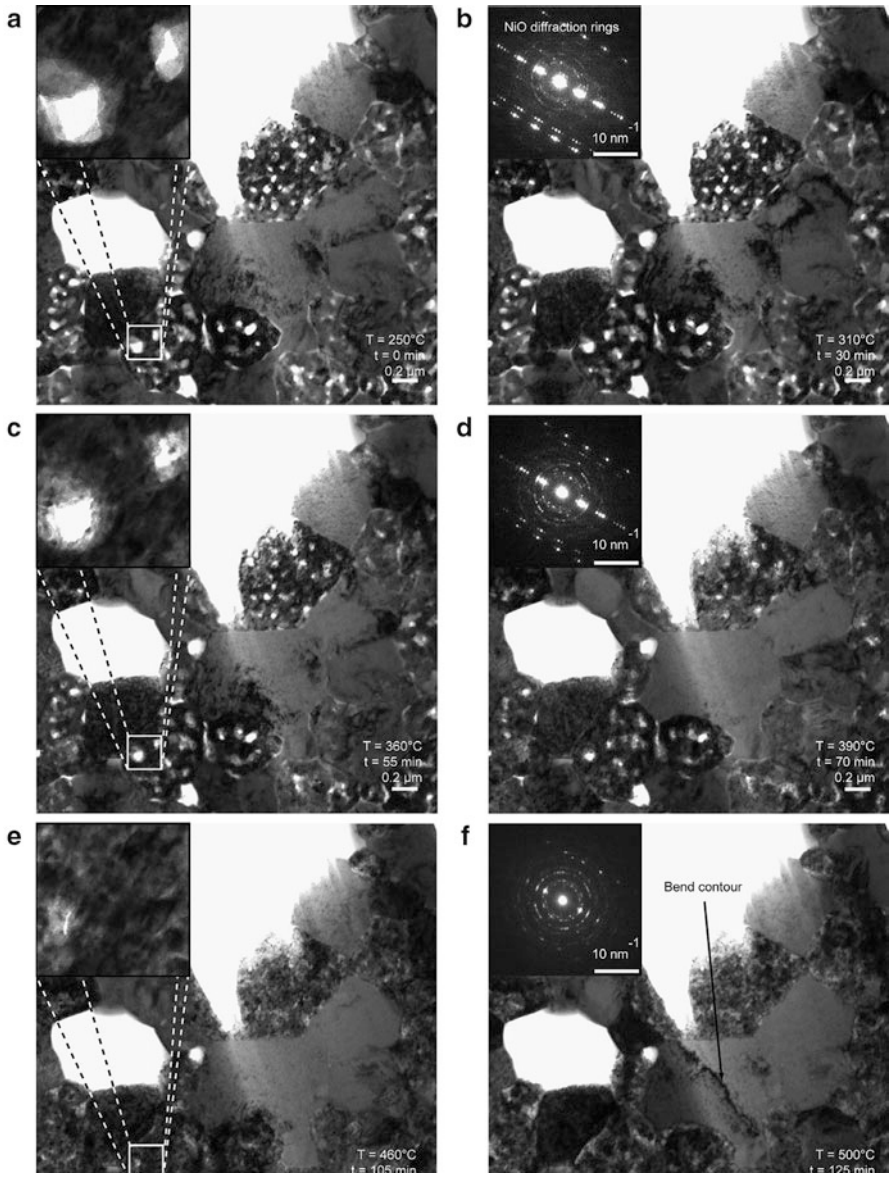

Fig. 8.13 Bright-field TEM images acquired during in situ reoxidation in 320 Pa O_2. Higher magnification images and diffraction patterns are shown as *insets* (Jeangros et al. 2010)

similar temperature increase and data acquisition as during reduction was performed, see Fig. 8.13. During reoxidation, the voids formed during reduction are filled with polycrystalline nickel oxide. Contrary to the reduction process, the reoxidation process occurs uniformly throughout the nickel grains starting at ca. 290 °C.

In this study, results obtained from ETEM support previous experimental observations (Waldbillig et al. 2005) and theoretical predictions (Jeangros et al. 2010). The results were further corroborated by investigations of oxidation properties of nickel particles under similar conditions (Jeangros et al. 2014).

8.5 Conclusions

The investigation of catalysts in a reactive environment can be a daunting feat scientifically as well as technically. Catalysts are dynamic entities and their state and structure changes with their surroundings and over time. ETEM provides a powerful tool for imaging samples at the atomic scale with simultaneous acquisition of spectroscopic information, all in a simulated working environment. Having this tool in the toolbox provides information on the local level that can ultimately dictate the development of the next generation of catalysts and functional materials when combined with other more globally probing characterization and analysis tools.

References

T. Akita, P. Lu, S. Ichikawa, K. Tanaka, M. Haruta, Analytical TEM study on the dispersion of Au nanoparticles in Au/TiO_2 catalyst prepared under various temperatures. Surf. Interface Anal. **31**, 73–78 (2001)

T. Akita, M. Kohyama, M. Haruta, Electron microscopy study of gold nanoparticles deposited on transition metal oxides. Acc. Chem. Res. **46**, 1773–1782 (2013)

T.S. Askgaard, J.K. Norskov, C.V. Ovesen, P. Stoltze, A kinetic-model of methanol synthesis. J. Catal. **156**, 229–242 (1995)

R.T.K. Baker, P.S. Harris, R.B. Thomas, Direct observation of particle mobility on a surface in a gaseous environment. Surf. Sci. **46**, 311–316 (1974)

A.D. Benavidez, L. Kovarik, A. Genc, N. Agrawal, E.M. Larsson, T.W. Hansen, A.M. Karim, A.K. Datye, Environmental transmission electron microscopy study of the origins of anomalous particle size distributions in supported metal catalysts. ACS Catal. **2**, 2349–2356 (2012)

M. Boudart, Turnover rates in heterogeneous catalysis. Chem. Rev. **95**, 661–666 (1995)

S.H. Brodersen, U. Gronbjerg, B. Hvolbaek, J. Schiotz, Understanding the catalytic activity of gold nanoparticles through multi-scale simulations. J. Catal. **284**, 34–41 (2011)

M. Cabie, S. Giorgio, C.R. Henry, M.R. Axet, K. Philippot, B. Chaudret, Direct observation of the reversible changes of the morphology of Pt nanoparticles under gas environment. J. Phys. Chem. C **114**, 2160–2163 (2010)

A. Carlsson, A. Puig-Molina, T.V.W. Janssens, New method for analysis of nanoparticle geometry in supported fee metal catalysts with scanning transmission electron microscopy. J. Phys. Chem. B **110**, 5286–5293 (2006)

F. Cavalca, A.B. Laursen, B.E. Kardynal, R.E. Dunin-Borkowski, S. Dahl, J.B. Wagner, T.W. Hansen, In situ transmission electron microscopy of light-induced photocatalytic reactions. Nanotechnology **23**, 075705 (2012)

F. Cavalca, A.B. Laursen, J.B. Wagner, C.D. Damsgaard, I. Chorkendorff, T.W. Hansen, Light-induced reduction of cuprous oxide in an environmental transmission electron microscope. ChemCatChem **5**, 2667–2672 (2013)

S.R. Challa, A.T. Delariva, T.W. Hansen, S. Helveg, J. Sehested, P.L. Hansen, F. Garzon, A.K. Datye, Relating rates of catalyst sintering to the disappearance of individual nanoparticles during Ostwald ripening. J. Am. Chem. Soc. **133**, 20672–20675 (2011)

S. Chenna, P.A. Crozier, Operando transmission electron microscopy: a technique for detection of catalysis using electron energy-loss spectroscopy in the transmission electron microscope. ACS Catal. **2**, 2395–2402 (2012)

I. Chorkendorff, J.W. Niemantsverdriet, *Concepts of Modern Catalysis and Kinetics* (Wiley-VCH, Weinheim, 2003)

A.K. Datye, Electron microscopy of catalysts: recent achievements and future prospects. J. Catal. **216**, 144–154 (2003)

A.T. DeLaRiva, T.W. Hansen, S.R. Challa, A.K. Datye, In situ transmission electron microscopy of catalyst sintering. J. Catal. **308**, 291–305 (2013)

D.J. Flannigan, A.H. Zewail, 4D Electron microscopy: principles and applications. Acc. Chem. Res. **45**, 1828–1839 (2012)

P.L. Gai, E.D. Boyes, S. Helveg, P.L. Hansen, S. Giorgio, C.R. Henry, Atomic-resolution environmental transmission electron microscopy for probing gas-solid reactions in heterogeneous catalysis. MRS Bull. **32**, 1044–1050 (2007)

S. Giorgio, M. Cabie, C.R. Henry, Dynamic observations of Au catalysts by environmental electron microscopy. Gold Bull. **41**, 167–173 (2008)

C.G. Granqvist, R.A. Buhrman, Statistical-model for coalescence of islands in discontinuous films. Appl. Phys. Lett. **27**, 693–694 (1975)

J.D. Grunwaldt, A.M. Molenbroek, N.Y. Topsøe, H. Topsøe, B.S. Clausen, In situ investigations of structural changes in Cu/ZnO catalysts. J. Catal. **194**, 452–460 (2000)

J.D. Grunwaldt, J.B. Wagner, R.E. Dunin-Borkowski, Imaging catalysts at work: a hierarchical approach from the macro- to the meso- and nano-scale. ChemCatChem **5**, 62–80 (2013)

B. Hammer, J.K. Nørskov, Why gold is the noblest of all the metals. Nature **376**, 238 (1995)

T.W. Hansen, *Sintering and Particle Dynamics in Supported Metal Catalysts, in Department of Chemistry* (Lyngby, Technical University of Denmark, 2006)

T.W. Hansen, J.B. Wagner, Environmental transmission electron microscopy in an aberration-corrected environment. Microsc. Microanal. **18**, 684–690 (2012)

T.W. Hansen, J.B. Wagner, Catalysts under controlled atmospheres in the transmission electron microscope. ACS Catal. **4**, 1673–1685 (2014)

T.W. Hansen, J.B. Wagner, P.L. Hansen, S. Dahl, H. Topsøe, C.J.H. Jacobsen, Atomic-resolution in situ transmission electron microscopy of a promoter of a heterogeneous catalyst. Science **294**, 1508–1510 (2001)

P.L. Hansen, J.B. Wagner, S. Helveg, J.R. Rostrup-Nielsen, B.S. Clausen, H. Topsøe, Atom-resolved imaging of dynamic shape changes in supported copper nanocrystals. Science **295**, 2053–2055 (2002a)

T.W. Hansen, P.L. Hansen, S. Dahl, J.H. Jacobsen, Support effect and active sites on promoted ruthenium catalysts for ammonia synthesis. Catal. Lett. **84**, 7–12 (2002b)

P.L. Hansen, S. Helveg, A.K. Datye, Atomic-scale imaging of supported metal nanocluster catalysts in the working state. Adv. Catal. **50**, 77–95 (2006)

T.W. Hansen, A.T. Delariva, S.R. Challa, A.K. Datye, Sintering of catalytic nanoparticles: particle migration or Ostwald ripening? Acc. Chem. Res. **46**, 1720–1730 (2013)

M. Haruta, N. Yamada, T. Kobayashi, S. Iijima, Gold catalysts prepared by coprecipitation for low-temperature oxidation of hydrogen and of carbon-monoxide. J. Catal. **115**, 301–309 (1989)

M. Haruta, S. Tsubota, T. Kobayashi, H. Kageyama, M.J. Genet, B. Delmon, Low-temperature oxidation of CO over gold supported on TiO_2, alpha-Fe_2O_3, and Co_3O_4. J. Catal. **144**, 175–192 (1993)

S. Helveg, C. Lopez-Cartes, J. Sehested, P.L. Hansen, B.S. Clausen, J.R. Rostrup-Nielsen, F. Abild-Pedersen, J.K. Nørskov, Atomic-scale imaging of carbon nanofibre growth. Nature **427**, 426–429 (2004)

K. Honkala, A. Hellman, I.N. Remediakis, A. Logadottir, A. Carlsson, S. Dahl, C.H. Christensen, J.K. Norskov, Ammonia synthesis from first-principles calculations. Science **307**, 555–558 (2005)

C.J.H. Jacobsen, Boron nitride: a novel support for ruthenium-based ammonia synthesis catalysts. J. Catal. **200**, 1–3 (2001)

T.V.W. Janssens, A. Carlsson, A. Puig-Molina, B.S. Clausen, Relation between nanoscale Au particle structure and activity for CO oxidation on supported gold catalysts. J. Catal. **240**, 108–113 (2006)

Q. Jeangros, A. Faes, J.B. Wagner, T.W. Hansen, U. Aschauer, J. Van Herle, A. Hessler-Wyser, R.E. Dunin-Borkowski, In situ redox cycle of a nickel-YSZ fuel cell anode in an environmental transmission electron microscope. Acta Mater. **58**, 4578–4589 (2010)

Q. Jeangros, T.W. Hansen, J.B. Wagner, R.E. Dunin-Borkowski, C. Hebert, J. Van Herle, A. Hessler-Wyser, Oxidation mechanism of nickel particles studied in an environmental transmission electron microscope. Acta Mater. **67**, 362–372 (2014)

Z. Kowalczyk, S. Jodzis, J. Sentek, Studies on kinetics of ammonia synthesis over ruthenium catalyst supported on active carbon. Appl. Catal. A **138**, 83–91 (1996)

Z. Kowalczyk, S. Jodzis, W. Raróg, J. Zieliński, J. Pielaszek, A. Presz, Carbon-supported ruthenium catalyst for the synthesis of ammonia. The effect of the carbon support and barium promoter on the performance. Appl. Catal. A **184**, 95–102 (1999)

G. Kresse, J. Hafner, Ab-initio molecular dynamics for open-shell transition metals. Phys. Rev. B **48**, 13115–13118 (1993)

A. Kudo, Y. Miseki, Heterogeneous photocatalyst materials for water splitting. Chem. Soc. Rev. **38**, 253–278 (2009)

R.J. Liu, P.A. Crozier, C.M. Smith, D.A. Hucul, J. Blackson, G. Salaita, In situ electron microscopy studies of the sintering of palladium nanoparticles on alumina during catalyst regeneration processes. Microsc. Microanal. **10**, 77–85 (2004)

B.K. Miller, P.A. Crozier, Visible and UV irradiation of ETEM samples for in-situ studies of photocatalysts. Microsc. Microanal. **17**(Suppl 2), 472–473 (2011)

B.K. Miller, P.A. Crozier, In situ visible and UV illumination of ETEM samples. Microsc. Microanal. **18**(Suppl 2), 1074–1075 (2012)

B.K. Miller, P.A. Crozier, System for in situ UV-visible illumination of environmental transmission electron microscopy samples. Microsc. Microanal. **19**, 461–469 (2013)

L.M. Molina, S. Lee, K. Sell, G. Barcaro, A. Fortunelli, B. Lee, S. Seifert, R.E. Winans, J.W. Elam, M.J. Pellin, I. Barke, V. von Oeynhausen, Y. Lei, R.J. Meyer, J.A. Alonso, A.F. Rodriguez, A. Kleibert, S. Giorgio, C.R. Henry, K.H. Meiwes-Broer, S. Vajda, Size-dependent selectivity and activity of silver nanoclusters in the partial oxidation of propylene to propylene oxide and acrolein: a joint experimental and theoretical study. Catal. Today **160**, 116–130 (2011)

W. Raróg, Z. Kowalczyk, J. Sentek, D. Skladanowski, J. Zieliński, Effect of K, Cs and Ba on the kinetics of NH_3 synthesis over carbon-based ruthenium catalysts. Catal. Lett. **68**, 163–168 (2000)

J.R. Rostrup-Nielsen, *Steam Reforming Catalysts* (Danish Technical Press, Copenhagen, 1975)

J. Rostrup-Nielsen, L.J. Christiansen, in *Concepts in Syngas Manufacture*, ed. by G.J. Hutchings. Catalytic Science Series, vol. 10 (Imperial College Press, London, 2011)

J. Sehested, Four challenges for nickel steam-reforming catalysts. Catal. Today **111**, 103–110 (2006)

D. Shindo, K. Takahashi, Y. Murakami, K. Yamazaki, S. Deguchi, H. Suga, Y. Kondo, Development of a multifunctional TEM specimen holder equipped with a piezodriving probe and a laser irradiation port. J. Electron. Microsc. **58**, 245–249 (2009)

S.B. Simonsen, S. Dahl, E. Johnson, S. Helveg, Ceria-catalyzed soot oxidation studied by environmental transmission electron microscopy. J. Catal. **255**, 1–5 (2008)
S.B. Simonsen, I. Chorkendorff, S. Dahl, M. Skoglundh, J. Sehested, S. Helveg, Direct observations of oxygen-induced platinum nanoparticle ripening studied by in situ TEM. J. Am. Chem. Soc. **132**, 7968–7975 (2010)
S.B. Simonsen, I. Chorkendorff, S. Dahl, M. Skoglundh, J. Sehested, S. Helveg, Ostwald ripening in a Pt/SiO(2) model catalyst studied by in situ TEM. J. Catal. **281**, 147–155 (2011)
D. Szmigiel, J. Zieliński, H. Bielawa, M. Kurtz, O. Hinrichsen, M. Muhler, W. Rarog, S. Jodzis, Z. Kowalczyk, L. Znak, The kinetics of ammonia synthesis over ruthenium-based catalysts: the role of barium and cesium. J. Catal. **205**, 205–212 (2002)
S.J. Tauster, Strong metal-support interactions. Acc. Chem. Res. **20**, 389–394 (1987)
S.J. Tauster, S.C. Fung, R.L. Garten, Strong metal-support interactions. Group 8 noble metals supported on TiO_2. J. Am. Chem. Soc. **100**, 170–175 (1978)
N.Y. Topsoe, H. Topsoe, FTIR studies of dynamic surface structural changes in Cu-based methanol synthesis catalysts. J. Mol. Catal. A Chem **141**, 95–105 (1999)
N.Y. Topsøe, H. Topsøe, FTIR studies of dynamic surface structural changes in Cu-based methanol synthesis catalysts. J. Mol. Catal. A **141**, 95–105 (1999)
T. Uchiyama, H. Yoshida, Y. Kuwauchi, S. Ichikawa, S. Shimada, M. Haruta, S. Takeda, Systematic morphology changes of gold nanoparticles supported on CeO_2 during CO oxidation. Angew. Chem. Int. Ed. Engl. **50**, 10157–10160 (2011)
B. van Setten, M. Makkee, J.A. Moulijn, Science and technology of catalytic diesel particulate filters. Catal. Rev. Sci. Eng. **43**, 489–564 (2001)
S.B. Vendelbo, C.F. Elkjaer, H. Falsig, I. Puspitasari, P. Dona, L. Mele, B. Morana, B.J. Nelissen, R. van Rijn, J.F. Creemer, P.J. Kooyman, S. Helveg, Visualization of oscillatory behaviour of Pt nanoparticles catalysing CO oxidation. Nat. Mater. (2014)
J.B. Wagner, *In Situ Transmission Electron Microscopy of Catalyst Particles*, in *NBIfAPG*. 2002, University of Copenhagen.
J.B. Wagner, P.L. Hansen, A.M. Molenbroek, H. Topsøe, B.S. Clausen, S. Helveg, In situ electron energy loss spectroscopy studies of gas-dependent metal-support interactions in Cu/ZnO catalysts. J. Phys. Chem. B **107**, 7753–7758 (2003)
D. Waldbillig, A. Wood, D.G. Ivey, Electrochemical and microstructural characterization of the redox tolerance of solid oxide fuel cell anodes. J. Power Sources **145**, 206–215 (2005)
P. Wynblatt, N.A. Gjostein, Supported metal crystallites. Prog. Solid State Chem. **9**, 21–58 (1975)
H. Yoshida, Y. Kuwauchi, J.R. Jinschek, K.J. Sun, S. Tanaka, M. Kohyama, S. Shimada, M. Haruta, S. Takeda, Visualizing gas molecules interacting with supported nanoparticulate catalysts at reaction conditions. Science **335**, 317–319 (2012)
S.R. Zhang, L. Nguyen, Y. Zhu, S.H. Zhan, C.K. Tsung, F. Tao, In-situ studies of nanocatalysis. Acc. Chem. Res. **46**, 1731–1739 (2013a)
L.X. Zhang, B.K. Miller, P.A. Crozier, Atomic level in situ observation of surface amorphization in anatase nanocrystals during light irradiation in water vapor. Nano Lett. **13**, 679–684 (2013b)

Chapter 9
Liquid Phase Experiments: Describing Experiments in Liquids and the Special Requirements and Considerations for Such Experiments

Niels de Jonge

Abstract Electron microscopy of specimens in liquid is possible using several different approaches. A cooled sample can be studied in a modified vacuum chamber containing a wet environment comprising vapor and liquid, whereby a thin liquid layer is maintained over the specimen via environmental scanning electron microscopy (ESEM). The sample can also be hermetically sealed from the vacuum by enclosure in a liquid chamber containing at least one thin and electron transparent window. Liquid specimen holders for transmission electron microscopy (TEM) and scanning TEM (STEM) or scanning electron microscopy (SEM) are now commercially available. A variant of this concept is the closure of the vacuum chamber by a window, whereby the electron beam penetrating through a thin window irradiates a sample in liquid outside the vacuum chamber. This chapter provides an overview of the most popular experimental approaches, including correlative light- and electron microscopy. Examples from our research demonstrate how three of these approaches were applied to the study of epidermal growth factor receptor (EGFR) dimerization in the plasma membranes of intact cells, the native structure of yeast, gold nanoparticle uptake, and the formation of gold dendrites.

9.1 Introduction

Electron microscopy achieves sub-Ångstrom resolution in thin solid samples in a high vacuum (Nellist et al. 2004). Many scientific questions, however, relate to specimens in a liquid environment. A liquid environment is of particular relevance for the study of biological specimens, nanoparticle growth, colloidal self-assembly, and electrochemical processes at nanoscale interfaces (de Jonge and Ross 2011).

N. de Jonge (✉)
INM—Leibniz Institute for New Materials, Campus D2 2, 66123, Saarbrücken, Germany

Department of Physics, Saarland University, Campus A5 1, 66123, Saarbrücken, Germany
e-mail: niels.dejonge@leibniz-inm.de

T.W. Hansen, J.B. Wagner (eds.), *Controlled Atmosphere Transmission Electron Microscopy*, DOI 10.1007/978-3-319-22988-1_9

Dating back to the early days of electron microscopy, various approaches have been developed to image samples in a liquid environment (Ruska 1942; Abrams and McBain 1944; Parsons et al. 1974; Parsons 1974). Two different concepts can be distinguished: (1) an open environment in which a liquid layer is maintained in equilibrium with a vapor in the specimen chamber of the electron microscope (Ruska 1942); (2) a closed environment in which the vacuum in the instrument is hermetically sealed from the specimen (Abrams and McBain 1944). The concept of an open environment has formed the basis for the so-called ESEM developed in the 1970s (Danilatos and Robinson 1979; Stokes 2008). Although ESEM has mostly been used to explore dry samples in a gaseous environment, it is actually very useful for studying samples in a thin liquid layer in a wet environment of saturated water vapor. Closed systems have become commercially available in the past decade (Thiberge et al. 2004; de Jonge et al. 2009; Nishiyama et al. 2010; Klein et al. 2011). Initiated by the availability of practical liquid systems for TEM (Williamson et al. 2003; Zheng et al. 2009b; de Jonge et al. 2009), the research field of electron microscopy of liquid specimens has experienced an upsurge of activity in the past few years (de Jonge 2014). Scientists from the field of chemistry, materials science, and biology explored new phenomena not visible before with other microscopy techniques. However, in many cases it turned out that the experiments were not so easy as hoped for. Electron microscopy in liquid poses several practical difficulties on account of the interaction of the electron beam with the liquid (Woehl et al. 2013; Schneider et al. 2014; de Jonge et al. 2014). Yet, these interactions can sometimes be used in one's favor to trigger reactions (Zheng et al. 2009b), can be surmounted with increased knowledge about these types of experiments (Smeets et al. 2015), and do not necessarily present a problem when the electron dose remains within the limit of radiation damage (de Jonge et al. 2009).

It is the aim of this chapter to provide an overview of the available techniques, including the practical aspects of these experiments, and possible application areas. Four of the most popular experimental setups will be presented. We also describe how correlative light- and electron microscopy can be implemented. The chapter is intended to give a flavor of what is possible with electron microscopy of liquid specimens for the interested reader not familiar with the field. This chapter includes a limited selection of references only. A comprehensive review of the field (de Jonge and Ross 2011), as well as a detailed description of all involved practical aspects, can be found elsewhere in literature (de Jonge et al. 2014). To exemplify the use of electron microscopy of liquid specimens, examples of our research are included.

9.2 Systems for Electron Microscopy of Liquid Specimens

Several different approaches exist to study liquid specimens (de Jonge and Ross 2011) (Fig. 9.1), and each has advantages and disadvantages depending on the specific application.

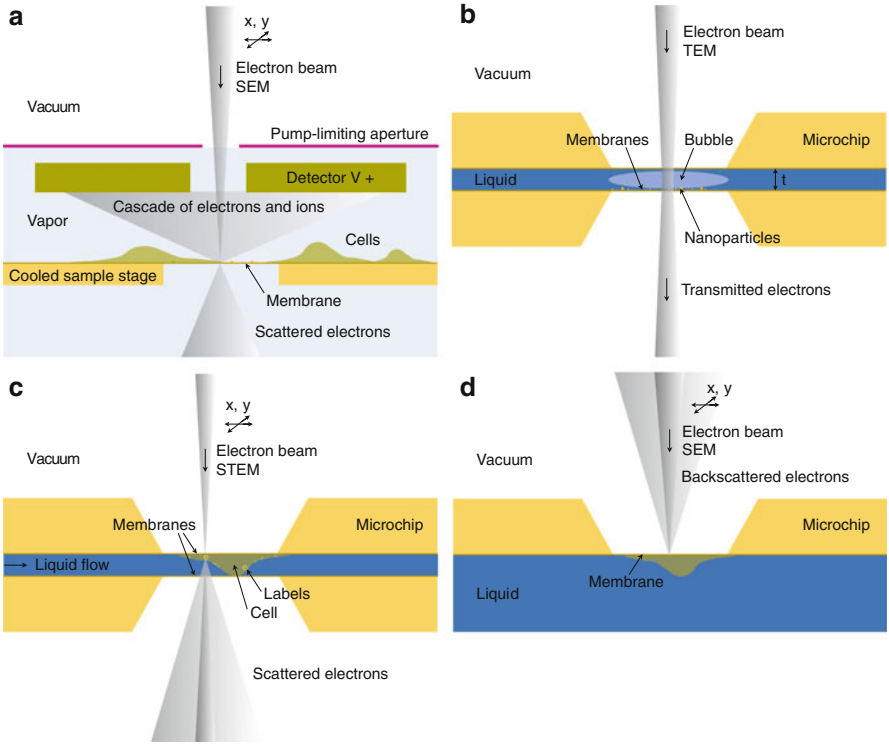

Fig. 9.1 Schematic representations of the most popular systems for electron microscopy of liquid specimens. (**a**) ESEM of cells immobilized on a membrane mounted on a cooled sample stage. The specimen chamber is differentially pumped, and vapor is maintained around the specimen. Detection is typically done using a detector above the specimen at a positive electric potential. STEM detection below the specimen is also possible. (**b**) TEM of a specimen containing nanoparticles fully enclosed between two thin windows supported by microchips. A gas bubble is sometimes formed in the liquid so that the effective liquid thickness is reduced. The focus is adjusted at the bottom membrane. (**c**) STEM of a cell containing nanoparticle protein labels. A flow of liquid runs between the two microchips so that fresh liquid is provided to the sample region. The focus is adjusted at the top membrane. (**d**) SEM of a specimen separated from the vacuum by a thin membrane. Detection is via backscattered electrons. The specimen can in principle be placed in a large or open liquid bath. Modified from (de Jonge and Ross 2011)

9.2.1 Environmental Scanning Electron Microscopy

Figure 9.1a shows the schematics of environmental scanning electron microscopy (ESEM) (Stokes 2008). ESEM has been most popular for imaging solid specimens in a gaseous environment, but it is also very useful for liquid specimens, for example, polymer wetting (Jansson et al. 2014), cells in liquid (Peckys et al. 2013), and even nanoparticle movements can be observed (Novotny et al. 2014). The sample chamber of the microscope is maintained at a certain base pressure of up to 4000 Pa for certain systems. The high vacuum in the electron

optics is protected from the gaseous environment via a differential pumping system with a pump limiting aperture mounted in the objective lens. The specimen stage is cooled with a Peltier element. The vapor pressure of water at 4 °C is 814 Pa, so that a sample at this temperature and pressure can be maintained at equilibrium between water and vapor. The sample is typically introduced in a water layer and a few additional droplets of water are placed on the cooling stage. The specimen chamber is then carefully evacuated via several pump cycles, so that most excess water is evaporated. Finally, the sample is covered by a thin film of water and the pressure is gradually decreased to a value close to 814 Pa until the water layer is thin enough for imaging. The exact pressure needs to be determined experimentally, as it depends on the heat conductance of the sample to the stage, the sample morphology, the type of liquid in the sample; ideally, pure water is used but in practice, organics or salts are contained in the liquid as well. When working with cells, these need to be chemically fixed and washed with pure water prior to ESEM (Kirk et al. 2009).

Imaging can be accomplished in three ways. Most users employ the gaseous secondary electron detector (Stokes 2008). The detector is mounted above the sample and is connected to a power supply, so that it is at positive electrical potential with respect to the sample. Electrons transmitted from the sample surface are accelerated towards the detector. Thereby gas molecules are ionized, resulting in a cascade of electrons and ions so that a high contrast level is obtained if the gas pressure is optimal. This contrast is the most sensitive for the very surface of the sample. The standard backscatter detector can also be used, and it is also sensitive for generating contrast at objects somewhat below the surface of the liquid. The spatial resolution achieved with these two detection principles is typically around 10 nm for liquid conditions.

As third detection principle, transmitted electrons can be collected using the STEM detector underneath the sample (Fig. 9.2). The wet-STEM detector (Bogner et al. 2005) is capable of detecting nanoscale objects of a high density within a liquid layer of lower density on account of the atomic number (Z) contrast of STEM. We demonstrated a resolution of 3 nm on gold nanoparticles (Peckys et al. 2013). The resolution is limited by beam broadening of the electron probe, the deeper the object under observation lies within the liquid. Secondly, scattering reduces the signal-to-noise ratio in the image. Wet-STEM at higher beam voltages than 30 keV available in commercial scanning electron microscopes (Danilatos and Robinson 1979) would be highly advantageous for the imaging of thicker sample regions but have so far not been realized, although several experiments have demonstrated wet-TEM in a laboratory setting (Ruska 1942; Parsons 1974; Sugi et al. 1997).

In particular for biological samples, it is important to image the specimens also with light microscopy prior to electron microscopic investigations. We have developed a procedure for correlative light microscopy and ESEM-STEM of eukaryotic cells (Peckys et al. 2014a). Cells grown on a silicon chip were first imaged with high resolution light microscopy by placing a microchip with the cells facing down in a cell culture dish with glass bottom. An oil immersion lens with high numerical aperture (NA) of 1.3 was applied to record fluorescence images of the sample

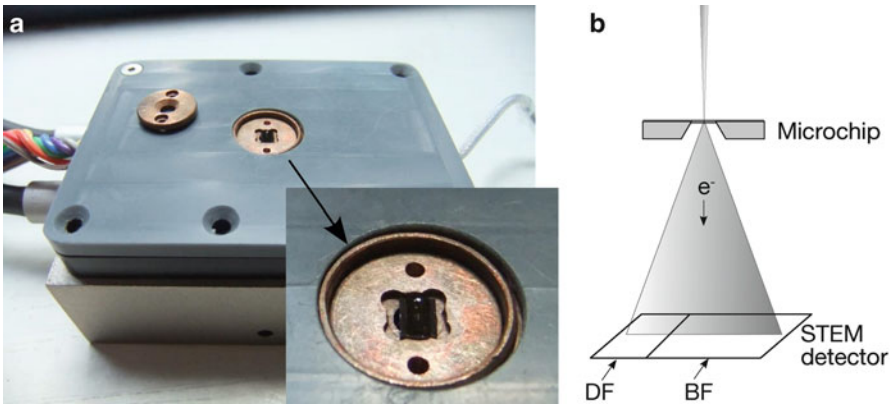

Fig. 9.2 ESEM-STEM equipment. (**a**) Photograph of a Peltier-cooled ESEM stage (Quanta 400 FEG ESEM, FEI, Hillsboro, OR, USA). The microchip with an SiN membrane window (a close-up is shown in the *inset* at the *right lower corner*) resides in a round copper holder such that it is positioned above an integrated STEM detector. Before the closing of the ESEM specimen chamber, the microchip is fixed with the second copper ring, seen at the *left side* of the stage. (**b**) Scheme of the integrated STEM detector below the microchip composed of two segments for bright-field (BF) and dark-field (DF) imaging. The dimensions are not to scale. With permission from (de Jonge et al. 2014)

(the oil was placed between the dish and the lens as is done in standard protocols). The location of each cell was determined relative to the corners of the silicon nitride window. The cells were fixed with glutaraldehyde, and the saline was replaced by pure water. The sample was then imaged with ESEM-STEM, while the cells were maintained in a thin liquid layer at all times. Each cellular position was easily located via its distance to the edge of the window. This protocol allows the combination of a top class light microscope with state-of-the-art ESEM-STEM using standard equipment.

9.2.2 Liquid Cell TEM

Thin membranes are used to enclose a liquid specimen and separate the specimen from the vacuum in the electron microscope (Fig. 9.1b). Standard silicon processing can be used to fabricate microchips supporting silicon nitride membranes (Williamson et al. 2003; Ring et al. 2011). Scatter contrast in TEM is used for imaging, whereby the focus is adjusted at the bottom membrane with respect to a downward traveling electron beam. Various groups have used commercial devices (Fig. 9.3) (Klein et al. 2011; Schuh and de Jonge 2014) to image the growth of nanoparticles (Evans et al. 2011; Liao et al. 2013), biominerals (Nielsen et al. 2014; Smeets et al. 2015) and biological specimens (Gilmore et al. 2013) or produced their own devices to study nanomaterial growth trajectories (Zheng et al. 2009b;

Fig. 9.3 Liquid flow specimen TEM/STEM holder system ("Poseidon" Protochips Inc., NC., USA). Microchips in a *box* are shown at the *lower left corner*. A microfluidic syringe pump (Harvard Apparatus, MA, USA) is connected to the holder via plastic tubing (Upchurch Scientific PEEK Tubing). With permission from (Schuh and de Jonge 2014)

Liao et al. 2012), electrochemical processes (Williamson et al. 2003; Radisic et al. 2006), and corrosion (Chee et al. 2014). Liquid cell TEM can also be employed to image proteins (Mirsaidov et al. 2012; Evans et al. 2012; Dukes et al. 2014), and is relevant for the study of energy related materials, such as research on the formation of SEI dendrites by Li deposition (Sacci et al. 2014). Time-resolved TEM is available with fast cameras, whereby the noise at high speeds is the limiting factor.

The experiment needs to be carefully designed in order to minimize the influence of the electron beam on the specimens (Abellan et al. 2014; Smeets et al. 2015), which implies chosing a balance between the liquid thickness, the electron dose, and the achieved resolution. Nanoscale resolution is achieved with silicon nitride windows of typical thicknesses ranging between 20 and 50 nm. Thinner windows of graphene have been used, for example, to obtain atomic resolution in TEM (Yuk et al. 2012), and to image bacteria (Mohanty et al. 2011). However, the resolution is typically not limited by the window thickness but rather by the thickness of the water layer. The electron beam suffers from inelastic scattering and a broadening of the energy spread. This in turn leads to a reduced spatial resolution on account of the chromatic aberration of the projection lenses (de Jonge and Ross 2011). The user should evaluate the amount of scattering from both the liquid and the top window, in the design of the experiment. Practical aspects involve outward bulging

of the windows when placed in the vacuum, so that the liquid thickness will reach well over a micrometer in the middle of the window for a typical window width of 20 μm even when a thin (<200 nm) spacer is used.

One approach to reduce the liquid thickness is via the creation of a bubble (Peckys et al. 2009; Klein et al. 2011; Woehl et al. 2013). In case the liquid is static, i.e. not continuously replaced in a flow (Ring and de Jonge 2010), gas bubbles are often formed upon the impact of the electron beam with the liquid, probably hydrogen gas. As a result, the liquid thickness is reduced and high resolution is possible in TEM. Various studies not explicitly stating an experimentally determined liquid thickness possibly involve this type of configuration. It is thus highly recommended to measure the liquid thickness, for example, by recording the electron energy-loss spectrum or by measuring the amount of elastic scattering by the liquid using the STEM detector (de Jonge et al. 2010). If liquid flow is initiated and one can be sure that the entire device is filled with liquid, then it is also possible to determine the liquid thickness via tilting the specimen and recording the shifts of fiducial markers on the top and bottom window; the thickness then follows from the parallax equation. The sample loading should be done in a very careful way such as to avoid particles, for example, aggregates, or pieces of chipped-off silicon to hinder the placement of the two membranes at the desired distance.

Future challenges include the development of systems with ultrathin but still practically applicable windows and well-controllable liquid layers. On the other hand, additional knowledge and experimental solutions are needed to discriminate the processes and objects under observation from influences of the electron beam.

9.2.3 Liquid STEM

In case the liquid thickness needs to be of several hundreds of nanometer or larger (Fig. 9.1c), then STEM is advantageous is many cases, especially for the imaging of dense materials (de Jonge et al. 2009). Several groups have observed the movement of gold nanoparticles in liquid (White et al. 2012; Ring and de Jonge 2012). Interestingly, it appears that the movements are several orders of magnitude slower than what is expected on the basis of Brownian motion, so that nanoparticle movements in liquid can actually be observed as long as the nanoparticles are in nanoscale proximity of the membrane window (Verch et al. 2015). Nanoparticle growth and self-assembly processes (van de Put et al. 2015) can readily be studied (Liu et al. 2013). Also biological molecules (Evans et al. 2012) and cells (de Jonge et al. 2009; Peckys et al. 2011) can be studied with Liquid STEM. The usage of the STEM probe also makes analytical studies possible, for example, with electron energy-loss spectroscopy (Jungjohann et al. 2012), or energy dispersed X-ray analysis (Zaluzec et al. 2014). Fast time-resolved STEM is possible in principle with a pixel dwell time of 2 μs but frame times in practical conditions are usually not shorter than 1 s.

The Z-contrast of STEM results in an almost quadratic dependence of the contrast with the atomic number. It is thus readily possible to resolve, for example, gold nanoparticles in micrometers-thick water layers (de Jonge et al. 2010). The focus of the electron microscope is adjusted at the top window, so that nanoparticles are imaged with a fine electron probe. At 200 keV beam energy, the probe is only minimally broadened by penetration through a 50 nm-thick silicon nitride window, and even atomic resolution is possible (Ramachandra et al. 2011; Jungjohann et al. 2012). A resolution of several nanometers is possible for a liquid thickness of 5 μm for nanoparticles in the top layer of the liquid (de Jonge et al. 2010), but the resolution reduces the deeper an object is positioned (Schuh and de Jonge 2014). The resolution is lower than 10 nm below a depth of 1 μm and is too low to be useful below 2 μm.

Once the beam is scattered on an object, the elastically scattered electrons need to travel through the liquid layer towards the detector. But this process is not critical and some degree of scattering, which mostly occurs at small angles anyway, will not change the signal in an annular dark field detector with an opening semi-angle of 50 mrad. The amount of current deposited in the sample is much lower than in case of TEM, but the local electron dose may by higher sometimes. It is of advantage to flow the liquid, so that radicals, free electrons, and gas are continuously flushed away. Liquid layers of several hundreds of nanometer are of advantage for the study of the solid/liquid interface and for the growth and self-assembly processes of nanomaterials. In our research, we have focused on the imaging of whole eukaryotic cells for biomedical research (Peckys and de Jonge 2014b), requiring a liquid thickness of 5 μm for thin cells, such as COS7 cells. The liquid thickness should be checked via measuring the amount of electrons collected in the annular dark-field detector or via tilting the stage (de Jonge et al. 2010, 2014).

Two different protocols for correlative light microscopy and Liquid STEM were developed. In the first protocol, cells grown on a silicon microchip were first imaged in a cell culture dish using standard high resolution light microscopy and an oil immersion lens. Thereafter, the microfluidic chamber was assembled from this microchip and a second one, and Liquid STEM images were recorded (Dukes et al. 2010; Peckys et al. 2014b). In the second protocol, a sample with live cells was prepared directly in the microfluidic chamber in the tip of the specimen holder. This sample was first imaged with light microcopy and subsequently with Liquid STEM (Peckys and de Jonge 2011, 2014b; Peckys et al. 2011). There was no need of additional sample preparation, however, the cells died after the electron beam irradiation.

9.2.4 SEM with Closed Device

Several groups have developed closed systems for SEM (Fig. 9.1d). The paper of Thiberge et al. (Thiberge et al. 2004) inspired many scientists to start experimenting with electron of liquid specimens (Joy and Joy 2005). They manufactured a capsule for placement in a standard SEM containing a liquid chamber enclosed by a thin

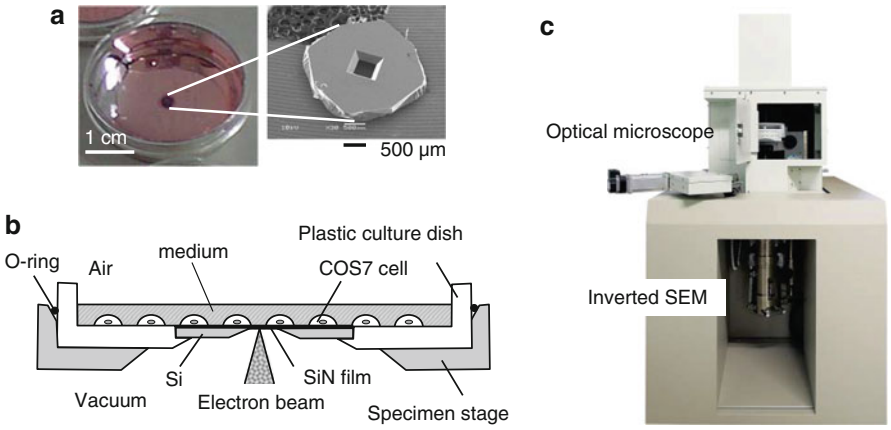

Fig. 9.4 Components of Atmospheric SEM (ASEM). (**a**) A removable cell culture dish contains a silicon nitride film window in its *bottom* plate (**a**, *right*). (**b**) A cell culture in liquid is maintained in the dish. The electron beam penetrates from the bottom through the SiN window to create contrast via backscatter detection. The dish is at air pressure and complete open from the top. (**c**). Prototype of the ASEM. An optical microscope is arranged above an inverted SEM with the specimen dish between them

polymer membrane. Contrast was obtained via backscatter detection. But the membrane was too thick to allow a resolution better than 20 nm and the system could not compete with the newly introduced super resolution fluorescence microscopy (Hell 2007). Others have used silicon nitride membranes integrated in silicon microchips (Jensen et al. 2013) and obtained a remarkably high resolution using STEM detection (Grogan and Bau 2010). The group of Sato demonstrated the full integration of cell culture light microscopy with SEM (Nishiyama et al. 2010), see Fig. 9.4. They mounted a silicon chip in the bottom of a standard plastic cell culture dish. The dish was placed on an upward electron microscope, whereby the silicon nitride separated vacuum from liquid. Cells in the dish were first imaged with light microscopy from the top. The electron beam irradiated the sample from the bottom and used backscattered electrons for contrast achieving a maximal resolution on gold nanoparticles of 8 nm. The resolution of the integrated light microscope was optimized using a high numerical aperture (NA) water immersion lens dipped in the liquid. The advantage of this system is the capability to work with an open cell culture dish, so that all kinds of biological experiments, such as incubation with receptor ligands, or even patch clamping can be carried out, after which the cells are fixed and studied with SEM. One of the latest developments is the integration of a high NA optical lens in an SEM equipped with a microfluidic chamber (Liv et al. 2014). Correlative light microscopy and SEM is thus achieved with a high optical resolution in the same instrument. An interesting new option is presented by the so-called Air SEM. This instrument comprises an electron optical column closed by a thin silicon nitride window. The system does not contain a specimen chamber but instead a specimen in air is irradiated with the electron beam passing through the window and the air and liquid beyond. The surfaces of samples can thus be inspected

using back scatter detection. The surfaces of samples in air are readily imaged and studies of samples covered in a thin water layer seem feasible (Vidavsky et al. 2014).

9.3 Examples of Applications

9.3.1 ESEM of Whole Cells

We have achieved 3 nm resolution on gold nanoparticles used as specific protein labels located at the edges of whole eukaryotic cells in hydrated state (Peckys et al. 2013), see Fig. 9.5. In this study, whole A549 lung cancer cells were grown on silicon nitride supporting membranes mounted on silicon chips (Ring et al. 2011; Peckys et al. 2014a). A nanoparticle label was prepared consisting of a gold nanoparticle conjugated to epidermal growth factor protein via a streptavidin–biotin bond. The cells were incubated with the label for 5 min at room temperature, so that the label specifically bound to the epidermal growth factor receptor (EGFR). The cells were then fixed with glutaraldehyde and imaged with ESEM. Just prior to ESEM, a sample was washed with pure water to remove salt. The overview image of Fig. 9.5a shows three adjacent cells. Due to electron beam scattering in the sample, it was not possible to achieve nanoscale resolution in the thicker regions of the cells, white in the image. But high resolution was obtained at the cell edge, where it was sufficiently thin (Fig. 9.5b). Finally, the nanoparticle labels became visible in Fig. 9.5c with a spatial resolution of 3 nm. This resolution allowed to distinguish individual labels, dimers, and clusters (Fig. 9.5d–g). The electron dose was of the order of 2×10^2 $e^-/Å^2$, a factor of two larger than used for TEM of cryo sections (Kourkoutis et al. 2012) (note that a much lower dose was erroneously mentioned in error in the original paper (Peckys et al. 2013)). The electron beam radiation damage did not damage the samples to such extent that the positions of the labels were changed, so that we assume that the label positions reflect those of the EGFR proteins in the natural state. The EGFR dimerizes after activation with its ligand EGF. A molecular model of the dimer including gold nanoparticle labels is shown in Fig. 9.6. Here, the center-to-center distance of the labels is expected to be 19 nm, consistent with the distances between pairs of labels found in Fig. 9.5, and with the most probably distance determined from statistics obtained from 1411 labels (Peckys et al. 2013). The obtained information can thus be used to determine the nanoscale location and stoichoimetry of EGFR in the plasma membrane, for example, to study the cellular regions in which the EGFR dimers reside, or to explore clustering of EGFR. Since the sample preparation and ESEM is relatively easy, similar as those protocols used for fluorescence microscopy, it is readily possible to study tens of whole cells, as we have shown for the EGFR (Peckys et al. 2013). Our latest research involves dimerization of the HER2 protein with relevance for research on breast cancer (Peckys et al. 2015).

We have also studied gold nanoparticle uptake in whole cells with ESEM-STEM (Peckys and de Jonge 2014a). A547 cells were incubated for 2 h with citrate

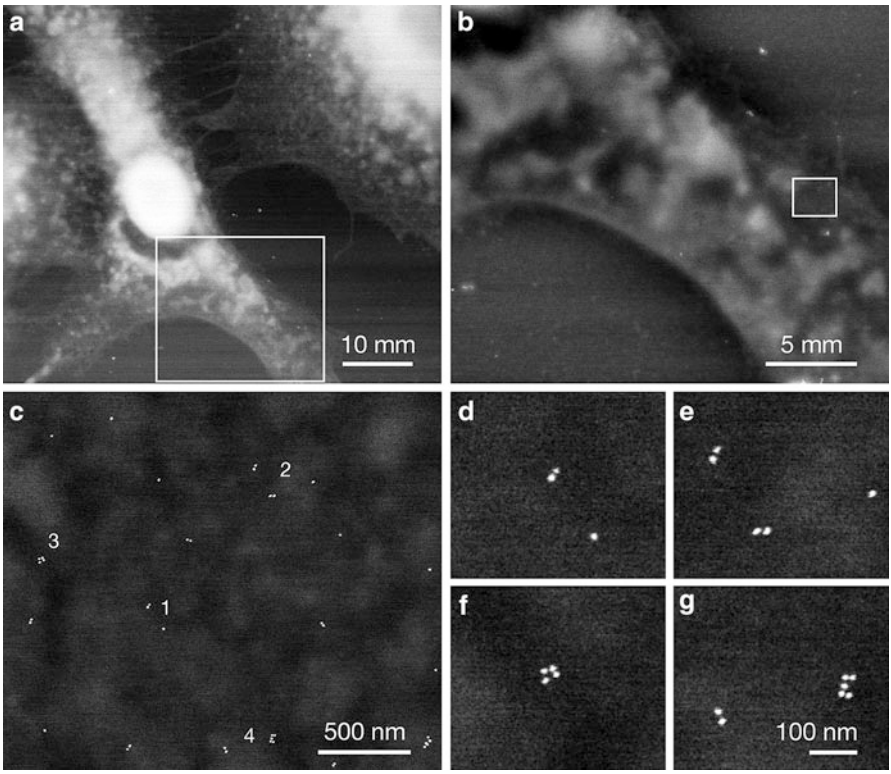

Fig. 9.5 ESEM of a whole fixed A549 cell in hydrated state. (**a**) Overview dark-field ESEM-STEM image at the edge of the cell showing the contours of the cell in *gray*, and the thicker cellular regions in *white*. The magnification $M = 1{,}500\times$. (**b**) Image recorded at the location of the *rectangle* in a using $M = 5{,}336\times$. (**c**) Image showing individual gold nanoparticles attached to epidermal growth factor receptors (EGFRs) as *white spots* for the region shown as *rectangle* in (**b**), $M = 50{,}000\times$. (**d–g**) Magnified regions from (**c**) showing the positions of individual proteins, EGFR dimers, and larger clusters indicated with numbers 1–4, respectively, in (**c**). From (Peckys et al. 2013)

stabilized and subsequently serum protein-coated gold nanoparticles of 30 nm diameter. The cells were then grown in standard cell culture medium for 24 h, so that the uptaken nanoparticles were collected and transported in lysosomes. It was found that the cell contained many clusters of nanoparticles (Fig. 9.7). Data was collected from 145 whole cells revealing that the size of the clusters depended on the nanoparticle diameter (Peckys and de Jonge 2014a). The strength of the ESEM approach is the ability to collect statistics of many (>100) whole cells, which is not practically feasible using conventional electron microscopy samples such as the thin plastic or cryo sections. In addition, the preparation of conventional thin samples inevitably leads to a loss of information, for example, the vesicles are sliced through, or the nanoparticles are smeared out of the section by the cutting process.

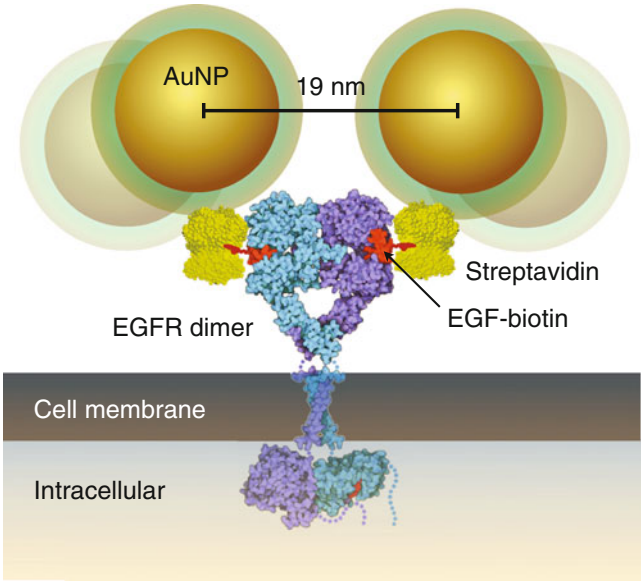

Fig. 9.6 Molecular model of the epidermal growth factor receptor (EGFR) dimer with gold nanoparticles (Au-NPs) conjugated via a streptavidin–biotin bond to the epidermal growth factor (EGF). The distance between the centers of the two AuNPs was estimated to amount to ~19 nm for a tightly packed structure. A larger distance of up 29 nm can be accomplished by rotating the AuNP on the streptavidin. The scaled drawings of streptavidin, EGF, and the EGFR were derived from CPK models of the 1 stp (streptavidin), 1EGF (EGF), 1NQL, 2JWA, 1M17, 1IVO, and 2GS6 (EGFR) structures as found in the RCSB Protein Databank, created by Jmol Version 12.2.15. Biotin size and structure was derived from the biotin model as drawn in RCSB Ligand Explorer Version 1.0. From (Peckys et al. 2013)

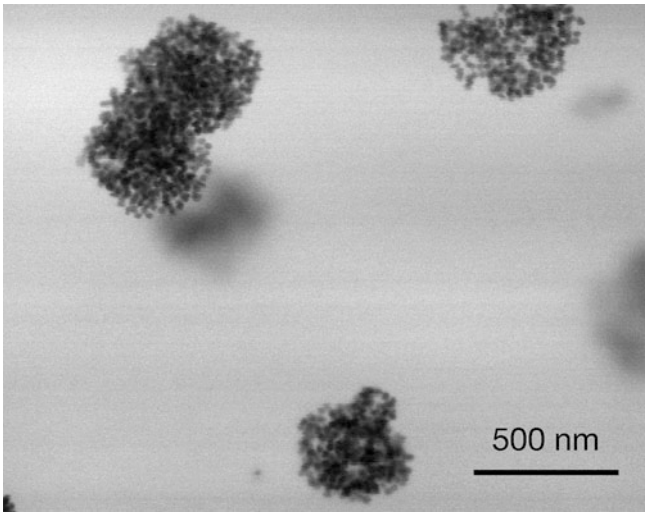

Fig. 9.7 ESEM-STEM images of 30 nm-diameter gold nanoparticles obtained after uptake and transport in A549 cells. The cells were AuNPs at later stages of the cellular uptake (2 h pulse and 22 h chase). $M = 40{,}000\times$. The AuNPs are homogenously distributed within clusters, presumably lysosomes. With permission from (Peckys and de Jonge 2014a)

9.3.2 Liquid Cell TEM of Gold Dendrite Growth

Liquid cell TEM was used to observe the growth of gold dendrites at the nanoscale (Kraus and de Jonge 2013). Gold seed nanoparticles were first grown on a silicon nitride membrane, and the membrane was dried. A droplet of growth solution containing $HAuCl_4$ was then applied to the microchip, and the microfluidic chamber was immediately closed and inserted into the electron microscope. The sample was then imaged with TEM until a bubble appeared, so that the seed nanoparticles covered by a thin layer of liquid became visible. That a liquid layer was present was concluded from the observation of moving particles. The sample was then continuously imaged at the same region. Growth of dendrites was initiated by the electron beam, as was observed each time a fresh region was imaged. The impact of the electron beam with the liquid, the nanoparticles, and the SiN window presumably generated free electrons in the liquid driving the electrochemistry of the dendrite growth (Kraus and de Jonge 2013). It is not likely that heat has played a significant role because electron beam-induced heating would amount to a few degrees Celsius only (Zheng et al. 2009a).

Several stills of an acquired movie are shown in Fig. 9.8. The dendrites grow larger from existing patches and then start to branch out. Dendrite nucleation was induced by the electron beam presumably reducing the liquid leading to an initial burst of growth. The growth then settled at tip velocities between 0.1 and 2.0 nm/s for different dendrites. Different dendrite geometries grew from the tips. From the presence of the branched shapes of the dendrites, it was concluded that the growth was diffusion limited. This experiment shows that the liquid cell TEM method can be used to study mechanisms of nanoscale dendrite growth and other types of anisotropic growth. However, these experiments need to be analyzed with great care because the electron beam influences the entire chemistry of the liquid (Grogan et al. 2014; Schneider et al. 2014; Abellan et al. 2014). The electron beam is known to create various reactive species in liquid, such as free electrons, oxygen and hydroxyl radicals, causing the formation of hydrogen gas, may even change the pH, and may reduce or oxidize the specimens under observation.

9.3.3 Liquid STEM of Whole Eukaryotic Cells

Our group was the first to detect the positions of labeled proteins in whole eukaryotic cells in liquid with nanometer resolution (de Jonge et al. 2009). COS7 cells were labeled with 10 nm-diameter gold-nanoparticles conjugated with EGF. The cells were grown, labeled, and fixed directly on the silicon microchips for

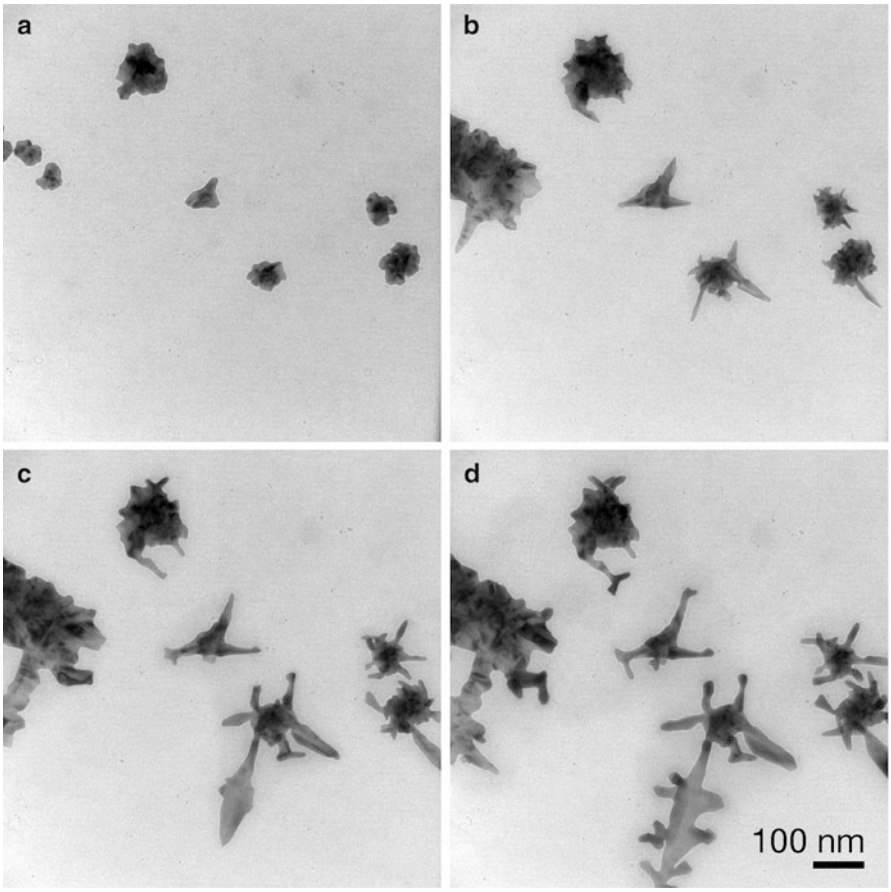

Fig. 9.8 Liquid cell TEM images selected from a time series acquired of growing gold dendrites. (**a**) Nanoscale objects appeared upon first imaging this location, presumably nuclei where the growth had already started. $M = 22{,}000\times$. (**b**) Frame recorded 70 s after (**a**). The growth directions of several dendrites are observed. (**c**, **d**) Frames recorded 120 and 245 s, respectively, after (**a**). With permission from (Kraus and de Jonge 2013)

Liquid STEM. Figure 9.9a shows the edge of a cell that was incubated for 5 min with EGF-gold labels. The localization of the labels at the cell edges is consistent with EGFR dispersed along the cell surface after 5 min of label incubation (Lidke et al. 2004). The electron dose used for one image was $q = 7 \times 10^2$ e$^-$/Å^2 and the pixel-dwell time was $t = 20$ µs. These experiments were not optimized for the lowest possible electron dose, and it can be calculated that a much smaller dose is needed to detect the nanoparticles (de Jonge et al. 2010).

To observe molecular rearrangements in the COS7 cells after ligand binding, in this case endocytosis of the labeled EGFRs, a second batch of cells was incubated for 10 min with EGF-gold, washed, and incubated an additional 15 min in buffer, see Fig. 9.9b. Circular clusters of labels are visible, consistent with clustering in

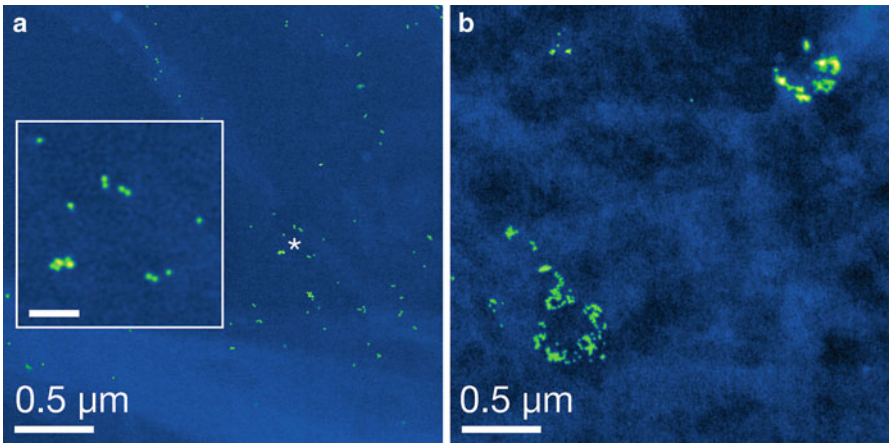

Fig. 9.9 Liquid STEM images of gold-labeled EGFRs on whole fixed COS7 cells in saline of a thickness of 6 µm. (**a**) Image of the edge of a cell. Gold labels are visible as *yellow spots* and the cellular material as *light-blue* matter over the *dark-blue* background. The signal level was color coded. The *box* is a magnified image (scalebar is 100 nm) of the region around the *asterisk* depicting the individual labels forming dimers and larger clusters. (**b**) Image of a cell showing two vesicles. Modified from (de Jonge et al. 2009)

internalized endosomes after receptor activation (Lidke et al. 2004). The spatial resolution was 4 nm, measured from the 20–80 % rising edge width (Reimer 1998), sufficient to distinguish adjacent labels.

The capability of Liquid STEM is important for the study of cellular function at the molecular level. A given functional state in a cell exhibits a specific molecular configuration of protein complexes and bound ligands. Changes in the functional state of the cell are tightly coupled to changes in molecular configuration. While the current data supporting these hypotheses are strong, they are based on indirect methods in structural biology, and biochemistry. Compared to biochemical methods providing information about the average of many cells in pooled cellular material, our methodology provides unique information at the molecular level. It is thus possible, for example, to study the assembly of protein complexes and protein clusters, as function of their cellular location. An application area is research on cancer associated with growth factor receptors. Certain cancer drugs target these receptors, and aim to prevent dimerization triggering cell growth. We expect that the causes of certain therapeutic resistance, associated with intra-tumoral heterogeneity (Seol et al. 2012), can be studied directly with Liquid STEM by scanning through many cells in a cell population and searching for the exceptions in the average cell response.

We have also demonstrated correlative fluorescence microscopy and Liquid STEM on QD-labeled EGFRs in fixed COS7 cells (Dukes et al. 2010). Correlative phase contrast light microscopy, fluorescence microscopy, and Liquid STEM was used to image unfixed yeast cells, alive at the onset of STEM, using an average electron dose of only 0.2 $e^{-}/Å^{2}$ (Peckys et al. 2011), see Fig. 9.10. Furthermore, we

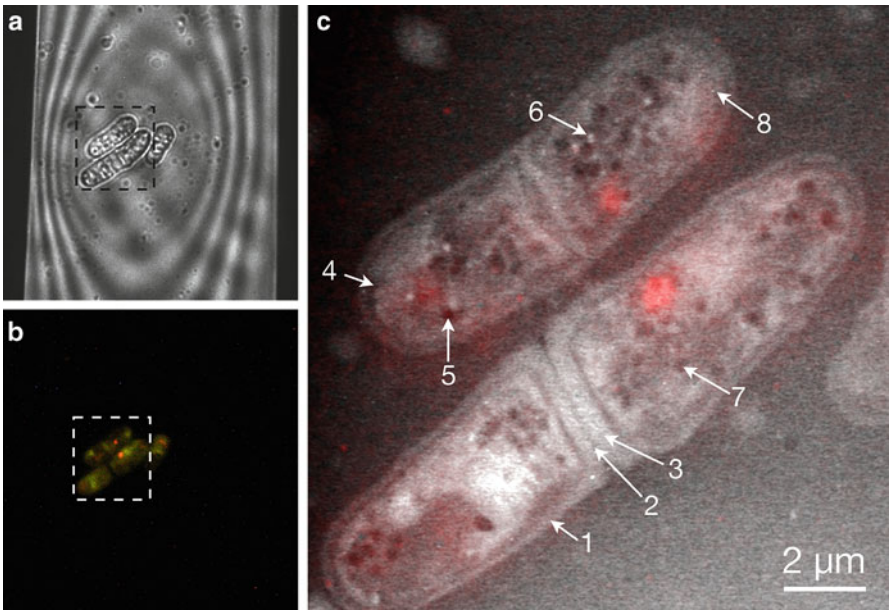

Fig. 9.10 Light microscopy and Liquid STEM of fully hydrated wild type *S. pombe* yeast cells alive at the onset of the recording of the first STEM image. (**a**) Phase contrast image showing *S. pombe* cells within a portion of the viewing window of the microfluidic chamber. (**b**) In the corresponding fluorescence image, it can be seen that all cells accumulated FUN-1 dye and emitted a punctuated *red* fluorescence, the typical signal of living yeast cells. (**c**) Liquid STEM image recorded in fully hydrated state of the same pristine yeast cells as shown in (**a**) and (**b**). *Numbered arrows* indicate examples of allocated organelles: (1) cell wall, (2) primary septum, (3) secondary septum, (4) cell membrane invagination, (5) lipid droplet, (6) peroxisome, and (7) unclassified vesicle. (8) Gold nanoparticle. The color is an overlay of the *red channel* of the fluorescence image (**b**). With permission from (Peckys et al. 2011)

studied the uptake of 30 nm-diameter gold nanoparticles in live COS7 cells (Peckys and de Jonge 2011). Since the cells were not prepared into thin sections, as is standard in electron microscopic studies, we were able to quantitative analyze the locations of the uptaken nanoparticles. The nanoparticles were collected in vesicles possibly lysosomes, and those assembled in a large cluster. The nanoparticles appeared to be bound to the membranes of the vesicles, and did not seem to fill the interior of the lysosomes.

9.4 Conclusions

Electron microscopy of specimen in a liquid environment is possible on a routine basis using several different approaches. ESEM is relatively easy to apply for samples embedded in a thin liquid layer. A resolution of a few nanometer can be

achieved for the imaging of heavy nanoparticles using STEM detection. However, it is difficult to control the exact water layer thickness. The enclosure of specimens in a liquid chamber allows a better control of the liquid environment, so that even higher resolution is possible. But the actual liquid thickness should be measured because the electron beam irradiation may cause gas bubbles to form in the liquid. The safest is to continuously flow the liquid using a microfluidic chamber. The separation of liquid and vacuum in SEM has several interesting options. It is, for example, possible to image the bottom side of entire cell cultures open at the top for experiments in liquid. The examples of experiments given here demonstrate that electron microscopy is useful for addressing research questions in both biology and materials science involving the nanoscale study of samples in liquid. Unique information about the EGFR dimerization in the plasma membranes of intact cells was obtained. Gold nanoparticle uptake was studied in whole cells, whereby the nanoparticle containing vesicles were preserved, and data was obtained of over a hundred of cells. The native structure of yeast was imaged. The formation of gold dendrites was studied at the nanoscale in a time-lapse experiment. The main limitation of the approach is the impact of the electron beam with the specimen, leading to radiation damage, and the formation of a range of reactive species. For stationary "snap shot" images recorded with an electron dose within the limit of damage, it is readily possible to study biological structure and proteins positions of the native state (de Jonge et al. 2009; Peckys et al. 2011). But as soon as processes are studied, it should be realized that the observed process is intertwined with a multiple of effects caused by the electron beam. In some cases, the electron beam effect was useful because it triggered the reactions (Zheng et al. 2009b) but in other cases, the experiment might become rather complex to interpret (Schneider et al. 2014). Yet, with ever increasing knowledge about this type of experiment (Woehl et al. 2013; Abellan et al. 2014; de Jonge et al. 2014) the effect of the beam can be taken into account so that even formation processes of beam-sensitive biominerals can be usefully studied (Smeets et al. 2015).

Acknowledgment We thank D.B. Peckys for discussions and E. Arzt for his support through INM. Research in part supported by the Leibniz Competition 2013.

References

P. Abellan, T.J. Woehl, L.R. Parent, N.D. Browning, J.E. Evans, I. Arslan, Factors influencing quantitative liquid (scanning) transmission electron microscopy. Chem. Commun. **50**(38), 4873–4880 (2014). doi:10.1039/c3cc48479c

I.M. Abrams, J.W. McBain, A closed cell for electron microscopy. J. Appl. Phys. **15**, 607–609 (1944)

A. Bogner, G. Thollet, D. Basset, P.H. Jouneau, C. Gauthier, Wet STEM: A new development in environmental SEM for imaging nano-objects included in a liquid phase. Ultramicroscopy **104**, 290–301 (2005)

S.W. Chee, D.J. Duquette, F.M. Ross, R. Hull, Metastable structures in Al thin films before the onset of corrosion pitting as observed using liquid cell transmission electron microscopy. Microsc. Microanal. **20**(2), 462–468 (2014). doi:10.1017/S1431927614000221
G.D. Danilatos, V.N.E. Robinson, Principles of scanning electron microscopy at high specimen pressures. Scanning **18**, 75–78 (1979)
N. de Jonge, Introduction to special issue on electron microscopy of specimens in liquid. Microsc. Microanal. **20**, 315–316 (2014). doi:10.1017/S143192761400052X
N. de Jonge, F.M. Ross, Electron microscopy of specimens in liquid. Nat. Nanotechnol. **6**(11), 695–704 (2011)
N. de Jonge, D.B. Peckys, G.J. Kremers, D.W. Piston, Electron microscopy of whole cells in liquid with nanometer resolution. Proc. Natl. Acad. Sci. **106**, 2159–2164 (2009)
N. de Jonge, N. Poirier-Demers, H. Demers, D.B. Peckys, D. Drouin, Nanometer-resolution electron microscopy through micrometers-thick water layers. Ultramicroscopy **110**(9), 1114–1119 (2010)
N. de Jonge, M. Pfaff, D.B. Peckys, Practical aspects of transmission electron microscopy in liquid. Adv. Imag. Electron. Phys. **186**, 1–37 (2014)
M.J. Dukes, D.B. Peckys, N. de Jonge, Correlative fluorescence microscopy and scanning transmission electron microscopy of quantum-dot-labeled proteins in whole cells in liquid. ACS Nano **4**(7), 4110–4116 (2010). doi:10.1021/nn1010232
M.J. Dukes, R. Thomas, J. Damiano, K.L. Klein, S. Balasubramaniam, S. Kayandan, J.S. Riffle, R.M. Davis, S.M. McDonald, D.F. Kelly, Improved microchip design and application for in situ transmission electron microscopy of macromolecules. Microsc. Microanal. **20**(2), 338–345 (2014). doi:10.1017/S1431927613013858
J.E. Evans, K.L. Jungjohann, N.D. Browning, I. Arslan, Controlled growth of nanoparticles from solution with in situ liquid transmission electron microscopy. Nano Lett. **11**(7), 2809–2813 (2011). doi:10.1021/nl201166k
J.E. Evans, K.L. Jungjohann, P.C.K. Wong, P.L. Chiu, G.H. Dutrow, I. Arslan, N.D. Browning, Visualizing macromolecular complexes with in situ liquid scanning transmission electron microscopy. Micron **43**, 1085–1090 (2012)
B.L. Gilmore, S.P. Showalter, M.J. Dukes, J.R. Tanner, A.C. Demmert, S.M. McDonald, D.F. Kelly, Visualizing viral assemblies in a nanoscale biosphere. Lab Chip **13**(2), 216–219 (2013). doi:10.1039/c2lc41008g
J.M. Grogan, H.H. Bau, The nanoaquarium: a platform for in situ transmission electron microscopy in liquid media. J. Microelectromech. Syst. **19**, 885–894 (2010)
J.M. Grogan, N.M. Schneider, F.M. Ross, H.H. Bau, Bubble and pattern formation in liquid induced by an electron beam. Nano Lett. **14**(1), 359–364 (2014). doi:10.1021/nl404169a
S.W. Hell, Far-field optical nanoscopy. Science **316**, 1153–1158 (2007)
A. Jansson, C. Boissier, M. Marucci, M. Nicholas, S. Gustafsson, A.M. Hermansson, E. Olsson, Novel method for visualizing water transport through phase-separated polymer films. Microsc. Microanal. **20**(2), 394–406 (2014). doi:10.1017/S143192761400021X
E. Jensen, C. Kobler, P.S. Jensen, K. Molhave, In-situ SEM microchip setup for electrochemical experiments with water based solutions. Ultramicroscopy **129**, 63–69 (2013). doi:10.1016/j.ultramic.2013.03.002
D.C. Joy, C.S. Joy, Scanning electron microscope imaging in liquids—some data on electron interactions in water. J. Microsc. **221**, 84–99 (2005)
K.L. Jungjohann, J.E. Evans, J.A. Aguiar, I. Arslan, N.D. Browning, Atomic-scale imaging and spectroscopy for in situ liquid scanning transmission electron microscopy. Microsc. Microanal. **18**(3), 621–627 (2012). doi:10.1017/S1431927612000104
S.E. Kirk, J.N. Skepper, A.M. Donald, Application of environmental scanning electron microscopy to determine biological surface structure. J. Microsc. **233**(2), 205–224 (2009). doi:10.1111/j.1365-2818.2009.03111.x
K.L. Klein, I.M. Anderson, N. de Jonge, Transmission electron microscopy with a liquid flow cell. J. Microsc. **242**(2), 117–123 (2011). doi:10.1111/j.1365-2818.2010.03484.x

L.F. Kourkoutis, J.M. Plitzko, W. Baumeister, Electron microscopy of biological materials at the nanometer scale. Annu. Rev. Mater. Res. **42**, 33–58 (2012)

T. Kraus, N. de Jonge, Dendritic gold nanowire growth observed in liquid with transmission electron microscopy. Langmuir **29**(26), 8427–8432 (2013). doi:10.1021/la401584z

H.-G. Liao, L. Cui, S. Whitelam, H. Zheng, Real-time imaging of Pt3Fe nanorod growth in solution. Science **336**(6084), 1011–1014 (2012). doi:10.1126/science.1219185

H.G. Liao, K. Niu, H. Zheng, Observation of growth of metal nanoparticles. Chem. Commun. (Camb.) **49**(100), 11720–11727 (2013). doi:10.1039/c3cc47473a

D.S. Lidke, P. Nagy, R. Heintzmann, D.J. Arndt-Jovin, J.N. Post, H.E. Grecco, E.A. Jares-Erijman, T.M. Jovin, Quantum dot ligands provide new insights into erB/HER receptor-mediated signal transduction. Nat. Biotechnol. **22**, 198–203 (2004)

Y. Liu, X.-M. Lin, Y. Sun, T. Rajh, In Situ visualization of self-assembly of charged gold nanoparticles. J. Am. Chem. Soc. **135**(10), 3764–3767 (2013). doi:10.1021/ja312620e

N. Liv, I. Lazic, P. Kruit, J.P. Hoogenboom, Scanning electron microscopy of individual nanoparticle bio-markers in liquid. Ultramicroscopy **143**, 93–99 (2014). doi:10.1016/j.ultramic.2013.09.002

U.M. Mirsaidov, H. Zheng, Y. Casana, P. Matsudaira, Imaging protein structure in water at 2.7 nm resolution by transmission electron microscopy. Biophys. J. **102**(4), L15–17 (2012). doi:10.1016/j.bpj.2012.01.009

N. Mohanty, M. Fahrenholtz, A. Nagaraja, D. Boyle, V. Berry, Impermeable graphenic encasement of bacteria. Nano Lett. **11**(3), 1270–1275 (2011). doi:10.1021/nl104292k

P.D. Nellist, M.F. Chisholm, N. Dellby, O.L. Krivanek, M.F. Murfitt, Z.S. Szilagyi, A.R. Lupini, A. Borisevich, W.H. Sides, S.J. Pennycook, Direct sub-angstrom imaging of a crystal lattice. Science **305**, 1741 (2004)

M.H. Nielsen, S. Aloni, J.J. De Yoreo, In situ TEM imaging of CaCO(3) nucleation reveals coexistence of direct and indirect pathways. Science **345**(6201), 1158–1162 (2014). doi:10.1126/science.1254051

H. Nishiyama, M. Suga, T. Ogura, Y. Maruyama, M. Koizumi, K. Mio, S. Kitamura, C. Sato, Atmospheric scanning electron microscope observes cells and tissues in open medium through silicon nitride film. J. Struct. Biol. **169**(3), 438–449 (2010). doi:10.1016/j.jsb.2010.01.005

F. Novotny, P. Wandrol, J. Proska, M. Slouf, In situ WetSTEM observation of gold nanorod self-assembly dynamics in a drying colloidal droplet. Microsc. Microanal. **20**(2), 385–393 (2014). doi:10.1017/S1431927614000208

D.F. Parsons, Structure of wet specimens in electron microscopy. Science **186**, 407–414 (1974)

D.F. Parsons, V.R. Matricardi, R.C. Moretz, J.N. Turner, Electron microscopy and diffraction of wet unstained and unfixed biological objects. Adv. Biol. Med. Phys. **15**, 161–270 (1974)

D.B. Peckys, N. de Jonge, Visualization of gold nanoparticle uptake in living cells with liquid scanning transmission electron microscopy. Nano Lett. **11**, 1733–1738 (2011)

D.B. Peckys, N. de Jonge, Gold nanoparticle uptake in whole cells in liquid examined by environmental scanning electron microscopy. Microsc. Microanal. **20**(1), 189–197 (2014a). doi:10.1017/S1431927613013986

D.B. Peckys, N. de Jonge, Liquid scanning transmission electron microscopy: imaging protein complexes in their native environment in whole eukaryotic cells. Microsc. Microanal. **20**, 189–198 (2014b). doi:10.1017/S1431927614000099

D.B. Peckys, G.M. Veith, D.C. Joy, N. de Jonge, Nanoscale imaging of whole cells using a liquid enclosure and a scanning transmission electron microscope. PLoS One **4**(12), e8214 (2009). doi:10.1371/journal.pone.0008214

D.B. Peckys, P. Mazur, K.L. Gould, N. de Jonge, Fully hydrated yeast cells imaged with electron microscopy. Biophys. J. **100**, 2522–2529 (2011)

D.B. Peckys, J.P. Baudoin, M. Eder, U. Werner, N. de Jonge, Epidermal growth factor receptor subunit locations determined in hydrated cells with environmental scanning electron microscopy. Sci. Rep. **3**(2626), 2621–2626 (2013). doi:10.1038/srep02626

D.B. Peckys, V. Bandmann, N. de Jonge, Correlative fluorescence and scanning transmission electron microscopy of quantum dot-labeled proteins on whole cells in liquid. Methods Cell Biol. **124**, 305–322 (2014a). doi:10.1016/B978-0-12-801075-4.00014-8

D.B. Peckys, M.J. Dukes, N. de Jonge, Correlative fluorescence and electron microscopy of quantum dot labeled proteins on whole cells in liquid. Methods Mol. Biol. **1117**, 527–540 (2014b). doi:10.1007/978-1-62703-776-1_23

D.B. Peckys, U. Korf, N. de Jonge, Local variations of HER2 dimerization in breast cancer cells discovered by correlative fluorescence- and liquid electron microscopy. Sci. Adv. 1(6) e1500165 (2015). doi: 10.1126/sciadv.1500165

A. Radisic, F.M. Ross, P.C. Searson, In situ study of the growth kinetics of individual island electrodeposition of copper. J. Phys. Chem. B **110**(15), 7862–7868 (2006). doi:10.1021/jp057549a

R. Ramachandra, H. Demers, N. de Jonge, Atomic-resolution scanning transmission electron microscopy through 50 nm-thick silicon nitride membranes. Appl. Phys. Lett. **98**(9), 093109 (2011)

L. Reimer, *Scanning Electron Microscopy: Physics of Image Formation And Microanalysis* (Springer, Berlin, 1998)

E.A. Ring, N. de Jonge, Microfluidic system for transmission electron microscopy. Microsc. Microanal. **16**(5), 622–629 (2010)

E.A. Ring, N. de Jonge, Video-frequency scanning transmission electron microscopy of moving gold nanoparticles in liquid. Micron **43**(11), 1078–1084 (2012)

E.A. Ring, D.B. Peckys, M.J. Dukes, J.P. Baudoin, N. de Jonge, Silicon nitride windows for electron microscopy of whole cells. J. Microsc. **243**(3), 273–283 (2011)

E. Ruska, Beitrag zur uebermikroskopischen Abbildungen bei hoeheren Drucken. Kolloid Zeitschrift **100**, 212–219 (1942)

R.L. Sacci, N.J. Dudney, K.L. More, L.R. Parent, I. Arslan, N.D. Browning, R.R. Unocic, Direct visualization of initial SEI morphology and growth kinetics during lithium deposition by in situ electrochemical transmission electron microscopy. Chem. Commun. **50**(17), 2104–2107 (2014). doi:10.1039/c3cc49029g

N.M. Schneider, M.M. Norton, B.J. Mendel, J.M. Grogan, F.M. Ross, H.H. Bau, Electron–water interactions and implications for liquid cell electron microscopy. J. Phys. Chem. C **118**(38), 22373–22382 (2014). doi:10.1021/jp507400n

T. Schuh, N. de Jonge, Liquid scanning transmission electron microscopy: Nanoscale imaging in micrometers-thick liquids. C. R. Phys. **15**(2–3), 214–223 (2014). doi:10.1016/j.crhy.2013.11.004

H. Seol, H.J. Lee, Y. Choi, H.E. Lee, Y.J. Kim, J.H. Kim, E. Kang, S.W. Kim, S.Y. Park, Intratumoral heterogeneity of HER2 gene amplification in breast cancer: its clinicopathological significance. Mod. Pathol. **25**(7), 938–948 (2012). doi:10.1038/modpathol.2012.36

P.J. Smeets, K.R. Cho, R.G. Kempen, N.A. Sommerdijk, J.J. De Yoreo, Calcium carbonate nucleation driven by ion binding in a biomimetic matrix revealed by in situ electron microscopy. Nat. Mater. (2015). doi:10.1038/nmat4193

D.L. Stokes, *Principles and Practice of Variable Pressure/Environmental Scanning Electron Microscopy (VP-SEM)* (Wiley, Chichester, West-Sussex, 2008)

H. Sugi, T. Akimoto, K. Sutoh, S. Chaen, N. Oishi, S. Suzuki, Dynamic electron microscopy of ATP-induced myosin head movement in living muscle filaments. Proc. Natl. Acad. Sci. **94**, 4378–4392 (1997)

S. Thiberge, A. Nechushtan, D. Sprinzak, O. Gileadi, V. Behar, O. Zik, Y. Chowers, S. Michaeli, J. Schlessinger, E. Moses, Scanning electron microscopy of cells and tissues under fully hydrated conditions. Proc. Natl. Acad. Sci. **101**(10), 3346 (2004)

M.W. van de Put, C.C. Carcouet, P.H. Bomans, H. Friedrich, N. de Jonge, N.A. Sommerdijk, Writing silica structures in liquid with scanning transmission electron microscopy. Small **11**(5), 585–590 (2015). doi:10.1002/smll.201400913

A. Verch, M. Pfaff, N. de Jonge, Exceptionally slow movement of gold nanoparticles at a solid: liquid interface investigated by scanning transmission electron microscopy. Langmuir 31 (25), 6956–6964 (2015). doi: 10.1021/acs.langmuir.5b00150

N. Vidavsky, S. Addadi, J. Mahamid, E. Shimoni, D. Ben-Ezra, M. Shpigel, S. Weiner, L. Addadi, Initial stages of calcium uptake and mineral deposition in sea urchin embryos. Proc. Natl. Acad. Sci. **111**(1), 39–44 (2014). doi:10.1073/pnas.1312833110

E.R. White, M. Mecklenburg, B. Shevitski, S.B. Singer, B.C. Regan, Charged nanoparticle dynamics in water induced by scanning transmission electron microscopy. Langmuir **28**(8), 3695–3698 (2012). doi:10.1021/la2048486

M.J. Williamson, R.M. Tromp, P.M. Vereecken, R. Hull, F.M. Ross, Dynamic microscopy of nanoscale cluster growth at the solid-liquid interface. Nat. Mater. **2**, 532–536 (2003)

T.J. Woehl, K.L. Jungjohann, J.E. Evans, I. Arslan, W.D. Ristenpart, N.D. Browning, Experimental procedures to mitigate electron beam induced artifacts during in situ fluid imaging of nanomaterials. Ultramicroscopy **127**, 53–63 (2013). doi:10.1016/j.ultramic.2012.07.018

J.M. Yuk, J. Park, P. Ercius, K. Kim, D.J. Hellebusch, M.F. Crommie, J.Y. Lee, A. Zettl, A.P. Alivisatos, High-resolution EM of colloidal nanocrystal growth using graphene liquid cells. Science **336**(6077), 61–64 (2012). doi:10.1126/science.1217654

N.J. Zaluzec, M.G. Burke, S.J. Haigh, M.A. Kulzick, X-ray energy-dispersive spectrometry during in situ liquid cell studies using an analytical electron microscope. Microsc. Microanal. **20**(2), 323–329 (2014). doi:10.1017/S1431927614000154

H. Zheng, S.A. Claridge, A.M. Minor, A.P. Alivisatos, U. Dahmen, Nanocrystal diffusion in a liquid thin film observed by in situ transmission electron microscopy. Nano Lett. **9**(6), 2460–2465 (2009a). doi:10.1021/nl9012369

H. Zheng, R.K. Smith, Y.W. Jun, C. Kisielowski, U. Dahmen, A.P. Alivisatos, Observation of single colloidal platinum nanocrystal growth trajectories. Science **324**(5932), 1309–1312 (2009b). doi:10.1126/science.1172104

Chapter 10
In Situ TEM Electrical Measurements

Silvia Canepa, Sardar Bilal Alam, Duc-The Ngo, Frances M. Ross, and Kristian Mølhave

Abstract Transmission electron microscopy (TEM) offers high spatial and temporal resolution that provides unique information for understanding the function and properties of nanostructures on their characteristic length scales. Under controlled environmental conditions and with the ability to dynamically influence the sample by external stimuli, e.g. through electrical connections, the TEM becomes a powerful laboratory for performing quantitative real time in situ experiments. Such TEM setups enable the characterization of nanostructures and nanodevices under working conditions, thereby providing a deeper understanding of complex physical and chemical interactions in the pursuit to optimize nanostructure function and device performance. Recent developments of sample holder technology for TEM have enabled a new field of research in the study of functional nanomaterials and devices via electrical stimulation and measurement of the specimen. Recognizing the benefits of electrical measurements for in situ TEM, many research groups have focused their effort in this field and some of these methods have transferred to ETEM. This chapter will describe recent advances in the in situ TEM investigation of nanostructured materials and devices with the specimen being contacted by electrical, mechanical or other means, with emphasis on in situ electrical measurements performed in a gaseous or liquid environment. We will describe the challenges and prospects of electrical characterization of devices and processes induced by a voltage in gas and liquids. We will also provide a historical perspective of in situ TEM electrical measurements and applications using electrical contacts.

10.1 Introduction

From an early stage in the development of transmission electron microscopy, it was desired that the microscope should be transformed into a micro-laboratory in which the response of the specimen to both external stimuli and the surrounding

S. Canepa • S.B. Alam • D.-T. Ngo • K. Mølhave (✉)
DTU Nanotech Department of Micro- and Nanotechnology, Technical University of Denmark, Lyngby, Denmark
e-mail: Kristian.molhave@nanotech.dtu.dk

F.M. Ross
IBM T. J. Watson Research Center, Yorktown Heights, New York, NY, USA

T.W. Hansen, J.B. Wagner (eds.), *Controlled Atmosphere Transmission Electron Microscopy*, DOI 10.1007/978-3-319-22988-1_10

environment could be recorded in real time (Butler 1979). Such a TEM system would be a powerful analytical tool, being able to record the state of materials at high spatial resolution under varying conditions of environment, temperature, stress, irradiation and/or voltage bias, etc.

Recent progress in materials science and nanotechnology has yielded new nanostructured materials that serve as the active components in electronics, optoelectronics, and sensing applications and for electrochemical energy storage and conversion. To improve the performance of functional nanomaterials, a deep understanding of their structure, response, and stability under relevant operational conditions is essential.

Development of nanostructured materials and devices can benefit substantially from in situ TEM observation as they can be investigated in environments that can be made to approximate the ex situ operation. Increasing interest and development in the in situ environmental TEM (ETEM) techniques has gradually matured to a point where experiments under near-realistic conditions have become feasible while maintaining high spatial resolution (Wagner et al. 2012).

In situ TEM electrical characterization can enhance our understanding of nanostructured materials such as nanowires, nanotubes and nanoparticles by establishing a quantifiable direct correlation between composition and/or structure and the electrical characteristics. Moreover, the changes in the electrical characteristics of the nanostructures can be correlated with changes made to the composition and structure, as a response to reactive gases or liquid processes that can be investigated in real time.

TEM operation with a reactive environment present around the sample can be realized in an ETEM, where the microscope's chamber provides an active surrounding gas phase environment. ETEM also enables experiments in volatile liquids from condensed vapour by using a cooling holder. For non-volatile liquids, experiments can also be performed in a standard TEM system by making use of enclosed gas or wet-cell systems, typically realized as microchip systems mounted in specialized specimen holders (see Chap. 6).

To apply an external stimulus, a custom specimen holder is generally required for transferring the stimulus to the sample. Such holders can typically be used in both TEM and ETEM systems. The external stimulus can be an electrical bias, optical radiation, heat, or mechanical forces. A wide range of TEM holders enable controlled application of these to the sample. To mention a few: heating holders have been in use for many years, nanomanipulators realizing STM, AFM or quantitative indentation functionalities have been developed in the last two decades, and chip-based systems for electrical contact to nanostructures and liquid samples have emerged most recently. All these holders have been used extensively in standard TEM. Apart from the heating holder, the combination of external stimuli with in situ ETEM is still a young and unexplored field that seems to have a wide range of possible applications. The recent developments in the ability to image in water and other liquids, as well as high pressure gases using closed cell systems (see Chaps. 6 and 9) has, however, quickly changed the scene and made environmental experiments possible in any TEM and hence also a recent increase in

published experimental results based on such systems (de Jonge and Ross 2011). The advancement in chip-based in situ TEM has occurred via the proliferation of micro- and nanofabrication technology. This resulted in the development of lab-on-chip systems that can be integrated with special TEM specimen holders and serve as miniature laboratories to perform experiments under controlled environmental conditions and desired stimulus to the specimen.

This chapter discusses such recent advances in in situ TEM investigation of nanostructured materials and devices, with focus on in situ TEM electrical characterization of materials and voltage bias-induced processes, particularly in the presence of gas or liquid phases in ETEM mode, or liquid-cell-based TEM.

10.1.1 Historical Perspective of In Situ TEM Electrical Measurements

Early examples of employing electrical contacts for in situ TEM experiments can be found as far back as the 1970s (Butler 1979). At that time, when the semiconductor industry was in its infancy, degradation and failure of integrated circuits due to electromigration were pressing problems. Blech and Meieran investigated electromigration in aluminium thin films using in situ TEM in the late 1960s (Blech and Meieran 1967, 1969). This required passing current through 300 nm thin Al strips supported on a silicon oxide membrane while imaging in situ. These experiments allowed the evolution of voids created in the Al strips by electromigration to be observed. From such direct observations of electromigration it was possible to estimate the rate of mass transport and the activation energy. Later examples of such investigations have included video recording of carbon nanotubes during immersion into mercury droplets to observe quantized conductance (Poncharal et al. 1999a) and electric current-induced breakdown of a carbon nanotube (Yuzvinsky et al. 2005b). More recently, all the steps involved in the formation of a silicon nanowire device have been recorded: starting from nucleation of a catalytic droplet, followed by catalytic growth of a Si nanowire bridge, and finally current-voltage characterization of the bridge until failure occurs (Kallesøe et al. 2012).

Dynamic processes of magnetization were also investigated in the early 1960s using TEM holders with electrical contacts. It was shown that domain walls in thin films of nickel and cobalt could not only be observed, but also moved in a relatively controlled manner (Silcox 1963). The domain walls were imaged in situ using high defocus, and were moved using a specially fabricated specimen holder with an electrically connected wire located in the vicinity of the specimen. By passing an electric current through the wire, the non-uniform magnetic field produced by current flow could be altered which in turn moved the domain walls. Holders for applying magnetic fields are still being improved (Lim et al. 2003; Arita et al. 2014).

By the 1960s, the potential of in situ TEM techniques for characterization of semiconductor devices was already identified by researchers working in academia and industry. Visualisation of the electrostatic potential distribution due to dopant atoms in semiconductors can give deep insight into the operation of a semiconductor device. One of the first experiments to investigate a silicon p-n junction in situ was carried out by Titchmarsh et al. (1969) in the late 1960s. The group used the technique of Foucault imaging (displaced aperture method) to examine the electric field strength and width across a biased p-n junction. The application of this technique was to study the effect of defects on the electric fields in a p-n junction device.

Since those early innovations, in situ TEM analysis of semiconductor devices has come a long way. For instance with the development of the electron holography TEM technique originally proposed by Gabor (1948), quantitative information on the electrostatic potential of doped semiconductors can be extracted (Midgley et al. 2009). Three dimensional maps of the electrostatic potential of a biased p-n junction can been determined quantitatively at nanometer spatial resolution (Twitchett et al. 2007). This was accomplished by combining electron holography with electron tomography. In such ways, the intricate details of complex nanodevices can be thoroughly characterized.

Electron holography, especially under applied bias, is clearly an interesting technique with potential for real-space mapping of electrostatic potentials with high spatial resolution. However, so far work combining holography with ETEM has been limited. One example has been the demonstration of electron holography imaging in an oxygen atmosphere of an in situ heated yttria-stabilized zirconia (YSZ)–Pt hetero-interface (Tavabi et al. 2011).

It is of course possible to apply other kinds of external stimulus to a specimen in the TEM. Heating in ETEM has been used for many years and is discussed in Chaps. 2 and 6 of this book. The application of sample heating in ETEM has relied on both commercial heating holders and custom made holders (Helveg et al. 2004) and chip systems. The use of custom made chip systems allows great flexibility. As an example, electrical measurements have been made on carbon nanotubes reaching ultrahigh temperatures up to 3200 K in UHV (Begtrup et al. 2007).

Optical stimuli have so far received relatively little attention, but suggest equally exciting possibilities. Recently, several groups have started to develop systems capable of illuminating samples inside the TEM (Shindo et al. 2009; Miller and Crozier 2013; Cavalca et al. 2013) with highly intense visible and UV illumination and in the presence of gas and variable temperatures. The motivation for these studies is the importance of understanding photocatalytic reaction mechanisms. Although complex, there is no reason that such stimuli cannot also be combined with electrical measurements.

10.1.2 Advantages and Pitfalls of Electrically Contacted In Situ Measurements

The continued interest in performing in situ TEM electrical measurements stems from the exceptional opportunity for correlated, quantitative information that can be gathered from such experiments:

1. TEM provides detailed knowledge of the pre-existing state of the specimen, for example, composition, surface morphology, crystal structure, defects, and contamination that can alter the electrical properties.
2. Precise measurement of nanostructure dimensions. For example, a correct interpretation of current-voltage (IV) characteristics of many nanostructures requires information on exact cross-sectional areas and the thickness of any surface coatings.
3. Real-time observation during the electrical probing of the specimen helps in establishing causality, where IV measurements on the device may change the structure due to electromigration effects, Joule heating or chemical reactions.
4. Quantitative data for the in situ experiments can be extracted from different TEM analysis techniques including diffraction, electron holography and EELS while electrically probing the sample.

These advantages make in situ TEM electrical experiments an attractive tool for researchers; however, such multi-parameter experiments require resolution of multiple technological challenges. A key challenge is to create a robust electrical interface between the nano-/micro-scale of the delicate thin and suspended specimen and the macro-scale of the sample holder of the TEM. This requires a custom holder with electrical leads and a contact interface to the specimen. The task has recently become easier with the availability of commercial electrical biasing sample holders.

One must however also be careful of the many pitfalls of in situ experiments: one important issue is the influence of the electron beam on electrical measurements. The electrical and magnetic fields and high-energy electron bombardment disturbs operation of the investigated device and those effects need to be decoupled during analysis of the results. For instance, irradiation by electrons can create electron-hole pairs on a semiconductor sample, plasmons in metals, and trapped electrons that can charge insulating regions and interfaces which might influence for instance the IV behaviour of a sample. Trace amounts of gases present in vacuum systems can also strongly influence the experiments. Chemical reactions involving radiolytic processes must also be kept in mind. This is especially a concern for carbon nanostructures that under irradiation can be influenced by traces of water vapour (Yuzvinsky et al. 2005a; Molhave et al. 2007). Hence, interpretation of the experimental results of in situ measurements of a nanodevice needs careful consideration of the sample surface, its preparation methods, sample history, as well as irradiation dose and radiolytic effects.

10.2 Application of In Situ TEM Electrical Measurements

The combination of electrical and structural measurements enabled by in situ electrical experiments becomes increasingly important in analysis of nanoelectronic devices in which the properties may change due to changes in the structure, or vice versa. Hence, many research groups have focused their effort in this field, developing applications for different physical environments. In order to perform in situ electrical measurements in different environments, special TEM holders, contacting methods and often designs of TEM microfabricated chip systems are required.

The following sections will describe various applications of in situ TEM electrical measurements, focusing on three environments:

1. In vacuum with fixed contacts, and in vacuum where the contact is achieved by in situ TEM manipulators such as TEM-STM and TEM-AFM systems.
2. In reactive gas environments.
3. In liquids for studying electrochemical processes.

10.2.1 In Situ TEM Electrical Measurements in Vacuum

Understanding the modes of failure and electric breakdown of nanostructured conductors (nanowires, nanotubes, ribbons), as well as other current-induced effects, is important for reliable design of novel electronic materials. In situ TEM has been used to study these mechanisms in materials such as carbon nanotubes, gallium nitride nanowires, boron nitride nanotubes and lead zirconate titanate ceramics, to mention a few. Many research groups have focused their efforts on in situ TEM electrical measurements in vacuum and to give a perspective on the diversity of the research carried out, the following section presents an example of such experimental work and gives a literature overview in Table 10.1.

The examples in Table 10.1 show that there is a well-established interest for in situ TEM electrical investigation of nanodevices. State-of-the-art research of nanowire/nanotube-based electrochemical devices and sensors is approaching the development stage where in situ investigation will help improve our understanding of their operation and for in-depth characterization. Literature on such devices is abundant, with applications getting close to market (Petkov 2013).

10.2.1.1 Contacting by Nanomanipulators

The combination of TEM with in situ manipulation offers a powerful tool for providing a fast and direct approach to conduct mechanical and electrical testing of a nanostructure during simultaneous imaging.

Table 10.1 Example of vacuum in situ TEM experiments requiring electrical interfaces

In situ TEM experiment	Materials
Electrical characterization	• Silicon nanowire (Kallesøe et al. 2012)
	• Carbon nanotube (CNT) (Wang et al. 2000, 2001; Poncharal et al. 2002)
	• Boron nitride nanotubes (Golberg et al. 2006)
	• Gold molecular wire (Ohnishi et al. 1998)
	• Metallic nanowires (Liu et al. 2008)
	• Graphene (Lu et al. 2011; Westenfelder et al. 2011)
Electromigration	• Aluminium thin film (Blech and Meieran 1967, 1969; Chang et al. 1990)
	• Copper wire (Chen et al. 2007)
	• Gold wires (Heersche et al. 2007)
	• Pd–Pt nanobridges (Kozlova et al. 2013)
Electric field-induced studies	• CNT field emission (Gao et al. 2001; Xu et al. 2005, 2006)
	• Electrospray of ionic liquid (Wang 2004; Terhune et al. 2013)
	• Ferroelectric oxides (Tan et al. 2005)
In situ specimen modification during IV characterization	• Platinum nanobridge annealing (Gao et al. 2011)
	• Transformation from graphene oxide to graphene (Xu et al. 2011)
	• Breakdown of GaN and Ag wires (Zhao et al. 2011)
	• Breakdown of carbon nanotubes (Yuzvinsky et al. 2005b)
Electron holography of biased specimen	• Silicon–silicon *p*–*n* junctions (Twitchett et al. 2002, 2006, 2007; Wang et al. 2002)
	• Silicon nanowires (He et al. 2013)
IV response to electron irradiation	• ZnO tetrapod nanostructures (Ahmad et al. 2010)
Mechanical studies using electric field-induced deformation	• CNT (Poncharal et al. 1999b)
	• Tungsten oxide nanowires (Liu et al. 2006)
	• GaN nanowires (Nam et al. 2006)
	• Oxide nanobelts (Wang 2004)
	• Piezoelectric crystal (PMN-PT) (Xu 2003)
	• ZnO nanowires (Yang et al. 2012)
Electrochemical processes	• Lithiation and delithiation of Si and Ge nanowires (Liu et al. 2012; Mehdi et al. 2014)
	• Lithiation of a single SnO_2 nanowire electrode (Huang et al. 2010; Ghassemi et al. 2011)

Various experimental techniques, including nanoindentation (Kushima et al. 2012; Palacio and Bhushan 2013) and atomic force microscopy (AFM) or scanning tunnelling microscopy (STM) have been combined with TEM to determine and to image nanoscale electromechanical properties.

In situ TEM STM experiments (Ohnishi et al. 1998) have demonstrated direct TEM imaging of suspended gold wires consisting of strings made from a few

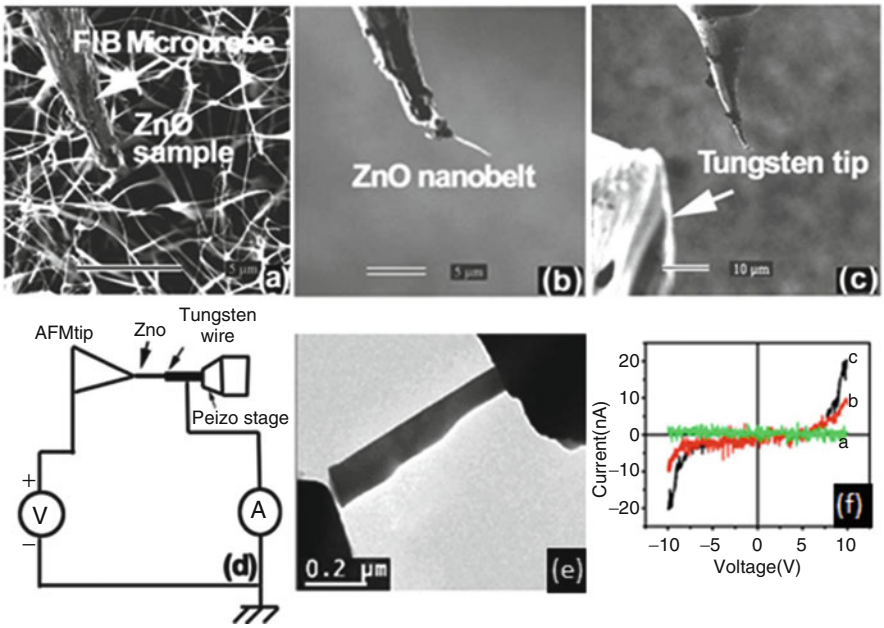

Fig. 10.1 Images recorded in an FIB system showing (**a**) the as grown ZnO sample and the FIB probe, (**b**) a single nanobelt attached to the FIB probe, (**c**) the FIB probe with a nanobelt approaching the tip of the tungsten wire, and (**d**) Schematic of the current-voltage measurement setup. In situ in the TEM, the current-voltage characteristics were measured and found strongly dependent on the applied stress. Adapted from (Asthana et al. 2009)

individual atoms. These 'wires' were made by withdrawing an STM tip from a sample within the TEM. More recently, force measurements have been added to form TEM-AFM systems or even dual manipulator systems (Kuzumaki et al. 2001). As an example, Asthana et al. (2009) introduced a system in which an AFM tip was placed on a small piezoelectric controller on the TEM holder to contact the specimen for I-V characteristics and tensile measurements via electrical contacts on the biasing holder (Fig. 10.1). The change in electrical properties of a ZnO belt from insulating to semiconducting behaviour could be measured when stress was applied.

Mechanical stimuli have not been pursued as intensively in the reactive environment of the ETEM, but fascinating work on hydrogen embrittlement (Sofronis and Robertson 2002) shows the potential that combined ETEM and mechanical studies can offer.

In situ TEM electrical measurements involving liquid, with electrical localized contacts made by TEM-STM systems, provide a new practical approach for studying electrochemical reactions in open cells without encapsulation. These experiments are applicable to non-volatile materials such as solid electrolytes and certain ionic liquids. This is of particular interest for the development of lithium ion batteries (LIBs) because of the possibility of studying the interlinked chemical, physical and electrical changes. This in situ technique allows one to develop a

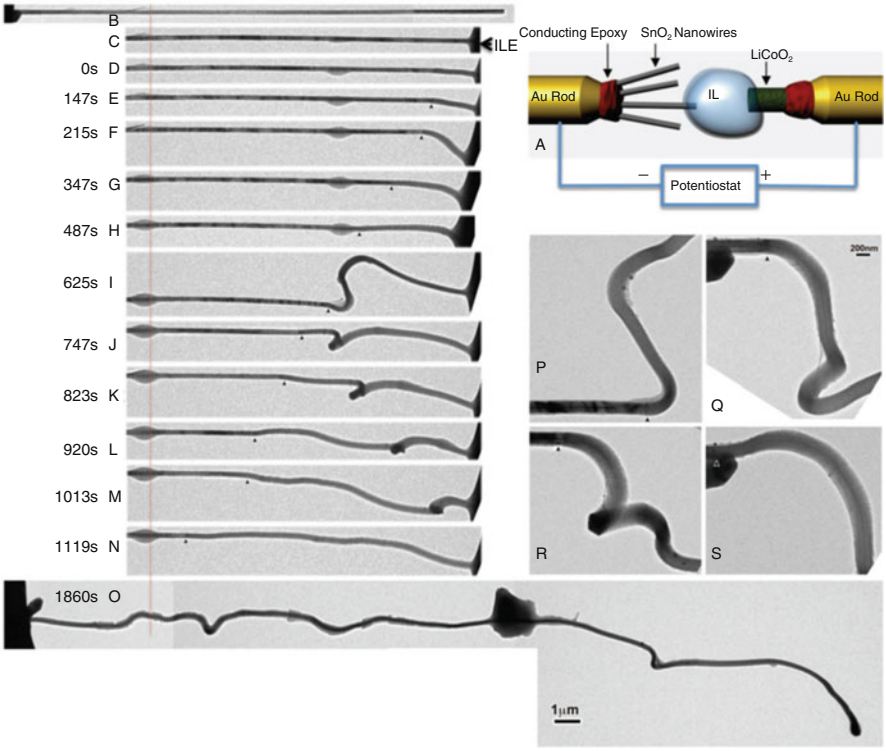

Fig. 10.2 (**a**) Schematic of the experimental set-up to examine lithiation of a nanowire electrode. Time-lapse structure evolution of a SnO_2 nanowire anode during charging at –3.5 V against a $LiCoO_2$ cathode. The initially straight nanowire (**b**, **c**) became significantly twisted and bent after charging (**d–s**). Reprinted with permission from (Huang et al. 2010)

'nano-battery' inside the TEM chamber. The first such experiments (Huang et al. 2010) showed in situ observations of electrochemical lithiation of a single SnO_2 nanowire electrode creating a nanoscale electrochemical device inside a TEM (Fig. 10.2) (Huang et al. 2010). A vacuum-compatible ionic liquid-based electrolyte (ILE) was used instead of a volatile electrolyte in order to eliminate the need for a complicated membrane encapsulation that would otherwise be necessary to prevent evaporation into the TEM column. The electrodes used were a single SnO_2 nanowire as the anode, and a cathode of $LiCoO_2$ particles (Fig. 10.2a). An applied potential drove the electrochemical lithiation reaction. During the lithiation process, the structure of the nanowire changes, including swelling, elongation and spiralization (Fig. 10.2b–s). After the entire nanowire had been affected by the charging process, the authors measured a 90 % increase in length and a diameter expansion of 35 %. These results are important in understanding the lithiation-induced changes in electrode geometry that may occur in batteries. In this experiment, beam-induced effects were also observed as long-term exposure to the electron beam caused some of the ionic liquid electrolyte to form a gel on the nanowire.

Such in situ TEM-STM methods have offered a unique capability for resolving fundamental aspects of nanowire-based battery operation that were poorly understood, such as electrode degradation, atomic level mechanisms of lithiation and delithiation, evolution of solid electrolyte interphase (Su et al. 2013) or microstructural changes (Liu et al. 2011).

10.2.1.2 Chip-Based Contacts

Creating multiple electrical connections between the specimen and TEM specimen holder can be a daunting task, as it requires the development of special TEM holders, ideally where the specimen chip can be easily plugged in. Recent commercially available TEM chip-based heater systems are showing promising new ways to form reliable plug-and-play set-ups for this.

In some cases, the specimen must be connected to contact leads on the TEM holder by wire bonding. In this technique, contact pads are connected through fine metallic wires, which is bonded to each contact pad with the assistance of an ultrasonic welding mechanism (Rodwell and Worrall 1985). Wire bonding offers a more flexible contacting regime in which connections between the specimen and the specimen holder can be established in any desired combination. Moreover, wire bonding has fewer restrictions on the location and micro-scale variations in height of the contact pad on the specimen. However, wire bonding can be time consuming and prone to errors.

10.2.2 In Situ TEM Electrical Measurements in Reactive Gas Environments

Although many groups have performed in situ TEM experiments involving electrical contacts, there are much fewer examples where in situ TEM electrical experiments are combined with experiments in a gas environment (Alam et al. 2013). Kallesøe et al. (2012) grew silicon nanowires (SiNWs) on locally heated regions of micro cantilevers in situ in the TEM. The wires were grown in an ultrahigh vacuum TEM (UHV-TEM) using the gold catalysed vapour–liquid–solid (VLS) mechanism (Wagner and Ellis 1964; Ross 2010) Extended growth allowed the nanowires to form bridges between adjacent microcantilevers. Creating such bridging SiNW devices in situ can give insight into the complete life cycle of the SiNW, from creation, to electrical characterization measurements and ending with breakdown when high bias voltages are applied. In order to grow the SiNWs in situ, the CVD precursor gas disilane was introduced in the UHV-TEM column. Growth was continued until one SiNW formed a bridge from one locally heated cantilever to an adjacent (unheated) cantilever. When the impinging SiNW

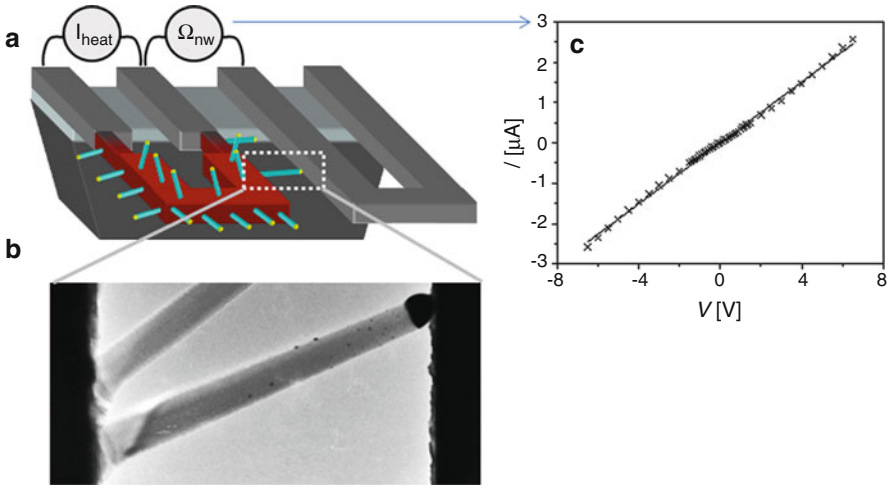

Fig. 10.3 SiNW is grown from one cantilever to an adjacent cantilever in situ by the VLS mechanism, via a catalytic gold-silicon eutectic liquid droplet at the tip of the nanowire (**a**). On contact to the unheated adjacent cantilever, the droplet solidifies, creating an SiNW bridge between the two cantilevers (**b**). After cooling by turning off the heating current I_{heat}, the electrical current-voltage characteristics of the nanowire can be probed (**c**)

made contact with the sidewall of the adjacent cantilever (Fig. 10.3), the catalyst droplet on the tip of the wire solidified, resulting in the creation of a mechanical, thermal and electrical contact between the wire tip and the adjacent cantilever. The SiNW was thus electrically connected at its two ends, base and tip, through the two cantilevers, making it possible to measure its electrical properties in situ.

Carrying out both growth and electrical measurements in situ allows measurements to be made before any oxidative surface effects that would arise due to exposure to air. The creation of electrically connected pristine SiNW bridges in situ therefore provides the ability to observe in real time the effect of introducing a reactant gas on the composition and structure of a SiNW surface and the subsequent effect on the electrical properties. For example, the structural and electrical response of the SiNW to further deposition of Si on the wire surface, or surface oxidation due to introduction of oxygen in the TEM, can be recorded. Such measurements will likely be useful in the field of SiNW photovoltaics or biosensors, where details of the nanowire surface state plays a key role in degradation of functionality.

10.2.3 In Situ TEM Electrical Measurements in Liquid

We can distinguish between TEM and ETEM by noting that the first operates in (moderately) high vacuum while the latter offers relatively high pressures with various gases present at the sample, including the possibility of condensed liquid

phases available at a cooled specimen holder. The term 'environmental' as applied only to differentially pumped 'ETEM' is recently losing its meaning, since microchip-based systems having a gas or liquid container and electron-transparent windows offer contained fluid environments for the sample and can be mounted and used in a standard high-vacuum TEM. Such systems were considered as early as 1944 (Abrams and McBain 1944). Much later, chip systems were developed to observe gas phase (Creemer et al. 2010) and liquid phase reactions (Williamson et al. 2003) in standard TEM. It was not until very recently that liquid cells became commercially available and a larger number of papers were published on liquid TEM (Yuk et al. 2012; Li et al. 2012; Liao et al. 2012; de Jonge and Ross 2011).

In the field of in situ TEM, the technique known as liquid cell microscopy has opened a new pathway for direct imaging and study of complex chemical and electrochemical processes occurring in a liquid environment (de Jonge and Ross 2011). Other methods do not allow such a direct characterization of electrochemical process dynamics at nanoscale resolution within a native electrolyte environment under realistic testing conditions and with site-specific chemical analysis. In situ TEM electrochemistry allows for the dynamic observation of redox processes on the electrodes and corresponding modifications of the materials.

Electron microscopy of liquids has become a field in itself characterized by two different experimental approaches that use either the open cell, previously described, with no encapsulation to the vacuum, or closed liquid cells. The closed cell can be made from clamped or glued microchips with thin membranes, typically made from silicon nitride (see Chap. 9). Given the pressure difference across the membranes from the liquid to the vacuum, both membranes bulge outwards which increases the mass thickness and reduces resolution in parts of the windowed area. Alternative systems include liquids encapsulated between graphene layers, and suspended microfluidic channels on a single chip that provide smaller membranes with less bulging and without the need for clamping (Jensen et al. 2014). The microchip-based closed cell is a useful tool for studying electrochemical process in aqueous or volatile solutions and electrolytes, and in some systems flow can be introduced as well. Since it is possible to pattern electrodes lithographically on the membrane itself, the system is flexible in allowing a multitude of electrode geometries and materials.

In the most common set-up for electrochemical measurements in closed cells, the reactions take place in a small integrated cell made from two clamped microchips each with an electron-transparent membrane, where one is a passive sealing window, while the other has electrodes lithographically patterned on the membrane. Such cells have a restricted volume available so it is important to verify that the TEM experiment mimics the process in bulk experiments. The cell is coupled with potentiostatic control to provide the necessary external stimuli for inducing the electrochemical reactions inside the chamber and allowing quantitative reading of the phenomena. Such cells were first demonstrated for performing direct electrochemical experiments during metal deposition in aqueous solutions (Williamson et al. 2003). It was possible to analyse directly dynamic observations of the

nucleation and growth of nanoscale copper clusters during electrodeposition on a polycrystalline Au electrode. Since then, liquid cell electron microscopy has seen rapid development and application. In addition to the TEM systems, similar enclosed liquid cells are being developed for SEM (Jensen et al. 2013) and photoelectron spectroscopy (Kolmakov et al. 2011; Jensen et al. 2013).

Dedicated commercial electrochemical TEM holders have been introduced. These provide solutions for electrochemical experiments and refined commercial products are continuously coming on the market. Recently, electrical biasing capabilities have been integrated in the flow cell design, enabling a wide variety of electrochemical experiments, e.g. involving materials for electrical energy storage devices. In the dedicated liquid holder, the biasing contacts are directly incorporated in the in situ TEM holder tip along with internal microfluidic channels leading to the electrochemical cell, which allows liquid to be introduced under a constant flow rate.

The assembly of a flow electrochemical cell in the biasing specimen holder is achieved by placing two chips in the holder and clamping using o-rings (Fig. 10.4). An electrical contact is made between the electrodes in the chip and the external electrochemical controller. It is possible to manipulate the liquid dynamics within the cell by using an external pump. Deposited thin films or Focused Ion Beam (FIB) welded samples held within the liquid cell can be studied electrochemically.

Nucleation, cluster growth and correlations are accessible by liquid cell TEM. An example (Radisic et al. 2006) showing the electrochemical nucleation and growth of nanoclusters in real time is given in Fig. 10.5. A series of images obtained during electrodeposition of Cu nanoclusters onto an electron-transparent Au

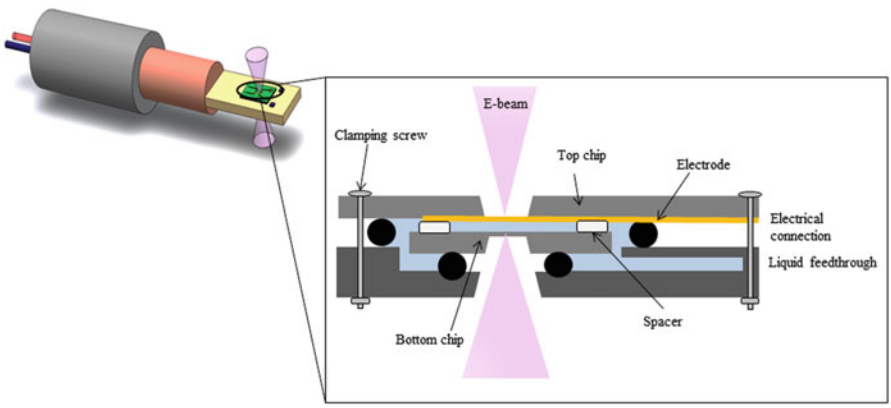

Fig. 10.4 Schematic view of one possible set-up for an in situ TEM closed cell for electrochemical measurements

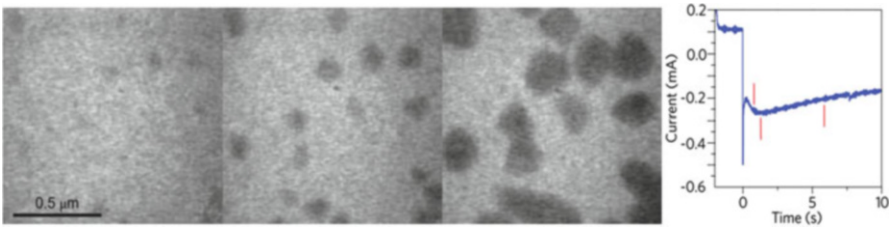

Fig. 10.5 Time sequence of potentiostatic deposition of Cu on a polycrystalline Au electrode and current-time transient curve with indications of the times the images were recorded. Adapted from (Radisic et al. 2006)

electrode from acidified copper sulfate solution can be compared with the current flowing at each time. This comparison of structural and electrical information revealed discrepancies between the growth kinetics measured for individual nanoscale copper clusters and the predictions of models, helping to improve the understanding of the initial stages of electrochemical growth, which is useful for a more quantitative control of nanoscale materials formed by electrochemical methods.

Another important application of electrochemical measurements is the study of corrosion and electrodeposition from solution. An example is the study of pitting corrosion of metal films (Cu and Al) in an aqueous sodium chloride (NaCl) solution (Chee et al. 2015), with the authors discussing the challenges associated with making electrochemical measurements during TEM imaging. A detailed discussion of electron beam-induced processes, which can strongly affect the measurements, can be found in (Schneider et al. 2014)

Gu et al. (2013) used a liquid holder to study the complex mechanisms involved in volumetric changes of a silicon nanowire during the lithiation and delithiation processes under potentiostatic conditions with both cathode and anode fully submersed in a $LiClO_4$ liquid battery electrolyte. Their observations are illustrated in Fig. 10.6a–d. A 100 nm silicon nanowire was coated on one surface with Cu to give high contrast. When a voltage is applied, the Si swells due to lithium intercalation in the nanowire while the Cu is unaltered. Since the wire is fully wetted at all times, the lithiation proceeds homogeneously along the length of the wire. This can be compared to the lithiation front that moves along the wire from the contact point in the previously discussed work by Huang et al. (Fig. 10.6), showing the importance of the diffusion field geometry in determining how the reaction proceeds.

The availability of these unique in situ holders has opened up new research directions that can be used to answer critical scientific questions regarding materials functionality for a broad range of materials and to perform a variety of operando studies of nanoscale energy and catalytic materials.

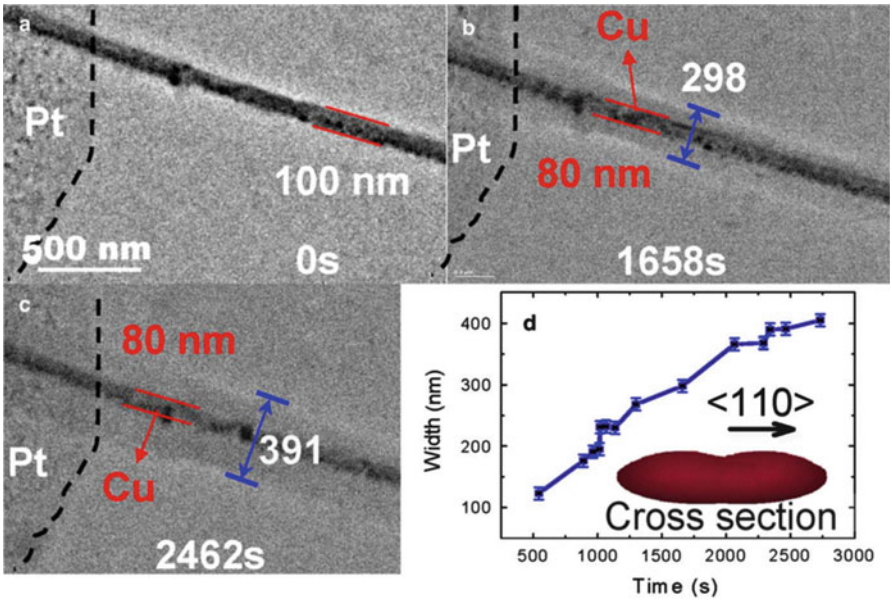

Fig. 10.6 In situ liquid-cell TEM tracking of the lithiation of a Cu-coated silicon nanowire contacted by Pt that had been deposited by FIB (visible on the left part of the images). TEM images (**a-c**) show the structural evolution of the nanowire upon lithiation over time: (**a**) pristine Cu−Si NW at 0 s; (**b**) core−shell formation of the Cu−Si NW at 1658 s; (**c**) Cu−Si NW at 2462 s. The expansion in width with time is shown in the graph (**d**) and the large width expansion indicates the wire is oriented as indicated in (**d**) with expected anisotropic lithiation process primarily in the <110> direction. Reprinted with permission from (Gu et al. 2013)

10.3 Conclusions and Outlook

In this chapter, we have shown several examples of the application of electrical measurements during in situ TEM and ETEM experiments in vacuum, liquid and reactive gas environments, for the study of gas–solid, gas–liquid–solid, and liquid–solid interactions—in some cases showing atomic level resolution. Under controlled conditions, in situ/ETEM with electrical measurement or stimulation is a powerful tool for conducting quantitative real-time property and structure investigations.

Electrical measurements in chemically active environments can be correlated with high spatial resolution information, using ETEM or a closed cell system in TEM. The sample holders must integrate specific units for application of external stimuli such as electrical bias, forces or light. Closed cells for liquid samples in TEM are undergoing rapid development, with application of heat and light likely to be introduced soon in addition to the electrochemical control.

Improving the capability of controlled electrical stimuli in ETEM can open up new perspectives to study directly functional nanomaterials and specific reactions

on the nanoscale that are essential to solve many of society's challenges for sustainable energy supply and energy storage, as well as solving fundamental scientific questions.

References

I.M. Abrams, J.W. McBain, A closed cell for electron microscopy. J Appl Phys **15**(8), 607 (1944). doi:10.1063/1.1707475

M. Ahmad, C. Pan, J. Zhao, J. Iqbal, J. Zhu, Electron irradiation effect and photoluminescence properties of ZnO-tetrapod nanostructures. Mater Chem Phys **120**(2-3), 319–322 (2010). doi:10.1016/j.matchemphys.2009.11.015

S.B. Alam, E. Jensen, F.M. Ross, O. Hansen, A. Burrows, K. Mølhave, Suspended microsystems for in-situ TEM studies of processes in gases and liquids. Microsc Microanal **19**(S2), 402–403 (2013). doi:10.1017/S1431927613004005

M. Arita, R. Tokuda, K. Hamada, Y. Takahashi, Development of TEM holder generating in-plane magnetic field used for in-situ TEM observation. Mater Trans **55**(3), 403–409 (2014). doi:10.2320/matertrans.md201310

A. Asthana, K. Momeni, A. Prasad, Y.K. Yap, R.S. Yassar, In situ probing of electromechanical properties of an individual ZnO nanobelt. Appl Phys Lett **95**(17), 172106 (2009). doi:10.1063/1.3241075

G.E. Begtrup, K.G. Ray, B.M. Kessler, T.D. Yuzvinsky, H. Garcia, A. Zettl, Probing nanoscale solids at thermal extremes. Phys Rev Lett **99**(15), 239904 (2007)

I.A. Blech, E.S. Meieran, Direct transmission electron microscope observation of electrotransport in aluminum thin films. Appl Phys Lett **11**(8), 263–266 (1967). doi:10.1063/1.1755127

I.A. Blech, E.S. Meieran, Electromigration in thin Al films. J Appl Phys **40**(2), 485–491 (1969). doi:10.1063/1.1657425

E.P. Butler, In situ experiments in the transmission electron microscope. Rep Prog Phys **42**(5), 833–895 (1979). doi:10.1088/0034-4885/42/5/002

F. Cavalca, A.B. Laursen, J.B. Wagner, C.D. Damsgaard, I. Chorkendorff, T.W. Hansen, Light-induced reduction of cuprous oxide in an environmental transmission electron microscope. Chemcatchem **5**(9), 2667–2672 (2013)

C.Y. Chang, V.D. Vankar, Y.C. Lee, R.W. Vook, A.J. Patrinos, J.A. Schwarz, Electromigration studies using in situ TEM electrical resistance measurements. Vacuum **41**(4-6), 1434–1436 (1990)

S.W. Chee, S.H. Pratt, K. Hattar, D. Duquette, F.M. Ross, R. Hull, Studying localized corrosion using liquid cell transmission electron microscopy. Chem Commun **51**(1), 168–171 (2015). doi:10.1039/c4cc06443g

K.-C. Chen, C.-N. Liao, W.-W. Wu, L.-J. Chen, Direct observation of electromigration-induced surface atomic steps in Cu lines by in situ transmission electron microscopy. Appl Phys Lett **90**(20), 203101 (2007)

J.F. Creemer, S. Helveg, P.J. Kooyman, A.M. Molenbroek, H.W. Zandbergen, P.M. Sarro, A MEMS Reactor for Atomic-Scale Microscopy of Nanomaterials Under Industrially Relevant Conditions. J Microelectromech Syst **19**(2), 254–264 (2010)

N. de Jonge, F.M. Ross, Electron microscopy of specimens in liquid. Nat Nanotechnol **6**, 695–704 (2011). doi:10.1038/nnano.2011.161

D. Gabor, A new microscopic principle. Nature **161**, 777–778 (1948)

R. Gao, Z. Pan, Z.L. Wang, Work function at the tips of multiwalled carbon nanotubes. Appl Phys Lett **78**(12), 1757–1759 (2001). doi:10.1063/1.1356442

B. Gao, M. Rudneva, K.S. McGarrity, Q. Xu, F. Prins, J.M. Thijssen, H. Zandbergen, H.S.J. Van Der Zant, In situ transmission electron microscopy imaging of grain growth in a platinum

nanobridge induced by electric current annealing. Nanotechnology **22**(20), 205705 (2011). doi:10.1088/0957-4484/22/20/205705

H. Ghassemi, M. Au, N. Chen, P.A. Heiden, R.S. Yassar, In situ electrochemical lithiation/delithiation observation of individual amorphous Si nanorods. ACS Nano **5**(10), 7805–7811 (2011). doi:10.1021/nn2029814

D. Golberg, M. Mitome, K. Kurashima, C.Y. Zhi, C.C. Tang, Y. Bando, O. Lourie, In situ electrical probing and bias-mediated manipulation of dielectric nanotubes in a high-resolution transmission electron microscope. Appl Phys Lett **88**(12), 123101 (2006)

M. Gu, L.R. Parent, B.L. Mehdi, R.R. Unocic, M.T. McDowell, R.L. Sacci, W. Xu, J.G. Connell, P. Xu, P. Abellan, X. Chen, Y. Zhang, D.E. Perea, J.E. Evans, L.J. Lauhon, J.G. Zhang, J. Liu, N.D. Browning, Y. Cui, I. Arslan, C.M. Wang, Demonstration of an electrochemical liquid cell for operando transmission electron microscopy observation of the lithiation/delithiation behavior of Si nanowire battery anodes. Nano Lett **13**(12), 6106–6112 (2013). doi:10.1021/nl403402q

K. He, J.-H. Cho, Y. Jung, Silicon nanowires: electron holography studies of doped p-n junctions and biased Schottky barriers. Nanotechnology **24**(11), 115703 (2013)

H.B. Heersche, L. Gn, K. O'Neill, H.S.J. Van Der Zant, H.W. Zandbergen, In situ imaging of electromigration-induced nanogap formation by transmission electron microscopy. Appl Phys Lett **91**(7), 072107 (2007). doi:10.1063/1.2767149

S. Helveg, C. Lopez-Cartes, J. Sehested, P.L. Hansen, B.S. Clausen, J.R. Rostrup-Nielsen, F. Abild-Pedersen, J.K. Norskov, Atomic-scale imaging of carbon nanofibre growth. Nature **427**(6973), 426–429 (2004)

J.Y. Huang, L. Zhong, C.M. Wang, J.P. Sullivan, W. Xu, L.Q. Zhang, S.X. Mao, N.S. Hudak, X.H. Liu, A. Subramanian, H. Fan, L. Qi, A. Kushima, J. Li, In situ observation of the electrochemical lithiation of a single SnO_2 nanowire electrode. Science **330**(6010), 1515–1520 (2010). doi:10.1126/science.1195628

E. Jensen, C. Købler, P.S. Jensen, K. Mølhave, E. Jensen, C. Købler, P.S. Jensen, K. Mølhave, In-situ SEM microchip setup for electrochemical experiments with water based solutions. Ultramicroscopy **129**, 63–69 (2013). doi:10.1016/j.ultramic.2013.03.002

E. Jensen, A. Burrows, K. Mølhave, Monolithic chip system with a microfluidic channel for in situ electron microscopy of liquids. Microsc Microanal **20**(2), 445–451 (2014). doi:10.1017/s1431927614000300

C. Kallesøe, C.-Y. Wen, T.J. Booth, O. Hansen, P. Bøggild, F.M. Ross, K. Mølhave, In situ TEM creation and electrical characterization of nanowire devices. Nano Lett **12**(6), 2965–2970 (2012). doi:10.1021/nl300704u

A. Kolmakov, D.A. Dikin, L.J. Cote, J.X. Huang, M.K. Abyaneh, M. Amati, L. Gregoratti, S. Gunther, M. Kiskinova, Graphene oxide windows for in situ environmental cell photoelectron spectroscopy. Nat Nanotechnol **6**(10), 651–657 (2011). doi:10.1038/Nnano.2011.130

T. Kozlova, M. Rudneva, H.W. Zandbergen, In situ TEM and STEM studies of reversible electromigration in thin palladium-platinum bridges. Nanotechnology **24**(50), 505708 (2013). doi:10.1088/0957-4484/24/50/505708

A. Kushima, J.Y. Huang, J. Li, Quantitative fracture strength and plasticity measurements of Lithiated silicon nanowires by in situ TEM tensile experiments. ACS Nano **6**(11), 209425–209432 (2012). doi:10.1021/nn3037623

T. Kuzumaki, H. Sawada, H. Ichinose, Y. Horiike, T. Kizuka, Selective processing of individual carbon nanotubes using dual-nanomanipulator installed in transmission electron microscope. Appl Phys Lett **79**(27), 4580–4582 (2001). doi:10.1063/1.1430022

D. Li, M.H. Nielsen, J.R.I. Lee, C. Frandsen, J.F. Banfield, J.J. De Yoreo, Direction-specific interactions control crystal growth by oriented attachment. Science **336**(6084), 1014–1018 (2012). doi:10.1126/science.1219643

H.-G. Liao, L. Cui, S. Whitelam, H. Zheng, Real-time imaging of Pt_3Fe Nanorod growth in solution. Science **336**(6084), 1011–1014 (2012). doi:10.1126/science.1219185

C.K. Lim, G. Yi, J.N. Chapman, W.A.P. Nicholson, S. McVitie, C.D.W. Wilkinson, TEM studies of the switching characteristics of small permalloy elements as a function of field orientation. J Phys D Appl Phys **36**(24), 3099–3102 (2003). doi:10.1088/0022-3727/36/24/001

K.H. Liu, W.L. Wang, Z. Xu, L. Liao, X.D. Bai, E.G. Wang, In situ probing mechanical properties of individual tungsten oxide nanowires directly grown on tungsten tips inside transmission electron microscope. Appl Phys Lett **89**(22), 221908 (2006)

X. Liu, J. Zhu, C. Jin, L.-M. Peng, D. Tang, H. Cheng, In situ electrical measurements of polytypic silver nanowires. Nanotechnology **19**(8), 085711 (2008). doi:10.1088/0957-4484/19/8/085711

X.H. Liu, H. Zheng, L. Zhong, S. Huang, K. Karki, L.Q. Zhang, Y. Liu, A. Kushima, W.T. Liang, J.W. Wang, J.H. Cho, E. Epstein, S.A. Dayeh, S.T. Picraux, T. Zhu, J. Li, J.P. Sullivan, J. Cumings, C. Wang, S.X. Mao, Z.Z. Ye, S. Zhang, J.Y. Huang, Anisotropic swelling and fracture of silicon nanowires during lithiation. Nano Lett **11**(8), 3312–3318 (2011). doi:10.1021/nl201684d

X.H. Liu, Y. Liu, A. Kushima, S. Zhang, T. Zhu, J. Li, J.Y. Huang, In situ TEM experiments of electrochemical lithiation and delithiation of individual nanostructures. Adv Energy Mater **2**(7), 722–741 (2012). doi:10.1002/aenm.201200024

Y. Lu, C.A. Merchant, M. Drndić, A.T.C. Johnson, In situ electronic characterization of graphene Nanoconstrictions fabricated in a transmission electron microscope. Nano Lett **11**(12), 5184–5188 (2011). doi:10.1021/nl2023756

B.L. Mehdi, M. Gu, L.R. Parent, W. Xu, E.N. Nasybulin, X. Chen, R.R. Unocic, P. Xu, D.A. Welch, P. Abellan, J.-G. Zhang, J. Liu, C.-M. Wang, I. Arslan, J. Evans, N.D. Browning, In-situ electrochemical transmission electron microscopy for battery research. Microsc Microanal **20**(2), 484–492 (2014). doi:10.1017/S1431927614000488

P.A. Midgley, R.E. Dunin-Borkowski, P.A. Midgley, R.E. Dunin-Borkowski, Electron tomography and holography in materials science. Nat Mater **8**(4), 271–280 (2009). doi:10.1038/nmat2406

B.K. Miller, P.A. Crozier, System for in situ UV-visible illumination of environmental transmission electron microscopy samples. Microsc Microanal **19**(2), 461–469 (2013). doi:10.1017/S1431927612014122

K. Molhave, S.B. Gudnason, A.T. Pedersen, C.H. Clausen, A. Horsewell, P. Boggild, Electron irradiation-induced destruction of carbon nanotubes in electron microscopes. Ultramicroscopy **108**(1), 52–57 (2007). doi:10.1016/j.ultramic.2007.03.001

C.-Y. Nam, P. Jaroenapibal, D. Tham, D.E. Luzzi, S. Evoy, J.E. Fischer, Diameter-dependent electromechanical properties of GaN nanowires. Nano Lett **6**(2), 153–158 (2006)

H. Ohnishi, Y. Kondo, K. Takayanagi, Quantized conductance through individual rows of suspended gold atoms. Nature **395**(6704), 780–783 (1998). doi:10.1038/27399

M.L.B. Palacio, B. Bhushan, Depth-sensing indentation of nanomaterials and nanostructures. Mater Charact **78**, 1–20 (2013)

N. Petkov, In situ real-time TEM reveals growth, transformation and function in one-dimensional nanoscale materials: from a nanotechnology perspective. ISRN Nanotechnol **2013**, 1–21 (2013). doi:10.1155/2013/893060

P. Poncharal, S. Frank, Z.L. Wang, W.A. De Heer, Conductance quantization in multiwalled carbon nanotubes. Eur Phys J D **9**(1-4), 77–79 (1999a)

P. Poncharal, Z.L. Wang, D. Ugarte, W.A. De Heer, Electrostatic deflections and electromechanical resonances of carbon nanotubes. Science **283**(5407), 1513–1516 (1999b). doi:10.1126/science.283.5407.1513

P. Poncharal, C. Berger, Y. Yi, Z.L. Wang, W.A. de Heer, Room temperature ballistic conduction in carbon nanotubes. J Phys Chem B **106**(47), 12104–12118 (2002). doi:10.1021/jp021271u

A. Radisic, P.M. Vereecken, J.B. Hannon, P.C. Searson, F.M. Ross, Quantifying electrochemical nucleation and growth of nanoscale clusters using real-time kinetic data. Nano Lett **6**(2), 238–242 (2006)

R. Rodwell, D.A. Worrall, Quality control in ultrasonic wire bonding. Microelect Int **2**(3), 67–72 (1985). doi:10.1108/eb044187

F.M. Ross, Controlling nanowire structures through real time growth studies. Rep Prog Phys **73** (11), 114501 (2010). doi:10.1088/0034-4885/73/11/114501

N.M. Schneider, M.M. Norton, B.J. Mendel, J.M. Grogan, F.M. Ross, H.H. Bau, Electron-water interactions and implications for liquid cell electron microscopy. J Phys Chem C **118**(38), 22373–22382 (2014). doi:10.1021/jp507400n

D. Shindo, K. Takahashi, Y. Murakami, K. Yamazaki, S. Deguchi, H. Suga, Y. Kondo, Development of a multifunctional TEM specimen holder equipped with a piezodriving probe and a laser irradiation port. J Electron Microsc (Tokyo) **58**(4), 245–249 (2009). doi:10.1093/jmicro/dfp018

J. Silcox, Magnetic domain walls in thin films of nickel and cobalt. Philos Mag **8**(85), 7–28 (1963)

P. Sofronis, I.M. Robertson, Transmission electron microscopy observations and micromechanical/continuum models for the effect of hydrogen on the mechanical behaviour of metals. Philos Mag A Phys Condens Matter Struct Defects Mech Prop **82**(17-18), 3405–3413 (2002)

Q. Su, L. Chang, J. Zhang, G. Du, B. Xu, In situ TEM observation of the electrochemical process of individual CeO_2/graphene anode for lithium Ion battery. J Phys Chem C **117**(8), 204292–204298 (2013). doi:10.1021/jp312169j

X.L. Tan, H. He, J.K. Shang, In situ transmission electron microscopy studies of electric-field-induced phenomena in ferroelectrics. J Mater Res **20**(7), 1641–1653 (2005). doi:10.1557/JMR.2005.0213

A.H. Tavabi, Z. Yasenjiang, T. Tanji, In situ off-axis electron holography of metal-oxide hetero-interfaces in oxygen atmosphere. J Electron Microsc (Tokyo) **60**(5), 307–314 (2011). doi:10.1093/jmicro/dfr056

K.J. Terhune, L.B. King, K. He, J. Cumings, In Situ Study of Ionic Liquid Taylor Cones Using Electron Microscopy, in *49th AIAA/ASME/SAE/ASEE Joint Propulsion Conference*, San Jose, California, 2013. American Institute of Aeronautics and Astronautics

J.M. Titchmarsh, A.J. Lapworth, G.R. Booker, A new method for investigating the electric field regions of p-n junctions. Phys Status Solidi **34**(2), K83–K86 (1969)

A.C. Twitchett, R.E. Dunin-Borkowski, P.A. Midgley, Quantitative electron holography of biased semiconductor devices. Phys Rev Lett **88**(23), 2383021–2383024 (2002)

A.C. Twitchett, R.E. Dunin-Borkowski, P.A. Midgley, Comparison of off-axis and in-line electron holography as quantitative dopant-profiling techniques. Philos Mag **86**(36), 5805–5823 (2006). doi:10.1080/14786430600815385

A.C. Twitchett, T.J.V. Yates, S.B. Newcomb, R.E. Dunin-Borkowski, P.A. Midgley, A.C. Twitchett, T.J.V. Yates, S.B. Newcomb, R.E. Dunin-Borkowski, P.A. Midgley, High-resolution three-dimensional mapping of semiconductor dopant potentials. Nano Lett **7**(7), 2020–2023 (2007). doi:10.1021/nl070858n

R.S. Wagner, W.C. Ellis, Vapor-liquid-solid mechanism of single crystal growth. Appl Phys Lett **4**(5), 89–90 (1964). doi:10.1063/1.1753975

J.B. Wagner, F. Cavalca, C.D. Damsgaard, L.D.L. Duchstein, T.W. Hansen, P.A.C. Renu Sharma, Exploring the environmental transmission electron microscope. Micron **43**(11), 1169–1175 (2012). doi:10.1016/j.micron.2012.02.008

Z.L. Wang, Properties of nanobelts and nanotubes measured by in situ TEM. Microsc Microanal **10**(1), 158–166 (2004). doi:10.1017/S1431927604040371

Z.L. Wang, P. Poncharal, W.A. de Heer, Nanomeasurements in transmission electron microscopy. Microsc Microanal **6**(3), 224–230 (2000)

Z.L. Wang, R.P. Gao, P. Poncharal, W.A. de Heer, Z.R. Dai, Z.W. Pan, Mechanical and electrostatic properties of carbon nanotubes and nanowires. Mater Sci Eng C Biomimetic Supramol Syst **C16**(1-2), 3–10 (2001)

Z.G. Wang, T. Hirayama, K. Sasaki, H. Saka, N. Kato, Electron holographic characterization of electrostatic potential distributions in a transistor sample fabricated by focused ion beam. Appl Phys Lett **80**(2), 246–248 (2002). doi:10.1063/1.1432746

B. Westenfelder, J.C. Meyer, J. Biskupek, G. Algara-Siller, L.G. Lechner, J. Kusterer, U. Kaiser, C.E. Krill, E. Kohn, F. Scholz, Graphene-based sample supports for in situ high-resolution TEM electrical investigations. J Phys D **44**(5), 055502 (2011). doi:10.1088/0022-3727/44/5/055502

M.J. Williamson, R.M. Tromp, P.M. Vereecken, R. Hull, F.M. Ross, Dynamic microscopy of nanoscale cluster growth at the solid-liquid interface. Nat Mater **2**(8), 532–536 (2003). doi:10.1038/nmat944

Z. Xu, In situ TEM study of electric field-induced microcracking in piezoelectric single crystals. Mater Sci Eng B **B99**(1-3), 106–111 (2003)

Z. Xu, X.D. Bai, E.G. Wang, Z.L. Wang, Field emission of individual carbon nanotube with in situ tip image and real work function. Appl Phys Lett **87**(16), 163106 (2005)

Z. Xu, X.D. Bai, E.G. Wang, Geometrical enhancement of field emission of individual nanotubes studied by in situ transmission electron microscopy. Appl Phys Lett **88**(13), 133107 (2006). doi:10.1063/1.2188389

Z. Xu, Y. Bando, L. Liu, W. Wang, X. Bai, D. Golberg, Electrical conductivity, chemistry, and bonding alternations under graphene oxide to graphene transition as revealed by in situ TEM. ACS Nano **5**(6), 4401–4406 (2011). doi:10.1021/nn103200t

J.C. Yang, M.W. Small, R.V. Grieshaber, R.G. Nuzzo, Recent developments and applications of electron microscopy to heterogeneous catalysis. Chem Soc Rev **41**(24), 8179–8194 (2012). doi:10.1039/c2cs35371g

J.M. Yuk, J. Park, P. Ercius, K. Kim, D.J. Hellebusch, M.F. Crommie, J.Y. Lee, A. Zettl, A.P. Alivisatos, High-resolution EM of colloidal Nanocrystal growth using graphene liquid cells. Science **336**(6077), 61–64 (2012). doi:10.1126/science.1217654

T.D. Yuzvinsky, A.M. Fennimore, W. Mickelson, C. Esquivias, A. Zettl, Precision cutting of nanotubes with a low-energy electron beam. Appl Phys Lett **86**(5), 083103 (2005a)

T.D. Yuzvinsky, W. Mickelson, S. Aloni, S.L. Konsek, A.M. Fennimore, G.E. Begtrup, A. Kis, B.C. Regan, A. Zettl, Imaging the life story of nanotube devices. Appl Phys Lett **87**(8) (2005b)

J. Zhao, H. Sun, S. Dai, Y. Wang, J. Zhu, Electrical breakdown of nanowires. Nano Lett **11**(11), 4647–4651 (2011). doi:10.1021/nl202160c

Chapter 11
ETEM Studies of Electrodes and Electro-catalysts

Christian Jooss, Stephanie Mildner, Marco Beleggia, Daniel Mierwaldt, and Vladimir Roddatis

Abstract Environmental TEM is an excellent tool for gaining insight into the atomic and electronic structure of electro-catalysts under operating conditions. Several electrochemical reactions such as oxidation/reduction processes of electrodes, heterogeneous gas phase catalysis of water splitting/oxygen evolution and electrochemical corrosion processes of materials have been studied in some pioneering experiments which will be summarized in this chapter. These experiments often reveal a strong change of the electrode due to the adsorption of gas species from the environment as well as due to the impact of the electron beam. We show that inelastic scattering of the high-energy electrons can induce electric potentials in the studied samples influencing the observed state of the catalyst. After an introduction to electrochemistry and ETEM investigations, we address, experimentally and theoretically, beam-induced potentials, their dependence on several parameters such as electron flux, electric conductivity, and geometry of samples, aiming at learning how to disentangle them from radiation damage. Our second focus is to control the electric potential distribution within and around samples by dedicated electrical TEM sample holders. To illustrate how this can be achieved, we present the results of a bias-controlled electro-corrosion experiment. We will discuss some of the main experimental and theoretical challenges for the development of controlled electrochemistry studies in transmission electron microscopes.

C. Jooss (✉) • S. Mildner • D. Mierwaldt • V. Roddatis
Institute of Materials Physics, University of Goettingen, Friedrich-Hund-Platz 1, Goettingen 37077, Germany
e-mail: jooss@ump.gwdg.de

M. Beleggia
Center for Electron Nanoscopy, Technical University of Denmark, Fysikvej 307, Kongens Lyngby 2800, Denmark

Helmholtz-Zentrum Berlin für Materialen und Energie, Hahn-Meitner-Platz 1, Berlin 14109, Germany

T.W. Hansen, J.B. Wagner (eds.), *Controlled Atmosphere Transmission Electron Microscopy*, DOI 10.1007/978-3-319-22988-1_11

11.1 Introduction into Electro-catalysis

Electrochemistry, i.e., chemical reactions involving electron transfer, has been a subject of scientific investigation for more than 200 years. Its relevance has increased in recent years due to the need of developing a sustainable energy basis. Electrochemical reactions are of tremendous importance in energy storage (e.g., electrolysis, fuel cells, and batteries), controlled low energy conversion of materials (e.g., metal extraction from ores) and are also involved in undesired reactions such as degradation and corrosion. Electro-catalysis is the increase in the rate of an electrochemical reaction induced by the change of reaction barriers due to the involvement of the electrode surface. Real electrode materials, therefore, do not only mediate the electrochemical electron transfer but in many cases also participate as electro-catalysts. The development of suitable electro-catalysts is essential for high efficiency of electrochemical reactions since they allow for controlling the activation barriers for the electron transfer mediated reactions and thus the activity and selectivity of a reaction. Since electro-catalysts are involved in the reaction process, their atomic and electronic structure typically changes substantially in their active state. Consequently, gaining a deeper understanding of catalysts performance in operation requires atomic scale studies under controlled operating conditions, i.e., at defined electrical conditions, redox state, and chemical environments.

11.1.1 The Equilibrium State of the Electrode Surface

TEM studies of the near surface atomic and electronic structure of electrodes and electro-catalysts in gas or liquid environments can give rise to fundamentally different results compared to high vacuum environments due to changes in the electrochemical equilibrium state of the electrode. The electrochemical equilibrium at the interface between the electrode and the gas/liquid environment is determined by the adsorption/desorption of environmental gas or liquid species g at electrode sites s.

$$s + g \leftrightarrows s_\mathrm{a} + g_\mathrm{a}, \tag{11.1}$$

where g_a denotes the gas atom adsorbed at the surface site s_a. Both the surface sites and the adsorbed atoms are modified in atomic structure, bonding, and charge state compared to the desorbed configuration. The free enthalpy of adsorption is given by

$$\Delta G = \Delta G_0 + \mathrm{RT}\,\ln\left(\frac{a_\mathrm{g}}{a_\mathrm{s}}\right) \quad \text{with} \quad \Delta G_0 = \mu_{s_\mathrm{a}} - \mu_\mathrm{s} + \mu_{g_\mathrm{a}} - \mu_\mathrm{g}. \tag{11.2}$$

μ_i denotes the chemical potential of the involved species under standard conditions. In order to find the pressure dependence of ΔG, the activities of the gas species and surface sites must be related to the respective surface concentrations $a_\mathrm{i} = \gamma_\mathrm{i} c_\mathrm{i}$, via

the activity coefficient γ_i. In the following, we assume that $\gamma_g = 1$ and that the number of surface sites c_s does not change with pressure (which may be unrealistic due to adsorption induced changes in surface structure), giving

$$\Delta G = \Delta G_0 + \mathrm{RT} \ln\left(\frac{p}{p_0}\right). \tag{11.3}$$

Here, p denotes the pressure of the gas and $p_0 = 1$ bar is taken as standard condition. At high enough concentrations of surface adsorbates, gas species can condense into liquid (e.g., for H_2O) or even solid layers (e.g., for some C_nH_m).

Generally, the formation of electrochemical equilibrium at the electrode surface is performed by charge transfer between the electrode and the adsorbents forming a space charge layer with a potential drop given by the Nernst equation

$$\Delta\varphi = \frac{\Delta G_0}{\mathrm{nF}} + \frac{\mathrm{RT}}{\mathrm{nF}} \ln\left(\frac{p}{p_0}\right). \tag{11.4}$$

F denotes the Faraday constant and n the number of moles. The total electric potential drop $\Delta\varphi = \Delta\phi_s + \Delta\phi_g$ is composed of the potential of the electrode and the adsorbed gas species, respectively, forming a Helmholtz double layer. The electric potential formed in electrochemical equilibrium is controlled by the concentration of surface adsorbents as well as the difference of the electrode's work function and the redox potential of the surface species. Figure 11.1 shows a sketch of such a situation for the example of a perovskite oxide electrode.

We want to emphasize here that this equilibrium state of the electrode in contact with a gaseous or liquid environment is a dynamic state, where the reaction rate of the forward reaction $k_+ c_s c_g$ and of the backward reaction $k_- c_{s_a} c_{g_a}$ are equal. Under standard conditions they are related to the equilibrium rate constant by

$$k_0 = \frac{k_+}{k_-} = \frac{c_{s_a} c_{g_a}}{c_s c_g} = e^{-\frac{\Delta G_0}{\mathrm{RT}}}. \tag{11.5}$$

Consequently, pressure-dependence ETEM observations of electrodes or electro-catalysts even near equilibrium conditions exhibit atomic and electronic double space charge layer like structures which are formed by a dynamical process of gas absorption/desorption with possible surface condensation and induced surface and subsurface reorganization.

11.1.2 Electrochemical Activity Driven by Beam Induced or Applied Electric Potentials

Electrochemical equilibrium of the electrode in contact with gas/liquid environments in an ETEM can be shifted by the electronic excitations and atomic displacements which are induced by the high-energy electron beam. Emission of excited

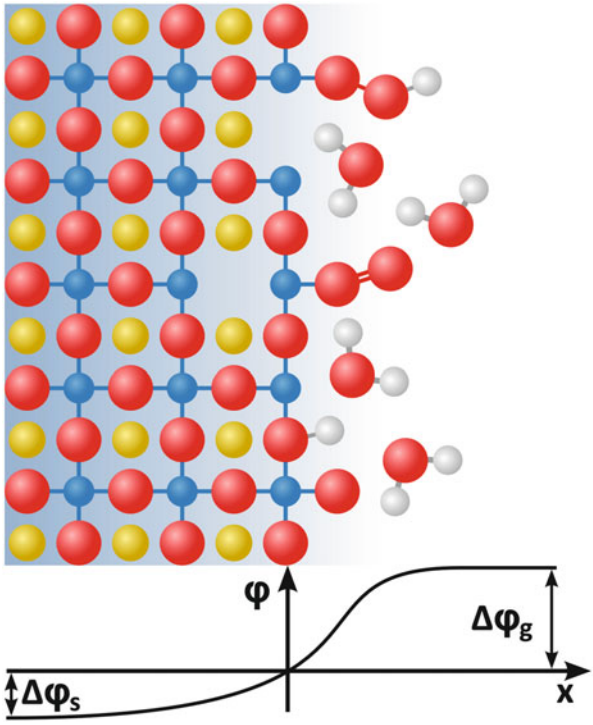

Fig. 11.1 Sketch of the equilibrium state of an electrode surface in contact with water vapor. This example shows a perovskite oxide forming oxygen vacancies and oxygen-based adsorbates leading to a potential drop across the surface

electrons may induce an electric potential at the illuminated sample area. In addition, using appropriate sample holders, an external electric potential can be applied to the TEM sample.

Applying such potentials can give rise to a net charge flow from the electrode to the surface adsorbent and thus to driving a surface redox process. The rate constants for the forward and backward reactions are modified by the application of a potential V as follows:

$$k_+ = k_+^0 \exp\left[\frac{\alpha F}{\mathrm{RT}}(V - V_0)\right] \quad \text{and} \quad k_- = k_-^0 \exp\left[-\frac{(1-\alpha)F}{\mathrm{RT}}(V - V_0)\right] \tag{11.6}$$

leading to a net current density

$$\begin{aligned} j &= \frac{\mathrm{nF}}{A}\left\{k_+ c_{\mathrm{s}} c_{\mathrm{g}} - k_- c_{\mathrm{s_a}} c_{\mathrm{g_a}}\right\} \\ &= j_0\left\{\exp\left[\frac{\alpha F}{\mathrm{RT}}(V - V_0)\right] - \exp\left[-\frac{(1-\alpha)F}{\mathrm{RT}}(V - V_0)\right]\right\}, \end{aligned} \tag{11.7}$$

known as the Butler–Volmer equation. It describes electrode kinetics for charge transfer limited reactions. The surface area of the electrode is denoted by A. In the

case of a one electron reaction, α is called symmetry factor and describes the sensitivity of the transition state to the applied voltage for the forward and backward reactions, respectively. If the effect on the potential barrier is the same for the forward and backward reactions, then $\alpha = 1 - \alpha = 0.5$. The exchange current density is related to the equilibrium rate constant by

$$j_0 = \frac{\mathrm{nF}}{A} k_0 \left(c_s c_g\right)^{1-\alpha} \left(c_{s_a} c_{g_a}\right)^{\alpha} \approx \frac{\mathrm{nF}}{A} c_s k_0 c_g^{1-\alpha} c_{g_a}^{\alpha}. \tag{11.8}$$

Note that $c_s^{1-\alpha} c_{sa}{}^{\alpha} = c_s$ for $c_s \approx c_{sa}$. If the reaction takes place via an activation barrier ΔE_a, the equilibrium rate constant is modified to

$$k_0 = k_{00} e^{-\frac{\Delta E_a}{RT}}. \tag{11.9}$$

With k_{00} denoting an attempt frequency. Electrodes which exhibit pronounced electro-catalytic activity show a reduced activation barrier compared to non-catalytic electrodes.

11.2 Critical Assessment of What Kind of Electrochemical Electrode Properties Can Be Observed in ETEM Experiments

Environmental Transmission Electron Microscopy (ETEM) using aberration corrected microscopes offers the opportunity to access the atomic and electronic structure of electro-catalysts as a function of gas species and pressure ranging from high vacuum ($p \approx 10^{-7}$ mbar) to pressures of about 10 mbar in differentially pumped configurations (Chang et al. 2010; Hansen et al. 2002; Helveg et al. 2004). Using gas or liquid cell holders, the pressure range can be extended to pressures above 1 bar (Creemer et al. 2010). The high spatial resolution capabilities can be combined with a variety of analytical methods for chemical and band structure analysis by using local X-ray and electron energy loss spectroscopy (EELS) (Hansen et al. 2010).

11.2.1 Pressure-Dependent Equilibrium State of the Electrode

Observing the atomic and electronic surface and subsurface structure of the equilibrium state of an electrode as a function of gas species and pressure requires guaranteeing low dose conditions specifically valid for maintaining the electrochemical equilibrium. As a first guess we assume that if the deposited energy due to

inelastic scattering of high energy electrons is much smaller than the potential energy of the double charge layer, electrochemical equilibrium is maintained. Another very critical issue for observing pressure-dependent equilibrium states of electrodes is the initial state of the TEM sample. Its surface and subsurface structure may be modified by preparation processes. Consequently, depending on the preparation conditions, the observed structure under high-vacuum conditions typically may not represent the corresponding equilibrium state but a kinetically frozen metastable state. Changing the Gibbs free energy of adsorption by changing the gas pressure may then allow for the observation of transition processes towards the relevant equilibrium state of the electrode interface to the environment. One example presented in Sect. 11.3.2 of this chapter is the oxidation of an oxygen deficient surface layer on a manganite upon increasing water vapor pressure. Here, however, an electron beam is required to drive this reaction.

11.2.2 Control of Sample Potential V

One of the main challenges for ETEM electrochemistry studies is the control of the sample potential, since according to (11.7), it directly drives electrochemical activity of a TEM sample/electrode. The availability of electrical sample holders on the one side offers great opportunities for the application of electric bias to TEM samples and thus to study their structure in contact with reactants as a function of an applied potential (see Sects. 11.3.4 and 11.3.5). On the other hand, understanding and controlling the effect of the high energy electron beam on the catalyst state poses several obstacles since the effect of beam induced sample charging must be well addressed and separated from other beam induced effects such as beam damage (see Sect. 11.4). Despite electron dose, the electric contact conditions and electric conductivity of the TEM sample or TEM grid may have a tremendous effect on the induced potential. Electric potential experiments such as the electrically controlled corrosion of Ca-manganite presented below represent two-electrode experiments, where the sample potential is measured against the TEM ground. Three-electrode experiments, typically performed in electrochemical cells outside TEM in order to get access to the potential drop between the electrode and the electrolyte, are at present out of reach for gas phase ETEM experiments.

11.2.3 Active Sites and States

Assuming that well-defined electric potential conditions have been established at a TEM sample by either using beam induced or sample holder controlled bias, access to active sites and active states may become achievable. Not all areas of the electrode surface may exhibit the same activity in electro-catalysis. The surface concentration of the active sites c_{s_a} (here identified as the concentration of sites with

adsorbed gas molecules) may be significantly smaller than the concentration of non-active surface sites c_s. The concentration of active sites may even change during activation of the catalyst. Typically, since electro-catalysts are partially involved in the reaction process, their atomic and electronic structure can substantially change during activation (Hutchings et al. 1994; Trotochaud and Boettcher 2014). Even one of the most studied noble metal catalysts, i.e., Pt, shows structural transformation upon polarization, such as the formation of Pt surface oxides even below the threshold of oxygen evolution (Arrigo et al. 2013). In situ XPS shows that CO-oxidation at Pd surfaces requires the formation of a highly reactive PdO surface (Blomberg et al. 2013) In situ X-ray absorption studies reveal that Co_3O_4 catalysts can change in Co valence as well as surface coordination in oxidizing or reducing environments (Zheng et al. 2011). In Sect. 11.3.1 of this chapter, an example of an ETEM study of the nucleation of an oxide wetting layer at a surface step of metallic Cu is shown. Understanding the detailed structure and nature of the active site is a central paradigm in modern molecular- or atomic-level catalysis.

11.2.4 Turn Over

The turn over frequency $\mathrm{TOF} = R_{\mathrm{net}}/s_a$ is defined as the number of reactions per active site per time, whereas the turn over number $\mathrm{TON} = g_{a^*}/s_a$ of a catalyst can be defined as the number of reacted gas molecules per number of active catalyst sites before it corrodes. A serious limitation for the determination of these numbers in ETEM experiments is the large gas volume compared to very small amounts of catalyst material in TEM samples. A coarse estimate of the number of reacted gas species via an ideal catalyst TEM specimen with $\mathrm{TOF} = 0.01$ 1/s, size of 1 μm × 1 μm × 100 nm and fraction of active sites $s_a = 1$ with a density of $1/(5\ \text{Å})^2$ shows that one has to accumulate reaction products for >5 min in order to be able measuring concentration changes in the order of 1 % at a total gas pressure of 1 μbar. This does not rule out measuring reaction products in differentially pumped ETEM experiments via the mounted mass spectrometers. However, any quantification of *TOF*'s or *TON*'s via such a configuration is hardly possible. The gas volume can be significantly reduced using gas or liquid cell sample holders (Zandbergen 2012; Kein et al. 2011). However, as we will show by experiments using a sacrificial agent in order to monitor catalytic activity by the growth of a solid phase on top of the electrode, rough estimates of *TON*'s are possible (Sect. 11.3.3).

11.2.5 Transient and Transition States

Microscopically, the presence of an activation barrier is due to complex atomic and electronic dynamics, which evolve during the charge transfer and the related oxidation/reduction reaction at the electrode surface. Such transient states can result

in a rich activation barrier landscape. The transition state is defined as the state along the reaction coordinate which has the highest potential energy. It may involve non-equilibrium atomic structure, electronic excitations, and electron-lattice-coupled dynamics at the electrode surface as well as in the reacted species. Simple theories, such as transition state theory (Truhlar et al. 1996), are based on strong assumptions, such as the absence of recrossing of the barrier, the presence of Boltzmann-like equilibrium distribution of energies, and a classical motion over a rigid barrier. Since charge transfer happens on time scales of fs to ns, ETEM is not suitable to directly access such processes. However, observation of transient states during slowly evolving electrochemical oxidation or reduction processes such as observed during oxidation of metal surfaces (Sect. 11.3.1) or during lithiation (Sect. 11.3.5) is already possible. In future, electrochemical studies with ultrafast electron microscopy may build a pathway to directly access ultrafast structure and electronic changes related to charge transfer dynamics.

11.3 Case Studies of Model Systems

11.3.1 In Situ Studies of Thermally Activated Redox Reactions

Electrochemical reactions can be studied in ETEM even in the absence of an externally applied or beam induced electric potentials either by changing the partial pressure of an oxidizing/reducing gas species or by changing the sample temperature. Changing the gas pressure directly modifies the Gibbs free energy (11.3), thus inducing an electrochemical non-equilibrium state that can drive a redox reaction until a new equilibrium is established. If the reaction is kinetically limited, an increase of temperature can dramatically increase the reaction constant (11.9) and thus enabling ETEM observations in a reasonable time scale. In addition, temperature changes may modify the Gibbs free energy of the interface.

Oxidation of metal surfaces requires the transfer of electrons from the metal to the oxygen atoms. Such reactions are often accompanied by complex structure and morphology changes. Zhou et al. (2013) have observed the formation of oxide islands during the oxidation of Cu surfaces via in situ ETEM studies (Fig. 11.2). The growth of islands follows the formation of a Cu_2O wetting layer of thickness of a few atomic layers on the virgin Cu surface. The study shed light onto the preferential formation of the oxide at Cu surface steps and the role of Cu_2O-Cu interfacial strain on the transition from layer to island growth. The experiments were performed at elevated temperatures and an oxygen partial pressures p_{O_2} in the range of several μbar.

The growth of a metal oxide layer due to oxidation of a metal surface requires the migration of either metal cations or oxygen anions through the oxide layer. In situ ETEM oxidation studies of Ni and NiCr alloys were able to shed light onto the

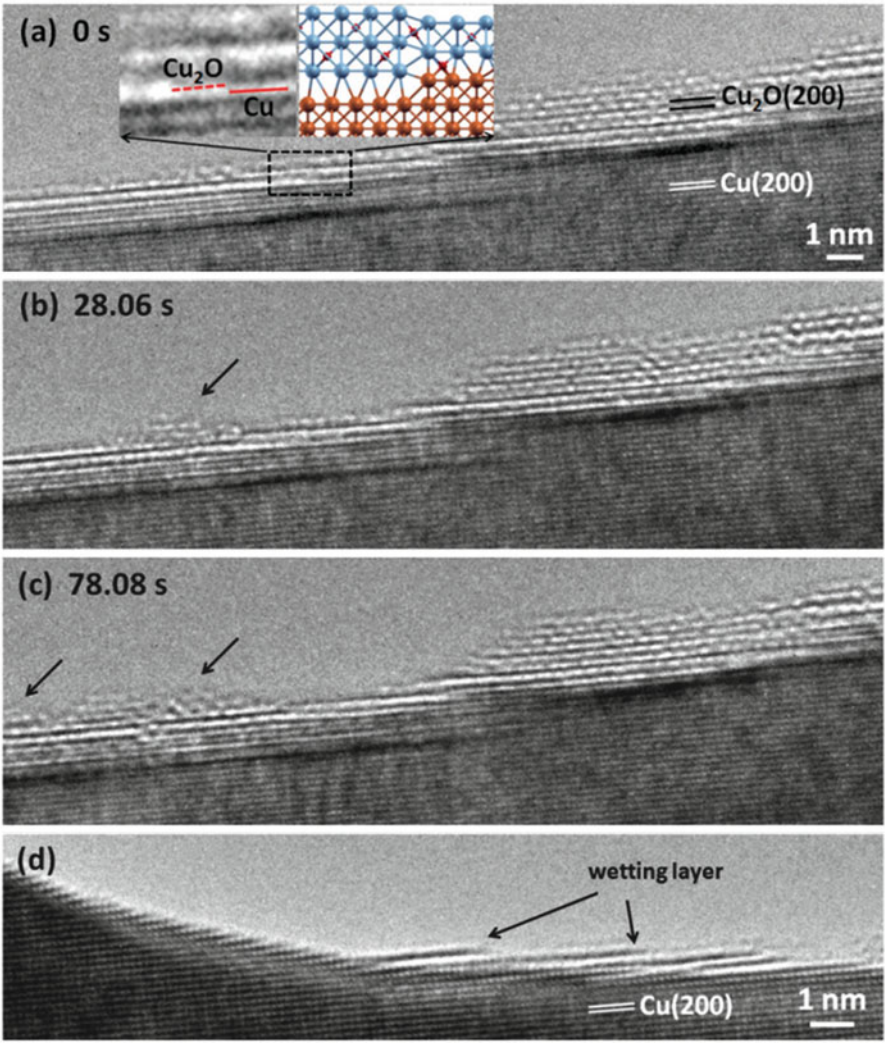

Fig. 11.2 (**a**–**c**) In situ TEM observations of the nucleation and growth of a Cu_2O island on the oxide wetting layer during oxidation of Cu(100) at 350 °C and $p_{O_2} = 6.7$ mbar. *Inset* in (**a**) shows the formation of a disconnection at the buried Cu–Cu_2O interface due to the presence of an atomic Cu surface step. (**d**) TEM image revealing that the oxide wetting layers initiate at Cu surface steps (Reproduced with permission (pending) from G. Zhou et al. Chem. Commun., 2013, 49, 10862)

role of vacancy injection for the oxidation process (Chenna and Crozier 2012; Wang et al. 2014). The study of SiO_2 supported Ni nanoparticles in a mixture of O_2 and CH_4 in a temperature range between 400 and 500 °C showed that the formation and growth of NiO happens via the migration of Ni atoms through the oxide layer which gives rise to the development of large voids within the oxidized nanoparticles

(Chenna and Crozier 2012). Remarkably, reduction of such NiO shell-void structures in CH_4 forms metallic Ni at the interior of the particles. The in situ ETEM study of NiCr particle oxidation in 1 mbar of an O_2 and Ar gas mixture at elevated temperatures reveals preferential oxidation of Cr and void formation due to vacancy injection (Wang et al. 2014). ETEM studies of oxidation and reduction processes thus enable to study a variety of transient states which evolve until completion of the reaction.

11.3.2 Manganese Oxide Redox Reactions via Beam Induced Potentials

Oxidation of an oxygen depleted manganite area can be studied by observation of the recrystallization of an initially amorphous edge of a $Pr_{1-x}Ca_xMnO_3$ (PCMO) film on MgO substrate in contact with pure water vapor as depicted in Fig. 11.3. We have selected an approximately 50 nm thick crystalline sample which is covered by an up to 3 nm thick surface layer of ion beam damaged, amorphous PCMO. The thickness of the layer was measured under high vacuum conditions, where no changes were observed on time scales of 30 min during irradiation with 300 keV electrons. During the exposure to pure water vapor at a pressure of $p(H_2O) =$ 20 µbar and an electron flux of 9000 e/Å^{2}s, the amorphous edges start to recrystallize. Recrystallization of thin amorphous areas also affects the surfaces normal to the incident electron beam as indicated by the inhomogeneous image contrast (Mildner et al. 2015). An FFT-analysis of the high resolution TEM images shows that the structure of the formed nanocrystals is consistent with the perovskite Pbnm structure, although some traces of other phases cannot entirely be excluded.

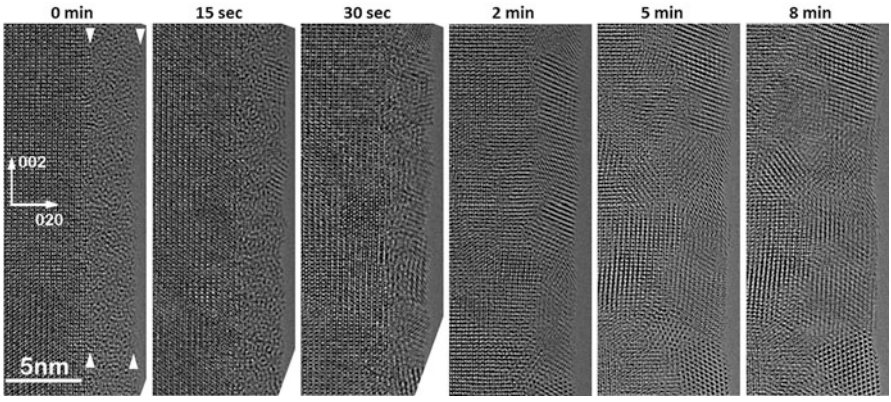

Fig. 11.3 Time series of HRTEM images showing the recrystallization of an initially amorphous edge (marked with *white arrowheads*) of a PCMO film in water vapor at $p_{H_2O} = 47$ µbar and an electron flux of 3.7×10^4 e/Å^{2}s. The initial state is shown in the left image at $t = 0$ min

In order to better understand the influence of electron flux and partial water pressure on the recrystallization process we have performed several experiments observing recrystallization at different pressures and electron fluxes. We have recorded movies with a frame rate of 1 s to detect the appearance of first nanocrystals in the amorphous area. The specimen was kept out of the electron beam during the beam current setting. The results of these experiments are depicted in Fig. 11.4. The onset time for the recrystallization drops nearly exponentially with an increase of electron flux. Such an approximate dependence is expected according to the Butler-Volmer (11.7), if the reaction is driven by an electric potential which increases proportional to the electron flux (see Sect. 11.4).

Post-reaction EELS of the recrystallized areas has been performed at the Mn L-edge in high vacuum at 80 kV beam energy. The ratio of the integral Mn L_3- and L_2-edge intensities can be interpreted as a measure of the Mn valence state. Depending on beam flux, a systematic oxidation of the surficial Mn species in 5.5 µbar water vapor in contrast to a reduction in 47 µbar is observed. Figure 11.5a summarizes the results of the differently treated sample areas. The intensity ratios

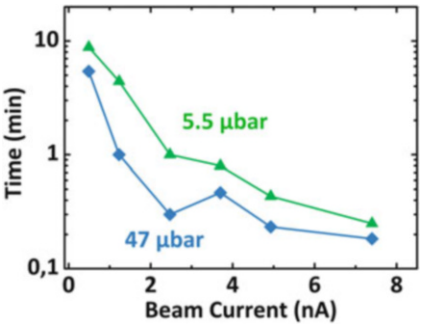

Fig. 11.4 Dependence of the onset time for recrystallization of an initially amorphous PCMO edge on the beam current

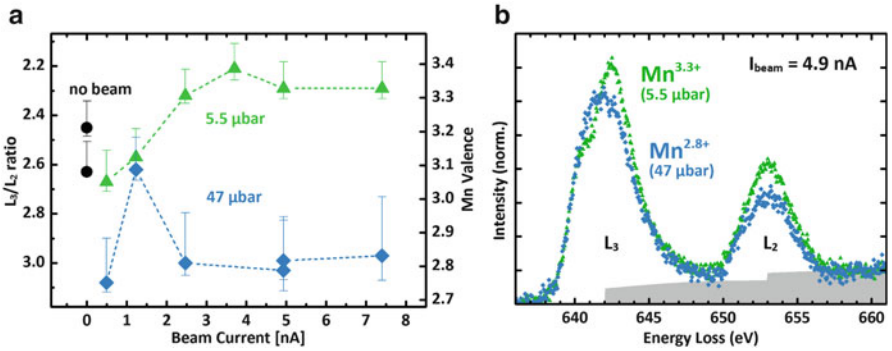

Fig. 11.5 EELS of the PCMO sample at Mn L-edge after exposure to the electron beam in water vapor. Beam flux-dependent recrystallization leads to oxidation (5.5 µbar) or reduction (47 µbar) of the Mn surface species, shown by the Mn L_3/L_2-ratio (**a**). Examples for spectra of oxidized/reduced areas are given in (**b**)

have been translated into Mn valence state using the relationship found by Varela et al. for $La_{1-x}Ca_xMnO_3$ powders (Varela et al. 2009). Figure 11.5b shows an example of spectra, which have been corrected for the power-law pre-edge background and normalized to unity at 658–661 eV. The energy has been calibrated according to X-ray absorption spectra of PCMO thin film samples (Mierwaldt et al. 2014) so that the L_2-edge is at 653 eV. The Hartree–Slater background model taken from Gatan Digital Micrograph is indicated by the filled grey curve. The two non-illuminated areas (black dots in Fig. 11.5a) exhibit a mean Mn valence below the expected value of 3.3+ due to the reduced amorphous surface layer. Recrystallization driven by a beam of 2.5 nA or more in 5.5 μbar water vapor leads to oxidation of the surficial Mn to roughly 3.3+ matching the expectation for stoichiometric PCMO. Sample oxidation is likely to be driven by the positive beam induced surface potential. In contrast, illumination in 47 μbar nominally reduces the Mn valence to roughly 2.8+. This reduction is consistent with other observations of surface/subsurface reduction of Mn valence in a H_2O pressure range between 13 and 100 μbar under oxygen evolution conditions (Mierwaldt et al. 2014; Raabe et al. 2012). Whether it is intrinsically related to the active non-equilibrium state during oxygen evolution or it is driven by acidic conditions due to the increasing proton production during oxygen evolution at higher water partial pressure cannot be clarified at present.

11.3.3 Oxygen Evolution at Manganite Electrodes Visualized by Sacrificial Reactions

Electrochemical gas-phase reactions at solid electrode surfaces can be studied by using sacrificial agents which allow for monitoring electrochemical activity of the electrode via the induced growth of a solid phase on active areas. Raabe et al. (2012) presented an ETEM study of an oxygen evolution catalyst in a gas mixture of 1 mbar He with 0.01 mbar H_2O and a small amount of SiH_4. Electron beam driven SiO_{2-x} growth was observed at active crystalline edges of $Pr_{1-x}Ca_xMnO_3$ ($x = 0.32$) (see Fig. 11.6) and interpreted as a direct solid state indicator for electro-catalytic activity for electrochemical water splitting and oxygen evolution.

The authors can exclude direct SiH_4 oxidation via reaction with H_2O,

$$SiH_4 + 2H_2O \rightarrow SiO_2 + 8H^+ + 8\,e^-,$$

or via deoxygenation of PCMO, since SiO_{2-x} growth is absent under the electron beam at inactive PCMO edges, such as amorphous areas (see Fig. 11.6h, i) or at negative applied potentials. The electro-catalytic O_2 evolution

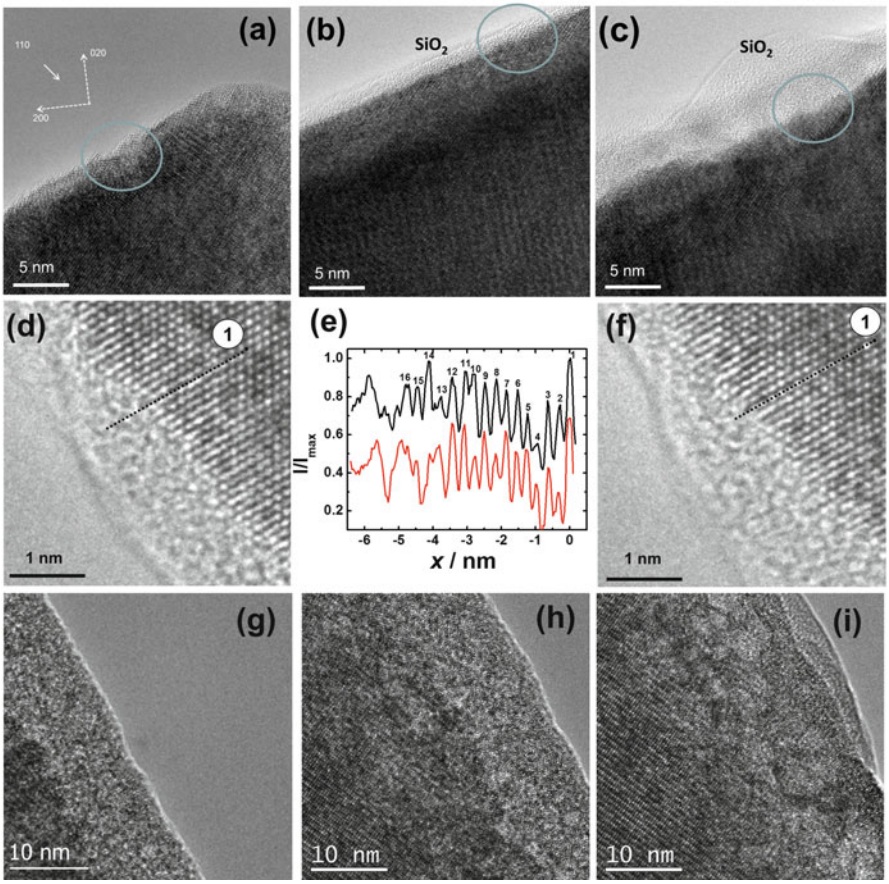

Fig. 11.6 ETEM study of crystalline PCMO ($x = 0.32$) in contact with a He/H_2O mixture (p(H_2O) ≈ 0.13 mbar) with small amounts of SiH_4 under electron flux of 5×10^4 $e^-/(Å^2 s)$. (**a**) HRTEM image acquired in high vacuum showing the pristine state of a crystalline edge on [001] axis. The same section as in (**a**) after injecting the gas mixture is shown in (**b**) 20 s and (**c**) 70 s after start of the electron beam stimulation. The growth of an amorphous SiO_{2-x} layer indicates oxygen evolution activity. The *grey circle* is a marker for a specific edge location. (**d**, **f**) Show high-resolution TEM images of another area of the sample on [201] axis after 300 s and 310 s of electron beam exposure in H_2O and resulting SiO_{2-x} coverage. (e) Intensity modulation along the same line depicted in (**d**, **f**). The first atomic column of this line is labeled as "1." (**g**, **h**) demonstrates the interplay between catalysis and corrosion and is used to analyze the catalytic TON (see text). (**g–i**) Absence of SiO_{2-x} growth at an amorphous PCMO edge under the same conditions leading to SiO_{2-x} growth at crystalline PCMO edges. (**g**) Virgin state of the amorphous sample edge in vacuum. (**h**, **i**) Morphology changes of that edge 40 and 160 s after start of electron beam stimulation, respectively. Parts of the figure have been published in Figs. 3 and S4 in Raabe et al. (2012)

$$2H_2O \rightarrow O_2 + 4H^+ + 4e^-$$

and the related SiO_{2-x} growth via reaction with atomic or molecular oxygen

$$SiH_4 + 2O/O_2 \rightarrow SiO_2 + 4H^+ + 4e$$

is visible by the increase of the O, O_2, and H_2 mass signals on time scales of minutes after shifting the electron beam to a catalytically active sample edge (Figure S8 in the Supplemental Material of Raabe et al. 2012).

All experiments involving H_2O/SiH_4 at catalytic edges show a strong slowing down of the SiO_{2-x} growth with increasing SiO_{2-x} thicknesses, which stops above a thickness of approximately 5–10 nm. We assume that after full coverage, SiO_{2-x} forms a diffusion barrier for the migration of the gas species. In addition, there is a slow transformation of crystalline PCMO into amorphous oxygen deficient PCMO at the PCMO-SiO_{2-x} interface (Fig. 11.6d, f). The study of the interplay between the rates of SiO_{2-x} growth and PCMO amorphization thus allows for the analysis of the competition between catalysis and corrosion and thus for an estimate of the TON under such conditions. The line profiles in Fig. 11.6e taken from Fig. 11.6d, f show the change from a periodical oscillation (half *b*-lattice parameter $b/2 = 0.29$ nm) to a disordered oscillation, indicating the crossover from well-crystalline PCMO to corroded amorphous PCMO followed by SiO_{2-x}, respectively. The comparison of the transformation rate of amorphous PCMO at ≈1.8 nm/min with the growth rate of SiO_{2-x} at ≈10 nm/min at the same region indicates TON of about 10 under the specified ETEM conditions. Thus, reduction of the PCMO ($x = 0.32$) is not a main source of oxygen for SiO_{2-x} formation.

11.3.4 Two Electrode Experiments in Gas Phase: Bias Control of Corrosion

The Nanofactory STM-TEM holder shown in Fig. 11.10a is an example of an electrical TEM holder which can provide control over electric potentials at TEM specimens and allow for the realization of two electrode experiments by using the STM tip as a counter electrode. In particular, control over sample potential emerging within the electron irradiated specimen area due to secondary electron emission is possible by applying a compensating electric potential to the sample. As an example, Fig. 11.7 shows an ETEM experiment in $He/H_2O/SiH_4$ gas mixture with a water partial pressure of 0.013 mbar under electron exposure with 10^4 e/(Å^{2}s) with and without potential control via the STM tip. SiH_4 has been used as a sacrificial agent in order to visualize electrochemical oxygen evolution activity via the growth of SiO_2 at active surface (see Sect. 11.3.3) (Raabe et al. 2012). In Fig. 11.7a, b, a Ca-rich PCMO ($x = 0.95$) sample area is shown before and after electron irradiation in gas without contact to the STM tip. The beam induced potential results in a

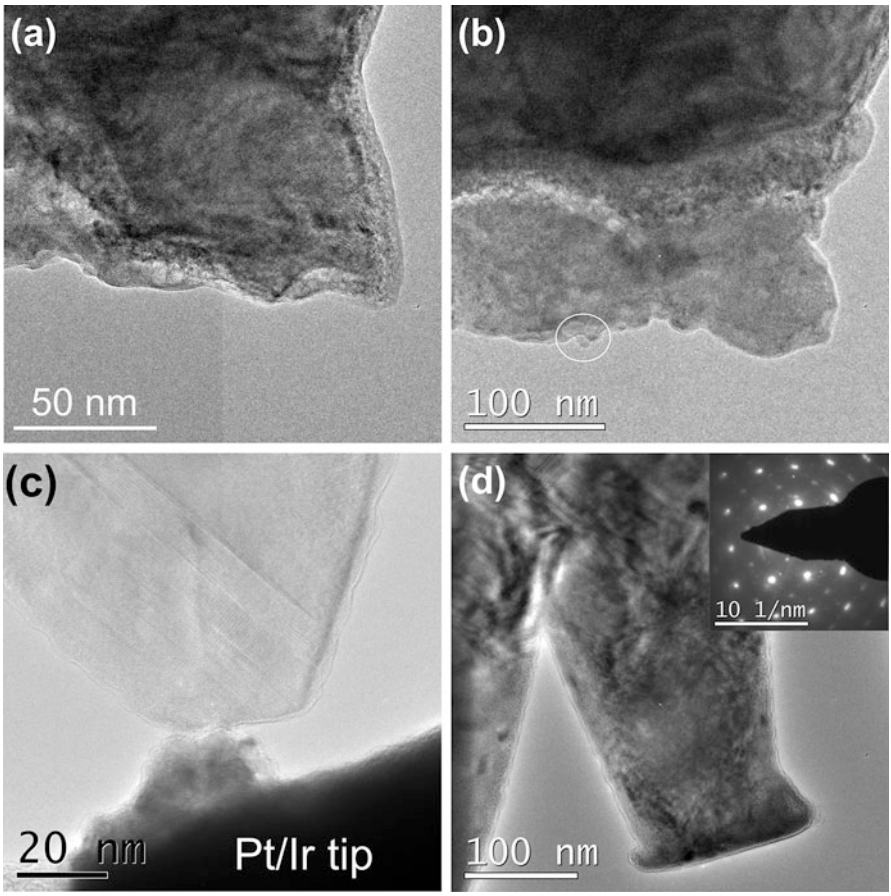

Fig. 11.7 Two electrode electrochemical cell in the ETEM with PCMO $x = 0.95$ working electrode and Pt/Ir as a counterelectrode. (**a**) Bright field overview TEM image of a crystalline PCMO grain in the virgin state. The corresponding diffraction pattern (*inset*) reveals the [001] zone axis. (**b**) Same area after 2 min irradiation with an electron flux of 10^4 e/Å^{2}s in 0.013 mbar H_2O. A pronounced corrosion due to recrystallization and subsequent amorphization is observed. The *insets* show diffraction patterns of a recrystallized and an amorphous region, respectively. (**c**) Bright field overview TEM image of a crystalline PCMO edge in the [001] zone axis in the virgin state just before contact with the Pt/Ir tip. (**d**) State of the sample with –1 V bias after an ETEM experiment under the same conditions as in (**b**). No recrystallization or amorphization is observed and the perovskite structure of the electrode remains entirely intact as revealed by the corresponding diffraction pattern (*inset*) of the final state. See Figs. 5 and 6 in Raabe et al. (2012)

recrystallization followed by amorphization of the irradiated crystalline PCMO region in presence of water (Fig. 11.7b). EELS analysis of the amorphous area reveals a reduced Mn oxidation state compared to virgin areas which we interpret as a consequence of electrochemical reduction of PCMO generally proceeding at positive potentials of ≈1 V, i.e., the generation of oxygen vacancies results in an

intermediate recrystallization towards a non-perovskite structure and a subsequent amorphization (Fig. 11.7b).

The SiO_{2-x} growth which monitors oxygen evolution activity is strongly suppressed in Ca-rich samples because of their high corrosion instability under applied electrochemical conditions. Another area of the same sample under the same gas and electron illumination conditions but with an applied voltage of −1 V is shown in Fig. 11.7c, d. The application of a negative potential at the sample in contact with the STM tip completely suppresses the corrosion observed without the application of an external potential (Fig. 11.7b). As can be seen in Fig. 11.7d, the initial perovskite structure is conserved. In addition, SiO_{2-x} growth is absent since the electrochemical oxygen evolution potential is seemingly not achieved under −1 V bias. However, mechanical stress resulting from the contact between sample and tip leads to a slight modification of the sample shape (c.f. Fig. 11.7c, d). Our observation that the application of −1 V can suppress the PCMO corrosion indicates that the beam induced potentials of the order of a volt can be compensated in a controlled manner by applied external potentials.

The observed electrochemical corrosion process of Ca-rich manganites in ETEM suggests an oxidation reaction at a positive beam induced potential as

$$ABO_3 + 3H_2O \rightarrow AO + BO_{2-y} + \left(\frac{1}{2} + y\right)O_2 + 2H_3O^+ + 2e^-.$$

Indeed, such an electrochemical decomposition is observed in ex situ cyclovoltammetry experiments using Ca-rich PCMO ($x \geq 0.8$) electrodes in contact with liquid electrolytes. At pH = 7, the electrode corrosion is typically observed at an equilibrium potential in a range of $V_0 = 0.2-0.35$ V versus standard hydrogen electrode (SHE) (Grygar 1999). Here, the perovskite decomposition leads to A-site cation dissolution in the liquid electrolyte which is absent in ETEM experiments in gas environment. In the presented two-electrode ETEM experiment, the application of a negative potential at the perovskite working electrode suppresses the anodic current from the gas species into the electrode. In contact with the Pt tip an overcompensation of beam-induced positive potential by an applied negative potential may even give rise to cathodic currents from the working electrode into the Pt working as a counter electrode.

11.3.5 Two Electrode Experiments with Liquid Electrolytes: Lithium Intercalation

One of the major challenges in gas phase electrochemistry is the absence of an electrolyte with sufficiently large ionic conductivity. Consequently, ion mass transport may represent a major reaction limiting step when comparing gas phase ETEM experiments at pressures below 20 mbar with real world electrochemical reactions

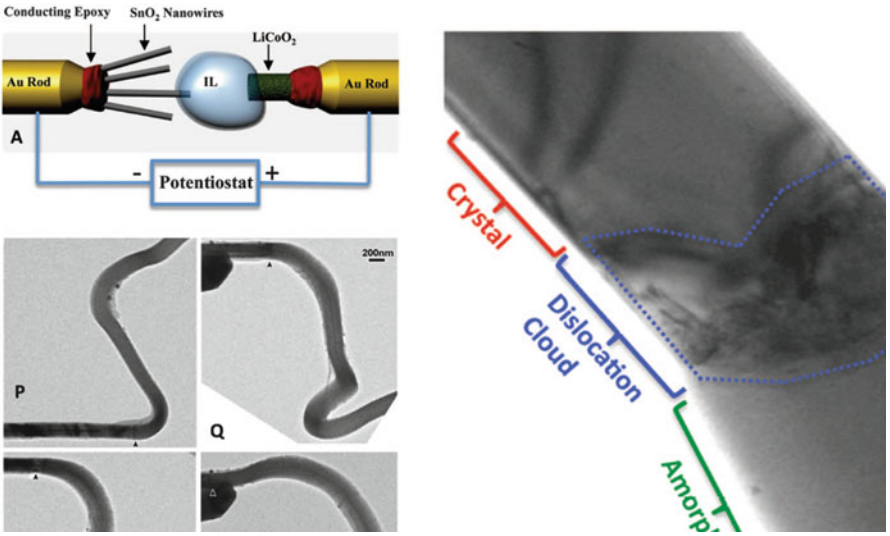

Fig. 11.8 (**a**) Set-up of an in situ TEM electrochemical lithiation experiment of SnO_2 nanowire electrodes using a $LiCoO_2$ counter electrode and an ion liquid electrolyte with low vapor pressure. (P) to (S) are sequential high-magnification images showing the progressive migration of the reaction front, swelling, and the twisted morphology of the nanowire after the reaction front passed by. (G) TEM image showing the high density of dislocations that appeared at the reaction front. (Reproduced with permission The American Association for the Advancement of Science from J. Y. Huang et al. Science 330 (2010) 1515-1520)

with gaseous or liquid reactants. An important class of electrochemical in situ experiments was therefore carried out in recent years based on ionic liquid (ILE) (Huang et al. 2010; Zhong et al. 2011) and solid state Li_2O or carbon based electrolytes (Liu et al. 2012; Ebner et al. 2013; Zhong et al. 2013). The ionic liquid is a molten organic salt with very low vapor pressure, enabling its use in high vacuum ($\approx 10^{-7}$ mbar) inside TEM's without differential pumping while still solvating and transporting Li ions effectively.

As an example, we summarize here an in situ TEM lithiation study of SnO_2 nanowires which was presented by Huang et al. (2010); see Fig. 11.8. The nanoscale battery was arranged by mounting SnO_2 nanowire electrodes, a $LiCoO_2$ counter electrode and ILE based electrolytes in a Nanofactory STM–TEM holder (Fig. 11.10). Electrochemical lithiation takes place at negative potentials of the order of -3.5 V. The lithium intercalation into SnO_2 happens via a reaction front, where a moving dislocation cloud enables an enhanced Li mobility in the SnO_2 phase resulting in a phase transformation from the crystalline SnO_2 into a phase which contains nanocrystalline Li_xSn and Sn particles embedded into an amorphous Li_2O phase, i.e.,

$$SnO_2 + 4Li^+ + 4e^- \rightarrow 2Li_2O + Sn$$

with Li_xSn reaction intermediates. The volume change of the phase transformation gives rise to nanowire expansion and thus some twisting and bending during the

evolution of the reaction front through the nanowire. Discharging at positive potential does not affect the Li_2O matrix and thus is not fully reversible.

Another in situ TEM study of electrochemical oxidation of

$$Li_2O_2 \rightarrow Li^+ + O_2 + 2e^-$$

shows that the reaction is charge-transfer limited since the low electronic conductivity of Li_2O_2 gives rise to high overpotentials (Zhong et al. 2013).

11.4 Electron Beam Induced Electric Potentials

Electric potentials of a magnitude relevant for electrochemistry can be easily generated by inelastic scattering of high energy electrons incident on a thin TEM foil specimen which results in the emission of Auger electron, core electrons as well as secondary electrons (SE). Electron emission from a TEM specimen leaves hole carriers, i.e., positive charges, within the specimen. Thus, depending on the electric conductivity of the sample, positive charges can accumulate within the electron beam exposed specimen areas resulting in a positive electric potential. This potential, on the one hand, generates an energy barrier for subsequent electrons trying to escape from the sample, i.e., the emission rate decreases with increasing potential. On the other hand the positive potential attracts negative charges from grounding or the environment, which compensate the holes generated by SE emission. The induced sample potential thus depends sensitively on the primary electron flux as well as on the electric conductivity of the sample and electric contact conditions. The evolving steady state potential is thus governed by the balance of the emission, I_{SE}, and the neutralization, I_N, currents:

$$\frac{dQ}{dt} = I_{SE} + I_N = 0. \tag{11.10}$$

Even under low-dose conditions, where the effect of beam damage due to atomic displacements may be absent, beam induced electric potentials can have a major effect on the electrode/catalyst state. In the following we present a theoretical model of the beam induced potential in combination with experimental approaches for measuring it. Since SE emission is the predominant fraction of electron emission processes (Cazaux 2010), we restrict our calculation on that species in Sect. 11.4.1. A short discussion of possible charge neutralization sources is subject of Sect. 11.4.2. Furthermore, we introduce methods for measuring electron beam induced potentials in a TEM by using electrical holders in Sect. 11.4.3 and by using off-axis holography in Sect. 11.4.4.

11.4.1 Determination of Secondary Electron Emission Yields from Electron Transparent Thin Foils

Electron emission from a condensed matter sample involves two basic steps: First, the beam induced excitation of a specimen electron to energies above the ionization edge and, second, the propagation of the excited (hot) electron to the surface of the specimen. The former depends on materials properties. The latter considers scattering of the SE within the specimen and is also affected by the specimen geometry. Electron emission further depends on the beam induced potential which will be discussed later. These two steps form the basis for theoretical treatments of the secondary electron yield Y, which relates the emission current I_{SE} and the primary beam current through the sample I_P via $Y = I_{SE}/I_P$, in the literature (Cazaux 2010; Henke et al. 1979; Chung and Everhart 1974). In 1974 Chung and Everhart derived an equation applicable to macroscopic metallic samples (Chung and Everhart 1974) with thicknesses d much larger than the inelastic mean free path λ of generated SE in the material. We adapt the Chung–Everhart equation to TEM thin foils with $d = \lambda$ by introducing the factor $1 - \exp\left(-\frac{d}{\lambda(E)}\right)$ which takes into account the limitation of Y by the finite thickness.[1]

$$\frac{dY}{dE}(E,\phi) = 2 \cdot \frac{S(E)\lambda(E)}{4} \cdot F(E,\phi) \cdot \left[1 - \exp\left(-\frac{d}{\lambda(E)}\right)\right] \tag{11.11}$$

Equation (11.11) describes the energy distribution of emitted SE per incident electron current and unit time. The term $F(E,\phi) = 1 - (E_F + \phi)/E$ depends on the work function ϕ. It accounts for energy losses during the propagation of an SE excited to energies above the ionization edge, $E > E_F + \phi$, across the specimen surface to vacuum. In other words, it reflects the escape probability of an excited SE with energy E. SE energies E are given relative to the bottom of the conduction band. $S(E) = C_Y(E_P)/(E - E_F)^2$ denotes the number of electrons excited to an energy interval $E + dE$ per primary electron and unit path. C_Y is a material specific constant and E_P denotes the energy of the primary electrons. C_Y can be obtained either theoretically (Streitwolf 1959) or in a semi-experimental way using common rate equations on the basis of scattering cross sections

[1] In the derivation of (11.10), we approximate the term $\exp(-d/\lambda \cos\theta)$ with $\exp(-d/\lambda)$ (c.f. (11.5) in Chung and Everhart 1974) when integrating over the allowed angular range of SE trajectories. In doing so, we effectively underestimate by a small amount the contribution to the yield of those secondaries with energies just above the work function. Numerical comparisons show that this approximation affects the yield spectrum dY/dE at most by about 1 %.

$$\frac{dn_{\text{ion}}}{dt\,dx} = n_s \cdot \sigma_{\text{ion}}(E_{\text{P}}) \cdot \frac{dn_{\text{P}}}{dt} \ . \tag{11.12}$$

Equation (11.12) relates the number of ionization processes per unit time and unit primary electron path dx with the specimen atomic density n_{s}, the primary particle current $\frac{dn_{\text{P}}}{dt}$ and the material specific ionization cross sections σ_{ion}. Experimental values of σ_{ion} are available in literature and online databases (http://dbshino.nifs.ac.jp). For PCMO it amounts to $\sigma_{\text{ion}}(E_{\text{P}}) = 3 \times 10^{-23}\,\text{m}^2$ at $E_{\text{P}} = 300\,\text{keV}$. According to (11.12) $n_{\text{s}} \cdot \sigma_{\text{ion}}(E_{\text{P}})$ gives the number of ionization processes per primary electron and unit path which is equal to the total number of electron excitations $S(E)$ with final energies $E > E_{\text{F}} + \phi$.

$$n_{\text{s}} \cdot \sigma_{\text{ion}}(E_{\text{P}}) = \int_{E_{\text{F}}+\phi}^{\infty} S(E)dE \ = \frac{C_{\text{Y}}(E_{\text{P}})}{\phi} \ . \tag{11.13}$$

We calculate (11.13) for PCMO ($x = 0.35$) using $n_{\text{s}} = 8.76 \times 10^{28}\text{m}^{-3}$, $\phi = 4.9$ eV (Reagor et al. 2004), $E_{\text{F}} = 1.84$ eV calculated via $E_{\text{F}} = \frac{\hbar^2}{2m}(3\pi^2 n_{\text{e}})^{\frac{2}{3}}$, where $n_{\text{e}} = (1-x)/V_{\text{SC}}$ with hole doping level $x = 0.35$ and the simple cubic unit cell volume $V_{\text{SC}} \approx (3.8\ \text{Å})^3$.

Finally, we calculate the inelastic mean free $\lambda(E)$ path of the generated SE with the semi-empirical expression given by Seah and Dench (1979) for inorganic compounds

$$\frac{\lambda(E)}{a} = 2170(E - E_{\text{F}})^{-2} + 0.72(a(E - E_{\text{F}}))^{\frac{1}{2}}, \tag{11.14}$$

where a denotes the monolayer thickness (for PCMO $a = 0.38$ nm). Inserting (11.13) and (11.14) in (11.11) and integration over the kinetic energy of the SE gives a total secondary electron yield Y_0

$$Y_0 = \int_{E_{\text{F}}+\phi}^{\infty} \frac{dY}{dE}\,dE = 0.0034. \tag{11.15}$$

A positive potential V arising from SE emission creates a barrier for ionized electrons that reduces their escape probability. This effect can be easily included in (11.11) by increasing the effective work function to $\phi + \text{eV}$:

$$\frac{dY}{dE}(E, \phi, V) = 2 \cdot \frac{S(E)\lambda(E)}{4} \cdot \left(1 - \frac{E_{\text{F}} + \phi + \text{eV}}{E}\right) \cdot \left[1 - \exp\left(-\frac{d}{\lambda(E)}\right)\right] \tag{11.16}$$

In Fig. 11.9a the energy distribution $\frac{\text{dY}}{\text{dE}}(E, \phi, V)$ has been calculated for different potentials V. The total yield as a function of potential V is shown in Fig. 11.9b.

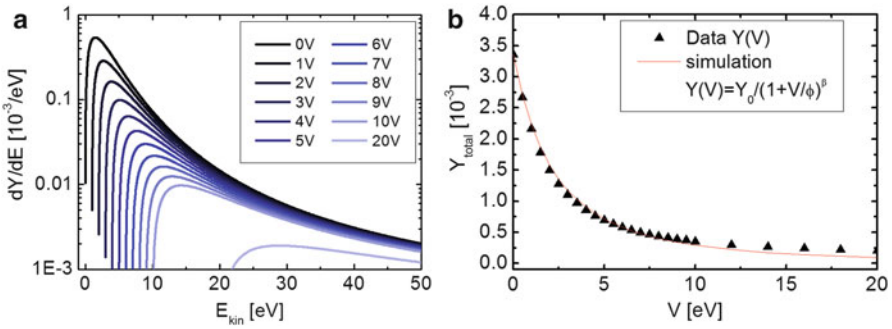

Fig. 11.9 The secondary electron yield depending on the beam induced electric potential V calculated according to (11.16). (**a**) The energy distribution of emitted SE per primary electron for different values of V and (**b**) the total yield as a function of V and a power law fit (*red line*) giving rise to the equation (11.17)

It reveals a rapid decrease of $Y(V)$ following a power law $Y(V) = Y_0/\left(1+\frac{V}{\phi}\right)^{\beta}$ with the exponent β~2.2 which leads to a self-limitation of the evolving potential. We define $v \equiv \frac{V}{\phi}$, write $Y(V) = I_{\mathrm{SE}}(V)/I_{\mathrm{P}}$, and obtain $I_{\mathrm{SE}}(v) = \frac{Y_0 I_{\mathrm{P}}}{(1+v)^{\beta}}$. In the stationary state emission currents and neutralization currents balance, $I_{\mathrm{N}}(v) = I_{\mathrm{SE}}(v)$. Describing $I_{\mathrm{N}}(V)$ as a function of the sample resistance $R(V)$ yields

$$v(1+v)^{\beta} = \frac{Y_0 I_{\mathrm{P}} R(V)}{\phi}. \tag{11.17}$$

Thus, the steady state potential strongly depends on the sample resistance which governs the neutralization currents.

11.4.2 Neutralization Currents

In TEM samples with low-resistive (metallic-like) pathways to ground the neutralization of holes generated within the electron irradiated specimen occurs via grounding currents. The high grounding currents may provide an almost entire compensation of generated holes and limit the evolving potential to vanishingly small values. However, grounding currents in cross section TEM samples of electrode/electro-catalysts sensitively depend on the chosen support material.

A second contribution to charge neutralization may be provided by a gaseous environment in the TEM similar to observations in SEM (Meredith et al. 1996; Moncrieff et al. 1978). Ionization of gas species or rather secondary electron emission from gas species may provide negative charges for compensating holes within the TEM specimen. However, simple calculations considering the cross sections for electron attachment to gas species (here H_2O and He) as well as

electron emission from gas species yield negligible neutralization currents on the order of 1 fA at conventional ETEM gas pressures. To give an example, a He pressure of 0.3 mbar using 300 keV electrons with a primary beam current density of $10^4\,\mathrm{e/\AA^2 s}$ results in a negative charge generation yield of 10^{-8}–10^{-6} per primary electron which is at least four orders of magnitude lower than the total yield per primary electron in solid samples. Thus, we conclude that even in high resistive samples the grounding current is the primary charge compensation mechanism in TEM thin foils.

11.4.3 Direct Measurement of Beam Induced Potentials

In this section we show two experiments in the TEM that support the theoretical considerations above. First, we show an experiment where we measure the sample resistance using an electrical biasing TEM holder equipped with a piezo-driven PtIr-STM tip (Fig. 11.10a). Additionally, we show electron holography experiments which reveal a phase shift of electron waves traversing the specimen and the vacuum nearby which carries information about the electric potentials within the specimen.

With an electrical biasing TEM holder we measure I-V characteristics of a PCMO/MgO cross section TEM sample (see Fig. 11.10). We obtain a resistance that strongly depends on the sample potential. It can be adequately simulated with a Frenkel–Poole conduction mechanism (Fig. 11.10b). By fitting the measured $R(V)$ curve via a Frenkel–Poole $R(V)$ dependence, we obtain $R(V_0) \cong 1\,\mathrm{M\Omega}$. Depending on sample preparation and surface adsorbents, a resistance of MgO lamellas of similar geometry of up to $R(V \rightarrow 0) \cong 67\,\mathrm{G\Omega}$ has been measured.

Removing the tip from the specimen and interconnecting a 200 TΩ resistance leads to a development of a positive electric potential of several volts under electron irradiation (Fig. 11.10d), depending on primary beam current and gas pressure. The induced potential evolving in 5 μbar water vapor pressure is higher than in vacuum. This is a surprising result since a gaseous environment is commonly considered to reduce beam induced charging effects. However, the combination of water vapor presence and electron exposure turns out to remove carbon contamination on the specimen surface and, thus, increases the leakage resistance.

In the following, we provide a test of the results obtained from the balance of current (11.10) and the estimated yield (11.15) by the measurement of the time evolution of the sample voltage (Fig. 11.10d). In this experimental configuration, the connection to ground is severed ($I_\mathrm{N} \ll I_\mathrm{SE}$ for $V < 10\,\mathrm{V}$ and $I_\mathrm{P} = 5.4\,\mathrm{nA}$)[2] and the balance of currents reads simply

[2] Due to the 200 TΩ input resistance $I_\mathrm{N}(10\,V)$~50 fA $\ll I_\mathrm{SE}(10V)$~1.5 pA for $I_\mathrm{P} = 5.4\,\mathrm{nA}$. Calculation of I_SE via $I_\mathrm{SE}(v) = (Y_0\ I_\mathrm{P})/(1+v)^\beta$. With increasing V, I_N increases to values of more than 10 % of I_SE and $I_\mathrm{N} \ll I_\mathrm{SE}$ is not fulfilled.

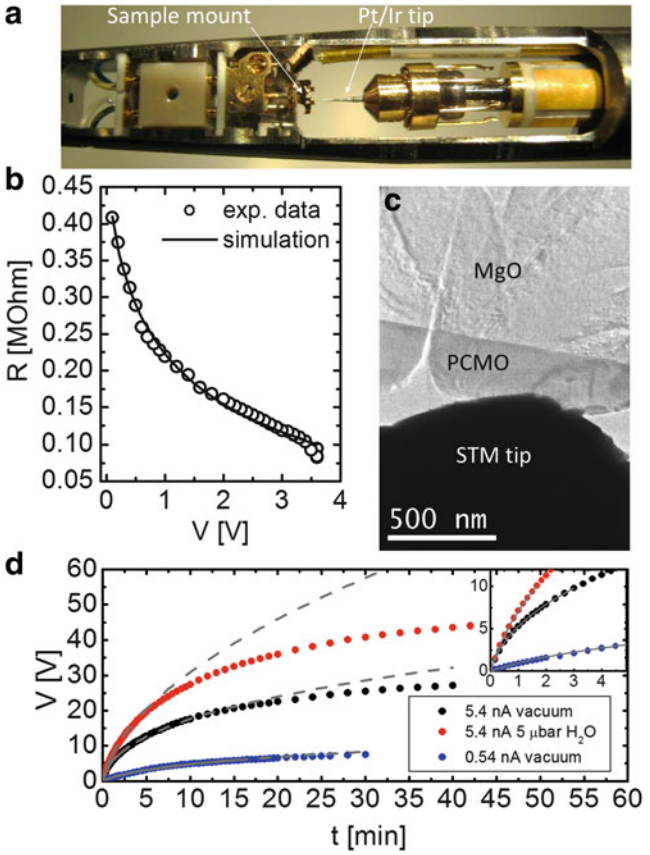

Fig. 11.10 Sample resistance and potential built-up measured in a cross section TEM sample cut from a PCMO thin film sample on insulating MgO substrate using a TEM holder equipped with a STM tip. (**a**) A photo of the electrical biasing holder showing the sample support and the piezo-driven STM tip. (**b**) The measured sample resistance as a function of applied potential without electron irradiation. (**c**) TEM image depicting the PCMO/MgO TEM sample in contact with a PtIr STM tip. (**d**) The measured electric potential as a function of time after starting electron exposure of a PCMO area with a diameter of 300 nm with a primary beam current through the sample $I_P = 0.54\,\text{nA}$ (*blue*) and $I_P = 5.4\ nA$ in vacuum (*black*) and in water pressure of $p_{H_2O} = 5$ µbar (*red*). The potential is measured using an electrometer with an internal resistance of 200 TΩ. For this configuration, the measured increase of the potential with time, $V(t)$, is fitted (*grey lines*) in the range $0 < V < 10V$ for ($I_P = 5.4$ nA) and $0 < V < 6V$ for ($I_P = 0.54$ nA) with a capacitor model described in the text below according to (11.22). This model is valid in a voltage range, where $I_N \ll I_{SE}$. The resulting time constants are summarized in Table 11.1

$$\frac{dQ}{dt} = I_{SE} = Y(V)I_P, \tag{11.18}$$

implying that the object will keep charging up, although at a rate that decreases with time. For a floating metallic object, each dQ of charge added or removed from its

Table 11.1 Results of fitting $V(t)$ data presented in Fig. 11.10d with (11.22) and (11.21)

Data (presented in Fig. 11.10c)	τ (s)	α	C (pF)
Blue data [$I_P = 0.54$ nA, p~10^{-7} mbar]	73.62	0.308	90
Black data [$I_P = 5.4$ nA, p~10^{-7} mbar]	9.18	0.363	95
Red data [$I_P = 5.4$ nA, p~5×10^{-3} mbar]	12.63	0.513	92

interior changes its potential, measured with respect to infinity, by an amount dV, where $C = \mathrm{d}Q/\mathrm{d}V$ is the self-capacitance of the body. Therefore, we can write

$$dV/dt = Y(V)I_P/C, \tag{11.19}$$

which can be solved in closed form if we take the $Y(V)$ as discussed above

$$dv \cdot (1+v)^{\beta} = \alpha \cdot dt/\tau, \tag{11.20}$$

where we reintroduce $v = V/\phi$ and define

$$\tau = \alpha \cdot \phi \cdot C/(Y_0 \cdot I_P) \quad \text{with} \quad \alpha = \frac{1}{\beta + 1}, \tag{11.21}$$

Giving

$$v(t) = -1 + \left(1 + \frac{t}{\tau}\right)^{\alpha}. \tag{11.22}$$

Equation (11.22) is used as a model to fit the data shown in Fig. 11.10d. The results of the fit are summarized in Table 11.1. The determination of the specimen capacity via (11.21) gives reasonable values. Minor variations of the obtained capacity presumably result from variations of the specimen thickness at the different sample regions where the measurements shown in Fig. 11.10d are performed. The deviations between the measured and fitted curve at $V \geq 10$ V are due to the increasing contribution of residual leakage currents (see Footnote 2). These observed deviations from a capacitive charging approximation is important, since it indicates that the beam induced potential tends to saturates at high enough potential values even for insulating samples.

The measurement of the potential-dependent sample resistance shown in Fig. 11.10b provides additional information for a semi-experimental determination of the beam induced potential via equation (11.17). We use the $R(V)$ characteristics of a TEM sample cut from the MgO catalyst support to simulate the implicit expression (11.17) for different values v and I_P. The result is shown in Fig. 11.11. The higher the primary current I_P is the higher the emission current I_{SE} and the higher the induced positive potential. The value of the steady state potential for the different parameters v and I_P are labeled with open circles.

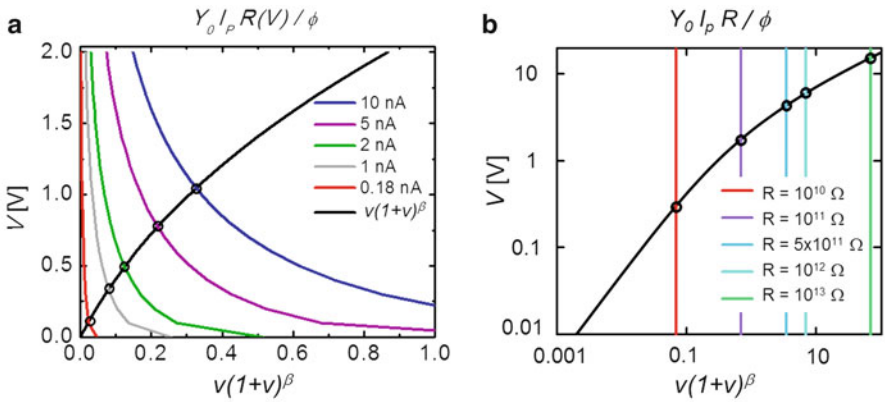

Fig. 11.11 Graphical solution of (11.17) by plotting the left side (lower axis) and the right side (upper axis) for different beam and sample parameter. (**a**) Sample potential V for the measured Frenkel–Poole like resistance of a MgO catalyst support for different primary beam currents. Limiting cases are $R(V \to 0) = 6.7 \times 10^{10}\ \Omega$ and $R(V = 10\ V) = 4 \times 10^9 \Omega$. (**b**) Sample potential V for a constant beam current of $I_P = 10$ nA, and different sample/contact resistances of ohmic type. Materials parameters are chosen for the manganite PCMO with total scattering yield of $Y_0 = 0.0034$ and work function $\phi = 4.9$ eV

We have to note here that the total resistance of a TEM lamella with respect to ground does not only depend on the specific resistance of the involved materials and the involved contact/interface resistances. There can be orders of magnitude changes due to surface defects and contamination which depend on the TEM sample preparation as well as on the sample cleaning procedure and the vacuum conditions of the ETEM. For example, from the bulk resistivity of MgO of $\rho = 10^{15}$ Ωcm (Cazaux et al. 1991) one would expect a total resistance of ~ 10^{20} Ω for a typical FIB cut TEM lamella of dimensions of 50 nm thickness, 1 μm width, and 1 mm length. Our measured resistances are in the MΩ to GΩ range and can even vary during an experiment due to change in surface contamination.

11.4.4 Measurement of Beam Induced Potentials by Off-Axis Electron Holography

Off-axis electrons holography allows for reconstruction of the phase and the amplitude of the electron wave traversing the TEM specimen, information that is lost in conventional TEM. Electric potentials V(**r**) influence the phase of the beam electron wave propagating in z direction and lead to a phase shift $\Delta\phi$ of

$$\Delta\phi(x,y) = C_{\mathrm{E}} \int_{-\infty}^{+\infty} V(x,y,z)\, dz. \tag{11.23}$$

The constant C_{E} depends on the kinetic energy of the beam electrons. For 300 keV electrons $C_{\mathrm{E}} = 6.53$ rad $\mathrm{V}^{-1}\mu\mathrm{m}^{-1}$.

The creation of a hologram is based on the separation of an electron wave into two parts via a positively charged metal wire before passing the specimen. One part of the wave passes through the sample and suffers a phase shift due to the electric field present within and around the (charged) object. The other part of the wave passes through vacuum, i.e., a region of space where, ideally, no electric fields are present. The coherent superposition of the two portions of the electron wave produces an interference pattern—the hologram. A reconstruction of the hologram via numerical methods allows the extraction of the phase shift, which enables us to estimate the potential.

Figure 11.12a shows the phase image of a PCMO ($x = 0.35$) sample region on MgO substrate during irradiation with an electron flux of 80 $\mathrm{e}^{-}/\mathrm{Å}^2\mathrm{s}$. In order to get an estimate of the surface potential we analyze the phase shift at the PCMO/vacuum interface on the vacuum side. Inside the specimen the phase shift of the beam electrons is governed by the mean inner potential arising from the magnetic properties and the charge density distribution of specimen electrons and atomic nuclei. Figure 11.12b presents the line profile of the phase shift along the blue arrow. In order to get a rough order-of-magnitude estimate of the surface potential, we assume a hemispherical specimen shape with radius R kept at a constant surface potential V_{S} with respect to a grounded plane (see Fig. 11.12a). The solution of the Laplace equation for this problem, computable analytically as a series of Legendre Polynomials, yields the electrostatic potential in the vacuum area outside the object. By integrating this potential along the beam path (z-axis), and focusing on the region just outside the object, we obtain the following approximation for the phase gradient:

$$\frac{d\Delta\phi(R)}{dx} \cong -2C_{\mathrm{E}}V_{\mathrm{S}}. \tag{11.24}$$

From Fig. 11.12b we get a phase shift gradient of $\nabla\phi = 8\,\mathrm{mrad/nm}$ at electron flux of 80 $\mathrm{e/Å}^2\mathrm{s}$ which yields an electric potential of $V \sim 0.6$ V (based on (11.24)). The phase shift gradient and accordingly the surface potential increases with increasing electron flux as shown in Fig. 11.12c.

A more sophisticated model for the determination of beam induced potentials from electron holography experiments based on more realistic approximations is given in (Mildner et al. 2015).

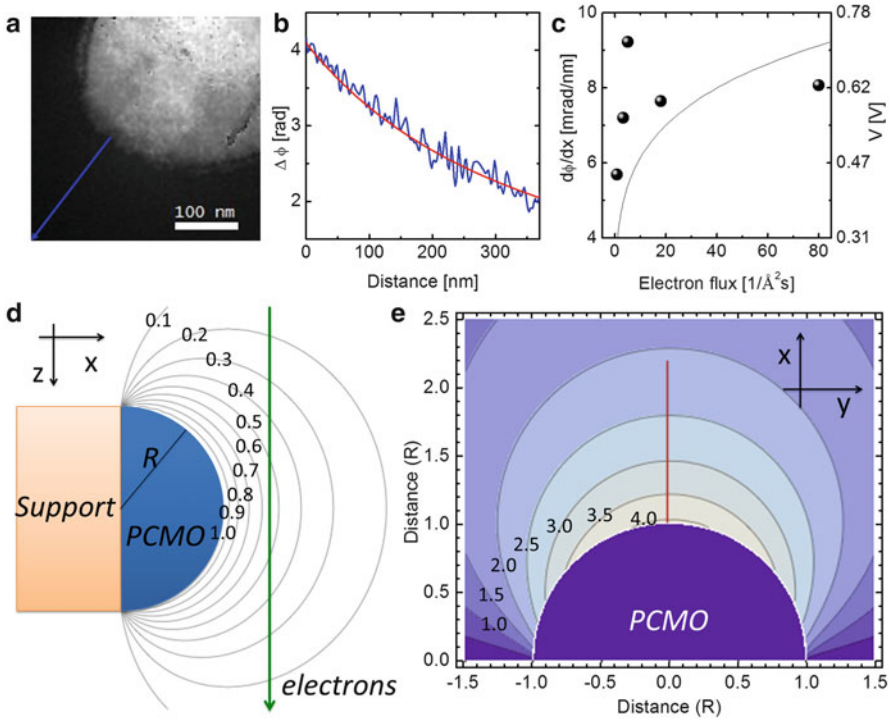

Fig. 11.12 (**a**) Phase image of a roughly semi-circular PCMO ($x = 0.35$) region. (**b**) Phase shift profile in vacuum along the blue line in (**a**). (**c**) Phase shift gradient at the PCMO/vacuum edge as a function of the primary electron flux; the thin line represents a simulation of the data based on the balance of currents (see Sect. 11.4.3 and Fig. 11.11). (**d**) Simplified geometry of the PCMO region modeled as an equipotential hemisphere generating an electrostatic potential in its surroundings (potential contours in fractions of the surface potential). (**e**) Phase shift (*contours* in rad) corresponding to the geometry in (**d**); the phase profile along the *red line* is shown as the *red curve* in (**b**)

11.5 Summary and Conclusions

We have shown that in situ TEM experiments in gas and liquid environments can give insights into many important aspects of electrode and electro-catalyst behavior during electrochemical reactions. The change in Gibbs energy of the catalyst surface in contact with gas or liquid species can give rise to the development of new states of electrochemical equilibrium with modified surface and interface atomic and electronic structure. One example is the formation of oxide nanocrystals during oxidation and reduction of an oxygen deficient amorphous region in the transition to the new electrochemical equilibrium structure in contact with water vapor.

Crucial for the understanding of electrode and catalyst behavior are studies of active states in redox experiments. The study of active states at manganite

perovskites during water splitting exhibits a reduction of the formal valence state from $Mn^{3.3+}$ to Mn^{2+} due to the formation of surface oxygen vacancies. Slowly enough evolving transient states of catalysts, electrodes and reactions zone can enable a deeper understanding of the nature of barriers. Stranski–Krastanov-like formation of metal-oxide islands on a wetting layer during oxidation of the metal and the moving interaction zone during lithiation of battery electrodes with a high density of dislocations are examples showing a rich world of structures which are not present in the initial and final state of the chemical transformation. Active sites and zones have been demonstrated in surface oxidation which nucleates at surface steps as well as at catalytic activity at crystalline edges of manganites which is absent at amorphous areas. The use of sacrificial agencies can be of high value for monitoring gas phase electrochemical reactions by the growth of a solid layer, as was demonstrated by using silane for monitoring oxygen evolution.

While such in situ experiments show fascinating atomic scale dynamics under different conditions, the realization of well-defined electrochemical studies is challenged by several effects. First of all, even below the threshold of beam damage under vacuum conditions, the electron beam induced charging of semiconducting or insulating electrodes or catalyst supports can have a strong effect on the catalyst state, since the evolving potentials easily can access values, where electrochemical reactions are possible. Consequently, the control of beam induced potentials and the application of well-defined external potentials is absolutely necessary in order to study electrochemistry under controlled conditions. An additional challenge in ETEM electrochemistry experiments is the establishment of clean chemical environments, clean sample surfaces and understanding the effects of thin TEM lamella preparation. Measurement of reaction products by mass spectrometry of the gas flowing through in the sample chamber is only possible by accumulating the small amounts of chemical reaction products over times of tenth of minutes. Whereas qualitative analysis of change of gas composition is possible, quantification of reaction products and combination to measured quantities of transferred charge seems to be far of reach at present, due to beam effects and limited measurement sensitivity for chemical species.

One of the most promising developments in ETEM electrochemistry is the application of well-defined external potential by a set of electrical sample holders. Various options have been developed in recent years which involve two-electrode geometries based on the Nanofactory STM holder as well as two and three electrode geometries which are accessible by microelectromechanical systems solutions.

Acknowledgements We are grateful for the support of Sadegh Yazdi and Takeshi Kasama from the Center for Electron Nanoscopy, Technical University of Denmark, for the acquisition of holography data presented in Fig. 11.12. Financial support is acknowledged by the DFG through the SFB1073/project C02.

References

R. Arrigo, M. Hävecker, M.E. Schuster, C. Ranjan, E. Stotz, A. Knop-Gericke, R. Schlögl, Angew. Chem. Int. Ed. **52**, 11660 (2013)
S. Blomberg, M.J. Hoffmann, J. Gustafson, N.M. Martin, V.R. Fernandes, A. Borg, Z. Liu, R. Chang, S. Matera, K. Reuter, E. Lundgren, Phys. Rev. Lett. **110**, 117601 (2013)
J. Cazaux, Ultramicroscopy **110**, 242 (2010)
J. Cazaux, K.H. Kim, O. Jbara, G. Salace, J. Appl. Phys. **70**, 960 (1991)
L.Y. Chang, A.S. Barnard, L.C. Gontard, R.E. Dunin-Borkowski, Nano Lett. **10**, 3073 (2010)
S. Chenna, P.A. Crozier, Micron **43**, 1188 (2012)
M. Chung, T. Everhart, J. Appl. Phys. **45**, 707 (1974)
J.F. Creemer, S. Helveg, P.J. Kooyman, A.M. Molenbroek, H.W. Zandbergen, P.M. Sarro, J. of Microelektromechanical Systems **19**, 254 (2010)
M. Ebner, F. Marone, M. Stampanoni, V. Wood, Science **342**, 716 (2013)
T. Grygar, J. Solid State Electrochem. **3**, 412 (1999)
P.L. Hansen, J.B. Wagner, S. Helveg, J.R. Rostrup-Nielsen, B.S. Clausen, H. Topsøe, Science **295**, 2053 (2002)
T.W. Hansen, J.B. Wagner, R.E. Dunin-Borkowski, Mater. Sci. Technol. **26**, 1338 (2010)
S. Helveg, C. López-Cartes, J. Sehested, P.L. Hansen, B.S. Clausen, J.R. Rostrup-Nielsen, F. Abild-Pedersen, J.K. Nørskov, Nature **427**, 426 (2004)
B.L. Henke, J. Liesegang, S.D. Smith, Phys. Rev. B **19**, 3004 (1979)
http://dbshino.nifs.ac.jp
J.Y. Huang, L. Zhong, C.M. Wang, J.P. Sullivan, W. Xu, L.Q. Zhang, S.X. Mao, N.S. Hudak, X.H. Liu, A. Subramanian, H. Fan, L. Qi, A. Kushima, J. Li, Science **330**, 1515 (2010)
G.J. Hutchings, A. Desmartin-Chomel, R. Olier, J.-C. Volta, Nature **368**, 41 (1994)
K.L. Kein, I.M. Anderson, N. De Jonge, J. Microsc. **242**, 117 (2011)
X.H. Liu, J.W. Wang, Y. Liu, H. Zheng, A. Kushima, S. Huang, T. Zhu, S.X. Mao, J. Li, S. Zhang, W. Lu, J.M. Tour, J.Y. Huang, Carbon **50**, 3836 (2012)
P. Meredith, A.M. Donald, B. Thiel, Scanning Vol. **18**, 467 (1996)
D. Mierwaldt, S. Mildner, R. Arrigo, A. Knop-Gericke, E. Franke, A. Blumenstein, J. Hoffmann, Jooss, Ch. Catalysts **4**, 129 (2014)
D.A. Moncrieff, V.N.E. Robinson, L.B. Harris, J. Phys. D Appl. Phys. **11**, 2315 (1978)
S. Raabe, D. Mierwaldt, J. Ciston, M. Uijttewaal, H. Stein, J. Hoffmann, Y. Zhu, P. Blöchl, C. Jooss, Adv. Func. Mat. **22**, 3378 (2012)
D.W. Reagor, S.Y. Lee, Y. Li, Q.X. Jia, J. Appl. Phys. **95**, 7971 (2004)
S. Mildner, M. Beleggia, D. Mierwaldt, T. W. Hansen, J. B. Wagner, S. Yazdi, T. Kasama, J. Ciston, Y. Zhu, C. Jooss J. Phys. Chem. C **119,** 5301 (2015).
M.P. Seah, W.A. Dench, Surf. Interface Anal. **1**, 2 (1979)
H.W. Streitwolf, Ann. Phys. (Leipz.) **458**, 183 (1959)
L. Trotochaud, S.W. Boettcher, Scr. Mater. **74**, 25 (2014)
D.G. Truhlar, B.C. Garrett, S.J. Klippenstein, J. Phys. Chem. **100**, 12771 (1996)
M. Varela, M.P. Oxley, W. Luo, J. Tao, M. Watanabe, A.R. Lupini, S.T. Pantelides, S.J. Pennycook, Phys. Rev. B **79**, 085117 (2009)
C.-M. Wang, A. Genc, H. Cheng, L. Pullan, D.R. Baer, S.M. Bruemmer, Sci. Rep. **4**, 3683 (2014)
H. Zandbergen, Microsc. Microanal. **18**, 1114 (2012)
F. Zheng, S. Alayoglu, J. Guo, V. Pushkarev, Y. Li, P.-A. Glans, J.-L. Chen, G. Somorjai, Nano Lett. **11**, 847 (2011)
L. Zhong, X.H. Liu, G.F. Wang, S.X. Mao, J.Y. Huang, PRL **106**, 248302 (2011)
L. Zhong, R.R. Mitchell, Y. Liu, M. Gallant, C.V. Thompson, J.Y. Huang, S.X. Mao, Y. Shao-Horn, Nano Lett. **13**, 2209 (2013)
G. Zhou, L. Luo, L. Li, J. Ciston, E.A. Stach, W.A. Saidi, J.C. Yang, Chem. Commun. **49**, 10862 (2013)

ERRATUM

Controlled Atmosphere Transmission Electron Microscopy

Thomas Willum Hansen and Jakob Birkedal Wagner

T.W. Hansen, J.B. Wagner (eds.), *Controlled Atmosphere Transmission Electron Microscopy*, DOI 10.1007/978-3-319-22988-1

DOI 10.1007/978-3-319-22988-1_12

Production team had inadvertently introduced the following errors in this book. These errors have now been fixed in this version.

Page	Line	Error	Corrected text
144	Line 9 from top	1 k æ1 k	1 k × 1 k
	Line 9 from top	4 k æ 4 k	4 k × 4 k
145	Figure 5.1 caption	Û	®
148	Figure 5.2 caption	Û	®
	Line 8 from bottom	4 k æ 4 k	4 k × 4 k
149	Equation 5.2	ì	×
150	Equation 5.5	ì	×
	Line 2 from bottom	>3æ	>3×
151	Line 3 from bottom	2æ	2×
152	Line 10 from top	4 k æ 4 k	4 k × 4 k
155	Line 10 from bottom	1 k æ1 k	1 k × 1 k
157	Figure 5.6 caption	1.3 æ 10	1.3 × 10
	Figure 5.6 caption	590 -	590 °

(continued)

The online version of the original book can be found at http://dx.doi.org/10.1007/978-3-319-22988-1

T.W. Hansen, J.B. Wagner (eds.), *Controlled Atmosphere Transmission Electron Microscopy*, DOI 10.1007/978-3-319-22988-1_12

Page	Line	Error	Corrected text
160	Line 4 from top	4 k æ 4 k	4 k × 4 k
160	Line 4 from top	æ2	×2
	Figure 5.8 caption	217 -	217 °
	Line 10 from top	90-	90°
	Line 11 from top	217 -	217 °
162	Line 13 from bottom	5æ	5×
179	Figure 6.11 caption	(a) 6 20, (b) 6 10, and (c) 35 μm	(a) 6 × 20, (b) 6 × 10, and (c) 3 × 5 μm
180	Table 6.3, row 3	35, 6 10, 6 20,	3 × 5, 6 × 10, 6 × 20,
	Last line from bottom	0.5 0.5 mm^2, 0.2 2 mm^2, 0.9 9 mm^2	0.5 × 0.5 mm^2, 0.2 × 2 mm^2, 0.9 × 9 mm^2
198	Line 12 from top	4 k 4 k	4 k × 4 k
205	Line 3 from bottom	15 μm 5 μm100 nm	15 μm × 5 μm × 100 nm